Advances in Materials Science and Engineering

Rock Unloading Failure Characteristics and Acoustic Emission Precursors

Lead Guest Editor: Depeng Ma
Guest Editors: Qing Ma, Huiqiang Duan, and Xuezhen Wu

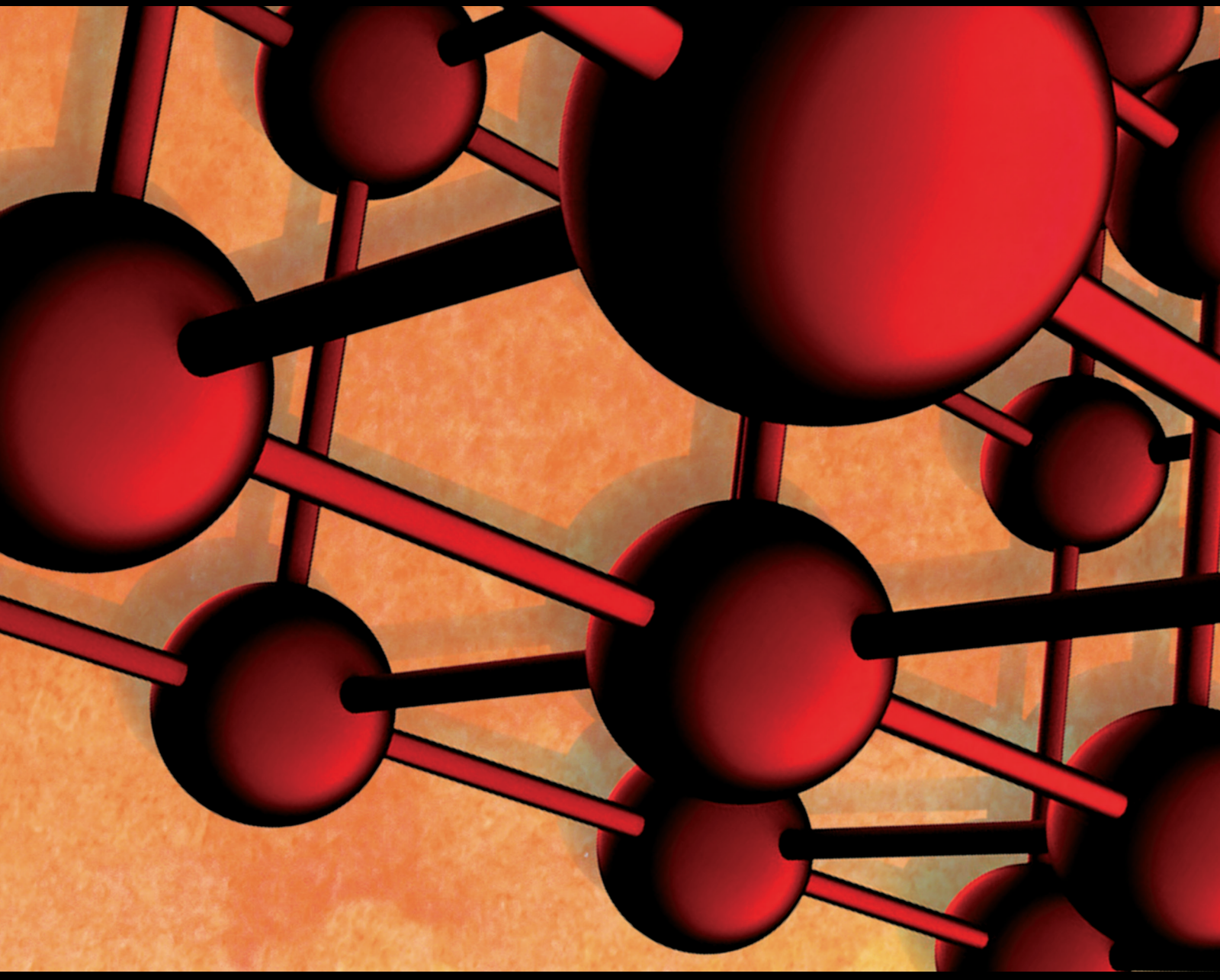

Rock Unloading Failure Characteristics and Acoustic Emission Precursors

Advances in Materials Science and Engineering

Rock Unloading Failure Characteristics and Acoustic Emission Precursors

Lead Guest Editor: Depeng Ma
Guest Editors: Qing Ma, Huiqiang Duan, and Xuezhen Wu

Contents

Contents

Hindawi
Advances in Materials Science and Engineering
Volume 2023, Article ID 8790995, 9 pages
https://doi.org/10.1155/2023/8790995

Research Article

Numerical Simulation of Acoustic Emission Events in Supporting Roadways under Different Dynamic Loads

Wenzheng Shang,[1] **Zhigang Liu**,[1,2,3] **Jianbo Yuan**,[1] **Wuchao You**,[4] **Shuai Han**,[4] **Lei Yu**,[4] **and Shihua Zhang**[3]

[1]*Institute of Mining Engineering, Shandong University of Science and Technology, Tai'an 271019, China*
[2]*Shandong Energy Group, Jinan 250013, China*
[3]*A Key Laboratory of Deep Coal Resource Mining, School of Mines, Ministry of Education of China, China University of Mining and Technology, Xuzhou 221116, China*
[4]*Shandong Jingtai Engineering Technology Co., Ltd., Zibo 255425, China*

Correspondence should be addressed to Zhigang Liu; 15865721818@163.com

Received 1 September 2022; Accepted 8 December 2023; Published 18 December 2023

Academic Editor: Tomasz Trzepieciński

This paper studies the distribution characteristics of acoustic emission (AE) events in supporting roadways under different dynamic load conditions through numerical simulation and theoretical analysis. According to the principle of AE numerical simulation, the roadway model is established by FLAC3D software, and the supporting structure of the bolt cable is established by editing the Fish function. According to the model dynamic load application criterion, the relationship between the peak velocity of the particle, the distance from the source center to the dynamic impact damage point, and the dynamic load intensity is introduced. The velocity-distance-energy relationship is deduced from the relationship to determine the magnitude of the dynamic load energy. The simulation results show that the intensity of the dynamic load source and the distance of the dynamic load source directly impact the AE events. The larger the dynamic load intensity and the closer to the dynamic load source, the more concentrated the AE events. The roadway has a blocking effect on the transmission of the dynamic load stress waves. According to this characteristic, the roadway can be protected by a high-pressure relief roadway. Rock lithology greatly influences the transmission of dynamic load stress waves and the number of AE events. When the dynamic load stress wave passes through the rock strata of different lithologies, the attenuation of the dynamic load energy and the number of AE events are large. However, when the dynamic load stress wave passes through the rock strata of the same lithology, the attenuation of the dynamic load energy and AE events is small. The surrounding rock structure in the bottom corner area of the roadway is susceptible to disturbance from dynamic load sources above the roadway. The results are greatly significant for studying the AE characteristics of support roadways with disturbance-typeimpact failure.

1. Introduction

With the deepening of coal mining, rock burst [1, 2] disasters have become increasingly serious, which seriously restricts the safe mining of coal. Due to the complexity of rock burst disaster-causing factors and the uncertainty of time and space, the current stage of rock burst research work cannot completely prevent or warn against disasters. As the last line of defense for the prevention and control of rock bursts, the support is affected by three highs and one disturbance effect [3–5]. Several dynamic stress phenomena in the mining process are likely to become factors of fracture and instability of the surrounding rock in the supporting roadway. Therefore, the support roadway faces new challenges. The disturbance-type shock failure of the roadway surrounding the rock source [6] has a great influence on roadway support design. The impact failure type of the source disturbance is accompanied by the transfer of energy, and the energy transmitted to the roadway in the form of waves damages the rocks around the roadway and along the energy propagation

path, resulting in rock fracture. The fracture damage of the rock releases elastic energy, resulting in acoustic emission (AE) events. Using AE detection technology [7, 8] and numerical simulation software to study the fracture characteristics of rock with source disturbance impact damage is of great significance for roadway support design.

For a long time, scholars worldwide have conducted several studies on applying AE-monitoring technology in coal mining. Based on the laboratory simulation test, Lin et al. [1] used the impact loading device to conduct loading and unloading tests on the surrounding rock model under four different stress gradients. By capturing the AE energy events of loading and unloading specimens and infrared monitoring anomalies, the energy evolution characteristics of the model during the entire loading process were quantitatively analyzed. Li et al. [9] conducted hydraulic fracturing (HF) tests under true triaxial stress on three-dimensional coal samples in the laboratory and studied the time variation of injection pressure curves and AE waveform parameters at different stages through AE-monitoring technology. The results showed that the characteristics of the AE waveform parameters well reflect the growth behavior of coal HF. Zhili et al. [10] studied the AE, energy, and damage evolution of coal samples under three uniaxial cyclic loading and unloading conditions. Based on the Brazilian-splitting test and uniaxial and triaxial compression tests, Su et al. [11] and Yang et al. [12], respectively, studied the evolution of rock failure and AE characteristics under different loading rates, which further deepened the understanding of rock failure process and provided theoretical support for rock stability analysis in mining design and construction. Using laboratory test methods, Xue et al. [13] utilized a high-accuracy automatic testing machine with a controllable loading rate and an AE experimental system to detect and locate stratal instability in the laboratory. The results show that the greater the energy released by the AE signal, the more prone to rock burst. In the numerical simulation of AE, Lv et al. [14] used RFPA2D software to study the compressive strength, crack generation and propagation, and failure mode of coal with combined defects. According to the distribution characteristics of the AE energy of combined coal simulated by RFPA2D software, the failure process of coal with combined defects was analyzed. Based on the cohesive zone model in ABAQUS, Meng et al. [15] studied the influence of bedding plane properties on rock strength, fracture, and AE characteristics.

Most of the above scholars' research contents are based on AE technology to study the damage evolution law of rock. However, there are few AE simulation studies on the surrounding coal mine rock-supporting roadways under dynamic load. Therefore, based on FLAC3D numerical simulation [16–18] software, this study uses numerical simulation and theoretical analyses to study the AE characteristics of the surrounding rock of supporting roadways under dynamic load. Under dynamic loads, the surrounding rock of roadways is often in an unstable state of repeated loading and unloading, and the process of fracture, expansion, and fracture occurs inside. In this process, the rock produces an AE phenomenon. By detecting the AE phenomenon inside the rock, the unloading failure of the rock can be observed and predicted, which is greatly significant for roadway support design.

2. Numerical Simulation Scheme Design of AE in Supporting Roadways under Different Dynamic Loads

2.1. Numerical Simulation Principle of AE. AE is a phenomenon in that the internal structure of the local part of the rock material is changed under the action of external, which causes the stress redistribution in the rock material, releases energy, and produces transient elastic waves. Its energy conversion is from mechanical energy to acoustic energy. AE is closely related to the generation of cracks in rocks. The expansion and closure of cracks in rocks produce the AE. FLAC3D numerical simulation software has significant advantages in simulating the mechanical properties of a rock mass. By constructing the model, the constitutive relationship is given to the model so that the model has the mechanical properties of rock. The model causes the fracture of the model unit under the condition of applying an external load, and the model unit releases elastic energy during fracture. In FLAC3D numerical simulation, the function is introduced into the calculation model by Fish language, and the strain energy of the unit is calculated in each operation. The rupture of each model unit releases energy to produce an AE event. In the record of AE events, the history command provided by FLAC3D numerical simulation software creates sampling record variables to sample and store the target object.

2.2. Model Unit Rupture Event Judgment Basis. During the numerical simulation, the generation of AE events is related to whether the elastic energy stored in the model unit is released. Therefore, the elastic energy stored in the model unit is calculated by the following equation:

$$W = \frac{1}{2E}\left[\sigma_1^2 + \sigma_2^2 + \sigma_3^2 - 2\mu\left(\sigma_1\sigma_2 + \sigma_1\sigma_3 + \sigma_2\sigma_3\right)\right], \quad (1)$$

where E is the elastic modulus of the medium, μ is the Poisson's ratio of the medium, and σ_1, σ_2, and σ_3 are the maximum, intermediate, and minimum principal stresses applied by the model, respectively.

In the process of model calculation under dynamic load, the elastic energy in the model unit changes continuously with the calculation time step. As shown in equation (2), if the calculated energy density difference is positive, it represents the energy storage. If it is negative, it represents the energy release of the model unit. At this time, the energy release state of the model unit is recorded as an AE event.

$$\Delta U_e = U_e - U_e', \quad (2)$$

where U_e is the elastic energy of the existing state of the model unit and U_e' is the elastic energy of the previous state of the model unit.

2.3. Simulation Program. The numerical model herein is based on the actual conditions of the Xinjulong Coal Mine. The study aims to investigate the deformation of the roadway and fracture of the rock mass around the roadway under different dynamic loads applied to different positions of the arched roadway under supporting measures and its AE characteristics. The arch tunnel model is established by FLAC3D numerical simulation software, and the Mohr–Coulomb constitutive model is provided. The Fish language is compiled to add a bolt-cable support structure to the roadway model (Figure 1). To study the deformation of the supporting roadway and the fractured state of the rock around the roadway under different dynamic loading conditions, the dynamic loads with the energy values of 1×10^3, 1×10^4, 1×10^5, and 1×10^6 J are applied at different positions of the model end face. As for the location selection of the dynamic load, the above, upper left 45°, and horizontal directions of the model are selected, and a 10×10 m dynamic load is applied in the middle of the model at the above position (Figure 2).

Observing the AE phenomenon within the rock around the roadway by numerical simulation and predicting the deformation of the roadway surrounding rock have certain practical significance in studying the roadway support and controlling the deformation of the surrounding rock.

3. Model Establishment, Parameter Selection, and Dynamic Load Application Criteria

3.1. Establishment of Numerical Model. Herein, FLAC3D numerical simulation software is selected to establish an arch roadway model with a model size of $50\,\text{m} \times 50\,\text{m} \times 50\,\text{m}$. The boundary of both sides of the model is set as a horizontal simple support constraint, and the horizontal displacement of the boundary on both sides is fixed. The lower boundary is set as a fixed support constraint to fix its horizontal and vertical displacements, and the upper boundary applies a uniform load according to the buried depth condition. The model grid is divided by the embedded cylindrical and rectangular roadway radial gradient rectangular grids. Two problems are studied herein. One is the influence of the dynamic load energy at different sizes on the AE characteristics of the supporting roadway model. The second is the influence of the dynamic load energy at different positions on the AE characteristics of the model.

3.2. Parameter Analysis. After dividing the grid unit, the FLAC3D model can provide different lithological mechanical characteristics of the unit. According to the actual geological conditions and lithology borehole histogram, the model is given siltstone and fine sandstone from top to bottom (Figure 3). The mechanical parameters of rock mass are presented in Table 1.

3.3. Dynamic Load Application Criterion. The magnitude of the dynamic load applied in the model is determined according to the relationship proposed by A. McGarr [19] between the peak particle velocity, the distance R from the source center to the dynamic impact damage point, and the rockburst intensity.

$$\lg(\text{Rv}) = 3.95 + 0.57M_L, \tag{3}$$

$$\lg E_L = 1.8 + 1.9M_L, \tag{4}$$

where R is the distance from the dynamic load location to the monitoring point (unit: cm) and V is the peak velocity of the surrounding rock vibrating particle detected by the monitoring point (unit: cm/s). The unit of Rv is cm^2/s, E_L is the unit of energy size J, and M_L is the magnitude.

According to equations (3) and (4), it is deduced that

$$v = \frac{10^{3.41+\lg E_L}}{R}. \tag{5}$$

In FLAC3D, the dynamic load is applied to the model by calling the Fish function, and the dynamic load arrangement of the interface source is used to apply the dynamic load with an area of $10\,\text{m} \times 10\,\text{m}$ on the end face of the model. To facilitate the analysis, the dynamic load stress wave is simplified as a section of the cosine wave harmonics. According to the different distances and positions of the source, it is applied to the roadway model, and the vibration period is 0.1 s. To ensure that the energy of the applied dynamic load is within the scope of the scheme design, the relationship between the velocity, distance, and energy of equation (5) is used to achieve different source strength characteristics by setting different source velocities $V_{\max}$. To ensure that the applied dynamic load is within the scope of the design scheme, the survey line is set on the roadway surface, and the velocity of the source stress wave reaching the surface of the roadway is measured to determine the size of the applied dynamic load. The measuring line arrangement is shown in Figure 4. The corresponding relationship between the parameters taken by different intensity dynamic loads and the source distance is shown in Table 2.

4. Simulation Result Analysis

4.1. Application of Dynamic Load Directly above the Model. As shown in Figure 5, when the dynamic load is applied above the end face of the model, the dynamic load of 1×10^4, 1×10^5, and 1×10^6 J is applied, respectively, and the AE distribution map under the three conditions is obtained. According to the AE distribution map, the following analysis is conducted.

As shown in Figure 5(a), when a dynamic load with the energy of 1×10^4 J is applied directly above the model, several four-party AE events are gathered on the end face directly above the model. From the distribution of the AE events, the energy of the dynamic load is transferred from the upper direction of the model to the surrounding roadway. As the dynamic load energy is transmitted in the form of waves, the energy passes through the rock strata of different lithologies in the transfer process, and the energy is attenuated. When the fourth power energy is transferred to the roadway, the energy has been attenuated to the third power energy, so there are few fourth power energy events around the roadway. From the 3D

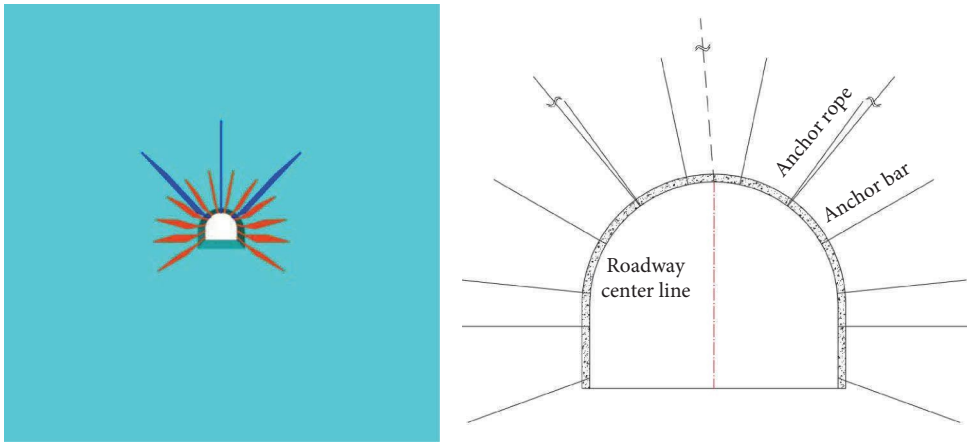

Figure 1: Numerical simulation model diagram of roadway support.

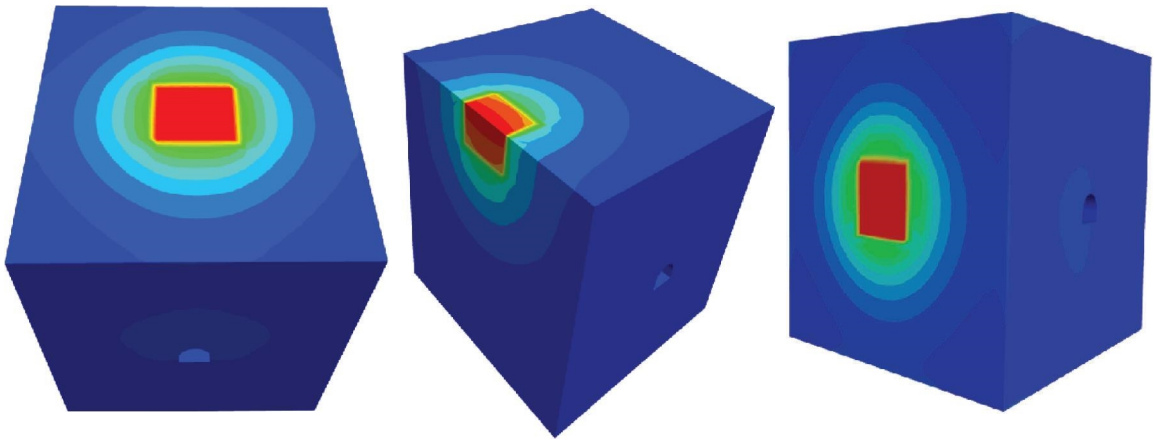

Figure 2: Numerical simulation diagram of dynamic load application position.

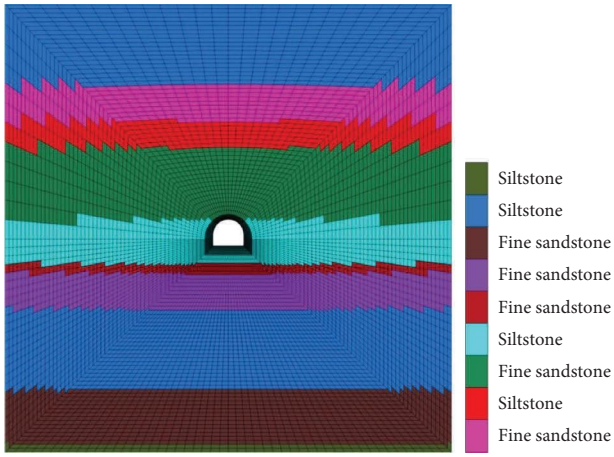

Figure 3: Model layer lithology diagram.

Table 1: Mechanical parameters of rock mass.

	Density ($kg{\cdot}m^{-3}$)	Bulk modulus (GPa)	Shear modulus (GPa)	Angle of internal friction (°)	Tensile strength (MPa)
Siltstone	2.75	8.10	4.84	35.7	3.41
Fine sandstone	2.7	7.87	3.38	38.8	5.79

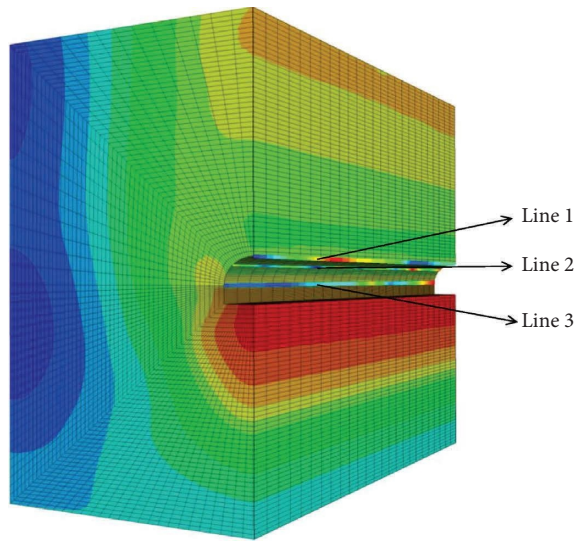

Figure 4: Line layout diagram.

Table 2: Dynamic load intensity and source distance parameters.

Energy of source	Hypocentral distance (m)	Line monitoring peak velocity (v_{max}, unity: m·s^{-1})
1×10^3–1×10^4 J	23.45	0.17
	33.49	0.12
	22.35	0.18
1×10^4–1×10^5 J	23.45	0.35
	33.49	0.24
	22.35	0.36
1×10^4–1×10^5 J	23.45	0.69
	33.49	0.48
	22.35	0.73

distribution state of the AE events, the number of AE events in the middle of the roadway is relatively denser than at both ends of the roadway because the dynamic load is applied directly above the middle of the roadway. Due to the barrier effect of the roadway on the dynamic load stress waves, the AE events near the roadway floor are few, but the AE events at the roadway bottom angle are many, and the energy of the AE events is less than the fourth power. Therefore, the tunnel bottom angle support should be strengthened in engineering construction.

Figure 5(c) shows the case where a dynamic load with the energy of 1×10^5 J is applied above the model. As the applied dynamic load energy increases, the number of AE events significantly increases. During the dynamic load energy transfer process, the fifth power dynamic load energy also decayed, and from the AE event distribution state, the fifth power energy events were mainly distributed above the model, which was the same as the case of applying the fourth power dynamic load energy. According to the 3D distribution state of the AE events, the AE events with the third power energy are mainly distributed around the roadway, and the distribution state of the AE energy in the middle of the roadway and near the floor is similar to the case when the fourth power dynamic load is applied.

Figure 5(c) shows the case where a dynamic load with the energy of 1×10^6 J is applied above the model. The transfer path of the dynamic load energy is the same as that of the fourth and fifth power dynamic load energy. However, on the transfer path of the dynamic load energy, most of the AE events on the transfer path with the sixth power dynamic load energy are the fifth power energy. From the 3D distribution state of the AE events, several AE events with the fifth and fourth power energies appear around the roadway, indicating that under the dynamic load disturbance of the sixth power energy, the model elements around the roadway release elastic strain energy greater than the fourth power energy. The AE event distribution in the bottom angle area of the roadway is similar to the dynamic load with the fourth and fifth power energy, but the AE of the model with the dynamic load with the sixth power energy exceeds the third power energy, which is related to the dynamic load energy applied by the model.

4.2. Dynamic Load Applied 45° from Top Left of Model. As shown in Figure 6, in the upper left of the model end face 45° direction were applied to 1×10^4 J, 1×10^5 J, and 1×10^6 J dynamic load case, the propagation path of the dynamic

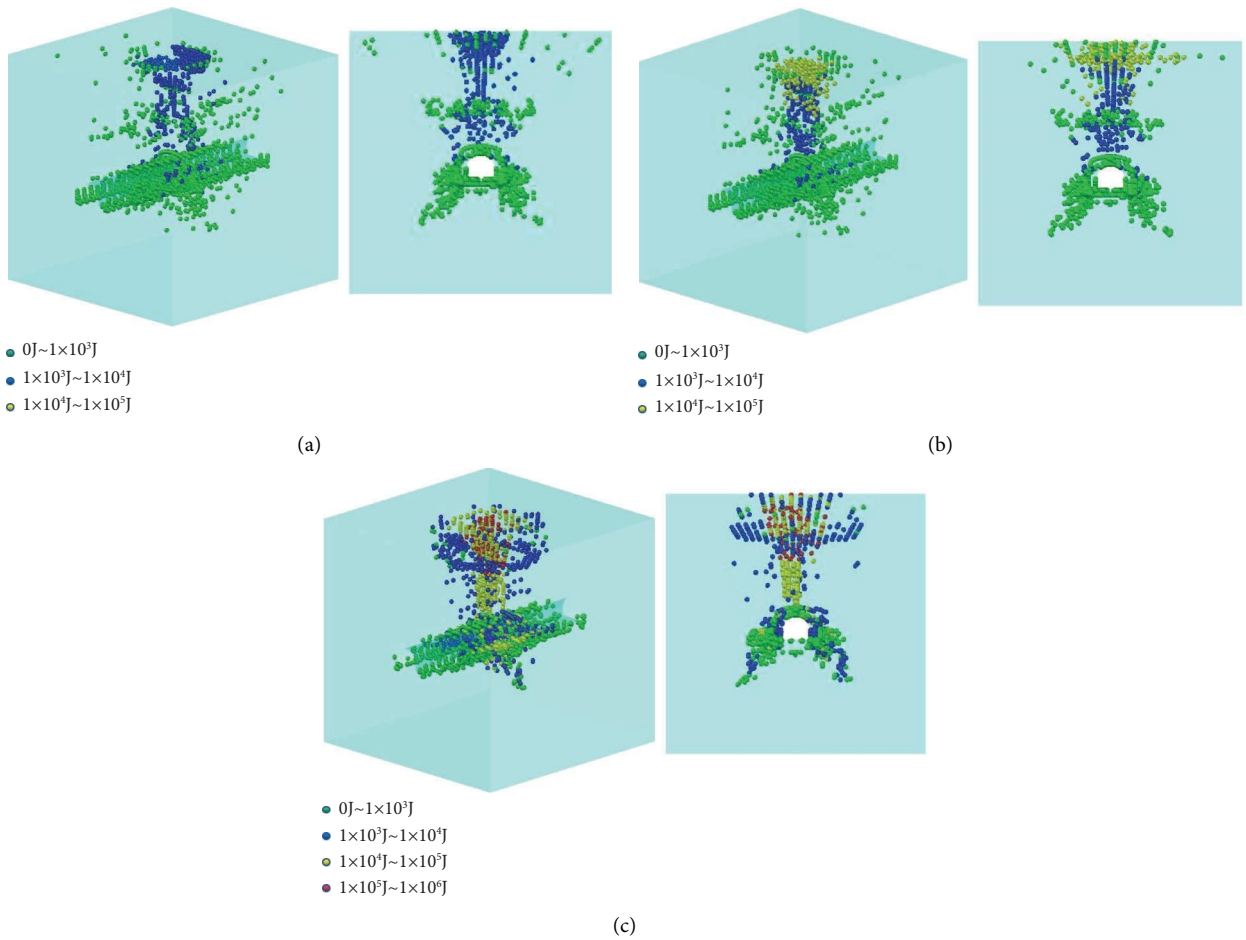

Figure 5: Distribution state diagram of acoustic emission right above the model. (a) State distribution diagram of four-power dynamic load energy acoustic emission. (b) State distribution diagram of five-power dynamic load energy acoustic emission. (c) State distribution diagram of six-power dynamic load energy acoustic emission.

stress wave is almost the same. However, the dynamic load of different energies induced by distributing the AE events is very different.

As shown in Figure 6(a), when a dynamic load energy of 1×10^4 J is applied at 45° above the left of the model, several four-power energy events appear near the dynamic load source and propagate down to the surface of the tunnel, indicating that a large amount of elastic strain energy stored inside the model element is released under the applied dynamic load disturbance. During the energy transfer, the energy is greatly attenuated by the influence of the distance and model layer, which is similar to the case of applying the dynamic load directly above the model. From the perspective of the AE distribution, the roadway is surrounded by many AE events of cubic energy. The number of AE events in the middle of the roadway greatly exceeds that at both ends of the roadway because the dynamic load position is projected in the middle of the roadway, and the distance from both ends of the roadway to the dynamic load source is farther.

As shown in Figure 6(b), when a dynamic load energy of 1×10^5 J is applied at 45° above the left of the model, the dynamic load source area mostly reaches the fifth power energy. However, compared with the AE events of the fourth power, the AE events of the fifth power are still relatively few, indicating that the dynamic load energy of the fifth power does not induce most of the AE events of the fifth power. In the energy transfer path, the most distribution is the fourth power energy of the AE events, and the energy transfer process also occurred in the inevitable attenuation. From the distribution of the AE events, there are four square energy AE events around the roadway, which shows that the dynamic load of the five square energy makes the model unit around the roadway break, thus inducing the model unit to release four square elastic strain energy.

As shown in Figure 6(c), the dynamic load energy of 1×10^6 J is applied at 45° above the left side of the model. As the applied dynamic load energy increases, the energy of the AE event in the dynamic load source area reaches the energy of the sixth power. There are many AE events with more than the fourth power energy on the energy transfer path, indicating that the dynamic load of the sixth power energy induces a larger range of small energy AE events. The several fourth power energy AE events also appeared on the surface of the tunnel, indicating that the greater the applied dynamic load energy, the more the energy that can induce AE events will also increase.

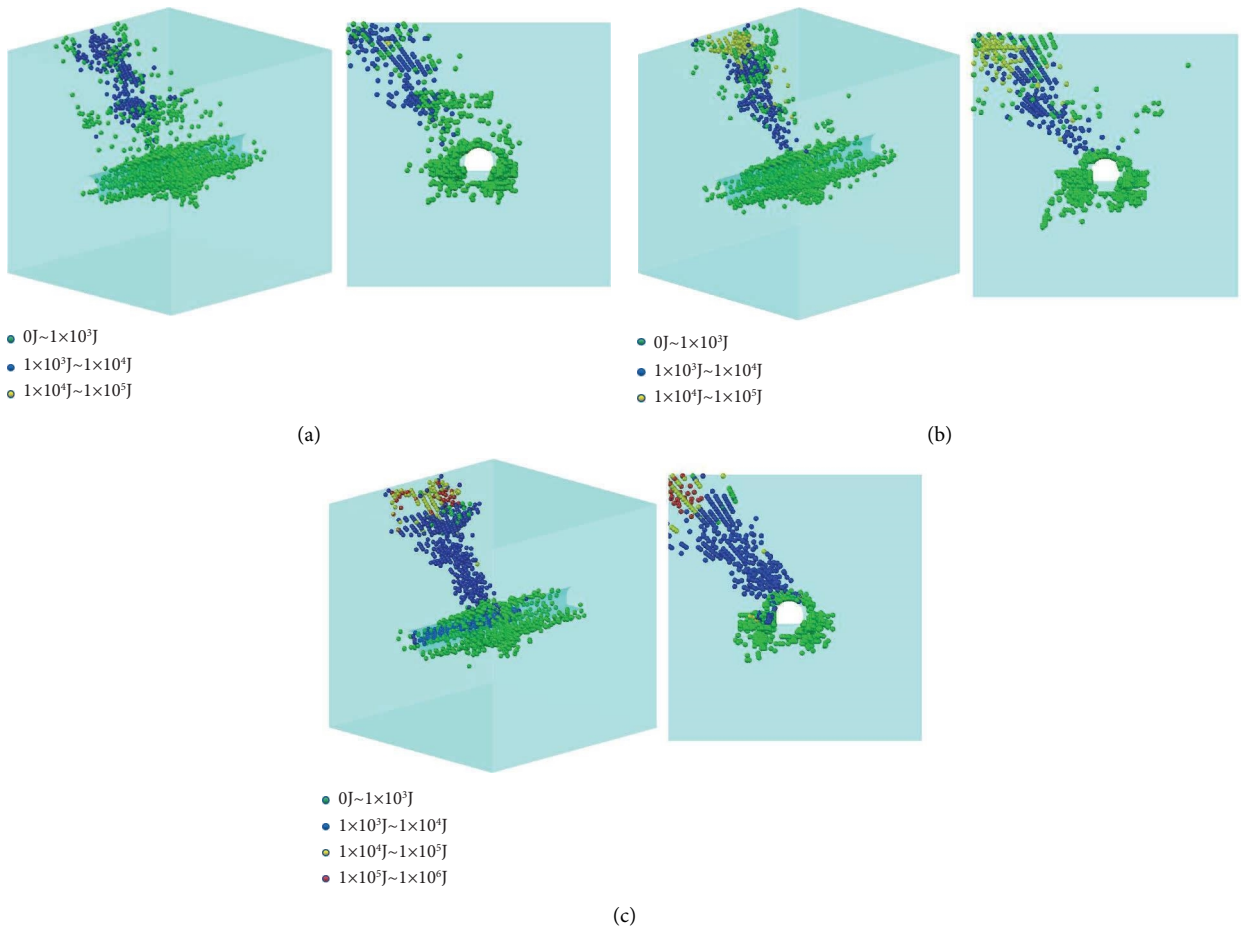

Figure 6: Distribution state diagram of acoustic emission at 45° upper left of the model. (a) State distribution diagram of four-power dynamic load energy acoustic emission. (b) State distribution diagram of five-power dynamic load energy acoustic emission. (c) State distribution diagram of six-power dynamic load energy acoustic emission.

4.3. Model Applying Dynamic Load Horizontally. As shown in Figure 7, when the dynamic loads of 1×10^4, 1×10^5, and 1×10^6 J are applied in the horizontal direction of the model, according to the distribution state diagram of the AE events, the transmission path of the dynamic load stress wave is transmitted from the horizontal direction to the roadway. In addition, because the dynamic load stress wave is transmitted in the same layer during transmission, the propagation of the dynamic load energy is less affected by the lithology of the rock layer.

As shown in Figure 7(a), when the applied dynamic load is the fourth power, the AE events on the dynamic stress wave transmission path are mainly the fourth power, but there are some AE events with energy exceeding the fourth power. This may be because the rock on the dynamic stress wave propagation path breaks under the action of the dynamic-static load coupling, thereby releasing energy to produce AE events with energy exceeding the fourth power. Around the roadway, the AE events are mainly dominated by three square energy events, and the AE events of the fourth power energy are mainly distributed in the middle of the roadway. At both ends of the roadway, the number of AE events is small.

As shown in Figure 7(b), when the applied dynamic load is the fifth power, the AE events on the stress wave transmission path of the dynamic load are mainly the fifth power dynamic load energy. The model unit is subjected to the dynamic–static load coupling. Like the application of the fourth power dynamic load energy, the model applying the fifth power dynamic load energy also has AE events that exceed the fifth power energy on the dynamic load stress wave propagation path. The AE events gathered in the middle of the roadway are mainly the dynamic load energy of the fourth and fifth powers. The number of AE events at both ends of the roadway is small, most of which are the dynamic load energy of the third power.

As shown in Figure 7(c), when the applied dynamic load is the sixth power, the AE events on the transmission path of the dynamic load stress wave are mainly the sixth power dynamic load energy, and the AE events in the middle of the roadway are mainly the fourth and fifth power dynamic load energy. The number of AE events at both ends of the roadway is similar to that of the model that applied the fourth and fifth power dynamic loads.

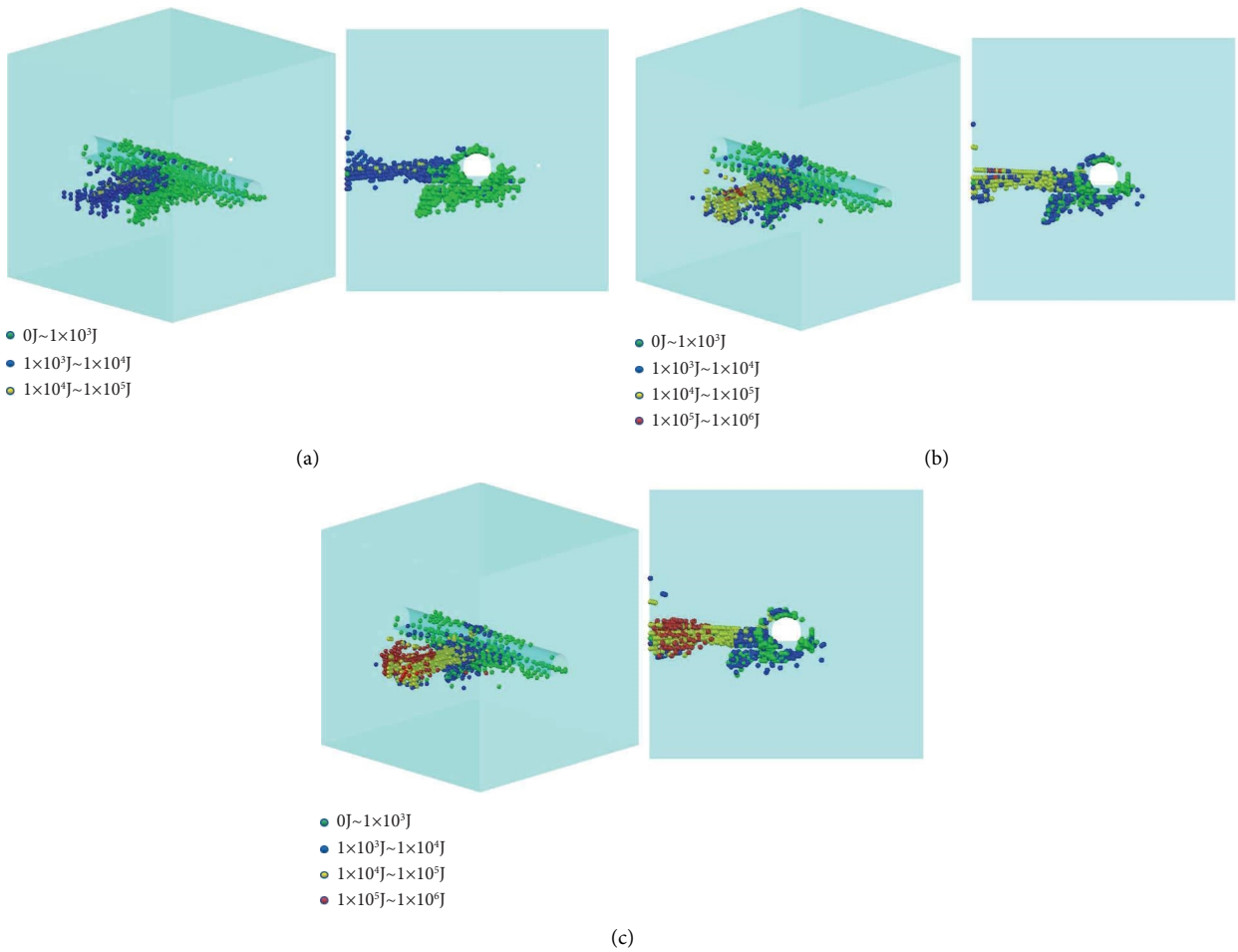

Figure 7: Distribution state diagram of horizontal acoustic emission of the model. (a) State distribution diagram of four-power dynamic load energy acoustic emission. (b) State distribution diagram of five-power dynamic load energy acoustic emission. (c) State distribution diagram of six-power dynamic load energy acoustic emission.

5. Conclusion

Through numerical simulation, this paper explores the AE characteristics of supporting roadways when different dynamic load energy values are applied at different positions. According to the theoretical analysis, the following conclusions are drawn:

(1) The strength and distance of the dynamic load source directly impact the AE events. When the dynamic load energy is applied to the end face of the model, the AE energy events near the source location are larger, and the AE events are denser. However, in the propagation path of the dynamic stress wave to the roadway because the dynamic stress wave passes through the rock strata of different lithologies during transmission, the energy attenuates during propagation. Therefore, the AE events near and around the roadway are mainly small energy, and the AE events in the middle of the roadway are denser than those at both ends of the roadway.

(2) When the dynamic stress wave propagates in the rock strata of the same lithology, the energy attenuation of the AE event is smaller than that in the rock strata of different lithologies, and the AE event is more concentrated.

(3) The roadway has a barrier effect on the dynamic load stress wave. According to the 3D distribution state diagram of the AE, when the dynamic load stress wave passes through the roadway, the number of AE events on the other side of the roadway decreases sharply, especially when the dynamic load is applied directly above the model and 45° on the left. According to this phenomenon, roadways are arranged in mines prone to mine earthquakes, and high-level measure roadways can be constructed above the roadways to protect the roadways.

(4) The dynamic load source above the roadway induces the deformation and failure of the bottom angle of the roadway, resulting in the instability of the surrounding rock structure of the roadway.

Therefore, the bottom angle support of the roadway should be strengthened in the process of roadway support.

Data Availability

The data in the manuscript were obtained by experiments and were effectively collected and correctly presented. Data used to support the findings of this study are included in the article.

Conflicts of Interest

The authors declare that they have no conflicts of interest.

Authors' Contributions

The work presented herein was carried out in collaboration between all the authors. Zhigang Liu and Wenzheng Shang proposed the innovative points and wrote the paper. Wenzheng Shang and Wuchao You carried out numerical simulation tests. Jianbo Yuan, Lei Yu, and Shihua Zhang contributed to the design. Shang Wenzheng and Han Shuai contributed to the writing.

References

[1] M. Lin, C. Gao, Y. Xia, D. Zhang, X. Liu, and X. Liang, "Rock burst initiation and precursors in a model specimen based on acoustic emission and infrared monitoring," *Arabian Journal of Geosciences*, vol. 15, no. 4, 2022.

[2] Y. Chen, J. Zhang, J. Chen, and X. Deng, "Special issue: rock burst disasters in coal mines," *Energies*, vol. 15, p. 4846, 2022.

[3] M. Xu, K. Li, and Y. Xu, "Partitioning control mechanism and engineering practice of rebuilding bearing arch in surrounding rock under high ground stress," *Advances in Civil Engineering*, vol. 2021, Article ID 6667182, 9 pages, 2021.

[4] C. Yuan, W. Wang, and C. Huang, "A study on the mechanism and controlling techniques of roadway deformations under high in situ stress conditions," *Geotechnical and Geological Engineering*, vol. 38, no. 1, pp. 605–620, 2020.

[5] R. Peng, R. Xue, H. Sun, and H. Zhou, "Characteristics of strong disturbance to rock mass in deep mining," *Journal of China Coal Society*, vol. 44, no. 5, pp. 1359–1368, 2019.

[6] M. S. Gao, Y. C. Zhao, Y. Y. Wen, Z. C. Cheng, and X. C. Quan, "Stress and energy criterion of the roadway destruction subjected to disturbance type rock burst and its practice," *Meitan Xuebao/Journal of the China Coal Society*, vol. 41, no. 4, pp. 808–814, 2016.

[7] K. Du, X. Li, M. Tao, and S. Wang, "Experimental study on acoustic emission (AE) characteristics and crack classification during rock fracture in several basic lab tests," *International Journal of Rock Mechanics and Mining Sciences*, vol. 133, Article ID 104411, 2020.

[8] T. Jie, S. Zhaoyang, W. Zaihai, and N. Fangbo, "Experimental study on acoustic emission frequency characteristics of granite under different cyclic loading and unloading," *IOP Conference Series: Earth and Environmental Science*, vol. 619, Article ID 012018, 2020.

[9] N. Li, L. Fang, B. Huang et al., "Characteristics of acoustic emission waveforms induced by hydraulic fracturing of coal under true triaxial stress in a laboratory-scale experiment," *Minerals*, vol. 12, p. 104, 2022.

[10] S. Zhili, J. Shengguo, X. Wenbing, and T. Qingteng, "Research on coal acoustic emission characteristics and damage evolution during cyclic loading," *Frontiers in Earth Science*, vol. 10, 2022.

[11] X. Su, H. Ji, D. Quan, T. Zhang, Z. Zhang, and J. Li, "Evolution of the circumferential axial strain ratio and acoustic emission response of loaded rocks," *Arabian Journal of Geosciences*, vol. 15, no. 3, 2022.

[12] J. Yang, K. Zhao, Y. Song et al., "Acoustic emission characteristics and fractal evolution of rock splitting and failure processes under different loading rates," *Arabian Journal of Geosciences*, vol. 15, no. 3, 2022.

[13] J. Xue, Z. Chen, Y. Li, J. Wang, and X. Li, "Failure characteristics of coal-rock combined bodies based on acoustic emission signals," *Arabian Journal of Geosciences*, vol. 15, no. 2, 2022.

[14] H. Lv, Z. Cheng, Y. Dong, J. Zhang, and Y. Ma, "Numerical simulation on the crack initiation and propagation of coal with combined defects," *Structural Engineering and Mechanics, An International Journal*, vol. 79, no. 2, pp. 237–245, 2021.

[15] Y. Meng, H. Jing, X. Liu, Q. Yin, and X. Wei, "Experimental and numerical investigation on the effects of bedding plane properties on the mechanical and acoustic emission characteristics of sandy mudstone," *Engineering Fracture Mechanics*, vol. 245, Article ID 107582, 2021.

[16] X. Li, H. Li, Z. Yang, X. Wang, and W. He, "Numerical simulation case study by using FLAC-3D of the composite coal-rock on the load-free fracture," *Journal of Safety and Environment*, vol. 20, no. 6, pp. 2187–2195, 2020.

[17] D. Xia, K. Leng, Z. Zhang, and Y. Hou, "Research on surrounding rock stability and layout scheme of soft rock roadway based on FLAC3D," *Ming Research and Development*, vol. 40, no. 12, pp. 92–99, 2020.

[18] G. J. Liu, S. L. Li, Z. L. Mu et al., "Numerical study on the impact instability characteristics induced by mine earthquake and the support scheme of roadway," *Shock and Vibration*, vol. 2021, Article ID 7697905, 16 pages, 2021.

[19] G. F. Wang, L. M. Dou, Z. L. Li, S. Gong, J. He, and W. Cai, "Anti-impact abilities calculation and feasibility analysis of seismic reverse for supporting," *Chinese Journal of Rock Mechanics and Engineering*, vol. 34, pp. 4125–4131, 2015.

Hindawi
Advances in Materials Science and Engineering
Volume 2023, Article ID 9508173, 17 pages
https://doi.org/10.1155/2023/9508173

Research Article

Mechanical Properties of Deep Variable Dip Joint Rock Mass in Reservoir Area under Wet and Dry Conditions

Fei Li,[1,2,3] **Huafeng Deng**,[1,3] **Wenwen Liu**,[4] **and Guoyong Duan**[1,5,6]

[1]*Key Laboratory of Geological Hazards on Three Gorges Reservoir Area (China Three Gorges University), Ministry of Education, Yichang, Hubei, China*
[2]*College of Civil Engineering, Hubei Three Gorges Polytechnic, Yichang, Hubei, China*
[3]*College of Civil Engineering and Architecture, China Three Gorges University, Yichang, Hubei, China*
[4]*Hubei Xinmin Construction Group Co. LTD, Yichang, Hubei, China*
[5]*Hubei Provincial Engineering Technology Research Center for Power Transmission Line, China Three Gorges University, Yichang, Hubei, China*
[6]*College of Electrical Engineering and New Energy, China Three Gorges University, Yichang, Hubei, China*

Correspondence should be addressed to Guoyong Duan; duanguoyong@ctgu.edu.cn

Received 4 July 2022; Accepted 10 August 2022; Published 29 April 2023

Academic Editor: Depeng Ma

The mechanical property of deep complex jointed rock mass is a hot topic in rock mechanics. In order to grasp the deformation and damage rules of through-going variable dip joint rock masses, the triaxial compression test and joint surface morphology scan test were conducted on cylindrical specimens in dry and wet conditions under 0, 5, 10, and 20 MPa water pressure. Through these tests, the deterioration law of rock samples under different pore water pressure in dry and wet conditions was studied. The effect of pore water pressure on the strength of saturated jointed rock sample is nonlinear. The imposed pore water pressure can significantly increase the axial deformation of rock samples, and higher pore water pressure can facilitate the deformation deterioration of samples. When the pore pressure is high, the rock samples show the characteristics of sliding shear failure. Under different pore pressure, the compressive strength of dry jointed rock is significantly higher than that of saturated jointed rock, and the saturated rock is more susceptible to sliding in the joint plane than dry rock. Dry jointed rock samples have stronger deformation ability than saturated jointed rock samples. The change rate of the morphologic parameters and the distribution of the failure cracks indicate that the stress concentration is evident in the middle of the joint plane.

1. Introduction

Reservoir earthquakes are one of the problems encountered during water resource development and utilization. Tens of thousands of earthquakes, large and small, have occurred since the Three Gorges Reservoir was impounded, and nearly one-third of them [1, 2] are inextricably linked to the local Gaoqiao Fault (Figure 1) [3–6]. Under the effect of vertical load loading and unloading brought by the periodic change of reservoir water, which triggers the increase of elastic stress of the reservoir base rock, the rise in pore water pressure is caused by the compaction of the rock pore, the change of groundwater level, and the diffusion of reservoir water outside the reservoir area, and the deterioration of mechanical rock properties leads to fault rupture and induces reservoir earthquake.

Many scholars have studied the mechanical properties of jointed rock mass, focusing on single jointed rock samples. Nonhole connected jointed rock masses with different connectivity rates exhibit anisotropic mechanical properties under loading and unloading conditions [7], and the joint direction has a greater effect on the strength and deformation of the rock mass than joint connectivity [8]. Renani established linear and nonlinear failure criteria using an analytical model of rock masses with nonpenetrating joints and predicted that increasing the joint strength and

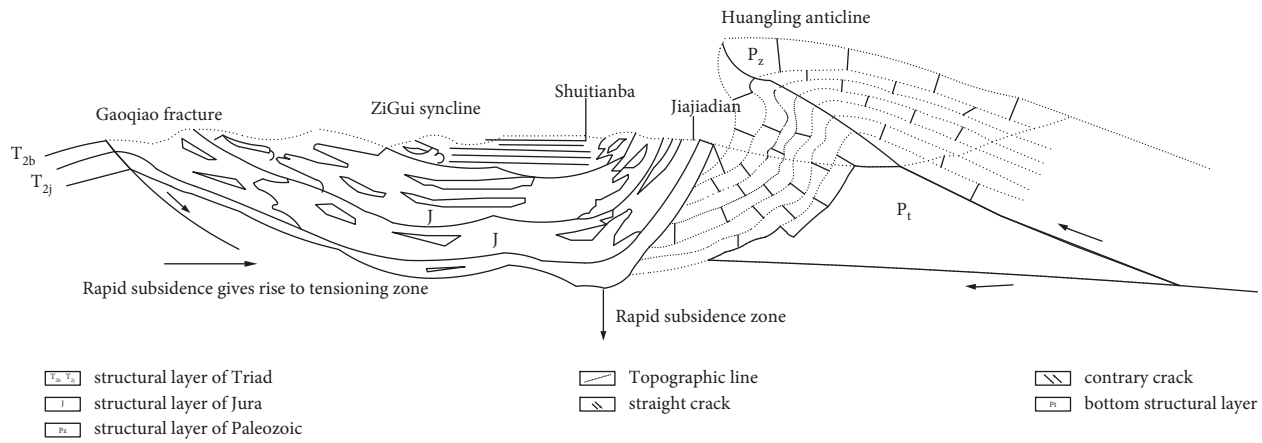

Figure 1: Profile of Gaoqiao fracture formation mechanism.

decreasing the joint shear strength would reduce the bond and friction of rock mass strength [9]. In terms of the failure mechanism of the jointed rock mass, Liu investigated the fatigue mechanism of the jointed rock mass under cyclic loading conditions from an energy perspective through routine tests [10]. The ductility of the joint with the magnitude of the positive stress has a significant influence on the fracture roughness and residual shear modulus of the rock bridge, which can be of great help in assessing the resistance of the rock bridge to evaluate the stability of the rock excavation [11]. However, there are fewer studies on rock masses with variable dip joints.

In terms of dry and wet states, current studies have demonstrated that the mechanical properties of rock samples in water-saturated states deteriorate significantly [12]. The deterioration of rock samples is exacerbated by the water-mechanical-chemical coupling state of mechanical loading and chemical interaction [13, 14]. Acoustic emission signals indicated that various shear-tensile damage modes or rock bridge modes occur in dry and saturated samples during rock failures [15], and rock moisture properties affect the peak strength, plastic deformation, and strength of rock failure [16].

Nicolas et al. [17] suggest that water mainly affects the diffusion aspect of rock samples in the brittle phase and has a more negligible effect on the peak strength. Tang [18] found that the peak shear strength decreases in dry and saturated fractures, where the shear parameter has a negative exponential trend, but the mechanical properties evolve differently. The diffusion of pore water pressure causes the activation of rock faults and the release of elastic energy [19], mainly manifest as the decrease of strength and the deterioration of deformation properties of rock masses. Li [20, 21] found that the permeability of dolomite is positively correlated with pore water pressure by the NMR technique, and the strength and the deformation properties of sandy slate decreased with increasing water pressure. Water pressure affects cohesion, deformation modulus, and internal friction angle differently. The cohesive force decreases sharply with the increased water pressure until the coherent power is lost. In rock mechanics indoor tests, most studies generalize natural joints as linear or planar, and the fugacity form is either through joints or nonthrough joints [11, 22, 23], which cannot realistically describe the actual joints morphology and in fact, different strata and fractures are primarily curved. This study simulates the rapid change of pore water pressure in the rock layer triggered by the short-time rise and fall of the water level in the reservoir area under different dry and wet conditions of the original stratum. Successive variable dip joints were set in the tuff rock samples to simulate the real fracture orientation to investigate the deterioration of mechanical properties under pore water pressure. The results can help understand the mechanical properties and damage modes of faults when rupture occurs, providing some reference to analyze the cause of earthquakes in the Three Gorges reservoir area.

2. Materials and Tests

2.1. Material and Rock Specimen Preparation. In this test, the tuffs of the Triassic Badong Formation near the Gaoqiao Fault in the Three Gorges Reservoir area were first drilled and core sampled into cylindrical rock samples with a diameter of 50 mm and a height of 100 mm (Figure 2(a)). The waterjet was used to cut out a joint surface with a gradual change in dip angle from 40° to 20° in the sample, which was used to simulate the production of the Gaoqiao fracture. A hole was punched in the center of the lower half of the rock sample to facilitate the application of water pressure (Figure 2(b)).

In this study, rock samples in both dry and saturated states were used, and a total of 8 working conditions with 4 levels of water pressure were applied, 2–3 rock samples for each condition. The saturation method was performed by vacuum saturation.

2.2. Test Procedure

2.2.1. Rock Mechanics Test Procedure. The rock samples were loaded with axial pressure (rate: 2 MPa/min) and circumferential pressure (rate: 1 MPa/min) simultaneously, reaching 100 MPa (axial pressure) and 50 MPa

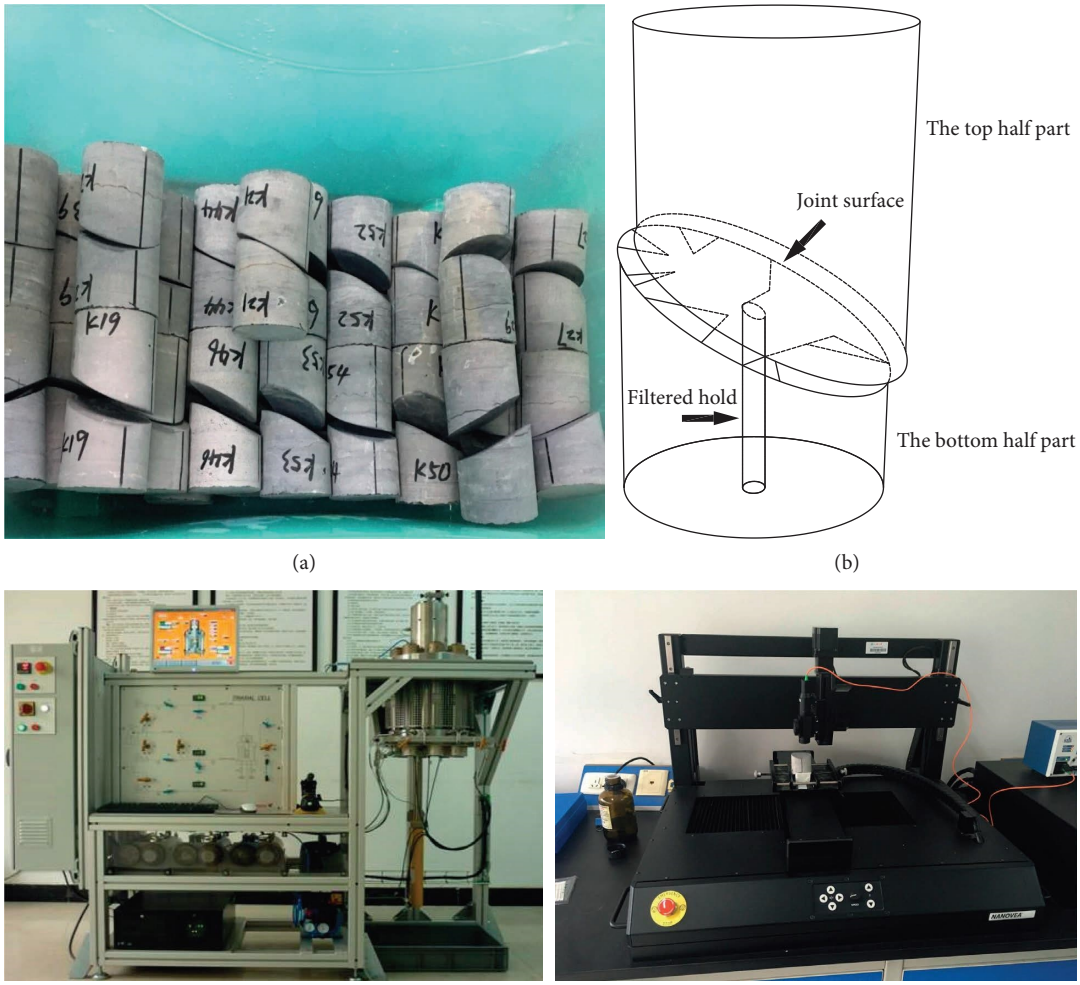

Figure 2: (a, b) Limestone rock specimens and (c, d) test equipment.

(circumferential pressure), respectively; keeping the circumferential pressure axial pressure unchanged, the water pressure was loaded to 0 MPa, 5 MPa, 10 MPa, and 20 MPa (2–3 rock samples were used for each level of water pressure test), and the water pressure loading rate was 1 MPa/min. After the water pressure was loaded to a predetermined value, anisotropic stress of rock samples was maintained for 30 minutes, and then the axial pressure continued to increase (at a rate of 2 MPa/min) until the failure occurred.

2.2.2. Analysis of the Fine Morphological Characteristics of the Joint Surface. A three-dimensional morphological scanner was used to scan the microscopic morphological characteristics of the joint surface of the rock sample before and after the test.

2.3. Test Equipment. The main equipment are TOP INDUSTRIE rock triaxial tester (Figure 2(c)), ST500 3D noncontact surface profiler (Figure 2(d)), and so on.

2.4. Stress-Strain Relation. The stress-strain curves of jointed rock specimen during the test are shown in Figure 3.

3. Mechanical Test Results of Variable Dip Nodular Rock Samples under Different Water Pressure

3.1. Stress-Strain Curve. The stress-strain curves of the jointed rock samples during the test are shown in Figure 3.

The pore water pressure was applied to the dry jointed rock sample, and the water pressure acted directly on the joint surface through the small holes in the lower part of the rock sample. From Figures 3(a)–3(d), it can be seen that with the increase of pore water pressure, the transverse strain of the rock sample has a tendency to gradually decrease, and the proportion of the plastic deformation stage in the test process further decreases. It should be noted that the transverse strains of the dry samples all tend to decrease in the front part when the pore water pressure is 5 MPa but start to increase gradually near the time of damage, which is caused by the rupture of the sheath that wraps the rock samples.

The triaxial compression tests were carried out on saturated jointed rock samples with different pore water pressures, and the stress-strain curves are shown in

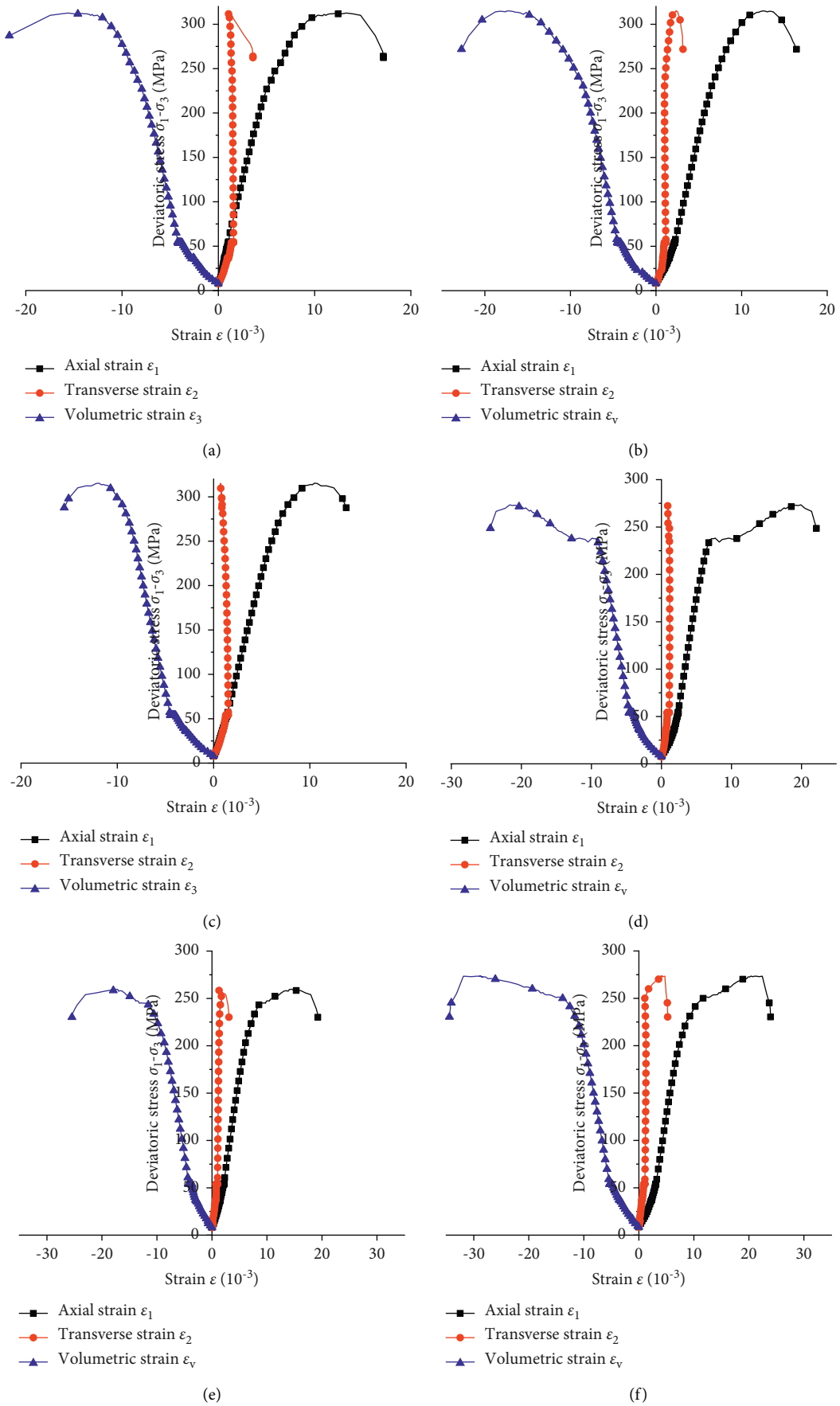

Figure 3: Continued.

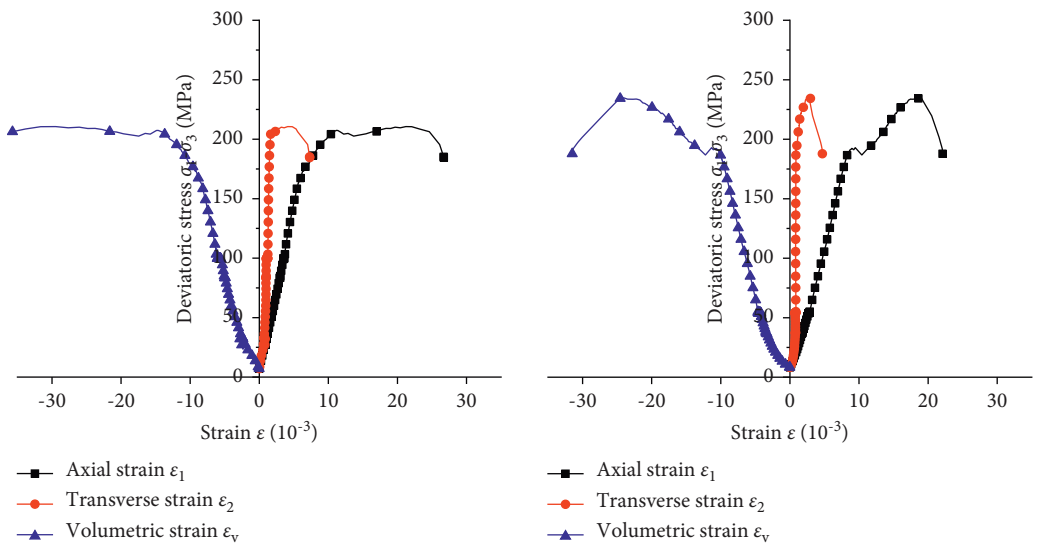

Figure 3: Stress-strain curves of jointed rock specimens under different pore pressures in wet and dry conditions.

Figures 3(e)–3(h). The saturated rock samples showed obvious plastic deformation during the test, and the proportion of plastic deformation before damage tended to rise with the increase of pore water pressure. During the loading process, the rate of change of transverse strain is much smaller than that of axial strain, but it suddenly rises when the rock sample approaches the peak strength of the first section until the rock sample is destroyed. For the axial strain, strain hardening occurs to varying degrees as the rock sample approaches the peak strength, i.e., the material must increase the stress to continue the strain after yield slip, and the ability of the material to resist deformation is improved at this stage. Observing the stress-strain curves, it can be seen that the rock samples under water pressure of 20 MPa have more sampling points in the strain-hardening stage than other water pressure conditions, while the strain in the elastic stage is smaller, indicating that the rock samples under higher water pressure enter the strain-hardening stage earlier while becoming less brittle.

The strain-hardening phenomenon of the saturated samples was most obvious at the pore water pressure of 20 MPa, the rock samples reached the first peak strength at the end of the elastic stage, and the second peak strength appeared after further loading was significantly higher than the first peak strength. However, the total peak strength is significantly smaller than that of the rock samples under pore water pressure of 0, 5, and 10 MPa.

3.2. Strength Characteristics. When the surrounding pressure is constant, the peak strength of the dry nodular rock samples shows a decreasing trend at different pore water pressures (Figure 4(a)).

Through data fitting, the relationship between water pressure of saturated sample and triaxial compressive strength can be obtained:

$$\sigma_1 = \frac{P_0}{18.758 - 0.965P_0} + 339.400. \quad (1)$$

The correlation coefficient R^2 was 0.9992. According to Figure 4(a) and the fitting (1), it can be seen that at low pore water pressure (0, 5, and 10 MPa), the triaxial compressive strength of dry jointed rock samples did not show large changes; when the pore water pressure increased to 20 MPa, the triaxial compressive strength showed a significant decrease; the minimum value of rock sample strength decreased about 11% compared with the maximum value.

The pore water pressure reaches the threshold value of 10 MPa before the strength of the rock sample is greatly deteriorated and has a significant impact on the rock properties. Considering that there are a large number of micropores in the rock sample, the lower pore water pressure is not enough to make the pores inside the rock sample rupture and connect, and the pores still have the pressure-bearing capacity at this time; when the pore water pressure increases, the micropores gradually connect with each other and produce obvious damage to the rock sample, which leads to the strength decrease.

Under the influence of different pore water pressure, the triaxial compressive strength of saturated nodular rock samples shows a phase change (Figure 4(c)).

Through data fitting, the relationship between water pressure of saturated sample and triaxial compressive strength can be obtained:

$$\sigma_1 = \frac{P_0}{0.897 - 0.128P_0} + 284.517. \quad (2)$$

The correlation coefficient R^2 was 0.97025. According to Figure 4(c) and the fitting (2), the maximum value of triaxial compressive strength occurs at 5 MPa pore water pressure and the minimum value occurs at 10 MPa pore

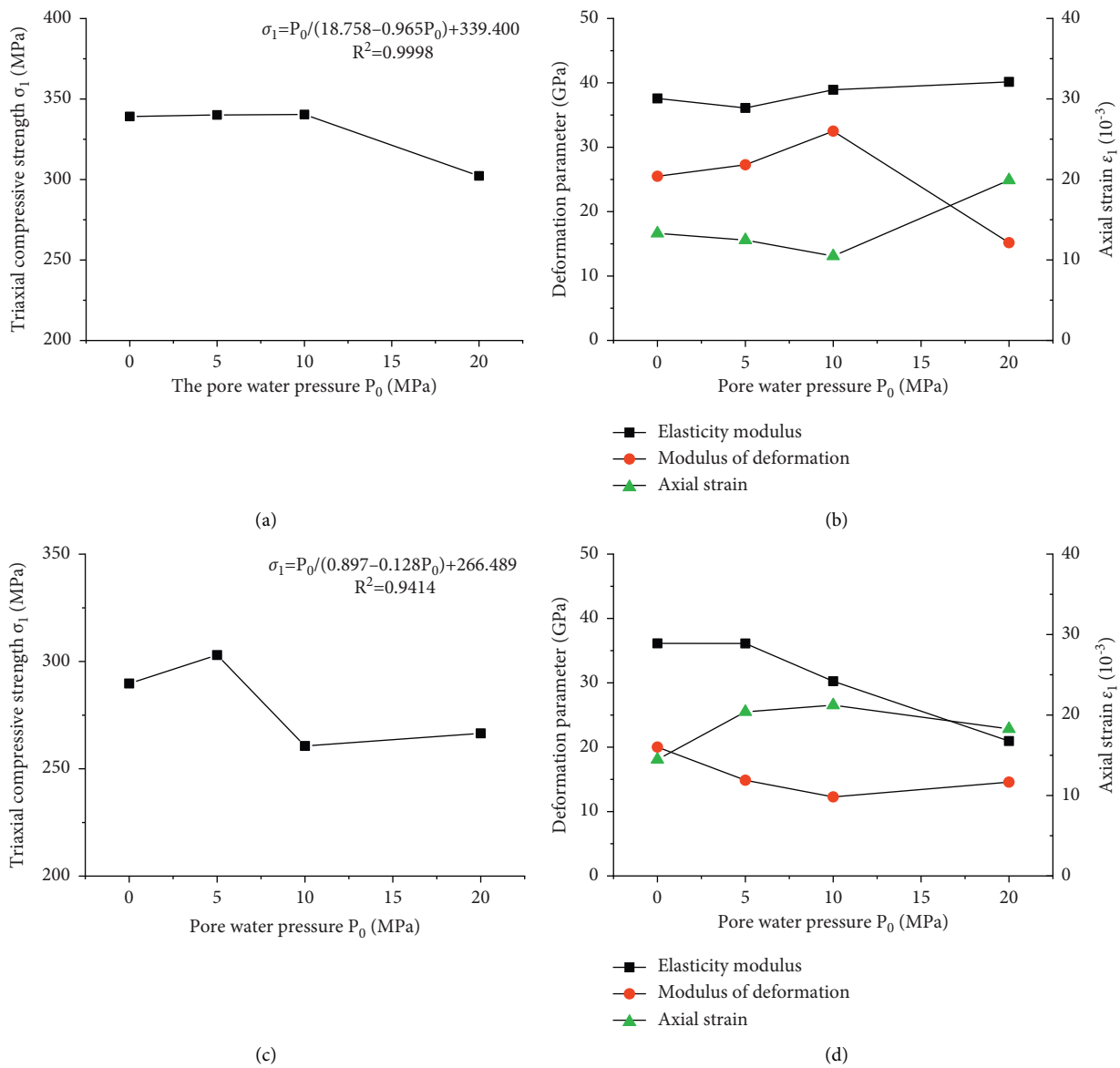

Figure 4: Strength and deformation curves of rock specimens in different states in wet and dry conditions.

water pressure. The triaxial compressive strength of the rock samples is closer at 0 and 5 MPa of pore water pressure; the triaxial compressive strength of the rock samples is closer at 10 and 20 MPa of pore water pressure. Therefore, it can be divided into two stages: the first stage with pore water pressure of 0–10 MPa and the second stage with pore water pressure of 10–20 MPa, and the compressive strength of the second stage decreased by about 13%. The pore water pressure is 5 MPa, and the measured value at this time has a large deviation from the fitted value, which is mainly due to the discrete nature of the specimen. For saturated nodular rock samples, the phase change of strength indicates that the effect of pore water pressure on strength is nonlinear, and the strength of rock samples changes significantly only when the pore water pressure changes by an order of magnitude.

3.3. Rock Deformation Characteristics. The elastic modulus and deformation modulus of dry nodular rock samples under different pore water pressure are shown in Figure 4(b), the difference between elastic modulus and deformation modulus is closer when the pore water pressure is 0, 5, and 10 MPa, indicating that the deformation of rock samples before reaching the peak strength under the application of lower pore water pressure is dominated by elastic deformation, and the proportion of plastic deformation is very small. In the process of increasing the pore water pressure from 0 MPa to 10 MPa, the deformation parameter values showed an increasing trend, while the peak strength did not change significantly, and the axial deformation of the specimen when the damage occurred under the lower pore water pressure showed a decrease. When the pore water pressure

increased to 20 MPa, the axial deformation showed a large increase. At lower pore water pressure, the stress concentration of internal microfractures is partially eliminated due to the adsorption of dissolved pores or microporosity near the surface of the rock sample, which makes the axial deformation rate of the specimen decrease. When the pore water pressure increased to 20 MPa, a larger deformation appeared in the axial direction, at which time the pore water pressure promoted the mutual penetration between micropores, which showed that the time from the initial loading to the final damage was shortened, indicating that the higher pore water pressure had an obvious effect on the deterioration of the specimen.

The deformation parameters of the saturated nodular rock samples under different pore water pressures are shown in Figure 4(d). The maximum value of the elastic modulus appears at the pore water pressure of 0 MPa and the minimum value appears at the pore water pressure of 20 MPa; the maximum value of the deformation modulus also appears at the pore water pressure of 0 MPa, but the minimum value appears at the pore water pressure of 10 MPa. According to the trend of deformation parameters with pore water pressure, the elastic modulus and deformation modulus both show a decreasing trend with the increase of pore water pressure, and the variation between the maximum and minimum values is about 25%. The axial strain of the rock samples showed an overall increasing trend with the increase of pore water pressure, and the maximum value of axial strain increased by about 50%, compared with the minimum value. It can be concluded that the application of pore water pressure can significantly increase the axial deformation of the rock samples but weaken the elastic deformation and enhance the plastic deformation capacity of the rock samples.

3.4. Damage Characteristics. The coarse solid line is the primary crack, and the fine solid line is the secondary crack.

As shown in Figures 5(a)–5(d), the common characteristics of the damage of dry nodular rock samples under different pore water pressure are obvious primary cracks and more secondary cracks concentrated in the lower part, and this phenomenon indicates that the softening effect of the rock samples is more obvious the closer to the pore water pressure source during the loading damage. Under the action of different pore water pressure, the damage characteristics show different characteristics. From the damage characteristics of rock samples before and after the application of pore water pressure (Figures 5(a) and 5(b)), it can be found that the cracks in the lower part of the rock samples increase significantly after the application of pore water pressure, and the distribution also shows a certain pattern with the change of pore water pressure. When the pore water pressure is 5 MPa, the primary and secondary cracks are partially parallel to the rock sample axis at the initial stage and then deflected, showing signs of cleavage and shear damage. When the pore water pressure rises to 10 MPa and 20 MPa, the main feature of crack orientation is a deviation from the axis at a certain angle, showing the characteristics of shear damage. At the pore water pressure of 20 MPa, a large number of secondary cracks were produced in the lower part of the rock sample.

The damage characteristics of the saturated sample under different pore water pressure are shown in Figures 5(e)–5(h). When the pore water pressure is 0 MPa, i.e., no pore water pressure is applied, the cracking trend of the rock sample is from horizontal and inclined to flat main cracks through the lower part of the rock sample, accompanied by secondary cracks. When the pore water pressure is 5 MPa, the main crack penetrates the whole rock sample through the middle of the joint surface, and the rock sample shows obvious shear damage characteristics. When the pore water pressure is 10 MPa, the main crack appears in the lower part of the sample, and the horizontal and inclined cracks extend to the bottom edge of the sample, mainly caused by the sliding and pulling of the upper and lower parts along the joint surface. When the pore water pressure is 20 MPa, the main crack penetrates through the center of the joint surface in the upper and lower parts of the sample, there are more cracks in the upper part than in the lower part, and secondary cracks are produced between the parallel main cracks.

The above phenomenon indicates that the elevated pore water pressure greatly weakens the shear strength of the rock sample. Since the joint surface has a certain roughness, during the sliding process of the rock sample along the joint surface, multiple stress concentrations occur on the joint surface and cause the generation and expansion of cracks. At the same time, different pore water pressures lead to different damage patterns of the jointed rock mass.

4. Analysis of the Effect of Pore Water Pressure on the Degradation of Variable Dip Nodular Rock Samples

4.1. Effect of Pore Water Pressure on Strength Properties of Saturated and Dry Nodular Rock Samples. For the nodular rock samples, the different states (dry or saturated) had significant effects on the strength of the rock samples, as shown in Figure 6. Under the influence of different pore water pressures, the compressive strength of the nodular dry rock samples was higher than that of the nodular saturated rock samples with the same water pressure. The compressive strengths of dry rock samples were 17.0%, 12.2%, 30.6%, and 13.4% higher than those of saturated rock samples under the pore water pressure of 0 MPa, 5 MPa, 10 MPa, and 20 MPa, respectively. During the loading damage, the friction coefficient of the joint surface of the dry rock samples was larger, and the friction coefficient of the joint surface of the saturated rock samples was smaller due to the influence of pore water. Therefore, the dry joint surface can provide a larger friction force during the loading damage, which makes the rock samples have a higher bearing capacity. The saturated rock samples are more prone to slip of the joint surface than the dry rock samples, so the load-bearing capacity of the saturated rock samples is lower.

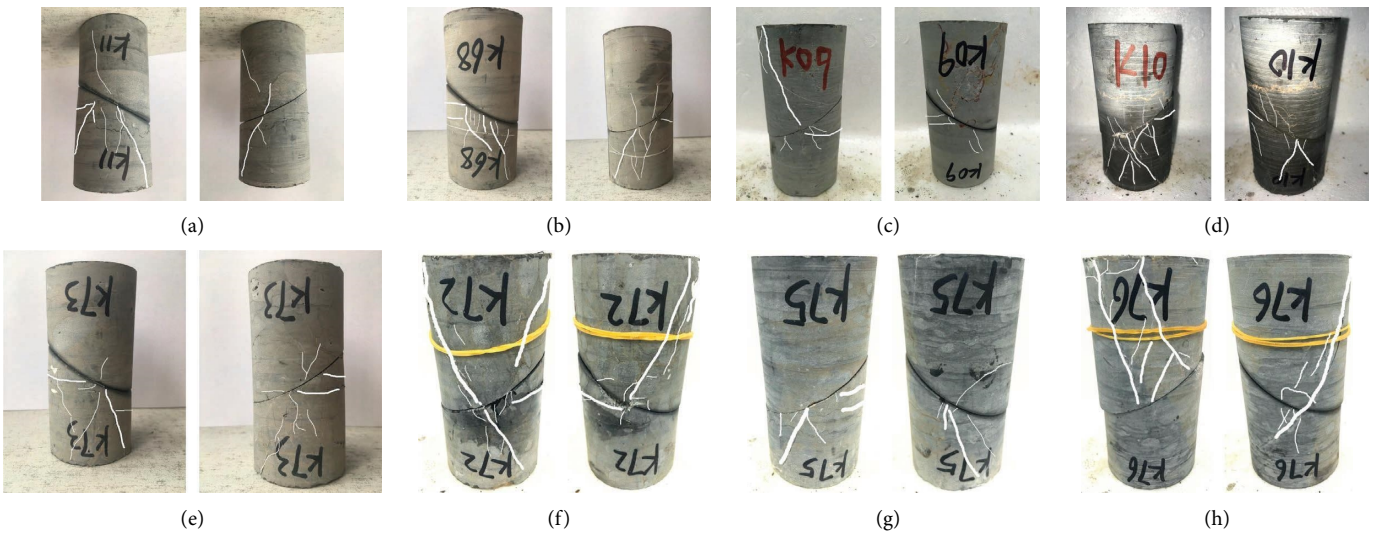

Figure 5: Failure characteristics of jointed rock specimens under different pore pressure in wet and dry conditions (The coarse solid line is the primary crack, and the fine solid line is the secondary crack).

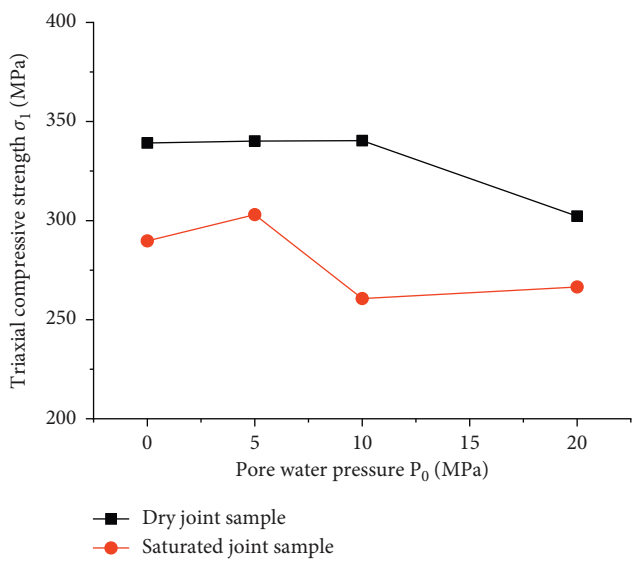

Figure 6: Strength comparison of rock specimens in different states.

4.2. Influence of Pore Water Pressure on Deformation Parameters of Saturated and Dry Nodular Rock Samples. Dry nodular rock samples at lower pore water pressure partially eliminate the stress concentration of internal microfractures due to the adsorption of the dissolved pores or microporosity near the surface of the rock samples, which decreases the axial deformation rate of the specimens. When the pore water pressure continues to increase, the micropores penetrate each other, which shows that the time from the initial loading to the final damage is shortened and the deformation appears to be larger growth, indicating that the effect of higher pore water pressure on the deterioration effect of the specimen is more obvious.

The elastic modulus and deformation modulus of saturated nodular rock samples both show a decreasing trend with the increase of pore water pressure, and the variation between the maximum and minimum values is about 20%–30%. The axial strain of the rock samples showed an overall increasing trend with the increase of pore water pressure, and the maximum value of axial strain increased about 50% compared with the minimum value. It can be concluded that the applied pore water pressure can significantly increase the axial deformation of the rock samples but weaken the elastic deformation and enhance the plastic deformation.

The comparison of deformation parameters of rock samples in dry and saturated states is shown in Figure 7. At 0–5 MPa, the difference between the elastic modulus of rock samples in the dry state and that in the saturated state is small, and at 5–20 MPa, the elastic modulus of rock samples in the saturated state gradually decreases, while that in the dry state slightly increases, resulting in a larger difference between the two.

From Figure 7(a), it can be seen that the elastic modulus of rock samples in different states is similar in dry and saturated states when the pore water pressure is 0–5 MPa. The modulus of elasticity of dry nodular rock samples is greater than that of saturated nodular rock samples only when the pore water pressure is 10–20 MPa. Under different pore water pressure, the elastic modulus of saturated rock samples fluctuates more and the elastic modulus of dry rock samples fluctuates less, which indicates that saturated rock samples are more sensitive to the change of pore water pressure. By the water pressure setting in accordance with the isometric series, the effect on the strength and deformation of the rock sample is more obvious under the larger water pressure. After exceeding 5 MPa, the larger the water pressure is, the larger the difference of elastic modulus between different states.

The deformation modulus of dry rock samples was 27.3%, 83.6%, 164.5%, and 4.1% higher than that of saturated rock samples at a pore water pressure of 0 MPa, 5 MPa, 10 MPa, and 20 MPa, respectively. In the interval from 0 to 10 MPa, the difference between the deformation modulus of the dry sample and the saturated sample gradually increased.

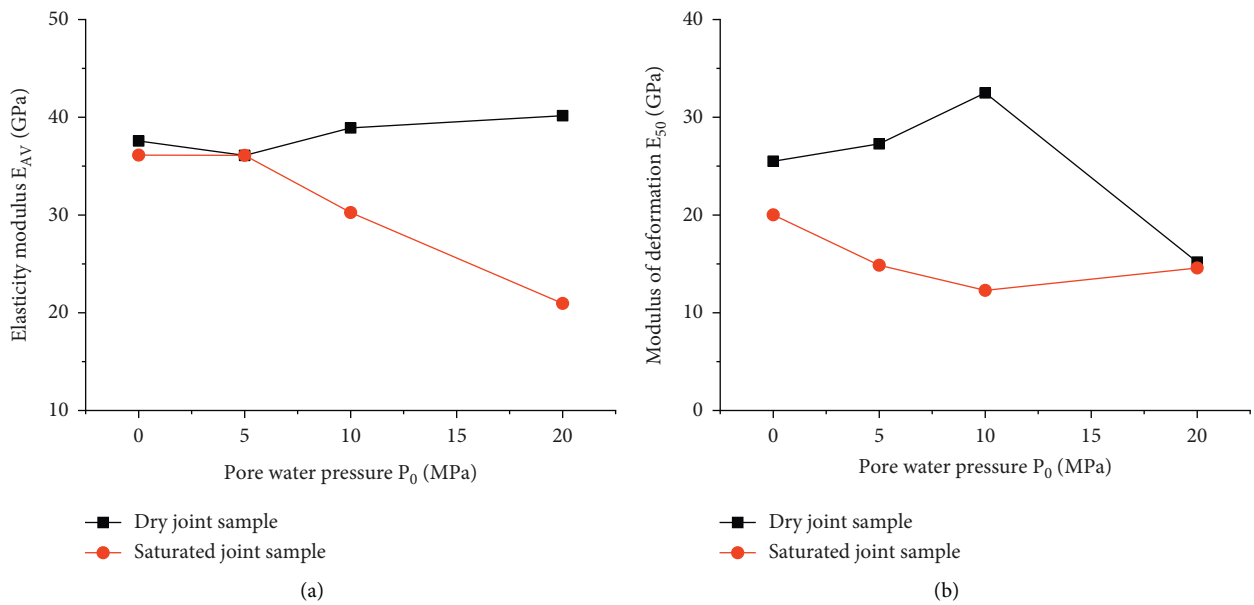

Figure 7: Deformation parameters include Elastic modulus and Deformation modulus.

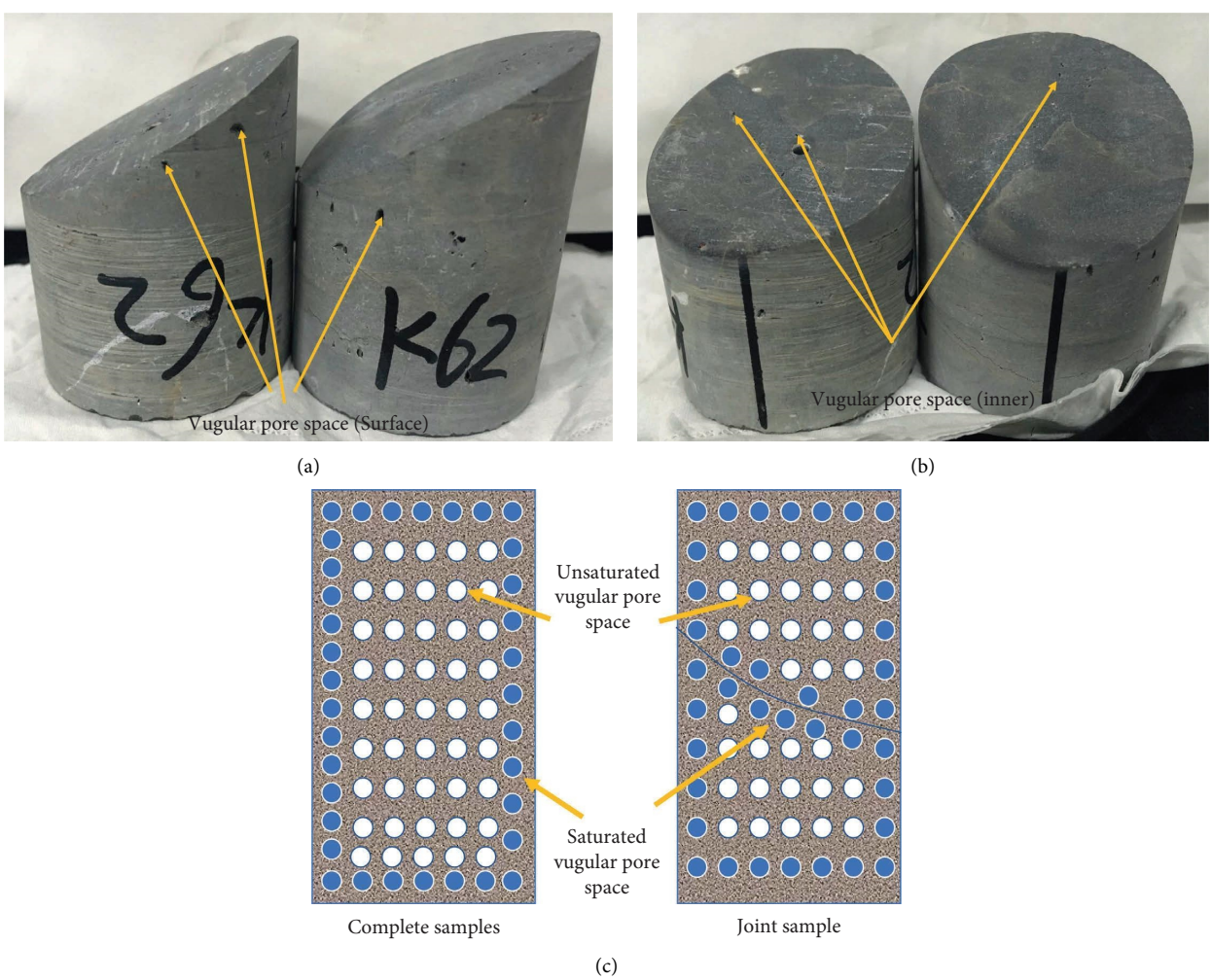

Figure 8: Solution pores in limestone samples (a, b) and schematic diagram of solution pore saturation (c).

However, at 20 MPa, the plastic deformation of the dry sample increased substantially compared with that of 0–10 MPa, and the maximum peak stress became smaller, resulting in a significant decrease in the deformation modulus at 20 MPa; the plastic deformation of the saturated sample increased slightly compared with that of 0–10 MPa, but the maximum peak stress increased substantially compared with that of 0–10 MPa, resulting in a small increase in the deformation modulus at 20 MPa. When the water pressure is 20 MPa, the deformation modulus values of dry and saturated rock samples are closer. The anomaly of deformation modulus at 20 MPa pore water pressure may be caused by the ratio of pore water pressure to axial pressure of 100 MPa reaching a certain threshold value, which reduces the friction coefficient of the variable dip joint surface and leads to the reduction of the strength of the joint surface, that is, the softening effect of water. This phenomenon indicates that the dry jointed rock sample has a stronger deformation capacity than the saturated jointed rock sample, although the fluctuation of deformation parameters of the saturated rock sample is smaller due to the softening effect of water, but the bearing capacity of the dry rock sample is significantly larger, which eventually affects the deformation capacity of the rock sample.

4.3. Characterization of Pore Evolution of Chert Specimens. Observations reveal a variable number and uneven distribution of dissolution pores on the surface and inside the tuff, hereafter referred to as dissolution pores (Figure 8). There are veins intruded in the rock layer, along with some laminations.

During the test, the main factors that produce deterioration of mechanical properties of dry nodular rock samples and saturated nodular rock samples are as follows: the saturation state and the size of pore water pressure. Due to the existence of dissolved pores of different sizes in the chert rock samples (Figures 8(a) and 8(b)), the processes of pore generation, saturation by immersion, interconnection, and formation of microcracks are affected by the pore water pressure (Figure 8(c)). First, the presence of pore water pressure decreases the friction coefficient of the joint surface for both dry and saturated joint rock samples. Second, the pore water gradually expands from the outer layer to the inner layer, which makes the dissolution pore linkage and leads to the increase of fracture penetration, thus reducing the mechanical properties of the rock sample. In addition, when the pore water pressure is less than the tensile strength of the rock sample, the change of the dissolved pore size is not enough to make the pore rupture, and it cannot significantly reduce the effective stress in the rock. This results in the deterioration of the mechanical properties of the joint surface of the rock sample.

5. Morphological Parameters of Nodular Rock Samples

The relevant parameters before and after the test were collected by 3D morphological scanning, and some parameters were selected to analyze the roughness of the joint surface. The rate of change of the following morphological parameters was analyzed by combining the 3D scanned images of the convex and concave surfaces of the joints.

The root mean square height and arithmetic mean height were selected for height parameters; the inverse loading area rate was used for functional parameters; the minimum autocorrelation length was used for spatial parameters to characterize the roughness of the joint surface.

The root mean square height S_q represents the root mean square of the height of each point in the region and characterizes the standard deviation of the height, equation (3) is used to characterize the discrete change in height of each point of the joint surface before and after the test, and the rate of change increases the surface joint surface roughness:

$$S_{q1} = \sqrt{\frac{1}{A}\iint_A Z^2(x, y)dxdy}. \tag{3}$$

Here, S_q represents the root mean square height, A represents the scanning area, and Z represents the high function.

S_a represents the average of the absolute value for the height difference of each point relative to the average surface, as shown in equation (4). It represents the alteration in the mean height of each point in the area. A positive change rate indicates an increase in the average height of each point on the joint wall and an increase in the roughness of the joint wall. On the other hand, a negative change rate indicates a decrease in the average height of each point on the joint wall and a decrease in the roughness of the joint wall:

$$S_a = \frac{1}{A}\iint_A |Z(x, y)|dxdy. \tag{4}$$

Here, S_a represents the arithmetic mean height, A represents the scanning area, and Z represents the high function.

S_{mc} represents the height C satisfying the load area ratio p%, which characterizes the overall concave-convex degree of the joint wall before and after the test. When the rate of change is positive, the curvature of the joint surface increases. A positive change rate indicates an increase in the wear degree for concave surfaces, while it indicates a partially disturbed connection surface due to failure for convex surfaces. When the change rate is negative, the curvature of the joint plane decreases. At this point, the edge part of concave surfaces has greater wear than the middle part, while the convex surface has the opposite.

S_{al} indicates the horizon distance, in which the function of autocorrelation decays rapidly toward the specified value s (default: 0.2). It represents the wavelength of the surface. A larger value indicates a larger wavelength on the surface. A positive change rate indicates a large wear degree of the joint surface, while a negative change rate indicates a small wear degree. The morphology parameters rate of change depends on the wear degree of the joint wall and the failure mode of the rock specimen. Different pore pressure may change joint

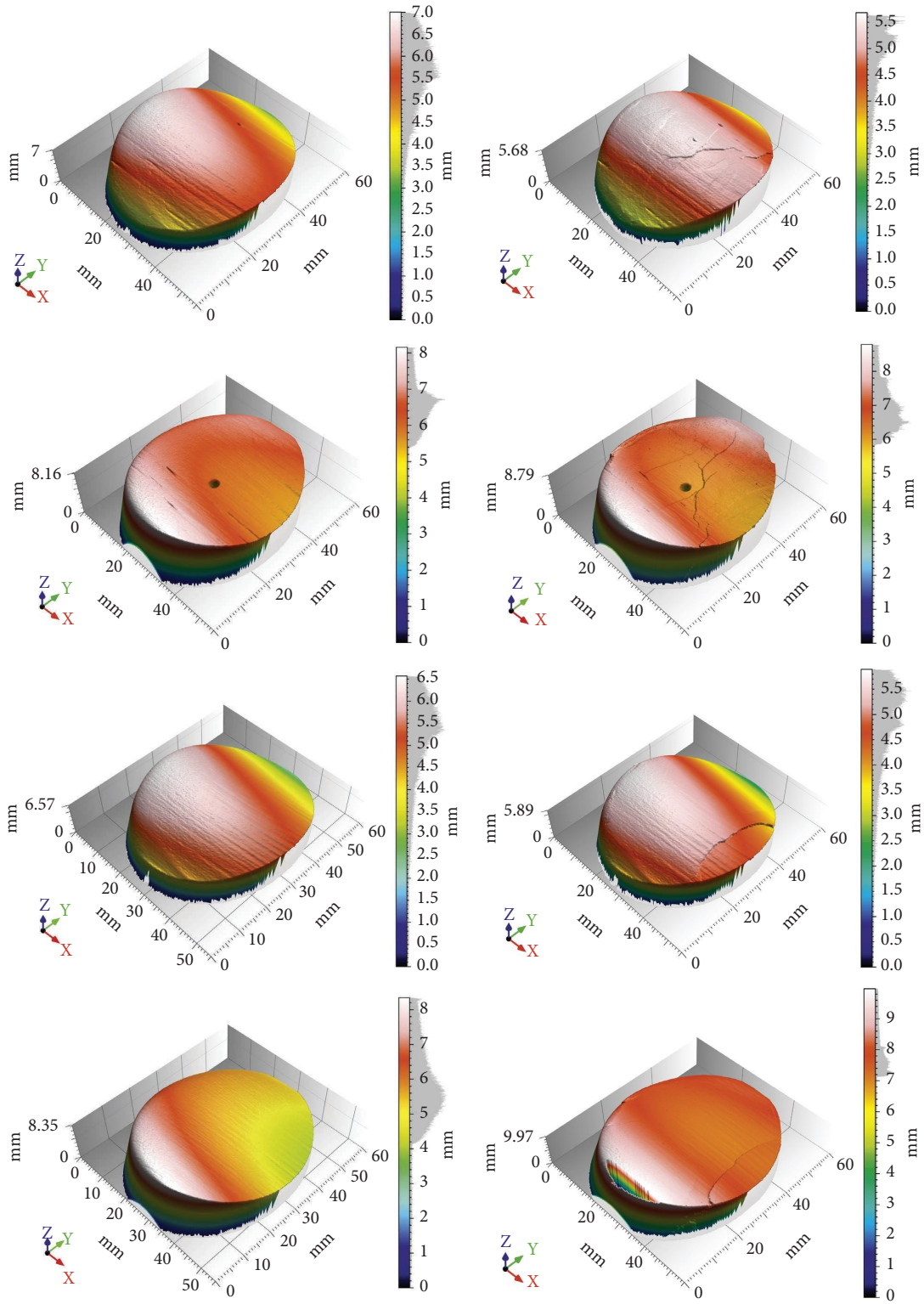

(a)

Figure 9: Continued.

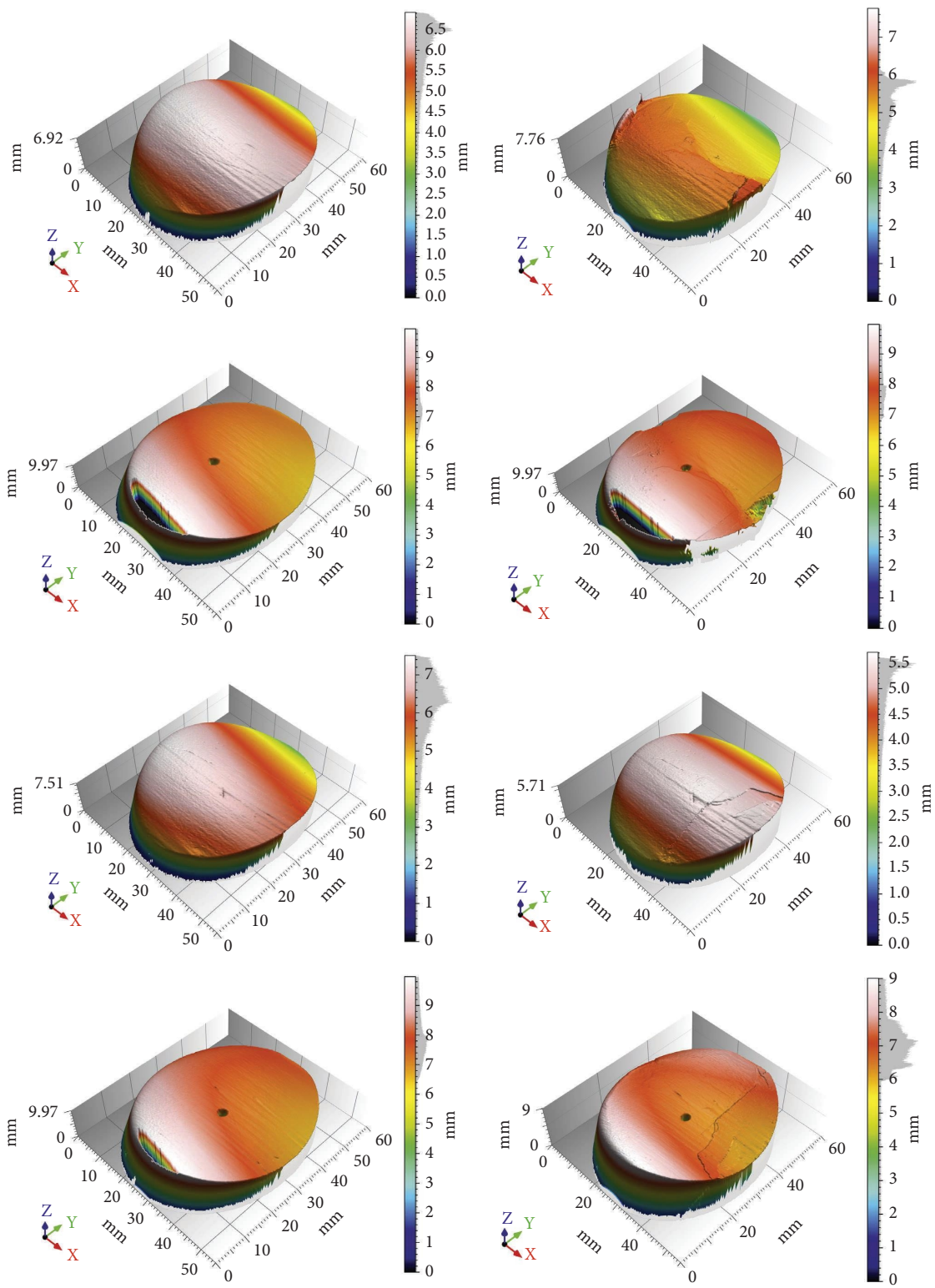

(b)

Figure 9: Continued.

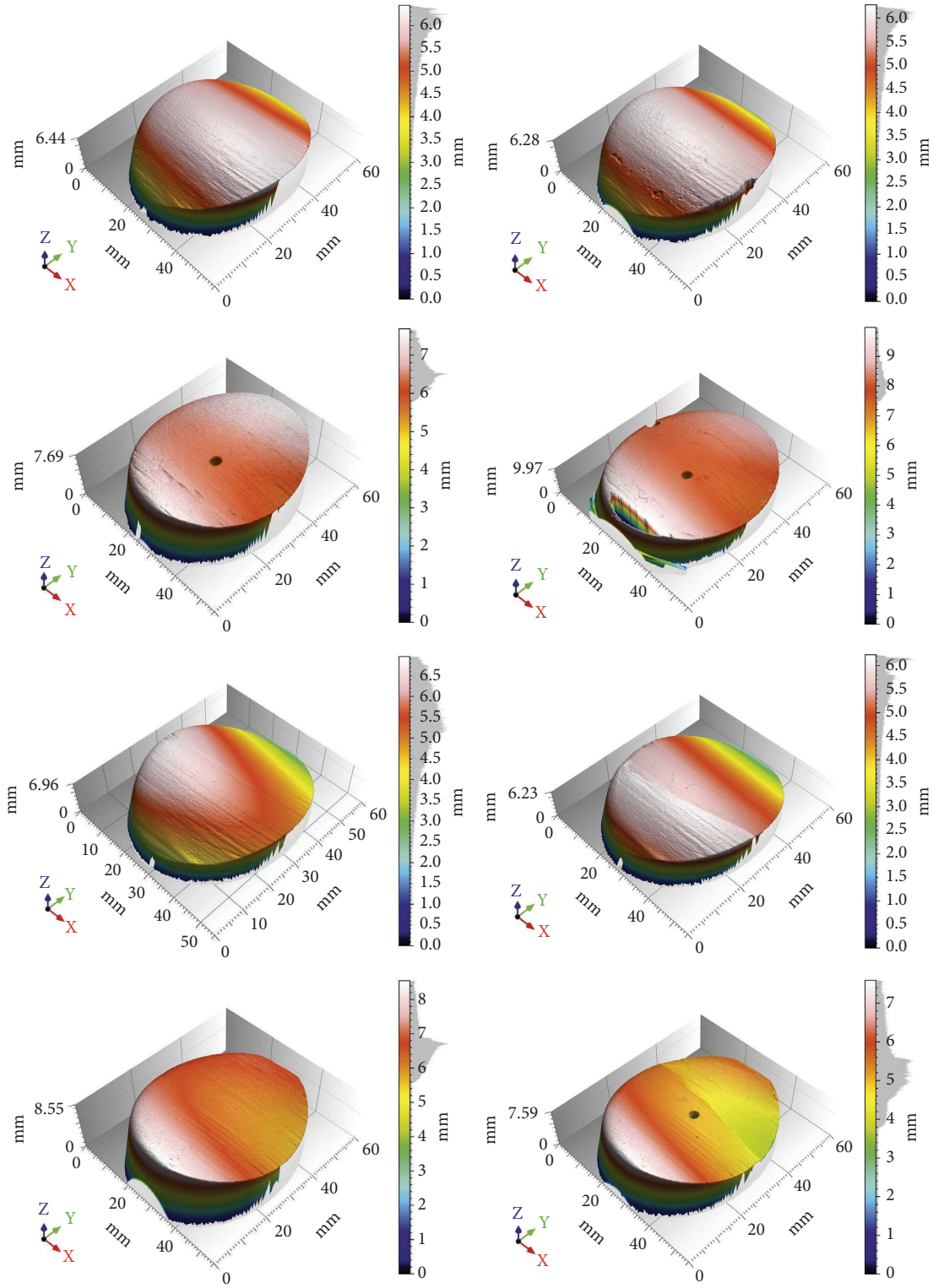

(c)

Figure 9: Continued.

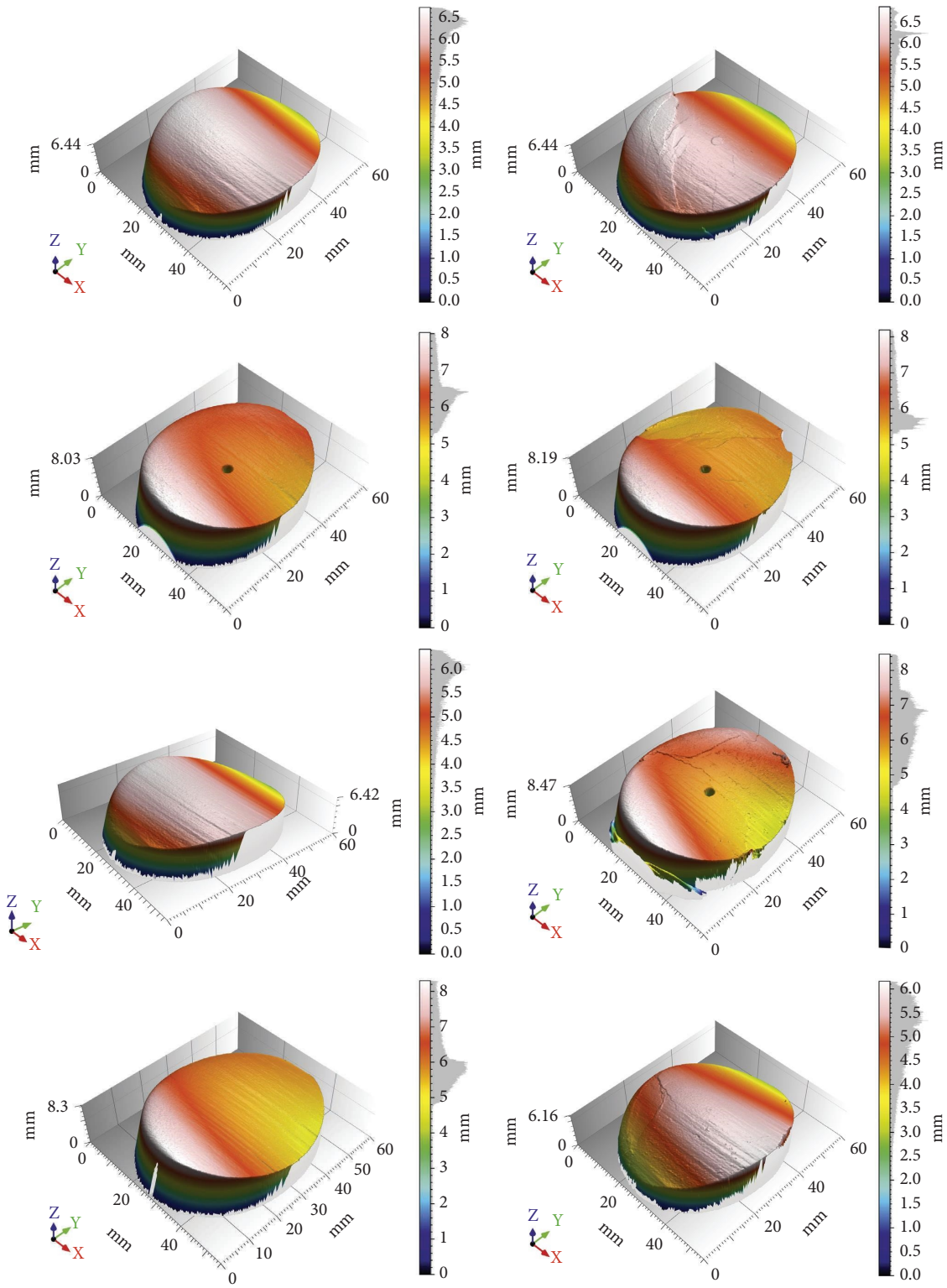

(d)

Figure 9: Three-dimensional view of joint plane scanning (the picture on the left is before the test, and the right is after the test).

Table 1: The change rate of joint rock morphology parameters (%).

Sample status	Pore water pressure (MPa) Morphology parameters	0	5	10	20	0	5	10	20
		The lower part of the sample (concave surface)				The upper part of the rock specimen (convex surface)			
Dry samples	S_q	31.88	−34.02	−0.62	−8.90	−14.80	−35.77	4.19	−13.88
	S_a	−6.22	−30.04	14.83	3.27	−13.00	−31.65	6.22	−11.65
	S_{mc}	−11.44	−29.05	18.38	−16.60	−16.05	−41.29	−7.45	4.02
	S_{al}	−4.78	−5.71	−0.03	−9.31	1.66	0.72	1.31	−0.87
Saturated samples	S_q	0.21	4.99	75.30	1.29	−24.06	−18.77	−7.87	−2.87
	S_a	3.78	2.59	67.57	9.20	−20.11	−14.16	−6.37	−0.61
	S_{mc}	3.48	−8.35	46.55	18.90	−29.41	−7.54	−5.26	2.79
	S_{al}	−0.24	−3.62	−9.52	4.35	0.40	−6.44	1.73	−2.86

plane morphology, affecting the destructional forms of the rock specimen.

5.1. Morphological Parameters of Jointed Rock Samples in Different States. Before and after the test, the upper and lower joint surfaces of the dry and saturated jointed rock samples were scanned in 3D morphology, as shown in Figure 9.

Under different water pressures, the dry sample nodal surface showed a transition from partial shear damage to overall shear damage, which was more obvious on the concave surface of the rock sample. When the pore water pressure was 0 MPa, there was only obvious shearing on the concave surface near the edge; when the pore water pressure was 5 MPa, the shearing range on the concave surface shifted toward the middle of the rock sample; when the pore water pressure was 10 MPa, the shearing range was already close to the middle line of the joint surface, indicating further expansion of the range; when the pore water pressure was 20 MPa, in addition to the shearing cracks extending toward the middle, there were secondary cracks produced on the concave surface This indicates that multiple damage occurred.

The cracks on the joint face of the saturated rock sample are more toward the middle, and the edges of the joint face in the lower half of the rock sample show obvious collapse cracks. At a pore water pressure of 0 MPa, there are obvious shear cracks on the convex surface, and the main crack in the middle of the concave surface derives several secondary cracks and a small part of chipping at the edge; at a pore water pressure of 5 MPa, in addition to a linear crack in the middle of the concave surface, small pieces of chipping appear at the junction between the crack and the edge of the joint surface; at a pore water pressure of 10 MPa, several small craters appear on the convex surface, indicating that the when the pore water pressure is 20 MPa, there are obvious shear cracks on the convex surface, and at the same time, there are cylindrical bumps in the middle due to the water pressure applied to the round hole of the concave surface, which indicates that the pore water pressure has a significant softening effect on the rock sample.

5.2. Analysis of morphological parameters. According to Table 1, it can be seen that the dry sample parameter S_q values are mainly decreasing under different water pressures, indicating that the dispersion of the height difference values at each point on the surface of the joint surface under the action of extrusion and friction decreases after the test. The saturated sample parameter S_q values were mainly decreasing in the upper part of the rock sample and increasing in the lower part of the rock sample, indicating that the test reduced the roughness of the convex surface and increased the roughness of the concave surface.

The dry sample parameter S_a value decreases when the pore water pressure is 0 MPa and 5 MPa, indicating that the average height of each point on the joint surface decreases, reflecting the reduction of the roughness of the joint surface by friction; it mainly shows an increase when the pore water pressure is 10 MPa and 20 MPa, mainly due to the misalignment of the sheared part. The saturation sample parameter S_a value also mainly decreases in the upper part of the rock sample and mainly increases in the lower part of the rock sample, indicating that the average height of the points on the convex surface decreases and the average height of the points on the concave surface increases. It reflects the decreasing effect of water pressure on the roughness of the rock sample.

From Table 1, it can be seen that the parameter S_q and S_a values of the upper half of the dry sample rock sample (convex surface) under the pore water pressure of 10 MPa have different trends from those under other pore water pressures. By observing the stress-strain curve of the dry sample at 10 MPa, it is found that the strain value increases the most from the stage of reaching the peak strength to the occurrence of damage, and at the same time, due to the local contact between the upper and lower parts of the through-variable dip joint surface, the rock sample joint surface produces the most relative sliding, which eventually leads to the increase of the roughness of the joint surface, and the parameter S*q* and S*a* values show a small increase.

The parameter S_{mc} value of the dry sample is mainly decreasing, reflecting the decrease of the curvature of the joint surface, which shows more wear in the middle for the convex surface, and indirectly reflects the shearing of the peak in the lower part of the rock sample for the concave surface. The saturated sample parameter S_{mc} values are also mainly decreasing in the upper half of the sample and increasing in the lower half of the sample, reflecting more wear in the middle than in the ends of the joint surface. This

indicates that the stress is more concentrated in the middle of the sample.

The S_{al} value of the dry sample decreases in the lower part of the sample and increases in the upper part, which indicates that the test process wears the lower part of the sample more obviously. The saturated sample parameter S_{al} value did not show a monotonic trend under different water pressure, which is due to the interaction of surface wear and shear part misalignment.

Different rock samples have different original roughness, so it is meaningful to compare the morphological scanning parameters of the same joint surface. The analysis of the rate of change of morphological parameters before and after the rock sample test shows that under different water pressure, the dry sample joint surface roughness decreases, the middle of the convex surface wears more, and the concave surface wears more obviously; the saturated sample convex surface roughness decreases, the concave surface roughness increases, and the middle of the joint surface wear is higher than the ends. There is no monotonic trend, the force in the middle of the joint surface of the rock sample is concentrated, and the joint surface appears partly misshapen.

6. Conclusion

This work mainly carries out the experimental research on the mechanical properties of variable dip angle jointed tuff rock samples, using the comparative analysis of mechanical properties of different types of rock samples and the analysis of surface morphological parameters of joints, etc. By establishing the dissolved pore model of tuff rock samples, the dry rock samples of variable dip angle jointed tuff were analyzed for factors such as variable pore water pressure, and the main conclusions obtained are as follows:

(1) The pore water pressure reaches the threshold value of 10 MPa before it produces a large deterioration of the strength of the dry nodular rock samples and has a significant effect on the rock properties. For saturated nodular rock samples, the effect of pore water pressure on strength is nonlinear, and the strength of rock samples only changes significantly when the pore water pressure changes by an order of magnitude. The main effect of pore water pressure is the deterioration of the rock sample and the change of frictional properties of the joint surface. Due to the smaller friction coefficient of the joint surface, the saturated rock samples are more prone to slip of the joint surface than the dry rock samples.

(2) In the case of applying lower pore water pressure, the elastic deformation is dominant in the deformation of dry jointed rock samples before reaching the peak strength. For saturated jointed rock samples, the application of pore water pressure can significantly increase the axial deformation of rock samples but weaken the elastic deformation and enhance the plastic deformation capacity of rock samples, and the higher pore water pressure has a more obvious effect on the deterioration of specimens. When the pore water pressure is higher, the rock samples show the characteristics of slip shear damage, and when the pore water pressure is lower, the rock samples are mainly in integral shear damage.

(3) Under different pore water pressure, the elastic modulus of saturated jointed rock samples fluctuates more, the elastic modulus of dry rock samples fluctuates less, and saturated rock samples are more sensitive to the change of pore water pressure. The dry nodular rock sample has a stronger deformation ability than the saturated nodular rock sample.

(4) Under different water pressure, the roughness of the dry sample nodular surface decreases, the middle of the convex surface is more worn, and the concave surface is worn more obviously; the roughness of the convex surface of the saturated sample decreases, the roughness of the concave surface increases, the middle of the nodular surface wear is higher than the two ends; there is no monotonic change trend, the force in the middle of the nodular surface of the rock sample is concentrated, and the nodular surface is partially misshapen.

Data Availability

The data (triaxial compression test) used to support the findings of this study are included within the supplementary information files.

Conflicts of Interest

The authors declare that they have no conflicts of interest.

Acknowledgments

This research was supported by the Joint Fund of the National Nature Science Foundation of China (U2034203), the Open Fund of the Key Laboratory of Geological Hazards on Three Gorges Reservoir Area (China Three Gorges University), Ministry of Education (2020KDZ12), the National Nature Science Foundation of China (52009067), the China National Natural Science Foundation Joint Funded Project (U1965109), and the Hubei Provincial Natural Science Foundation Innovation Group Project (2020CFA049).

Supplementary Materials

The following contents have been modified this time: the four formulas have been re-edited by Microsoft Word's formula editor. To represent Figure 9 more systematically, the numbers 3 and 4 have been moved to the original positions of the numbers 1 and 2. (*Supplementary Materials*)

References

[1] G. Duan, L. Wang, H. Deng, J. Zhang, Z. Luo, and Q. Jiang, "Mechanical response of listric faults in the three Gorges reservoir area based on three-dimensional morphological characteristics," *Frontiers in Physics*, vol. 9, Article ID 766920, 2021.

[2] G. Duan, Y. Wang, J. Chen, and J. Zhang, "Analysis of reservoir seismic law based on three-dimensional morphological characteristics of joint surface related to listric fault," *Frontiers in Physics*, vol. 9, Article ID 811609, 2022.

[3] J. Deng and L. Zhou, "Features and activity of Gaoqiao Fault zone along the north-western margin of zigui basin in Hubei province," *Geology and Mineral Resources of South China*, vol. 03, pp. 18–23, 2003.

[4] J. Xia, L. Zhou, and S. Liu, "Study on the characteristics and activity of main faults in Zigui Basin and its periphery in western Hubei province," *Hydrogeology & Engineering Geology*, vol. 01, pp. 10–14, 1996.

[5] L. Zhou and J. Z. J. Xia, "Characteristics of the Gaoqiao Fault zone and its influence of the three Gorges Project," *The people of the Yangtze river*, vol. 03, pp. 17–19, 1996.

[6] S. J. Gao, *Crustal Stress Field and Earthquakes in the Three Gorges Region of the Yangtze River Crustal Stress Field and Earthquakes in the Three Gorges Region of the Yangtze River*, 1992.

[7] L. H. Wang, "Experimental study on mechanical properties of jointed rock mass with different connectivity under triaxial loading and unloading," *Journal of rock mechanics and engineering*, vol. 34, no. 12, pp. 2500–2508, 2015.

[8] G. Duan, J. Li, J. Zhang, E. Assefa, and X. Sun, "Mechanical properties and failure modes of rock specimens with specific joint geometries in triaxial unloading compressive test," *Advances in Materials Science and Engineering*, pp. 1–14, Article ID 1340934, 2019.

[9] H. Rafiei Renani, C. D. Martin, and M. Cai, "An analytical model for strength of jointed rock masses," *Tunnelling and Underground Space Technology*, vol. 94, Article ID 103159, 2019.

[10] Y. Liu, F. Dai, L. Dong, N. W. Xu, and P. Feng, "Experimental investigation on the fatigue mechanical properties of intermittently jointed rock models under cyclic uniaxial compression with different loading parameters," *Rock Mechanics and Rock Engineering*, vol. 51, no. 1, pp. 47–68, 2018.

[11] X.-X. Yang and P. H. S. W. Kulatilake, "Laboratory investigation of mechanical behavior of granite samples containing discontinuous joints through direct shear tests," *Arabian Journal of Geosciences*, vol. 12, no. 3, p. 79, 2019.

[12] H. F. Deng, J. C. Fang, J. L. Li, Y. Xiao, and M. L. Zhou, "Influence mechanism of water state on mechanical properties of red bed soft rock," *Journal of coal*, vol. 42, no. 08, pp. 1994–2002, 2017.

[13] D. Hu, H. Zhou, Q. Hu, J. Shao, X. Feng, and H. Xiao, "A hydro-mechanical-chemical coupling model for geomaterial with both mechanical and chemical damages considered," *Acta Mechanica Solida Sinica*, vol. 25, no. 4, pp. 361–376, 2012.

[14] S. Rafieepour, H. Jalayeri, C. Ghotbi, and M. R. Pishvaie, "Simulation of wellbore stability with thermo-hydro-chemo-mechanical coupling in troublesome formations: an example from Ahwaz oil field, SW Iran," *Arabian Journal of Geosciences*, vol. 8, no. 1, pp. 379–396, 2015.

[15] R. Shen, T. Li, H. Li et al., "Study on the effect of water on electromagnetic radiation characteristics of fractured sandstone under load," *Environmental Earth Sciences*, vol. 80, no. 3, p. 87, 2021.

[16] X. Liu, L. Wu, Y. Zhang, Z. Liang, X. Yao, and P. Liang, "Frequency properties of acoustic emissions from the dry and saturated rock," *Environmental Earth Sciences*, vol. 78, no. 3, p. 67, 2019.

[17] A. Nicolas, J. Fortin, J. B. Regnet, A. Dimanov, and Y. Guéguen, "Brittle and semibrittle behaviours of a carbonate rock: influence of water and temperature," *Geophysical Journal International*, vol. 206, no. 1, pp. 438–456, 2016.

[18] Z. C. Tang, L. Li, X. C. Wang, and J. P. Zou, "Influence of cyclic freezing-thawing treatment on shear behaviors of granite fracture under dried and saturated conditions," *Cold Regions Science and Technology*, vol. 181, Article ID 103192, 2021.

[19] Y. Zhu, X. Liu, and E. Wang, "Influence of impoundment gravity and pore pressure on reactivation of faults," *Geomechanics and Geophysics for Geo-Energy and Geo-Resources*, vol. 6, no. 4, pp. 1–19, 2020.

[20] J. Li, J. Xu, L. Wang, H. Yang, and Z. Yang, "Water-rock coupling tests on mechanical properties of sandy slate rock mass," *Yantu Gongcheng Xuebao/Chinese Journal of Geotechnical Engineering*, vol. 35, no. 3, pp. 599–604, 2013.

[21] K. G. Li, "Experimental study on unloading damage and permeability characteristics of dolomite based on NMR technology," *Journal of rock mechanics and Engineering*, vol. 38, no. S2, pp. 3493–3502, 2019.

[22] X. Wang, W. Yuan, Y. Yan, and X. Zhang, "Scale effect of mechanical properties of jointed rock mass: a numerical study based on particle flow code," *Geomechanics and Engineering*, vol. 21, no. 3, pp. 259–268, 2020.

[23] J. Yu, X. Chen, Y.-y. Cai, and H. Li, "Triaxial test research on mechanical properties and permeability of sandstone with a single joint filled with gypsum," *KSCE Journal of Civil Engineering*, vol. 20, no. 6, pp. 2243–2252, 2016.

Hindawi
Advances in Materials Science and Engineering
Volume 2023, Article ID 9030449, 10 pages
https://doi.org/10.1155/2023/9030449

Research Article

Acoustic Emission Characteristics and Damage Evolution Analysis of Sandstone under Three-Point Bending Test

Tao Qin, Chen Jiang, Yanwei Duan, Yiwei Wang, and Chao Ju

Key Laboratory of Mining Engineering of Heilongjiang Province College, Heilongjiang University of Science and Technology, Harbin 150022, China

Correspondence should be addressed to Yanwei Duan; 1354070597@qq.com

Received 8 September 2022; Revised 2 October 2022; Accepted 5 October 2022; Published 1 February 2023

Academic Editor: Depeng Ma

In order to study the prevention of roadway roof bending, sinking, and breaking and the prevention of dynamic disasters such as the appearance of rock bursts, three-point bending experiments of sandstone under different spans were carried out. By using stress loading system and acoustic emission technology, the acoustic emission characteristic parameters of the sandstone fracture process were analyzed, the precursory information of rock bending fracture was explored, and the evolution law of sandstone damage based on acoustic emission characteristics was obtained. The results showed that according to the variation of acoustic emission ringing count, the load-time curve was divided into four typical stages: the first stage showed an overall increasing trend; the second stage showed an obvious increasing trend; the third stage showed obvious accelerated growth and the acoustic emission ringing count reached the maximum at the moment of rupture. In the fourth stage, the amplitude and frequency of the ringing count are large and high. With the increase in span, the cumulative ringing counts of AE decreased, and the rate of change gradually decreased. The fracture process of three-point bending sandstone can reflect the precursor information of rock fracture from time domain, frequency domain, and R value (ratio of cumulative acoustic emission ringing count to cumulative energy count). In time domain, the evolution characteristics of AE cumulative ringing count stage II can be used to predict the three-point bending fracture of sandstone. The peak frequency shows a linear increase after a spike and then an accelerated increase to a rupture, and the boundary point between the spike and the linear and nonlinear can be obtained. The decrease in R value can indicate that the main crack is growing in the specimen. According to the damage rate, the characteristics of the damage variables can be divided into five stages: stationary and low, gradually increasing, gradually decreasing, main crack coalescence, and complete fracture. With the increase in span, the fracture damage shows a decreasing trend. The residual damage fluctuates between 0.38 and 0.40 due to the difference in crack propagation trajectory. It has theoretical research value for revealing the internal mechanism of rock bending and fracture and has engineering guiding significance for mine pressure and rock strata control and dynamic disaster prevention.

1. Introduction

Underground mining causes the surrounding rock to be subjected to tensile, compressive, shear, or compound stresses, the root cause of rock damage is that the tensile or shear stresses reach their limits, and the roof bending and sinking fracture process is an important reason for the emergence of mine pressure and dynamic disasters [1–5]. Rock fracture has obvious local characteristics, and scholars have carried out a large number of studies related to the regional and overall damage laws of rock fracture, which have played an important role in understanding the mechanical characteristics and damage mechanisms in the process of rock damage. However, during the fracture and failure process of rock materials, the internal force and deformation process are very complex, and the deformation and damage characteristics of the internal and external zones of rock under different stress states will show obvious differences. The study of the internal microscopic change characteristics of rock during the instability and failure process has been one of the hot and difficult problems in rock mechanics research. In the study of rock fracture

mechanics, three-point bending specimens are simple to produce and easy to operate, and the results are representative, so the study of the fracture process of three-point bending has become particularly important [6–9].

For rock materials or rock-like materials, scholars have carried out a large number of three-point bending tests to study the fracture behavior of rock. Wei et al. [10] analyzed the fracture toughness and tensile strength characteristics of sandstone through a three-point bending test with an incision. Zuo et al. [11] studied the fracture characteristics and crack propagation law of granite under three-point bending through heat treatment. Through comparative analysis of the three-point bending test and the Brazilian splitting test, Heng et al. [12] studied the fracture propagation and evolution mechanism of shale. Lu et al. [13] studied the influence of the prefabricated crack method and prefabricated length on the fracture process through three-point bending test. Zhao et al. [14] studied the influence of particle size on the failure of rock-like materials based on bending test. Through numerical simulation, Han et al. [15] studied the influence of the strength properties of different bedding planes on rock failure during three-point bending.

A large number of scholars have carried out researches on the application of acoustic emission in rock fracture monitoring and achieved fruitful results. Yang [16] studied the microfracture behavior and acoustic emission characteristics of rock under hydraulic coupling through machine learning. Wang et al. [17] used acoustic emission technology to explain the law of granite crack growth by carrying out true triaxial tests on granite and building a cooperative prediction model for rock failure time. Liu et al. [18] carried out the Brazilian splitting test and used acoustic emission technology to explore the relationship between RA (the ratio of rise time to amplitude) and AF (average frequency) of acoustic emission characteristic parameters and crack failure mode. Li et al. [19] carried out a uniaxial loading test of coal and rock mass, used acoustic emission technology for monitoring, and analyzed the instability and failure process of coal and rock mass by analyzing acoustic emission waveform characteristics through the HHT method. Yang et al. [20] carried out triaxial unloading confining pressure experiments with different unloading rates and initial confining pressures and discussed the relationship between fractal characteristics of the AE time series of coal and rock mass and its instability and failure.

Based on the above research, this paper uses stress loading system and acoustic emission technology to carry out three-point bending experiments of sandstone with different spans, analyzes the acoustic emission characteristic parameters of the sandstone fracture process, explores the precursory information of rock bending and fracture, and obtains the sandstone damage evolution law based on acoustic emission characteristic representation. It is of great significance to study the prevention of bending and subsidence fractures of roadway roof and the prevention of dynamic disasters such as rock burst.

2. Introduction to the Three-Point Bending Test

2.1. Experimental Scheme. Dense and uniform sandstone specimens were selected and processed into rectangular specimens of 50 mm × 50 mm × 200 mm, and the six end faces of the specimens were polished by grinding machines, with the dimensional error of the specimens within ±0.3 mm and the verticality error less than 0.25°. The specimens were calibrated one by one by rock sample ultrasound, and specimens with similar wave speed were selected to reduce the influence of discrete sandstone specimens on the experimental results. Rubber bands were attached to the ends of both sides of the specimens to fix the acoustic emission sensor probes, and the damage evolution and precursor information of rock bending fracture at different span distances were obtained through the acoustic emission system for sandstone specimens, see Figure 1.

The sandstone three-point bending experiments were set up in five groups of tests with different lower pivot spans, the spans of the pivot points were set to 180 mm, 170 mm, 160 mm, 150 mm, and 140 mm, and three specimens were carried out in each group of experiments, as shown in Figure 2.

2.2. Experimental System. The experimental setup mainly includes stress loading system and acoustic emission system, see Figure 3.

① Applying vertical load to the specimen by TAW-500 microcomputer-controlled electro-hydraulic servo system, the experimental device load control accuracy is 0.001 kN, and displacement control accuracy is 0.001 mm.

② Application of SH-II acoustic emission system to monitor the acoustic emission signal of the loading process, the frequency measurement range is 1 kHz~3 MHz, the acoustic emission probe model is Nano30, the measurement threshold value is 40 dB under no-load condition, the sampling rate is 1 MSPS, and the waveform signal and characteristic parameters are collected in real time.

3. Analysis of Acoustic Emission Characteristics of Sandstone Fracture Process

Figure 4 shows the relationship between load time and acoustic emission ringing counts for different span spans, and the experiments were loaded with equal displacement, and time was positively correlated with displacement. The load-time curve is divided into four typical stages by the fluctuation of acoustic emission ringing count. At the initial loading to a certain load, there is an obvious concentration of ringing counts, which divides the first stage; with the increase of load, there is a second obvious concentration of ringing counts, which divides the second stage; at the peak moment, there is a third high concentration of ringing counts, which divides the third stage, after the peak is divided into the fourth stage. The rupture of the sandstone under the three-point bending condition is localized and random, so the acoustic emission in the first and second stages also has random sudden rise and aggregation. The auxiliary line added by the load-time curve found that the curve before the peak can be divided into two typical stages,

Figure 1: Specimen preparation.

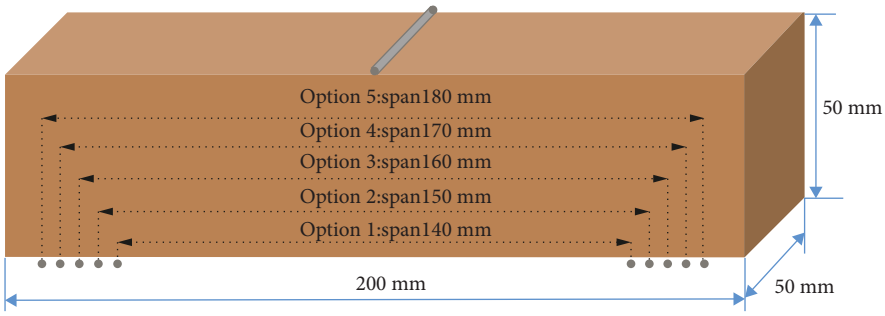

Figure 2: Layout of fulcrum span.

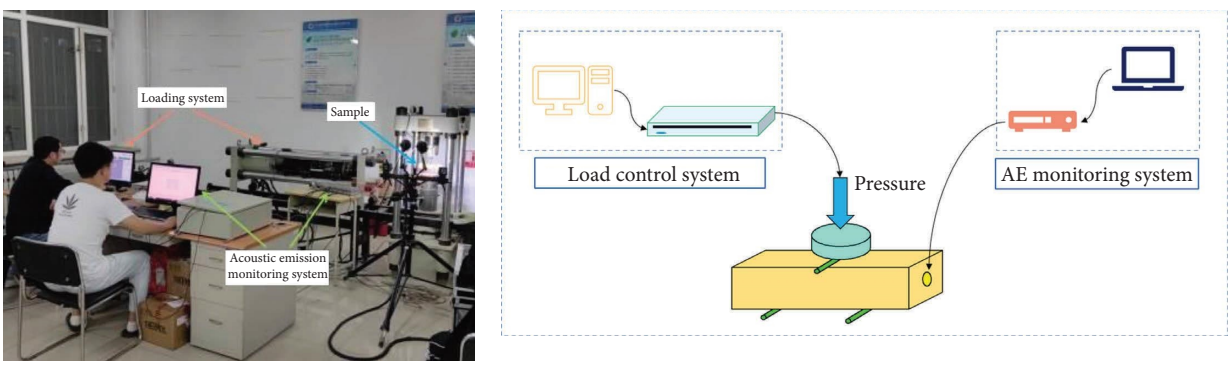

(a) (b)

Figure 3: Experimental system: (a) physical diagram of the experimental system and (b) schematic diagram of the experimental system.

linear elastic stage and nonlinear yielding stage, which indicates that the rock three-point bending experiment is essentially different from the typical uniaxial and triaxial compression deformation process, and the linear change in stage I makes it difficult to judge the compression-density stage by the load-time curve. The so-called neutral layer refers to the plane in the middle of the height direction of the rock sample. Accordingly, with the help of acoustic emission ringing count, fluctuation aggregation characteristics can determine the three-point bending compressive density stage.

The elasto-plastic cutoff point delineated by the load-time curve is not at the same location as the elasto-plastic cutoff point delineated by the acoustic emission ringing count, such as the span 180 mm and 150 mm curves tend to be earlier than the acoustic emission ringing count, and the span 160 mm curve tends to lag behind the acoustic emission ringing count. The consistency of the load-time curve fluctuation and peak moment with the acoustic emission ringing count indicates that the feedback of acoustic emission ringing count on the crack is significant, while the load-time curve trend responds to the characteristics of the sandstone as a whole, which is not sensitive to the change of microcracking.

The analysis of the acoustic emission ringing counts at each stage of different span spans revealed that stage I contains two cases, the acoustic emission signal was collected at the beginning of the experiment (no-load) (180 mm and 160 mm) and the acoustic emission signal was collected after the load was increased (170 mm, 150 mm, and 140 mm). With the increase of span distance, the overall trend of acoustic emission ringing count in stage I is increasing.

Stage II contains three cases, the acoustic emission ringing counts calmly vary slightly (span 170 mm, 150 mm, and 140 mm), slightly increase (span 180 mm), and more drastic fluctuating changes (span 160 mm). The first case is the change from disorderly to orderly microcracks under load, and the area near the rupture zone is more significant; the second case is a higher degree and number of primary crack adjustments, and

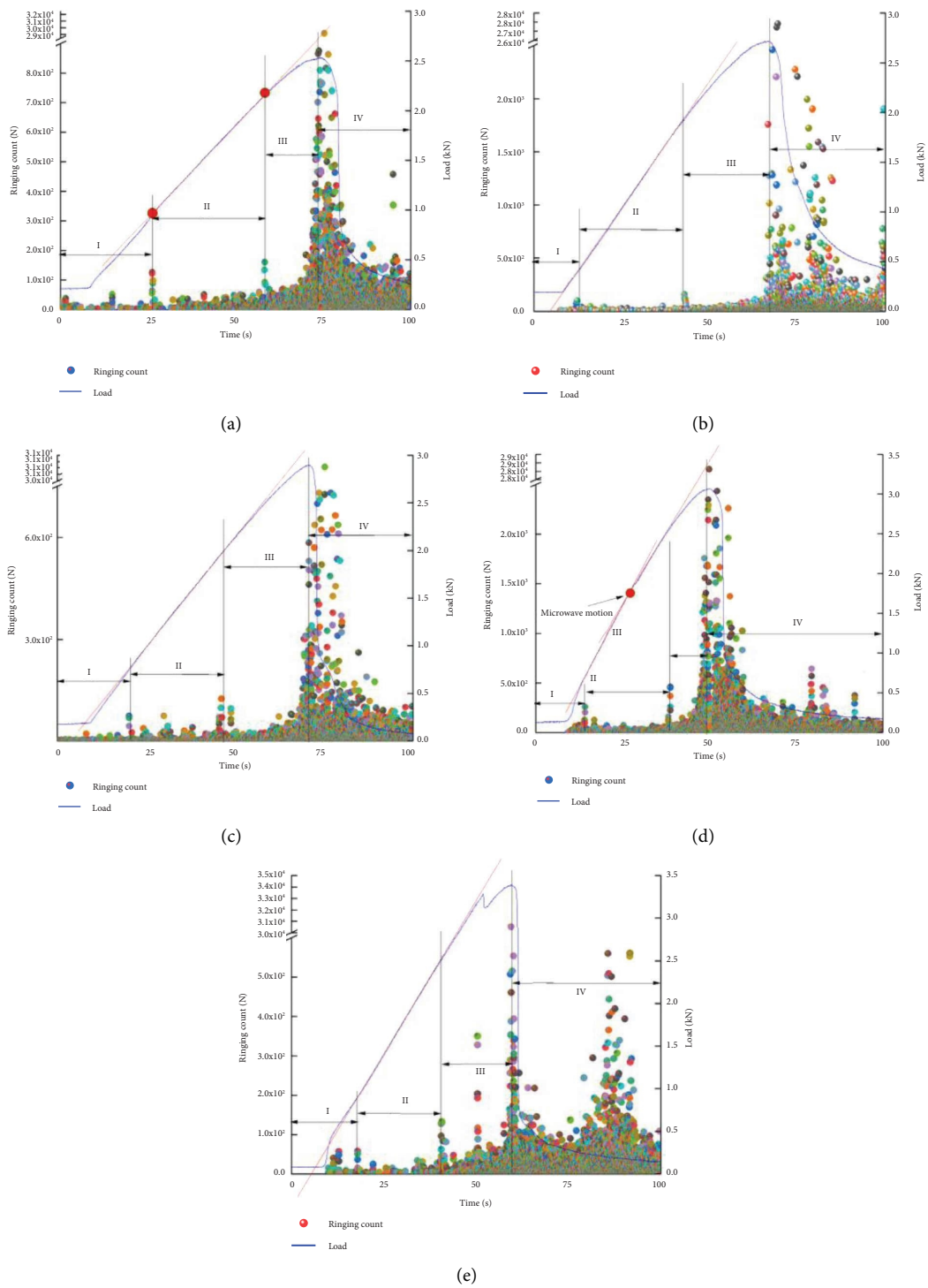

Figure 4: Acoustic emission characteristic parameters and load-time curve of different spans: (a) span 180 mm, (b) span 170 mm, (c) span 160 mm, (d) span 150 mm, and (e) span 140 mm.

the acoustic emission signal is active; the third case is the expansion of local primary cracks under load or has produced newborn cracks, indicating that the specimen has more primary defects or local weak areas, and the smaller load action that the crack sprouting. From the above three cases, we get that the specimen primary state has a significant influence on the crack evolution, and the specimen primary state has a certain randomness. With the increase in span distance, the stage II shows an obvious increasing trend.

The acoustic emission signal enters the active stage in stage III, which is also an important stage for prediction and forecasting. With the increase of load, the acoustic emission ringing count shows obvious accelerated growth, and the acoustic emission ringing count reaches the maximum at the

moment of rupture. This stage contains the expansion of primary microcracks near the rupture zone in the lower part of the neutral layer, the sprouting of new cracks, the penetration of primary cracks, the penetration of newborn cracks and primary cracks, especially at the moment of rupture, the initial fracture in the lower middle has been formed, the high-energy rupture event occurs, and the high ringing counts also appear. Therefore, the arrival of rupture can be judged by the sudden increase in acoustic emission ringing count.

Stage IV is more complicated, including the loss of bearing capacity phase and residual stress phase. By analyzing the crack extension process, it is found that the three-point bending crack penetration is completed under low load, followed by the crack extension period after the peak. Under the load, the crack extension, extension direction, and speed are related to the acoustic emission ringing count. The acoustic emission signal maintains a high amplitude and frequency of ringing counts, according to which also indicates that the sandstone completes the crack extension. The acoustic emission ringing counts in the postpeak residual phase show two situations, one is to keep continuously active (spanning 180 mm, 160 mm, and 150 mm), mainly because the fracture initiation near the lower middle of the sandstone has been formed, and the fracture continues to extend upward under the push of continuous displacement, and the fracture extension speed is relatively smooth; one is aggregation active (spanning 170 mm and 140 mm), and the acoustic emission ringing counts. The high-frequency high count signal occurs again after the active period, indicating that the crack extension is intermittent, and the extension occurs again after the deformation reaches a certain degree. It is found that the acoustic emission ringing count is more active postpeak than prepeak, mainly because of the difference in the intensity and frequency of the elastic wave released by the crack sprouting and expansion.

Figure 5 shows the cumulative acoustic emission ringing counts at the peak of different spans. With the increase of the span, the accumulated acoustic emission ringing counts show a decreasing trend, and the rate of change is gradually decreasing, which indicates that the intensity of rupture is gradually decreasing, but the decay. The rate of change is decreasing, indicating that the intensity of rupture is decreasing, but the decay is getting faster.

4. Analysis of Sandstone Rupture Precursor Information

Prerupture of coal rock leads to obvious acoustic emission phenomenon due to intensive activity of cracks, and this stage is relatively short compared to the prepeak period, so accurate capture and judgment of acoustic information are the key stage of early warning forecasting. In order to explore the precursor information of rock rupture more comprehensively, we analyze the acoustic law of three-point bending sandstone prerupture from the time domain, frequency domain, and ratio of acoustic emission cumulative ringing count to cumulative energy count (R value) and give the rupture warning characteristics in this way.

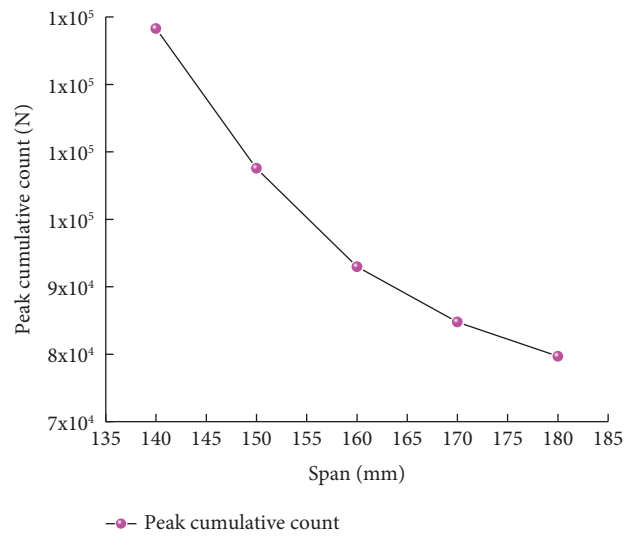

Figure 5: Cumulative ringing count curve of acoustic emission in different spans.

4.1. Time Domain Analysis. From the perspective of time domain precursor information identification, it is crucial to find the acoustic emission ringing count anomaly at the prefracture stage. The whole curve of acoustic emission cumulative ringing count shows a significant and rapid growth in stage II, which needs to be refined and analyzed to dig deeper into the dynamic properties of acoustic emission cumulative ringing count at the prerupture stage, taking the span of 140 mm as an example, as shown in Figure 6.

Initially, there is a sudden jump in growth, indicating that at this time, the rock sample breaking. The first-stage and second-stage slopes are 59 and 134, respectively, and the microcrack extension enters a more stable period; after the linear end point, the accumulated acoustic emission ringing counts show an accelerated growth trend, a virtual circle is drawn with the linear end point as the vertical line, the end point of the arc is the starting point of the accelerated growth, and the acceleration phase calculated by the angle of the acceleration stage is 64.6° by diameter and arc length, and the microcracks converge and coherence at this stage.

The above analysis can be used to predict the sandstone three-point bending rupture by the evolution characteristics of the acoustic emission cumulative ringing count stage II. The initial feedback is the jump growth of acoustic emission ringing count, the secondary feedback is the dividing point of the linear growth of stage II, and the third feedback is the starting point of the arc, whose corresponding percentage of forecast time is 81%, 87%, and 97%, respectively, and the forecast data are evenly distributed and progressive step by step, indicating that the selected characteristic parameters and cutoff points are reliable.

4.2. Frequency Domain Analysis. According to the frequency spectrum law at different crack evolution stages of three-point bending test, the peak frequency shows an increasing trend before the peak point, which can reveal the precursor information of fracture from the perspective of frequency

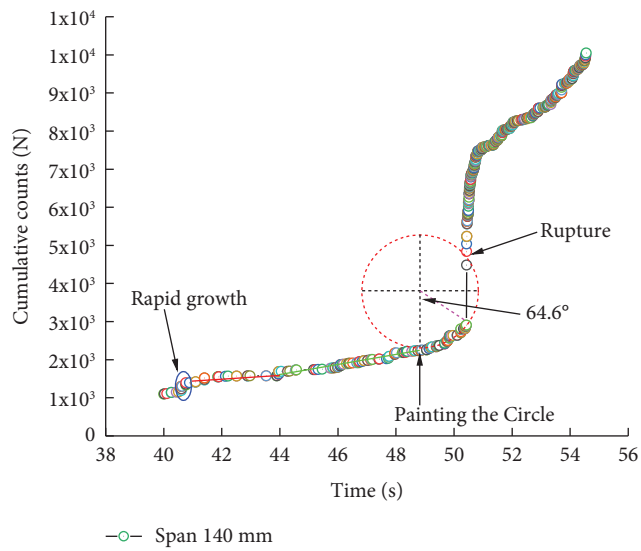

Figure 6: Variation curve of acoustic emission cumulative ringing count in the whole loading process.

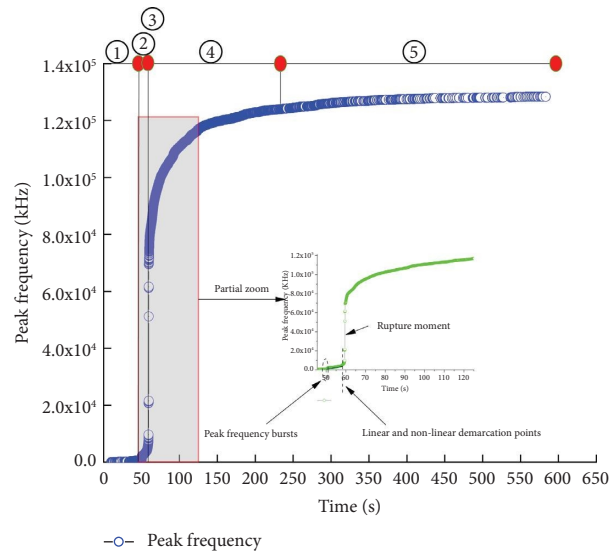

Figure 7: Cumulative peak frequency curve of acoustic emission.

domain. Figure 7 gives the change curve of the accumulated peak frequency of acoustic emission, which can be divided into five stages according to the analysis of its change law, the first stage of low peak frequency and slow growth rate is the microcrack adjustment and budding activity period; the second stage of peak frequency accelerated growth is the crack expansion and penetration period; the third stage of the rapid growth of peak frequency is the crack local penetration period, in the lower part of the specimen to form. The fourth stage of peak frequency deceleration growth is the crack extension period, and the lower part of the specimen cracks gradually to the upper loading line extension; the fifth stage of peak frequency remains stable; at this time, the main control fracture has been formed, three-point bending rupture surface separation process of sandstone rupture zone tear and slip caused by changes. The second and third stages of peak frequency are important intervals for precursor information identification, so it is locally amplified. The analysis found that the peak frequency showed a sudden increase followed by linear growth and then accelerated growth to rupture, and the two characteristic points of peak frequency were obtained as sudden increase and linear and nonlinear demarcation point, whose corresponding percentage of forecast time was 85% and 97%, respectively, indicating that it is reasonable and feasible to forecast rupture from frequency domain perspective.

4.3. Acoustic Emission R Value. Acoustic emission ringing counts characterize the active degree of cracking, and acoustic emission energy characterizes the energy released from the crack source. Using the ratio of cumulative acoustic emission ringing counts and cumulative energy counts defined as the R value [21], the R value can characterize the degree of internal energy concentration, which is given by

$$R = \frac{\sum N}{\sum E}. \tag{1}$$

Figure 8 gives the variation pattern of R value during the loading to fracture of the three-point bending sandstone. The R value remains basically unchanged in the late peak period, indicating that weaker cracking activity occurs after the peak. The R value changes are more drastic in the prepeak period and the early postpeak period, and local amplification analysis is performed for this stage.

The initial loading stage R value shows a sharp increase and then decreasing trend; at this time, the acoustic emission signal experienced a relative low-energy high ringing count and high-energy high ringing count stage; the decrease of R value is not the generation of large fissures, the initial loading energy and ringing count are relatively small, the primary defect adjustment triggered the growth of energy ringing count leads to the decrease of R value, and the initial loading stage R value change law reference value is not significant.

The sudden increase of R value in the middle of loading shows linear growth and one sudden increase, which indicates that the acoustic emission activity is becoming more and more intense, the slope of the curve increases significantly after the sudden increase of R value, the growth rate of acoustic emission energy decreases, and the growth rate of acoustic emission ringing count increases. R value of sudden increase can be used as a precursor feature, and the unstable deformation of the specimen occurs.

The R value decreases and then increases to the peak and then decreases again at the moment of rupture, which also indicates that the R value can characterize the degree of crack expansion and the stage in which it is located. R value decreases indicate that the through crack is breeding the main rupture, so the low point of the R value decreasing process and the high point of the increasing process at this stage can be used as the precursor of rupture.

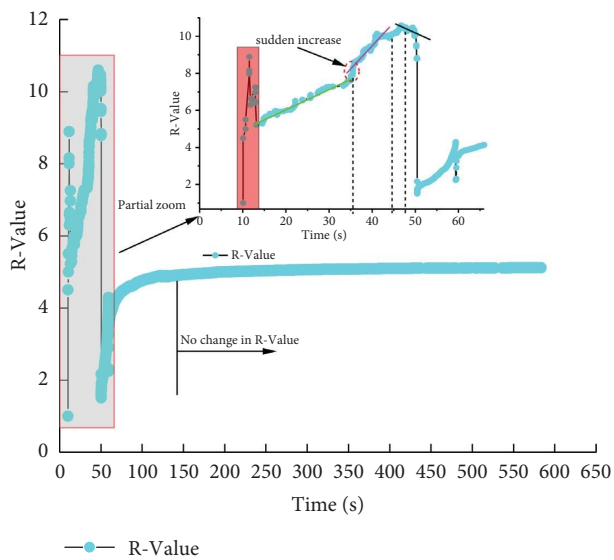

Figure 8: Variation curve of R value in the whole loading process.

5. Analysis of the Damage Evolution Law Characterized by Acoustic Emission Characteristic Parameters

During the sandstone three-point bending experiment, the crack emerges and forms a cracking point, and the crack extends upward from the cracking point to the fracture of the specimen. The sandstone damage evolution process of the three-point bending experiment can be divided into two stages, namely, the damage formation stage and the residual damage stage. Based on the consistency of damage and crack evolution, this section uses acoustic emission characteristic parameters to characterize the damage, analyze the damage evolution law of the whole process of three-point bending damage, and study the damage evolution characteristics of sandstone experimental sandstone with different span three-point bending.

Under the load, the sandstone loading line corresponding to the effective cross-sectional area will decrease, and the equivalent cross-sectional area after fracture is 0. In this way, the concept of damage is proposed [22], namely,

$$D = \frac{A_{\text{orig}} - A_{\text{loss}}}{A_{\text{orig}}}, \\ = 1 - \frac{A_{\text{loss}}}{A_{\text{orig}}}, \tag{2}$$

where D is the damage variable, between 0 and 1, 0 is no damage, 1 is complete fracture; A_{orig} is the longitudinal cross-sectional area of the loading line of the undamaged specimen; A_{loss} is the longitudinal cross-sectional area of the loading line of the damaged specimen.

In the practical application process, the effective area of the longitudinal section of the three-point bending loading line is difficult to determine, and referring to the method proposed in the paper [23] to determine the damage variable through the effective stress, the effective stress can be determined during the single and triaxial experiments, and the stress cannot be calculated for the three-point bending experiments, so the damage variable is determined by the effective load as follows:

$$F' = \frac{F}{1 - D}, \tag{3}$$

where F' is the effective load, and F is load, unit kN.

According to the theory of elastic mechanics, the relationship between the displacement of sandstone and the load and damage variables is obtained as follows:

$$d = \frac{F'}{k}, \\ = \frac{F}{k(1 - D)}, \tag{4}$$

where d is the displacement of the sandstone loading line in mm; k is the elastic constant.

Since the rock particles and cementation components are random, the strength of microunits is also random, and assuming that the microunit strength obeys the Weibull statistical distribution [16].

$$\varphi(a) = \frac{m}{a_0}\left(\frac{a}{a_0}\right)^{m-1} e^{-(a/a_0)^m}, \tag{5}$$

where a is the microelement mechanical parameter, a_0 is the average microelement mechanical parameter, and m is the homogeneity of the sandstone.

Under the action of load, the sandstone particle microelement transforms from the stable state to the unstable state, and the probability density function is the damage rate calculated by counting the unstable state of the microelement, by which the macroscopic damage degree of the specimen can be characterized. Assuming that the number of unstable microelements is n when a certain load is reached, the number of unstable microelements inside the specimen when the displacement increases is, and the number of microelements when the displacement is d is obtained as follows:

$$n(d) = \int_0^d N\phi(x)\mathrm{d}x, \\ = N\left(1 - e^{-(d/a_0)^m}\right). \tag{6}$$

The rock will release strain energy outward during the crack extension process, and the acoustic emission characteristic parameters are consistent with the strain energy [24], and the damage degree of the rock can also be characterized by the acoustic emission characteristic parameters, and the relationship between the damage variable D and the acoustic emission characteristic parameters and statistical microelement changes is given by

$$D = \frac{N_1}{N_m}, \\ = 1 - e^{-(d/a_0)^m}, \tag{7}$$

where N_1 is the cumulative acoustic emission ringing count when the displacement is d, and N_m is the cumulative

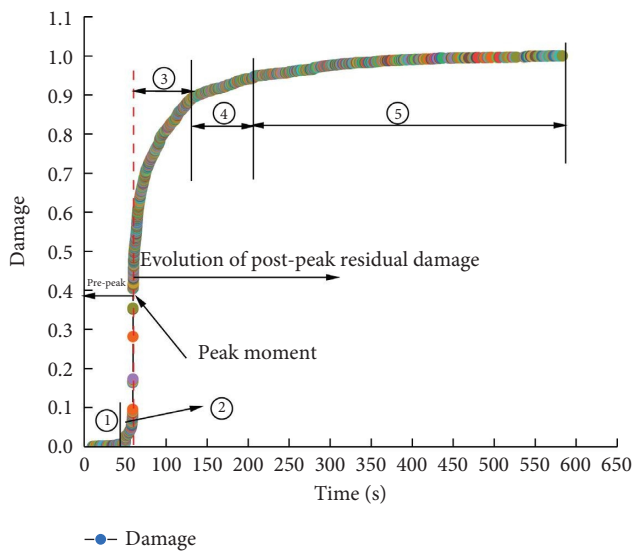

Figure 9: The change law of damage variables characterized by acoustic emission characteristic parameters.

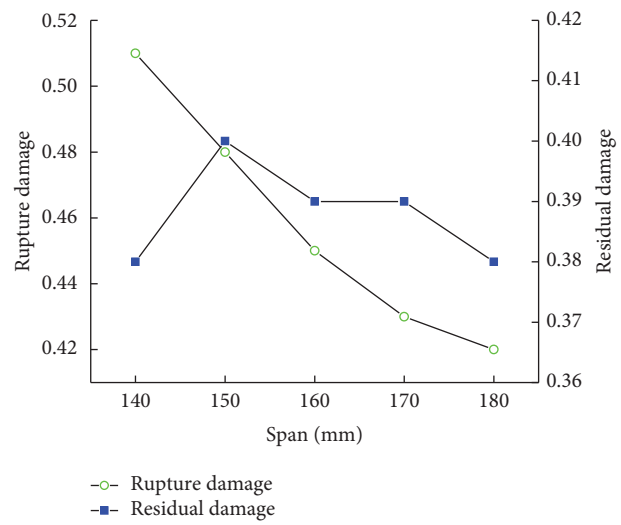

Figure 10: Characteristic analysis of different span damage evolution stages.

acoustic emission ringing count when the sandstone is completely fractured.

The above analysis is based on the fracture of the rock when it reaches the ultimate bearing capacity. The specimen cracked when the peak load was reached in the three-point bending experiment and did not fracture, and the degree of damage was still increasing during the extension and expansion of the crack. According to the characteristics of the three-point bending experiments, the residual damage variable D_t is proposed, and the damage variable expression is

$$D_t = \frac{N_m - N_1}{N_m}. \tag{8}$$

Through the acoustic emission cumulative ringing count and theoretically derived damage formula, the damage characteristics of the specimen parameters are calculated, the damage degree of the peak moment of the specimen is only 0.51, the residual damage variable of the fracture process after cracking reaches 0.49, uniaxial, triaxial, and shear of the experimental peak moment damage are generally above 0.8, and the residual damage of the residual stage after the peak of the three-point bending experiment has the significance of the discussion [25–27].

Specimen damage variable changes pattern, see Figure 9. According to the damage variable, curve characteristics will be divided into five stages, stage I damage is small, the rate of change is smooth and low, it can be considered that this stage of sandstone specimens under the action of the load did not occur damage; stage II damage change rate gradually increased, the damage entered a violent evolutionary stage, this stage formed the initial fracture, the peak moment of load damage variable increased to 0.51, stage III damage rate shows a gradually decreasing trend, the specimen crack occurs relatively stable extension, and this stage damage variable increased by 0.38; stage IV main control crack has penetrated, the sandstone has lost the load-bearing capacity, the specimen completely fractured, and damage variable reached 0.94; stage V is mainly sandstone specimen completely fractured after the slip and friction between the fractured rock blocks.

In order to analyze the damage evolution characteristics of sandstone in three-point bending experiments with different span distances, the curves of rupture damage and residual damage with different span distances were drawn, as shown in Figure 10. With the increase of span distance, the rupture damage showed a decreasing trend; the residual damage fluctuated between 0.38 and 0.40, and the crack extension trajectories were different, but the unfolding lengths were similar, so the residual damage results were similar.

6. Conclusion

Three-point bending experiments were carried out on sandstone samples with different spans using a press and acoustic emission system. AE characteristic parameters, fracture law, and damage evolution law of sandstone were obtained. The main conclusions are as follows:

(1) According to the fluctuation of acoustic emission ringing count, the load-time curve was divided into four typical stages: the first stage showed an increasing trend; the second stage showed an obvious increasing trend. The third stage showed an obvious acceleration of growth, and the acoustic emission ringing count reaches the maximum at the moment of rupture. In the fourth stage, the amplitude and frequency of the ringing count are large and high. With the increase in span, the cumulative ringing counts of AE showed a decreasing trend, and the rate of change gradually decreased.

(2) The failure process of three-point bending sandstone can reflect the precursor information of rock failure from time domain, frequency domain, and R value. In time domain, the evolution characteristics of stage II of acoustic emission cumulative ringing count can

be used to predict the three-point bending fracture of sandstone. The peak frequency shows a linear increase after a spike and then an accelerated increase to a rupture, and the boundary point between the spike and the linear and nonlinear can be obtained. The decrease in R value can indicate that the main crack is growing in the specimen.

(3) According to the damage rate, the damage variable characteristics of the specimen can be divided into five stages: stationary and low, gradually increasing, gradually decreasing, main crack through, and complete fracture. With the increase in span, the fracture damage shows a decreasing trend. The residual damage fluctuates between 0.38 and 0.40 due to the difference in crack propagation trajectory.

Data Availability

The data used to support the study are available within the article.

Conflicts of Interest

The authors declare that they have no conflicts of interest.

Acknowledgments

This study was supported by the Outstanding Young Talents Project of Central Government for the Reform and Development of Local Universities (2020YQ13) and Scientific and Technological Key Project of "Revealing the List and Taking Command" in Heilongjiang Province: Study on Geological Model and Ventilation Model of Intelligent Mining in Extremely Thin Coal Seam (2021ZXJ02A03).

References

[1] T. Li, K. X. Li, X. Y. Pi, and C. Fang, "Time-dependent behavior of acoustic emission feature parameters of sandstone under bending load," *Journal of China Coal Society*, vol. 43, no. 11, pp. 3115–3121, 2018.

[2] H. P. Kang, "Seventy years development and prospects of strata control technologies for coal mine roadways in," *China" Chinese Journal of Rock Mechanics and Engineering*, vol. 40, no. 01, pp. 1–30, 2021.

[3] H. P. Kang, G. Xu, B. M. Wang et al., "Forty years development and prospects of underground coal mining and strata control technologies in China," *Journal of Mining and Strata Control Engineering*, vol. 1, no. 02, pp. 7–39, 2019.

[4] Q. X. Qi, Y. Z. Li, S. K. Zhao et al., "Seventy years development of coal mine rockburst in China: establishment and consideration of theory and technology system," *Coal Science and Technology*, vol. 471, no. 09, pp. 1–40, 2019.

[5] S. J. Chen, Z. H. Zhao, F. Feng, and M. Z. Zhang, "Stress evolution of deep surrounding rock under characteristics of bi-modulus and strength drop," *Journal of Central South University*, vol. 29, no. 2, pp. 680–692, 2022.

[6] C. F. Deng, J. F. Liu, L. Chen, Y. Li, and G. Xiang, "Study on the mechanical behavior and acoustic emission characteristics of fracture of granite with different grain sizes," *Geotechnics*, vol. 37, no. 08, pp. 2313–3232, 2016.

[7] W. C. Zhu, S. L. Wang, and C. A. Tang, "Computer simulation of concrete three-point bending test," *Journal of Northeastern University*, vol. 20, no. 5, pp. 533-534, 1999.

[8] H. P. Xie and Z. H. Chen, *Rock Mechanics*, Science Press, Beijing, China, 2004.

[9] J. P. Zuo, H. W. Zhou, and Y. J. Liu, "Study of characteristic parameters of three-point bending damage of sandstone at different temperatures," *Journal of Rock Mechanics and Engineering*, vol. 29, no. 04, pp. 64–71, 2010.

[10] J. Wei, W. C. Zhu, R. F. Li, L. L. Niu, and Q. Y. Wang, "Experiment of the tensile strength and fracture toughness of rock using notched three point bending test," *Journal of Water Resources and Architectural Engineering*, vol. 14, no. 03, pp. 128–132, 2016.

[11] J. P. Zuo, H. W. Zhou, X. Fan, and Y. Ju, "Research on fracture behavior of BEISHAN granite after heat treatment under three-point bending," *Chinese Journal of Rock Mechanics and Engineering*, vol. 32, no. 12, pp. 2422–2430, 2013.

[12] S. Heng, X. Liu, X. Z. Li, X. D. Zhang, and C. H. Yang, "Study on the fracture propagation mechanisms of shale under tension," *Chinese Journal of Rock Mechanics and Engineering*, vol. 38, no. 10, pp. 2031–2044, 2019.

[13] H. Lu, X. F. Feng, C. X. Yang, and X. W. Zhang, "Effect of different notch prefabrication methods and notch lengths on rock three-point bending test," *Rock and Soil Mechanics*, vol. 42, no. 04, pp. 1115–1125, 2021.

[14] K. Zhao, Y. T. Zhou, P. Zeng, and C. Y. Lu, "Experimental study on acoustic emission characteristics of rock-like materials with different particle sizes under three-point bending," *Journal of China Coal Society*, vol. 43, no. 11, pp. 3107–3114, 2018.

[15] D. X. Yang, "Acoustic emission behavior characteristics of rock micro-fracture evolution based on deep learning," *Chinese Journal of Rock Mechanics and Engineering*, vol. 41, no. 8, p. 1728, 2022.

[16] C. L. Wang, C. Cao, C. F. Li, X. S. Chuai, G. M. Zhao, and H. Lu, "Experimental investigation on synergetic prediction of granite rockburst using rock failure time and acoustic emission energy," *Journal of Central South University*, vol. 29, no. 4, pp. 1262–1273, 2022.

[17] X. L. L Z. Liu, X. B. Li, M. S. Han, and L. Q. Yang, "Acoustic emission and micro-rupture characteristics of rocks under Brazilian splitting load," *Chinese Journal of Engineering*, vol. 41, no. 11, pp. 1422–1432, 2019.

[18] X. L. Li, S. J. Chen, S. M. Liu, and Z. H. Li, "AE waveform characteristics of rock mass under uniaxial loading based on Hilbert-Huang transform," *Journal of Central South University*, vol. 28, no. 6, pp. 1843–1856, 2021.

[19] R. Yang, L. Jiakun, B. Zhou, and D. P. Ma, "Rock unloading failure precursor based on acoustic emission parametric fractal characteristics," *Lithosphere*, vol. 2022, Article ID 8221614, 2022.

[20] W. G. Han, Z. D. Cui, T. W. Tang, J. Y. Zhang, and Y. Z. Wang, "Effects of different bedding plane strength on crack propagation process under three points bending," *Journal of China Coal Society*, vol. 44, no. 10, pp. 3022–3030, 2019.

[21] G. Liu, Y. M. Li, F. K. Xiao, S. J. Huang, and R. F. Zhang, "Study on failure mechanics behavior and damage evolution law of yellow sandstone under uniaxial triaxial and pore water action," *Chinese Journal of Rock Mechanics and Engineering*, vol. 38, no. S2, pp. 3532–3544, 2019.

[22] C. B. Li, H. P. Xie, and L. Z. Xie, "Experimental and theoretical study on the shale crack initiation stress and crack damage

stress," *Journal of China Coal Society*, vol. 42, no. 4, pp. 969–976, 2017.

[23] X. R. Wang, E. Y. Wang, F. Liu, X. L. Li, H. Wang, and D. X. Li, "Macro-crack propagation process and corresponding AE behaviors of fractured sandstone under different loading rates," *Chinese Journal of Rock Mechanics and Engineering*, vol. 37, no. 6, pp. 1446–1458, 2018.

[24] Y. N. Rabotnov, "On the equation of state of creep," *Proceedings of the Institution of Mechanical Engineers, Conference Porceedings*, vol. 178, no. 1, pp. 2117–2122, 1963.

[25] J. Lemaitre, "A continuous damage mechanics model for ductile fracture," *Journal of Engineering Materials and Technology*, vol. 107, no. 1, pp. 83–89, 1985.

[26] C. A. Tang, S. L. Wang, and Y. F. Fu, *Numerical Experiments on Rock Fracture Process*, Science Press, Beijing, China, 2003.

[27] K. Zhao, J. F. Jin, X. J. Wang, and K. Zhao, "Study on the relationship between sound velocity of rock and its damage and acoustic emission," *Geotechnical Mechanics*, vol. 28, no. 10, pp. 2105–2109, 2007.

Hindawi
Advances in Materials Science and Engineering
Volume 2023, Article ID 4596586, 12 pages
https://doi.org/10.1155/2023/4596586

Research Article

Experimental Study on the Effect of Supercritical CO_2 on Mechanical Properties and Fracture Characteristics of Longmaxi Shale

Ran Zhang,[1,2] **Hao Yan**,[1] **Lin Yang**,[3] **Kun Liao**,[1] **and Lei Tao**[4]

[1]*School of Mechanical Engineering, Xihua University, Chengdu 610039, China*
[2]*State Key Laboratory of Oil and Gas Reservoir Geology and Exploitation, Southwest Petroleum University, Chengdu 610500, China*
[3]*Tight Oil and Gas Exploration and Development Project Department of PetroChina Southwest Oil and Gasfield Company, Chengdu, China*
[4]*Chengdu University of Technology, Chengdu 610039, China*

Correspondence should be addressed to Ran Zhang; zhangran87@foxmail.com

Received 28 July 2022; Revised 15 October 2022; Accepted 19 January 2023; Published 30 January 2023

Academic Editor: Qing Ma

Conventional hydraulic fracturing techniques typically consume large amounts of water when producing shale gas. Fracking fluids may cause environmental pollution. In contrast, supercritical carbon dioxide ($scCO_2$) (above 31.8°C, 7.29 MPa) can displace CH_4 in shale reservoirs. Achieve CO_2 sequestration while increasing the shale gas production. We studied the mechanical properties and fracture characteristics of a shale under the action of $scCO_2$, nitrogen, helium, and water by comparing the triaxial compression tests of shale samples with seven coring angles. The results show that: (1) $scCO_2$ effectively reduced compressive strength of the shale and weakened the anisotropy of shale; (2) $scCO_2$ caused the content of dolomite, calcite, and illite to decrease by 4.7%~13.5%, respectively; (3) $scCO_2$ produced micropores and microfractures 10 times larger than the original size in the microstructure. These microstructures can help improve the seepage and gathering of shale gas, leading to enhanced shale gas recovery and CO_2 storage.

1. Introduction

Current hydraulic fracturing of shale needs thousands of tons of water and proppant. Besides, the flow-back fluid is typically harmful to the environment, making its handling difficult and costly. In addition, recent research showed large-scale multistage hydraulic fracturing will generate microseismic [1], which may further trigger stronger geological movements and be a serious threat to people's lives and properties. China is a country with scarce water resources per capita, and the distribution of water resources is uneven. Most of the shale gas-rich areas in China are water-scarce, such as mountains and hills [2], and conventional hydraulic fracturing requires large amounts of water. Shale gas extraction will increase water pressure on local water resources. The large amounts of water injection into shale formations may cause ground sliding and trigger earthquakes. This dramatically increases the cost of hydraulic fracturing methods; therefore, new nonwater fracturing methods for shale gas production become very attractive in these regions. On the other hand, carbon capture and storage (CCS)-technologies are becoming more practical in reducing greenhouse gas emissions [3]. Carbon capture has already been applied commercially in certain industry branches, and CO_2 is widely used in the natural gas processing industry [4–7]. Supercritical CO_2 has the characteristics of low viscosity, low-surface tension, high diffusivity, no hydration with clay, nontoxic. Injecting the industrial liquefied CO_2 into shale can realize the following: (1) $scCO_2$ jet fracturing; (2) effective increase of shale

permeability; (3) replacement or displacement of shale gas to enhance its recovery; (4) carbon geological sequestration [8–11]. Currently, $scCO_2$ injection has become an environment-friendly alternative to the conventional hydraulic fracturing. Hence, to better understand its application in shale gas production and carbon sequestration, it is important to study the interaction between $scCO_2$ and shale.

1.1. Breaking Rocks with $scCO_2$ Jet. Kolle and Marvin [12, 13] introduced $scCO_2$ in the coiled tubing drilling method. He found that $scCO_2$ jet has a stronger permeability in the reservoir rock and can effectively reduce the fracture pressure of the rock. Du et al. [7, 14] carried out an experimental study on sandstones breaking with the $scCO_2$ jet. Their study indicated that $scCO_2$ caused the phenomena of large volumetric layered broken. Liu et al. [15] studied the fracture extension behaviour under the influence of supercritical CO_2 jets and different fracture types.

1.2. Chemical Reaction between $scCO_2$ and Minerals in Sandstone. Many researchers [16–25] studied the chemical reactions of CO_2-sandstone-brine under the supercritical condition of CO_2. They found that $scCO_2$ corroded the mineral surface and disrupted the original pore structure. Irregular etching marks were found on the surface of the mineral crystals under the scanning electron microscope.

1.3. Chemical Reactions between $scCO_2$ and Minerals in Shale. Lahann et al. [26] put shale caprock in CO_2-brine under high temperature and pressure to study their reactions. Results showed that the relative contents of some elements in the filtrate were higher than that in the control case. Xu et al. [27] found that kerogen decomposed stably and continuously in CO_2 with high pressure. In addition, Angeli et al. [28] detected hydrogen (1% in content) at the CO_2 outlet during his experiments on the $scCO_2$-shale caprock, which confirmed shale organic matter decomposed under $scCO_2$ condition. Moreover, Allawzi et al. [29] found that kerogen debris also decomposed under the $scCO_2$ condition.

1.4. Changes of Rock Physical Properties. Lu et al. [30] found that the shale treated with supercritical CO_2 slickwater had a significant increase in the number of micropores, and its pore area and volume increased. Yang et al. [31] investigated the effect of porosity change on the adsorption performance of CH_4 after supercritical CO_2 action on the shale at different temperature and pressure conditions. Fatah et al. [32] tested the effect of different mineral contents and temperatures on the hydrophilicity of shale under the action of supercritical CO_2. The results show that shales with high-quartz content are highly hydrophilic. Wollenweber et al. [33] studied the carbon sequestration efficiency and found that CO_2 could decrease the breakthrough capillary pressure of the caprock by two-thirds. In addition, repeated CO_2 treatments led to decreased capillary sealing efficiency and increased shale caprock permeability. Vialle and Vanorio [34] observed permanent change in microporous structures when studying the reaction between carbonate rocks and injected CO_2-saturated water.

While the study of the properties of $scCO_2$ and its effect on the microstructure of different types of rocks is important, its influence on the properties of shale gas formations cannot be ignored. Shale from Longmaxi shale gas formation in the Fuling shale gas field, Chongqing City, China, is rich in organic matter with an average content of 2.5%, thermal maturity of 2.5%, and porosity of 2.5% [35–37]. Due to its special characteristics, it is critical to clear the interactions and effects between $scCO_2$ and shale. In this study, we collected specimens from the aforementioned location and carried out strength tests at 7 dissimilar coring angles under $scCO_2$ condition. The mechanical characteristics and fracture properties were studied systematically at the microscopic scale.

2. Experimental Section

2.1. Preparation of Shale Samples. The Longmaxi Formation rocks and minerals are highly brittle, mainly because they contain a large number of silicified graptolites, radiolarians, and other fossils [38]. Collect original shale outcrops and remove the regolith.

Figures 1 and 2 show that the test samples are drilled from the same outcrop shale to reduce errors caused by differences in mineral compositions. Set the coring angle β as 0°, 15°, 30°, 45°, 60°, 75°, and 90°, respectively. These samples were further cut into standard cylinders to ensure smoothness, parallelism, and perpendicularity to the axis on both end faces.

Then the porosity of specimens is measured by helium, which is based on the principle of pressure pulse [39], and the test pore pressure and confining pressure are 2 MPa and 5 MPa, separately. The results show that most of the specimens belong to the bedrock (the density is 2.55 g/cm^3 on average). Porosity is 3.5% on average, and the permeability is on the level of nanodarcy and varies from 141 nD to 323 nD with an average of 200 nD. So, the sample-to-sample variation is so small that the specimens can be considered as the same.

2.2. Experimental Apparatus and Method. The experimental equipment is shown in Figure 3. To create $scCO_2$ condition (above 31.8°C, 7.29 MPa), the following improved experimental system main components and workflows are used [40]. (1) An air-driven and liquefied gas booster are used to increase the gas pressure, as shown in Figures 3(a) and 3(b). Then, they are connected to the inlet line at the top of the specimen through pipelines. Finally, pumped high-pressure CO_2 into the sealed specimen through the confining pressure barrel. (2) A heating ring is installed around the confining pressure barrel to increase temperature. A temperature sensor is located beside the specimen to measure the temperature of the specimen, as shown in Figure 3(b). (3) A confining unit provides the pressure required to fracture the specimen by pressurizing hydraulic oil in the confining pressure barrel.

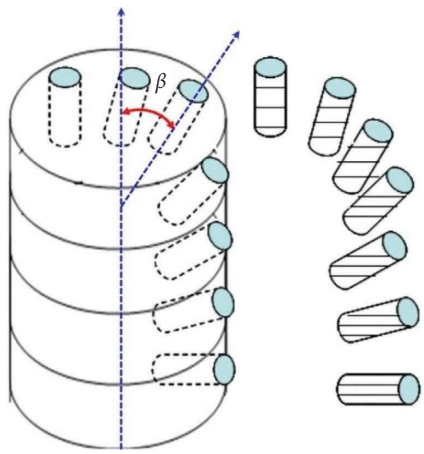

Figure 1: Shale specimens of 7 different coring angles.

Figure 2: Prepared shale specimens. The 7 specimens in the first row were used for the test 1 at scCO2 condition; those in the second row were used for the test 2 with N_2 at the same temperature and pressure condition as test 1; those in the third row were used for the test 3 with helium gas at the same temperature as test 1.

The specimen is placed into the triaxial apparatus as shown in Figure 3(c). The experiment procedures are listed as follows: (1) wrap the specimen with heat shrinkable tubing; (2) install the displacement sensor and temperature sensor; (3) seal the barrel; (4) adjust experimental conditions; (5) maintain the experimental conditions to ensure shale pores filled with $scCO_2$, (6) impose the axial load to begin the test under the uniform loading rate of 0.04 mm/min until specimen damages.

Table 1 shows that the experiments are designed to include four test groups. Each group were carried out at seven different coring angles (0°, 15°, 30°, 45°, 60°, 75°, and 90°), with 28 triaxial compression experiments in total. Nitrogen gas, Helium gas, and clear water at the same temperature and pressure ([a] Confining pressure. [b] Pressure of the test gas in Table 1). were selected as the control groups.

3. Results and Discussion

3.1. Rock Mechanics and Characteristics of the Longmaxi Shale. The shale's mechanical anisotropy is notable. The triaxial compression strength in the helium group (with an average of 310 MPa) is lower than that in the $scCO_2$ experimental group (with an average of 314 MPa), in the water control group (with an average of 321 MPa), and in the nitrogen control group (with an average of 328 MPa). The main reason is that gas injection at high pressure leads to high pore pressure, which decreases the absolute value of the confining pressure. Some literature [41, 42] showed that natural damages are compressed more heavily under higher confining pressure, which increases the triaxial compression strength of the shale. In contrast, hydration leads to a reduction in the compression strength of the shale.

Table 2 shows the results of core strength tests with different coring angles under the action of different media. Compared to the nitrogen control group, the compression strength of the shale decreased by between 2% and 20% under the influence of $scCO_2$, with a maximum absolute decrease of 49 MPa. The reduced compression strength of the Longmaxi shale is 2–5% greater than that found in the Zheng's et al. experimental results [41] under the CO_2–NaCl solution environment. The compression strength of the shale under the influence of $scCO_2$ decreased by between 1% and 6% more than the water control, with a maximum absolute decrease of 15 MPa. Some studies [43, 44] have shown that the hydration of shales leads to a reduction in strength due to the dissolution of some minerals and the dislodging of particles from microperspectives. This study aims to investigate the effect of $scCO_2$ on the mechanical properties of shale. The mechanical properties of shale under the action of clear water will change due to the influence of hydration and other factors. To exclude interference, this study will mainly conduct a comparative experimental study with inert gases.

Figure 4 shows that the relation of triaxial compression strength and coring angle can be fitted by a sine curve with high R^2. Triaxial compression strength increases gradually with β and reaches its maximum at $\beta = 15°$. Then, it decreases and reaches the minimum value at $\beta = 60°$. However, it increases again when β is added from 60° to 90°.

Figures 5–8 show that there are no distinct phases representing fractures and pores being compacted on the curves. The stress-strain curves are approximately straight until the peak stress is reached. As the stress increases, the stress-strain curve begins to bend. This is because the shale is fractured after the peak stress is reached. A clear brittle fracture sound can be heard when the shale is fractured. After peaks, the stresses decrease rapidly to the lowest stress points. These results show that Longmaxi shale has high brittleness under all three experimental conditions.

By comparing the stress-strain curves in Figures 5–10, the $scCO_2$ experimental group has the lowest yield strain into the damage phase. Meanwhile, the peak stresses of the $scCO_2$ experimental group are lower than that in the control groups. After the maximum stress points, the stresses of the $scCO_2$ experimental group drop sharply than that in the other two groups.

3.2. The Failure Modes of Specimens. Rock failure modes are affected by many factors. Among them, test conditions are the main factors [45]. Besides, different coring angles also lead to different failure modes. The failure modes can be mainly divided into splitting failure and shear failure modes.

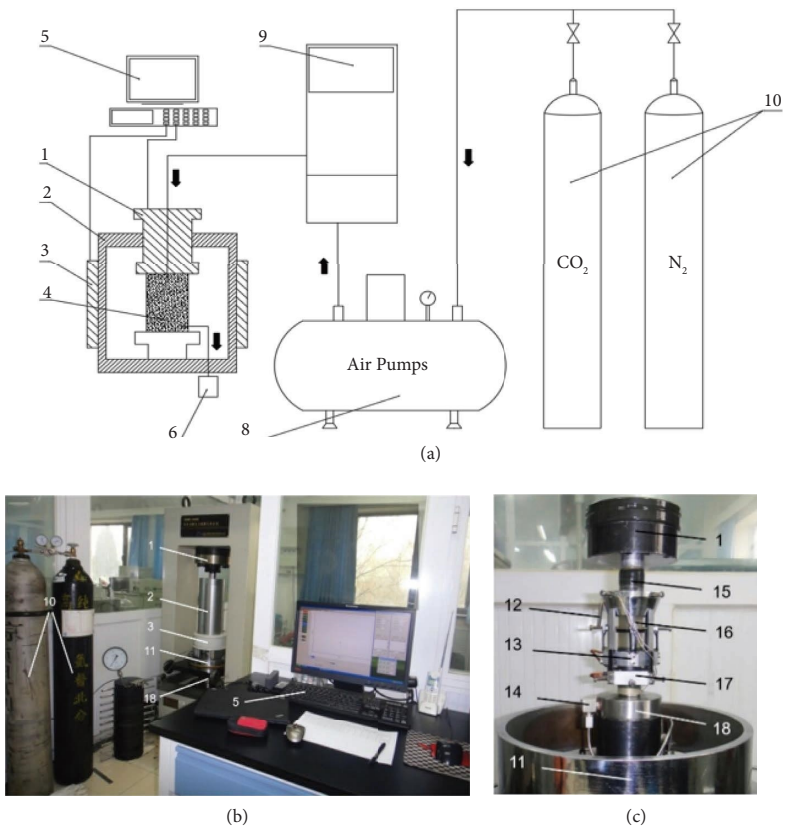

1. top plate; 2. confining pressure barrel; 3. heating ring; 4. assembled specimen with sensors; 5. data acquisition and control system; 6. gas outlet device; 7. confining unit; 8. air driven; 9. liquefied gas booster; 10. CO_2 or N_2 bottle; 11. seal ring; 12. temperature sensor; 13. radial displacement transducer; 14. gas outlet (the gas inlet is invisible behind the top plate); 15. heat shrinkable tubing; 16. specimen wrapped with heat shrinkable tubing; 17. axial displacement transducer; 18. bottom plate.

Figure 3: (a) Schematic diagram of the experimental system, (b) main components of the experimental system, and (c) specimen set up between the top and the bottom plates in the confining pressure barrel.

Table 1: The experimental parameters.

No	Test content	Pc (MPa[a])	T (°C)	Pg (MPa[b])	Gas
1	$scCO_2$ test	20	40	10	$scCO_2$
2	N_2 test	20	40	10	N_2
3	Helium gas test	20	40	10	Helium
4	H_2O test	20	40	10	H_2O (Liquid)

Table 2: Core strength at different coring angles with different media.

Media conditions	Triaxial strengths with different coring angles (MPa)						
	0°	15°	30°	45°	60°	75°	90°
$scCO_2$	341	390	375	324	241	245	285
N_2	376	403	386	301	248	293	293
He	361	387	373	298	227	243	294
H_2O	354	394	384	318	246	260	291

Figure 11 shows the shale failure modes under diverse experiment conditions and coring angles. When the coring angle is less than 15°, the failure modes of the shale specimen contain both splitting and shear modes (Figure 12) and have formed *Y*-type fracture geometry. The failure condition is similar in the other two control groups. However, the specimens in the $scCO_2$ experimental group break more thoroughly at 15° coring angle, showing more fractures. At the coring angle of 15°, the $scCO_2$ group has a higher strain value than the nitrogen control group before reaching peak stress (Figure 6). This means shale failed after a longer period of compression under the action of $scCO_2$. During this process, $scCO_2$ repeatedly acted on the fractured fractures, producing more complex fractures.

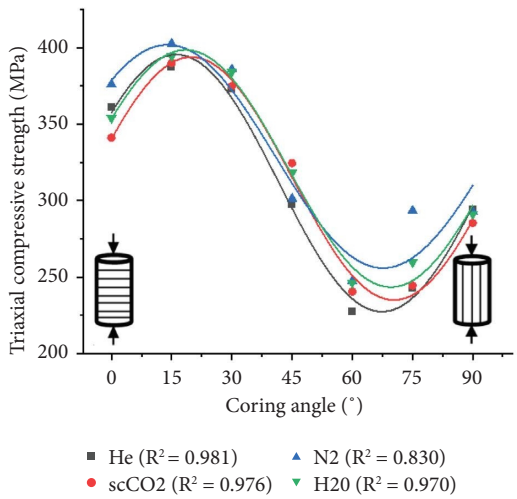

Figure 4: The relationship between triaxial strength and coring angle.

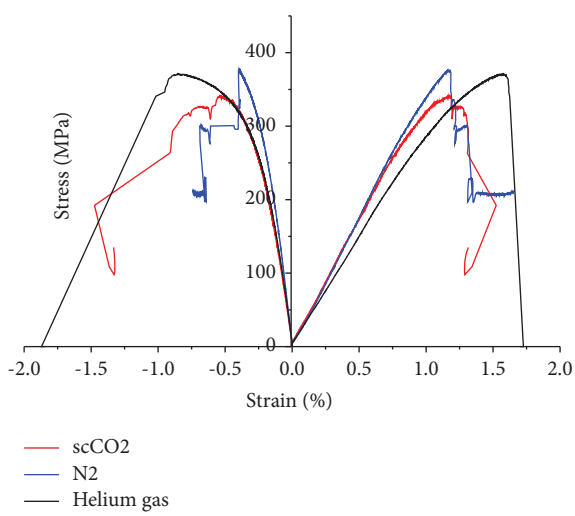

Figure 5: Stress-strain curves at the coring angle of 0° (positive and negative values of strain represent axial and radial strains, respectively, the same in the other stress-strain plots).

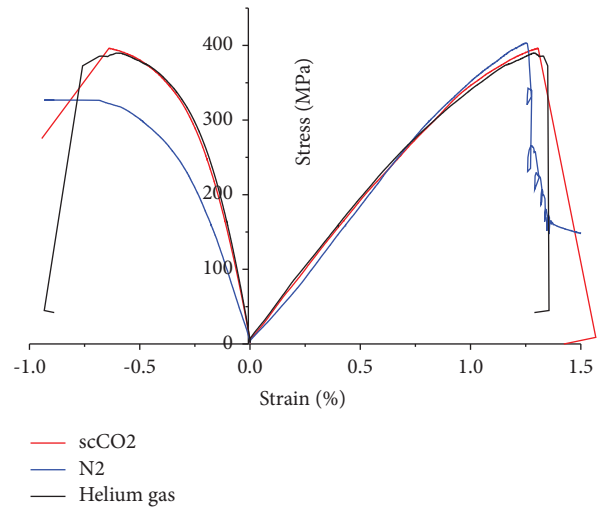

Figure 6: Stress-strain curves at the coring angle of 15°.

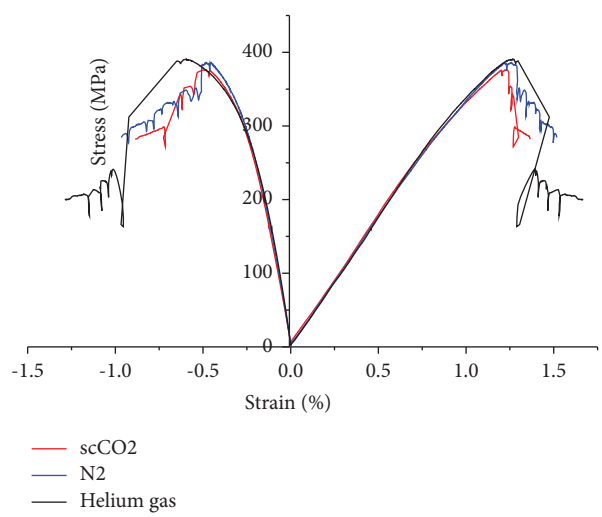

Figure 7: Stress-strain curves at the coring angle of 30°.

At $\beta = 30°$, 45°, or 60°, the failure modes are the single shear or the double shear modes due to the slipping between the bedding planes (Figure 13). Some graptolites are observed on the fracture surfaces. The splitting failure modes of rock samples with low coring angles are not obvious due to the confining pressure and high coring angle. In addition, smooth shear fractures were formed on the bedding planes with severe slip. Therefore, the triaxial compression strength of the shale decreases as the angle increases.

At $\beta = 75°$ or 90°, the failure modes mainly follow the splitting mode. The main reason is that the direction of axial loading is almost parallel to the shale bedding planes.

In summary, the combined effects of $scCO_2$ and bedding planes led to various failure modes in the experiments. At low coring angles (0°–15°), the specimens in the $scCO_2$ experimental group produced more fractures compared to the other control groups due to more reactions between $scCO_2$ and shale. At moderate coring angles (30°–60°), the fractures could easily cross the specimens along the bedding planes. At high coring angles (75°–90°), some fractures were found on the specimens, due to the tensile damage.

3.3. Changes of Mechanical Anisotropy. Figures 14 and 15 show that the mechanical parameters of the Longmaxi shale changed with the internal bedding directions. At low coring angles (0°–15°), the elastic modulus of the $scCO_2$ experimental group is lower than that of the N_2 control group. However, at moderate and high coring angles (45°–90°), the elastic modulus of the $scCO_2$ experimental group is higher than that in both control groups. However, at moderate and high coring angles (45°–90°), the elastic modulus of the $scCO_2$ experimental group is higher than that in both control groups with an exception at the 60° coring angle, where it is slightly smaller than that of the N_2 control group.

To describe the anisotropic characteristics of the shale, an anisotropic in-dex R_c is defined as follows [46]:

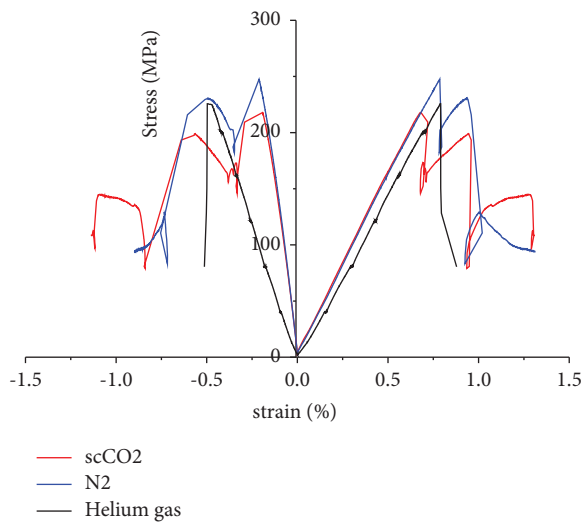

Figure 8: Stress-strain curves at the coring angle of 60°.

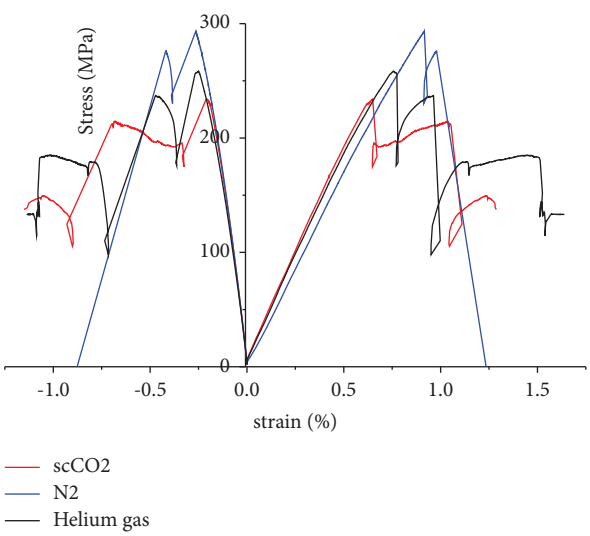

Figure 9: Stress-strain curves at the coring angle of 75°.

$$R_c = \frac{X_{ci(0)}}{X_{ci(90)}}, \quad (1)$$

where $X_{ci(0)}$ and $X_{ci(90)}$ are the shale mechanical parameters at the coring angle of 0° and 90°, respectively. Anisotropic indexes of triaxial strength, elastic module, and Poisson's ratio are listed in Table 3. The anisotropic indexes of triaxial strength and elastic modulus in the $scCO_2$ experimental group are much lower than those in the N_2 control group, whereas the anisotropic index of Poisson's ratio in the $scCO_2$ experimental group is much higher than that of the N_2 control group. The decreased shale mechanical anisotropic indexes of triaxial strength and elastic modulus in the $scCO_2$ experimental group indicate that $scCO_2$ tends to make the shale more isotropic.

3.4. Mineralogical Changes. The components of shale minerals in each experimental group have been obtained by the X-ray diffraction experiments. According to Kaszuba's et al. test method [47], the samples were analyzed by XRD. In addition, analyzed the clay composition of the samples.

The several tests were performed within each group to reduce the error induced by rock heterogeneity. The mineral components and the clay components are shown in Tables 4 and 5.

Little difference was found in the mineral components of the N_2 and Helium control groups. However, compared with the two control groups, the relative contents of calcite, dolomite, and illite in the $scCO_2$ group reduce significantly. The content of calcite decreases about 5.6% on average (the maximum is 7.1%, and the minimum is 4.7%). The content of the dolomite and illite decreased by 6.9% (the maximum is 8.6%, and the minimum is 5.1%) and 10.6% (the maximum is 13.5%, and the minimum is 8.5%), respectively. The relative content of quartz in the $scCO_2$ group increases due to very little reaction of quartz with CO_2 in the short term and the decrease of other minerals.

Wu et al. [48] tested the water content of shale. CO_2 gas becomes corrosive when contact with water. As a result, shale minerals and organic matter will be corroded by H^+ [4–7, 49]. The following equation [49] can express the dissolutions of the calcite and dolomite minerals:

$$\begin{aligned} &CaCO_3\,(\text{calcite}) + H^+ \longrightarrow Ca^{2+} + HCO_3^- \\ &CaMg(CO_3)_2\,(\text{dolomite}) + H^+ \longrightarrow Ca^{2+} + Mg^{2+} + HCO_3^-. \end{aligned} \quad (2)$$

Meanwhile, the $scCO_2$ condition facilitates the decomposing of minerals and organic matters through the generation of connected corrosion micropores and microcracks seen in Figures 16(c) and 16(d). This is the reason why notably changes of mineral components are observed in the $scCO_2$ experimental group. In contrast, mineral components in the other two control groups show few changes.

3.5. Microstructure Changing of Fracture Surface. The microscopic structure of shale plays an important role in shale gas production. The specimens were carefully

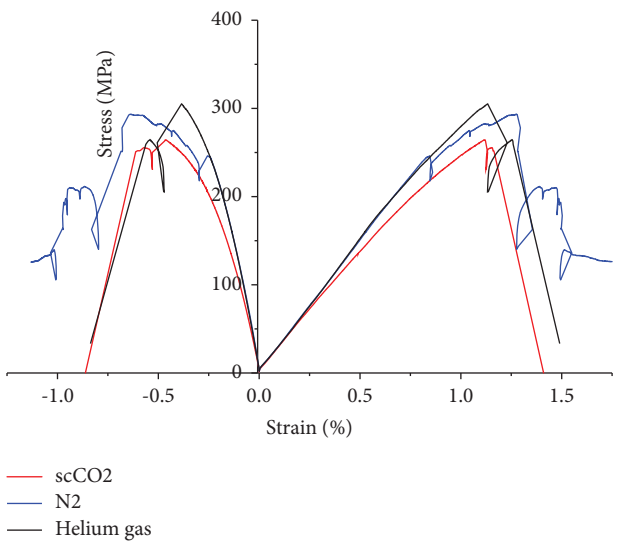

Figure 10: Stress-strain curves at the coring angle of 90°.

Figure 11: The shale failure modes picture of different experimental conditions and different coring angles.

observed with a Quanta-450 SEM device to study the microscopic structure of Longmaxi shale under three experimental conditions. Their microscopic structures are summarized in Figure 16, with each row representing each group.

It has been shown that [35, 36] the composition of the Longmaxi Shale includes dolomite, quartz, muscovite minerals, organic matter with a small number of micropores and microfractures of 0.1 to 5 μm. In the control group of helium, it can be seen that the brittle minerals are closely

0° 15°

(a) (b)

Figure 12: Fracture surface morphology of a typical splitting mode at the coring angle of 0° and 15° (the left specimen is from the $scCO_2$ experimental group; the right one is from the N_2 control group). (a) 0°, (b) 15°.

60° 70°

(a) (b)

Figure 13: Fracture surface morphology of a typical shearing mode at the coring angle of 60° and 75° (the left specimen is from the $scCO_2$ group; the right one is from the N_2 group). (a) 60°, (b) 70°.

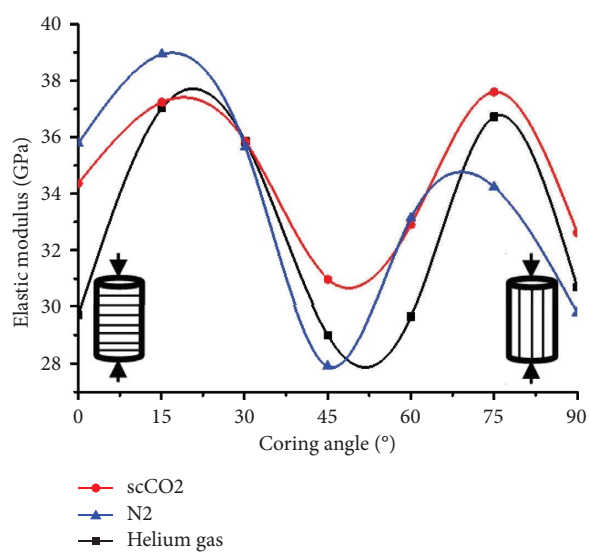

Figure 14: The relationship between elastic modulus and coring angles.

bonded to the clay minerals from Figures 16(i) and 16(l); Meanwhile, the experimental results show that the natural microcracks are less affected by the axial load (Figures 16(j) and 16(l)). The shale microstructure of the helium control group changes little during the experiments.

Figures 16(e) and 16(l) show that no significant differences in the shale microstructure are observed between the N_2 control group (Test 2) and the Helium control group (Test 3). Since the clay minerals are carried by N_2, more of them are found around the surface of the quartz, as shown in Figures 16(h) and 16(l).

However, the shale microstructure in the $scCO_2$ experiment (Test 1) corrodes severely (Figures 16(a)–16(d)). Due to the low viscosity and high diffusion rate of $scCO_2$, it is easy to invade the micropores and microfractures during the experiment, which increases the fracture connectivity. The $scCO_2$ forces some fractures to continually expand, generating long complex fractures (Figure 16(a)), and delamination sheets (Figure 16(b)). On the other hand, the high-speed $scCO_2$ fluid in the micropores leads to the denudation and migration of clays, generating complex microscopic structures (Figure 16(c)). Therefore, $scCO_2$ jets

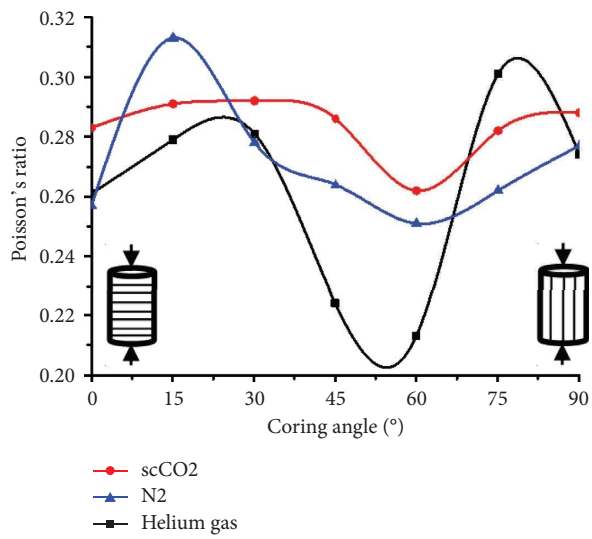

Figure 15: The relationship between the coring angle and the Poisson's ratio.

Table 3: The mechanical anisotropy of the three tests.

NO	Test name	Rc (S) [a]	Rc (E) [b]	Rc (μ) [c]
1	$scCO_2$ test	1.06	1.05	1.11
2	N_2 test	1.28	1.20	0.93
3	He test	1.22	0.97	0.95

[a] Anisotropic index of triaxial compression strength. [b] anisotropic index of elastic modulus. [c] anisotropic index of Poisson's ratio.

Table 4: Mineralogical analysis results of the three experiments (XRD).

Test name	Mineral contents (%)					
	Quartz	Feldspar	Plagioclase	Calcite	Dolomite	Clay and other minerals
$scCO_2$ test	33.5	0.4	0.6	16.1	27.1	22.3
	38.2	0.4	0.4	14.5	25.8	20.7
	28.4	0.3	0.9	16.8	29.3	24.3
	34	0.4	0.4	15.2	27.7	22.3
	31.3	0.6	0.6	16.4	26.4	24.7
	32.9	0.6	0.4	16.9	27.9	21.3
	32.2	0.4	0.6	16.1	28.4	22.3
N_2 test	22.1	0.5	0.8	22.1	33.1	21.4
	21.6	0.5	0.7	23.5	34.7	19
	23.4	0.6	0.4	22.4	32.7	20.5
	22.5	0.4	0.6	22.7	33	20.8
	23.2	0.6	0.4	23.8	32.7	19.3
	23.4	0.5	0.6	23.4	33.5	18.6
	22.9	0.7	0.6	23.6	32.9	19.3
Helium test	24.5	0.6	0.6	23.2	35.7	15.4
	23.7	0.5	0.8	22.6	33.2	19.2
	22.3	0.7	0.7	22.5	33.8	20
	23.2	0.5	0.6	23.8	34.3	17.6
	22.9	0.6	0.9	23.1	35.1	17.4
	23.1	0.5	0.5	23.3	34.9	17.7
	22.8	0.7	0.5	23.6	33.5	18.9

Table 5: Clay analysis results of the three experiments (XRD).

Test name	Clay contents (%)				
	Smectite	I/S	Illite	Kaolinite	Chlorite
$scCO_2$ test	33.5	4.1	19.2	16.1	27.1
	32.2	6.2	21.3	14.5	25.8
	28.4	4.5	21.0	16.8	29.3
	34	2.7	20.4	15.2	27.7
	31.3	4.8	21.1	16.4	26.4
	32.9	2.7	19.6	16.9	27.9
	32.2	2.8	20.5	16.1	28.4
N_2 test	22.8	2.5	31.7	17.2	25.8
	23.1	3.2	29.2	18.3	26.2
	23.4	2.1	30.1	17.9	26.5
	24.6	2.4	32.4	15.7	24.9
	24.4	4.5	29.3	16.7	25.1
	25.5	1.7	28.5	16.9	27.4
	26.3	3.3	30.1	15.9	24.5
Helium test	24.5	3.4	29.3	16.1	26.7
	25.8	2.0	31.8	14.6	25.8
	26.1	4.6	29.7	15.7	23.9
	25.9	3.7	27.5	16.2	26.7
	23.7	1.4	31.2	17.4	26.3
	25.4	2.6	29.8	16.8	25.4
	22.8	1.6	31.6	15.9	28.1

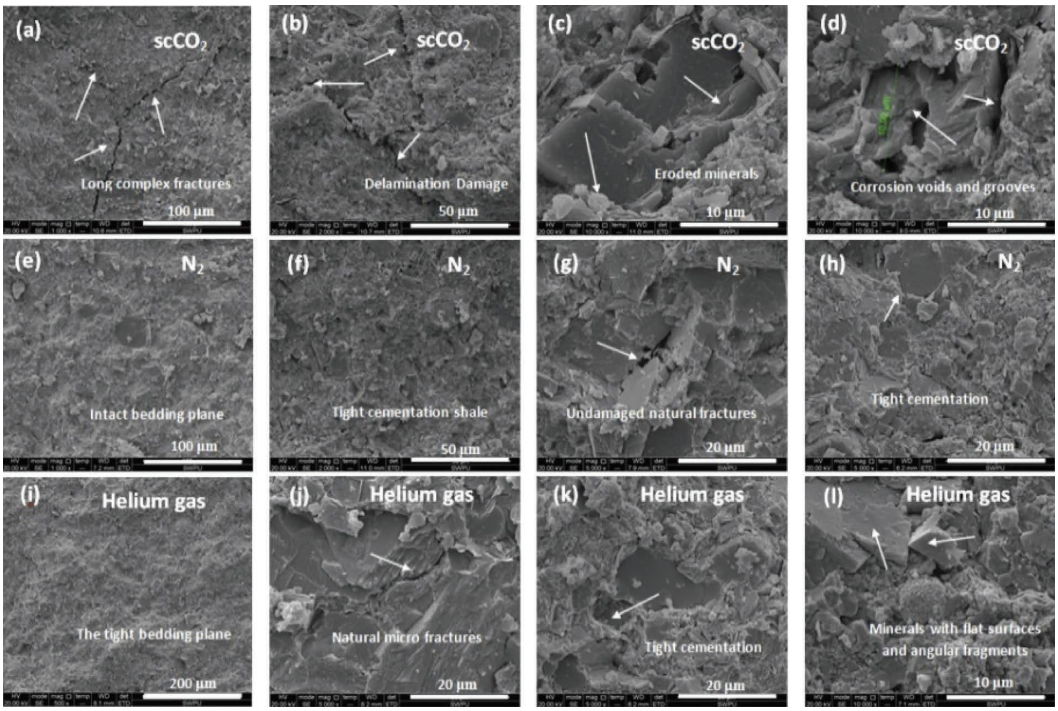

Figure 16: Microscopic structures picture of different experimental conditions.

can effectively reduce the threshold pressure of breaking and fracturing rock and improve the degree of rock fracturing.

The microstructures of shale corrode obviously in the $scCO_2$ condition. Some corrosive voids and grooves are observed. Figure 16(d) shows that the diameters of the corrosive voids and grooves are more than 10 μm, 10 times larger than the original size of microholes and microfractures.

Complex chemical and physical reactions between $scCO_2$ and shale can generate numbers of corrosion voids and grooves, which are conducive to the seepage and accumulation of shale gas, enhancing recovery. Meanwhile, these reactions severely damage the original microstructures of shale, reducing its strength and mechanical anisotropy.

4. Conclusions

In our experiments, $scCO_2$ reduces the triaxial strength of Longmaxi shale by 2% to 20% compared to the other two gases. It also decreases the shale mechanical anisotropic indexes. The combined effects of $scCO_2$ and the bedding plane lead to various failure modes in the experiments. At low coring angles of less than 15°, more fractures are observed on the specimens in the $scCO_2$ experimental group; at moderate coring angles (30°–60°), fractures cross the specimens more easily along the bedding planes; at high coring angles (75°–90°), some splitting fractures produced by tensile damage are found on the specimens.

The calcite, dolomite, and illite contents of Longmaxi shale decreased by 5.6%, 8.6%, and 10.6% in the $scCO_2$ experimental group, respectively. The microstructures of shale are remarkably corroded under the $scCO_2$ condition due to the complex chemical and physical reactions. Numbers of corrosive voids and grooves are produced with diameters of more than 10 μm, 10 times larger than those of the original microholes and microfractures. These microstructures can help improve the seepage and gathering of shale gas, leading to enhanced shale gas recovery.

Data Availability

Study data not yet publicly available.

Conflicts of Interest

The authors declare that there are no conflicts of interest regarding the publication of this paper.

Acknowledgments

The authors would like to thank the National Natural Science Foundation of China (Grant no: 52004225), Application Foundation Project in Sichuan Province (2022NSFSC1273), and Open Fund (PLN2020-1) of State Key Laboratory of Oil and Gas Reservoir Geology and Exploitation (Southwest Petroleum University) for financial support and permission to perceive this study.

References

[1] Z. Chen, Fa Zhao, F. Sun et al., "Hydraulic fracturing-induced seismicity at the hot dry rock site of the gonghe basin in China," *Acta Geologica Sinica - English Edition*, vol. 95, no. 6, pp. 1835–1843, 2021.

[2] Eiaus, *Shale Oil and Shale Gas Resources Are Globally Abundant*, US Energy Information Administration, Washington, DC, USA, 2013.

[3] P. Markewitz, W. Kuckshinrichs, W. Leitner et al., "Worldwide innovations in the development of carbon capture technologies and the utilization of CO_2," *Energy & Environmental Science*, vol. 5, no. 6, pp. 7281–7305, 2012.

[4] G. Brunner, "Supercritical process technology related to energy and future directions – an introduction," *The Journal of Supercritical Fluids*, vol. 96, pp. 11–20, 2015.

[5] R. Barati and J. T. Liang, "A review of fracturing fluid systems used for hydraulic fracturing of oil and gas wells," *Journal of Applied Polymer Science*, vol. 131, no. 16, pp. ID–40735, 2014.

[6] C. Xiao, H. Ni, R. Wang, H. Huo, X. Shi, and M. Li, "Study on horizontal wellbore flow of supercritical carbon dioxide drilling," *Applied Thermal Engineering*, vol. 175, Article ID 115381, 2020.

[7] Y. k Du, Rh Wang, Hj Ni, Zy Huang, and Mk Li, "Dynamical analysis of high-pressure supercritical carbon dioxide jet in well drilling," *Journal of Hydrodynamics*, vol. 25, no. 4, pp. 528–534, 2013.

[8] C. Palmer and Z. Sito, "Nitrogen and carbon dioxide fracturing fluids for the stimulation of unconventional shale plays," *AGH Drilling, Oil, Gas*, vol. 30, no. 1, p. 191, 2013.

[9] B. Jia, Z. Chen, and C. Xian, "Investigations of CO2 storage capacity and flow behavior in shale formation," *Journal of Petroleum Science and Engineering*, vol. 208, no. PD, Article ID 109659, 2022.

[10] X. Jin and S. Shah, "Fracture propagation direction and its application in hydraulic fracturing," in *SPE Hydraulic Fracturing Technology Conference*Society of Petroleum Engineers: The Woodlands, Texas, USA, 2013.

[11] M. Godec, G. Koperna, R. Petrusak, and A. Oudinot, "Potential for enhanced gas recovery and CO2 storage in the Marcellus Shale in the Eastern United States," *International Journal of Coal Geology*, vol. 118, pp. 95–104, 2013.

[12] J. J. Kolle and M. Marvin, "Jet-assisted coiled tubing drilling with supercritical carbon dioxide," in *ETCE/OMAE 2000 Joint Conference*ASME, New York, NY, USA, 2000.

[13] J. J. Kollé, "Coiled tubing drilling with supercritical carbon dioxide," in *SPE/CIM International Conference on Horizontal Well Technology*Tempress Technologies, Inc, Renton, WA, USA, 2000.

[14] Y. K. Du, R. H. Wang, H. J. Ni, M. K. Li, W. Q. Song, and H. F. Song, "Determination of rock-breaking performance of high-pressure supercritical carbon dioxide jet," *Journal of Hydrodynamics*, vol. 24, no. 4, pp. 554–560, 2012.

[15] J. Liu, Y. Hu, Y. Kang et al., "Experimental study on fracture propagation induced by supercritical CO2 jet fracturing in artificial samples with prefabricated bedding planes," *Journal of Natural Gas Science and Engineering*, vol. 72, Article ID 103037, 2019.

[16] A. Patmonoaji, Yi Zhang, Z. Xue, H. Park, and T. Suekane, "Experimental and numerical simulation of supercritical CO 2 microbubble injection into a brine-saturated porous medium," *International Journal of Greenhouse Gas Control*, vol. 91, Article ID 102830, 2019.

[17] P. Mavhengere, N. Wagner, and N. Malumbazo, "The effects of long-term supercritical CO2 exposure on Zululand Basin core samples," *Energy*, vol. 220, Article ID 119806, 2021.

[18] Z. Sun, X. Song, G. Feng, Y. Huo, Z. L. Wang, and S. Kong, "Influence of supercritical, liquid, and gaseous CO2 on fracture behavior in sandstone," *Energy Science & Engineering*, vol. 8, no. 11, pp. 3788–3804, 2020.

[19] X. Zhang, B. Wei, J. Shang et al., "Alterations of geochemical properties of a tight sandstone reservoir caused by supercritical CO_2 -brine-rock interactions in CO_2 -EOR and geosequestration," *Journal of CO_2 Utilization*, vol. 28, pp. 408–418, 2018.

[20] G. Zhang, D. Zhou, Pu Wang, K. Zhang, and M. Tang, "Influence of supercritical CO 2 -water on the micromechanical properties of sandstone," *International Journal of Greenhouse Gas Control*, vol. 97, no. C, Article ID 103040, 2020.

[21] F. Liu, P. Lu, C. Griffith et al., "CO2–brine–caprock interaction: reactivity experiments on Eau Claire shale and a review of relevant literature," *International Journal of Greenhouse Gas Control*, vol. 7, pp. 153–167, 2012.

[22] Q. R. Miller, C. J. Thompson, J. S. Loring et al., "Insights into silicate carbonation processes in water-bearing supercritical CO 2 fluids," *International Journal of Greenhouse Gas Control*, vol. 15, pp. 104–118, 2013.

[23] Y.-H. Huang, S.-Qi Yang, W.-P. Li, and M. R. Hall, "Influence of super-critical CO 2 on the strength and fracture behavior of brine-saturated sandstone specimens," *Rock Mechanics and Rock Engineering*, vol. 53, no. 2, pp. 653–670, 2020.

[24] F. Othman, M. Yu, F. Kamali, and F. Hussain, "Fines migration during supercritical CO 2 injection in sandstone," *Journal of Natural Gas Science and Engineering*, vol. 56, pp. 344–357, 2018.

[25] M. F. Irfan, T. M. Bisson, E. Bobicki et al., "CO2 storage in saline aquifers by dissolution and residual trapping under supercritical conditions: an experimental investigation," *Colloids and Surfaces A: Physicochemical and Engineering Aspects*, vol. 548, pp. 37–45, 2018.

[26] R. Lahann, M. Mastalerz, J. A. Rupp, and A. Drobniak, "Influence of CO 2 on new albany shale composition and pore structure," *International Journal of Coal Geology*, vol. 108, pp. 2–9, 2013.

[27] T. Xu, J. A. Apps, and K. Pruess, "Mineral sequestration of carbon dioxide in a sandstone–shale system," *Chemical Geology*, vol. 217, no. 3-4, pp. 295–318, 2005.

[28] M. Angeli, M. Soldal, E. Skurtveit, and E. Aker, "Experimental percolation of supercritical CO 2 through a caprock," *Energy Procedia*, vol. 1, no. 1, pp. 3351–3358, 2009.

[29] M. Allawzi, A. Al-Otoom, H. Allaboun, A. Ajlouni, and F. Al Nseirat, "CO2 supercritical fluid extraction of Jordanian oil shale utilizing different co-solvents," *Fuel Processing Technology*, vol. 92, no. 10, pp. 2016–2023, 2011.

[30] Y. Lu, J. Liu, J. Tang et al., "Pore changes of slickwater-containing shale under supercritical CO2 treatment," *Fuel*, vol. 312, Article ID 122775, 2022.

[31] K. Yang, J. Zhou, X. Xian et al., "Gas adsorption characteristics changes in shale after supercritical CO2-water exposure at different pressures and temperatures," *Fuel*, vol. 310, Article ID 122260, 2022.

[32] A. Fatah, Z. Bennour, H. B. Mahmud, R. Gholami, and M. Hossain, "Surface wettability alteration of shales exposed to CO2: implication for long-term integrity of geological storage sites," *International Journal of Greenhouse Gas Control*, vol. 110, Article ID 103426, 2021.

[33] J. Wollenweber, S. Alles, A. Busch, B. M. Krooss, H. Stanjek, and R. Littke, "Experimental investigation of the CO2 sealing efficiency of caprocks," *International Journal of Greenhouse Gas Control*, vol. 4, no. 2, pp. 231–241, 2010.

[34] S. Vialle and T. Vanorio, "Laboratory measurements of elastic properties of carbonate rocks during injection of reactive CO2-saturated water," *Geophysical Research Letters*, vol. 38, no. 1, p. 5, 2011.

[35] K. Jiao, S. Yao, C. Liu et al., "The characterization and quantitative analysis of nanopores in unconventional gas reservoirs utilizing FESEM–FIB and image processing: an example from the lower Silurian Longmaxi Shale, upper Yangtze region, China," *International Journal of Coal Geology*, vol. 128-129, pp. 1–11, 2014.

[36] Y. Wang, D. Dong, H. Yang et al., "Quantitative characterization of reservoir space in the lower silurian Longmaxi shale, southern sichuan, China," *Science China Earth Sciences*, vol. 57, no. 2, pp. 313–322, 2014.

[37] C. Zou, D. Dong, S. Wang et al., "Geological characteristics and resource potential of shale gas in China," *Petroleum Exploration and Development*, vol. 37, no. 6, pp. 641–653, 2010.

[38] T. Guo and H. Zhang, "Formation and enrichment mode of Jiaoshiba shale gas field, Sichuan Basin," *Petroleum Exploration and Development*, vol. 41, no. 1, pp. 31–40, 2014.

[39] H. Gao and H. A. Li, "Pore structure characterization, permeability evaluation and enhanced gas recovery techniques of tight gas sandstones," *Journal of Natural Gas Science and Engineering*, vol. 28, pp. 536–547, 2016.

[40] P. G. Ranjith and M. S. A. Perera, "A new triaxial apparatus to study the mechanical and fluid flow aspects of carbon dioxide sequestration in geological formations," *Fuel*, vol. 90, no. 8, pp. 2751–2759, 2011.

[41] H. Zheng, X. T. Feng, and P. Z. Pan, "Experimental investigation of sandstone properties under CO2–NaCl solution-rock interactions," *International Journal of Greenhouse Gas Control*, vol. 37, no. 0, pp. 451–470, 2015.

[42] Q. Li, M. Chen, Y. Jin, Y. Zhou, F. P. Wang, and R. Zhang, "Rock mechanical properties of shale gas reservoir and their influences on hydraulic fracture," in *International Petroleum Technology Conference 2013: Challenging Technology and Economic Limits to Meet the Global Energy Demand*, vol. 2, pp. 1180–1188, Society of Petroleum Engineers, Beijing, China, 2013.

[43] J. Liu, Z. Yang, J. Sun, Z. Dai, K. Lv, and Q. You, "Experimental investigation on hydration mechanism of Sichuan shale (China)," *Journal of Petroleum Science and Engineering*, vol. 201, Article ID 108421, 2021.

[44] Y. Liu, C. Yang, J. Wang, Y. Xiong, and P. Peng, "New insights into hydration-induced creep behavior of shale: a comparison study of brittle black shale and clayey oil shale at micro-scale," *Marine and Petroleum Geology*, vol. 138, Article ID 105554, 2022.

[45] X. Tang, A. Paluszny, and R. W. Zimmerman, "A study of the influence of fragmentation in ore-pass hang-up phenomena," in *Proceedings of the 47th US Rock Mechanics/Geomechanics Symposium*, March 2013.

[46] Y. Ran-Gang and T. Yong, "On the rock mechanics parameters anisotropy of sandstone," *Chinese Journal of Experimental Mechanics*, no. 3, pp. 368–375, 2013.

[47] J. P. Kaszuba, A. Navarre-Sitchler, G. Thyne, C. Chopping, and T. Meuzelaar, "Supercritical carbon dioxide and sulfur in the Madison Limestone: a natural analog in southwest Wyoming for geologic carbon–sulfur co-sequestration," *Earth and Planetary Science Letters*, vol. 309, no. 1, pp. 131–140, 2011.

[48] Y. Wu, T. Fan, S. Jiang et al., "Methane adsorption capacities of the lower paleozoic marine shales in the yangtze platform, south China," *Energy and Fuels*, vol. 29, no. 7, pp. 4160–4167, 2015.

[49] H. Tian, F. Pan, T. Xu, B. J. McPherson, G. Yue, and P. Mandalaparty, "Impacts of hydrological heterogeneities on caprock mineral alteration and containment of CO2 in geological storage sites," *International Journal of Greenhouse Gas Control*, vol. 24, pp. 30–42, 2014.

Hindawi
Advances in Materials Science and Engineering
Volume 2022, Article ID 7634951, 11 pages
https://doi.org/10.1155/2022/7634951

Research Article

Study on Rheological Characteristics of Uncemented Coal Gangue-Fly Ash Backfill (UCGFB) Slurry Based on Fractal Theory

Junyu Jin,[1,2] **Faguang Yang**,[1,2] **Chengjin Gu**,[1,2] **Yibo Zhou**,[1,2] **and Xiaolong Wang**[1,2]

[1]*School of Energy and Mining Engineering, China University of Mining & Technology-Beijing, D11 Xueyuan Road, Haidian District, Beijing 100083, China*
[2]*State Key Laboratory of Coal Resources and Safe Mining, China University of Mining and Technology-Beijing, D11 Xueyuan Road, Haidian District, Beijing 100083, China*

Correspondence should be addressed to Junyu Jin; junyupaper@outlook.com

Received 29 August 2022; Accepted 30 September 2022; Published 15 October 2022

Academic Editor: Depeng Ma

In order to explore the influence of gradation and concentration on the rheological parameters of uncemented coal gangue-fly ash backfill (UCGFB) slurry, based on the fractal theory, the particle size distribution of the mixture of coal gangue and fly ash under different mixing ratios are analyzed in this paper. On this basis, the influence of gradation and concentration on rheological parameters of UCGFB slurry are studied and a numerical simulation of slurry transportation is also carried out. The results show that (1) the fractal dimension can well characterize the grading characteristics of UCGFB mixtures, the larger the fractal dimension, the more fine particles in the material. (2) The fractal dimension of 2.628 is a critical point, when the fractal dimension of the mixture is greater than or equal to 2.628, the content of fine particles in the slurry can meet the requirements. On this basis, by adjusting the concentration of the slurry, the slurry can reach a good state. (3) When the slurry concentration reaches 79%, no matter how the gradation of the mixture changes, the rheological parameters of the slurry are at a high level. (4) In this paper, the average pressure loss per unit length pipeline is between 3000–8000 Pa for slurry with different mixing ratios, with a minimum value of 3070 Pa and the maximum value of 7697 Pa. Moreover, the pressure loss of bend is greater than that of straight pipe.

1. Introduction

Coal gangue is a kind of solid waste with a low calorific value produced in the process of coal mining and washing. According to statistics, by the end of 2019, China's accumulated amount of gangue has exceeded 6 billion tons, forming 1500–1700 gangue hills, covering an area of more than 200 thousand mu, the emission has increased by about 500–800 million t year by year [1]. Countries around the world have conducted a lot of exploration and practice on the comprehensive utilization of coal gangue, forming a comprehensive treatment and utilization system for power generation, road paving, production of building materials, production of chemical raw materials, agricultural application, and underground filling, but the comprehensive utilization rate of coal gangue is less than 30% [2–7]. The accumulation of coal gangue has brought great hidden dangers to the environment and personal safety. The main hazards caused are the occupation of land resources, pollution of groundwater, destruction of the soil environment, air pollution, and geological disasters [7, 8]. In order to realize the economic and efficient treatment of coal gangue, the UCGFB technology is slowly rising in China. The whole process is shown in Figure 1. The coal gangue is crushed to 3–6 mm, then according to the particle size distribution of the broken gangue, the appropriate proportion of fly ash is added, then water is added to mix to prepare a high-concentration slurry with a concentration of 76%–79%. The slurry is transported to the goaf through the filling pump and filling pipeline, which can not only achieve the purpose of economic and efficient treatment of the gangue but also play a certain supporting role on the roof of the goaf for reducing the ground surface subsidence [9–12].

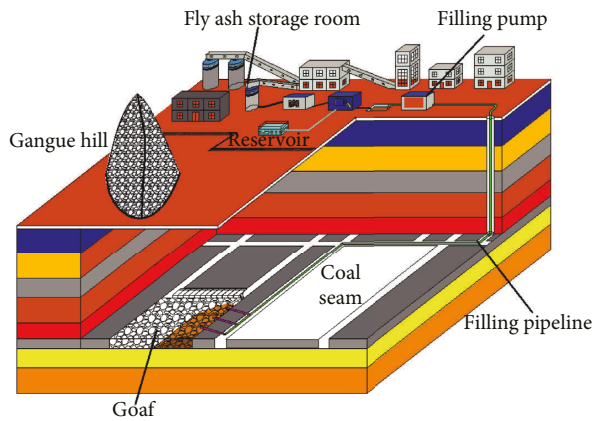

Figure 1: Schematic diagram of backfilling process.

The performance of filling slurry is very important to the transportation of slurry. The gradation of the materials is the key factor to determine the performance of the slurry, so it is necessary to study the influence of the gradation of the materials on the performance of the slurry [13, 14]. At present, the grading curve is often used to characterize the particle grading characteristics of materials, when grading parameters are directly used to evaluate the performance of filling slurry; it is difficult to establish a simple and clear evaluation relationship because there are several grading parameters. Therefore, it is of great significance to simply and quantitatively characterize the gradation of filling materials, then to evaluate the performance of filling slurry on this basis.

The fractal theory can quantitatively describe the complexity and space-filling capacity of geometric bodies and is suitable for characterizing the complex particle size distribution of mineral materials [15–19]. Many experts and scholars have applied it to rock mechanics, concrete, asphalt, and other fields and achieved certain results. Xu et al. [20] studied the fractal model of the particle size distribution of expansive soil, explained the physical mechanism of fractal particle size distribution, and obtained that the fractal dimension range of particle size distribution is between 2.0 and 3.0. Zhou [21] proposed a fractal model of rock-crushing particle size distribution, carried out ore-crushing tests, and pointed out that the fractal characteristics of ore are universal, and the fractal dimension, like other crushing indexes, can be used as an ideal index for evaluating crushing. Jiang et al. [22] combined fractal geometry with numerical simulation, used fractal dimension to characterize the distribution of rock joints, and studied its impact on the excavation of underground caverns. Hang and Yu [23] applied the fractal theory to the asphalt mixture, found that the asphalt mixture showed obvious fractal characteristics, and obtained the fractal dimensions of seven different gradations through calculation. Based on fractal theory, Chu et al. [24] obtained three algebraic expressions of fractal dimension, cumulative probability, and mass distribution of particles, which are functions of particle concentration, particle diameter, and maximum and minimum particle diameter. Konkol and Prokopski [25] measured the fractal dimension of the fracture surface of concrete containing variable kaolinite and speculated that the fracture toughness of this kind of concrete has a correlation with the fractal dimension. The Brazilian scholar Armandei and de Souza Sanchez Filho [26] took the fracture surface of steel fiber reinforced concrete as the research object, explored the relationship between the fractal dimension of the fracture surface, the content of steel fiber, and the concrete material, then based on this, discuss the material design scheme that can optimize the strength and fracture toughness.

Although the fractal theory has been applied to many fields, there is little research on the application of fractal theory to coal mine filling materials. Therefore, the purpose of this study is to analyze the gradation of filling materials based on fractal theory. Then on this basis, to study the influence of material gradation and concentration on the rheological properties of filling slurry.

2. Fractal Analysis of Material Gradation

2.1. Fractal Theory. According to the fractal theory, the number of particles passing through the sieve aperture r shall meet the formula (1), where D is the fractal dimension and $r_{\max}$ is the pore diameter of the screen when the particle passing rate is 100%.

$$N(r) = \left(\frac{r}{r_{\max}}\right)^{-D}. \tag{1}$$

The number of particles in the interval $(r, r+dr)$ is

$$dN(r) = -Dr_{\max}^{D} r^{-1-D} dr. \tag{2}$$

It is difficult to measure the number of particles passing through the sieve hole r during the experiment. In practice, the cumulative particle mass passing through the sieve hole r is used to represent the particle distribution. Assuming the density of particles isρ, the mass of particles in the interval $(r, r+dr)$ can be expressed as follows:

$$dM(r) = \rho V(r) dN(r) = -\rho k r^3 D r_{\max}^{D} r^{-1-D} dr, \tag{3}$$

where k is the particle volume factor based on the characteristic size, which is a constant.

The mass distribution function of particles is the following formula:

$$P(r) = \frac{M(r)}{M_0}, \tag{4}$$

where $P(r)$ is the mass distribution function of particles, which represents the passing rate of particles in the sieve hole r, and $M(r)$ is the mass of particles passing through the sieve hole r, that is the mass of particles (g) not larger than the particle size of r. M_0 is the total mass of particles, that is the mass of particles passing through the sieve aperture $r_{\max}$. Formula (5) can be obtained by combining formulas (3) and (4).

$$P(r) = \frac{\rho k(-D) r_{\max}^{D} r^{3-D}}{(3-D) M_0} + C. \tag{5}$$

$P(r_{\max}) = 1$ and $P(r_{\min}) = a$, which means that the ratio of particle mass is smaller than the minimum sieve aperture $r_{\min}$ to total mass is a. Formula (6) can be obtained by substituting the initial conditions into formula (5):

$$P(r) = \frac{(1-a)\left(r^{3-D} - r_{\max}^{3-D}\right)}{r_{\max}^{3-D} - r_{\min}^{3-D}} + 1. \quad (6)$$

2.2. Calculation of Fractal Dimension of UCGFB Mixture. In this paper, the raw materials used to study the performance of UCGFB slurry are the gangue of the "Wangjiata" coal mine and the fly ash of the "Linxi" coal mine. The density of coal gangue is 2350 kg/m^3 and the density of fly ash is 2480 kg/m^3. The chemical composition of both is shown in Table 1. The particle size distribution of coal gangue (broken to 6 mm) and fly ash is shown in Figure 2. It can be seen from Figure 2 that compared with coal gangue, the content of fine particles in fly ash is more, and the proportion of particles below 200um is about 90%. The content of fine particles in coal gangue can be improved by adding fly ash to coal gangue. The particle size distribution of fly ash and coal gangue (crushed to 6 mm) mixed in different proportions are shown in Table 2.

The particle size distribution and fractal distribution fitting of the mixture after the fly ash and gangue are mixed in different proportions are shown in Figure 3. The fractal dimension and correlation coefficient are shown in Table 3, it can be seen from Table 3 that the fractal dimension of the mixture is different under different mixing ratios. With the increase of fly ash content, the content of fine particles in the mixture increases, and the fractal dimension becomes larger. The correlation coefficient R^2 of fractal distribution fitting mixture gradation is higher than 0.98, which indicates that fractal dimension D can well characterize the gradation characteristics of gangue and fly ash mixture.

3. Rheological Behavior Analysis Based on Fractal Theory

3.1. Test Scheme. Taking the coal gangue of the "Wangjiata" coal mine (crushed to 6 mm) and the fly ash of the "Linxi" coal mine as raw materials, the influence of gradation and slurry concentration on the rheological characteristics of slurry is studied. The research scheme is shown in Table 4. Four levels are set for each factor to conduct full factor tests, with a total of 16 groups of experiments.

3.2. Test Instrument. In this paper, the RheolaQC rheometer of Anton Paar Company in Germany is selected and connected to the computer through RS232. Figure 4 is the physical diagram of the RheolaQC rheometer. When testing the rheological properties of the UCGFB slurry, the shear test is carried out by controlling the shear rate. Put the rotor into a 500 ml beaker for the rheological test. Set the shear rate range to 0–150 s^{-1} and the time to 120 s through special software. The corresponding shear stress and viscosity are recorded in real time. In order to eliminate the error, the average value is obtained through multiple measurements.

3.3. Test Results and Analysis

3.3.1. Rheological Characteristic Index. Yield stress and viscosity are two basic parameters to characterize the rheology of slurry. The yield stress is the maximum shear stress that the slurry can bear when it only deforms without flowing under the action of external force, which reflects the initial cohesion of the slurry and is closely related to whether the slurry contains cementitious materials, additives, and the content of fine particles in the material. The viscosity reflects the internal friction of the slurry when it flows and is the macroscopic expression of the microscopic action of the fluid molecules. The viscosity of the slurry is related to the particle size, distribution, momentum exchange between the solid particles and the liquid molecules, and other factors.

3.3.2. Rheological Model. The concentration of the backfill slurry is as high as 76%–79%, which is in the form of paste. When the backfill slurry flows in the pipeline, the movement state is "plunger" moving as a whole. For high-concentration backfill slurry, the most commonly used rheological model is mainly the H-B model, and its rheological equation is expressed as

$$\tau = \tau_0 + \eta\left(\frac{\mathrm{du}}{\mathrm{dy}}\right)^n, \quad (7)$$

where τ is shear stress, Pa;du/dy is the shear rate, s^{-1};η is the viscosity, Pa·s;$\tau_0$is the yield stress; $n$is the rheological index, when $n = 1$, $\tau_0 = 0$, it is Newtonian fluid; when $n = 1$, $\tau_0 > 0$, it is Bingham body; when $n > 1$, it is an expansion body; when $n < 1$, it is pseudoplastic.

3.3.3. Experimental Result. The rheological data and fitting of the UCGFB slurry when the gradation $D = 2.658$ and the concentration are 76%, 77%, 78%, and 79%, respectively, is shown in Figure 5. It can be seen from Figure 5 that the relationship between the shear rate and shear stress of UCGFB slurry is an approximate straight line, which belongs to the characteristics of the Bingham body of non-Newtonian material. The rheological parameters of 16 groups of UCGFB slurry are shown in Table 5.

The change of rheological parameters of slurry along with fractal dimension under different concentrations is shown in Figure 6. It can be seen from the figure that when the fractal dimension is 2.512, the yield stress and viscosity of the slurry are the maximum values under the same concentration, indicating that the content of fine particles in the slurry is very low and the content of coarse particles is too much, and the relative motion between particles in the slurry is mainly sliding friction, the friction resistance between particles is large, as shown in Figure 7(a). When the fractal dimension increases from 2.512 to 2.599, the yield stress and viscosity of the slurry decrease rapidly, this is because the fine particles are equivalent to small balls, with

Table 1: Chemical composition of coal gangue and fly ash.

Chemical composition	SiO_2	Al_2O_3	Fe_2O_3	TiO_2	K_2O	CaO	P_2O_5	SO_3
Gangue	50.6	23.9	7.7	1	2.3	5.1	0.1	8.1
Fly ash	52	29.3	9.83	2.03	3.63	2.34	0	0.89

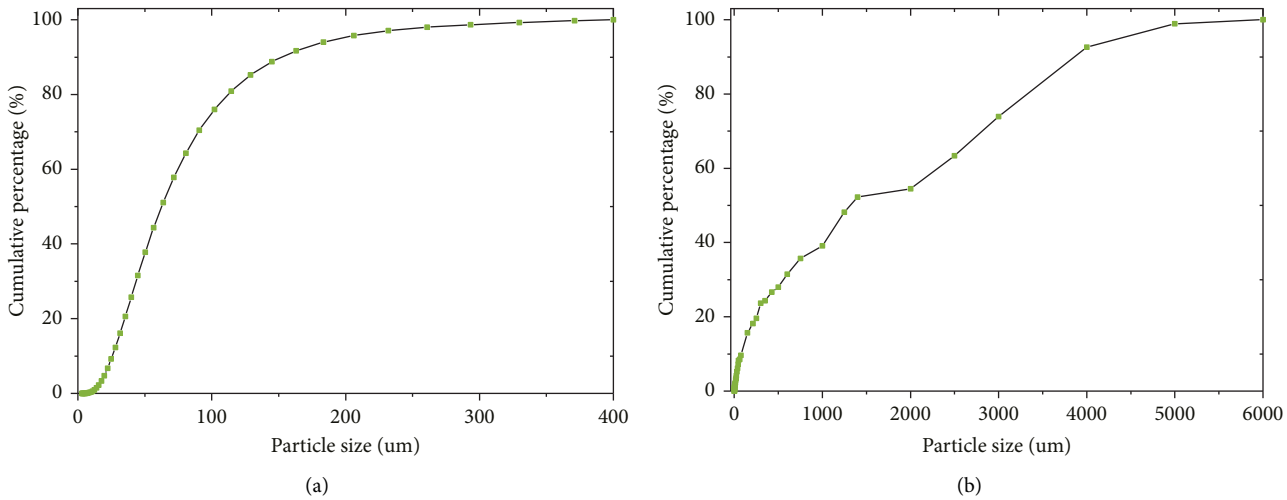

Figure 2: Cumulative distribution of particle size. (a) Fly ash. (b) Gangue.

Table 2: Particle size distribution of coal gangue and fly ash mixed in different proportions.

Particle size distribution (μm)	0 : 1	1 : 4	1 : 5.5	1 : 8	1 : 0
<5	1.61	1.22	1.29	1.35	0.02
<10	2.21	1.89	1.97	2.04	0.36
<25	4.18	5.19	4.95	4.74	4.77
<50	8.21	14.12	12.76	11.49	37.78
<75	9.64	19.92	17.55	15.35	61.00
<150	15.74	30.35	26.98	23.85	88.78
<300	23.70	38.71	35.24	32.04	98.72
<500	28.00	42.40	39.08	36.00	100.00
<1000	39.09	51.28	48.47	45.86	
<2000	54.46	63.57	61.47	59.53	
<3000	73.92	79.14	77.93	76.82	
<4000	92.58	94.07	93.73	93.41	
<5000	98.91	99.13	99.08	99.03	
<6000	100.00	100.00	100.00	100.00	

the increase of the content of fine particles in the slurry, part of the sliding friction between the coarse particles in the slurry changes to rolling friction, the rheological characteristics of the slurry will be improved to some extent, as shown in Figure 7(b). When the fractal dimension is increased from 2.599 to 2.628, the yield stress and viscosity of the slurry are further reduced, indicating that with the further increase of the content of fine particles in the slurry, the friction resistance between particles is further reduced, then the rheological property of the slurry is further improved.

When the fractal dimension is 2.628, the yield stress and viscosity of the slurry are at the lowest point under the same concentration. The yield stress and viscosity of the slurry with the concentration of 76% and 77% are basically the same, which indicates that the water content in the slurry with a fractal dimension of 2.628 and a concentration of 77% is an appropriate value, while the slurry with the fractal dimension of 2.628 and the concentration of 76% contains a small part of excess free water. When the fractal dimension increases from 2.628 to 2.658, the rheological parameters of the slurry with a concentration of 76% basically do not change, the yield stress and viscosity of the slurry with a concentration of 77%, 78%, and 79% gradually increase, and the larger the concentration, the greater the increase. The reason for this phenomenon is that when the fractal dimension is 2.628, the content of fine particles in the slurry has reached a sufficient or excessive state, and the coarse particles are suspended in the slurry and completely separated by the fine particles. The friction between particles is rolling friction, as shown in Figure 7(c). In this state, with the increase of fractal dimension, the content of fine particles in the slurry will further increase, but the friction between particles in the slurry will not decrease. For the slurry with the concentration of 77%, 78%, and 79%, the slurry concentration is high and the water content is low, when the concentration remains constant, the increase of the fine particle content will lead to the reduction of the thickness of the adsorption layer on the surface of the fine particles, which will lead to the reduction of the spacing between the particles. When the spacing between particles becomes smaller, the friction resistance between particles will become larger, which will lead to an increase in the yield stress and viscosity of the slurry. For the slurry with a concentration of 76%, the slurry contains a part of excess free water, which can meet the amount of water that needs to be adsorbed due to the increase of fine particles.

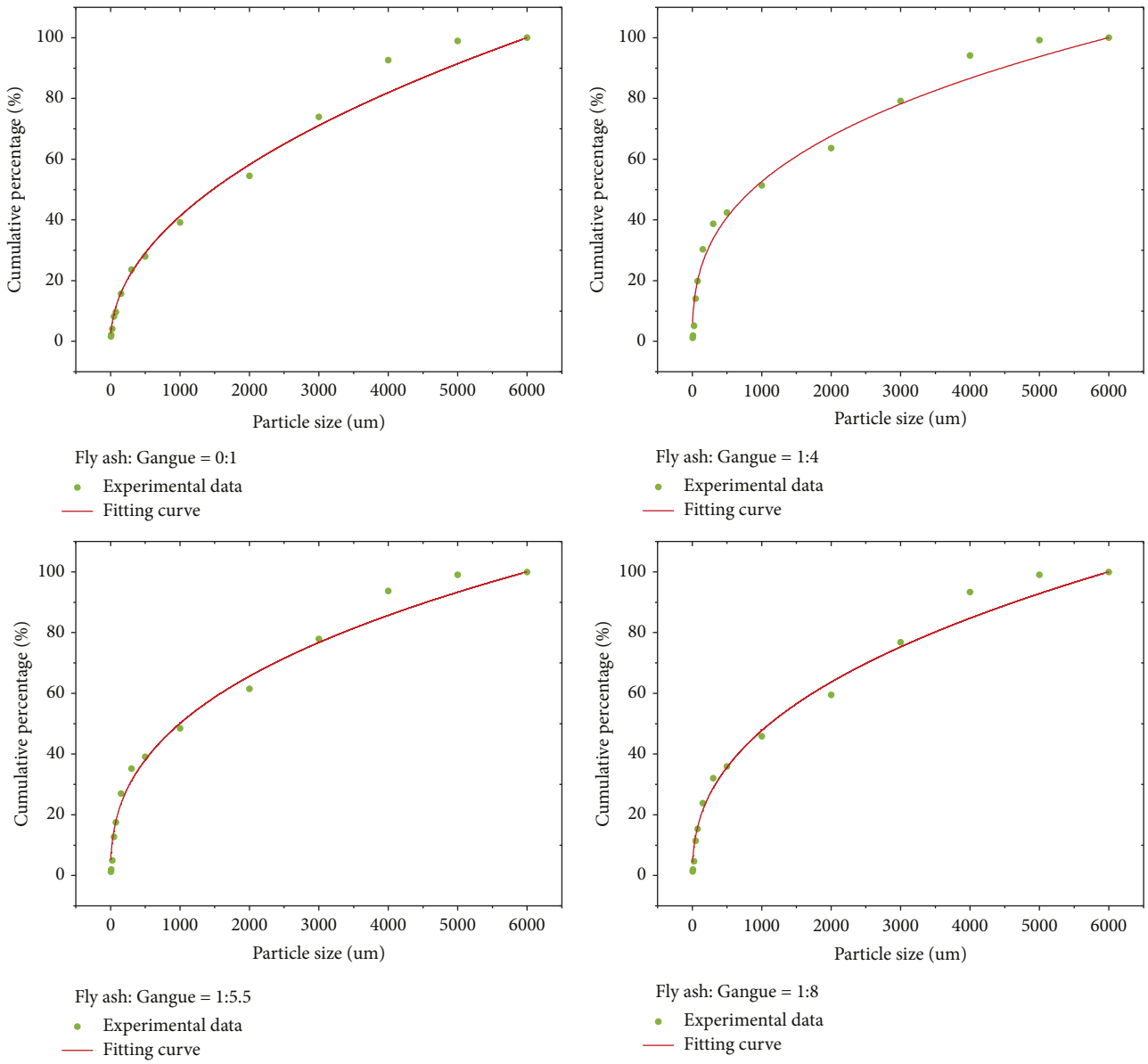

Figure 3: Particle size distribution and fitting of mixed materials.

Table 3: Fractal dimension and correlation coefficient.

Fly ash: coal gangue	Fractal dimension	Correlation coefficient R^2
0 : 1	2.512	0.989
1 : 4	2.658	0.984
1 : 5.5	2.628	0.987
1 : 8	2.599	0.988

Table 4: Test scheme.

Level	Factor		
	Grain gradation		Slurry concentration(%)
	Fly ash: coal gangue	Fractal dimension	
1	0 : 1	2.512	76
2	1 : 4	2.658	77
3	2 : 11	2.628	78
4	1 : 8	2.599	79

In addition, according to the fact that the yield stress and viscosity of the slurry with the fractal dimension of 2.628 and 2.658 are basically equal at the concentration of 76%, it can be concluded that the fractal dimension of 2.628 is a critical point, when the fractal dimension of particle gradation is greater than or equal to 2.628, the content of fine particles in the slurry is sufficient. This is because it is known from the previous analysis that the slurry with the fractal dimension of 2.628 and a concentration of 76% contains a part of excess free water, If the content of fine particles in the slurry with the fractal dimension of 2.628 is insufficient, when the fractal dimension changes from 2.628 to 2.658, the yield stress and viscosity of the slurry will inevitably be further reduced.

Figure 4: Rheometer.

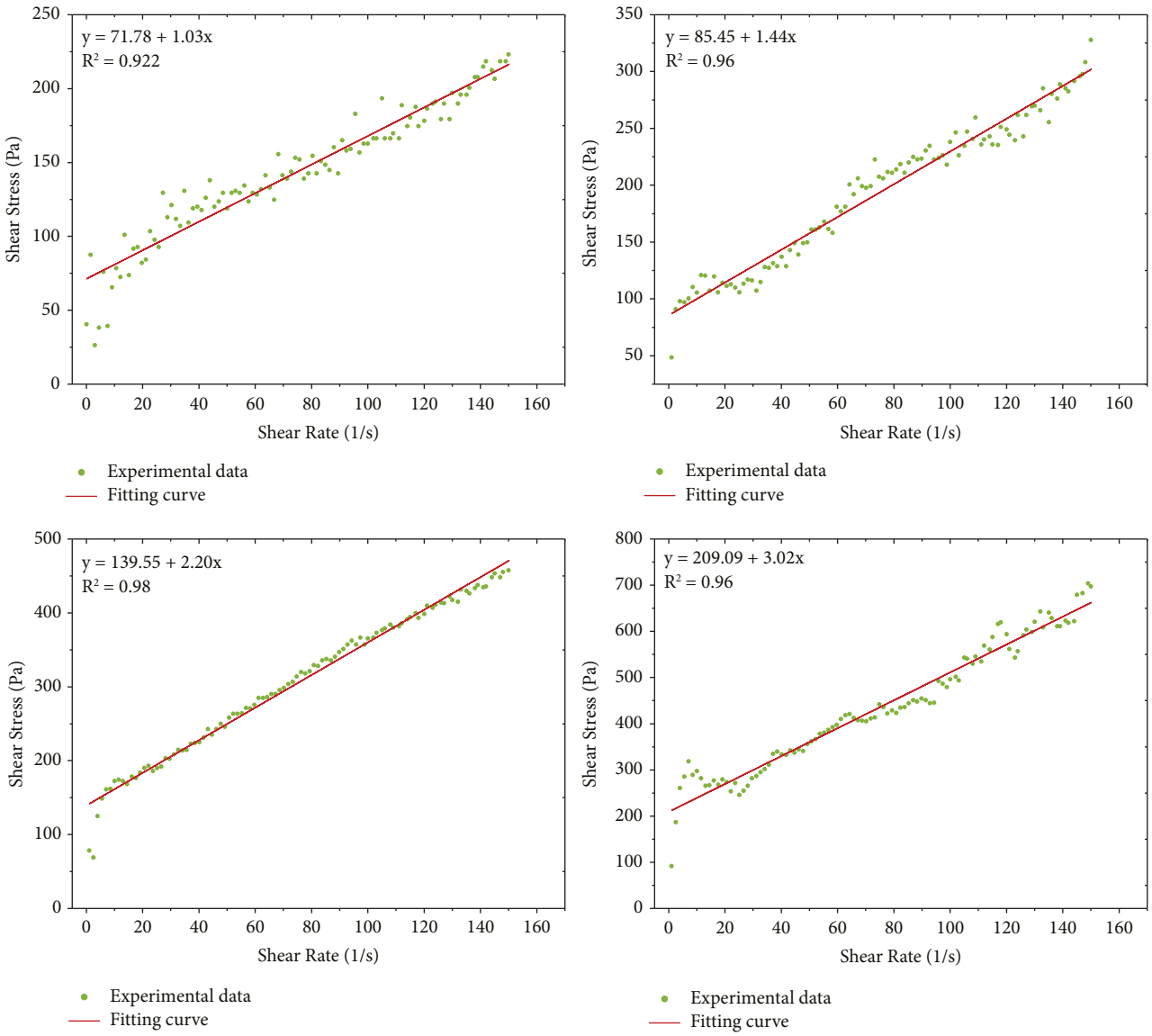

Figure 5: Rheological test results.

However, the test results show that there is no change in both, which indicates that the content of fine particles in the slurry has reached an appropriate content at this time.

The change of slurry rheological parameters with concentration under different fractal dimensions is shown in Figure 8. It can be seen from the figure that when the fractal

Table 5: Rheological parameters of slurry at different proportions.

Samples	Particle gradation		Slurry concentration (%)	Yield stress (Pa)	Dynamic viscosity (Pa·s)
	Fly ash: coal gangue	Fractal dimension (D)			
1	1 : 4	2.658	76	71.78	1.03
2			77	85.45	1.44
3			78	139.55	2.20
4			79	209.09	3.02
5	2 : 11	2.628	76	71.30	1.04
6			77	70.00	1.05
7			78	116.36	1.74
8			79	178.18	2.43
9	1 : 8	2.599	76	120.07	1.49
10			77	100.91	1.42
11			78	139.55	2.04
12			79	193.64	2.63
13	0 : 1	2.512	76	213.65	2.77
14			77	215.36	3.00
15			78	218.78	3.32
16			79	220.00	3.42

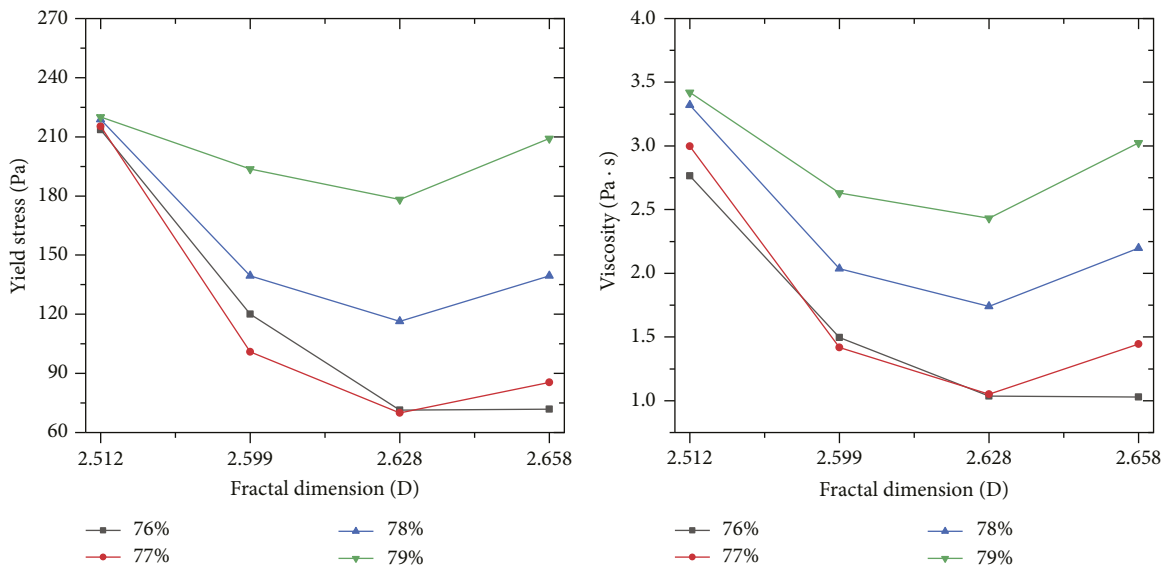

Figure 6: Effect of particle gradation on rheological parameters.

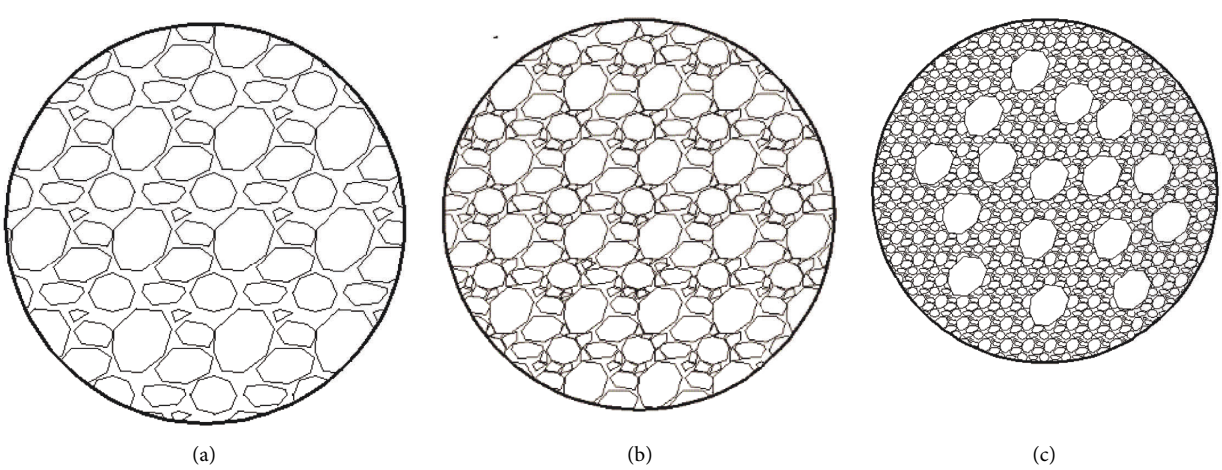

Figure 7: Stacking state of gangue particles.

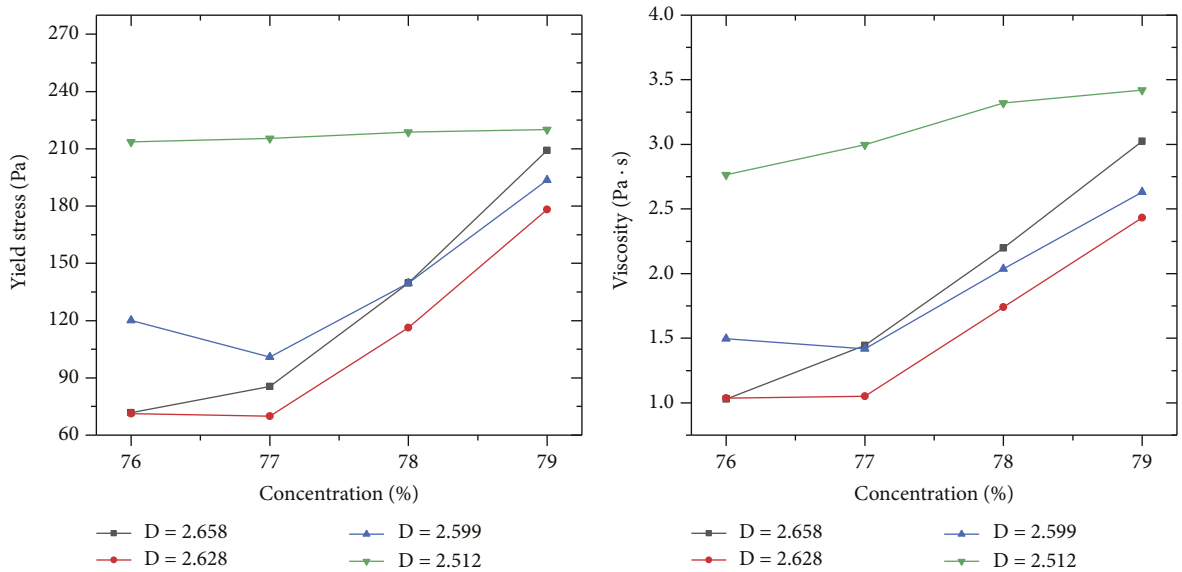

Figure 8: Effect of slurry concentration on rheological parameters.

dimension is 2.599, the yield stress and viscosity of the slurry will decrease as the slurry concentration increases from 76% to 77%, this is because the water content of the slurry with the fractal dimension of 2.599 and the concentration of 76% is too much, part of the free water could be secreted from the surface of the slurry, and some fine particles are suspended in the free water, which will cause the content of fine particles in the whole slurry system to decrease, the friction resistance between particles to increase, and the yield stress and viscosity of the slurry to increase. If the concentration of the slurry is increased, the bleeding amount of free water on the surface of the slurry can be reduced, which is equivalent to increasing the content of fine particles in the slurry system, so the yield stress and viscosity of the slurry will be reduced. When the fractal dimension is 2.628, as the slurry concentration increases from 76% to 77%, the yield stress and viscosity of the slurry remain basically unchanged, this is because at the concentration of 76%, the surface bleeding of the slurry is small, and the bleeding has little impact on the rheological parameters of the slurry, when the slurry concentration is increased to 77%, the bleeding amount on the slurry surface basically disappears, and the rheological property of the slurry basically does not change. When the fractal dimension is 2.658, as the slurry concentration increases from 76% to 77%, the yield stress and viscosity of the slurry gradually increase, the reason is that when the concentration is 76%, there is no redundant free water in the slurry, with the concentration increasing from 76% to 77%, the water content of the slurry is insufficient, resulting in the increase of the yield stress and viscosity of the slurry.

When the fractal dimension is 2.658, 2.628, or 2.599, the yield stress and viscosity of the slurry increase significantly with the slurry concentration increasing from 77% to 78% and then to 79%. The larger the fractal dimension, the faster the growth rate, which indicates that the larger the fractal dimension, the more sensitive the rheological parameters of slurry to the change of concentration. When the fractal dimension is 2.512, the yield stress and viscosity value of the slurry are at a very high level, and the change of the yield stress and viscosity value is very small with the change of the concentration, which indicates that when the content of fine particles in the slurry is too small, the rheological property of the slurry is very poor, and the rheological property of the slurry cannot be effectively improved only by adjusting the concentration of the slurry.

4. Numerical Simulation

4.1. Simulation Scheme. In this section simulation of the pipeline transportation of 16 different backfill slurry in Table 5 by ANSYS fluent soft will be conducted and the pipeline transportation resistance of backfill slurry will be analyzed. ICEM CFD is used to establish two models of straight pipe and elbow pipe (as shown in figure 9). The diameter of the pipeline is 0.2 m, the length of the straight pipe is 3 m, and the radius of curvature of the elbow is 0.6 m. In order to reduce the influence of the unstable transportation of slurry at the inlet and outlet due to the change of pipe diameter on the numerical simulation results, 1.6 m straight pipes are added at the inlet and outlet of the elbow. In order to facilitate the numerical simulation, the following assumptions are made in this paper: during the transportation process, the slurry is simplified as a single-phase flow, the filling slurry is incompressible and does not segregate, and has good integrity and uniformity. The solution settings are shown in Table 6.

4.2. Simulation Results and Analysis. Table 7 is a summary of the numerical simulation results of 16 kinds of slurries. Figure 10 is a numerical simulation cloud diagram of the

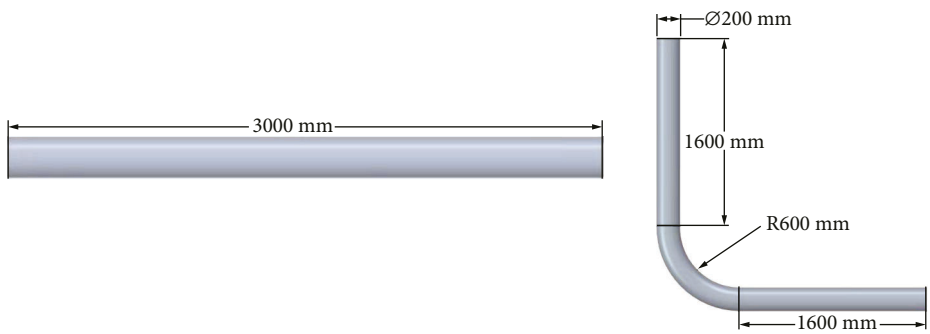

Figure 9: Pipeline model.

Table 6: Numerical simulation solution settings.

Model selection	Slurry density	Velocity-inlet	Pressure-out	Residual	Number of iterations
Viscous-laminar	1800 kg/m^3	1.5 m/s	$1 * 10^5$ Pa	0.001	500

Table 7: Summary of pressure loss per unit length of slurry with different proportions.

Particle grading (D)	Concentration (%)	Pressure loss per unit length (Pa)		
		Straight pipe	Bend	Mean value
2.658	76	3000	3139	3070
	77	3667	3863	3765
	78	5333	5311	5322
	79	7000	7243	7122
2.628	76	3000	3139	3070
	77	3000	3139	3070
	78	4333	4587	4460
	79	6000	6036	6018
2.599	76	4000	4346	4173
	77	3667	3863	3765
	78	5000	5070	5035
	79	6333	6519	6426
2.512	76	6667	6760	6714
	77	7000	7243	7122
	78	7667	7726	7697
	79	7667	7726	7697

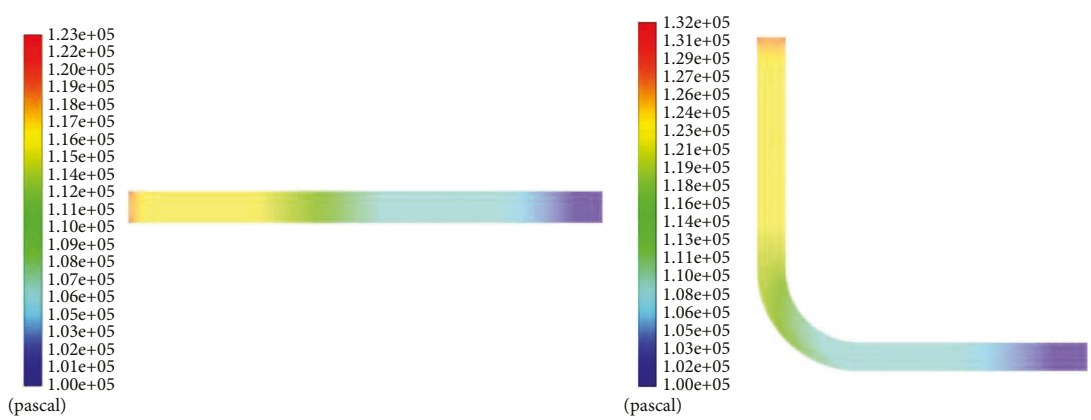

Figure 10: Numerical simulation diagram of slurry with a concentration of 79% and fractal dimension of 2.512.

backfill slurry with a concentration of 79% and a fractal dimension of 2.512. Figure 11 is a distribution diagram of the average pressure loss per unit length of the 16 kinds of slurries. It can be seen from the graph and table that (1) the average pressure loss per unit length pipeline of the slurry transported by the elbow and the straight pipe is between

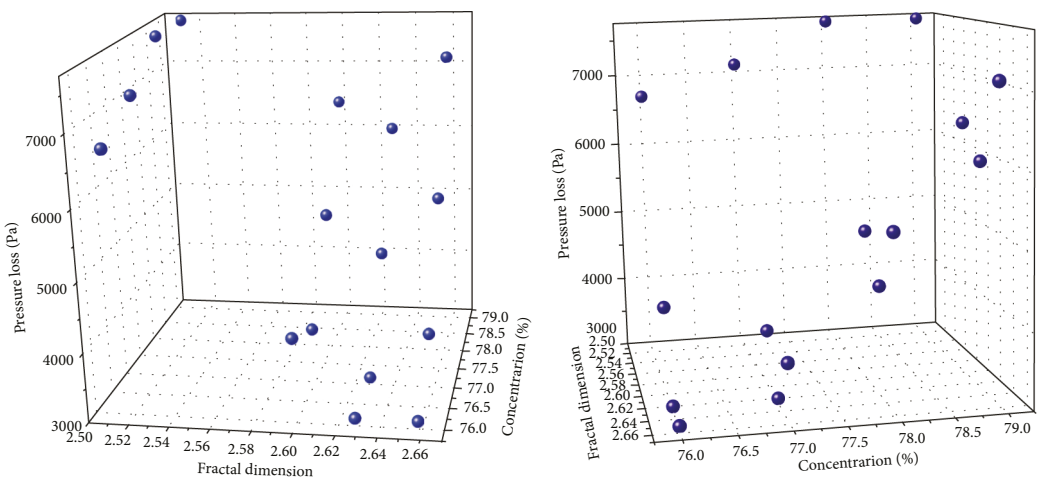

Figure 11: Average pressure loss per unit length of different slurries.

3000–8000 pa, the minimum value is 3070 Pa, the maximum value is 7697 Pa and the pressure loss of the elbow is greater than that of the straight pipe. (2) When the fractal dimension of the slurry gradation is 2.512, the pressure loss of the unit length of the pipeline is greater than 6000 Pa no matter what the slurry concentration is; when the slurry concentration is 79%, the pressure loss is greater than 6000 Pa regardless of the gradation, and the influence of gradation on the slurry performance is greater than the concentration. (3) When the fractal dimension $D \geq 2.599$ and the concentration $\leq$ 78%, the pressure loss per unit length of the pipeline is less than 5000 Pa.

5. Conclusion

(1) The fractal dimension can well characterize the gradation characteristics of the UCGFB mixture, and the larger the fractal dimension, the more fine particles in the material.

(2) The fractal dimension of 2.628 is a critical point. Only when the fractal dimension of the material is greater than or equal to 2.628, the content of fine particles in the slurry can meet the requirements. Based on this, by adjusting the concentration of the slurry, the UCGFB slurry can reach a good state.

(3) The average pressure loss per unit length pipeline of 16 kinds of backfill slurry is between 3000–8000 Pa, the minimum value is 3070 Pa, the maximum value is 7697 Pa, and the pressure loss of the elbow is greater than that of the straight pipe.

Data Availability

The data used to support the findings of this research are included within the paper.

Conflicts of Interest

The authors declare that there are no conflicts of interest.

Acknowledgments

This work was supported by the China Scholarship Council (No. 202106430021).

References

[1] L. J. Yu, Y. L. Feng, and W. Yan, "The current situation of comprehensive utilization of coal gangue in China," *Advanced Materials Research*, vol. 524-527, pp. 915–918, 2012.

[2] Y. Dong, X. Zhang, J. Lin, J. Zhao, and Z. Meng, "Experimental study on the compaction and deformation of filling gangue by reducing waste gangue for filling mining," *Frontiers in Materials*, vol. 8, Article ID 700118, 2021.

[3] B. Hao and C. Wang, "Influence on environment and comprehensive utilization measures of coal gangue," *Dynamics of Urban Agglomeration in China: Preferences of Energy-Saving and Environment-Friendly Society*, pp. 300–303, 2009.

[4] Y. Guo, C. Li, and M. Li, "Experimental study on cement stabilized macadam-gangue mixture in road base," *International Journal of Coal Preparation and Utilization*, vol. 42, no. 3, pp. 580–593, 2022.

[5] L. Li, G. Long, C. Bai, K. Ma, M. Wang, and S. Zhang, "Utilization of coal gangue aggregate for railway roadbed construction in practice," *Sustainability*, vol. 12, no. 11, p. 4583, 2020.

[6] Y. An, "Study on applicability of coal gangue at base layer of navigation airport pavement," *Materials Science, Energy Technology and Power Engineering III (MEP 2019)*, vol. 2154, Article ID 020014, 2019.

[7] T. Huang, S. M. Lei, Q. L. Ma, and E. W. Wang, "Progress of purification and applications of coal gangue," *Advanced Materials Research*, vol. 835-836, pp. 523–526, 2013.

[8] G. Hao, F. Yun, L. Zhanyuan, Y. Sen, and Z. Song, "Study on the property and reuse of coal gangue in Liupanshui, Guizhou Province, China," *International Journal of Mining, Reclamation and Environment*, vol. 27, no. 5, pp. 366–373, 2013.

[9] D. Wu, B. Yang, and Y. Liu, "Pressure drop in loop pipe flow of fresh cemented coal gangue–fly ash slurry: experiment and simulation," *Advanced Powder Technology*, vol. 26, no. 3, pp. 920–927, 2015.

[10] D. Wu, B. Yang, and Y. Liu, "Transportability and pressure drop of fresh cemented coal gangue-fly ash backfill (CGFB)

slurry in pipe loop," *Powder Technology*, vol. 284, pp. 218–224, 2015.

[11] D. Wu, T. Deng, and R. Zhao, "A coupled THMC modeling application of cemented coal gangue-fly ash backfill," *Construction and Building Materials*, vol. 158, pp. 326–336, 2018.

[12] D. Wu, Y. Hou, T. Deng, Y. Chen, and X. Zhao, "Thermal, hydraulic and mechanical performances of cemented coal gangue-fly ash backfill," *International Journal of Mineral Processing*, vol. 162, pp. 12–18, 2017.

[13] B. Yang, J. Jin, X. Yin, X. Wang, and H Yang, "Effect of concentration and suspension agent (HPMC) on properties of coal gangue and fly ash cemented filling material," *Shock and Vibration*, vol. 2021, Article ID 6643773, 12 pages, 2021.

[14] Y. Wang, Y. Huang, and Y. Hao, "Experimental study and application of rheological properties of coal gangue-fly ash backfill slurry," *Processes*, vol. 8, no. 3, p. 284, 2020.

[15] Y. Miao, "Rock fragmentation size distribution prediction and blasting parameter optimization based on the muck-pile model," *Mining, Metallurgy & Exploration*, 2021.

[16] Y. Xu, "Explanation of scaling phenomenon based on fractal fragmentation," *Mechanics Research Communications*, vol. 32, no. 2, pp. 209–220, 2005.

[17] J. A. Sanchidrián, F. Ouchterlony, P. Segarra, and P. Moser, "Size distribution functions for rock fragments," *International Journal of Rock Mechanics and Mining Sciences*, vol. 71, pp. 381–394, 2014.

[18] Y. Wang, W. Dan, Y. Xu, and Y. Xi, "Fractal and morphological characteristics of single marble particle crushing in uniaxial compression tests," *Advances in Materials Science and Engineering*, pp. 1–10, Article ID 537692, 2015.

[19] L. Rui Yang, "Rock unloading failure precursor based on acoustic emission parametric fractal characteristics," *Lithosphere*, 2022.

[20] Y. F. Xu, H. Matsuoka, and D. A. Sun, "Fractal model for grain-size distribution of soils," *Powders and Grains*, vol. 2001, 6 pages, 2001.

[21] H. P. Zhou, "Experiment study on crushing different ores based on fractal theory," *Manufacturing, Design Science and Information engineering*, vol. I AND II, pp. 591–598, 2015.

[22] Y. J. Jiang, Y. Tanabashi, B. Li, and J. Xiao, "Influence of geometrical distribution of rock joints on deformational behavior of underground opening," *Tunnelling and Underground Space Technology*, vol. 21, no. 5, pp. 485–491, 2006.

[23] J. B. Huang and X. Yu, "Relationship of high-temperature performance and aggregate gradation of asphalt mixtures based on fractal theory," *Applied Mechanics and Materials*, vol. 204-208, no. 1-5, pp. 3795–3798, 2012.

[24] H. Chu, F. Ren, Z. Zheng, and M. Gu, "Study on granularity distribution of powder by fractal models," *Fractals*, vol. 25, no. 4, Article ID 1740009, 2017.

[25] J. Konkol and G. Prokopski, "Fracture toughness and fracture surfaces morphology of metakaolinite-modified concrete," *Construction and Building Materials*, vol. 123, pp. 638–648, 2016.

[26] M. Armandei and E. de Souza Sanchez Filho, "Correlation between fracture roughness and material strength parameters in SFRCs using 2D image analysis," *Construction and Building Materials*, vol. 140, pp. 82–90, 2017.

Hindawi
Advances in Materials Science and Engineering
Volume 2022, Article ID 2779965, 16 pages
https://doi.org/10.1155/2022/2779965

Research Article

Development and Application of Analogous Materials for Fluid-Solid Coupling Physical Model Test

Mingyang Ren,[1] **Xiangjie Yin**,[2] **Ningjing Li**,[3] **Xuyang Wu**,[1] **and Heng Liu**[1]

[1]*School of Civil and Transportation Engineering, Henan University of Urban Construction, Pingdingshan, Henan, China*
[2]*Lixia Holding, Jinan, China*
[3]*China Petroleum Pipeline Engineering Corporation, Langfang, Hebei, China*

Correspondence should be addressed to Mingyang Ren; 20201017@hncj.edu.cn

Received 3 August 2022; Accepted 26 September 2022; Published 10 October 2022

Academic Editor: Depeng Ma

The coupling effect between the stress field formed by rock mass and the seepage field formed by groundwater has an important impact on the stability of underground engineering. In order to conduct the fluid-solid coupling physical model test in the laboratory, it is necessary to develop suitable analogous materials. In this study, a new type of analogous material reflecting the fluid-solid coupling effect is developed with iron powder, barite powder, and quartz sand as aggregates, white cement as a cementing agent, and silicone oil as a regulator. Through a large number of orthogonal experiments, the influence laws of different material contents on the mechanical properties and permeability characteristics of analogous materials are obtained. In addition, a method for quickly determining the proportion of components in fluid-solid coupling analogous materials is also proposed. The developed analogous material is employed in the fluid-solid coupling physical model test of a deep tunnel. The variation laws of rock stress, displacement, and seepage pressure around the tunnel during construction are obtained, which verifies the feasibility of the developed analogous material.

1. Introduction

With the rapid development of the global economy and the gradual expansion of human living space, many underground projects under construction and planning continue to march into the deep rock mass. In the fields of mining, transportation, water conservancy and hydropower, energy, and nuclear waste disposal, the buried depth of underground tunnels or caverns has reached more than 1000 kilometers. With the increase in buried depth, the stability of underground engineering is greatly threatened, especially the coupling effect of high ground stress and high external water pressure [1–5]. Therefore, it is of great significance for the safety and economy of underground engineering to study the distribution and evolution of stress, seepage pressure, and displacement in deep rock mass under fluid-solid coupling conditions.

For the complex coupling between the stress field and seepage field of rock mass, theoretical analysis, numerical simulation, and geomechanical model testing are the three main research methods. Moreover, the geomechanical model test can truly reflect the spatial relationship between geological structure and engineering structure and accurately simulate the construction process. Especially, for large and complex engineering problems, it plays an irreplaceable role than theoretical analysis and numerical simulation [6, 7]. The success of the fluid-solid coupling model test of deep rock mass mainly depends on the reliability of the fluid-solid coupling similarity criterion and fluid-solid coupling analogous materials. At present, scholars have studied the fluid-solid coupling similarity theory and analogous materials around these two aspects. Based on the fluid-solid coupling similarity criterion of continuum mechanics theory, Li et al. [8–10] developed a fluid-solid coupling analogous material composed of sand, barite powder, talc powder, cement, petrolatum, silicone oil, and an appropriate amount of mixing water, which can simulate different rock masses with different permeabilities. Hu et al. [11] systematically discussed the three-dimensional solid-fluid coupling similarity theory, which provided theoretical

guidance for the development of model test technology. From the perspective of fluid-solid coupling theory, Chen et al. [12] developed a kind of fluid-solid coupling analogous material for deep water barriers with paraffin and Vaseline as cementing agents, river sand and calcium carbonate as aggregates, and hydraulic oil as a regulator. Yu et al. [13] employed low-melting, high-quality paraffin as a binder, sand and talc powder as aggregate, and high-quality wear-resistant hydraulic oil as the regulator and developed a nonhydrophilic fluid-solid coupling analogous material. Bai et al. [14] developed a novel analogous material mixed with calcium carbonate, white cement, paraffin, quartz sand, silicone oil, talc, and iron powder and researched the effects of different mixing ratios on the mechanical properties of the analogous material. Based on the fluid-solid coupling similarity theory of continuous media, S. Liu and W. Liu [15] mixed river sand, calcium carbonate, talc powder, white cement, Vaseline, and hydraulic oil and developed a fluid-solid coupling analogous material that can simulate coal seam aquifers. Shi et al. [16] developed an analogous material with cement and gypsum as cementing agents and quartz sand as aggregate and studied the relationship between water absorption, softening coefficient, permeability coefficient, sand binder ratio, water paste ratio, and quartz sand particle size. Using cement and gypsum as cementing materials and sand as aggregate, Huang et al. [17] formulated a fluid-solid coupling analogous material that can simulate water inrush in tunnels under excavation disturbance.

Although some progress has been made in the study of fluid-solid coupling analogous materials, the current fluid-solid coupling analogous materials are based on the theory of continuum mechanics without considering the effects of high ground stress [18–24]. The existing fluid-solid coupling analogous materials are not suitable for high ground stress environments. Therefore, this study firstly deduces the fluid-solid coupling similarity criterion under high in situ stress and high water pressure. Then, under the guidance of the derived similarity criterion, a new type of fluid-solid coupled analogous material suitable for simulating deep rock mass engineering is developed, and the effects of different mixing ratios on the density, compressive strength, tensile strength, deformation modulus, and permeability coefficient of analogous materials are studied through orthogonal tests. Finally, taking Xianglu Mountain Tunnel as the engineering background, the effectiveness of the developed analogous material is verified by conducting a fluid-solid coupling model test.

2. Fluid-Solid Coupling Similarity Conditions under High In Situ Stress

According to the similarity principle, the fluid-solid coupling model test of deep rock mass must not only meet the similarity of geometric dimensions, boundary conditions, mechanical properties, and rock mass structure but also meet the similarity of hydraulic properties (mainly referring to the four parameters including permeability coefficient, seepage pressure, seepage flow, and flow velocity).

The fluid-solid coupling similarity criterion is the basis for the development of analogous materials. The current fluid-solid coupling similarity criterion is mostly derived from the homogeneous continuum mechanics model [11], which is expressed as follows:

$$\begin{cases} C_G \dfrac{C_\delta}{C_L^2} = C_\lambda \dfrac{C_V}{C_L} = C_G \dfrac{C_V}{C_L} = C_\rho \dfrac{C_\delta}{C_t^2} = C_\gamma \\ C_K = \sqrt{C_L}/C_\gamma \\ C_P = C_\gamma C_L \end{cases}, \tag{1}$$

where C_G is the similarity ratio of shear modulus, C_δ is the similarity ratio of displacement, C_L is the similarity ratio of geometric dimensions, C_λ is the similarity ratio of Lame's constant, C_V is the similarity ratio of volume, C_ρ is the similarity ratio of density, C_t is the similarity ratio of time, C_γ is the similarity ratio of unit weight, C_K is the similarity ratio of permeability coefficient, and C_P is the similarity ratio of seepage pressure.

When the rock mass is under the influence of high in situ stress and high seepage pressure, the similarity relationship of equation (1) will no longer be satisfied. Therefore, it is necessary to establish the fluid-solid coupling similarity criterion considering high in situ stress and high seepage pressure.

2.1. Similarity Criterion of Permeability Coefficient. Considering the influence of high ground stress on the permeability coefficient, Wu et al. [25] obtained the relationship between effective stress and permeability coefficient through a large number of field tests:

$$K_f = K_0 \sigma^{-a}, \tag{2}$$

where K_f is the permeability coefficient, K_0 is the permeability coefficient when the effective stress approaches 0, σ is the effective stress, and α is the fractal dimension of fracture distribution density.

In order to keep the dimension consistent, $\sigma_0 = 1$ MPa is introduced; then, equation (2) can be rewritten as

$$K_f = K_0 \left(\frac{\sigma}{\sigma_0}\right)^{-a}. \tag{3}$$

Combining equation (3) and similarity principle, we can obtain

$$\text{Prototype: } K_f = K_0 \left(\frac{\sigma}{\sigma_0}\right)^{-a} (\sigma > 0), \tag{4}$$

$$\text{Model: } K_f' = K_0' \left(\frac{\sigma'}{\sigma_0'}\right)^{-a'} (\sigma' > 0). \tag{5}$$

According to the similarity principle and in combination with equations (4) and (5), it can be deduced that

$$C_{K_f}K_f' = C_{K_0}K_0'\left(\frac{C_\sigma\sigma'}{C_{\sigma_0}\sigma_0'}\right)^{-C_a a'}. \quad (6)$$

Since α is a dimensionless quantity and σ_0 is a constant, we get $C_\alpha = 1$ and $C_{\sigma 0} = 1$. Therefore, equation (6) can be simplified as

$$\frac{C_K}{C_{K_0}C_\sigma^{-\alpha}}K_f' = K_0'\sigma'^{-\alpha'}. \quad (7)$$

So, the similarity ratio of permeability coefficient considering the influence of high stress is

$$C_K = C_{K_0}C_\sigma^{-\alpha}. \quad (8)$$

The similarity ratio formula of permeability coefficient in equation (1) is brought into equation (8), and the similarity condition of permeability coefficient considering high in situ stress is

$$C_K = C_\sigma^{-\alpha}C_\gamma^{-1}C_L^{1/2}. \quad (9)$$

2.2. Similarity Criterion of Seepage Flow. The relationship between the similarity ratio of seepage flow and permeability coefficient is

$$\text{Prototype: } Q = K_f A\frac{H_1 - H_2}{L}, \quad (10)$$

$$\text{Model: } Q' = K_f' A'\frac{H_1' - H_2'}{L'}, \quad (11)$$

where Q is the seepage discharge, K_f is the permeability coefficient, H_1 and H_2 are the water head heights along the seepage path, respectively, L is the length of seepage path, and A is the seepage cross-sectional area. According to the similarity principle, we can obtain

$$C_Q Q' = C_{K_f}K_f'C_L^2A'\frac{C_L H_1' - C_L H_2'}{C_L L'}. \quad (12)$$

After simplifying equation (12), it can be deduced that

$$C_Q = C_K C_L^2. \quad (13)$$

Taking equation (9) into (13), the similarity condition of seepage flow considering the influence of high ground stress is

$$C_Q = C_\sigma^{-\alpha}C_\gamma^{-1}C_L^{2/5}. \quad (14)$$

2.3. Similarity Criterion of Flow Velocity. The calculation formula of fluid velocity is

$$v = \frac{L}{t}, \quad (15)$$

where v is the velocity of the fluid, L is the movement path of the fluid, and t is the movement time of the fluid.

According to the similarity theory, the similarity ratios of flow velocity and acceleration satisfy

$$C_v = \frac{C_L}{C_t}, \quad (16)$$

$$C_a = \frac{C_v}{C_t} = \frac{C_v^2}{C_L}. \quad (17)$$

The gravity of two similar flow fields in the gravity field must also be similar. Therefore, the following formula holds

$$C_a = \frac{C_v}{C_t} = \frac{C_v^2}{C_L} = C_g. \quad (18)$$

Therefore, the similarity ratio relation of flow velocity is

$$C_v = \sqrt{C_L C_g}. \quad (19)$$

2.4. Similarity Criterion of Seepage Pressure. According to the definition of seepage pressure and the similarity principle, the following formula can be deduced:

$$\text{Prototype: } P = \frac{F}{A}, \quad (20)$$

$$\text{Model: } P' = \frac{F'}{A'}. \quad (21)$$

$$\begin{cases} P = C_P P' \\ F = C_F F' \\ A = C_A A' \end{cases}. \quad (22)$$

Combined with equation (20)–(22), the following formulas can be deduced:

$$C_P = \frac{C_F}{C_A} = \frac{C_F}{C_L^2}. \quad (23)$$

The similarity ratio of forces can be deduced as

$$C_F = \frac{\rho L^{3v/t}}{\rho' L'^{3v'/t'}} = C_\gamma C_L^2 C_v^2. \quad (24)$$

Combined with equations (23) and (24), the relationship of similarity ratio between seepage pressure and flow velocity is

$$C_P = C_\gamma C_v^2. \quad (25)$$

So, similar condition of seepage pressure can be written as

$$C_P = C_\gamma C_L. \quad (26)$$

3. Development of Fluid-Solid Coupling Analogous Materials

3.1. Selection of Raw Materials. The raw materials of fluid-solid coupling analogous materials mainly include aggregate,

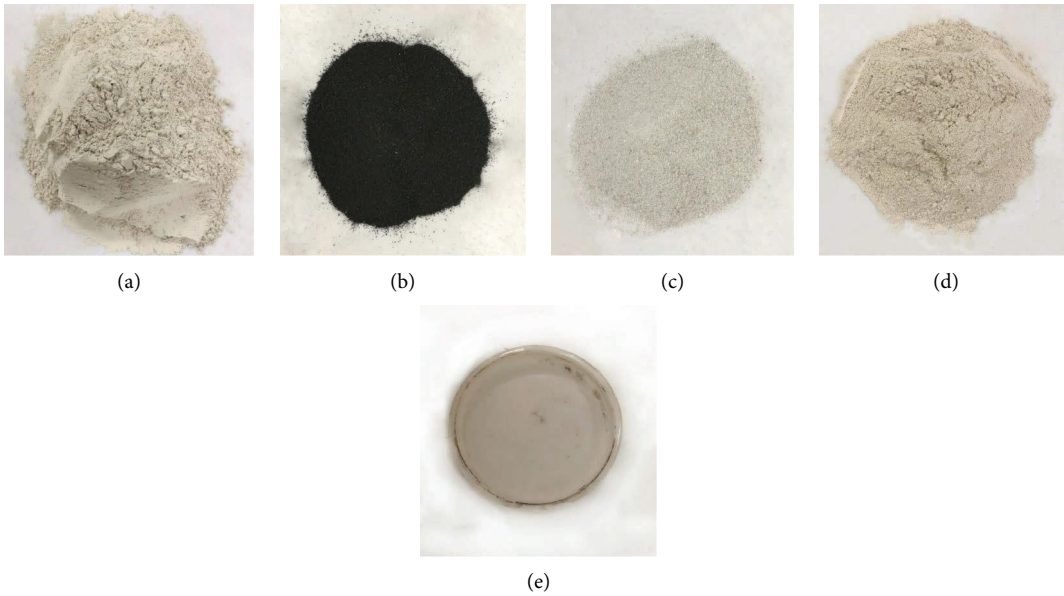

Figure 1: Raw materials used for developing fluid-solid coupling analogous materials. (a) Barite powder; (b) iron powder; (c) quartz sand; (d) white cement; (e) silicone oil.

cementing agent, and regulator. By consulting a large number of literature on fluid-solid coupling analogous materials and testing the relevant characteristics of raw materials [7–10], it is finally determined to select iron powder, quartz sand and barite powder as aggregates, white cement as a cementing agent, and silicone oil as a regulator to develop fluid-solid coupling analogous materials.

As the main raw material, aggregate plays the role of skeleton and support for the specimen. If no aggregate is added during the production of the test sample, the test sample will not be formed. In our test, the grain size of quartz sand particles is in the range of 300~1200 μm, the grain size of barite powder is in the range of 20~70 μm, and iron powder has a particle size in the range of 80~130 μm. A cementing agent refers to a substance with considerable strength that changes the properties of the material through physical and chemical actions and can be closely bonded with other materials. The cementation strength of white cement is between gypsum and cement, which can better adjust the strength of analogous materials. So, the materials will not collapse in the case of water and meet the two special conditions of deformation and permeability. In the development of fluid-solid coupling analogous materials, the role of the regulator is generally to adjust the permeability coefficient of materials. In this study, high-quality silicone oil with a viscosity of 10^{-3} m^2/s is selected, which has the functions of moisturizing and reducing dry cracking, and can improve the nonhydrophilic property of the material. Figure 1 illustrates the raw materials used for developing fluid-solid coupling analogous materials.

3.2. Experimental Scheme and Sample Preparation for Analogous Materials. The influence of components in raw materials on the mechanical properties and hydraulic properties of fluid-solid coupling analogous materials is studied by an orthogonal test. In the orthogonal experiment, the mass ratio of iron powder, quartz sand, and barite powder is selected as factor A, the ratio of white cement mass to aggregate mass is selected as factor B, and the ratio of silicone oil mass to aggregate mass is selected as factor C. Due to the important influence of aggregate on materials, factor A is set at 7 levels: 1 : 1 : 1, 2 : 1 : 1, 4 : 1 : 1, 1 : 2 : 1, 1 : 4 : 1, 1 : 1 : 2, and 1 : 1 : 4. Factor B is set at 4 levels of 0.1%, 2%, 4%, and 6%. Factor C is set at 4 levels of 0.1%, 3%, 6%, and 9%. The designed orthogonal experimental scheme L_{32} $(1^7 \times 2^4)$ is listed in Table 1.

Fluid-solid coupling analogous material tests include density test, uniaxial compression test, Brazilian splitting test, and permeability test, which are used to obtain its density, compressive strength, tensile strength, deformation modulus, and permeability coefficient. Figure 2 displays the preparation of fluid-solid coupling analogous material specimens. Figure 3 gives the process of testing analogous materials.

Figure 4 presents the axial stress-axial strain curve from uniaxial compression test. It can be seen that the axial stress-axial strain curve of analogous materials shows obvious strain softening characteristics, which is similar to the complete stress-strain curve of rock.

According to the orthogonal experimental scheme designed in Table 1, the density, uniaxial compressive strength, tensile strength, deformation modulus, and permeability coefficient of each group of fluid-solid coupling analogous materials are listed in Table 2.

4. Influence of Components in Raw Materials on Properties of Analogous Materials

Range is the reflection of the influence of different levels on specific test indicators under specific factors. For the results

Table 1: Orthogonal experimental scheme L_{32} ($1^7 \times 2^4$).

Experiment number	Experimental scheme	Mass ratio Iron powder : quartz sand : barite powder	Ratio of white cement mass to aggregate mass (%)	Ratio of silicone oil mass to aggregate mass (%)
1	A_1—B_1—C_1	1 : 1 : 1	0.1	0.1
2	A_1—B_1—C_4	1 : 1 : 1	0.1	9
3	A_1—B_2—C_2	1 : 1 : 1	2	3
4	A_1—B_2—C_3	1 : 1 : 1	2	6
5	A_1—B_3—C_2	1 : 1 : 1	4	3
6	A_1—B_3—C_3	1 : 1 : 1	4	6
7	A_1—B_4—C_4	1 : 1 : 1	6	9
8	A_1—B_4—C_1	1 : 1 : 1	6	0.1
9	A_2—B_1—C_3	2 : 1 : 1	0.1	6
10	A_2—B_2—C_4	2 : 1 : 1	2	9
11	A_2—B_3—C_1	2 : 1 : 1	4	0.1
12	A_2—B_4—C_2	2 : 1 : 1	6	3
13	A_3—B_1—C_1	4 : 1 : 1	0.1	0.1
14	A_3—B_2—C_2	4 : 1 : 1	2	3
15	A_3—B_3—C_3	4 : 1 : 1	4	6
16	A_3—B_4—C_4	4 : 1 : 1	6	9
17	A_4—B_1—C_3	1 : 2 : 1	0.1	6
18	A_4—B_2—C_4	1 : 2 : 1	2	9
19	A_4—B_3—C_1	1 : 2 : 1	4	0.1
20	A_4—B_4—C_2	1 : 2 : 1	6	3
21	A_5—B_1—C_2	1 : 4 : 1	0.1	3
22	A_5—B_2—C_1	1 : 4 : 1	2	0.1
23	A_5—B_3—C_4	1 : 4 : 1	4	9
24	A_5—B_4—C_3	1 : 4 : 1	6	6
25	A_6—B_1—C_4	1 : 1 : 2	0.1	9
26	A_6—B_2—C_3	1 : 1 : 2	2	6
27	A_6—B_3—C_2	1 : 1 : 2	4	3
28	A_6—B_4—C_1	1 : 1 : 2	6	0.1
29	A_7—B_1—C_2	1 : 1 : 4	0.1	3
30	A_7—B_2—C_1	1 : 1 : 4	2	0.1
31	A_7—B_3—C_4	1 : 1 : 4	4	9
32	A_7—B_4—C_3	1 : 1:4	6	6

(a) (b) (c)

Figure 2: Preparation of fluid-solid coupling analogous material specimens. (a) Dumping mixed materials; (b) compression moulding; (c) cured specimen.

of orthogonal test, the range analysis method is intuitive and easy to understand. The primary and secondary factors affecting the test results can be easily obtained through range analysis.

When the levels of each factor in the orthogonal experimental scheme are equal, the sensitivity order of all factors is completely determined by the range. Since the level of factor A in our orthogonal experiment is 7, the level of other factors is 4. Therefore, the range of factor A needs to be reduced. The reduction formula of the range is

$$R' = dR\sqrt{r}, \tag{27}$$

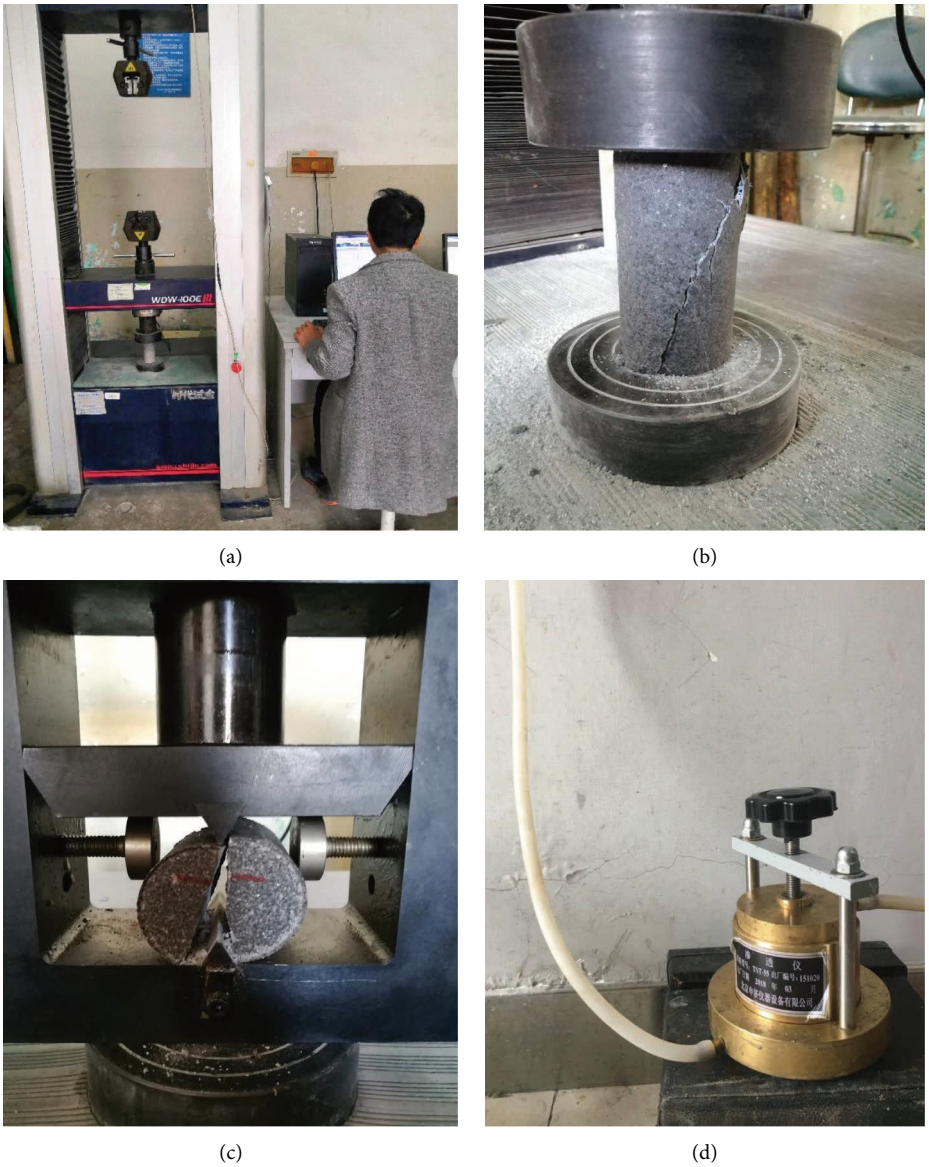

Figure 3: Process of testing analogous materials. (a) Uniaxial compression test; (b) failed specimen after compression; (c) brazilian splitting test; (d) permeability test.

where R' and R are the range before and after reduction, respectively, r is the repetition times of each level test of this factor, $r = n/m$, n is the number of tests, m is the number of levels, and d is the reduced coefficient, which is related to the level number of factor.

4.1. Influence of Material Components on Density. Table 3 and Figure 5 display the influence of material composition on density. From Table 3, it can be seen that the density is most affected by aggregate, followed by silicone oil, and least by white cement. Moreover, compared with silicone oil and white cement, aggregate has a dominant effect on density. The effect of white cement on density is almost negligible. The variation curves of density with various factors in Figure 5 can also prove this point. In addition, with the increase in the proportion of iron powder, the density of analogous materials showed a significant increasing trend. This is mainly due to the fact that the density of the iron powder is much higher than that of other components. Therefore, this can give us an enlightenment; when matching fluid-solid coupling analogous materials, the density of the analogous material can be adjusted by controlling the content of the iron powder.

4.2. Influence of Material Components on Compressive Strength. Table 4 and Figure 6 display the influence of material composition on compressive strength. From Table 4, it can be seen that the ranges of three factors A, B, and C are 0.33 MPa, 0.85 MPa, and 0.06 MPa, respectively. Therefore, the compressive strength is most affected by white cement, followed by aggregate, and least by silicone oil. Moreover, the effect of white cement on compressive

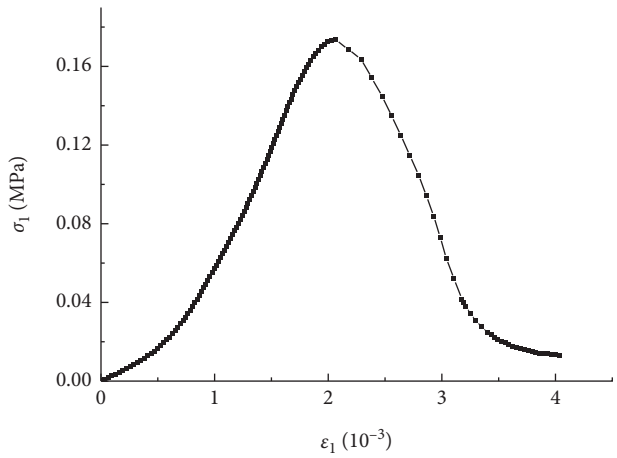

Figure 4: Axial stress-axial strain curve of fluid-solid coupling analogous material.

Table 2: Orthogonal experimental result.

Experiment number	Density (g/cm^3)	Compressive strength (MPa)	Tensile strength (kPa)	Deformation modulus (MPa)	Permeability coefficient (m/s)
1	2.51	0.51	71.3	86.5	$9.60e^{-8}$
2	2.7	0.65	30.2	101.4	$5.20e^{-8}$
3	2.61	0.91	50.6	77.3	$6.80e^{-8}$
4	2.65	0.98	42.3	53.8	$5.30e^{-8}$
5	2.63	1.12	82.5	137.2	$3.90e^{-8}$
6	2.66	1.19	80.8	98.7	$2.10e^{-8}$
7	2.69	1.42	61.4	110.3	$9.10e^{-9}$
8	2.53	1.37	124.7	152.1	$6.80e^{-8}$
9	2.86	0.72	39.6	49.8	$4.13e^{-8}$
10	2.88	0.95	47.7	55.9	$7.10e^{-9}$
11	2.77	1.21	79.8	130.5	$8.90e^{-8}$
12	2.8	1.44	114.5	174.9	$9.30e^{-9}$
13	2.86	0.55	51.7	82.3	$8.30e^{-8}$
14	2.88	0.82	60.3	117.6	$3.30e^{-8}$
15	2.91	1.07	67.6	137.8	$1.10e^{-8}$
16	2.93	1.48	75.4	172.3	$9.50e^{-9}$
17	2.54	0.35	34.1	42.5	$3.50e^{-8}$
18	2.57	0.69	39.7	48.6	$1.10e^{-8}$
19	2.49	0.97	45.3	54.3	$7.10e^{-7}$
20	2.52	1.34	79.8	57.2	$2.00e^{-7}$
21	2.31	0.21	19.3	34.2	$9.20e^{-7}$
22	2.29	0.46	36.4	38.5	$9.60e^{-7}$
23	2.36	0.83	43.7	41.8	$1.40e^{-7}$
24	2.33	1.08	84.6	47.6	$1.10e^{-7}$
25	2.47	0.29	20.7	30.3	$3.20e^{-8}$
26	2.45	0.51	31.8	36.1	$1.20e^{-8}$
27	2.44	0.85	43.7	41.8	$2.85e^{-9}$
28	2.42	1.13	82.4	48.2	$5.20e^{-8}$
29	2.3	0.34	21.5	33.2	$1.70e^{-8}$
30	2.28	0.59	42.5	34.8	$5.80e^{-8}$
31	2.34	0.92	48.7	40.6	$1.00e^{-9}$
32	2.32	1.15	82.6	49.3	$8.90e^{-9}$

strength is much greater than that of aggregate and silicone oil. This can also be confirmed from the variation curves of compressive strength with various factors in Figure 6. Figure 6 clearly shows that the compressive strength first increases and then decreases with the increase of iron powder content. That is to say, there is a critical proportion (50%) of iron powder content in terms of compressive strength. In general, the compressive strength of analogous materials increases linearly with the increase of white cement content, but is not sensitive to the content of silicone oil.

Table 3: Range analysis of the influence of material composition on density.

Level number	Density (g/cm^3)		
	Factor A	Factor B	Factor C
1	2.62	2.57	2.52
2	2.83	2.58	2.56
3	2.90	2.58	2.59
4	2.53	2.57	2.62
5	2.32		
6	2.45		
7	2.31		
R	0.59	0.009	0.099
R'	0.44		

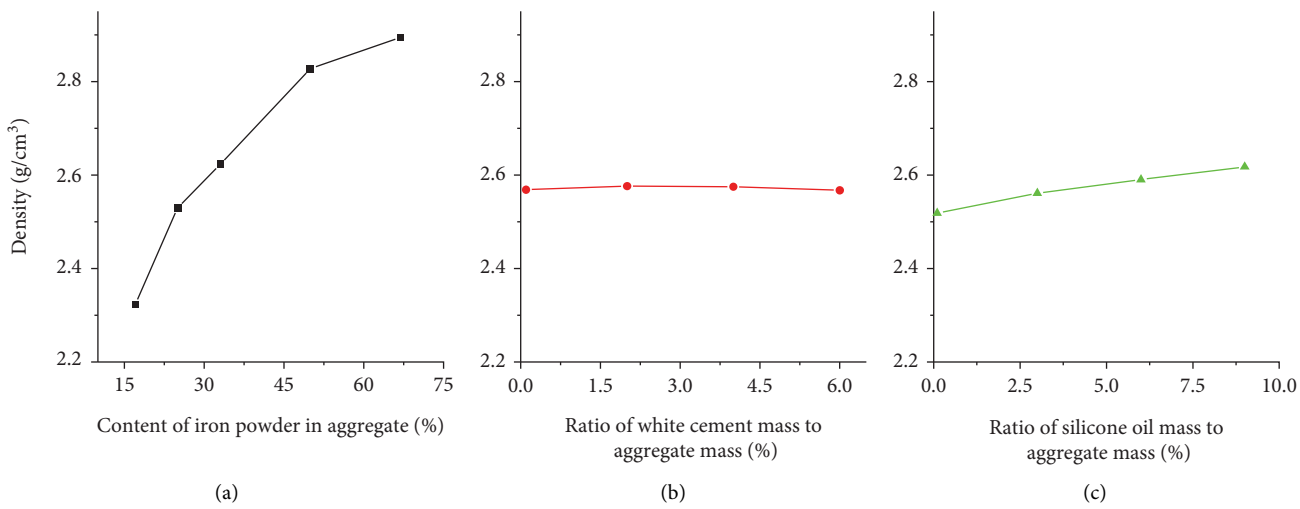

Figure 5: Influence of material composition on density.

Table 4: Range analysis of the influence of material composition on compressive strength.

Level number	Uniaxial compressive strength (MPa)		
	Factor A	Factor B	Factor C
1	1.02	0.45	0.85
2	1.08	0.74	0.88
3	0.98	1.02	0.88
4	0.84	1.30	0.90
5	0.65		
6	0.70		
7	0.75		
R	0.44	0.85	0.06
R'	0.33		

4.3. Influence of Material Components on Tensile Strength. Table 5 and Figure 7 display the influence of material composition on tensile strength. From Table 5, it can be seen that the ranges of three factors A, B, and C are 19.27 kPa, 52.13 kPa, and 20.83 kPa, respectively. Therefore, the tensile strength is most affected by white cement, which is consistent with its effect of compressive strength. In addition, the variation of tensile strength with the content of white cement and iron powder in Figure 7 is also consistent with the variation of compressive strength. However, the tensile strength decreases with the increase of silicone oil content. On the whole, both compressive strength and tensile strength are most affected by white cement. This also reflects the function of white cement as a cementing agent. Therefore, the strength of analogous materials can be adjusted by controlling the content of white cement.

4.4. Influence of Material Components on Deformation Modulus. Table 6 and Figure 8 display the influence of material composition on deformation modulus. From Table 6, it can be seen that the ranges of three factors A, B, and C

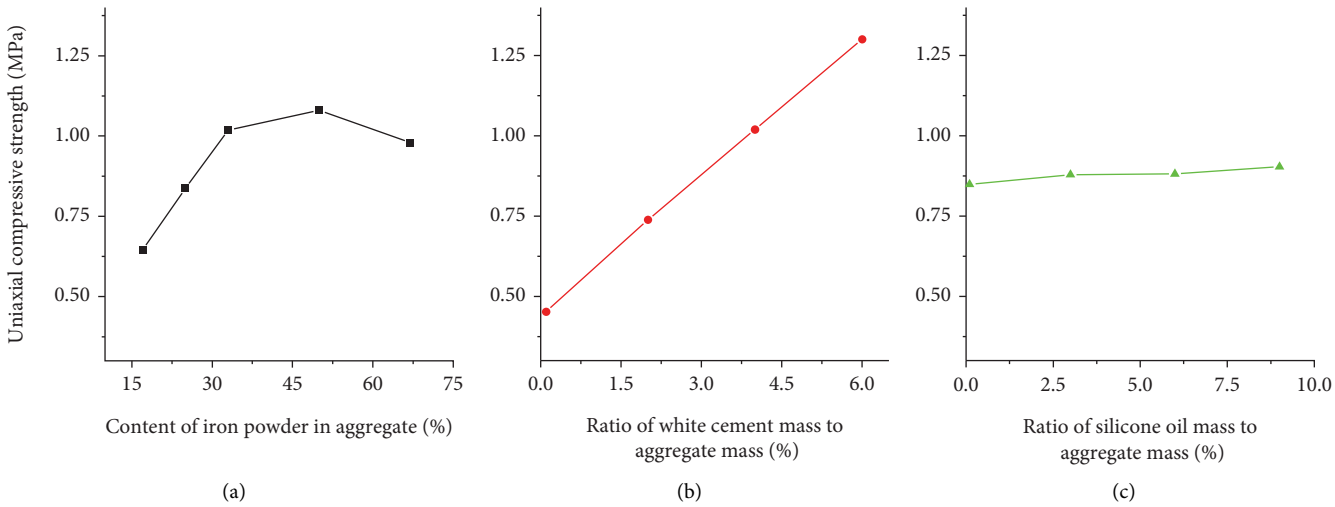

Figure 6: Influence of material composition on compressive strength.

Table 5: Range analysis of the influence of material composition on tensile strength.

Level number	Tensile strength (kPa)		
	Factor A	Factor B	Factor C
1	67.98	36.05	66.76
2	70.40	43.91	59.03
3	63.75	61.51	57.93
4	49.73	88.18	45.94
5	46.00		
6	44.65		
7	48.83		
R	25.75	52.13	20.83
R'	19.27		

are 66.15 MPa, 43.96 MPa, and 19.73 MPa, respectively. The influence of aggregate, white cement, and silicone oil on the deformation modulus decreases in turn. Figure 8 depicts that the deformation modulus generally increases with the increase of iron powder content and white cement content, but its change trend with silicone oil is not significant. The reason why the deformation modulus increases with the increase of iron powder content may be that iron powder improves the particle gradation of aggregate and increases its compactness. As a binder, white cement plays the role of bonding particles to stabilize the skeleton. The increase of its content will inevitably lead to the increase of deformation modulus.

4.5. Influence of Material Components on Permeability Coefficient. Table 7 and Figure 9 display the influence of material composition on permeability coefficient. From Table 6, it can be seen that the range of three factors A, B, and C are $3.83e^{-7}$ m/s, $1.01e^{-7}$ m/s, and $2.32e^{-7}$ m/s, respectively. Therefore, aggregate has the greatest influence on the permeability coefficient, followed by silicone oil, and white cement has the least influence. Figure 9 clearly shows that, with the increase of iron powder content, white cement content, and silicone oil content, the permeability coefficient of analogous materials shows a downward trend. The reason for this phenomenon may be that the increase in the content of iron powder improves the gradation of the particles of analogous materials and increases its compactness, while the increase in the content of white cement and silicone oil leads to the blockage of the permeable channels in the analogous materials, resulting in a decrease in the permeability coefficient. Different from the effect of white cement on the permeability coefficient, the effect of aggregate and silicone oil on the permeability coefficient has significant segmentation characteristics. For factor A, when the content of iron powder is lower than 33%, the change of permeability coefficient is very sharp, and when it exceeds 33%, the change of permeability coefficient is relatively gentle. Similarly, when the content of silicone oil is less than 6%, the permeability coefficient changes significantly, and when it is greater than 6%, the permeability coefficient basically remains unchanged. Therefore, the segmentation feature should be fully utilized when adjusting the permeability coefficient of fluid-solid coupling analogous materials.

To develop fluid-solid coupling analogous materials that meet certain requirements, it is usually necessary to carry out a large number of trial and error tests and repeatedly adjust the proportion of each material component. This is a rather

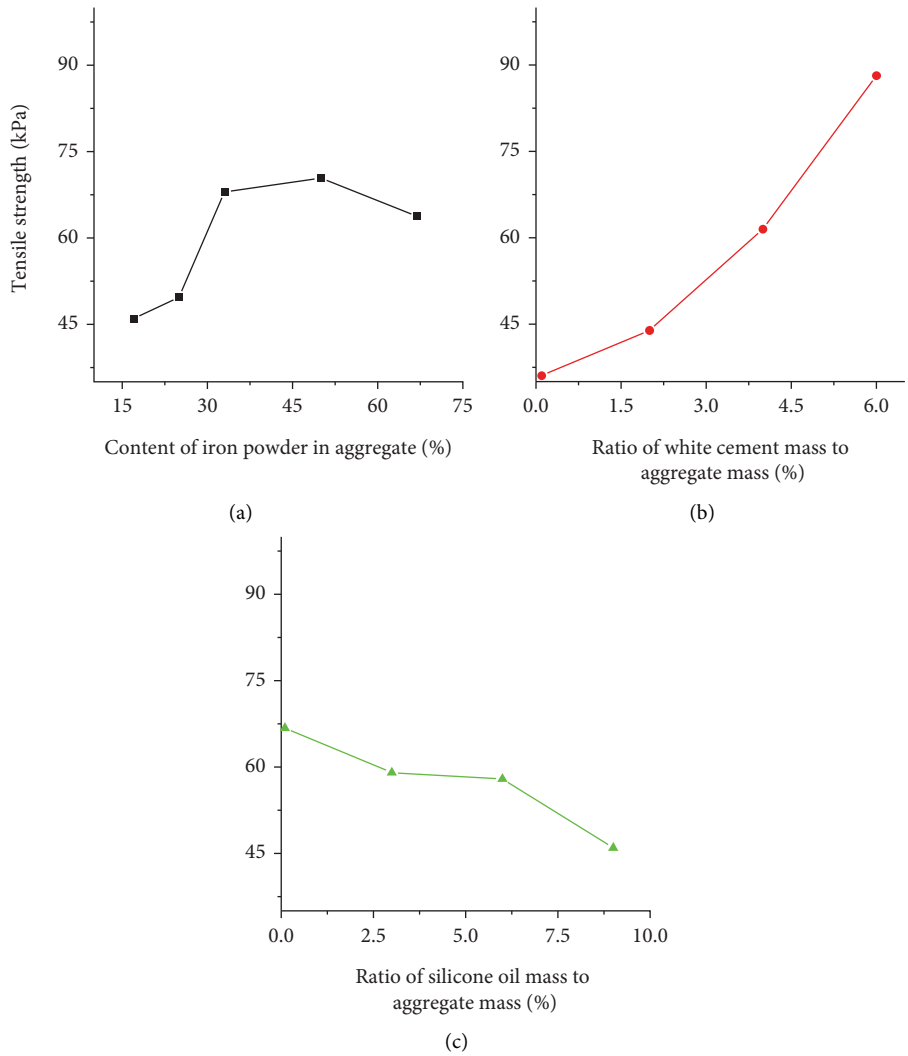

Figure 7: Influence of material composition on tensile strength.

Table 6: Range analysis of the influence of material composition on deformation modulus.

Level number	Deformation modulus (MPa)		
	Factor A	Factor B	Factor C
1	102.16	57.53	78.40
2	102.78	57.83	84.18
3	127.50	85.34	64.45
4	50.65	101.49	75.15
5	40.53		
6	39.10		
7	39.48		
R	88.40	43.96	19.73
R'	66.15		

tedious and arduous task. Therefore, based on the analysis of the influence of material components on the physical and mechanical properties of fluid-solid coupling analogous materials, we propose a method to quickly determine the proportion of components in analogous materials that meet certain requirements.

According to the above results, the role of aggregate is very important, especially the content of iron powder, which mainly affects the density, deformation modulus, and permeability of analogous materials. Therefore, the proportion of all components in aggregate is the main controlling factor in determining the proportioning

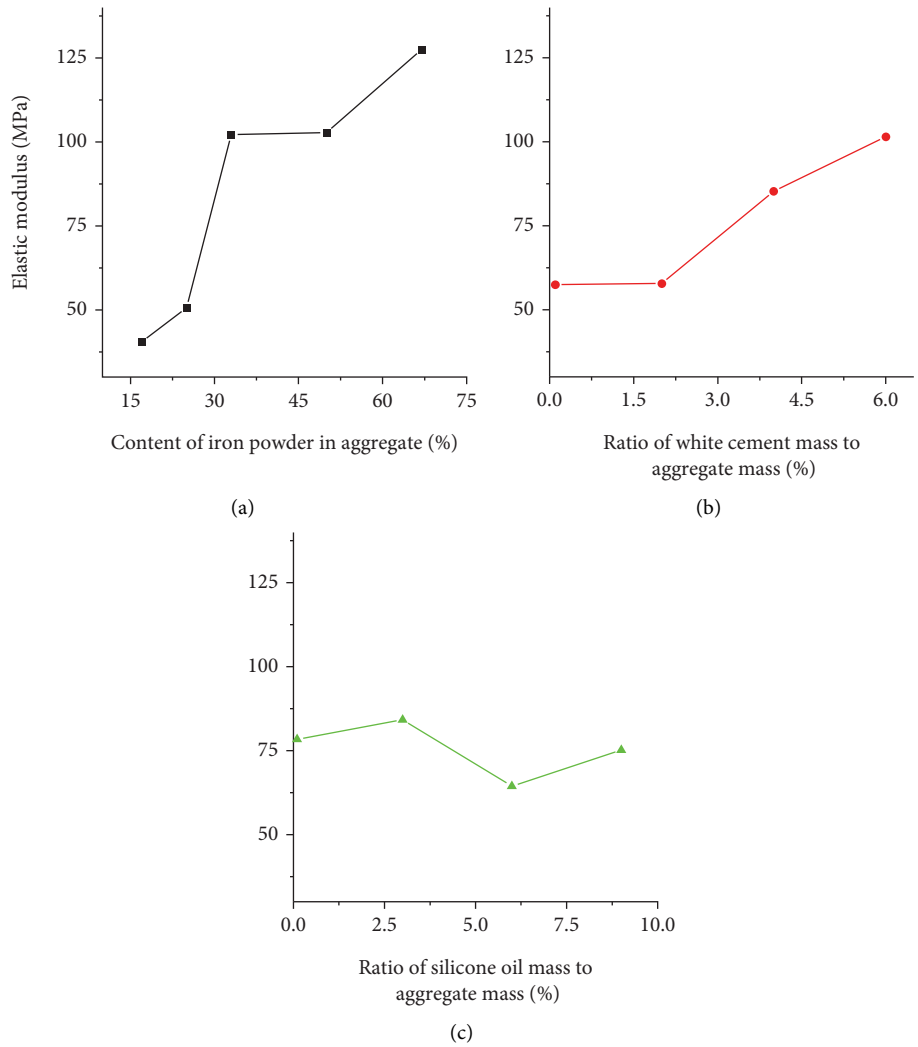

Figure 8: Influence of material composition on deformation modulus.

Table 7: Range analysis of the influence of material composition on permeability coefficient.

Level number	Permeability coefficient (m/s)		
	Factor A	Factor B	Factor C
1	$5.08e^{-8}$	$1.6e^{-7}$	$2.65e^{-7}$
2	$3.67e^{-8}$	$1.5e^{-7}$	$1.61e^{-7}$
3	$3.41e^{-8}$	$1.27e^{-7}$	$3.65e^{-8}$
4	$2.39e^{-7}$	$5.84e^{-8}$	$3.27e^{-8}$
5	$5.33e^{-7}$		
6	$2.47e^{-8}$		
7	$2.12e^{-8}$		
R	$5.11e^{-7}$	$1.01e^{-7}$	$2.32e^{-7}$
R'	$3.83e^{-7}$		

scheme of analogous material. White cement basically only controls the strength of the analogous material, while silicone oil mainly controls the permeability. Therefore, when formulating analogous materials, the approximate ratio range of each component in the aggregate should first be determined according to the desired density and deformation modulus. Secondly, the content range of white cement is determined according to the required compressive strength and tensile strength. Then, based on the desired permeability coefficient, the range of silicone oil content is roughly estimated. Finally, by fine-tuning the range of aggregate proportion, white cement content, and

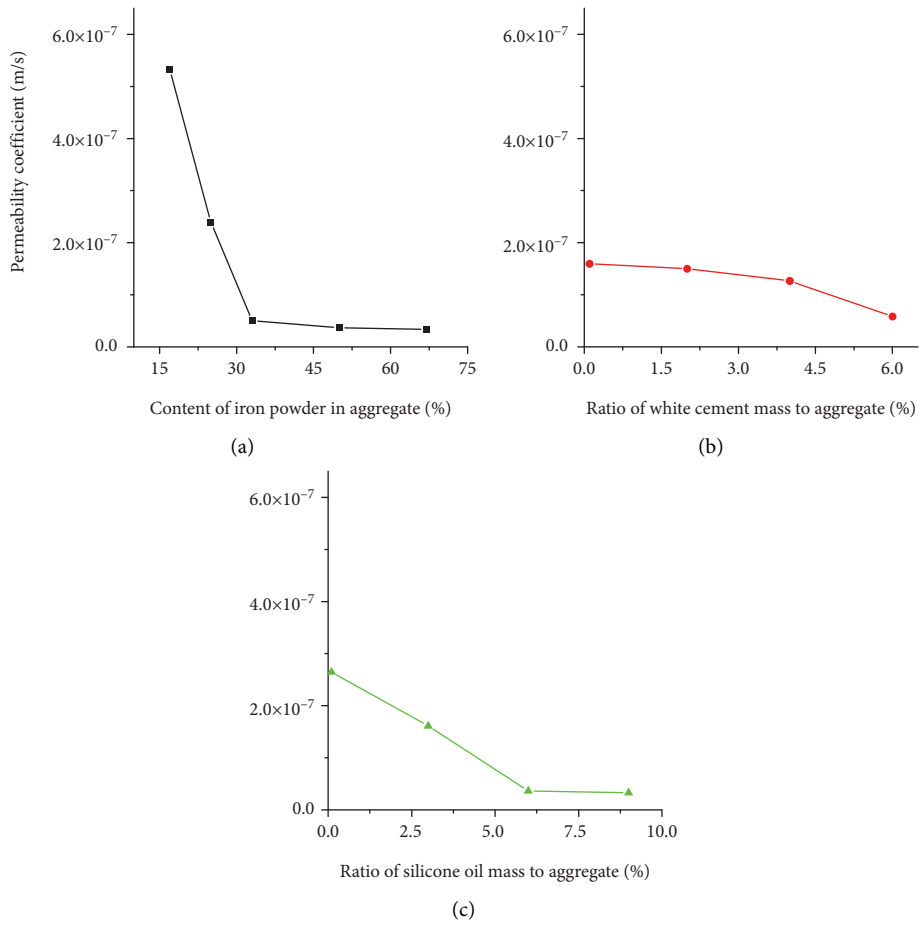

Figure 9: Influence of material composition on permeability coefficient.

silicone oil content, the proportion of each component of the fluid-solid coupling analogous material that meets the requirements can be quickly determined.

5. Application of Fluid-Solid Coupling Analogous Material

5.1. Model Test Overview. Taking Xianglu Mountain Tunnel as the engineering background, the fluid-solid coupling model test is carried out to verify the reliability of the developed fluid-solid coupling analogous material. Xianglu Mountain Tunnel is located in the first section of a large water diversion project in Yunnan Province, China. The tunnel has a total length of nearly 64 km and a maximum buried depth of nearly 1500 meters. It crosses the watershed of the Jinsha River and Lancang River. The geological conditions are very complex. There are many active faults along the tunnel line, and karst is relatively developed. When the tunnel crosses the fault fracture zone, major engineering geological disasters such as water and mud inrush may occur, which play a controlling role in the whole water diversion project [26, 27].

In this study, the typical deep-buried tunnel section (DL36 + 450-DL36 + 550) is selected to carry out the fluid-solid coupling model test. The buried depth of the tunnel in the test area is 1000~1250 m, and it crosses a fault with an inclination of 45° and a width of 15 m. The self-developed fluid-solid coupling true three-dimensional model test system was used in the test. According to the internal dimensions of the model box (length 1.0 m, width 1.0 m, and height 1.0 m) and the excavation requirements, the geometric similarity ratio is 100, the unit weight similarity ratio is 1, the stress similarity ratio is 100, and the permeability coefficient similarity ratio is 10.

According to the geological data, the physical and mechanical parameters of rocks inside and outside the fault are given in Table 8. Table 9 lists the proportion of components in analogous materials simulating rocks inside and outside the fault.

5.2. Model Test Process. The whole process of model testing is divided into the making of geological model, the installation of test elements, and the excavation and support of model tunnels. The geological model is made by layered compaction and layered air-drying curing. Since the test area contains a fault with an inclination of 45°, the test device shall be rotated by 45° before making the physical model (see Figure 10(a)). Then, the evenly mixed analogous material is paved in the model box (see Figure 10(b)). When the physical model is constructed to a specific height, the pressure cell, multipoint displacement meter, and seepage

Table 8: Physical and mechanical parameters of rocks inside and outside the fault.

Rock type	Density (g/cm^3)	Uniaxial compressive strength (MPa)	Tensile strength (kPa)	Deformation modulus (GPa)	Permeability coefficient (m/s)
Rock inside fault	2.6	44.7	2.8	11.6	$7.5e^{-7}$
Rock outside fault	2.5	18.2	1.2	3.9	$4.6e^{-6}$

Table 9: Proportion of components in analogous materials.

Material type	Mass ratio Iron powder : quartz sand : barite powder	Ratio of white cement mass to aggregate mass (%)	Ratio of silicone oil mass to aggregate mass (%)
Material inside fault	1.2 : 0.8 : 1.0	0.8	5.5
Material outside fault	0.4 : 0.6 : 1.0	0.5	3.1

(a) (b) (c) (d)

Figure 10: Continued.

(e) (f)

Figure 10: The process of fluid-solid coupling physical model test.

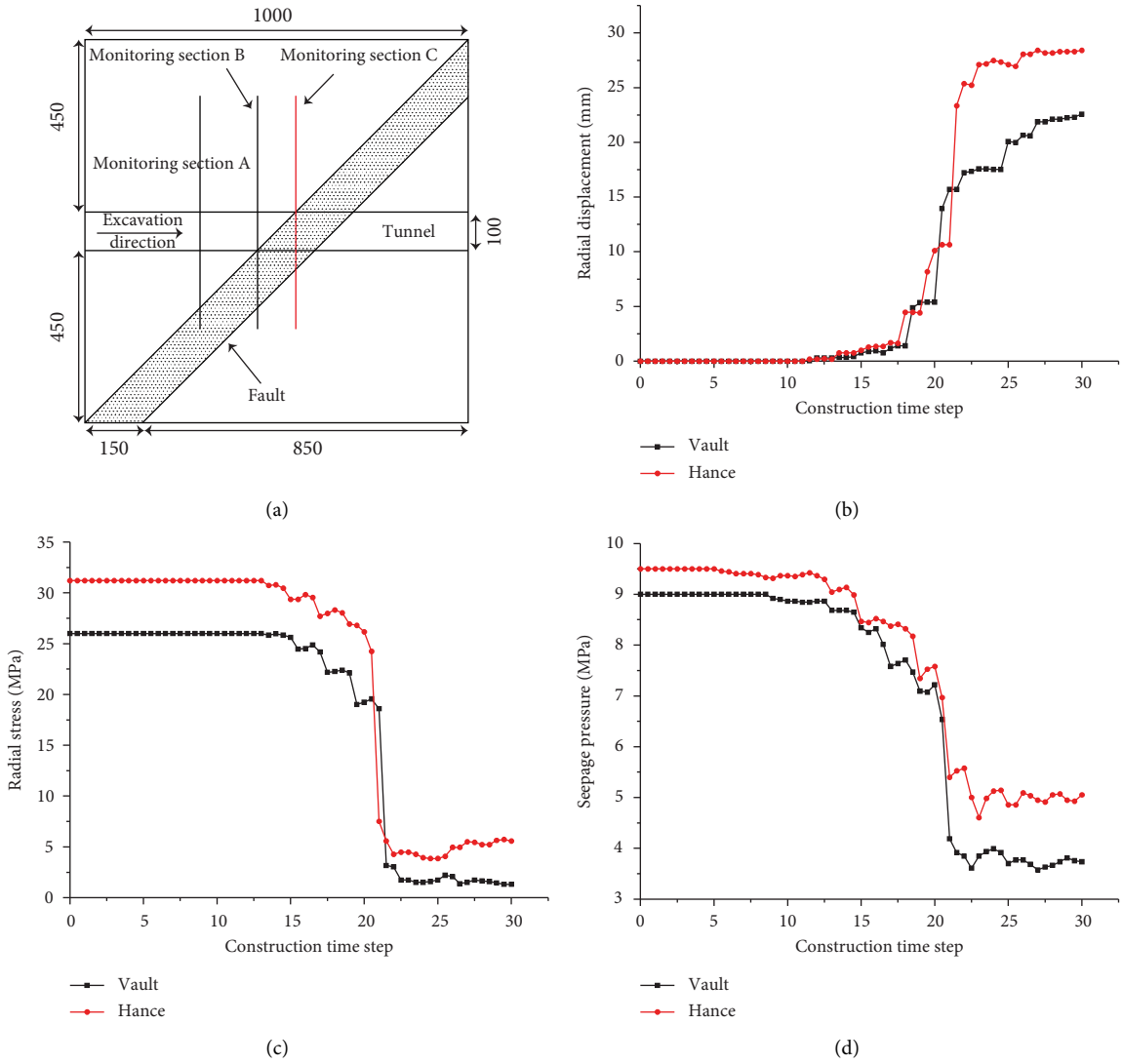

Figure 11: Variation curves of displacement, stress, and seepage pressure around the tunnel with construction time steps. (a) Monitoring section layout; (b) radial displacement; (c) radial stress; (d) seepage pressure.

pressure cell shall be buried around the tunnel (see Figure 10(c)). After the whole physical model is built, the boundary stress and water pressure need to be applied to the model to form a real stress environment and water environment in the physical model (see Figure 10(d)). Subsequently, special tools are used to excavate and support the model tunnel (see Figure 10(e)). Figure 10(f) shows the tunnel face after excavation. It can be clearly seen that there is seepage flow at the face, indicating that the developed analogous material can better simulate the seepage of groundwater.

5.3. Model Test Result. Taking monitoring Section 3 as an example, the variation curve of displacement, stress, and seepage pressure around the tunnel with the construction time step is shown in Figure 11. It can be clearly found that, with the advance of excavation, the radial deformation of rock around the tunnel increases gradually, while the radial stress and seepage pressure around the tunnel decreases gradually. After the support structure is installed, the deformation, stress, and seepage pressure of the surrounding rock gradually tend to be stable. These phenomena are consistent with common sense, which proves that the developed fluid-solid coupling analogous materials are feasible.

6. Conclusions

In this study, the fluid-solid coupling similarity conditions considering high in situ stress are derived. A new type of fluid-solid coupling analogous material is developed with iron powder, quartz sand, and barite powder as aggregates, white cement as a cementing agent, and silicone oil as a regulator and is applied to the fluid-solid coupling physical model test. The main conclusions are as follows:

(1) As three elements of analogous materials, the aggregate mainly affects the density and deformation characteristics, the white cement is mainly used to control the strength characteristics, and the role of the silicone oil is to adjust the permeability. Moreover, when the content of silicone oil is less than 6%, the permeability coefficient changes significantly. When its content is greater than 6%, the permeability coefficient basically remains unchanged.

(2) In order to quickly determine the proportion of all components in analogous materials that meet the requirements, the mass ratio of components in the aggregate should be determined first, followed by the content of white cement and finally the content of silicone oil.

(3) By using the developed materials to carry out physical model tests, the displacement, stress, and seepage pressure of rocks around the tunnel are accurately obtained. It proves the effectiveness of the developed materials.

Data Availability

The data presented in this study can be obtained from the corresponding author upon request.

Conflicts of Interest

The authors declare no conflicts of interest.

Acknowledgments

This research was funded by the https://doi.org/10.13039/501100001809Education Department of Henan Province of China (Grant no. 22A56008).

References

[1] H. Xie, T. Gao, and Y. Ju, "Research and development of rock mechanics in deep ground engineering," *Chinese Journal of Rock Mechanics and Engineering*, vol. 34, pp. 2161–2178, 2015.

[2] M. Wang, Z. Zhou, and Q. Qian, "Tectonic, deformation and failure problems of deep rock mass," *Chinese Journal of Rock Mechanics and Engineering*, vol. 23, pp. 448–455, 2006.

[3] L. Yuan, "Research progress of mining response and disaster prevention and control in deep coal mines," *Journal of China Coal Society*, vol. 46, pp. 716–725, 2021.

[4] M. He, "Progress and challenges of soft rock engineering in depth," *Journal of China Coal Society*, vol. 39, pp. 1409–1417, 2014.

[5] R. Yang, J. Lv, B. Zhou, and D. Ma, "Rock Unloading failure precursor based on Acoustic Emission Parametric fractal characteristics," *Lithosphere*, vol. 2022, Article ID 8221614, 2022.

[6] Y. Zhou, S. Li, L. Li, Q. Zhang, and S. Shi, "New technology for fluid-solid coupling tests of underground engineering and its application in experimental simulation of water inrush in filled-type karst conduit," *Chinese Journal of Geotechnical Engineering*, vol. 37, pp. 1232–1240, 2015.

[7] L. Li, S. Sun, J. Wang, W. Yang, S. Song, and Z. Fang, "Experimental study of the precursor information of the water inrush in shield tunnels due to the proximity of a water-filled cave," *International Journal of Rock Mechanics and Mining Sciences*, vol. 130, Article ID 104320, 2020.

[8] S. C. Li, H. L. Liu, L. P. Li, Q. Zhang, K. Wang, and K. Wang, "Large scale three dimensional seepage analysis model test and numerical simulation research on undersea tunnel," *Applied Ocean Research*, vol. 59, pp. 510–520, 2016.

[9] S. Li, D. Pan, and Z. Xu, "A model test on catastrophic evolution process of water inrush of a concealed Karst cave filled with confined water," *Rock and Soil Mechanics*, vol. 39, pp. 3164–3173, 2018.

[10] S. Li, C. Gao, Z. Zhou et al., "Analysis on the precursor information of water inrush in Karst tunnels: a true triaxial model test study," *Rock Mechanics and Rock Engineering*, vol. 52, no. 2, pp. 373–384, 2019.

[11] Y. Hu, Y. Zhao, and D. Yang, "Simulation theory and method of 3D solid-liquid coupling," *Journal of Liaoning Technical University*, vol. 26, pp. 204–206, 2007.

[12] J. Chen, L. Yin, and W. Sun, "Development and application for new solid-fluid coupling similar material of deep floor aquifuge," *Chinese Journal of Rock Mechanics and Engineering*, vol. 34, pp. 3956–3964, 2015.

[13] L. Yu, H. Jing, and B. Xu, "Solid-fluid coupling analogous material test for subsea tunnel," *Journal of Central South University*, vol. 46, pp. 983–990, 2015.

[14] J. Bai, M. Wang, Q. S. Zhang, Z. Zhu, R. Liu, and W. Li, "Development and application of a new similar material for fluid–solid coupling model test," *Arabian Journal of Geosciences*, vol. 13, no. 18, p. 913, 2020.

[15] S. Liu and W. Liu, "Experimental development process of a new fluid-solid coupling similar-material based on the orthogonal test," *Processes*, vol. 6, no. 11, p. 211, 2018.
[16] X. Shi, B. Liu, and Y. Qi, "Applicability of similar materials bonded by cement and plaster in solid-liquid coupling tests," *Rock and Soil Mechanics*, vol. 36, pp. 2624–2630, 2015.
[17] Z. Huang, X. Li, and S. Li, "Research and development of similar material for liquid-solid coupling and its application in tunnel water-inrush model test," *Journal of Central South University*, vol. 49, pp. 3029–3039, 2018.
[18] S. Li, X. Feng, S. Li, L. Li, and G. Li, "Research and development of a new similar material for solid-fluid coupling and its application," *Chinese Journal of Rock Mechanics and Engineering*, vol. 29, pp. 281–288, 2010.
[19] Z. Liu and Y. Hu, "Solid liquid coupling study on water inrush through faults in coal mining above confined aquifer," *Journal of China Coal Society*, vol. 32, pp. 1046–1050, 2007.
[20] J. Zhang and Z. Hou, "Experimental study on simulation materials for solid-liquid coupling," *Chinese Journal of Rock Mechanics and Engineering*, vol. 23, pp. 3157–3161, 2004.
[21] K. Wang, S. Li, Q. Zhang et al., "Development and application of new similar materials of surrounding rock for a fluid-solid coupling model test," *Rock and Soil Mechanics*, vol. 37, pp. 2521–2533, 2016.
[22] T. Han, W. Yang, and Z. Yang, "Development of similar material for porous medium solid-liquid coupling," *Rock and Soil Mechanics*, vol. 32, pp. 1411–1417, 2011.
[23] H. Zhou, Y. Tang, and D. Hu, "Study on coupled penetrating-dissolving model and experiment for salt rock cracks," *Chinese Journal of Rock Mechanics and Engineering*, vol. 25, pp. 946–950, 2006.
[24] Z. Li, M. Ma, and Y. Bao, "Development and application of fluid-solid coupling similar materials in discharge test of Old Goaf water," *Geofluids*, vol. 2020, Article ID 8834885, 2020.
[25] Y. Wu, "Study on the relationship between stress and seepage in fractured rock mass," *Hydrogeology & Engineering Geology*, vol. 22, pp. 30–35, 1995.
[26] M. Ren, Q. Zhang, and S. Chen, "Physical model test study on synergistic action of liningrock for deep tunnel under complex geological conditions," *China Civil Engineering Journal*, vol. 52, pp. 98–109, 2019.
[27] Q. Y. Zhang, M. Y. Ren, K. Duan et al., "Geo-mechanical model test on the collaborative bearing effect of rock-support system for deep tunnel in complicated rock strata," *Tunnelling and Underground Space Technology*, vol. 91, Article ID 103001, 2019.

Hindawi
Advances in Materials Science and Engineering
Volume 2022, Article ID 3097093, 14 pages
https://doi.org/10.1155/2022/3097093

Research Article

Research on the Strength Prediction Model of Softened Mudstone Based on Triaxial Compressive Test of Rock

Kai Yun,[1] **Yongquan Zhu**,[1] **Renyuan Wang**,[1] **and Zhichun Fang**[2]

[1]*State Key Laboratory of Mechanical Behavior and System Safety of Traffic Engineering Structures, Shijiazhuang Tiedao University, Shijiazhuang, Hebei 050043, China*
[2]*School of Civil Engineering, Shijiazhuang Tiedao University, Shijiazhuang, Hebei 050043, China*

Correspondence should be addressed to Yongquan Zhu; 7935526@163.com

Received 5 July 2022; Revised 2 September 2022; Accepted 13 September 2022; Published 4 October 2022

Academic Editor: Qing Ma

Mudstone is highly sensitive to water. When it comes into contact with water, the softening phenomena such as the decrease of strength and the increase of deformation are prominent. It is of great significance to clarify its related mechanical properties. For the tertiary mudstone, a triaxial compression test and a Brazilian splitting test are carried out under the conditions of four kinds of water content (0, 10.1%, 12.5%, and 14.1%) and four kinds of confining pressures (0 MPa, 2 MPa, 5 Mpa, and 10 MPa). The test results show that (1) with the increase of confining pressure and water content, the mudstone changes from brittle failure to ductile failure. The higher the confining pressure, the greater the strength and elastic modulus. The higher the water content, the significantly lower the strength and elastic modulus, and the higher the strain. (2) With the increase of water content, the influence of confining pressure on strength is more prominent. High confining pressure can effectively inhibit the trend of strength attenuation. (3) When the water content is low (0–10.1%), the strength of the mudstone is mainly related to its own water content. When the water content increases to 10.1%–14.1%, both the confining pressure and the water content are important factors affecting the strength of the mudstone. Then, the applicability of five commonly used strength criteria to the strength prediction of softened mudstone is compared and analyzed. The results show that the Rocker strength criterion can more accurately and conveniently predict the strength of mudstone under different water content. Finally, based on this strength criterion, a nonlinear strength prediction model of softened mudstone considering water content and confining pressure effect is proposed and its good applicability is verified.

1. Introduction

China is one of the countries with the widest distribution of mudstones in the world. Mudstone exists in more than 20 provinces. With the acceleration of China's infrastructure construction, a large number of structural stability and disease problems caused by mudstone have appeared in the construction of tunnels in railway engineering, highway engineering, subway engineering, oil and gas transportation engineering, and inter-basin water transfer engineering. The main reason is that the mechanical properties of mudstone are unstable, and softening phenomena such as strength reduction and the increase of deformation are easy to occur when it comes into contact with water. It will cause huge potential safety hazards to the construction and operation of the project. Therefore, it is necessary to study the mechanical properties of softened mudstone.

At present, many scholars have made a lot of valuable research on the mechanical properties of mudstone after long-term research. Zhang et al. [1] obtained the constitutive equation of four stages of the stress-strain curve of purplish red mudstone of the Badong Formation through the triaxial compression test. Wang and Li [2] took the soft rock in Western China as an example and obtained the variation law of strength and deformation with confining pressure under different water content. Xu et al. [3] established the fitting curve and fitting function of the four stages of the stress-strain curve through the strength and deformation

characteristics of mudstone under different confining pressures. Luo [4] obtained the stress-strain curve of strongly weathered mudstone after multiple drying and wetting cycles. Luo et al. [5] summarized the influence of water content of mudstone on its mechanical properties and Duncan-Zhang model parameters. Liu et al. [6] made the energy explanation of the water-saturated softening mechanism of mudstone and revealed the energy evolution mechanism of mudstone. Fu et al. [7] studied the functional relationship equation between shear strength and vertical deformation of pre-disintegrating carbonaceous mudstone.

The strength criterion is to study the yield condition and failure rule of rock under the real complex stress environment. The research and selection of appropriate strength criteria is of great significance to the judgment of rock strength and engineering design. Yuan et al. [8] estimated the mechanical parameters of rock mass based on the Hoek–Brown strength criterion. Zhu et al. [9] expounded the research progress and research results of the Hoek–Brown strength criterion and introduced related research work at present. Zou et al. [10] compared the Bieniawski criterion and the Balmar criterion and analyzed their advantages and disadvantages. You [11] summed up the variation characteristics of bonding force and friction force in the Mohr stress space based on the exponential strength criterion. Zhang et al. [12] constructed the exponential strength criterion through triaxial compression tests and verified its applicability. Shi et al. [13] compared and analyzed five strength criteria and evaluated the applicability of each strength criterion. Zhang and Liu [14] explored the prediction effect of different strength criteria on rock tensile strength.

At present, the applicability of many existing strength criteria to softened mudstone is seldom studied, and the scope of application is not very clear. In view of this, this paper takes the tertiary mudstone as the research object and carries out the triaxial compression test and Brazilian splitting test under different water content to reveal the influence law of water content and confining pressure on mechanical properties of mudstone. Then, based on the triaxial test data, the accuracy and applicability of the Mohr–Coulomb strength criterion, Hoek–Brown strength criterion, generalized Hoek–Brown strength criterion, Bieniawski strength criterion, and Rocker strength criterion for the prediction of mudstone strength under different water content and confining pressures are compared and analyzed. Finally, a nonlinear strength prediction model of softened mudstone considering water content and confining pressure effect is proposed.

2. Sample Preparation and Test Scheme

2.1. Field Sampling. The tertiary mudstone block in this test is taken from Xiangshan tunnel in Zhongwei City, Ningxia, China. By the mineral composition analysis, the mineral composition of the mudstone is mainly quartz, illite, and calcite, accounting for more than 70%. The rest contains a small amount of plagioclase, chlorite, and palygorskite. The pore type of the rock sample is mainly interlayer micropores of clay minerals, and the pore level is mainly micropores. The crack is highly developed and evenly distributed. According to the field measured data, the vertical in situ stress in this section is 4.21 Mpa, and the average horizontal in situ stress is 5.03 MPa. The rock block sampling location is at the top of the tunnel, and the location has the advantages of wide distribution of test rocks, prominent rock characteristics, litter disturbance, and easy collection.

After the collection, in order to prevent the weathering and water loss of the rock blocks, which is caused by the long transportation time or the long test period, the sealing wax method is used for sealing and preservation (as shown in Figure 1) so as to ensure the accuracy of the test data.

2.2. Sample Preparation. After the rock is sampled on-site and transported to the laboratory, the rock block shall be unpacked and processed. Since the mudstone is very sensitive to water, it is easy to become cracked and even disintegrate blocks when it comes into contact with water, which not only makes the sample formation rate low but also has a great impact on the test results. Therefore, in the process of the rock block drilling and coring, we do not cool down the rock block with water. Instead, we retrofit the original coring machine by connecting the high-pressure air pump (as shown in Figure 2). The high-pressure air can replace water to cool down the rock block (as shown in Figure 3). In this way, it will not only affect the water content of mudstone but also avoid the sticking of coring machine and rock sample damage caused by overheating. The result shows that this method works well and the size of the mudstone sample meets the test requirements. The mudstone sample is shown in Figure 4.

2.3. Test Scheme. This test mainly includes the triaxial compression test and Brazilian splitting test of mudstone with different water content. The sample for the triaxial compression test is a cylinder with a diameter of $D = 50$ mm and a height of $h = 100$ mm. The test equipment is a large-rigidity rock triaxial testing machine, as shown in Figure 5. The sample for the Brazilian splitting test is also a cylinder with a diameter of $D = 50$ mm and a height of $h = 50$ mm. The test equipment is a universal material testing machine, as shown in Figure 6. The tensile strength of rock is calculated according to the following formula:

$$\sigma_t = \frac{2P}{\pi D h}. \tag{1}$$

In the equation, σ_t is the tensile strength of the rock, P is the failure load, D is the diameter of the sample, and h is the height of the sample.

In order to explore the strength and deformation characteristics of mudstone under different water content and different confining pressures, the triaxial compression test and Brazilian splitting test are carried out for four kinds of water content: dry state, natural state, saturated state, and state between the natural state and saturated state. Mudstone samples in the dry state, the saturated state, and the state between the natural state and saturated state can be prepared

Figure 1: Sealing and preservation of the rock block with wax.

Figure 2: High-pressure air pump.

by the drying method, vacuum saturation method, and free immersion method, respectively. According to the water content test, when the rock sample is immersed for 1-2 hours, its water content only increases slightly, which is not very different from the water content in the natural state. When it is immersed for 3 hours, its water content will increase significantly. When it is immersed for 4 hours, the water content will reach the saturated stable state. Therefore, the free immersion time of rock samples with water content between the natural water content and saturated water content in this test will be 3 hours. The water content of mudstone samples under four water content states is 0 (dry state), 10.1% (natural state), 12.5% (water content state between the natural state and saturated state), and 14.1% (saturated state). According to the actual stress environment of the rock, four groups of confining pressures are selected for the triaxial compression test, which are 0 MPa, 2 MPa, 5 Mpa, and 10 MPa.

Figure 3: Automatic coring machine sampling.

Figure 4: Mudstone sample.

According to the principle of the parallel test, in order to eliminate the test error caused by individual differences of samples, the number of samples for each group of test should be 5 under the same water content state and the same loading direction. Therefore, under the same water content and the same confining pressure, take five groups of samples to repeat the triaxial compression test, and the total number of rock samples for the triaxial compression test under four water content and four groups of confining pressures is 80. Under the same water content, take five groups of samples to

Figure 5: Rock triaxial testing machine.

Figure 6: Universal material testing machine.

repeat the Brazilian splitting test, and the total number of Brazilian splitting test samples under four water content conditions is 20.

3. Analysis of Test Results

3.1. Analysis of Deformation Characteristics. According to the triaxial compression test results, the stress-strain curves of mudstone in four water content states under different confining pressures can be drawn, as shown in Figure 7.

It can be seen from Figure 7 that (1) when the water content of mudstone is low (0–10.1%), at low confining pressure (0 MPa–2 MPa), the stress-strain curve can be obviously divided into four stages: compaction stage, linear elasticity stage, yield stage, and failure stage. With the increase of water content, the compaction stage and linear elastic stage of the stress-strain curve become significantly shorter. The rock sample begins the yield stage relatively quickly, and there is no obvious yield point. The strain of the rock sample will continue to increase at a certain stress level and eventually lead to failure. The failure mode changes from brittle failure to ductile failure. The reason may be that with the increase of water content of mudstone, the argillization phenomenon is prominent and it is similar to the properties of general sand. The strength is reduced, and the rock samples are mostly ductile failure. (2) Under the same water content, with the increase of confining pressure, the compressive strength, residual strength, and elastic modulus of mudstone increase, and the value of axial strain is also increased. (3) Under the same confining pressure, the compressive strength, residual strength, and elastic modulus of mudstone decrease significantly with the increase of water content, and the value of strain when reaching the peak compressive strength is increased with the increase of water content. After the rock sample failure, the residual strength remains unchanged and the amount of plastic deformation continues to increase.

3.2. Analysis of Strength Characteristics. Through the triaxial compression test and Brazilian splitting test, the compressive strength under different confining pressures in different water content states and the tensile strength under different water content are obtained. The results are shown in Table 1.

Through the analysis of the data in Table 1, the characteristics of the compressive strength and tensile strength of mudstone are obtained: (1) When the water content is only increased from 0 to 14.1%, the uniaxial compressive strength of mudstone decreases from 9.2 MPa to 2.0 MPa and the tensile strength is reduced from 3.1 Mpa to 0.66 MPa. The decline rate is nearly 80%. It can be seen that this kind of mudstone is very sensitive to water, and the water content has a significant impact on the strength of mudstone. Under the same confining pressure, the compressive strength and tensile strength will decrease significantly with the increase of water content; (2) under the same water content, the compressive strength and tensile strength of mudstone increase with the increase of confining pressure; (3) when the mudstone is in the state of low water content (0–10.1%), with the increase of confining pressure from 0 MPa to 10 MPa, the strength increases by about 350%–400%. When the water content increases to 12.5%–14.1%, the strength increases by 600%–700%, which is about 1.5–2 times of the low water content state. It shows that the higher the water content of mudstone, the greater the influence of confining pressure on its strength; (4) when the mudstone is in a high confining pressure (5 MPa–10 MPa) environment, as the water content increases from 0 to 14.1%, its strength decreases by about 60%. When the confining pressure decreases (0 MPa–2 MPa), the decrease rate increases to about 70%, which indicates that the strength reduction of mudstone in the low confining pressure environment is more obvious.

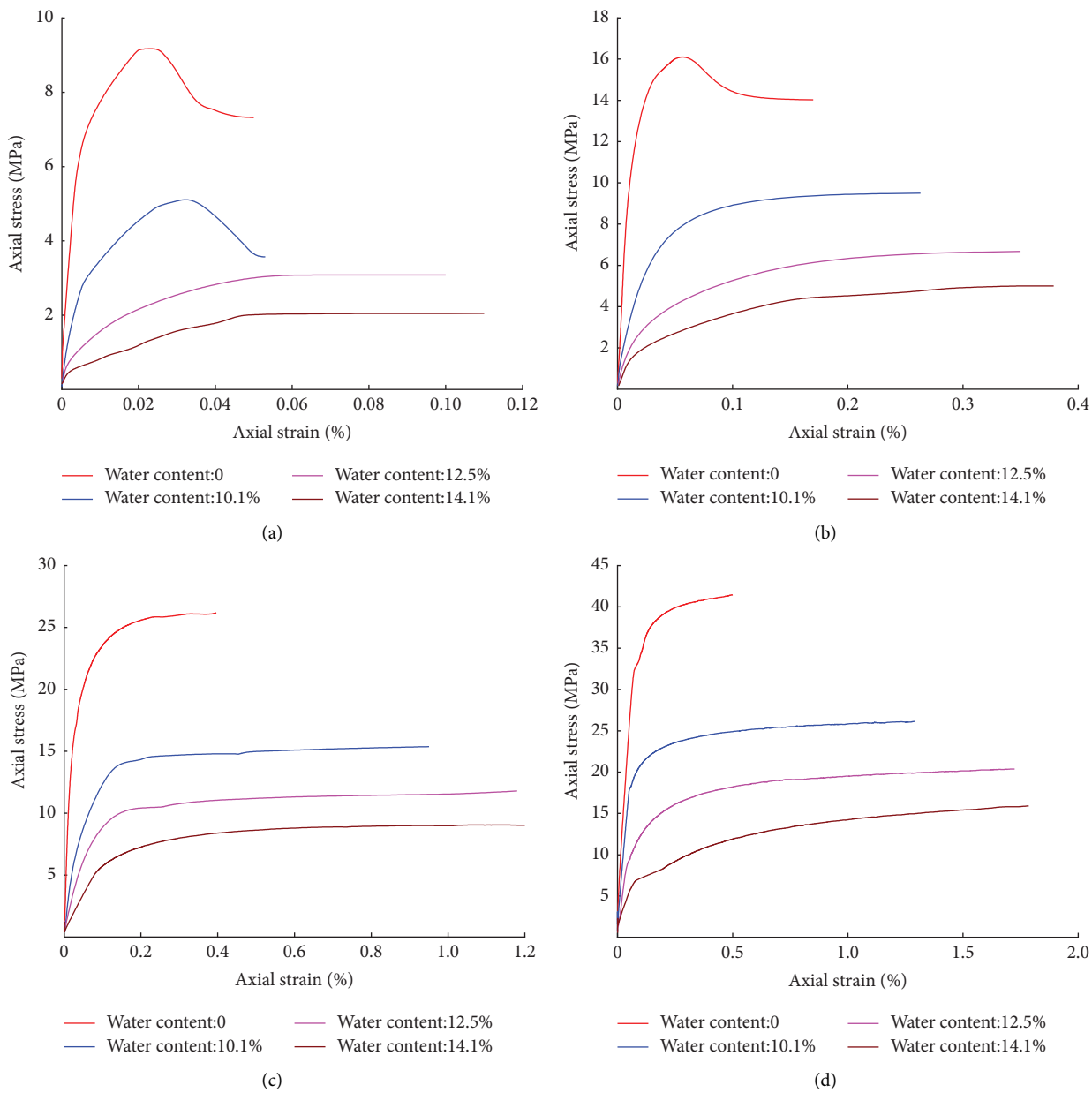

Figure 7: Stress-strain curves of mudstone under four water content under different confining pressures. (a) Confining pressure: 0 MPa. (b) Confining pressure: 2 MPa. (c) Confining pressure: 5 MPa. (d) Confining pressure: 10 MPa.

Because the high confining pressure can inhibit the development of cracks in mudstone, hinder the penetration of cracks, and delay the occurrence of the critical failure state. Hence, the macro-performance is the improvement of compressive strength and the strength decline is relatively small.

3.3. Analysis of Softening Characteristics. The property that the strength of rock changes after immersion in water is called softening. The softening coefficient is usually used to characterize the softening characteristics of rocks. In order to facilitate the analysis of the softening characteristics of mudstone under different water content and different confining pressure conditions, a triaxial softening coefficient is introduced. Under the same confining pressure, the calculation method of the triaxial softening coefficient is the ratio of the compressive strength of mudstone under different water content states to the compressive strength of mudstone in the dry state. The triaxial softening coefficient ξ' can be expressed as

$$\xi' = \frac{R_{cb}}{R_c}. \tag{2}$$

In the equation, R_{cb} is the compressive strength of mudstone in different water content states and R_c is the compressive strength of mudstone in the dry state.

Table 1: Summary of mudstone strength test results.

Water content (%)	Confining pressure (MPa)	Compressive strength (MPa)	Tensile strength (MPa)
0	0	9.2	3.10
	2	16.1	
	5	26.2	
	10	41.5	
10.1	0	5.2	1.75
	2	9.5	
	5	15.4	
	10	26.1	
12.5	0	3.0	1.05
	2	6.7	
	5	11.8	
	10	20.4	
14.1	0	2.0	0.66
	2	5.0	
	5	9.0	
	10	15.9	

Taking the compressive strength of mudstone in Table 1 into equation (2), the variation curve of the triaxial softening coefficient of mudstone with confining pressure under different water content conditions can be drawn, as shown in Figure 8.

It can be seen from Figure 8 that under different confining pressures, the variation law of the triaxial softening coefficient of mudstone with water content is roughly the same, showing a downward trend with the increase of water content. When the water content changes from 0 to 10.1%, there is little difference in the reduction range of the mudstone softening coefficient under the confining pressure state of the four groups. When the water content is 10.1%, the triaxial softening coefficients are all around 0.6, which means that when the water content is low, the strength is mainly related to its own water content. As the water content continues to increase, from 10.1% to 14.1%, the variation range of the softening coefficient is different. The higher the confining pressure is, the smaller the reduction range of the triaxial softening coefficient is, and the greater the strength is. It shows that when the water content increases to a certain range, not only the mudstone strength is related to its own water content but also the size of the confining pressure will become an important influencing factor. Confining pressure can weaken the downward trend of strength due to the increase of water content. Therefore, in practical engineering application, when considering the softening phenomenon of mudstone, the water content state and the actual stress environment should be comprehensively analyzed. In this way, the strength of the mudstone can be accurately determined.

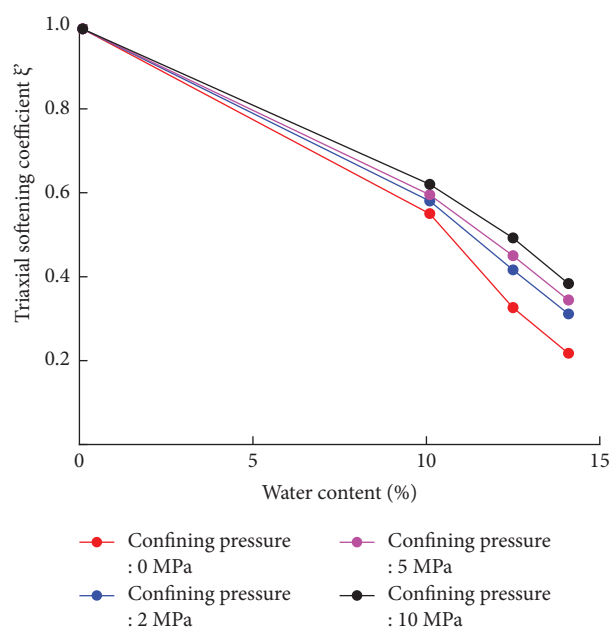

Figure 8: Triaxial softening coefficient curve of mudstone.

4. Applicability Study of Strength Criterion

The strength criterion can truly and objectively reflect and describe the strength characteristics and failure characteristics of rock, which is widely used in bridge, tunnel, water conservancy, mining, and other engineering fields. As the basic theory of rock mechanics, the strength criterion can also be used to predict and check the strength of rocks.

4.1. Strength Criterion and Its Expression

4.1.1. Mohr–Coulomb Strength Criterion. Since its establishment, the Mohr–Coulomb strength criterion has been widely used for its concise expression and clear physical concept. So far, the Mohr–Coulomb strength criterion is still one of the most classical strength theories in the field of rock mechanics. According to the criterion, the failure of rock is mainly the shear failure that occurs on a certain surface of the rock. The expression is

$$\sigma_1 = \sigma_c + k\sigma_3. \tag{3}$$

In the equation, σ_1 is the maximum principal stress (the same below), σ_3 is the minimum principal stress (the same below), σ_c is the uniaxial compressive strength (the same below), and k is the influence coefficient of different confining pressures on strength.

4.1.2. Hoek–Brown Strength Criterion. In 1980, Hoek and Brown [15, 16] first proposed the Hoek–Brown strength criterion by summarizing and analyzing a large number of triaxial test data and results. It can describe the nonlinear relationship between the internal ultimate principal stress of rock when failure occurs. The expression is

$$\sigma_1 = \sigma_3 + \sigma_c\left(m_i\frac{\sigma_3}{\sigma_c} + 1\right)^{0.5}. \tag{4}$$

In the equation, m_i is the empirical parameter of rock dimension (the same below), which can reflect the degree of softness and hardness of rock. Its value ranges from 0.001 to 25. The value of m_i can be obtained by looking up the table. In order to avoid the error of human subjectivity and make the calculation more accurate, in this paper, the value of m_i is determined by the uniaxial compressive strength and tensile strength. The calculation method is as follows:

$$m_i = 16\frac{\sigma_t}{\sigma_c} - \frac{\sigma_c}{\sigma_t}. \tag{5}$$

In the equation, σ_t is the tensile strength (the same below).

4.1.3. Generalized Hoek–Brown Strength Criterion. Hoek et al. [17] improved the Hoek–Brown strength criterion in 1992, which is called the generalized Hoek–Brown strength criterion. Its expression is

$$\sigma_1 = \sigma_3 + \sigma_c\left(m_b\frac{\sigma_3}{\sigma_c} + s\right)^{a}. \tag{6}$$

In the equation, m_b and a are dimensional empirical parameters for different rock masses and s is a parameter reflecting the degree of rock fragmentation. Hoek et al. [18, 19] proposed a method for obtaining rock mass parameters m_b, s, and a based on the geological strength index (GSI). The GSI can be obtained by looking up the table [20],

$$\left.\begin{aligned} m_b &= \exp\left(\frac{GSI - 100}{28}\right)m_i \\ s &= \exp\left(\frac{GSI - 100}{9}\right) \\ a &= 0.5 \end{aligned}\right\}. \tag{7}$$

4.1.4. Bieniawski Strength Criterion. The Bieniawski criterion is a two-dimensional rock empirical strength criterion summarized and proposed by Bieniawski [21] in 1974 on the basis of a large number of rock strength tests. It belongs to one of the power function strength criterion. Bieniawski believed that in general, the strength curve is not a straight line. Its expression is

$$\frac{\sigma_1}{\sigma_c} = 1 + e\left(\frac{\sigma_3}{\sigma_c}\right)^{f}. \tag{8}$$

In the equation, e and f are the relevant parameters determined by the triaxial compression test. Bieniawski determined the parameter f as a constant 0.75 after fitting the test results through the experimental analysis of five types of rocks. At this time, the above formula only contains one unknown parameter, which is called the single-parameter Bieniawski strength criterion.

Converting equation (8) into equation (9), there are two unknown parameters e and f, which is called the two-parameter Bieniawski strength criterion,

$$\ln\frac{\sigma_1 - \sigma_c}{\sigma_c} = \ln e + f\ln\left(\frac{\sigma_3}{\sigma_c}\right). \tag{9}$$

If equation (8) is modified into equation (10), it contains three unknown parameters e, f, and g, which is called three-parameter Bieniawski strength criterion,

$$\frac{\sigma_1}{\sigma_c} = g + e\left(\frac{\sigma_3}{\sigma_c}\right)^{f}. \tag{10}$$

The single-parameter Bieniawski strength criterion is based on the strength test data of five types of rocks. After fitting analysis, the value of parameter f in the expression is determined to be 0.75, and the value of e depends on the rock type, and its value ranges from 3 to 5. The expression of the two-parameter Bieniawski strength criterion is based on the single-parameter expression and obtained by taking logarithms on both sides of the formula. At this time, the value of parameter f is no longer fixed at 0.75. For other types of rocks except for the five types of rocks, the two-parameter expression is more applicable. The three-parameter Bieniawski strength criterion is also obtained by further modifying the parameters based on the single-parameter Bieniawski strength criterion. To sum up, the parameters in the Bieniawski strength criterion are all obtained by fitting the rock strength test data. The two-parameter and three-parameter Bieniawski strength criteria are evolved from the single-parameter Bieniawski strength criterion, which is applicable to all kinds of rocks with significant nonlinear or linear characteristics of strength curves.

4.1.5. Rocker Strength Criterion. The Rocker strength criterion was proposed by Carter et al. [22]. Its expression is

$$\sigma_1 = \sigma_c\left(\frac{\sigma_3}{\sigma_t} + 1\right)^{m}. \tag{11}$$

In the equation, the value of index m can be obtained by fitting and regression analysis of the triaxial compression test data, and its value range is 0.3–1.

The Rocker strength criterion is an empirical power function strength criterion. Its biggest feature is that the

expression includes the tensile strength parameter. Compared with other empirical strength criteria, the Rocker strength criterion considers not only the influence of uniaxial compressive strength but also the influence of rock tensile strength in the prediction of rock triaxial compressive strength, which makes the strength analysis of rock more complete.

In this paper, five widely used strength criteria are selected to predict the strength of mudstone under different water content states and different confining pressures. The purpose is to discuss and study the applicability of different kinds of strength criteria. Based on the strength test data (as shown in Table 1), through regression analysis, the relevant constants included in the five strength criteria are obtained, and in this way, the complete calculation expression of each strength criterion is obtained. The calculation expressions of the five strength criteria for mudstone under different water contents are shown in Table 2:

According to the calculation expressions listed in Table 2, five strength criterion prediction curves of mudstone under different water content can be obtained. In order to study the deviation between each strength criterion and the test value of strength more intuitively, the triaxial compression test data are marked. The curve is shown in Figure 9.

4.2. Applicability Evaluation Criteria of Strength Criteria. To evaluate the applicability of the strength criterion, the author intends to use the method of calculating the least mean standard fitting deviations and analyzing the strength criterion prediction curves and then find the best strength criterion for predicting the strength of mudstone. The least mean standard fitting deviations represent that when the mudstone is under the same water content condition, the average deviation between the calculated value of the fitting expression and the test value of the mudstone compressive strength under the four confining pressure conditions. It reflects the accuracy of each strength criterion expression in predicting the compressive strength of mudstone under different confining pressures under a certain water content state. The smaller the value, the smaller the deviation, and the better the prediction effect of the fitting expression. The formula of the least mean standard fitting deviations is as follows:

$$\eta = \sqrt{\frac{\sum_j \left(\sigma_{1j}^{\text{cal}} - \sigma_{1j}^{\text{test}}\right)^2}{n}}. \tag{12}$$

In the equation, η is the least mean standard fitting deviation, σ_{1j}^{cal} is the calculated value of the maximum principal stress, $\sigma_{1j}^{\text{test}}$ is the test value of the maximum principal stress, j is the test point under different confining pressures, and n is the number of test data and $n = 4$.

According to equation (12), the least mean standard fitting deviations of each strength criterion of mudstone under different water content states can be obtained, as shown in Table 3.

4.3. Applicability Study of Strength Criterion. According to the results in Figure 9 and Table 3, it is shown that the least mean standard fitting deviations of the Mohr–Coulomb strength criterion under different water content states is small and the difference is not significant. When the mudstone is in the state of low confining pressure (0 MPa–2 MPa), the Mohr–Coulomb strength criterion has a good effect on the prediction of mudstone strength. With the increase of confining pressure, the calculated value deviates from the test value, and both give a low estimation of the actual compressive strength of mudstone. It shows that the Mohr–Coulomb strength criterion is more suitable for predicting the strength of mudstone at a lower confining pressure level. At the same time, the calculated values of the tensile strength of mudstone under the four water content states have great deviations from the experimental values, and the higher the water content, the greater the deviation. The maximum deviation is about 2.5 times of the test value, indicating that when mudstone is in the state of tensile stress failure, its strength reflects the regular characteristics of nonlinearity, while the linear Mohr–Coulomb strength criterion cannot be applied.

The calculated compressive strength of mudstone under the Hoek–Brown strength criterion and generalized Hoek–Brown strength criterion is quite different from the experimental value. When the water content is low (0–10.1%), the calculated compressive strength values of the two strength criteria are significantly lower than the experimental values. In the dry state, the least mean standard fitting deviation of the generalized Hoek–Brown strength criterion reaches 11.15 MPa. The reason may be that the influence of the change of water content is not considered when determining the geological strength index (GSI), resulting in the low value of the parameters. The calculated value of compressive strength is low. With the increase of water content (12.5%–14.1%), the least mean standard fitting deviations of the two strength criteria decrease significantly, indicating that the prediction effect of the two criteria becomes better. At this time, the calculated value of compressive strength is close to the actual test value. Under the four water content states, the Hoek–Brown strength criterion has a good effect on the prediction of the tensile strength of mudstone, the calculated value is little different from the actual test value, and the calculated value of the generalized Hoek–Brown strength criterion is lower than the test value. Generally speaking, the Hoek–Brown strength criterion and generalized Hoek–Brown strength criterion have good prediction effect only when mudstone is within a certain water content range, but they are prone to large deviations in other water content states. The overall applicability is not good.

The Bieniawski strength criterion has little difference between the calculated value of compressive strength and the test value under different water content and different confining pressures, and the least mean standard fitting deviation is small, which can achieve good fitting effect. Among them, the three-parameter Bieniawski criterion is the best, followed by the two-parameter, and the single-parameter deviation is relatively the largest. However, the Bieniawski

Table 2: Calculation expression of the strength criterion under different water content.

Strength criterion	Water content (%)	Evaluate expression
Mohr–Coulomb	0	$\sigma_1 = 9.2 + 3.255\sigma_3$
	10.1	$\sigma_1 = 5.2 + 1.899\sigma_3$
	12.5	$\sigma_1 = 3 + 1.632\sigma_3$
	14.1	$\sigma_1 = 2 + 1.273\sigma_3$
Hoek–Brown	0	$\sigma_1 = \sigma_3 + 9.2\ (0.263\sigma_3 + 1)^{0.5}$
	10.1	$\sigma_1 = \sigma_3 + 5.2\ (0.464\sigma_3 + 1)^{0.5}$
	12.5	$\sigma_1 = \sigma_3 + 3\ (0.914\sigma_3 + 1)^{0.5}$
	14.1	$\sigma_1 = \sigma_3 + 2\ (1.125\sigma_3 + 1)^{0.5}$
Generalized Hoek–Brown	0	$\sigma_1 = \sigma_3 + 9.2\ (0.184\sigma_3 + 0.329)^{0.5}$
	10.1	$\sigma_1 = \sigma_3 + 5.2\ (0.325\sigma_3 + 0.329)^{0.5}$
	12.5	$\sigma_1 = \sigma_3 + 3\ (0.640\sigma_3 + 0.329)^{0.5}$
	14.1	$\sigma_1 = \sigma_3 + 2\ (0.787\sigma_3 + 0.329)^{0.5}$
Bieniawski (single-parameter)	0	$\sigma_1 = 9.2 + 9.2 \times 3.147\ (\sigma_3/9.2)^{0.75}$
	10.1	$\sigma_1 = 5.2 + 5.2 \times 2.306\ (\sigma_3/5.2)^{0.75}$
	12.5	$\sigma_1 = 3 + 3 \times 2.223\ (\sigma_3/3)^{0.75}$
	14.1	$\sigma_1 = 2 + 2 \times 1.965\ (\sigma_3/2)^{0.75}$
Bieniawski (two-parameter)	0	$\sigma_1 = 9.2 + 9.2 \times 3.268\,(\sigma_3/9.2)^{0.957}$
	10.1	$\sigma_1 = 5.2 + 5.2 \times 2.100\ (\sigma_3/5.2)^{1.028}$
	12.5	$\sigma_1 = 3 + 3 \times 1.814\ (\sigma_3/3)^{0.980}$
	14.1	$\sigma_1 = 2 + 2 \times 1.487\ (\sigma_3/2)^{0.984}$
Bieniawski (three-parameter)	0	$\sigma_1 = 9.2 \times 0.994 + 9.2 \times 3.257\ (\sigma_3/9.2)^{0.941}$
	10.1	$\sigma_1 = 5.2 \times 1.011 + 5.2 \times 2.061\ (\sigma_3/5.2)^{1.014}$
	12.5	$\sigma_1 = 3 \times 1.015 + 3 \times 1.798\ (\sigma_3/3)^{0.972}$
	14.1	$\sigma_1 = 2 \times 1.021 + 2 \times 1.456\ (\sigma_3/2)^{0.970}$
Rocker	0	$\sigma_1 = 9.2\ ((\sigma_3/3.1) + 1)^{0.998}$
	10.1	$\sigma_1 = 5.2\ ((\sigma_3/1.75) + 1)^{0.825}$
	12.5	$\sigma_1 = 3\ ((\sigma_3/1.05) + 1)^{0.808}$
	14.1	$\sigma_1 = 2\ ((\sigma_3/0.66) + 1)^{0.735}$

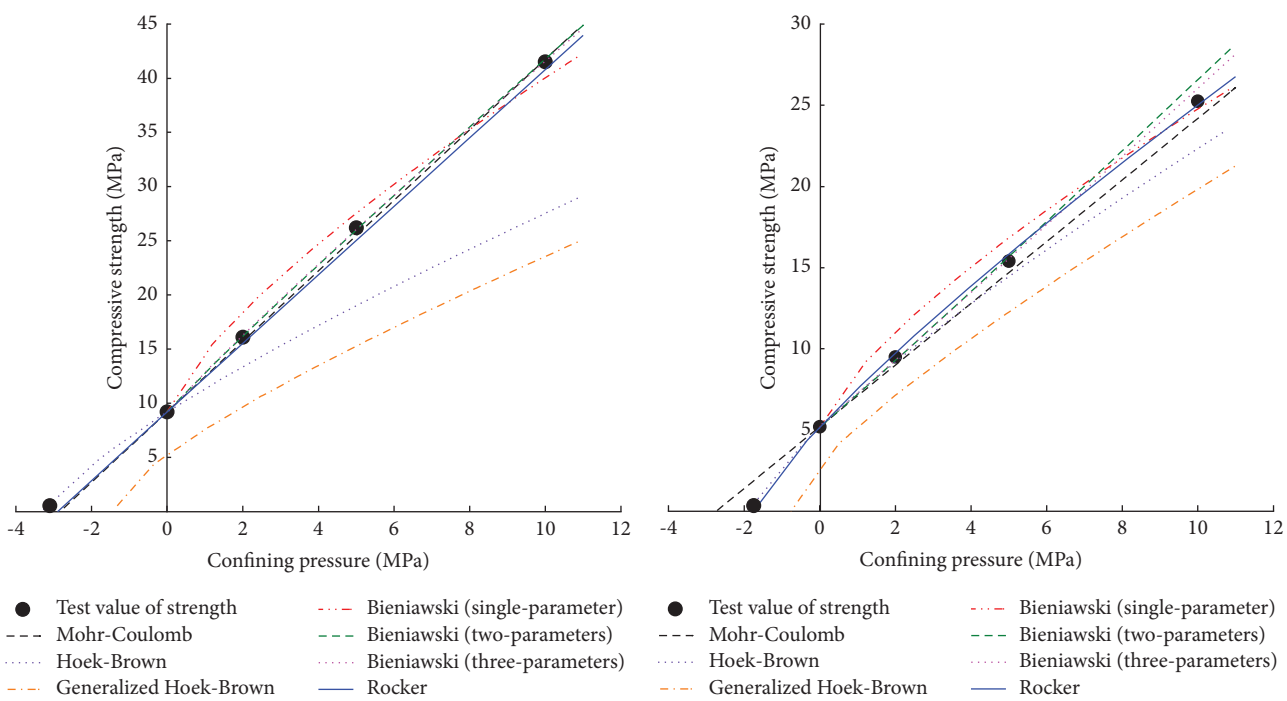

Figure 9: Continued.

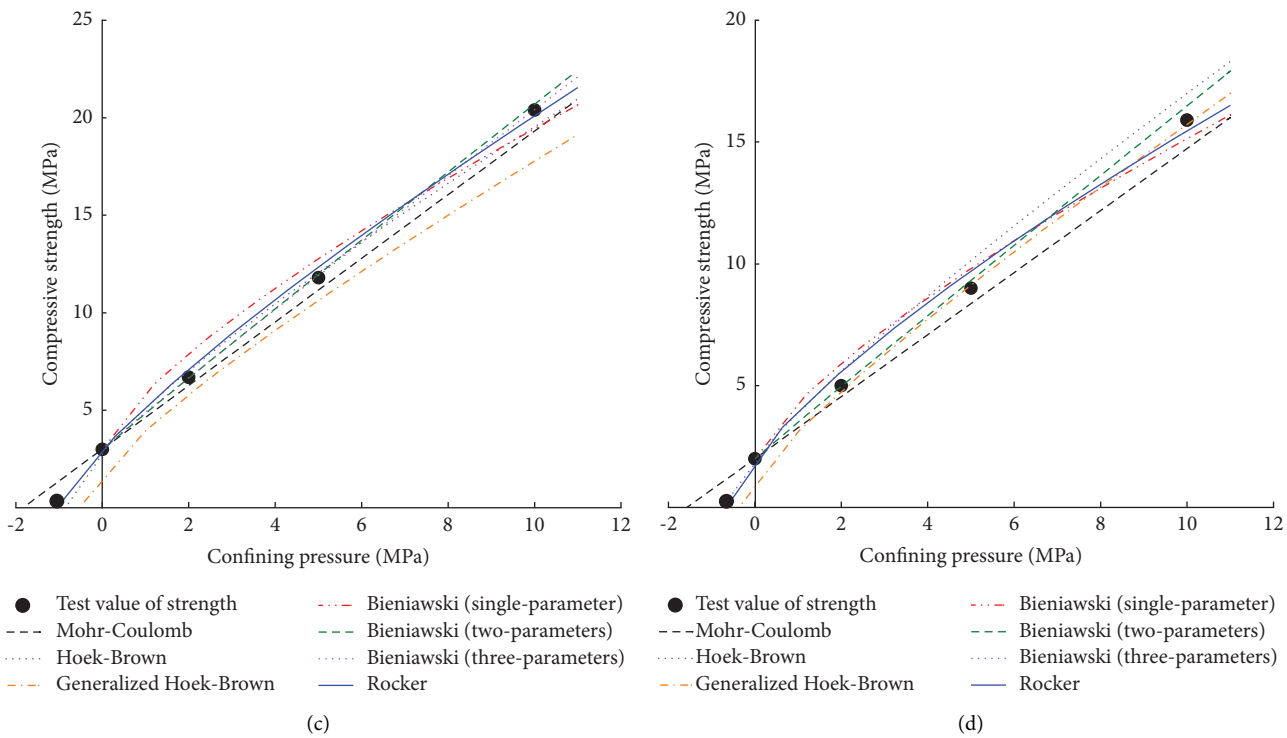

Figure 9: Strength criterion prediction curves of mudstone under different water content. (a) Water content: 0. (b) Water content: 10.1%. (c) Water content: 12.5%. (d) Water content: 14.1%.

Table 3: Least mean standard fitting deviations of each strength criterion.

Strength criterion	Water content (%)	Least mean standard fitting deviations (MPa)
Mohr–Coulomb	0	0.43
	10.1	0.60
	12.5	0.66
	14.1	0.70
Hoek–Brown	0	7.97
	10.1	1.94
	12.5	0.48
	14.1	0.85
Generalized Hoek–Brown	0	11.15
	10.1	3.86
	12.5	1.63
	14.1	0.46
Bieniawski (single-parameter)	0	1.53
	10.1	1.25
	12.5	0.92
	14.1	0.73
Bieniawski (two-parameter)	0	0.18
	10.1	0.30
	12.5	0.18
	14.1	0.34
Bieniawski (three-parameter)	0	0.13
	10.1	0.12
	12.5	0.06
	14.1	0.07
Rocker	0	0.75
	10.1	0.60
	12.5	0.37
	14.1	0.51

strength criterion is an empirical model, and the correlation coefficient in the calculation expression has no specific physical meaning, which is easy to cause human error. At the same time, this criterion can only predict the compressive strength of rock but cannot obtain the tensile strength of rock. The scope of application has obvious limitations.

The Rocker strength criterion can well fit the compressive strength values of mudstone under different water content states and different confining pressures, and the least mean standard fitting deviations are all below 1 MPa. It can be seen from the figure that as the confining pressure increases gradually, the Rocker strength criterion curve has a gradual slowing trend, indicating that the growth rate of the compressive strength value decreases with the increase of the confining pressure, which is also more consistent with the actual situation. Moreover, the physical meaning of the parameters in the expression of the Rocker strength criterion is clear, and the acquisition method is simple and reliable, so the Rocker strength criterion has strong applicability.

To sum up, by comparing and analyzing the applicability of the five strength criteria, it can be seen that the Rocker strength criterion can not only be well applied to the calculation and prediction of mudstone strength under different water content and different confining pressures but also the parameters in the expression are clear, simple, and easy to get. Generally speaking, the Rocker strength criterion is more applicable.

4.4. Rocker Strength Criterion Considering Water Content and Confining Pressure Effects. Through the comparative analysis of the applicability of the five strength criteria above, it is proposed to select Rocker strength criterion to describe and predict the strength index of mudstone. From the calculation expression of the Rocker strength criterion, it can be seen that the uniaxial compressive strength, the tensile strength, and the value of exponent m will affect the calculation and prediction of mudstone strength. At the same time, they are closely related to the water content of mudstone. The purpose of this subsection is to study the function correspondence between the uniaxial compressive strength, the tensile strength, the value of exponent m, and the water content of mudstone and then obtain the calculation expression of the modified Rocker strength criterion including both water content and confining pressure. Finally, a nonlinear strength prediction model for softened mudstone can be established.

According to the analysis of the triaxial compression test results, it can be seen that the relationship between the uniaxial compressive strength and the water content approximately satisfies the quadratic polynomial function relationship. The fitting curve is shown in Figure 10, and its relational expression is

$$\sigma_c = -0.028w^2 - 0.128w + 9.207. \tag{13}$$

Its correlation coefficient is $R^2 = 0.997$, indicating that the fitting effect is good.

The relationship between the tensile strength and water content of mudstone approximately meets the exponential function relationship. The fitting curve is shown in Figure 11, and its relational expression is

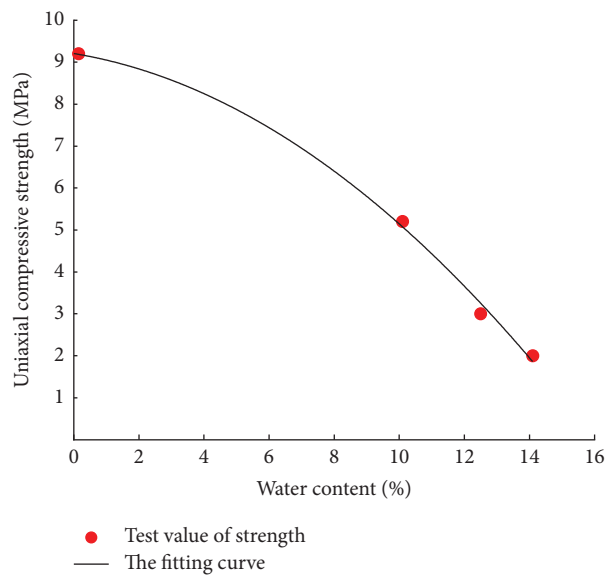

Figure 10: Fitting curve between the uniaxial compressive strength and water content.

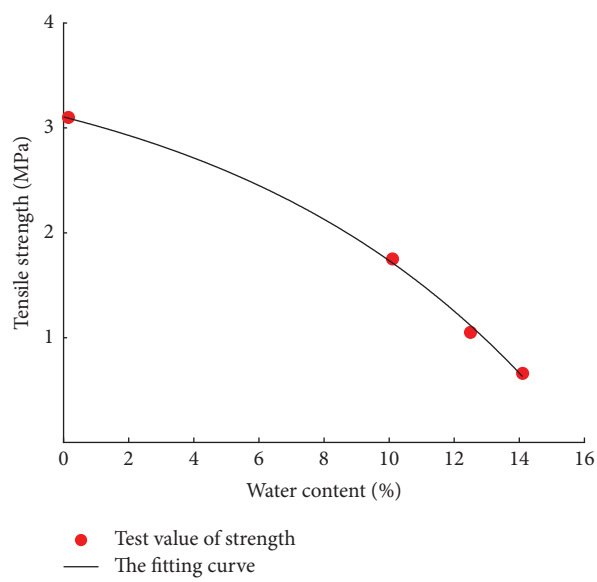

Figure 11: Fitting curve between the tensile strength and water content.

$$\sigma_t = 3.891 - 0.787 \exp\left(\frac{w}{9.915}\right). \tag{14}$$

Its correlation coefficient is $R^2 = 0.998$, indicating that the fitting effect is good.

When the water content of mudstone is 0, 10.1%, 12.5%, and 14.1%, the value of exponent m is 0.998, 0.825, 0.808, and 0.735, respectively. According to the corresponding relationship, they approximately meet the function relationship of the quadratic polynomial. The fitting curve is shown in Figure 12, and its relational expression is

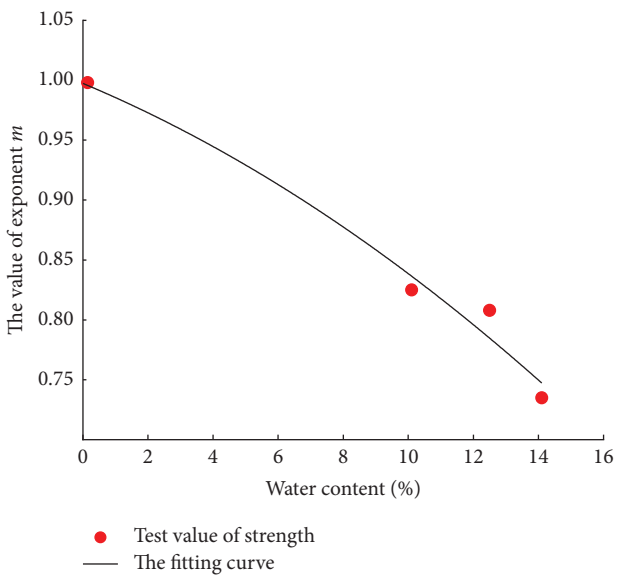

Figure 12: Fitting curve between the value of exponential m and water content.

$$m = -0.00045w^2 - 0.011w + 0.997. \quad (15)$$

Its correlation coefficient is $R^2 = 0.978$, indicating that the fitting effect is good.

Substituting equations (13)–(15) into (11), the following equation can be obtained:

$$\ln\left(\frac{\sigma_1}{-0.028w^2 - 0.128w + 9.207}\right) = \left(-0.00045w^2 - 0.011w + 0.997\right) \ln\left(\frac{\sigma_3}{3.891 - 0.787\exp(w/9.915)} + 1\right). \quad (16)$$

Equation (16) is the Rocker strength criterion expression for softened mudstone considering both water content and confining pressure. Substituting $\sigma_3 = 0$ MPa, 2 MPa, 5 Mpa, and 10 MPa into equation (16), we can get the Rocker strength criterion prediction curve considering the water content effect under different confining pressures, as shown in Figure 13.

It can be seen from Figure 13 that (1) the four predicted curves have basically the same trend, indicating that the strength of softened mudstone varies with water content in roughly the same law under different confining pressure states and the strength decreases significantly with the increase of water content. Under the same water content state, the strength increases with the increase of confining pressure. (2) When the water content of mudstone is higher than 10%, the influence of confining pressure on strength is more significant, and the amplitude of strength change caused by the change of confining pressure is greater. (3) When the water content of mudstone increases, high confining pressure can effectively inhibit the degree of strength attenuation. (4) Under different confining pressures, when the water content of mudstone is 0, 10.1%, 12.5%, and 14.1%, the average deviations between the calculated strength and the experimental strength of mudstone are 4%, 4%, 9%, and 11%, respectively.

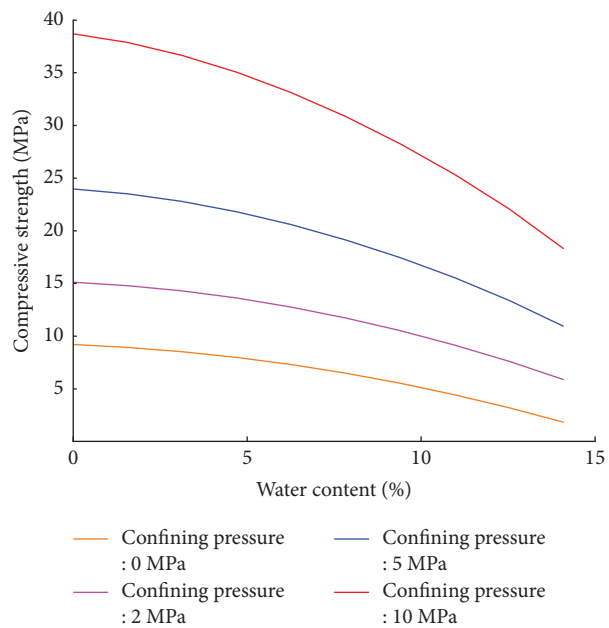

Figure 13: Prediction curve of the Rocker strength criterion considering the water content effect.

From the abovementioned relevant strength test results and softening characteristic law in Chapter 3, it can be seen that the results obtained by the prediction curve of the Rocker strength criterion are consistent with the actual situation. The prediction law is basically consistent with the test law, and the deviation between the calculated value and the test value is small. The prediction effect is good. The research results show that the strength prediction model considering the water content and confining pressure effect based on the Rocker strength criterion can well reflect the strength characteristics and softening characteristics of softened mudstone under different water content and different confining pressures. It has good applicability for the prediction and calculation of softened mudstone strength.

5. Conclusion

Taking the tertiary mudstone as the research object, this paper analyzes the triaxial strength characteristics and deformation law of softened mudstone through field sampling, triaxial compression strength test, and Brazilian splitting test and discusses the applicability of the strength criterion for softened mudstone. The main conclusions are as follows:

(1) In terms of deformation characteristics, with the increase of confining pressure and water content, the mudstone changes from brittle failure to ductile failure; under the same water content state, with the increase of confining pressure, the compressive strength, residual strength, and elastic modulus of mudstone increase significantly, and the amount of

deformation is also greatly increased; under the same confining pressure, the compressive strength, residual strength, and elastic modulus of mudstone decrease significantly with the increase of water content, and the value of strain will be increased when reaching the peak compressive strength.

(2) In terms of strength characteristics, the water content has a significant influence on the strength index of mudstone. The higher the water content of mudstone, the greater the effect of confining pressure on its strength, and the high confining pressure can effectively suppress the degree of strength attenuation.

(3) In terms of softening characteristics, under different confining pressures, the variation law of the triaxial softening coefficient of mudstone with water content is roughly the same, showing a downward trend with the increase of water content. When the water content is low (0–10.1%), the strength of the mudstone is mainly related to its own water content. When the water content increases to 10.1%–14.1%, both the confining pressure and the water content are important factors affecting the strength of the mudstone. Confining pressure can weaken the downward trend of strength due to the increase of water content.

(4) Five different forms of rock strength criteria are compared and analyzed from the aspects of the accuracy of the strength prediction of softened mudstone and the objectivity and convenience of expression parameter selection. The research shows that the applicability of the Rocker strength criterion is better.

(5) Based on the Rocker strength criterion, a nonlinear strength prediction model of softened mudstone considering the water content and confining pressure effect is obtained. The results show that the prediction law of the model is basically consistent with the test law, and the deviation between the calculated value and the test value is small. It can better describe the strength characteristics and softening characteristics of softened mudstone and has good applicability.

Data Availability

The data used to support the findings of this study can be obtained from the corresponding author upon request.

Conflicts of Interest

The authors declare that they have no conflicts of interest.

Acknowledgments

This research was supported by the National Science Foundation of China (Grant no. 52178391).

References

[1] J. M. Zhang, Y. H. Liu, C. H. Luo, and S. R. Shen, "Triaxial compression test and constitutive model for red mudstone of Badong formation," *Journal of Engineering Geology*, vol. 21, no. 1, pp. 138–142, 2013.

[2] L. Wang and Z. Y. Li, "Triaxial compression test analysis of weakly cemented mudstone in West China," *Journal of Yangtze River Scientific Research Institute*, vol. 33, no. 8, pp. 86–90, 2016.

[3] B. T. Xu, C. H. Yan, and H. F. Xu, "Triaxial tests on stress-strain of mudstone," *Chinese Journal of Geotechnical Engineering*, vol. 26, no. 6, pp. 863–865, 2004.

[4] Q. Luo, "Influence of dry-wet cycle on strength and disintegration of highly weathered mudstone," *Bulletin of the Chinese Ceramic Society*, vol. 33, no. 4, pp. 1248–1253, 2020.

[5] C. L. Luo, Y. Y. Yu, D. X. Bao, and P. Wang, "Duncan-Zhang model parameters of red mudstone based on triaxial tests," *China Earthquake Engineering Journal*, vol. 9, no. 2, pp. 436–444, 2019.

[6] W. L. Liu, E. C. Yan, H. Dai, Y. Du, W. B. Xiao, and S. Zhao, "Study on characteristic strength and energy evolution law of Badong formation mudstone under water effect," *Chinese Journal of Rock Mechanics and Engineering*, vol. 39, no. 2, pp. 311–326, 2020.

[7] H. Y. Fu, J. Liu, L. Zeng, H. B. Bian, and Z. N. Shi, "Deformation and strength tests of pre-disintegrating Carbonaceous mudstone under loading and soaking condition," *Rock and Soil Mechanics*, vol. 40, no. 4, pp. 1273–1280, 2019.

[8] Y. C. Yuan, M. X. Wang, S. S. Shi, B. L. Sun, and T. Lei, "Estimation of surrounding rock mass mechanical parameters of mountain tunnel based on Hoek-Brown criterion," *Chinese Journal of Underground Space and Engineering*, vol. 13, no. 1, pp. 22–28, 2017.

[9] H. H. Zhu, Q. Zhang, and L. Y. Zhang, "Review of research progresses and applications of Hoek-Brown strength criteriont," *Chinese Journal of Rock Mechanics and Engineering*, vol. 32, no. 10, pp. 1945–1963, 2013.

[10] Y. Q. Zou, D. P. Liu, and C. Q. Wang, "A comparison of two empirical strength criterion in power function for rock material," *Journal of Xi'an University of Architecture and Technology*, vol. 40, no. 2, pp. 213–217, 2008.

[11] M. Q. You, "Study on shear strength of rocks using the Exponential criterion in Mohr's stress space," *Chinese Journal of Theoretical and Applied Mechanics*, vol. 51, no. 2, pp. 607–619, 2019.

[12] Q. Zhang, C. Li, Q. Guo, M. Min, B. S. Jiang, and Y. N. Wang, "Exponential true triaxial strength criteria for rock," *Chinese Journal of Geotechnical Engineering*, vol. 40, no. 4, pp. 625–633, 2018.

[13] X. C. Shi, Y. F. Meng, and G. Li, "Comparative analyses of several rock strength criteria," *Rock and Soil Mechanics*, vol. 32, no. S1, pp. 209–216, 2011.

[14] L. Zhang and B. G. Liu, "A comparison study of rock strength criteria considering tensile strength," *Engineering Mechanics*, vol. 33, no. 11, pp. 201–207, 2016.

[15] E. Hoek and E. T. Brown, "Empirical strength criterion for rock masses," *Journal of the Geotechnical Engineering Division*, vol. 106, no. 9, pp. 1013–1035, 1980.

[16] E. Hoek and E. T. Brown, *Underground Excavations in Rocks*, Institution of Mining and Metallurgy, London, UK, 1980.

[17] E. Hoek, D. Wood, and S. Shah, *A Modified Hoek-Brown Criterion for Jointed Rock Masses*, British Geotechnical Society, London, UK, 1992.

[18] E. Hoek, "Strength of rock and rock masses," *International Society for Rock Mechanics News Journal*, vol. 2, no. 2, pp. 4–16, 1994.

[19] E. Hoek, P. K. Kaiser, and W. F. Bawden, *Support of Underground Excavations in Hard Rock*, Balkema, Rotterdam, Netherlands, 1995.

[20] S. M. Hu and X. W. Hu, "Estimation of rock mass parameters based on quantitative GSI system and Hoek-Brown Criterion," *Rock and Soil Mechanics*, vol. 32, no. 3, pp. 861–866, 2011.

[21] Z. T. Bieniawski, "Estimating the strength of rock materials," *Journal of the South African Institute of Mining and Metallurgy*, vol. 4, no. 8, pp. 312–320, 1974.

[22] B. J. Carter, E. J. Scott Duncan, and E. Z. Lajtai, "Fitting strength criteria to intact rock," *Geotechnical & Geological Engineering*, vol. 9, no. 1, pp. 73–81, 1991.

Hindawi
Advances in Materials Science and Engineering
Volume 2022, Article ID 4120287, 15 pages
https://doi.org/10.1155/2022/4120287

Research Article

Damage Evolution of Rocks Containing a Set of Cross-Joints Based on Acoustic Emission Characteristics

Xiao Li,[1,2,3] **Xinquan Wang**,[1,2,3] **Kangyu Wang**,[4] **Hongguo Diao**,[1,2,3] **and He Zhang**[5]

[1]*Department of Civil Engineering Zhejiang University City College, Hangzhou 310015, China*
[2]*Key Laboratory of Safe Construction and Intelligent Maintenance for Urban Shield Tunnels of Zhejiang Province, Hangzhou 310015, China*
[3]*Zhejiang Engineering Research Center of Intelligent Urban Infrastructure, Hangzhou 310015, China*
[4]*School of Civil Engineering, Zhejiang University of Technology, Hangzhou 310015, China*
[5]*College Civil Engineering & Architecture, Zhejiang University, Hangzhou 310015, China*

Correspondence should be addressed to Hongguo Diao; diaohg@zucc.edu.cn

Received 10 August 2022; Revised 19 September 2022; Accepted 22 September 2022; Published 30 September 2022

Academic Editor: Depeng Ma

The problem of damage rupture of jointed rocks is a hot topic of research in underground tunnel engineering. In this paper, the damage evolution characteristics of rocks containing a set of cross-joints are investigated based on particle flow code (PFC). Firstly, the jointed rock models, such as rock models with different joint cross-angles and with different joint lengths, are established based on PFC. Then, the uniaxial compression mechanical properties and acoustic emission (AE) evolution characteristics of different jointed rocks are analyzed. Finally, the damage evolution characteristics of jointed rocks are discussed based on the damage variable defined by AE counts. The research results show that the uniaxial compressive strength (UCS) and elastic modulus (E) of the jointed rock are highest when the joint cross-angle β is 60°. The UCS and E of jointed rocks show a trend of decrease with the increase of joint length. The overall trend of the AE evolution of jointed rocks does not change with the change of joint cross-angle and joint length. However, the time step of the occurrence of acoustic emission (crack initiation time) has changed. The damage evolution of jointed rocks shows three stages with the increase of stress (time): damage-free stage, slow damage increase stage, and sharp damage increase stage. The fluctuation characteristics of the damage evolution of jointed rocks are different with the change of β and LB. The damage rupture of jointed rocks begins to sprout from and expand along the tip of the joints.

1. Introduction

With the continuous increase of underground mining scale and depth, there are a number of disasters such as rock burst of roadway-surrounding rocks and instability of coal pillars. The occurrence of dynamic disasters in underground mining is related to the mechanical properties of surrounding rocks of roadways. Generally, there are a large number of defects such as joints and fractures in the surrounding rock of the roadway, which make the mechanical properties of the surrounding rock of the roadway vary greatly, leading to more difficult prevention and control of mine disasters [1–3]. Therefore, it is of great engineering significance to investigate the physical and mechanical properties of different defective rocks [4–6].

At present, the methods to study the mechanical properties and instability mechanisms of jointed rocks mainly focus on indoor experiments and numerical simulations. In terms of experimental studies, many scholars have used different materials (e.g., natural rocks, cement mortar, gypsum, and PMMA (poly(methyl methacrylate))) to explore the damage mechanical properties and characteristics of jointed rock masses with various joint characteristics [7]. For example, Lee and Jeon [8] experimentally investigated the mechanical properties of granite, PMMA, and gypsum specimens containing a noncrossing nonparallel joint under

uniaxial compression conditions. Yin et al. [9] studied the coalescence mechanism between two parallel three-dimensional (3D) preexisting surface cracks in the granite specimen under uniaxial compression. The bridge angles between the two preexisting cracks vary from 0° to 135°. Yang [10] investigated the crack coalescence behavior of brittle sandstone samples containing two coplanar fissures in the process of deformation. Zhou et al. [11] experimentally studied the crack coalescence behavior in rock-like materials containing multiple flaws under uniaxial compression. Compared with indoor experiments, numerical simulations are convenient and low cost in simulating mechanical properties and damage characteristics of different jointed rocks. At the same time, some complex joint experiments are produced with relatively large errors, and numerical simulation can ensure sufficient accuracy. Based on the finite element method (FEM) or discrete element method (DEM), Li and Wong [12], Zhang and Wong [13], and Chen et al. [14] have investigated the influence of inclination angle and loading condition on crack initiation and propagation. Vergara et al. [15] discussed the effect of joint geometrical parameters on the mechanical behavior of specimens containing nonpersistent joints using the UDEC. Sarfarazi et al. [16] studied the failure behavior of "H"-shaped nonpersistent cracks under uniaxial load using particle flow code (PFC), and the angles of "H"-shaped nonpersistent joints were 0°, 30°, 60°, and 90° degrees. Although many scholars have conducted a lot of research studies on the mechanical properties and crack extension forms of jointed rocks, the forms of engineering joints are complex and diverse, and there are still areas that need to be studied, such as the cross-angles of joints and the length of joints.

In addition, many studies have shown that the destruction process of rocks is accompanied by acoustic emission phenomenon, and the use of this phenomenon can effectively predict and analyze rock burst, envelope collapse, and other hazards [17–19]. Therefore, the acoustic emission phenomenon during the destruction of rocks with different joints is also a research hotspot for scholars. At present, many scholars have investigated the acoustic emission characteristics during rock destruction. For example, Moradian et al. [17] evaluated the damage during shear tests of rock joints using acoustic emissions. Hazzard and Young [18] provided a technique for recording AEs in bonded-particle models and applied the technique to a simulated compressive failure test on a model of granite core sample. Khazaei et al. [19] quantified the damage characteristics of intact rock based on acoustic emission technology. Lin et al. [20] experimentally studied the acoustic emission characteristics of jointed rock mass by a double disc cutter. Chong et al. [21] investigated the scale effect and anisotropy of jointed rock mass (JRM) from the perspective of acoustic emission characteristics and estimated the size of the representative element volume (REV). Zhang et al. [22] comparatively studied the fracture characteristics of coal and rock samples based on acoustic emission technology. Chen et al. [14] discussed the acoustic emission evolution characteristics of rocks with different joint dip angles under uniaxial conditions. Liu et al. [23] investigated the AE evolution characteristics and damage constitutive model of coal-rock combined body based on particle flow code. Zhang et al. [24] analyzed the effects of different joint positions on the mechanical properties, acoustic emission characteristics, and damage evolution characteristics of rock columns based on PFC models. Although many scholars have verified the relationship between rock damage and acoustic emission, studies on the acoustic emission damage evolution characteristics of jointed rocks are relatively insufficient, and there is still a need to further investigate the damage evolution characteristics of different jointed rocks.

In this paper, the damage evolution characteristics of rocks containing a set of cross-joints are investigated based on particle flow code. Firstly, the jointed rock models, such as rock models with different joint cross-angles and with different joint lengths, are established based on the parallel bond model (PBM) and the smooth joint model (SJM). Then, the uniaxial compression mechanical properties and acoustic emission evolution characteristics of different jointed rocks are analyzed. Finally, the damage evolution characteristics of jointed rocks are discussed based on acoustic emission counts.

2. Rock Models with a Set of Cross-Joints Based on Particle Flow Code

2.1. PFC Theory for Simulating Jointed Rock Mass. The particle flow code program simulates the motion of the rock medium and its interactions through the discrete particle approach. Compared with finite element and other discrete element software, the PFC has the following advantages: the basic unit of PFC is particles, and the collection of inter-particle adhesion fracture can simulate the macroscopic rock breakage; the contact between particles is better than that between angular objects, which greatly improves its computational efficiency [25].

The PFC reflects the macromechanical properties of the model by setting particles and the contact between particles. When simulating the medium (e.g., rock mass and soil), the PFC provides two contact models: the contact bond model (CBM) and the parallel bond model (PBM) [26]. Since the CBM is a point contact, it can only simulate force transfer and not moments, which in turn is only suitable for simulating materials such as soils. The PBM regards the bonding between particles as a set of parallel springs, which has the effects of tension, shear, and moment, so it can effectively simulate the bonding between particles in rocks. In this paper, we use the PBM to build the complete rock model. When the tensile or shear stress between the particles exceeds the parallel bond strength, the parallel bond will lose its function [27].

The smooth joint model (SJM) is usually used to simulate the joints and fractures in rocks in the PFC model [28, 29]. Simulation of jointed rocks was achieved by replacing the PB contact model in the PBM with the SJ contact model. As shown in Figure 1, the smooth joint model provides the macroscopic behavior of a linear elastic and either bonded or frictional interface with dilation [26]. The behavior of the bonded interface is linear elastic until the strength limit is

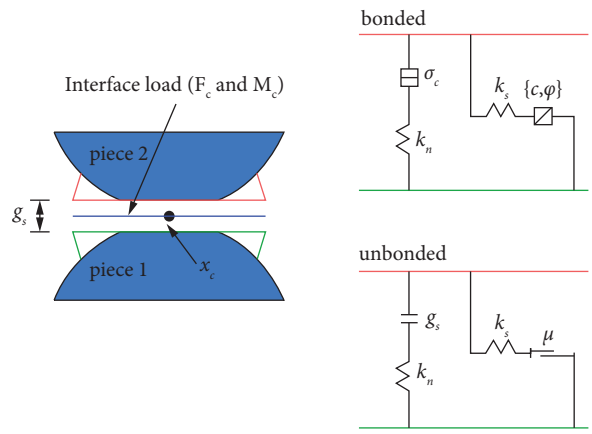

Figure 1: Smooth joint model [22].

exceeded and the bond breaks, making the interface unbonded; the behavior of an unbonded interface is linear elastic and frictional with dilation, with slip accommodated by imposing a Coulomb limit on the shear force. The interface does not resist relative rotation.

2.2. Numerical Models

2.2.1. Numerical Schemes. The purpose of this paper is to investigate the damage evolution characteristics of rocks containing a set of cross-joints, and the main considerations are the effects of the cross-angle and the length of joints, so the two schemes, as shown in Figure 2, are mainly considered in this paper. The model dimensions of the two schemes are the same, both are 50 mm × 100 mm, and both fixed the inclination angle (30° with the horizontal line) and the length LA (20 mm) of joint A. In Figure 2(a), the length LB of joint B is fixed as 30 mm, but its angle β with joint A is varied. The joint cross-angle β is taken as 30°, 60°, 90°, 120°, and 150° to investigate the effect of joint cross-angle on the damage evolution characteristics of rocks. In Figure 2(b), the joint cross-angle β is fixed as 100°, but the length LB of joint B is varied. The length LB of joint B is taken as 10 mm, 20 mm, 30 mm, 40 mm, and 50 mm to investigate the effect of joint length on the damage evolution characteristics of rocks.

2.2.2. Model Parameters. Since the PFC model reflects the macroscopic mechanics of rock by the mechanical properties of particles and the interparticle contact and these parameters cannot be obtained directly from the indoor experiments, the parameters of the model need to be calibrated before the numerical simulation. Typically, the parameters used by the PBM can be obtained from uniaxial compression tests [30]. The specific methods are as follows: firstly, a PBM with the same scale as the indoor uniaxial compression test model is established; secondly, the same mechanical loading scheme as the indoor experiments is used to obtain the mechanical properties of the numerical model; finally, the meso-parameters of the PBM are repeatedly calibrated by the "trial-and-error" method until the macroscopic parameters (e.g., elastic modulus and uniaxial compressive strength) and damage modes of the PBM are consistent with or similar to those of the indoor experiments. The final determined parameters can then be used for the analysis of different numerical schemes.

Due to the lack of indoor experimental data, the numerical parameters calibrated by Chen et al. [14] were used to establish the numerical models. The rock used in the research conducted by Chen et al. [14] was green sandstone, and the density, modulus of elasticity, and UCS of the rock were 2500 kg/m^3, 13.73 GPa, and 81.4 MPa, respectively. The deviation of E and UCS between the indoor experiment and the PFC numerical model is 0.39 GPa and 0.34 MPa.

The meso-parameters of the numerical green sandstone model calibrated by the "trial-and-error" method are shown in Table 1. The stress-strain curves and damage modes of the numerical model obtained by the uniaxial compression test based on meso-parameters are shown in Figures 3 and 4. As can be seen from the figures, the test results of the numerical model are in good agreement with the experimental results, so the meso-parameters in Table 1 can be used to build the PBM required in this paper.

Due to the difficulty of obtaining the mechanical and geometric parameters of actual joints, the bond properties of joints are set to 5% of the bond properties of particles (intact rock) by using the experience of Wang et al. [31], and the mechanical properties of joints in different parts of rock mass are assumed to be the same. The meso-parameters of joints are also obtained by referring to the study conducted by Chen et al. [14], and the specific parameters are shown in Table 2.

2.3. AE Simulation Based on PFC. When the force on the PBM as well as the SJM is greater than its bond strength (i.e., tensile strength or shear strength), the bond between the particles breaks, which corresponds to the creation of microcracks in the rock [32]. In general, during rock crack extension, damage energy will be rapidly released in the form of acoustic waves, which is the so-called acoustic emission phenomenon. Therefore, we can write FISH language to monitor the number of particle bond fractures during rock damage in real time and then analyze the acoustic emission characteristics during rock damage by counting the number of bond fractures at each moment (time step).

2.4. Loading Condition. This paper mainly investigates the mechanical properties, acoustic emission characteristics, and damage evolution law of rock models containing different cross-joints under uniaxial compression conditions, so the loading method in this paper is the same as the indoor uniaxial compression loading. In general, there are two modes of uniaxial compression experiments, displacement loading and stress loading, and this paper adopts the displacement loading mode. In order to improve the running efficiency, a loading speed of 0.001 m/s is adopted by moving the wall on top of the model. Although this loading speed is higher than that of general indoor experiments, many studies show that when the loading speed of PFC model is

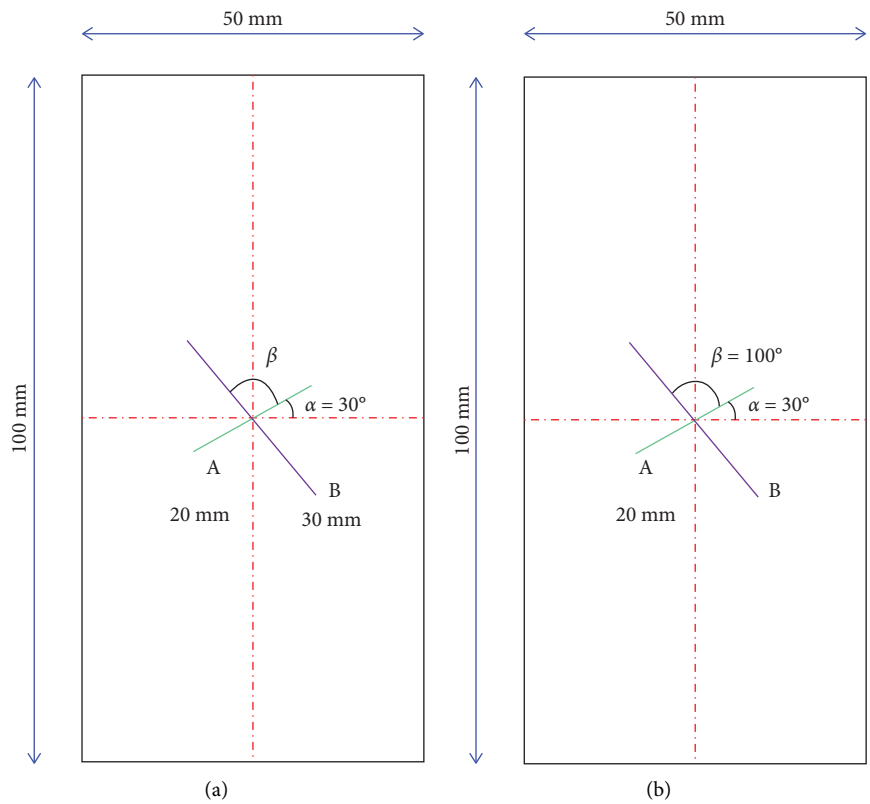

Figure 2: Schemes of rock models with a set of cross-joints with different (a) joint cross-angles and (b) joint lengths.

Table 1: Meso-parameters for the PBM [14].

Parameter	Value
Minimum particle diameter (mm)	0.3
Maximum particle diameter (mm)	0.5
Contact modulus of the particle (GPa)	10
Parallel bond deformation modulus (GPa)	16
Contact bond gap (mm)	0.05
Porosity	0.1
Density (kg/m^3)	2500
Parallel bond tensile strength (MPa)	21.7
Parallel bond cohesive force (MPa)	56
Stiffness ratio	1.5

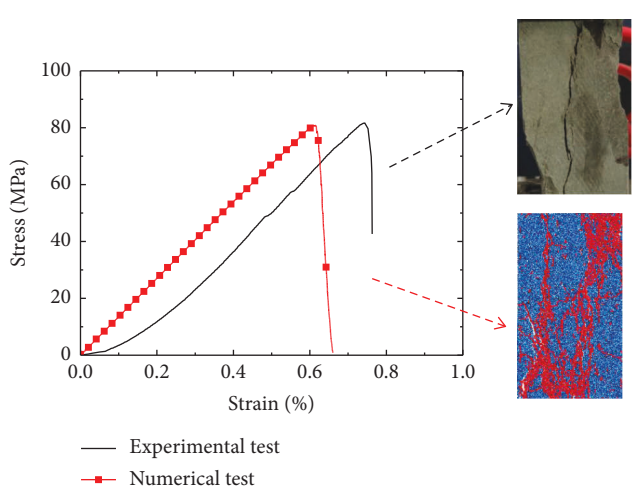

Figure 3: Comparison of experimental and numerical results of stress-strain curves and damage modes [14].

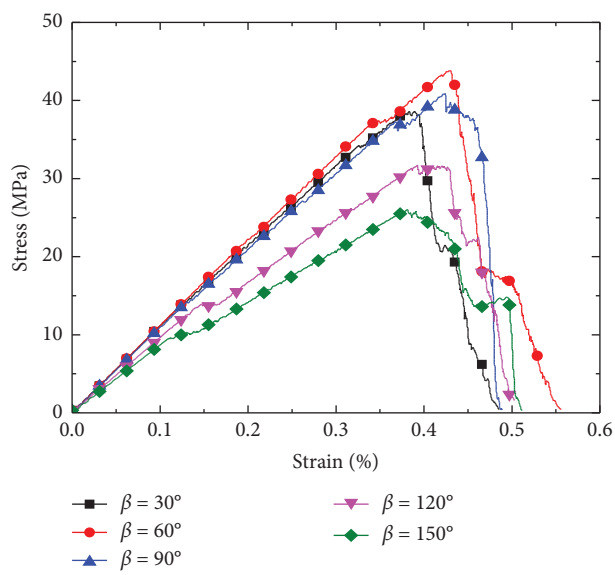

Figure 4: Stress-strain curves of rocks with different joint cross-angles.

Table 2: Meso-parameters for the SJM [11].

Parameter	Value
Joint tensile strength (MPa)	1.085
Joint cohesive force (MPa)	2.8
Joint friction angle	30
Joint normal stiffness (GPa/m)	15
Joint tangential stiffness (GPa/m)	10
Joint width (mm)	1

less than 0.1 m/s, the difference of axial stress-axial strain curve and strength parameters between numerical specimens is very small [33, 34].

3. Mechanical Properties and AE Evolution Characteristics of Different Rock Models

3.1. Mechanical Properties

3.1.1. Effect of Joint Cross-Angle. Figures 4 and 5 show the stress-strain curves as well as the uniaxial compressive strength and elastic modulus of rocks with different joint cross-angles, respectively. From the figures, it can be seen that the UCS and E of jointed rocks show a trend of increase and then decrease with the increase of joint cross-angle β. As the joint cross-angle β increases from 30° to 150°, the UCS of jointed rocks is 38.64 MPa, 43.85 MPa, 40.91 MPa, 31.74 MPa, and 26.02 MPa and the E is 11.21 GPa, 11.24 GPa, 10.96 GPa, 9.51 GPa, and 8.59 GPa, respectively. The UCS and E of jointed rocks are highest when the joint cross-angle β is 60°. The main reason is that when the cross-angle β is 60°, the dip angle of joint B with the horizontal direction (i.e., $\alpha + \beta$) is 90°, while many studies have shown that a 90° dip angle of joints has less effect on the mechanical properties of rocks [35].

3.1.2. Effect of Joint Length. Figures 6 and 7 show the stress-strain curves as well as the uniaxial compressive strength and elastic modulus of rocks with different joint lengths (the length of joint B, LB), respectively. From the figures, it can be seen that the UCS and E of jointed rocks show a trend of decrease with the increase of joint length. As the joint length increases from 10 mm to 50 mm, the UCS of jointed rocks is 42.41 MPa, 41.87 MPa, 37.18 MPa, 36.89 MPa, and 21.39 MPa and the E is 11.58 GPa, 11.31 GPa, 10.52 GPa, 9.22 GPa, and 7.09 GPa, respectively. The main reason is that as the length of joints increases, the penetration of joints increases and the extent of weak structure throughout the rock becomes larger, which in turn leads to a decrease in the mechanical properties of the jointed rock.

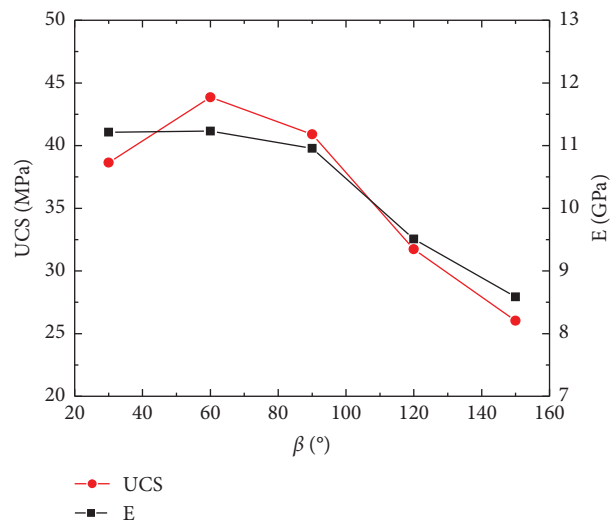

Figure 5: UCS and E of rocks with different joint cross-angles.

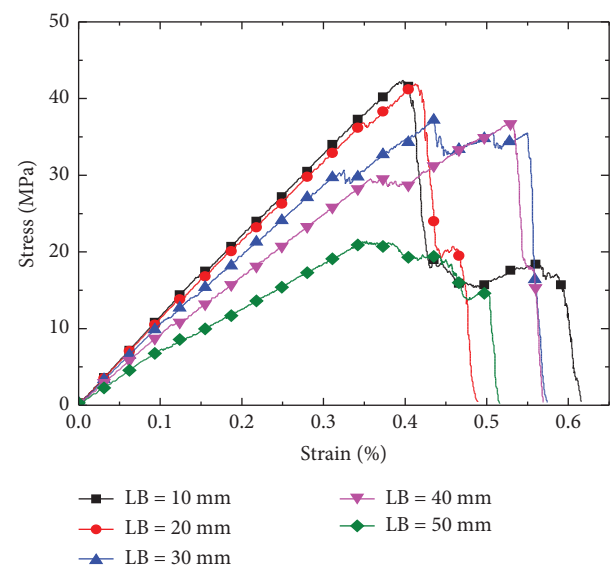

Figure 6: Stress-strain curves of rocks with different joint lengths.

3.2. AE Evolution Characteristics

3.2.1. Effect of Joint Cross-Angle. Figure 8 shows the acoustic emission evolution characteristic curves of rocks containing different joint cross-angles. From the figure, it can be seen that, with the increasing load loading time, the stress in the jointed rock shows a characteristic of fluctuating increase until the peak and then fluctuating decrease. Along with the evolution of stress, the acoustic emission counts of jointed rocks show three stages. The first stage is the stage of linear rise of the stress curve. At this time, no cracks are produced inside the jointed rocks, and the number of acoustic emission counts from the jointed rocks is zero. This stage can be called the acoustic emission-free stage. The second stage is the stage of rising fluctuation of stress curve. At this time, the cracks inside the jointed rocks are gradually developed, and the acoustic emission counts are jumping, i.e., there are moments of sudden increase, while others are not, which is related to the damage characteristics inside the jointed rocks. Overall, the increase in acoustic emission intensity (the number of acoustic emission counts at the same time step) in this phase is not very large and can be called the phase of slow increase of acoustic emission. The third stage is around the peak of the stress curve. At this time, the cracks inside the jointed rocks increase sharply, and the acoustic emission counts also jump, but the intensity of acoustic emission is much larger than that of the second stage. Therefore, the third stage can be called the stage of sharply increasing acoustic emission.

In addition, it can also be seen from Figure 8 that the overall trend of the acoustic emission evolution of jointed rocks does not change with the change of joint cross-angle. However, the time step of the occurrence of acoustic emission (crack initiation time) has changed. As the joint

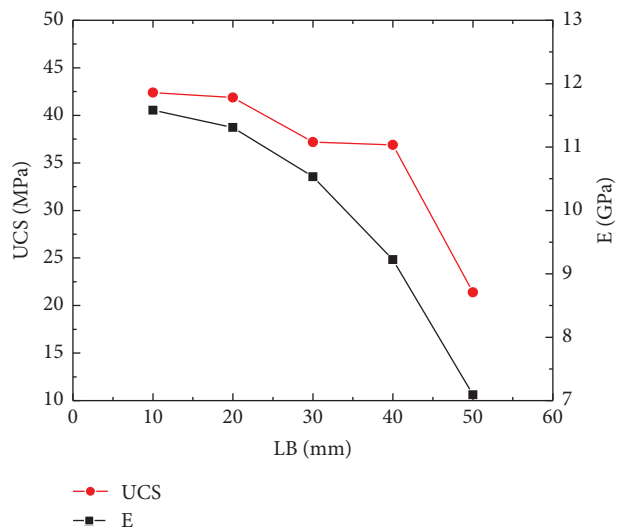

Figure 7: UCS and E of rocks with different joint lengths.

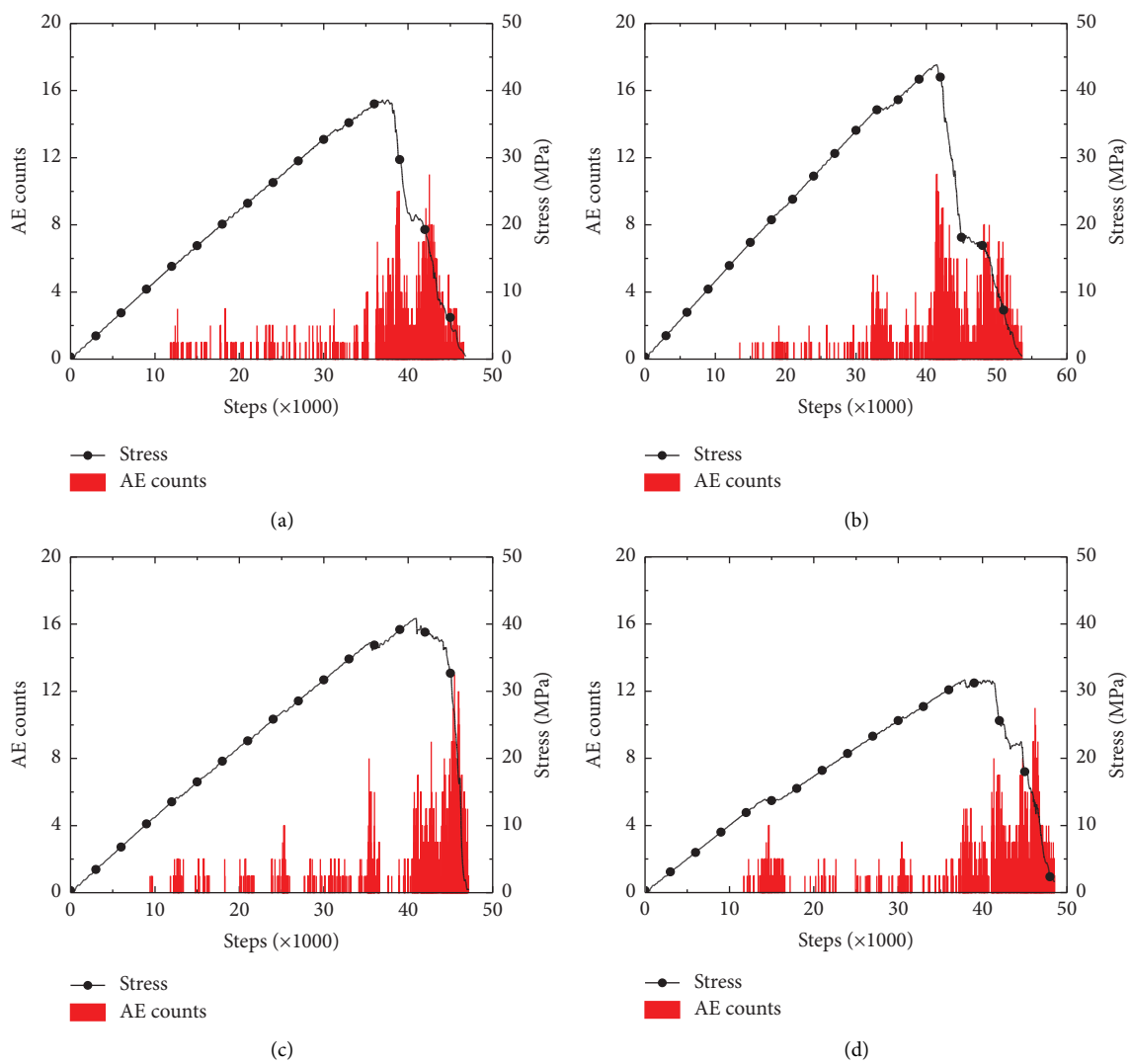

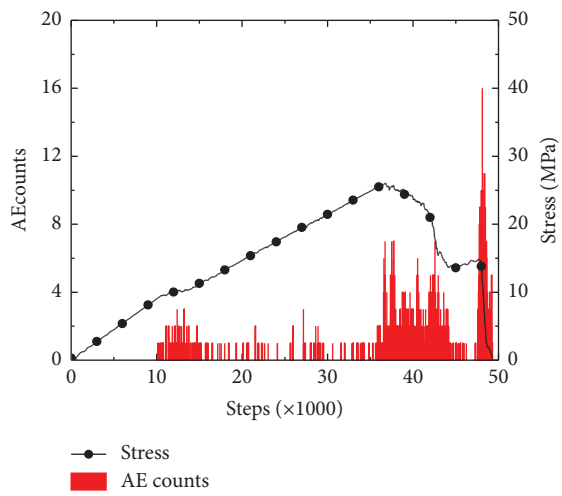

(e)

Figure 8: AE counts of rocks with different joint cross-angles. (a) $\beta = 30^\circ$. (b) $\beta = 60^\circ$. (c) $\beta = 90^\circ$. (d) $\beta = 120^\circ$. (e) $\beta = 150^\circ$.

cross-angle β increases from 30° to 150°, the time step of the occurrence of acoustic emission is 11776, 15321, 9598, 11582, and 10100, respectively. The largest time step of the occurrence of acoustic emission is for the rock with β equal to 60°, and the UCS and E of this jointed rock are the largest. Overall, the better the mechanical properties of the jointed rock, the less likely it is that internal cracks will form and the acoustic emission will be generated later. Besides, the maximum value of AE counts and the time of its occurrence vary with the variation of joint cross-angle β. As the joint cross-angle β increases from 30° to 150°, the maximum values of acoustic emission counts of jointed rocks are 11, 10, 13, 10, and 11, showing a "W"-type trend, and the time corresponding to the maximum values of acoustic emission counts is 42510, 41409, 45576, 46363, and 48347. Overall, the maximum value of acoustic emission and the occurrence time step have few relationships with the change of joint cross-angle β, and the relationship with UCS and E is also not obvious. Nevertheless, the evolution characteristics of acoustic emission changes are more closely related to the fluctuation characteristics of stress, and the time step of the acoustic emission jump is consistent with the time step of the stress fluctuation.

3.2.2. Effect of Joint Length. Figure 9 shows the characteristic curves of acoustic emission evolution of rocks with different joint lengths. As can be seen from the figure, the overall trend of the evolution of acoustic emission of jointed rocks does not change greatly as the length of joint B changes, and they all go through three stages: no acoustic emission, slowly increasing acoustic emission, and sharply increasing acoustic emission. However, with the increase of joint length, the phase of sharp increase of acoustic emission changes from two to one. Besides, the overall trend of the time step of the occurrence of acoustic emission decreases with the increase of joint length. As the joint length LB increases from 10 mm to 50 mm, the time step of the occurrence of acoustic emission is 11589, 9507, 9853, 8563, and 7411, respectively. The largest time step of the occurrence of acoustic emission is for the rock with LB equal to 10 mm, and the UCS and E of this jointed rock are the largest. Overall, the shorter the joint length of the rock (the smaller the penetration), the better its mechanical properties, the less likely its internal cracks will form, and the later the generation of acoustic emission. In addition, the maximum value of acoustic emission counts and the time of its occurrence vary with the variation of joint length. As the joint length LB increases from 10 mm to 50 mm, the maximum values of acoustic emission of jointed rocks are 10, 20, 16, 16, and 11, showing a trend of increase and then decrease, and the time corresponding to the maximum values of acoustic emission is 54878, 41028, 53734, 51846, and 48717. Overall, the maximum value of acoustic emission and its time step of occurrence are not obvious in relation to the variation of joint length and are not obvious in relation to UCS and E.

4. Damage Evolution of Different Rock Models Based on AE Characteristics

4.1. Damage Variables Based on AE Characteristics. The scholar Kachanov [36] of the former Soviet Union defined the damage variable as follows:

$$D = \frac{A_i}{A}, \tag{1}$$

where A_i is the damage cross-sectional area of the rock material in a certain period and A is the cross-sectional area of the material without damage at the initial stage.

If the cumulative acoustic emission count at the time when the nondestructive cross-sectional area A of the rock samples completely loses the bearing capacity is W, then the cumulative acoustic emission count W_u of the unit area of rock failure is

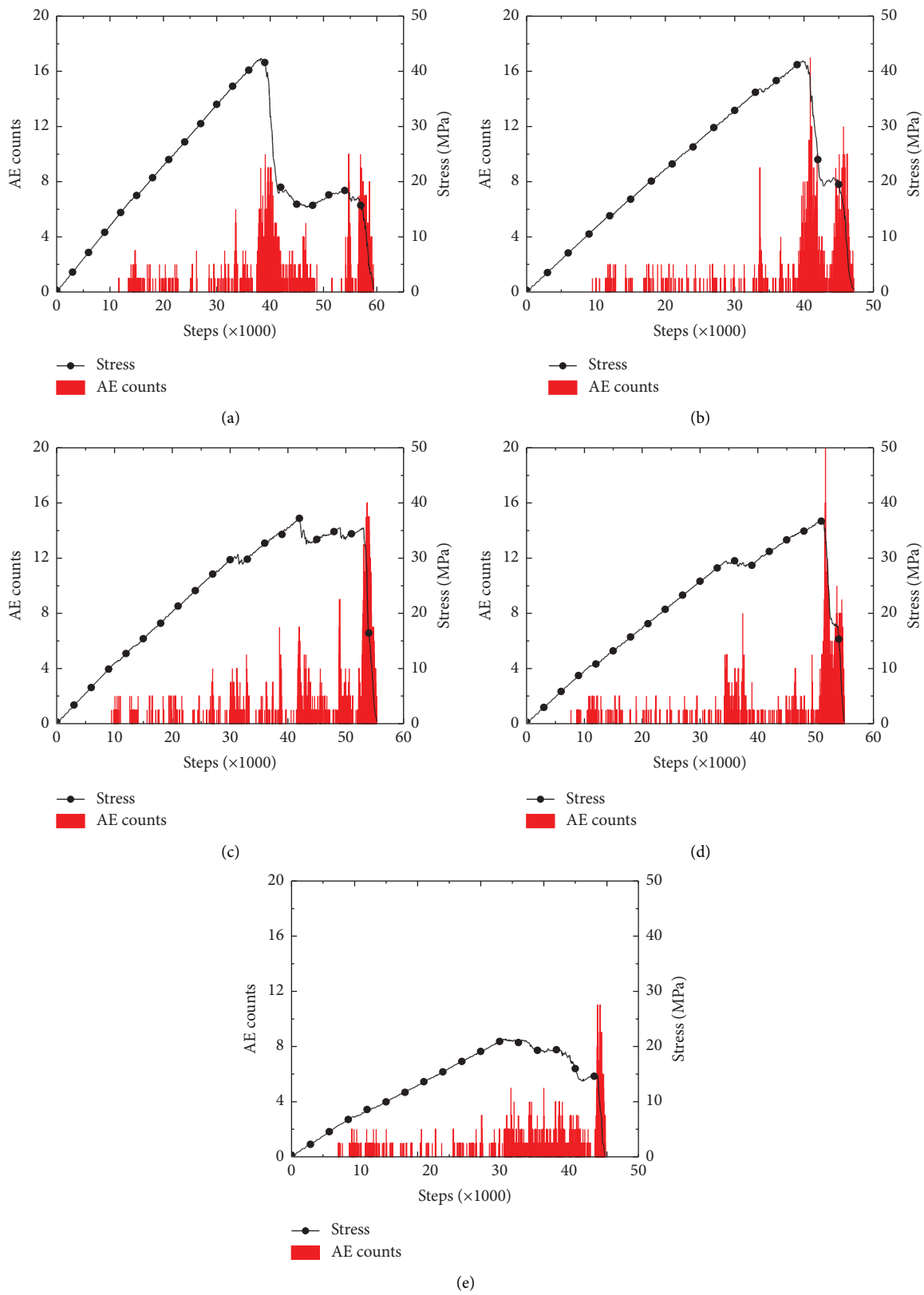

Figure 9: AE counts of rocks with different joint lengths. (a) LB = 10 mm. (b) LB = 20 mm. (c) LB = 30 mm. (d) LB = 40 mm. (e) LB = 50 mm.

$$W_u = \frac{W}{A}. \tag{2}$$

When the damage cross-sectional area of the rock samples reaches A_i, the number of cumulative acoustic emission counts W_t can be calculated as

$$W_t = W_u \cdot A_i = \frac{W}{A} \cdot A_i. \tag{3}$$

Thus,

$$D = \frac{A_i}{A} = \frac{W_t}{W}. \tag{4}$$

Many studies [3, 14] have shown that the damage variables using (4) can better respond to the damage characteristics of rocks, so we next explore the damage evolution patterns of different jointed rocks by using the damage variables defined by (4).

4.2. Damage Evolution of Different Jointed Rock Models

4.2.1. Effect of Joint Cross-Angle. Figure 10 shows the damage evolution characteristics of rocks with different joint cross-angles. From the figure, it can be seen that the damage evolution of jointed rocks shows three stages with the increase of stress (time). The first stage is the damage-free stage, which corresponds to the no acoustic emission stage in acoustic emission evolution characteristic curves. At this time, no cracks are produced inside the jointed rock, which mainly corresponds to points a ~ b in the figure. The second stage is the slow (fluctuating) increasing stage of damage, which corresponds to the slow increasing stage of acoustic emission evolution characteristics. Within this phase, cracks within the rock are continuously developed and acoustic emission occurs in jumps, which mainly corresponds to points b ~ d in the figure. The third stage is the stage of sharp increase of damage, which corresponds to the sharp increase of acoustic emission evolution characteristics. In this stage, the rock internal cracks develop rapidly and the acoustic emission signal is more intense, mainly corresponding to points d ~ f in the figure.

From Figure 10, we also know that the trend of damage evolution characteristics of jointed rocks does not change with the increase of joint cross-angle, and all go through three damage characteristic stages. However, the fluctuation characteristics during the damage evolution of jointed rocks are different with the change of joint cross-angle. When the joint cross-angle β is 30°, the slow increasing phase of jointed rock damage is relatively gentle, and the sharp increasing phase of damage is relatively steep and less fluctuating. When the joint cross-angle β is 60° ~120°, the slow increasing stage of the jointed rock damage shows two steps, the sharp increasing stage of damage also shows two steps, and the slope of the first step has the tendency to become larger with the increase of β. Overall, the damage evolution trend of jointed rocks is related to the stress characteristics, and the fluctuation of damage is also due to the fluctuation generated by stress. Therefore, the damage variables defined by using acoustic emission can better reflect the damage evolution characteristics of jointed rocks.

Figure 11 shows the damage evolution of rocks with different joint cross-angles. From the figure, it can be seen that the damage rupture of jointed rocks begins to sprout from and expand along the tip of the joints. In points a ~ c, cracks are mainly produced at the tips of the joints. When entering point d, the cracks develop continuously around the two joints. When entering points e ~ f, the development of cracks is more extensive and begins to spread throughout the model until the model is destroyed.

For rocks with different joint cross-angles, the damage rupture process during loading is different. When the joint angle is 30°~90°, the initial damage of the jointed rock is mainly at the tip of joint B, followed by cracks near joints A and B, and finally the damage block is formed on the left side of the jointed rock and detached from the rock. Of course, for the rock with a joint angle of 60°, the right side of the rock masses also formed a destruction block. When the joint angle is 120°, the initial damage of the jointed rock is at the right-hand tips of joints A and B, which then extends to the left-hand tips of the joints and finally forms larger cracks in the upper part of the jointed rock, thus leading to rock destruction. For a jointed rock with a joint angle of 150°, the initial damage is at the tip of joint A, then extends to the tip of joint B, and finally continues to extend along the tip of joint B until the rock breaks down.

4.2.2. Effect of Joint Length. Figure 12 shows the damage evolution characteristics of rocks with different joint lengths. From the figure, we can know that the trend of damage evolution characteristics of rocks does not change with the increase of the length of joints, and they all go through three characteristic stages as described in Section 3.2.1. However, the fluctuation characteristics of the damage evolution of jointed rocks are different with the variation of joint length. When the length of the joint is 10 mm, the slow damage phase of the rock is between point b and point c, with a small increase, and the sharp increase phase of the rock is between point c and point f, with a large increase and the existence of two steps. When the length of the joint is 20 mm, the slow damage phase of the rock is between point b and point d, with a small increase; the sharp increase phase of the rock is between point d and point f, with a larger increase; and the stage phase is small. When the length of joints is 30 mm, the slow damage phase of the rock is between point b and point c, the sharp increase phase of the rock is between point c and point f, and the increase rate in phase c~e is smaller than that in phase e ~ f. When the length of joints is 40 mm, the slow damage stage of the rock is between point b and point c; the sharp increase stage of the damage of the rock is between point c and point f; and there are two steps. The increase rate in the first step is slower than that in the second step. When the length of the joint is 50 mm, the slow damage phase of the rock is between point b and point c, the sharp increase phase of the rock is between point c and point f, and the increase rate in phase c to e is balanced and less than the sharp increase in phase e to f.

Figure 13 shows the damage evolution of rocks with different joint lengths. It can be seen from the figure the damage evolution process of jointed rocks shows some

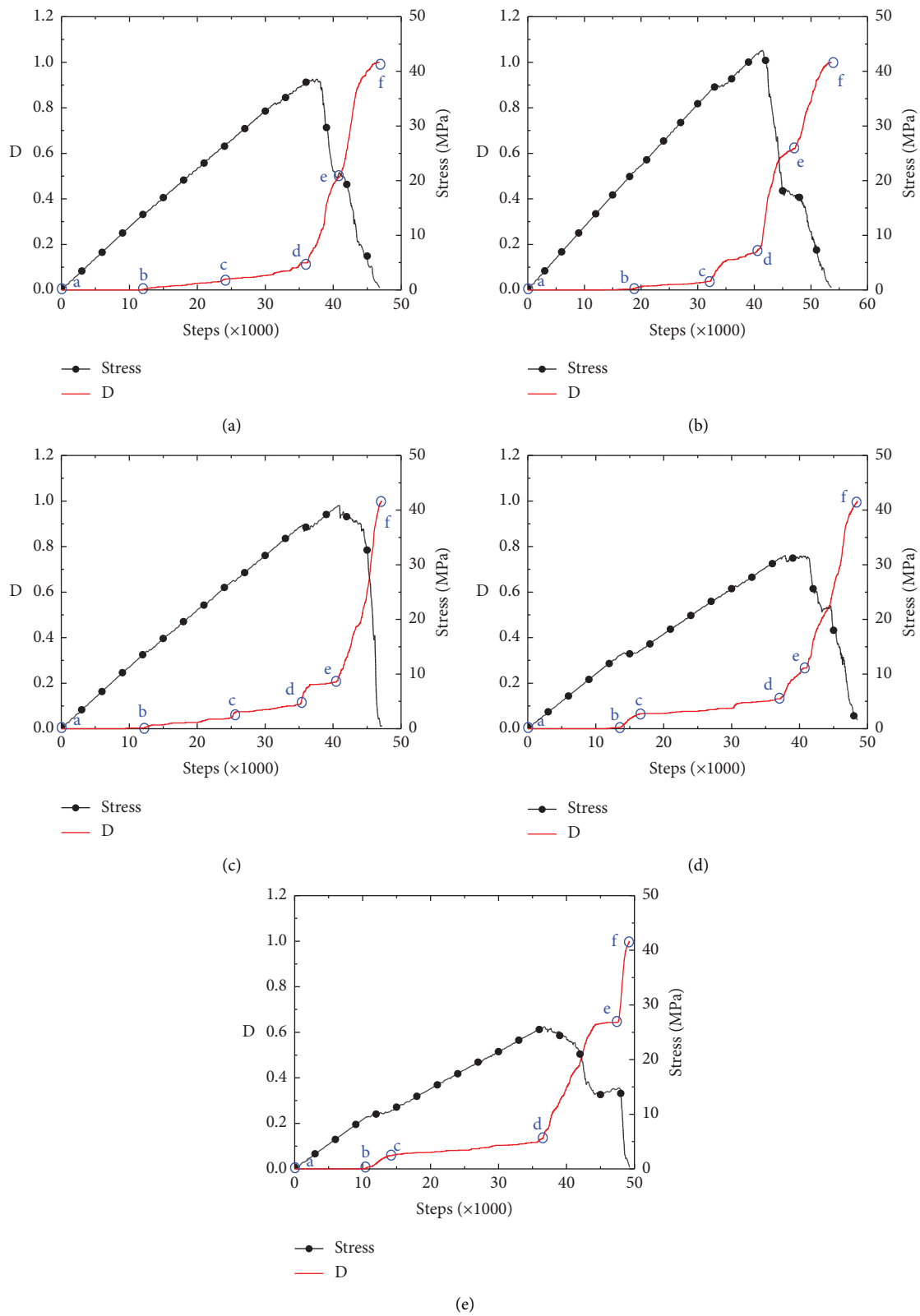

Figure 10: Damage evolution characteristics of rocks with different joint cross-angles. (a) $\beta = 30^{\circ}$. (b) $\beta = 60^{\circ}$. (c) $\beta = 90^{\circ}$. (d) $\beta = 120^{\circ}$. (e) $\beta = 150^{\circ}$.

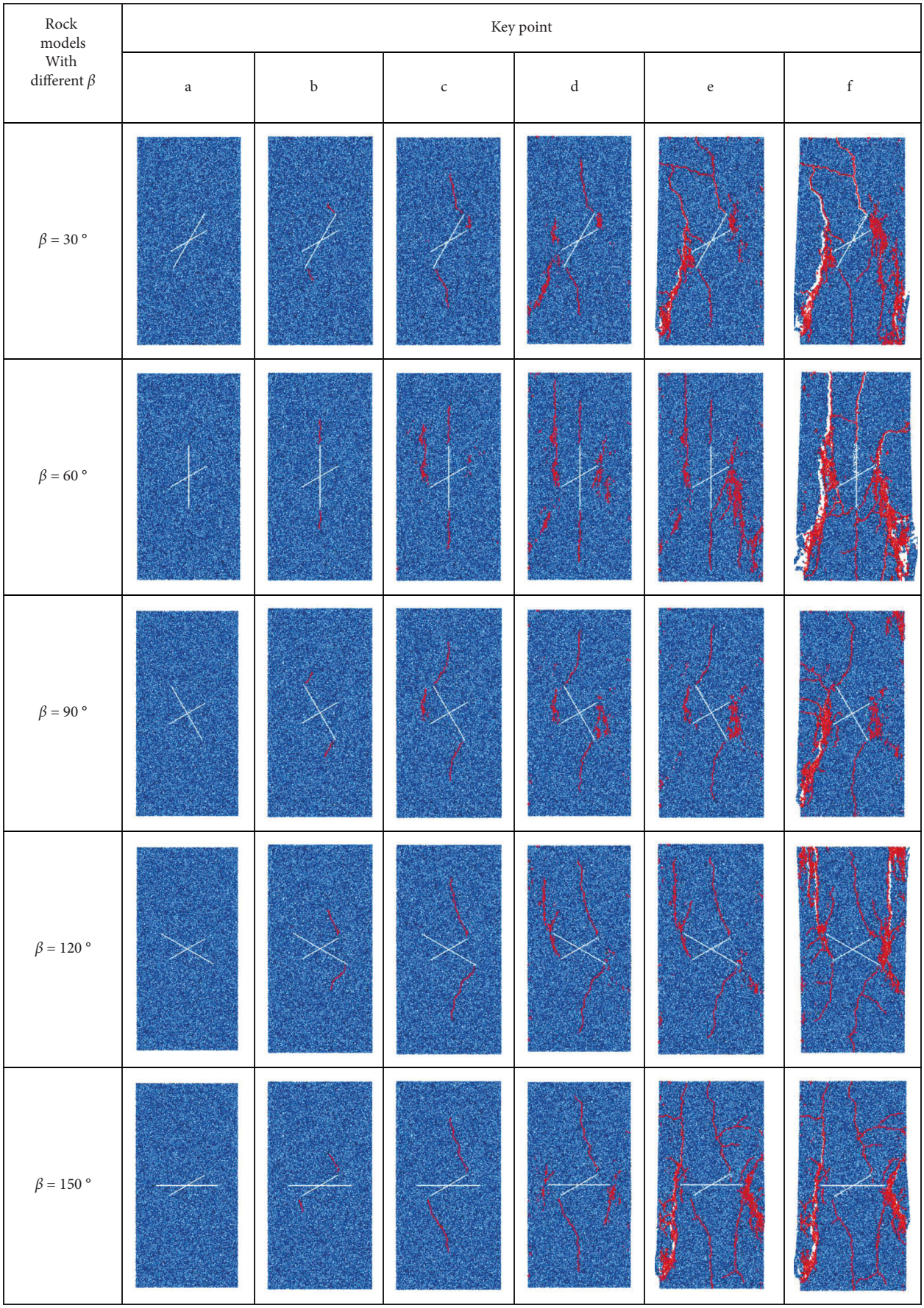

Figure 11: Damage evolution of rocks with different joint cross-angles.

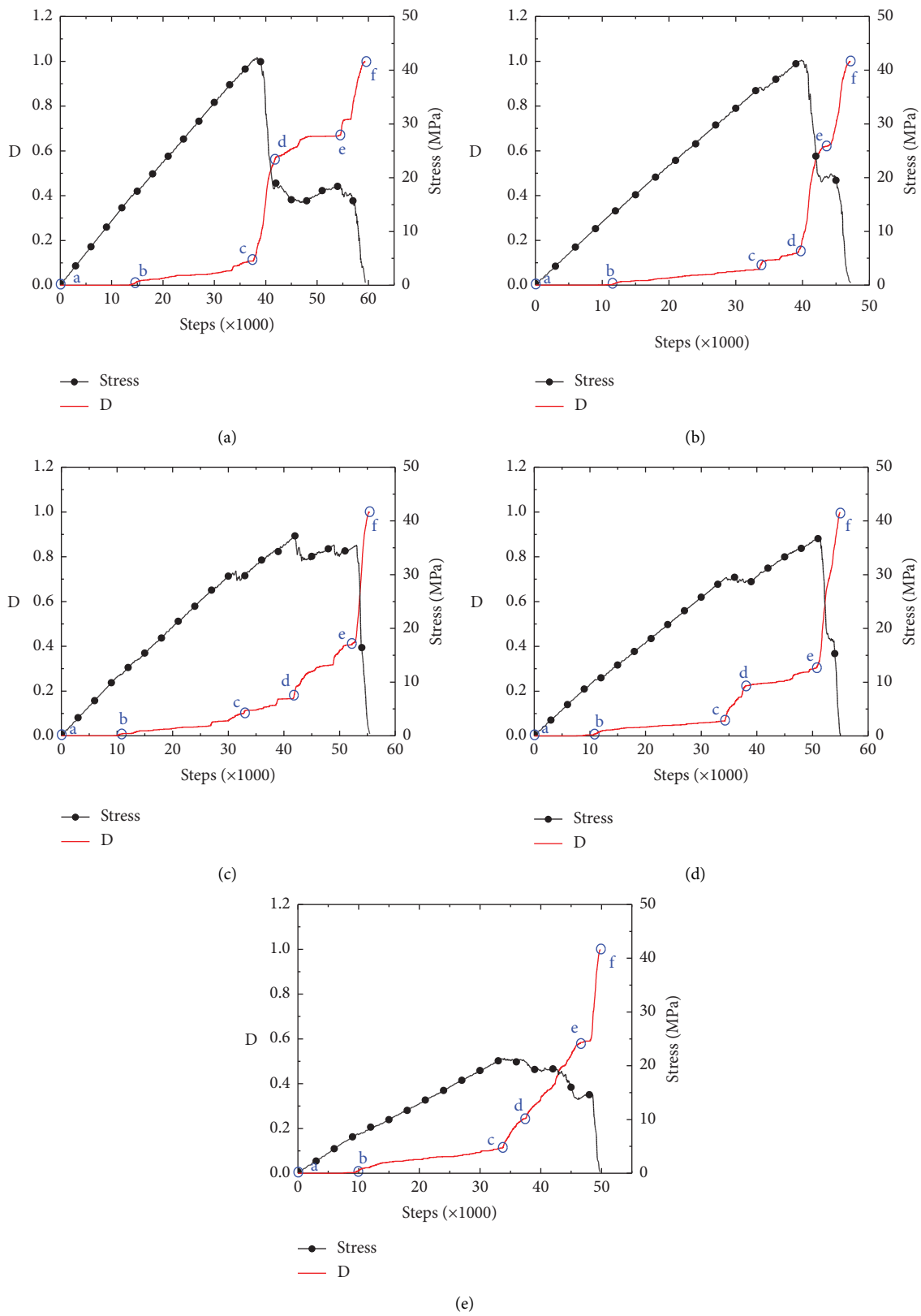

Figure 12: Damage evolution characteristics of rocks with different joint lengths. (a) LB = 10 mm. (b) LB = 20 mm. (c) LB = 30 mm. (d) LB = 40 mm. (e) LB = 50 mm.

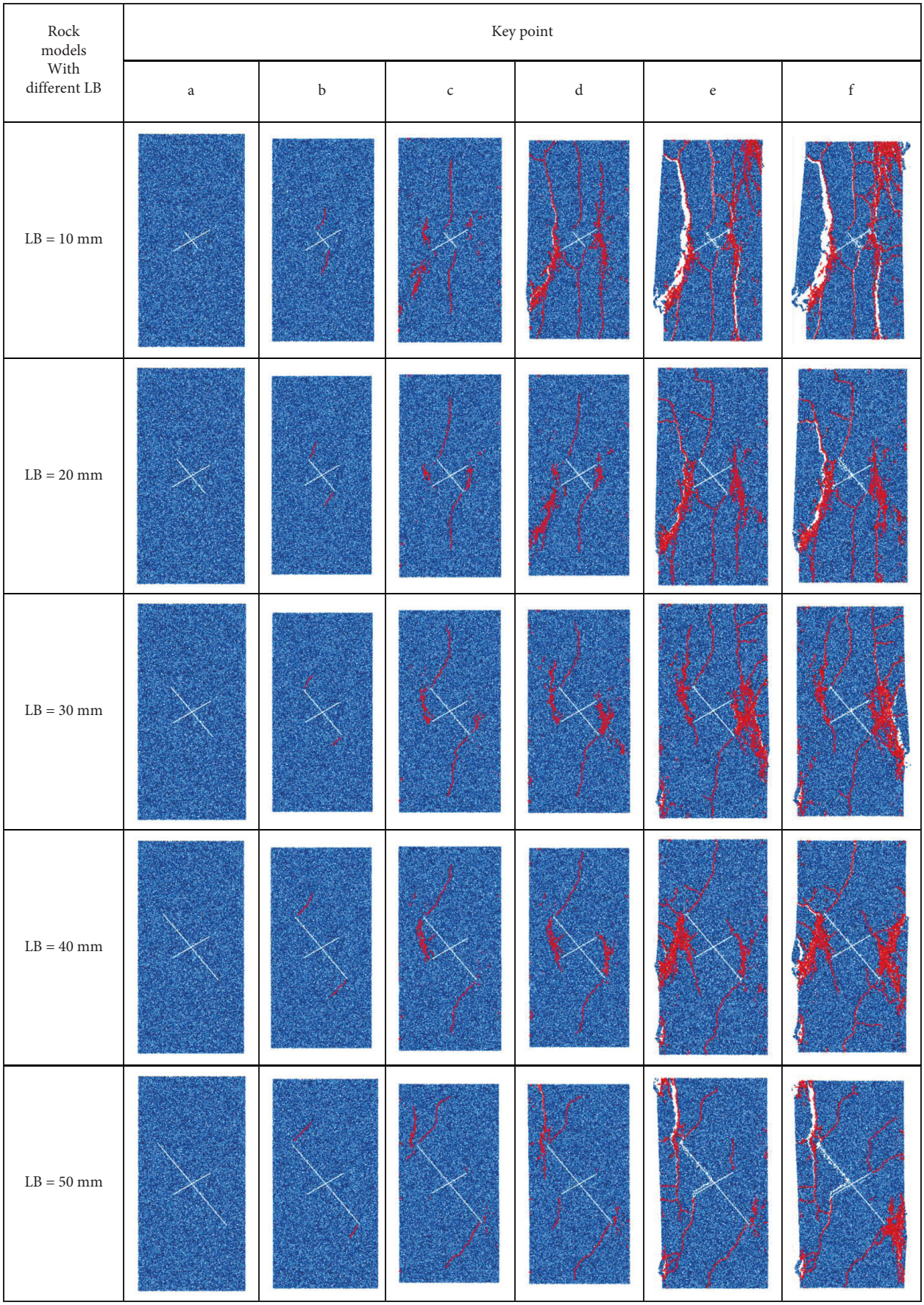

Figure 13: Damage evolution of rocks with different joint lengths.

similarity with the different lengths of joints, mainly in the crack budding stage and the slow development stage. In the crack initiation stage, the cracks are first produced at the tips of joint B. Subsequently, cracks along joint B are continuously expanded and mixed with cracks in joint A. However, the final damage state of jointed rocks varies with the length of joints. When the length of joints is small, the splitting block of the rock is larger and the cracks extend closer to the center of the rock. When the length of joints is large, the damage of the rock gradually breaks towards the edge of the rock, such as the upper left corner and the lower right corner.

5. Conclusions

This paper numerically investigates the effects of joint angle and joint length on the mechanical properties, acoustic emission characteristics, and damage evolution characteristics of jointed rocks based on particle flow code, and the following conclusions are obtained.

The UCS and E of jointed rocks show a trend of increase and then decrease with the increase of joint cross-angle β. The UCS and E of the jointed rock are highest when the joint cross-angle β is 60°. The UCS and E of jointed rocks show a trend of decrease with the increase of joint length.

Along with the evolution of stress, the acoustic emission counts of jointed rocks show three stages: acoustic emission-free stage, slow AE increase stage, and sharp AE increase stage. The overall trend of the AE evolution of jointed rocks does not change with the change of joint cross-angle and joint length. However, the time step of the occurrence of acoustic emission (crack initiation time) has changed. Overall, the better the mechanical properties of the jointed rock, the later the acoustic emission will be generated. The maximum value of AE and the occurrence time step have few relationships with the change of β and LB, and the relationship with UCS and E is also not obvious.

The damage evolution of jointed rocks shows three stages with the increase of stress (time): damage-free stage, slow damage increase stage, and sharp damage increase stage. The trend of damage evolution characteristics of jointed rocks does not change with the increase of joint cross-angle or joint length, and all go through three damage characteristic stages. However, the fluctuation characteristics of the damage evolution of jointed rocks are different with the change of β and LB.

The damage variables defined by using acoustic emission can better reflect the damage evolution characteristics of jointed rocks. The damage rupture of jointed rocks begins to sprout from and expand along the tip of the joints. The damage rupture of jointed rocks is different with the change of β and LB, which is mainly reflected in the crack initiation position and the final failure mode. For rocks with different β, the crack initiation position and the final failure mode are different; however, for rocks with different LB, the crack initiation position is similar.

Data Availability

The data used to support the findings of this study are included in the article.

Conflicts of Interest

The authors declare that they have no conflicts of interest.

Acknowledgments

This research was funded by the National Natural Science Foundation of China (52109139 and 52009122), the China Postdoctoral Science Foundation (2022M712724), the Natural Science Foundation of Zhejiang Province (LQ20E080022 and LQ21E090002), and the Science and Technology Project supported by the Department of Transportation of Zhejiang Province (2019007).

References

[1] D. Mas Ivars, M. E. Pierce, C. Darcel et al., "The synthetic rock mass approach for jointed rock mass modelling," *International Journal of Rock Mechanics and Mining Sciences*, vol. 48, no. 2, pp. 219–244, 2011.

[2] F. Ren, C. Zhu, and M. He, "Moment tensor analysis of acoustic emissions for cracking mechanisms during schist strain burst," *Rock Mechanics and Rock Engineering*, vol. 53, no. 1, pp. 153–170, 2020.

[3] W. Liu, J. Xu, Z. Wang, and C. Peng, "Experimental research on damage characteristics and safety damage threshold of jointed caverns based on acoustic emissions," *Geomechanics and Geophysics for Geo-Energy and Geo-Resources*, vol. 7, no. 3, pp. 72–14, 2021.

[4] Y. Wang, W. H. Tan, D. Q. Liu, Z. Q. Hou, and C. H. Li, "On anisotropic fracture evolution and energy mechanism during marble failure under uniaxial deformation," *Rock Mechanics and Rock Engineering*, vol. 52, no. 10, pp. 3567–3583, 2019.

[5] M. C. He, Q. R. Sui, M. N. Li, Z. J. Wang, and Z. G. Tao, "Compensation excavation method control for large deformation disaster of mountain soft rock tunnel," *International Journal of Mining Science and Technology*, 2022.

[6] G. Feng, X. C. Wang, Y. Kang, and Z. T. Zhang, "Effect of thermal cycling-dependent cracks on physical and mechanical properties of granite for enhanced geothermal system," *International Journal of Rock Mechanics and Mining Sciences*, vol. 134, Article ID 104476, 2020.

[7] R. H. Cao, P. Cao, H. Lin, X. Fan, C. Zhang, and T. Liu, "Crack initiation, propagation, and failure characteristics of jointed rock or rock-like specimens: a review," *Advances in Civil Engineering*, vol. 201931 pages, Article ID 6975751, 2019.

[8] H. Lee and S. Jeon, "An experimental and numerical study of fracture coalescence in pre-cracked specimens under uniaxial compression," *International Journal of Solids and Structures*, vol. 48, no. 6, pp. 979–999, 2011.

[9] P. Yin, R. H. C. Wong, and K. T. Chau, "Coalescence of two parallel pre-existing surface cracks in granite," *International Journal of Rock Mechanics and Mining Sciences*, vol. 68, pp. 66–84, 2014.

[10] S. Q. Yang, "Crack coalescence behavior of brittle sandstone samples containing two coplanar fissures in the process of deformation failure," *Engineering Fracture Mechanics*, vol. 78, no. 17, pp. 3059–3081, 2011.

[11] X. P. Zhou, H. Cheng, and Y. F. Feng, "A "n experimental study of crack coalescence behaviour in rock-like materials containing multiple flaws under uniaxial compression"," *Rock Mechanics and Rock Engineering*, vol. 47, no. 6, pp. 1961–1986, 2014.

[12] H. Li and L. N. Y. Wong, "Influence of flaw inclination angle and loading condition on crack initiation and propagation," *International Journal of Solids and Structures*, vol. 49, no. 18, pp. 2482–2499, 2012.

[13] X. P. Zhang and L. N. Y. Wong, "Cracking processes in rock-like material containing a single flaw under uniaxial compression: a numerical study based on parallel bonded-particle model approach," *Rock Mechanics and Rock Engineering*, vol. 45, no. 5, pp. 711–737, 2012.

[14] Z. Chen, L. Xu, and Y. Shang, "Influence of joint angle on the acoustic emission evolution characteristics and energy dissipation rule of rock mass," *Geotechnical & Geological Engineering*, vol. 39, no. 2, pp. 1621–1635, 2021.

[15] M. R. Vergara, M. Van Sint Jan, and L. Lorig, "Numerical model for the study of the strength and failure modes of rock containing non-persistent joints," *Rock Mechanics and Rock Engineering*, vol. 49, no. 4, pp. 1211–1226, 2016.

[16] V. Sarfarazi, R. K. zadeh, K. Asgari, and X. Wang, "H" shaped echelon joints under uniaxial loading," *Geotechnical & Geological Engineering*, vol. 40, no. 4, pp. 1765–1787, 2022.

[17] Z. A. Moradian, G. Ballivy, P. Rivard, C. Gravel, and B. Rousseau, "Evaluating damage during shear tests of rock joints using acoustic emissions," *International Journal of Rock Mechanics and Mining Sciences*, vol. 47, no. 4, pp. 590–598, 2010.

[18] J. F. Hazzard and R. P. Young, "Simulating acoustic emissions in bonded-particle models of rock," *International Journal of Rock Mechanics and Mining Sciences*, vol. 37, no. 5, pp. 867–872, 2000.

[19] C. Khazaei, J. Hazzard, and R. Chalaturnyk, "Damage quantification of intact rocks using acoustic emission energies recorded during uniaxial compression test and discrete element modeling," *Computers and Geotechnics*, vol. 67, pp. 94–102, 2015.

[20] Q. B. Lin, P. Cao, K. H. Li, R. H. Cao, K. P. Zhou, and H. W. Deng, "Experimental study on acoustic emission characteristics of jointed rock mass by double disc cutter," *Journal of Central South University*, vol. 25, no. 2, pp. 357–367, 2018.

[21] Z. Chong, Q. Yao, X. Li, and K. Shivakumar, "Acoustic emission investigation on scale effect and anisotropy of jointed rock mass by the discrete element method," *Arabian Journal of Geosciences*, vol. 13, no. 9, pp. 324–414, 2020.

[22] Z. Zhang, X. Liu, Y. Zhang, X. Qin, and M. Khan, "Comparative study on fracture characteristics of coal and rock samples based on acoustic emission technology," *Theoretical and Applied Fracture Mechanics*, vol. 111, Article ID 102851, 2021.

[23] W. Liu, W. Yuan, Y. Yan, and X. Wang, "Analysis of acoustic emission characteristics and damage constitutive model of coal-rock combined body based on particle flow code," *Symmetry*, vol. 11, no. 8, p. 1040, 2019.

[24] P. Zhang, Y. He, Z. Sun, and D. Yue, "Influence of parallel-joint position on mechanical behavior and acoustic emission characteristics of rock pillar," *Shock and Vibration*, vol. 2021, pp. 1–9, Article ID 1719553, 2021.

[25] J. Zhou, Y. Chi, Y. W. Chi, and J. P. Xu, "The method of particle flow and PFC2D Code," *Rock and Soil Mechanics*, vol. 21, no. 3, pp. 271–274, 2000.

[26] Itasca Consulting Group Inc, *PFC (Particle Flow Code), version 5.0*, ICG, Minnesota, MN, USA, 2014.

[27] M. Chen, S. Q. Yang, P. G. Ranjith, and Y. C. Zhang, "Cracking behavior of rock containing non-persistent joints with various joints inclinations," *Theoretical and Applied Fracture Mechanics*, vol. 109, Article ID 102701, 2020.

[28] S. Wu and X. Xu, "A study of three intrinsic problems of the classic discrete element method using flat-joint model," *Rock Mechanics and Rock Engineering*, vol. 49, no. 5, pp. 1813–1830, 2016.

[29] M. Bahaaddini, A. M. Sheikhpourkhani, and H. Mansouri, "Flat-joint model to reproduce the mechanical behaviour of intact rocks," *European Journal of Environmental and Civil Engineering*, vol. 25, no. 8, pp. 1427–1448, 2021.

[30] U. Castro-Filgueira, L. R. Alejano, J. Arzúa, and D. M. Ivars, "Sensitivity analysis of the micro-parameters used in a PFC analysis towards the mechanical properties of rocks," *Procedia Engineering*, vol. 191, pp. 488–495, 2017.

[31] P. Wang, M. Cai, F. Ren, C. Li, and T. Yang, "A digital image-based discrete fracture network model and its numerical investigation of direct shear tests," *Rock Mechanics and Rock Engineering*, vol. 50, no. 7, pp. 1801–1816, 2017.

[32] J. F. Hazzard, R. P. Young, and S. C. Maxwell, "Micromechanical modeling of cracking and failure in brittle rocks," *Journal of Geophysical Research: Solid Earth*, vol. 105, no. B7, pp. 16683–16697, 2000.

[33] P. Cheng, "Loading rate effect analysis on rock particle flow mode under uniaxial compression," *Chinese Journal of Underground Space and Engineering*, vol. 14, no. 3, pp. 635–642, 2017.

[34] X. p. Zhang, Q. Zhang, and S. Wu, "Acoustic emission characteristics of the rock-like material containing a single flaw under different compressive loading rates," *Computers and Geotechnics*, vol. 83, pp. 83–97, 2017.

[35] C. Huang, W. Yang, K. Duan, L. Fang, L. Wang, and C. Bo, "Mechanical behaviors of the brittle rock-like specimens with multi-non-persistent joints under uniaxial compression," *Construction and Building Materials*, vol. 220, pp. 426–443, 2019.

[36] L. M. Kachanov, "Rupture time under creep conditions," *International Journal of Fracture*, vol. 97, no. 1/4, pp. 11–18, 1999.

Hindawi
Advances in Materials Science and Engineering
Volume 2022, Article ID 8147186, 17 pages
https://doi.org/10.1155/2022/8147186

Research Article

Simulation of the Uniaxial Mechanical Properties and Crack Evolution of Coal Pillar-Artificial Dam in Abandoned Mines

Xin Lyu,[1] **Ke Yang**,[2] **Juejing Fang**,[1] **Minke Duan**,[1] **and Jinzhou Tang**[1,3]

[1]*State Key Laboratory of Mining Response and Disaster Prevention and Control in Deep Coal Mines, Anhui University of Science and Technology, Huainan 232001, China*
[2]*Institute of Energy, Hefei Comprehensive National Science Center, Hefei 230031, China*
[3]*Guizhou Provincial Key Laboratory of Rock and Soil Mechanics and Engineering Safety, Guizhou University, Guiyang, Guizhou 550025, China*

Correspondence should be addressed to Juejing Fang; juejing_fang@foxmail.com

Received 30 June 2022; Accepted 20 August 2022; Published 21 September 2022

Academic Editor: Depeng Ma

The key to the construction of underground reservoirs in abandoned mines is the construction of coal pillar-artificial dams, and the choice of bonding parameters between the coal pillars and artificial dams is the deciding factor that determines the engineering stability. Based on the analysis of the force state of coal pillar-artificial dams, the influence of the interface angle was analyzed. Seven sets of coal pillar-artificial dam specimens were prepared and a PFC^{3D} numerical model was constructed to carry out the uniaxial compression test without lateral pressure. Based on the strength, deformation, and energy evolution characteristics of the coal pillar-artificial dam, the influence of the angle of the coal pillar-artificial dam interface on the performance of the specimen was analyzed. The research results showed that the force state of the coal pillar-artificial dam can be divided into three types. The composite simulation curve showed obvious postpeak viscosity. The compressive strength, peak strain, and average dissipated energy curves of the coal pillar-artificial dam showed a unimodal trend that first increased and then decreased. The total energy and elastic energy of the coal pillar-artificial dam showed an increasing trend during loading. The simulated initiation stress and damage stress of the coal pillar-artificial dam specimens were intermediate to that of the coal pillars and the artificial dams, which first increased and then decreased with the increase in inclination, reaching the peak at 70°.

1. Introduction

The Fourteenth Five-Year Plan focuses clearly on increasing the concentration of coal production in resource-rich areas. As outdated coal production units are phased out, the number of closed/abandoned coal mines will continue to rise [1–3]. In this context, it is pertinent to develop overall strategies, basic theoretical research, and key technological breakthroughs for the development and utilization of resources and energy from closed/abandoned mines [4, 5]. In addition, the reuse of the resources contained in abandoned mines and underground spaces plays a vital role in the optimization and sustainable development of the industrial structure of coal enterprises [6]. The construction of underground reservoirs in coal mines provides a realistic basis for innovative ideas such as using abandoned mines to build pumped-storage power stations [7]. The construction of abandoned mines pumped-storage power stations can improve the integration of China's power source network and load storage, facilitating the establishment of a clean energy base with multiple complementary energy sources. [8]. The construction of safe and controllable underground reservoirs has important experimental and practical value for the protection of groundwater resources and the development and utilization of subterranean space in closed/abandoned mines [9]. To this end, many researchers have studied the safety and stability of the reuse of subterranean spaces in abandoned mines [10–13] and established a stability evaluation system for water storage systems in underground mines. Case evaluations for the structural stability of underground reservoirs in coal mines were also carried out [14, 15].

At the same time, the researchers also carried out a series of experimental studies on various parameters of the underground reservoir dam. Artificial dams were constructed to study the dynamic failure characteristics under different intensity conditions, and studies on the comprehensive strength measurement of ultrasonic rebound, cyclic loading, and uniaxial compression acoustic emission test were carried out [16, 17]. The seismic performance and dynamic response [14, 18] were tested, based on which a fuzzy multilevel comprehensive evaluation model for the safety of artificial dams was proposed [20]. The FLAC^{3D} numerical simulation software was used to establish an artificial dam model, on which graded water pressure was applied to study the water-rock migration interaction [21–23]. The limiting water head value that the artificial dam can bear, and the vulnerable position were determined, [24, 25] and the fluid-solid coupling numerical model of the underground reservoir under the coupled action of mining and flooding was constructed [16]. Through underground sampling, the rock fragmentation characteristics [27] and size effect test were carried out to analyze the deformation behavior of underwater coal and rock [28, 29]. Some researchers have also carried out the mechanical characteristics testing of coal-rock composite as per the existing state of coal-rock in the mine, [27] analyzing the deformation behaviors and individual characteristics of the coal-rock composite [31], [32] to understand the characteristics of damage and failure of the composite as well as progressive instability [33], [34]. Based on existing data regarding underground reservoirs, the dam thickness was optimized, [35] and the stability of the coal pillar-artificial dam connection was simulated [36–38]. These studies focus mainly on the analysis of the coal-rock-artificial dam structure, and the composite structure is considered only with respect to the plane bonding. However, the construction of the abandoned coal pillar-artificial dam is not a simple plane bonding process. Research on the instability characteristics of the bonded structure in the composite state is of great significance to the utilization of underground space in abandoned mines.

Considering the bonding angle as the research object, seven sets of coal pillar-artificial dam type coal-rock specimens were prepared and a PFC^{3D} numerical model was constructed. A uniaxial compression test was carried out without lateral pressure. Based on the strength, deformation, and energy evolution characteristics of coal pillar-artificial dams, the influence of the angle of the coal pillar-artificial dam on the performance of the specimen was analyzed. The PFC^{3D} model was used to explore the crack evolution, particle displacement, and spatial distribution behaviors, based on which the bonding structure of the water storage dam in the underground space of the abandoned mine was optimized.

2. Deformation Mechanics Analysis of Coal Pillar-Artificial Dam

2.1. Stress State of Coal Pillar-Artificial Dam. Different from complete coal seams or rock formations, coal pillar-artificial dams are composed of two different media, which differ significantly from the single structure when they are loaded. When bonding them to each other, it is necessary to consider not only the strength of the artificial dam, but also the coordinated bearing capacity of the remaining coal pillars. The interaction between the two media restricts each other and carries the load together. The tightness of the bond between the two media determines the stress state under loading (Figure 1).

(1) When the coal pillars and artificial dam are loosely bonded (Figure 1(a)), they are subjected to their respective loads, and stress concentration is easily formed at the interface. The stress states of the single structure on both sides are unidirectional, and they will break when each side reaches the critical value. At the same time, the damage on one side aggravates the damage on the other side.

(2) When the coal pillar-artificial dam bond is tight (Figure 1(b)), the amount of deformation of the coal pillar is larger due to its relatively weak physical properties as it is influenced by the structural change of the other side caused by stress. As a result, the unilateral bearing capacity of the composite is increased, with the coal pillar being subjected to bidirectional stress and the artificial dam being subjected to unidirectional stress.

(3) When the coal pillar-artificial dam is extremely tightly bonded (Figure 1(c)), the two will carry the load in a coordinated manner. The coal pillars share the deformation while transferring part of the stress to the side of the artificial dam, resulting in a unidirectional stress of the overall structure with a stable internal structure.

2.2. Mechanical Model of Coal Pillar-Artificial Dam. The coal pillar-artificial dam is composed of a coal pillar side and an artificial dam side, both of which are elastoplastic bodies that can be represented by Saint-Venant bodies (Figure 2).

At the same time, the elastomer part can be refined based on different lithologies. That is, the dual strain Hooke's law is applied with the coal pillar approximated as the soft part and the artificial dam as the hard part, which satisfies the Hooke's law, respectively. In addition, the mechanical components on the coal pillar side and the artificial dam side are connected in parallel according to the bonding method of the coal pillar-artificial dam.

$$\begin{cases} \sigma = \sigma_1 + \sigma_2, \\ \epsilon = \epsilon_1 = \epsilon_2. \end{cases} \tag{1}$$

The change of the overall strain of the composite considers the deformation of the single bodies on both sides, and there is also the influence of interface bonding. Therefore, the combined body will be deformed under the action of the external force; however, due to the difference of σ_S of the two sides and the different degrees of bonding, different mechanical models may be suitable for use:

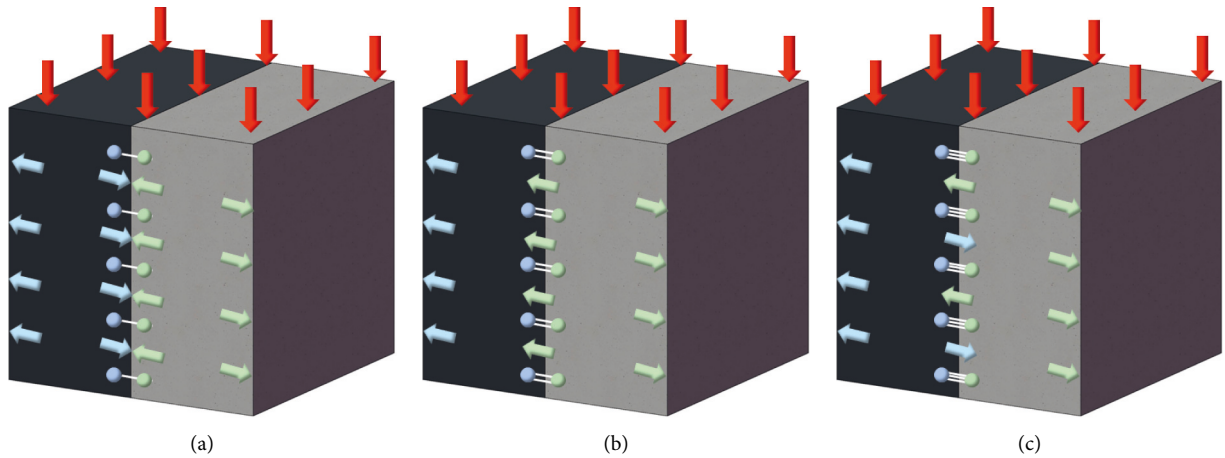

Figure 1: Stress state of coal pillar-artificial dam. (a) Split bearing, (b) shared bearing, and (c) coordinated bearing.

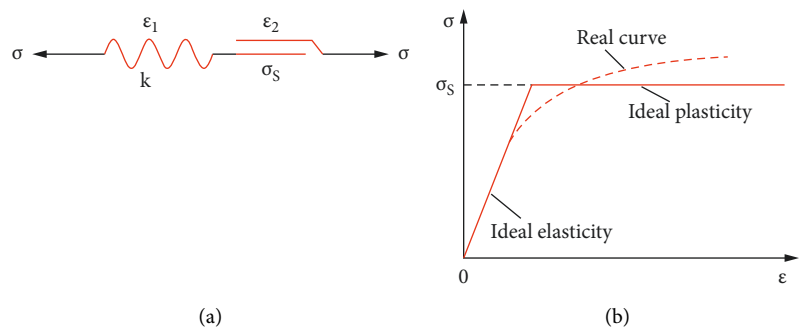

Figure 2: Schematic diagram of the constitutive relationship of Saint-Venant body. (a) Saint-Venant body mechanical model, (b) schematic diagram of elastoplastic model.

2.2.1. Split Loading Constitutive Model of Coal Pillar-Artificial Dam.

$$\begin{cases} \sigma_1 < \sigma_{S_1}, \epsilon = \dfrac{\sigma_1}{k_1} = \dfrac{\sigma_2}{k_2}, \\ \sigma_1 \geq \sigma_{S_1}, \epsilon \longrightarrow \infty, \end{cases} \tag{2}$$

where σ_1 and σ_2 are the stresses applied to the coal pillar side and the artificial dam side, respectively. The terms k_1 and k_2 are the elastic coefficients of coal pillars and artificial dams, σ_{S_1} and σ_{S_2} are the frictional resistance between the coal pillar side and the friction plate of the artificial dam, and m is the frictional resistance correction factor, with $\sigma_{S_1} + \sigma_{S_2}/m > \sigma_{S_2}$.

When the combined body is loosely bonded, the strain is dominated by the deformation of the coal pillar side. When σ_1 is smaller than the friction resistance σ_{S_1} of the friction plate on the side of the coal pillar, the combined body will be elastically deformed. At the same time, as $k_1 < k_2$ then $\sigma_1 < \sigma_2$. The artificial dam side inside the combined body bears most of the stress and maintains a complete structure. When $\sigma_1 \geq \sigma_{S_1}$, the deformation of the coal pillar side cannot be controlled, and the stress on the other side increases instantaneously with the failure of one side, leading to an overall stable structure.

2.2.2. Shared Loading Constitutive Model of Coal Pillar-Artificial Dam.

$$\begin{cases} \sigma_2 < \sigma_{S_2}, \epsilon = \dfrac{\sigma_1}{k_1} = \dfrac{\sigma_2}{k_2}, \\ \sigma_2 \geq \sigma_{S_2}, \epsilon \longrightarrow \infty. \end{cases} \tag{3}$$

When the combined body is tightly bonded, the stress in the coal pillar-artificial dam is dominated by the artificial dam side. At this time, the friction resistance of the friction plate σ_{S_2} shall prevail. Under the action of the external force, the combined body deforms elastically. At the same time, σ_2/σ gradually increases with the increase in the external load, and the overall deformation is in a controllable range. When $\sigma_2 \geq \sigma_{S_2}$, damage and deformation occur on the artificial dam side, and the overall structure becomes unstable.

2.2.3. Coordinated Loading Constitutive Model of Coal Pillar-Artificial Dam.

$$\begin{cases} \sigma < \dfrac{\sigma_{S_1} + \sigma_{S_2}}{m}, \epsilon = \dfrac{\sigma_1}{k_1} = \dfrac{\sigma_2}{k_2}, \\ \sigma \geq \dfrac{\sigma_{S_1} + \sigma_{S_2}}{m}, \epsilon \longrightarrow \infty. \end{cases} \tag{4}$$

When the combined body is extremely tightly bonded, the external load is carried together by the two parts. In such a situation, the friction resistance of the integrated body friction plate $\sigma_{S_1} + \sigma_{S_2}/m$ shall prevail, where the value of m depends on the bonding structure parameters of the two sides. Here, the overall frictional resistance of the combined body increases, which improves the overall load-bearing and deformation capacity until $\sigma \geq \sigma_{S_1} + \sigma_{S_2}/m$, where the overall structure of coal pillar-artificial dam is unstable and damaged.

3. Experiment and Numerical Modeling

3.1. Experiment Setup. The combined body specimen of this test is composed of two parts: coal pillar and artificial dam. Because the lithology of natural coal is relatively brittle and not suitable for processing, the coal pillar was made of coal powder and cement in a mass ratio of cement: coal powder: water = 1 : 2.5 : 1. The artificial dam was made by mixing river sand and cement, the mass ratio of which was cement: river sand: water = 1 : 1.5 : 0.5 where the sieving size of coal powder was 2.0 mm × 2.0 mm and the sieving size of river sand was 2.5 mm × 2.5 mm, as shown in Figure 3 (the material ratio was selected according to the existing literature).

Since the connection between the coal pillar and the artificial dam was a trapezoidal connection, it involved three factors: angle, width, and depth. This test focused on the impact of mechanical properties caused by angle changes (Table 1 and Figure 4). The width was fixed to 30 mm and the depth was fixed to 7.5 mm, resulting in a total of seven groups (including five coal pillars-artificial dam specimens, one coal pillar specimen, and one artificial dam single specimen) [30]. Each group had three test pieces, named according to the number angle (such as A-80°). The test pieces were cylinders with a size of Φ50 mm × L100 mm, all of which were taken from a large cubical test block.

The large cube test block was shaped by the model steel plate in the mold. The coal pillar part was poured first, and the steel plate was taken out after the vibration was completed, after which the artificial dam part was poured. After vibrating, the test block was left to stand for 48 h prior to demolding. After the large cube test block has been cured to 28 days under natural conditions, the core was extracted in a direction to the interface (Figure 5). The unevenness of both ends was polished with fine sand to ensure that the unevenness did not exceed 0.05 mm, and the non-perpendicularity of each adjacent surface did not exceed ±0.5°.

A rock mechanics testing machine was used to perform the uniaxial compression test without lateral pressure on the test pieces (Figure 6):

(1) The test piece was placed on the lower platen of the test machine. The center of the test piece was aligned with the center of the lower platen of the test machine, and a digital dial gauge was installed to connect to the computer system for debugging.

(2) The upper platen of the machine was lowered until it barely touched the test piece. At the same time, the axis of the test piece was kept coincident with the loading center line of the testing machine to avoid an eccentric force, which will affect the test results.

(3) A high-definition camera was set up. The loading rate and displacement acquisition frequency were set to be 0.1 kN/s and 100 ms, respectively. The sample was subjected to axial stress until the test piece was finally destroyed.

(4) The data collected in the experiment were recorded and saved for analysis and processing.

3.2. Model Establishment and Parameter Calibration. The PFC particle discrete element starts from the mesoscale, and does not need to assume a macroscopic constitutive model of the material, but analyzes the propagation and failure process of rock microcracks from the microscopic level, and establishes the macroscopic and microscopic correspondence of the rock. From the microlevel, the rock is formed by the bonding of tiny mineral particles inside, and the arrangement of its components affects the development characteristics of the microcrack system inside the rock. The bonding medium between the particles has different contact relations, controlled by a certain fracture criterion, and its deformation and strength parameters have different degrees of dispersion. These many microscopic factors all affect the macroscopic mechanical properties of the rock to a certain extent. Express. Compared with the traditional finite element, the discrete element has the following advantages: the microparticle model can reflect the process of microcracks in the rock propagating into macro-cracks, reflecting the mutual influence of the cracks in the process of propagation, and the redistribution of the contact force between particles. A microscopic particle model that accurately reflects the characteristics of the rock is constructed, which can reasonably simulate the dynamic fracture process of the rock microstructure. In order to study the crack evolution characteristics of the coal pillar-artificial dam from a mesoscopic perspective, based on the particle flow theory, the PFC^{3D} software was used to numerically simulate the uniaxial compression of the specimen.

The particle discrete element method is developed based on the discrete element theory of Cundall et al. It uses an explicit difference algorithm to alternately use the force-displacement law and Newton's law of motion in the calculation cycle, and update the contact force between contacting particles through the force-displacement law. The position of the particles is updated through the law of motion to form a new contact of the particles, thereby simulating the movement and interaction process of the particles. There are many types of bonding models built in the PFC. Here, a parallel bonding model is selected (Linearpbond), which is more suitable for simulating hard rock materials. The Linearpbond model can transmit force and moment. When the applied stress exceeds the bond strength, the bond of the parallel bond model will be broken. It is determined that the size of the simulated test piece is a cylinder of Φ50 mm × L100 mm, and the upper and lower

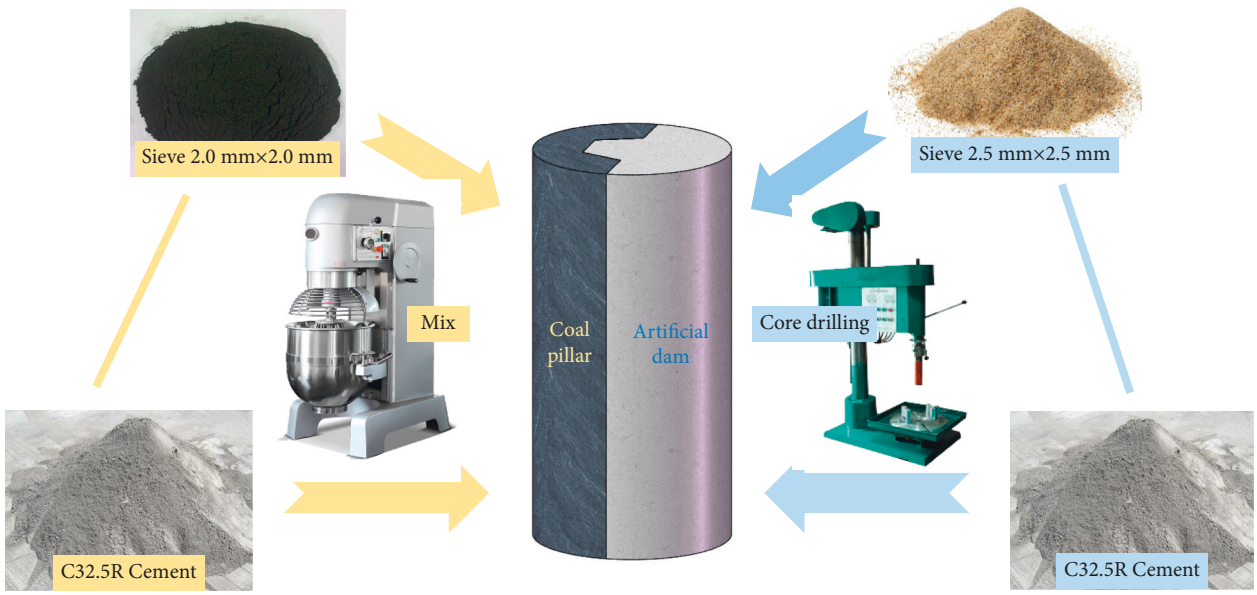

Figure 3: Sample preparation process.

Table 1: Test parameter design.

Factor	Angle (°)	Width (mm)	Depth (mm)
Gradient	50	30	7.5
	60	30	7.5
	70	30	7.5
	80	30	7.5
	90	30	7.5

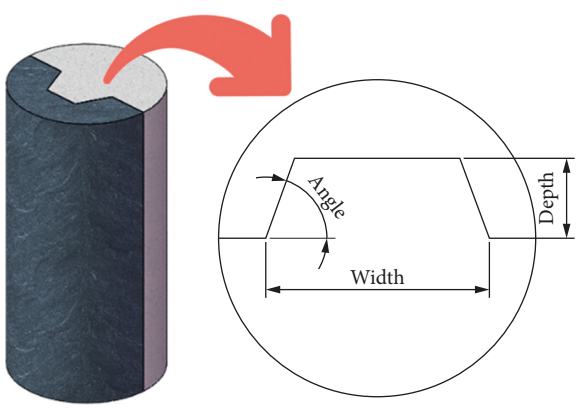

Figure 4: Structure of the coal pillars-artificial dam.

end faces are calculated with rigid walls, and the surrounding is a free boundary (Figure 7).

The microparameter calibration of numerical calculation involves tuning to obtain reasonable microparameters by the trial-and-error method based on the macro-parameters. That is, before the numerical calculation, micromechanical parameters are assigned to the model. Then, the calculated macromechanical parameters of the material are compared with the measured experimental values. The corresponding micromechanical parameters are varied to calibrate the macro-mechanical parameters of the material. When the numerical calculation results are consistent with the experimental results, the model is considered reliable. The material parameter calibration process is shown in Figure 8.

By calibrating the mechanical parameters, the micromechanical parameters of the coal pillar and artificial dam single bodies were obtained, respectively. The parameters can then be substituted into the combined body to calibrate the interface, as shown in Table 2.

The uniaxial compression experiment controlled by displacement loading was simulated by specifying the rates of downward and upward motion of the top and bottom walls of the model, respectively. The friction coefficient between the wall and the particles was set to 0.1 (to eliminate the influence of the end face), and the rate of movement was set to 0.05 m/s. At the same time, to obtain a complete stress–strain curve, loading was stopped when the stress dropped to 70% after the specimen was broken. During this process, the changes in the stress, strain, and number of cracks during the entire loading process were recorded using a code written in Fish.

4. Uniaxial Compression Characteristics of Coal Pillar-Artificial Dams

Through experiment and PFC^{3D} simulations, the stress–strain curves and test data were obtained after uniaxial compression (Figure 9, Table 3). Representative curves in the test group were plotted.

It can be seen from Figure 9 that the experimental data agreed with the simulated data. The small difference between them was due to the denser and more homogeneous particles used in the simulation. In addition, during the experiment, the pressure of the testing machine was released after detecting the damage and so, compared with the numerical simulation curve, it lacks the postpeak variation curve.

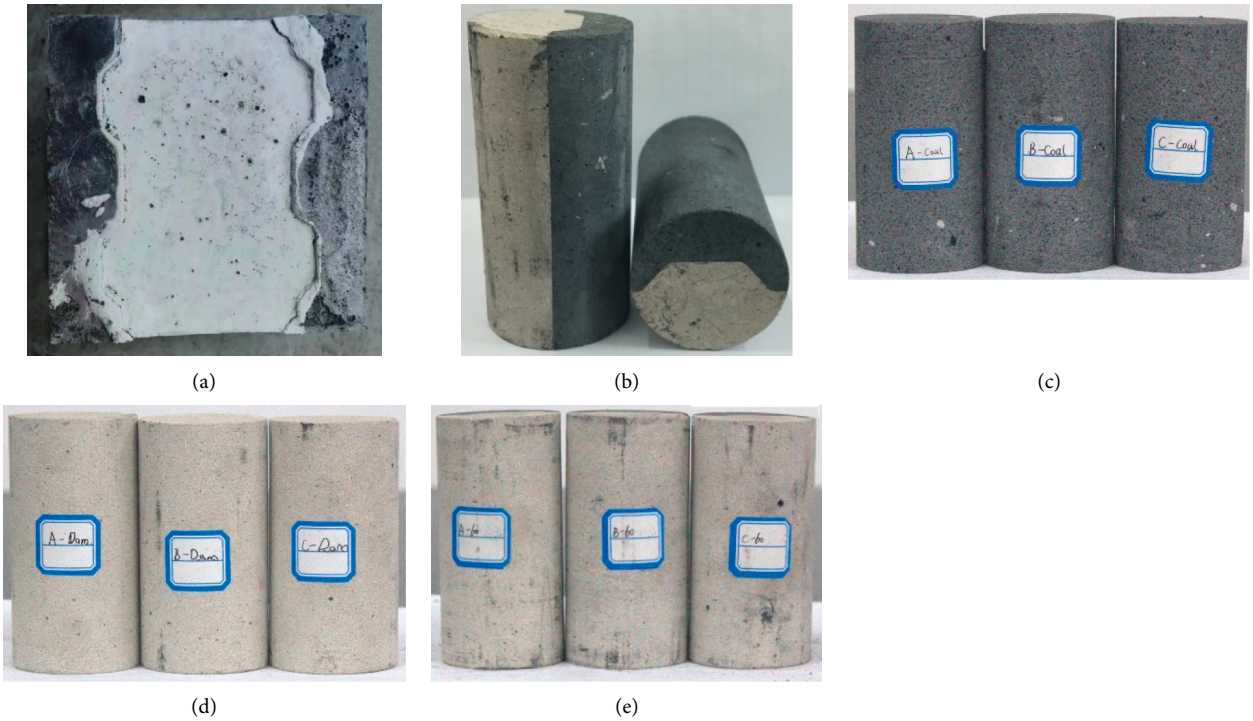

(a) (b) (c)

(d) (e)

Figure 5: Coal pillars-artificial dam samples. (a) Cube test block, (b) core drilling of test piece (c) coal pillar samples, (d) artificial dam samples, and (e) coal pillars-artificial samples.

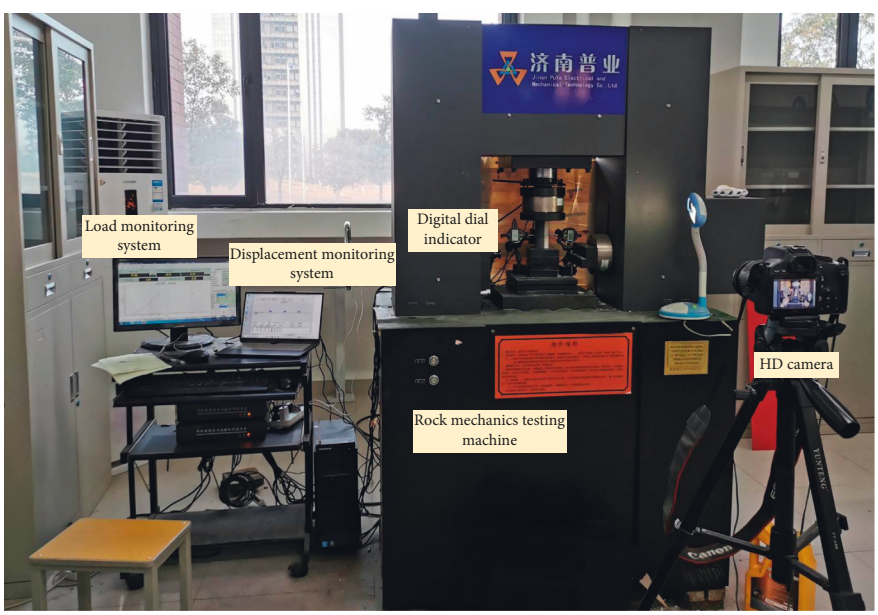

Figure 6: Test equipment.

The test curves had the complete five-stage characteristics of original void compaction–linear elasticity–elasto-plastic transition–plasticity–failure, while the simulation curves were monotonous. At the same time, the coal pillar test curves showed a certain postpeak viscosity, which was obvious in the simulation curves of the combined body. It can also be seen that the peak stress and strain of the viscosity curve decreased with the increase in the interface angle, and the distance between the peak compressive strength and the peak of the viscosity curve also decreased gradually with the increase in the inclination. It shows that as the angle increases, the structure of the combined body becomes more complete.

4.1. Analysis of Strength Characteristics of Coal Pillar-Artificial Dam. In order to analyze the coal pillar-artificial dam strength characteristics in depth, combined with the uniaxial

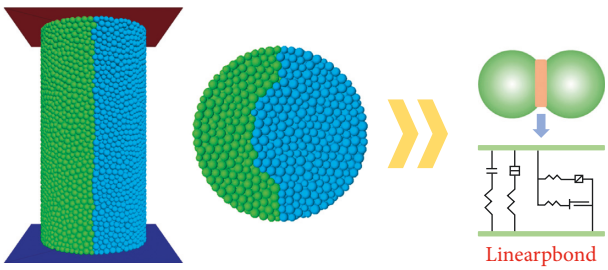

Figure 7: Simulated specimen and bonding model.

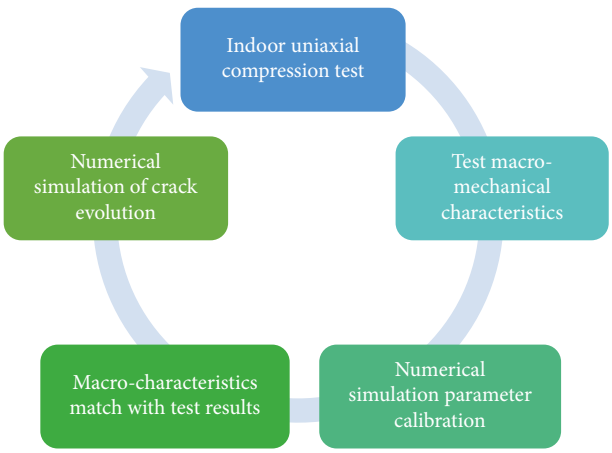

Figure 8: Calibration trial and error method.

Table 2: Micromechanical parameters of the numerical model.

Type	Name	Value
Coal pillar	Particle radius	1.0~1.5 mm
	Friction coefficient	0.4
	Effective modulus	0.4 GPa
	Normal stiffness	1.7 MPa
	Tangential stiffness	3.4 MPa
Interface	Particle radius	1.0~1.5 mm
	Friction coefficient	0.4
	Effective modulus	2 GPa
	Normal stiffness	6 MPa
	Tangential stiffness	12 MPa
Artificial dam	Particle radius	1.0~1.5 mm
	Friction coefficient	0.4
	Effective modulus	2 GPa
	Normal stiffness	10 MPa
	Tangential stiffness	20 MPa

compression laboratory test results, the relationship curve between the compressive strength of the composite specimen and the angle of the interface is obtained, as shown in Figure 10.

It can be seen that the strength of the composite specimen is mostly between the strength of the coal pillar and the individual strength of the artificial dam. As the angle changes, the average curve of the coal pillar-artificial dam test shows a single-peak change trend that first increases and then decreases. At the same time, the peak point is greater than the compressive strength of the single specimen of the artificial dam, which indicates that the strength of the composite specimen is not only determined by the proportion of the coal pillar and the volume of the artificial dam, but also related to the connection form and the angle of the interface; the reduction after the peak point, both the small rate and the increase rate are slightly larger than before the peak; the angle change of the interface changes the stress transmission conditions in the coal pillar and the artificial dam, thereby affecting the stress state of the two, and finally shows a clear difference.

Compared with the single body artificial dam, the compressive strength of the coal pillar-artificial dam was reduced by 8.16%, 5.17%, −0.70%, 4.09%, and 8.01% during the process of increasing the bonding angle of coal pillar-artificial dam from 50° to 90°. Compared with the single body coal pillar specimen, the increase was 498.48%, 517.90%, 556.19%, 524.95%, and 499.43%, respectively.

The test mean curve was fitted using the single-peak GussAmp formula:

$$\sigma_s = 31.36 + 3.11e^{-\frac{(x_s - 70.81)^2}{27.44^2}}, \tag{5}$$

where σ_s is the uniaxial compressive strength of the test piece and x_s is the interface angle of the coal pillar-artificial dam. The correlation coefficient R^2 is 1, indicating that the formula can fully characterize the relationship between the angle and the compressive strength of coal pillar-artificial dam, and can guide the construction of artificial dams on-site.

4.2. Analysis of Deformation Characteristics of Coal Pillar-Artificial Dam. Drawing the relationship between angle and peak strain (Figure 11), it can be seen that the strain of the coal pillar-artificial dam specimen is larger than that of the dam body specimen, and the peak strain of the coal pillar specimen is the smallest. This is due to the combined coal. The column not only has the deformation characteristics of a single unit, but also bears a much higher limit stress than the single unit. The severe deformation greatly increases the strain of the combined body; the average curve of the coal column-artificial dam test shows a single peak that first increases and then decreases, changes trend, and the increase rate before the peak is higher than the increase rate after the peak.

Compared with the single body artificial dam, the peak strain of coal pillar-artificial dam was increased by 12.04%, 12.96%, 14.81%, 11.11%, and 10.19% during the process of increasing the bonding angle of the coal pillar-artificial dam from 50° to 90°. Compared with the single body coal pillar test piece, the increase was 28.72%, 29.79%, 31.91%, 27.66%, and 26.60%, respectively. In the coal pillar-artificial dam test piece, the deformation of the pillars was shared by the coal pillar; therefore, the total deformation was much higher than that of the single body artificial dam test piece.

The mean curve from the test is fitted using the single-peak Laplace formula:

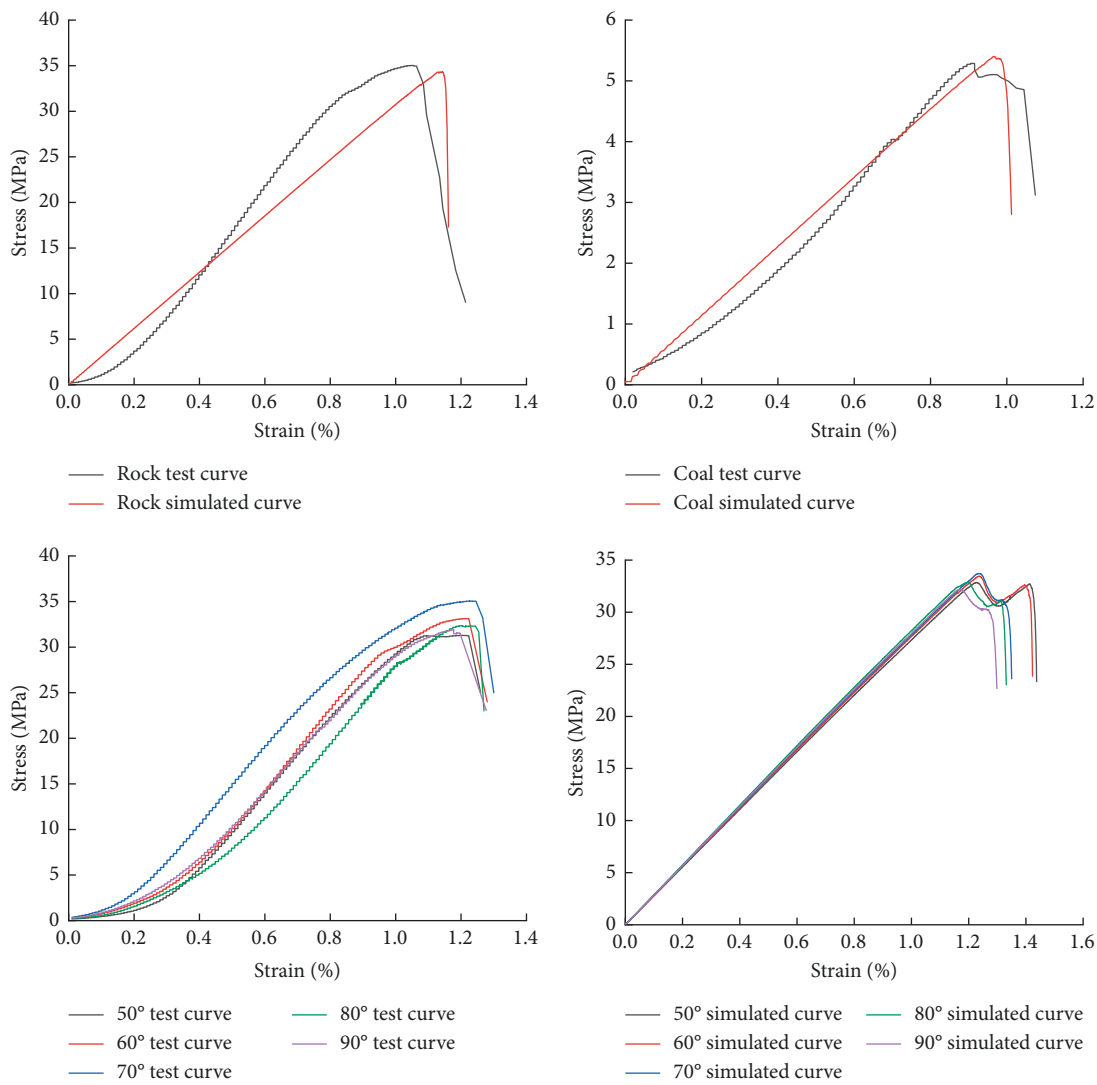

Figure 9: Test and simulated stress–strain curves.

Table 3: Test and simulation results.

Serial number	Test		Simulation	
	Mean stress (MPa)	Mean strain (%)	Stress (MPa)	Strain (%)
Dam	34.21	1.08	34.33	1.14
Coal	5.25	0.94	5.40	0.97
50°	31.42	1.21	32.85	1.23
60°	32.44	1.22	33.46	1.24
70°	34.45	1.24	33.71	1.24
80°	32.81	1.20	32.85	1.20
90°	31.47	1.19	32.20	1.17

$$\epsilon_s = 1.19 + \frac{1}{13.08} e^{-\frac{|x_s - 66.54|}{6.54}}, \quad (6)$$

where ϵ_s is the peak strain of the test piece and x_s is the interface angle of the coal pillar-artificial dam. The correlation coefficient R^2 is 0.79. The formula can characterize the relationship between the angle and the peak strain of coal pillar-artificial dam and can predict the stability of the site structure.

4.3. Energy Evolution of Coal Pillar-Artificial Dam. The specimen interacts energetically with its surroundings in the form of elastic energy, dissipated energy, surface energy, radiant energy, kinetic energy, thermal energy, etc. At the same time, the energy transfer and transformations of the specimen in the uniaxial loading process are divided into four parts: energy input, energy accumulation, energy dissipation, and energy release. Energy input refers to the mechanical energy supplied by the surroundings. In the test system, it refers to the work done by the test press on the rock. Energy accumulation refers to the elastic deformation energy during the load phase. The energy input from the outside is stored in the test piece in the form of elastic deformation energy. When the external force is removed, the elastic deformation is restored, and the elastic deformation energy is released to the surroundings. Energy dissipation refers to plastic strain energy and surface energy. Because

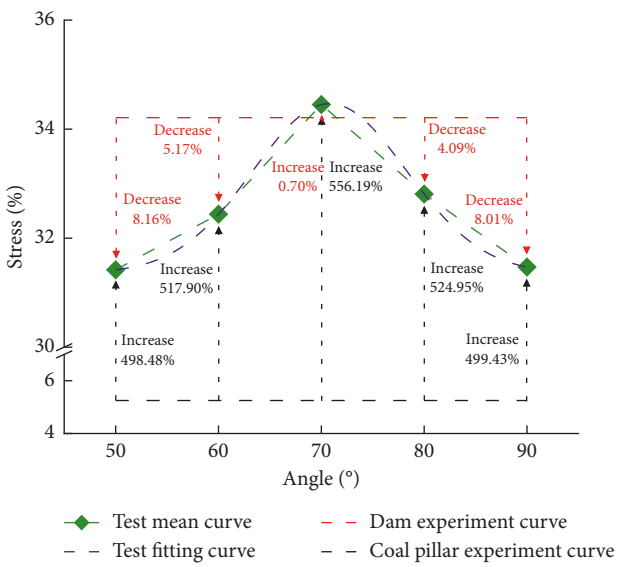

Figure 10: Relationship between angle and compressive strength.

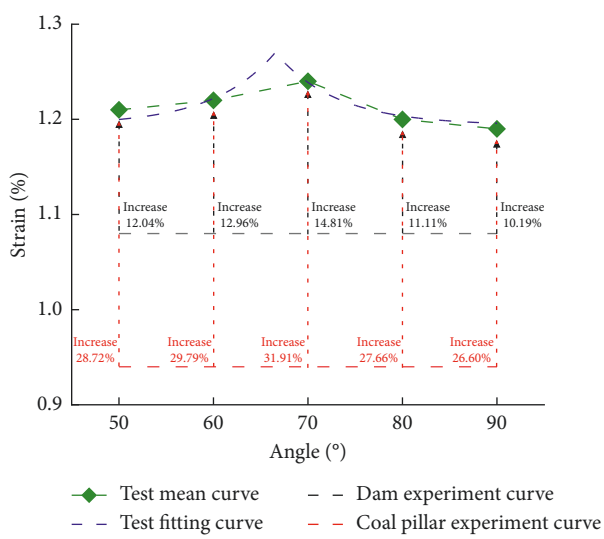

Figure 11: Relationship between angle and peak strain.

there are many discontinuous structures such as pores, cracks, and joints inside, under the action of external force, the energy input from the outside will not only bring about elastic deformation, but also produce irreversible plastic deformation, resulting in plastic deformation energy. With the development and expansion of internal microcracks, it also leads to the formation of new microcracks. In damage mechanics, the energy consumed by new cracks in the process of crack propagation is called surface energy. Energy is released as the kinetic energy of splashing and breaking, while acoustic energy, radiant energy, and thermal energy are generated by the instability and destruction due to failure. The energy released during failure comes from the elastic deformation energy accumulated in the early stage.

Energy evolution under uniaxial compression is shown in Figure 12. The coal pillar-artificial dam stress–strain curve peak area represents the work done by the testing machine

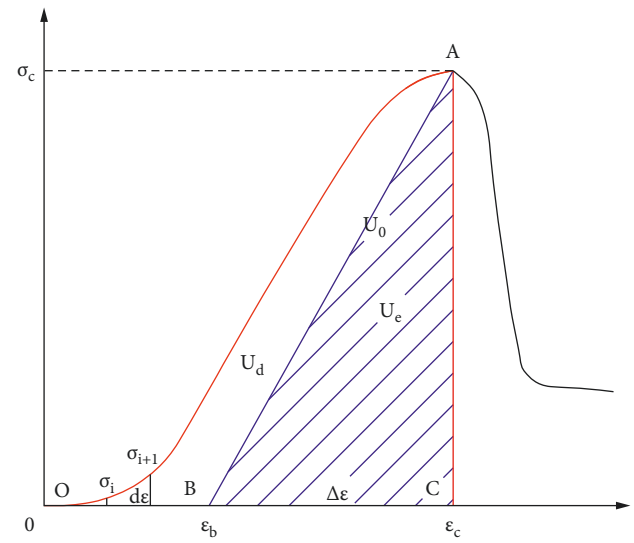

Figure 12: Schematic diagram of energy evolution relationship.

on the sample. Energy input U_o can be represented by the OAC area in Figure 12. A straight line parallel to the stress–strain plot along the peak point, and a straight line perpendicular to the axis at the peak point are drawn. The area of the triangle formed is the accumulated elastic energy U_e (ABC area in Figure 12). The area occupied by OAB shown in Figure 12 is the dissipation energy U_d.

The input energy supplied to the combined body U_o is the sum of elastic energy U_d and dissipated energy U_d.

$$U_o = U_e + U_d, \tag{7}$$

$$U_o = \int_0^{\epsilon_s} \sigma_i \mathrm{d}\epsilon, \tag{8}$$

$$U_e = \frac{\sigma_s \Delta\epsilon_s}{2}, \tag{9}$$

where σ_s (MPa) is the peak strength of the coal pillar-artificial dam, $\Delta\epsilon$ is the axial strain difference, ϵ_b and ϵ_c are the stress–strain curve edge nodes.

According to equations (7)–(9), the energy evolution process during each combined loading process can be obtained (Table 4). External energy is continuously input into the coal pillar-artificial dam test piece during the loading process. Part of the energy is transformed into dissipated energy, which is manifested in the plastic deformation of the combined body and microcrack initiation, expansion, and other microdamages. The rest of the energy is stored inside the test piece in the form of elastic energy.

The energy evolution behaviors of coal pillar-artificial dam test pieces with different angles were similar. The A-70° test piece was selected to draw the energy and stress relationship curve.

It can be found from Figure 13 that the total energy and elastic energy increase in the same manner as the stress–strain relationship curve. The rate of increase of the two in the early stage was relatively small, and the curve was relatively flat during the compaction stage of the stress–strain

Table 4: Uniaxial compression energy value of coal pillar-artificial dam test piece.

Group	Total energy ($J\cdot m^{-3}$)	Elastic energy ($J\cdot m^{-3}$)	Dissipated energy ($J\cdot m^{-3}$)	Percentage of elastic energy (%)
Dam	18.86	16.26	2.60	86.21
Coal	2.19	2.09	0.10	95.43
50°	17.72	16.76	0.96	94.58
60°	18.93	17.33	1.60	91.55
70°	22.70	20.0	2.62	88.11
80°	16.34	15.14	1.20	92.66
90°	17.44	16.47	0.97	94.44

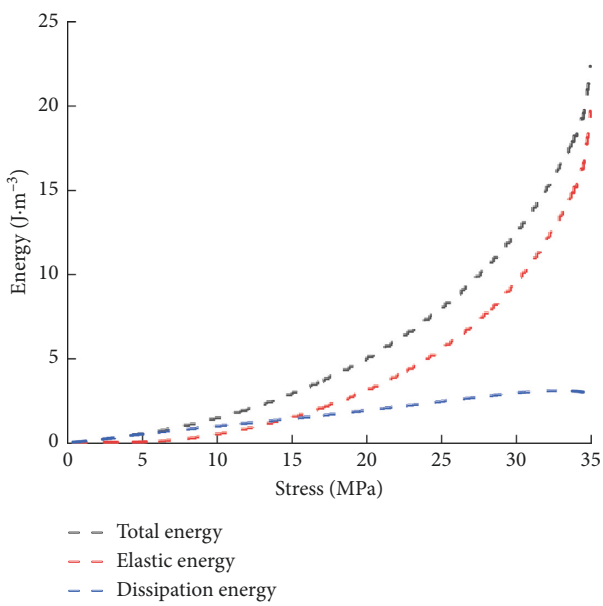

Figure 13: Relationship between energy and stress (A-70°).

curve, which was followed by a gradual increase in the rate. It can be observed that the total energy and elastic energy increased in a linear manner that corresponds to the elastic stage of the stress–strain curve. When the sample reached the peak stress, the total energy and elastic energy both reached the maximum, and the proportion of elastic energy gradually increased, subsequently starting to release. The internal cracks of the specimen rapidly expanded into macroscopic cracks, which eventually led to the destruction of the specimen. The dissipation energy curve increased obviously in the early stage, then tended to flatten, and finally decayed. It is related to the three stages before the peak of the stress–strain curve. In the initial compaction stage, not only the microcracks in the coal pillar and the artificial dam, but also on the interface between the coal pillar and the artificial dam were compacted. At this time, most of the work done by the testing machine on the sample was converted into work done on the compact structure surface, and the accumulated elastic energy was small. Then, in the elastic phase, almost all the work done by the testing machine was converted into elastic energy. Therefore, the dissipated energy density remained almost unchanged. When entering the prepeak plastic yield stage, the

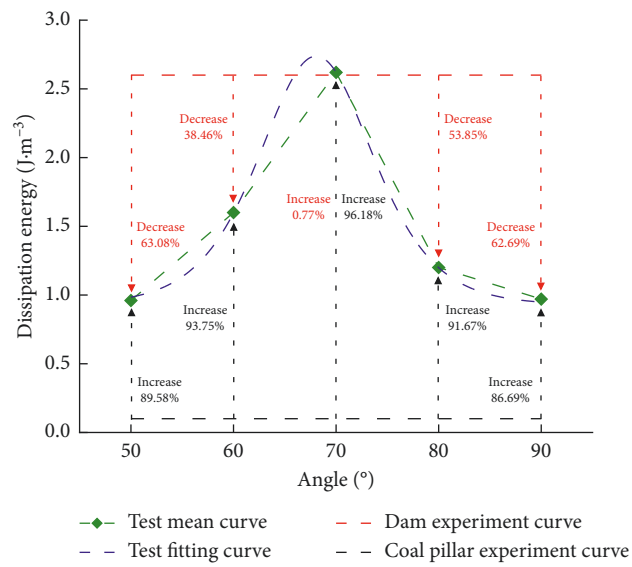

Figure 14: Relationship between angle and dissipated energy.

strength of the sample was close to the peak value and the deformation was reduced. At the same time, the internal energy accumulation entered the peak period, at which time the external radiation energy decreased.

It can be seen from Figure 14 that as the inclination changes, the dissipation energy curve of the combined sample shows a unimodal trend that first increases and then decreases. Like the stress curve, the peak point was greater than the single body specimen of the artificial dam, while the dissipation energy of the single body specimen of the coal pillar was much smaller than other curves.

Compared with the single body artificial dam, the compressive strength of coal pillar-artificial dam specimens was reduced by 63.08%, 38.46%, −0.77%, 53.85%, and 62.69% during the process of increasing the bonding angle from 50° to 90°. Compared with the single body coal pillar specimen, the increase was 89.58%, 93.75%, 96.18%, 91.67%, and 86.69%, respectively.

The test mean curve was fitted using the single-peak Logistpk formula:

$$U_d = 0.93 + \frac{7.24e^{-x_s - 68.06/3.72}}{\left(1 + e^{-x_s - 68.06/3.72}\right)^2}, \tag{10}$$

where U_d is the peak strain of the test piece and x_s is the interface angle of the coal pillar-artificial dam. The correlation coefficient R^2 is 0.99. The equation can characterize the relationship between the dissipated energy and the peak strain of coal pillar-artificial dam and can provide a basis for on-site safety monitoring.

5. Crack Evolution Study of the Coal Pillar-Artificial Dam

5.1. Analysis of Crack Evolution of the Coal Pillar-Artificial Dam. In the process of simulating the uniaxial compression of coal pillar-artificial dam specimens (Figure 15), the

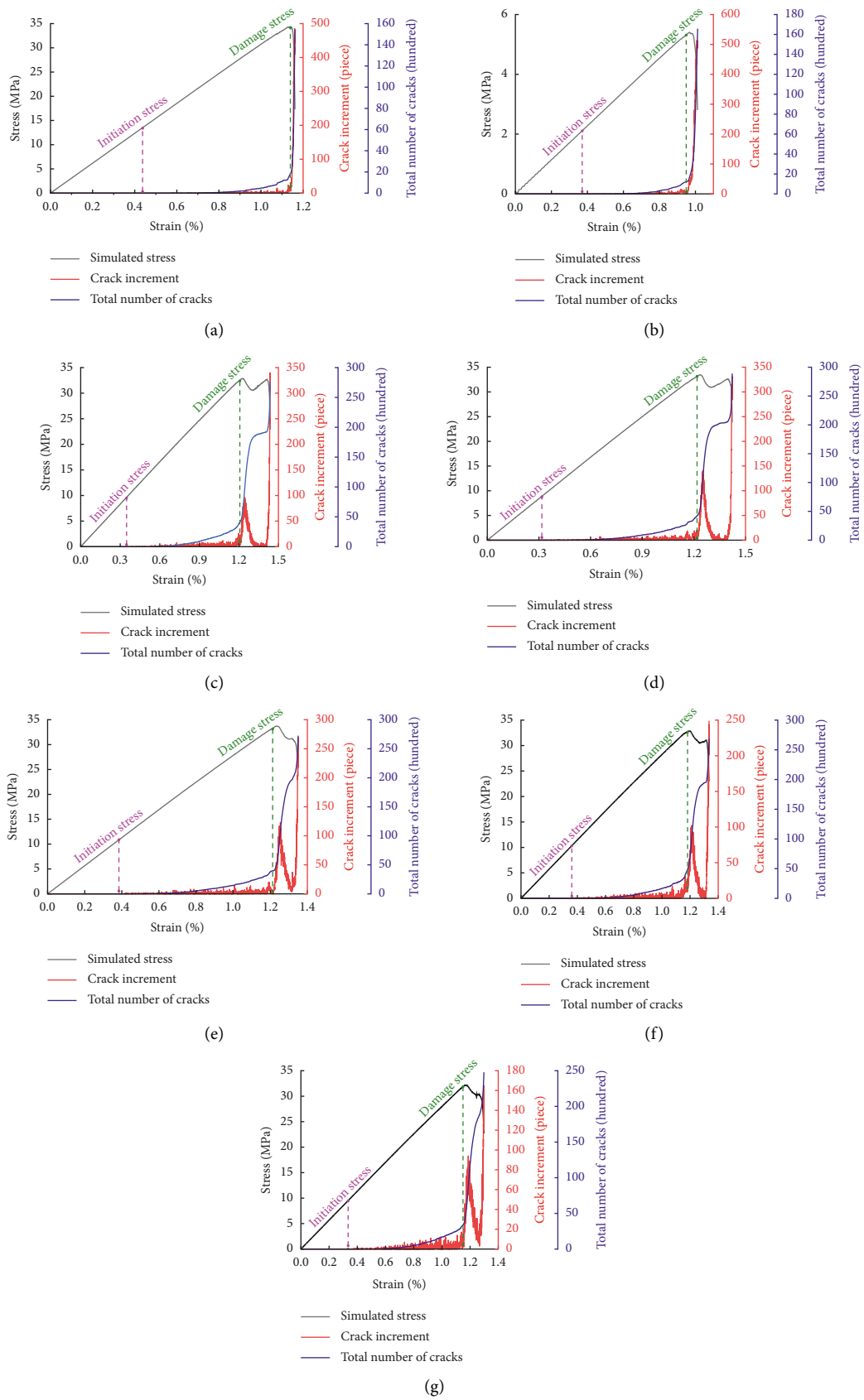

Figure 15: Crack evolution curves. (a) Single body artificial dam, (b) single body coal pillar, (c) 50° combined body, (d) 60° combined body, (e) 70° combined body, (f) 80° combined body, and (g) 90° combined body.

internal cracks in the combined body developed from initiation to evolution, which was followed by penetration, causing the overall structure to become unstable. The behaviors of the coal pillar-artificial dam were similar to those of the artificial dam, while the evolution of internal cracks in the coal pillar-artificial dam specimen was the same.

With the application of stress, coal pillar-artificial dam first experiences elastic strain. The contact stress between particles is less than the bonding strength between particles, and no cracks are generated inside at this time. The stress increases gradually, and the contact stress between the particles becomes greater than the bonding strength, which leads to the destruction of the bonds between the particles and the appearance of microcracks in the specimen. The number of microcracks grows rapidly until the specimen is damaged. The cracks in the specimen continue to increase after failure, showing the final failure form. The coal pillar-artificial dam specimen still has a certain degree of viscosity after reaching the compressive strength. It shows a stable period in the crack evolution curve, and the number of cracks does not increase. After the energy is released, the specimen collapses instantly with an even higher crack increase rate.

The axial stress corresponding to crack initiation is the initiation stress, and the stress corresponding to the point where the number of cracks in the coal pillar-artificial dam increases rapidly is called the damage stress. The initiation stress σ_i and damage stress σ_d of each combined body and their relationship with peak stress σ_s are shown in Table 5.

It can be seen from Figure 16 that the simulated crack initiation stress of the coal pillar-artificial dam specimen showed a trend of increasing first and then decreasing with the increase in the angle, reaching the peak value at 70°, which bore out the experimental values. Since the bonding contact stress between the particles in the artificial dam exceeded that of the coal pillar particles, the initiation stress of the artificial dam was larger than that of the coal pillar. The initiation stress of the combined body is mainly controlled by the contact stress between the filler particles. Therefore, the initiation stress of the coal pillar-artificial dam is mainly determined by the internal deformation of the coal pillar.

The test mean curve was fitted using the single peak extreme formula:

$$\sigma_i = 9.18 + 1.74e^{\left(-e^{-\frac{x_s - 71.76}{7.30}} - \frac{x_s - 71.76}{7.30} + 1\right)}, \quad (11)$$

where σ_i is the initiation stress of the simulated test piece and x_s is the interface angle of the coal pillar-artificial dam. The correlation coefficient R^2 is 0.99. The formula can characterize the influence of angle changes on crack initiation, and the occurrence of internal cracks can be predicted by observing the increase in stress.

It can be seen from Figure 17 that the increase in the angle caused the damage stress to increase first and then decrease, but both were intermediate to the single body coal pillar and the single body artificial dam. Since the damage

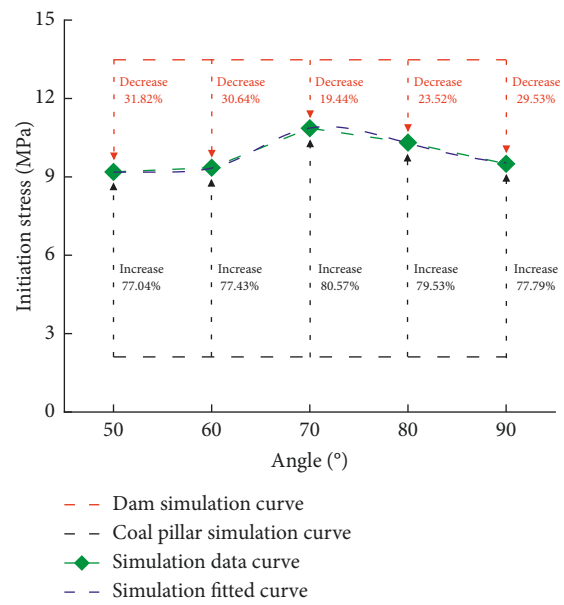

Figure 16: Relationship between angle and initiation stress.

Table 5: Crack evolution of coal pillar-artificial dam.

Group	Initiation stress (MPa)	Damage stress (MPa)	$\frac{\sigma_i}{\sigma_s}$ (%)	$\frac{\sigma_d}{\sigma_s}$ (%)
Dam	13.48	34.12	39.27	99.40
Coal	2.11	5.31	39.06	98.29
50°	9.19	32.38	27.97	98.56
60°	9.35	33.10	27.94	98.92
70°	10.86	33.22	32.22	98.55
80°	10.31	32.65	31.38	99.39
90°	9.50	31.83	29.50	98.86

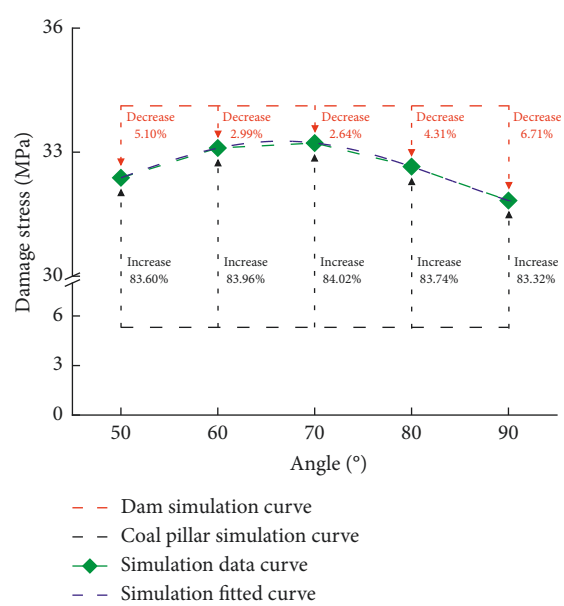

Figure 17: Relationship between angle and damage stress.

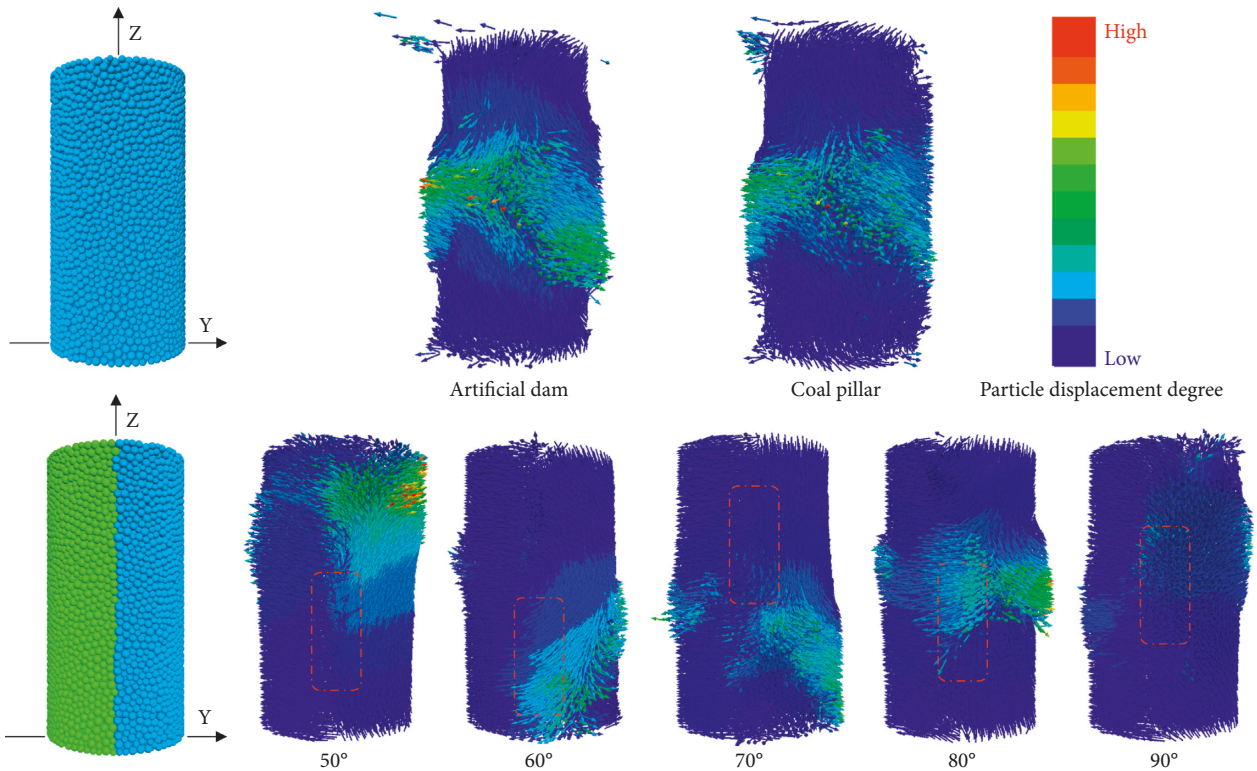

Figure 18: Particle displacement distribution.

stress corresponds to the point of rapid growth of the number of internal cracks in the model, it implies that the bonds between the internal particles have been destroyed at this time. Therefore, it is believed that the damage stress is mainly controlled by the contact stress between the particles on the side of the artificial dam, and the damage stress to the combined body is mainly affected by the internal bonds of the artificial dam.

The test mean curve was fitted using the single-peak Gauss formula:

$$\sigma_d = 30.84 + 106.2534.91\sqrt{\frac{\pi}{2}}e^{-2\frac{(x_s - 66.63)^2}{34.31^2}}, \quad (12)$$

where σ_d is the damage stress of the simulated test piece and x_s is the interface angle of the coal pillar-artificial dam. The correlation coefficient R^2 is 0.99. The formula can characterize the relationship between angle change and crack evolution, and the distribution and penetration of internal cracks can be judged by observing the increase in stress.

The initiation stress and damage stress of the two-material model were both intermediate to the values associated with the coal pillar and the artificial dam single bodies, while the ratio of the initiation stress to the peak stress was smaller than the single body models. The ratio of damage stress to peak stress was intermediate to that of the coal pillar and the artificial dam. Inside the coal pillar single body model, due to the low bond strength between the particles, when cracks occur, they will rapidly expand and coalesce, resulting in macroscopic damage to the coal pillar. In the coal pillar-artificial dam model, after cracks occur, the crack propagation and penetration speed were reduced due to the restriction of the particle bonds on the side of the artificial dam. Therefore, the macroscopic damage occurred later, which was between the coal pillar and the artificial dam single bodies.

5.2. Particle Displacement of Coal Pillar-Artificial Dam. By observing the particle displacement on both sides of the coal pillar-artificial dam interface (Figure 18), the combined body stress state can be obtained, and the mechanical model can be judged.

The particle displacements in the single body artificial dam and the single body coal pillar were comparable. Both moved along the axis from the center to either side, and the displacement on both sides was the same. In contrast, the main displacement of the coal pillar-artificial dam combined body model was on the side of the artificial dam, and there was an obvious interface.

As the angle increases, the particle displacement changed from collision to intrusion, then to interaction, and then again to intrusion and collision, respectively, corresponding to the stress states of split bearing–sharing bearing–coordinated bearing–split bearing–sharing bearing. On the side of the artificial dam, the collisional displacement occurred both along the vertical interface and in the opposite direction, with the outward expansion displacement being dominant (50° and 90° models). The monomers on both sides are, respectively, subjected to force, and the particles expand outward under the action of the force, and collide at the interface.

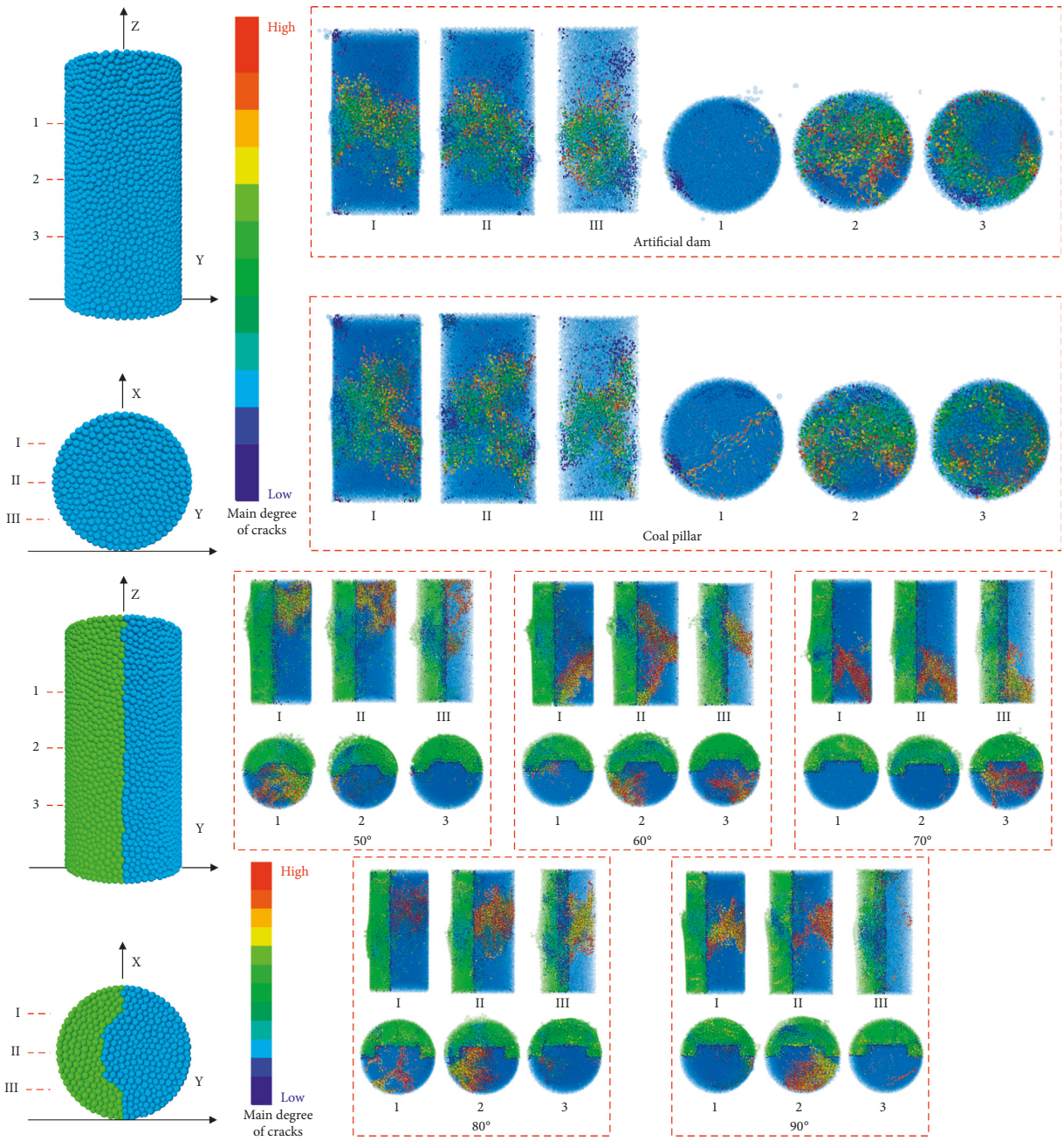

Figure 19: Numerical simulation of the spatial distribution of cracks.

The overall intrusive displacement was dominated by a single direction displacement, with the displacement of the coal pillar side increasing significantly (60° and 80° models). The monomer on one side is mainly stressed, and the particles move to the area with less stress, causing the intrusion of particles on one side.

The interactive displacement had strong displacement clusters on both the coal pillar side and the artificial dam side, and there was an interactive phenomenon at the interface. The particles have no obvious directionality under the action of stress, and the specimen expands outward as a whole.

5.3. Spatial Distribution of Coal Pillar-Artificial Dam Cracks. The final failure forms of coal-pillar single body, artificial-dam single body, and coal pillar-artificial dam were analyzed. The test pieces were sliced at 25 mm, 50 mm, and 75 mm heights to analyze the development of cracks in the horizontal direction. At the same time, the axial crack distribution was obtained by slicing at 12.5 mm, 25 mm, and 37.5 mm in the transverse direction (Figure 19).

It can be seen from Figure 19 that the distribution of cracks in the single body coal pillar and the single body artificial dam specimen was relatively uniform, and the main cracks were distributed throughout the test pieces.

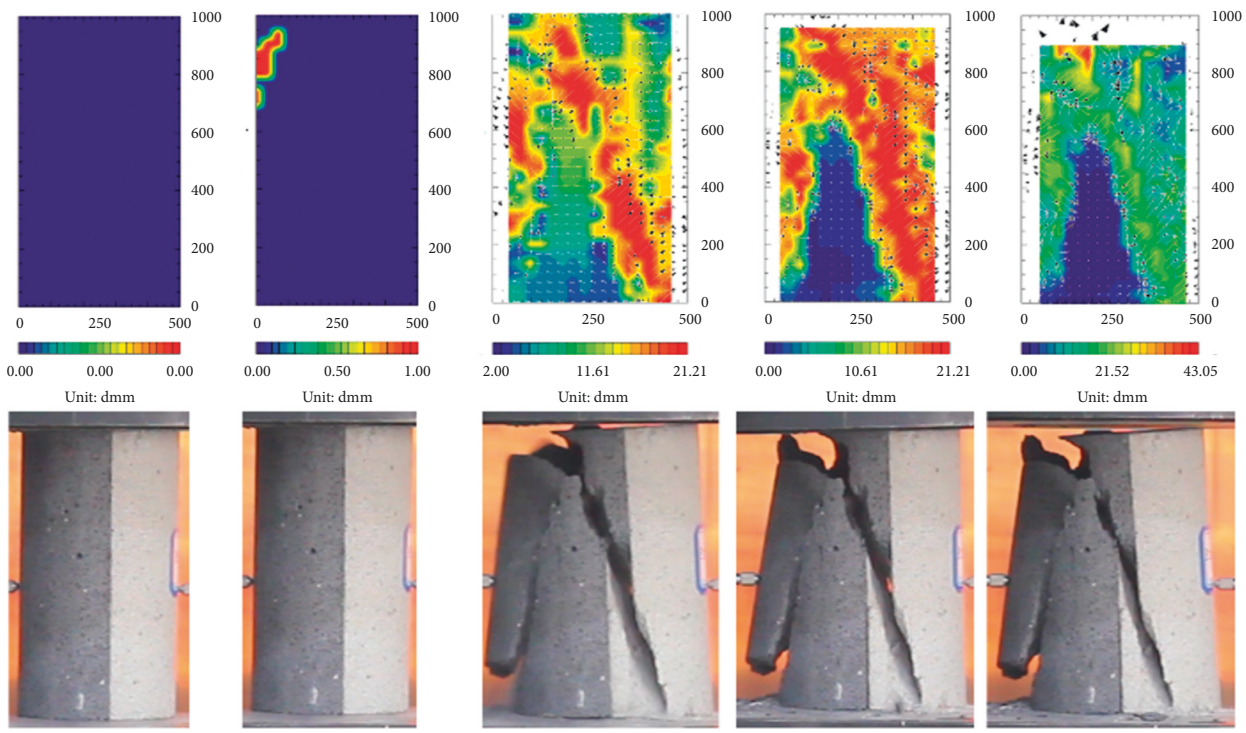

Figure 20: Coal pillar-artificial dam test failure forms.

Both were dominated by monoclinic splitting failure, while the evolution of individual coal pillar cracks was more complicated.

The cracks in the coal pillar-artificial dam combined body model were clearly demarcated along the interface. The main cracks of the specimen were concentrated on the artificial dam side with a clustered distribution, while the cracks on the coal pillar side were relatively scattered and basically covered the entire coal pillar area. At the same time, as the inclination increased, the position of the main cracks gradually shifted downwards and then upwards, and the macroscopic particle splashing also followed this trend. The damage of coal pillar-artificial dam was still dominated by monoclinic splitting. Taking the damage test of a 70° specimen as an example (Figure 20), the simulation and the test macroscopic damages were the same.

6. Conclusion

(1) Judging by the tightness of the bonding between the coal pillar and the artificial dam, the stress state can be divided into three types: split bearing, shared bearing, and coordinated bearing, corresponding to three different constitutive models.

(2) The test stress–strain curve had five stages, while the combined-body simulation curve showed an obvious postpeak viscosity. The compressive strength and mean peak strain curve for the coal pillar model showed a single-peak change trend that first increased and then decreased, and the peak value exceeded the compressive strength of the single body specimen of the artificial dam.

(3) The total energy and elastic energy of coal pillar-artificial dam under load showed the same trend. The dissipation energy curve showed an obvious increase in the early stage, then tended to flatten, and finally decayed. With the change in angle, the dissipation energy curve of the combined body specimen showed a unimodal trend of increasing first and then decreasing.

(4) The simulated initiation stress and damage stress of the coal pillar-artificial dam test piece were intermediate to the coal pillar and artificial dam single bodies. At the same time, with the increase in inclination, it showed a trend of increasing first and then decreasing, reaching a peak at 70°. The crack propagation and penetration speed were limited by the particle bonding on the artificial dam side.

(5) As the angle increased, the particle displacement of coal pillar-artificial dam model was collision–intrusive–interactive–intrusive–collision, corresponding to the stress state of split bearing–shared bearing–coordinated bearing–split bearing–shared bearing.

(6) Failure mechanism in both the single-body and combined body models was dominated by monoclinic splitting. The cracks of the coal pillar-artificial dam combined body model were clearly demarcated along the interface. The main cracks of the specimen were concentrated on the side of the artificial dam with a clustered distribution. At the same time, as the angle increased, the position of the main cracks gradually shifted downwards and then upwards [27, 30, 31].

Data Availability

The data used to support the findings of this study are included within the article.

Disclosure

This article was published as a preprint based on the link: https://assets.researchsquare.com/files/rs-929950/v1_covered.pdf?c = 1632931903"c = 1631877758.

Conflicts of Interest

The authors declare no conflicts of interest.

Acknowledgments

The authors are grateful for the financial support provided by Anhui Provincial University Scientific Research Project (YJS20210391), Institute of Energy Hefei Comprehensive National Science Center Project (21KZS215), Key Research and Development Plan of Anhui Province (202104a07020009), and Guizhou Provincial Science and Technology Projects ([2020]2004).

References

[1] L. Yuan and K. Yang, "Further discussion on the scientific problems and countermeasures in the utilization of abandoned mines," *Journal of China Coal Society*, vol. 46, no. 1, pp. 16–24, 2021.

[2] G. H. XieYQ and LiC. SuZG, "Exploitation and utilization of renewable energy from waste mine resources," *Renewable Energy Resources*, vol. 38, no. 3, pp. 423–426, 2020.

[3] C.W. J. LiuF, C.G. M. ZhangJM, and L. F Guo, "Current technological innovation and development direction of the 14th five-year plan period in China coal industry," *Journal of China Coal Society*, vol. 46, no. 1, pp. 1–15, 2021.

[4] J.Y. D. YuanL, Z.Y. X. WangK, and XuC. HaoXJ, "Precision exploitation and utilization of closed/abandoned mine resources in China," *Journal of China Coal Society*, vol. 43, no. 1, pp. 14–20, 2018.

[5] G.M. Z. XieHP, Z. R. GaoF, XuH. JuY, and Y. W Wang, "Strategic conceptualization and key technology for the transformation and upgrading of shut-down coal mines," *Journal of China Coal Society*, vol. 42, no. 6, pp. 1355–1365, 2017.

[6] B.Z. F. PuH and XuJ. C. ZhangJX, "Research on a reuse mode of geothermal resources in abandoned coal mines," *Journal of China Coal Society*, pp. 1–11, 2021.

[7] H.Z. M. XieHP, Z. L. GaoF, and Y. N. Gao, "A new technology of pumped-storage power in underground coal mine: principles, present situation and future," *Journal of China Coal Society*, vol. 40, no. 5, pp. 965–972, 2015.

[8] GuD. Z. LiT, D.B. Q. LiJF, and S. Q Liu, "Construction of pumped storage peak shaving system for mine water based on abandoned coal mine goaf," *Coal Science and Technology*, vol. 46, no. 9, pp. 93–98, 2018.

[9] F.Y. H. SuiS and Z.X. L. LiM, "Construction and application of evaluation system for operation effect of underground reservoir," *China Journal of Oceanology*, vol. 50, no. 6, pp. 126–133, 2020.

[10] R. Esmaeil, M. Ehsan, S. Reza, and G. Mehran, "Optimized algorithm in mine production planning, mined material destination, and ultimate pit limit," *Journal of Central South University*, vol. 25, no. 6, pp. 1475–1488, 2018.

[11] D. Z. Gu, "Theory framework and technological system of coal mine underground reservoir," *Journal of China Coal Society*, vol. 40, no. 2, pp. 239–246, 2015.

[12] F. Liu and S. Z. Li, "Discussion on the new development and utilization of underground space resources of transitional coal mines," *Journal of China Coal Society*, vol. 42, no. 9, pp. 2205–2213, 2017.

[13] T. B. Zhao, M. L. Xing, W. Y. Guo, C. W. Wang, and B. Wang, "Anchoring effect and energy-absorbing support mechanism of large deformation bolt," *Journal of Central South University*, vol. 28, no. 2, pp. 572–581, 2021.

[14] Z. G. Cao, "Study on aseismic performance of different artificial dam structures of coal mine underground reservoir," *Coal Science and Technology*, vol. 48, no. 12, pp. 237–243, 2020.

[15] P. Peng, Z. G. Shan, and Y. F. Dong, "Coupling model for assessing anti-seepage behavior of curtain under dam foundation," *Journal of Central South University*, vol. 19, no. 7, pp. 2016–2021, 2012.

[16] Q. L. Yao, Y. P. Liu, T. Chen, X. H. Li, S. Y. Yang, and H. F. Duan, "Experimental study of damage evolution of artificial dam strength of underground reservoir," *Journal of China Coal Society*, vol. 43, no. 4, pp. 1111–1117, 2018.

[17] D. Z. Gu, Y. G. Yan, Y. Zhang, E. Z. Wang, and Z. G. Cao, "Experimental study and numerical simulation for dynamic response of coal pillars in coal mine underground reservoir," *Journal of China Coal Society*, vol. 41, no. 7, pp. 1589–1597, 2018.

[18] S. Y. Wang and H. Y. Zuo, "Safety diagnosis on coal mine production system based on fuzzy logic inference," *Journal of Central South University*, vol. 19, no. 2, pp. 477–481, 2012.

[19] Q. M Huang, S. M Liu, W. M Cheng, and G. Wang, "Fracture permeability damage and recovery behaviors with fracturing fluid treatment of coal: an experimental study," *Fuel*, vol. 282, p. 118809, 2020.

[20] X Xu, L. Zhou, and Q. Y Feng, B Gao, Research progress of gas-water-rock interaction for gas occurrence and migration in abandoned coal mine," *Safety in Coal Mines*, vol. 47, no. 6, pp. 1–4, 2016.

[21] B. B. Wang, B. Liang, J. G. Wang, K. M. Sun, W. J. Sun, and H. B. Chi, "Experiment study on rock bulking of coal mine underground reservoir," *Rock and Soil Mechanics*, vol. 39, no. 11, pp. 4086–4092+4101, 2018.

[22] J. Z. Tang, S. Q. Yang, D. Elsworth, and Y. Tao, "Three-dimensional numerical modeling of grain-scale mechanical behavior of sandstone containing an inclined rough joint," *Rock Mechanics and Rock Engineering*, vol. 54, no. 2, pp. 905–919, 2020.

[23] C. Zhang, P. H. Han, F. T. Wang, and X. He, "The stability of residual coal pillar in underground reservoir with the effect of mining and water immersion," *Journal of China University of Mining and Technology*, pp. 1–8, 2021.

[24] T. R. Ma, D. P. Ma, and Y. J. Yang, "Fractal characteristics of coal and sandstone failure under different unloading confining pressure tests," *Advances in Materials Science and Engineering*, 2020.

[25] JuJ. F. BaiDY and LiJ. H. XuJL, "Stability analysis of mine underground reservoir artificial dam in Lijiahao mine," *Journal of China Coal Society*, vol. 42, no. 7, pp. 1839–1845, 2017.

[26] B. F. Wang, L. Wu, J. Zhang, B. Liang, and C. B. Liu, "Experiment on size effect for deformation characteristics of rock and coal in coal mine underground reservoir," *Journal of Mine Safety and Engineering*, pp. 1–10, 2021.

[27] Q. L. Yao, Q. Hao, X. Y. Chen, B. J. Zhou, and J. Fang, "Design on the width of coal pillar dam in coal mine groundwater reservoir," *Journal of China Coal Society*, vol. 44, no. 3, pp. 891–899, 2019.

[28] P. X. Zhao, Y. C. He, S. G. Li, H. F. Lin, Y. Y. Jia, and E. H. Yang, "Coal thickness effect on mechanics and energy characteristics of coal-rock combination model," *Journal of Mine Safety and Engineering*, vol. 37, no. 5, pp. 1067–1076, Article ID 106445, 2020.

[29] C. J. Li, Y. Xu, M. M. Feng, and B. Pan, "Deformation law and failure mechanism of coal-rock-like combined body under uniaxial loading," *Journal of China Coal Society*, vol. 45, no. 5, pp. 1773–1782, 2020.

[30] F. Du, K. Wang, X. L. Dong, and J. P. Wei, "Numerical simulation of damage and failure of coal-rock combination based on CT three-dimensional reconstruction," *Journal of China Coal Society*, pp. 1–12, 2021.

[31] Y. Rui, J. K. Lv, Z. Bo, and D. P. Ma, "Rock unloading failure precursor based on acoustic emission parametric fractal characteristics," *Lithosphere*, vol. 2022, 2020.

[32] K. Yang, W. J. Liu, L. T. Dou, X. L. Chi, Z. Wei, and Q. Fu, "Experimental investigation into interface effect and progressive instability of coal-rock combined specimen," *Journal of China Coal Society*, vol. 45, no. 5, pp. 1691–1700, 2020.

[33] Z. Y. Fang, J. F. Ju, Z. G. Cao, X. Z. Wang, and J. L. Xu, "Numerical simulation of damage and failure of coal-rock combination based on CT three-dimensional reconstruction," *Journal of China Coal Society*, pp. 1–12, 2021.

[34] M. K. Duan, C. B. Jiang, W. M. Yin, K. Yang, J. Z. Li, and Q. J. Liu, "Experimental study on mechanical and damage characteristics of coal under true triaxial cyclic disturbance," *Engineering Geology*, vol. 295, Article ID 106445, 2021.

[35] Z. Li and Q. H. Rao, "Quantitative determination of PFC3D microscopic parameters," *Journal of Central South University*, vol. 28, no. 3, pp. 911–925, 2021.

[36] K. Yang, X. Lyu, Q. P. Liu et al., "Experimental study on instability characteristics of coal pillar-artificial dam bond in abandoned mine," *J Min Safety Eng*, pp. 1–16, 2022.

[37] X. Lyu, K. Yang, J. J. Fang, Z. N. Zhang, Y. Wang, and Q. Fu, "Simulation of the uniaxial mechanical properties and crack evolution of coal pillar-artificial dam in abandoned mines," *Journal of China Coal Society*, 2021.

Hindawi
Advances in Materials Science and Engineering
Volume 2022, Article ID 6426279, 9 pages
https://doi.org/10.1155/2022/6426279

Research Article

Relationship between Mechanical Properties of Saturated Fissured Sandstone and Fissure Angle after Freeze-Thaw Cycles

Yiquan Luan, Zihao Liu, Guilei Song, Jinpeng Zhang, Longxiao Chen, Peng Qin, and Chuanxiao Liu

College of Water Conservancy and Civil Engineering, Shandong Agriculture University, Taian 271000, Shandong, China

Correspondence should be addressed to Chuanxiao Liu; lchuanx@163.com

Received 4 July 2022; Accepted 2 September 2022; Published 20 September 2022

Academic Editor: Baskaran Rangasamy

The change of mechanical properties of the surrounding rock of underground engineering in cold regions decreases engineering safety. In order to explore the influence of fissure angle on the mechanical properties of surrounding rocks, uniaxial compression and acoustic emission tests were carried out on the fissured sandstone in a saturated state. The results showed that the stress-strain curves of the fissured sandstone had "stress drop" phenomena, the acoustic emission ringing count rate and the cumulative ringing count versus time curve could describe the various stages of fissured sandstone failure, and the increase in the fissure angle made the acoustic emission activity more active. Fissures degraded the mechanical properties of sandstone. The peak strength and elastic modulus of the fissured sandstone increased with the increase of the fissure angle due to the large fissure width of the saturated sample and the freezing-thawing effect, and the peak strain and Poisson's ratio had no obvious regularity. As the fissure angle increased, the dominant cracks in the failure mode changed from tensile cracks to shear cracks and then to tensile cracks, and the failure mode changed from splitting failure to shearing failure and then to splitting failure. This study can provide guidance and suggestions for the design of underground engineering in cold regions.

1. Introduction

Underground engineering in cold regions experiences freeze-thaw cycles, and water-ice phase changes occur in water to cause uneven expansion and contraction of minerals in the rock, leading to further development of primary fissures and pores inside the rock, which affects the stability of the surrounding rocks of underground works in cold regions [1].

As a composite brittle material, the study on the effect of internal fissures on the mechanical properties of rocks is more mature. Yang et al. [2–4] used an acoustic emission monitoring system to analyze the mechanical properties and deformation rupture process of fissured sandstone under uniaxial compression conditions and found that the fissure angle had a significant effect on the strength and deformation modulus of the specimen, and the change in acoustic emission was associated with the degree of damage inside the specimen. Li et al. [5] analyzed the crack development pattern of fissure rocks under uniaxial compression and observed two forms of crack emergence: internal tip cracking together with external tip cracking and external tip cracking only. Lee et al. [6] conducted numerical simulations on fissured specimens with three different arrangements under uniaxial compression conditions and investigated the effects of different angles of rock bridges on the emergence and extension of cracks and the damage pattern of specimens. Feng et al. [7] conducted a true triaxial unloading test and conducted an in-depth study on the relationship between the crack propagation process and the stress in three directions. Cheng et al. [8] carried out uniaxial compression tests on prefabricated fissure-like rock materials and found that the peak strength and residual strength decreased as the prefabricated fissure length increased and the failure mode changed from shear to tensile failure. Chen et al. [9] found that the inclination and length of the structural plane have important effects on the crack propagation behavior, failure mode, energy evolution, and displacement distribution of

surrounding rocks. Chen et al. [10] deduced the macroscopic damage variable formula of rock mass considering the crack propagation length and the friction effect of joint closure by combining the energy principle and the fracture damage theory and established a coupled damage variable considering macroscopic and microscopic defects.

In addition, underground engineering in cold regions suffers from freeze-thaw cycles for a long time, and the proportion of ice content inside the rock during freezing plays an important role in the mechanical properties of the rock. The ice content is governed by the initial water content. Boone [11, 12] et al. studied the effect of temperature change on the pattern of freezing swelling. Wang et al. [13] explored the mechanical properties of tonalite after freeze-thaw cycles at different temperatures and found that the uniaxial compressive strength and Young's modulus of specimens decreased and structural face rupture increased after suffering freezing damage. Chen et al. [14, 15] proposed a shear creep intrinsic model considering the effects of freeze-thaw cycles and time-dependent damage based on NMR detection and shear creep tests. Mustafa Fener et al. [16] used polarized light microscopy to examine the structural changes in andesite after freeze-thaw cycles and determined the effect of the number of freeze-thaw cycles on the basic mechanical properties of the stone. Huang et al. [17] used the static elastic modulus to represent the freeze-thaw damage of rocks, established the damage principal structure model, and derived the final statistical damage principal structure equation. Liu et al. [18] proposed a new model for predicting freeze-thaw uniaxial compressive strength based on elastic-plasticity theory and fatigue damage mechanics, considering the actual state of rock stress distribution under freeze-thaw action. Based on the principle of static equilibrium, the law of conservation of energy, and the law of conservation of mass for rocks, Kang et al. [19] established a model undergoing controlling equations for the heat-water-force coupling of rocks undergoing freeze-thaw cycles.

In summary, current studies have focused on the mechanical properties of intact rocks in dry and saturated states [20] and ignored the fact that water-bearing rocks in nature have internal fractures and are often under freeze-thaw action. Fewer studies have been conducted on the mechanical properties of saturated water-bearing fractured rocks under freeze-thaw action. In view of this, the sandstone in this study was taken out during mine excavation as the background of the Jiangzhuang coal mine project in Jining City, Shandong Province, and produced standard specimens of fissure sandstone with 1.18% water content under 20 freeze-thaw cycles. This studies the influence of the fissure dip angle of water-saturated sandstone under the freeze-thaw action on the deterioration law of rock mechanical properties and acoustic emission characteristics. Moreover, it can provide suggestions for the construction and maintenance of underground projects in cold areas.

2. Materials and Methods

2.1. Sample Preparation. The rock samples used in this test were selected from the sandstone in the process of mine excavation in Jiangzhuang coal mine, Jining City, Shandong Province. After the drilling, cutting, and grinding, the rock was made into a standard specimen of Φ50 mm × 100 mm required for the test. A 25 mm long and 2 mm wide penetration fissure was cut in the center of the rock sample by using the SQ3020 CNC ultrahigh pressure water jet cutting machine (Figure 1(a)). The fissure dip angles were set at 0°, 15°, 30°, 45°, 60°, 75°, and 90°. The specific distribution of specimen fissures was shown in Figure 1(b).

This test used the natural water-saturated method to produce sandstone specimens in a water-saturated state, and the specific operation steps were as follows: firstly, the specimens were put in a drying oven at 105°C for 24 hours. Second, we waited for them to cool to room temperature and weighed their dry mass. Then, we soaked the rock samples in water to absorb water, took out the specimens every 30 minutes at the beginning of the soaking process, wiped off the water on the surface of the specimens, and weighed their mass until saturation. Finally, we measured the saturation of the sandstone used in this test. The saturated water content was measured to be 1.18%.

The prepared fissured sandstones were wrapped tightly with cling film, and we placed them in a freeze-thaw cycle chamber for a freeze-thaw cycle test with a freezing temperature of −20°C and a freezing time of 12 h. The dissolution temperature was set to 20°C and dissolution time to 12 h. In other words, each freeze-thaw cycle was 24 h. The number of freeze-thaw cycles was set to 20 times according to the corresponding test specification [21, 22]. The specimen numbers with different inclination angles under freeze-thaw action were shown in Table 1.

2.2. Test Equipment and Loading Procedure. Conventional uniaxial compression tests were performed on fissured sandstones under 20 freeze-thaw cycles using the STAC 600–50 multifunctional rock triaxial testing machine with stress-controlled axial loading. The axial loading rate was 0.05 MPa/s. During the loading process, it indicated that the sandstone lost its bearing capacity when the axial stress and hoop strain were greatly reduced, accompanied by a popping sound. The loading was stopped immediately. In addition, the acoustic emission signals were detected using an AE21C acoustic emission detector when the rock underwent uniaxial compression.

3. Mechanical Properties' Analysis

3.1. Stress-Strain Curve Analysis. The fissured sandstone samples with a water content of 1.18% after 20 freeze-thaw cycles were subjected to conventional uniaxial compression tests, and the full stress-strain curves were obtained from the test results as shown in Figure 2, where ε_1 was the axial strain, ε_3 was the hoop strain, and ε_v was the volumetric strain.

The stress-strain curves of fissured sandstones were similar. They were up-concave and went through four stages: the compaction stage, elastic deformation stage, plastic deformation stage, and destruction stage. The weakening effect of water made it possible to compress the

(a) (b)

Figure 1: A sample preparation diagram. (a) SQ3020 CNC ultrahigh pressure water jet cutting machine. (b) Arrangement of fissure rock samples.

Table 1: Sample number.

Number of freeze-thaw cycles	Water content (%)	Fissure angle (°)	Specimen number
20	1.18	Intact	A-intact
		0	A-0
		15	A-15
		30	A-30
		45	A-45
		60	A-60
		75	A-75
		90	A-90

microfractures inside the sandstone with relatively small load. In the elastic deformation stage, the phenomenon of "stress drop" appeared, and the full stress-strain curve showed "multiple peaks." The number of "peak" increased compared with the intact sandstone specimen, and the curve fluctuations were more. The decrease in the proportion of linear elastic phase indicated that elastic deformation gradually decreased. This was because the sandstone used in the test had high brittleness and weak tensile capacity. The tensile deformation may have occurred during the compression process. During the plastic deformation stage, the circumferential and volumetric strains increased significantly. The internal cracks and newly generated cracks in the rock samples began to expand and penetrate, followed by macroscopic cracks. After reaching the peak strength, the stress decreased rapidly, indicating that the specimen lost its load-bearing capacity, and the rock samples showed brittle damage characteristics.

3.2. Acoustic Emission Characterization. Figure 3 showed the experimental results of the acoustic emission cumulative ringing count rate of the fissured sandstone.

At the beginning of the compression-density and elastic-deformation phases, the primary fissures within the sandstone were compacted, and the acoustic emission activity was minimal. The accumulated elastic energy started to be released, and new cracks were generated in the plastic deformation stage. The cumulative ringing count curve fluctuated frequently, and the "stress drop" phenomenon made the acoustic emission events reach a small peak. Then, the acoustic emission events entered a "silent period," the ringing count rate weakened, and the cumulative ringing count rate curve tended to be flat in this phase. After the "silent period," the fissured sandstone entered the damage stage. The stress reached its peak, and a large number of new cracks were generated, expanded, and penetrated, at which time the acoustic emission event was extremely active. The ringing count rate appeared to peak, and the cumulative ringing count rose sharply. After the stress peak, the rock sample had been damaged, and the sandstone was in the residual damage stage.

With the increased fissured dip angle, the acoustic emission ringing count rate and cumulative ringing count rates of the sandstone showed an increasing trend. At the same time, the cumulative ringing count rate-time curve could be divided into stable periods and unstable periods. In the stable period, the cumulative ringing count was growing at a low rate, and the cracks were developed and expanded steadily. In the unstable period, the cumulative ringing count was growing at a high rate, and the rock samples produced irreversible damage cracks. The duration of the stable period

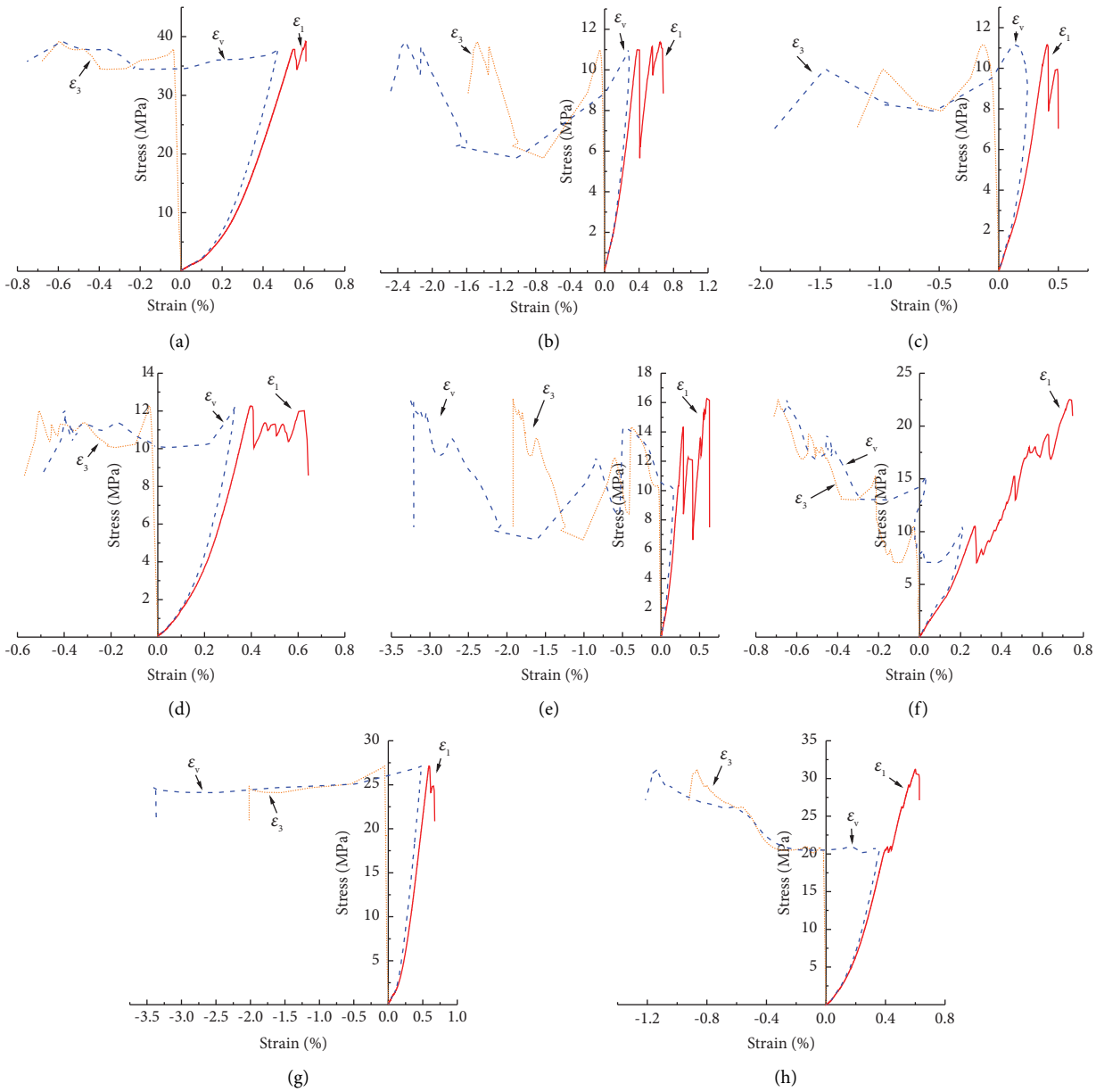

Figure 2: Conventional uniaxial compression stress-strain curves of fissured sandstone with different dip angles. (a) A-intact. (b) A-0. (c) A-15. (d) A-30. (e) A-45. (f) A-60. (g) A-75. (h) A-90.

of the cumulative ring count rate curve became longer with the increase of the dip angle, which indicated that the larger the angle was, the stronger the resistance of the sandstone to deformation.

3.3. Peak Strength Analysis. Figure 4(a) reflected the relationship between compressive strength of the water-saturated fissured sandstone and the fissure dip angle after freeze-thaw action. Figure 4(b) reflected the relationship between the effective bearing area of the fissured sandstone and the fissure dip angle.

As could be seen from the figures, the peak strengths of the fissured sandstone were smaller than those of the intact sandstone, which indicated that the presence of fissure had a weakening effect on the sandstone. The fissure opens up to form a larger sliding fault during fissured sandstone destruction, resulting in the weakening of strength. The lowest peak strength of the fissured sandstone was 11.16 MPa at a 15° fissure angle, and the highest peak strength of the fissured sandstone was 31.21 MPa at a 90° fissure angle. The peak strength increased with the increase in the fissure angle, but it was lower than that of the intact specimen. According to the literature, the test results of some scholars showed that the peak strength of the rock tended to decrease and then increase with the increase of the fissure angle. However, this phenomenon was not obvious in this paper, which was caused by the different fissure widths used in the specimens, and the fissure width in this study was 2 mm. The experimental results of Shen

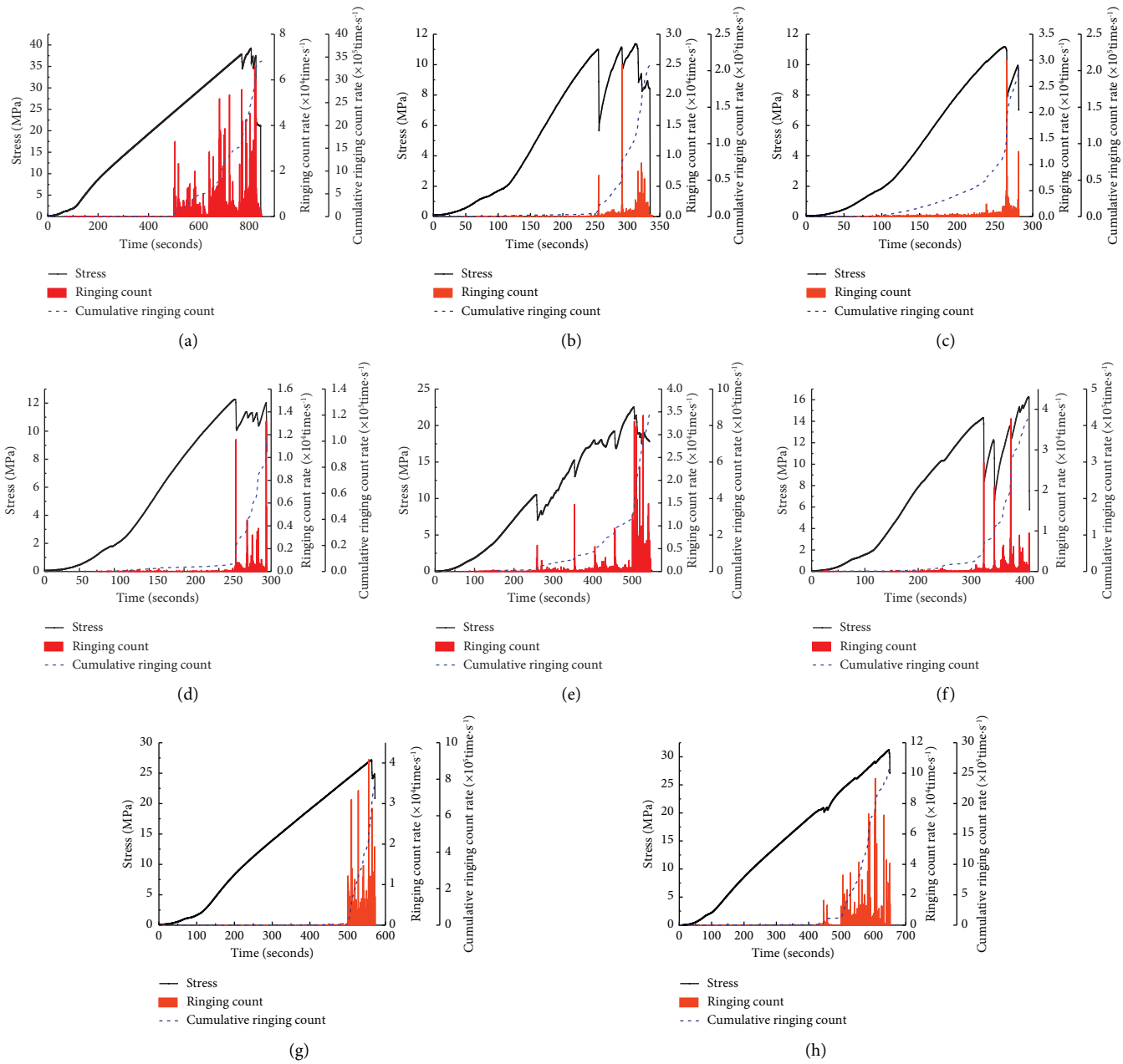

Figure 3: Acoustic emission ringing count rates and cumulative ringing count rates in fractured sandstones with different dip angles. (a) A-intact. (b) A-0. (c) A-15. (d) A-30. (e) A-45. (f) A-60. (g) A-75. (h) A-90.

et al. [23] showed that when the fissure width was lower than 0.8 mm, the peak strength showed an obvious trend of first decreasing and then increasing, and a more obvious trend of increasing when the fissure width was greater than 0.8 mm.

In addition, there was a significant jump in peak strength when the fissure dip angle was 60°, which was related to the damage caused by the fissure. The cross-sectional area of the sandstone specimen consisted of the total pore area and the effective bearing area. The effective bearing area of the fissured sandstone specimens was reduced compared with that of the intact sandstone specimen, so the peak strength was smaller than that of the intact sandstone. The effective bearing area increased with the increase of the fissure angle. When the fissure dip angle was 45°~60°, the effective bearing area increased more.

The fitting equation and correlation coefficient between the fissure angle and compressive strength of the fissured sandstone are shown as

$$UCS = 7.885 + 0.24281\alpha, R^2 = 0.92084. \quad (1)$$

Eq. UCS—peak fractured rock strength, MPa; $E = 3.24799 + 0.05372\alpha, R^2 = 0.96693$—fissured sandstone dip angle.

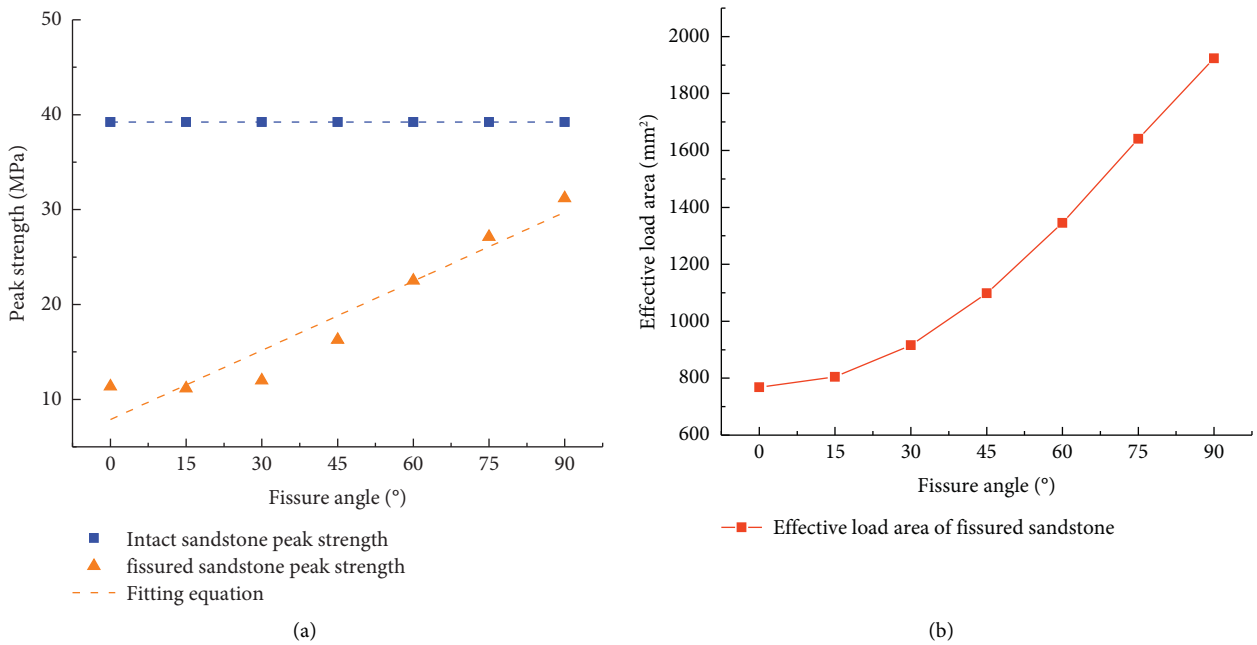

Figure 4: Peak strength of the fissured sandstone versus fissure dip angle. (a) Peak strength of the fissured sandstone versus fissure angle. (b) Relationship between the effective load area of the fissured sandstone and the fissure angle.

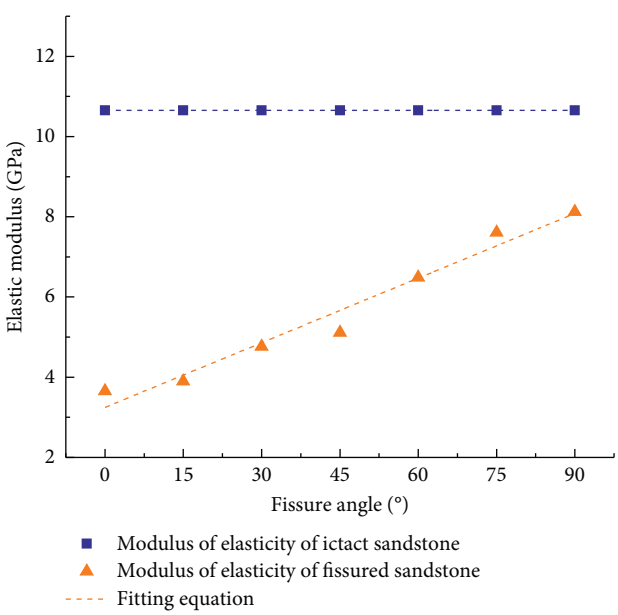

Figure 5: Relationship between the elastic modulus of the fissured sandstone and the fissure angle.

3.4. Elastic Modulus Analysis. Figure 5 reflected the relationship between the elastic modulus of the fissured sandstone and the fissure angle.

As could be seen from the figure, the lowest specimen elastic modulus was 3.66 GPa when the dip angle was 0°. When the dip angle was 90°, the highest peak strength was 8.13 GPa, which was lower than the intact sandstone elastic modulus. This was because there were more pores and cavities in the fissured sandstone, and this expanded the surface area in contact with water, which enhanced the softening effect of water. The elastic modulus of the fissured sandstone increased with the increase of the fissure angle, indicating that the larger the dip angle was, the stronger the ability of the specimen to resist deformation was. In other words, the increased fissure angle had an optimization effect on the ability of the sandstone to resist deformation. It was worth noting that at the fissure dip angle of 60°, the elastic modulus had a jump increase, followed by a monotonic increasing trend, and the change form was similar to Figure 5.

The fitted equations and correlation coefficients for the relationship between the dip angle and the elastic modulus of the fissured sandstone are shown as follows:

$$E = 3.24799 + 0.05372\alpha, R^2 = 0.96693. \quad (2)$$

Eq. E— modulus of elasticity of the fissured sandstone, GPa.

3.5. Peak Strain Characteristics. Figure 6 reflected the relationship between the peak axial strain of the fissured sandstone and the fissure dip angle.

It could be seen from the figure that there was no obvious pattern between the peak strain and the fissure dip angle of the fissured sandstone. This was because the "stress drop" phenomenon occurred; the specimen axial, circumferential, and volumetric strains increased largely, and their values could not be compared. Therefore, there was no obvious pattern of peak strains in the fissured sandstone when the peak strength was reached.

3.6. Poisson's Ratio Characteristics. Figure 7 reflected the relationship between Poisson's ratio of the fissured sandstone and the fissure angle.

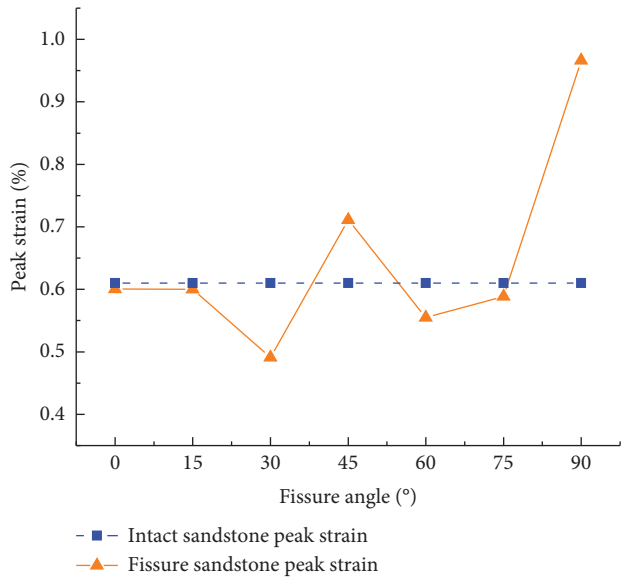

Figure 6: Peak strain of the fissured sandstone versus fissure angle.

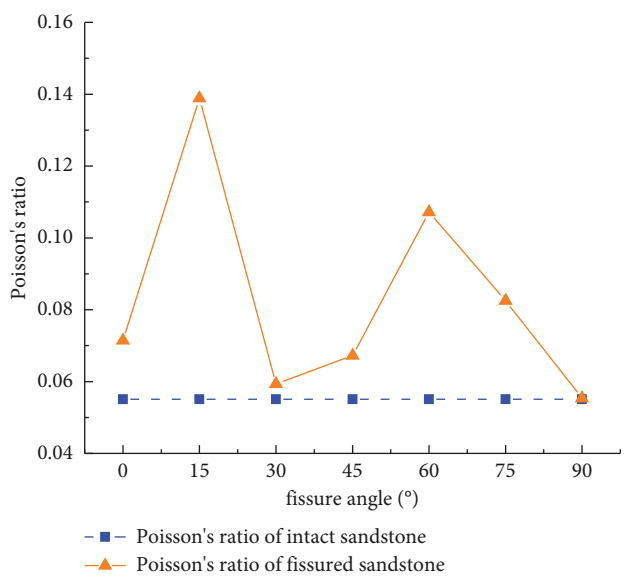

Figure 7: Relationship between Poisson's ratio and fissure dip in fissured sandstones.

From the figure, there was no obvious pattern between Poisson's ratio and the fissure angle of fissured sandstones. However, it could be found that the values of Poisson's ratio of fissured sandstones were larger than those of intact sandstones, which was due to the fact that plastic deformation had been generated during the preparation of fissured specimens, and the ratio of transverse strain to longitudinal strain of fissured specimens became larger. It could be found that the peak strain value of the fissured sandstone was similar to that of the intact sandstone when the fissure angle was small, but Poisson's ratio was relatively larger, which indicated that the rock was more prone to instability and swelling deformation under the external load. In addition, Poisson's ratio was almost the same as that of the intact sandstone, and the peak strain value was the largest and significantly larger than that of the intact sandstone when the fissure dip angle was 90°, indicating that the lateral deformation of the fissured sandstone was larger at this time.

3.7. Analysis of Macroscopic Damage Patterns in Fractured Sandstones. Figure 8 showed the macroscopic damage pattern of the fissured sandstone.

The macroscopic damage mode of intact sandstone specimens was splitting damage. Sandstone specimens with a fissure dip angle of 0° and 15° had wing cracks penetrating up and down to form the main rupture surface, which was typical of splitting failure. When the fissure dip angle increased from 30° to 45°, the development direction of wing cracks in sandstone specimens completely changed to the axial loading direction, and the failure mode changed from splitting failure to shear failure. Sandstone specimens with a fissure angle of 60° had the most abundant crack types, and wing cracks, secondary inclined cracks, secondary coplanar cracks, and far-field cracks all appeared. The development of wing cracks was incomplete, the secondary coplanar cracks and secondary inclined cracks penetrated up and down to form the main rupture surface, and the failure mode was shearing failure. Wing cracks were not obvious in the sandstone specimen with a fissure angle of 75°. The far-field cracks merge with the secondary cracks to form the secondary rupture surface, and the failure mode became splitting failure. Sandstone specimens with a fissure angle of 90° had obvious longitudinal penetration failure. The extension cracks were mainly far-field cracks, and the failure mode was splitting failure.

It could be found that the fissure angle gradually increased from 0°, the shear cracks were gradually more than tensile cracks in the failure mode, and the specimen failure mode changed from splitting failure to shear failure. The fissure angle increased to 60°; the peak strength had increased significantly. Therefore, there were more rock grains to reach weakening, resulting in more split surfaces. Moreover, tensile cracks gradually increased, and the failure mode gradually changed to splitting failure.

The number of wing cracks and their development gradually decreased, but the number of secondary cracks and their development gradually increased. From the energy point of view, each secondary crack could be regarded as a channel for strain energy consumption, and the greater number of them consumed more energy, thus requiring a greater load to destroy the rock sample [24], which also explained the phenomenon that the peak strength of the sandstone increased with the increase of the fissure dip angle.

4. Discussion

The fissures in the water-filled fissured sandstone under the freeze-thaw action deteriorate the mechanical properties of the sandstone, but the increase in the fracture angle has an optimized effect on the bearing capacity of the fractured sandstone. When the prefabricated fissure width is 2 mm, the peak strength increases with the increase of the fissure angle. Previous studies show that the peak strength decreases

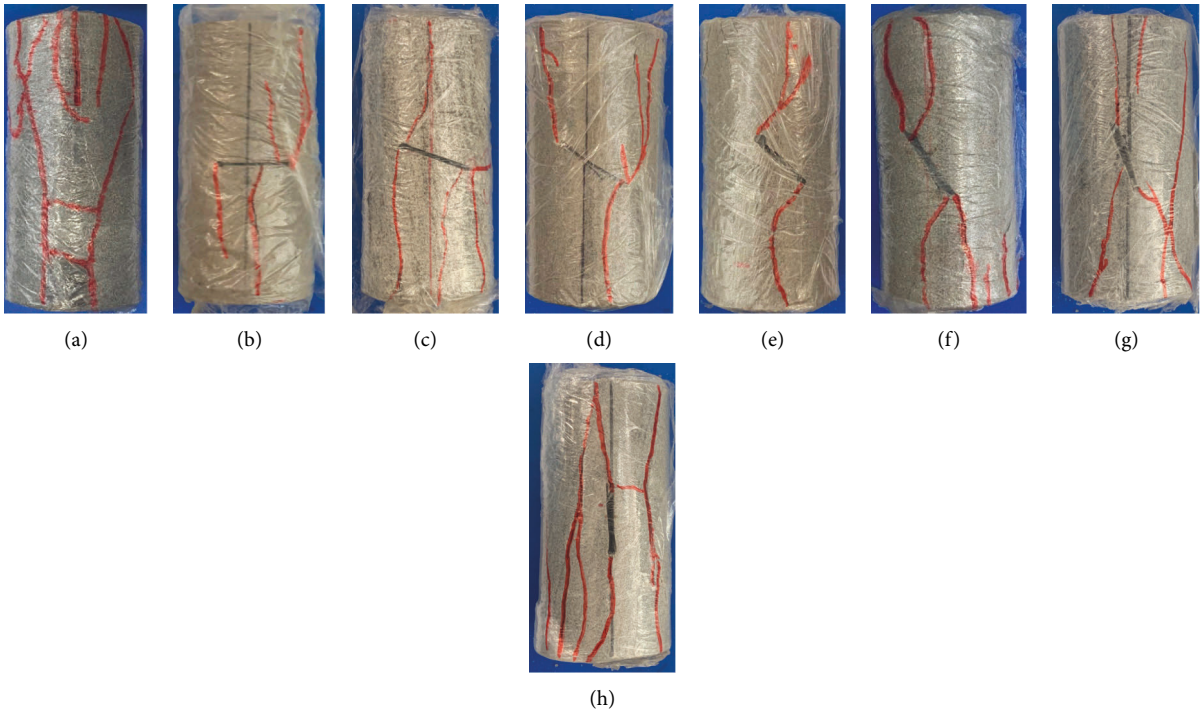

Figure 8: Destruction mode of fissured sandstones with different dip angles. (a) A-intact. (b) A-0. (c) A-15. (d) A-30. (e) A-45. (f) A-60. (g) A-75. (h) A-90.

first and then increases with the increase of the fissure dip angle, which is different from our experimental results. This is not only related to the different width of the prefabricated fissure and the brittleness of sandstones but may also be influenced by the strength of the specimen, the friction angle, and the tension-compression ratio [25]. Moreover, the fissure sandstone in this study was in a water-filled state and experienced 20 freeze-thaw cycles, which is one of the factors that caused the different results. In addition, the relationship between the fissure angle and the peak strain of the fractured sandstone in the test was unclear. On the one hand, the effect of water made the axial strains, circumferential strains, and volumetric strains increase largely, and they cannot be compared.

On the other hand, the fractured sandstone is more porous and more easily damaged under the load used; at the same time the damage in the initial state has produced a certain plastic deformation, resulting in a reduction of the axial deformation during formal compression [26].

In actual engineering, there will be temperature damage during freeze-thaw cycles, and frost heave forces caused by temperature changes can damage the rock. In addition, the rock is often in a three-dimensional loading state for a long time, and future work should be combined with the surrounding pressure for creep to better restore the construction environment at the site and explore the effect of water content on the fractured sandstone in the freeze-thaw state.

5. Conclusion

(1) The stress-strain curve of water-filled fractured sandstones after freeze-thaw showed a "multi-peak type." It was observed by acoustic emission that the greater the fissure angle, the longer the stable period of the cumulative ringing count rate curve of the fractured sandstone, and the stronger the resistance to deformation.

(2) The fissure played a deteriorating role in the mechanical properties of the sandstone. The peak strength and elastic modulus tended to increase with the increase of the fissure angle, and the peak strain and Poisson's ratio have no obvious relationship with the change of the fissure angle.

(3) As the fissure angle increased, the dominant crack in the failure changed from tensile cracks to shear cracks and then to tensile cracks, and the failure mode changed from splitting failure to shearing failure and then to splitting failure.

Data Availability

All experimental data generated or used during the study are available from the corresponding author upon request.

Conflicts of Interest

The authors declare no conflicts of interest.

Authors' Contributions

Yiquan Luan and Zihao Liu contributed equally to this work.

Acknowledgments

This work was supported by the Key Development Program for Research of Shandong Province 2018GNC110023, the National Natural Foundation of Shandong ZR2021QE233, and the National Natural Science Foundation of China (51574156).

References

[1] Y. L. Chen, J. Ni, L.-H. Jiang, M. L. Liu, P. Wang, and R. Azzam, "Experimental study on mechanical properties of granite after freeze–thaw cycling," *Environmental Earth Sciences*, vol. 71, no. 8, pp. 3349–3354, 2014.

[2] J. Yang, Z. L. Mu, and S. Q. Yang, "Experimental study of acoustic emission multi-parameter information characterizing rock crack development," *Engineering Fracture Mechanics*, vol. 232, Article ID 107045, 2020.

[3] W. L. Tian, S. Q. Yang, Z. L. Hu, and J. W. Lu, "Experimental study of the mechanical behavior of unfilled rough jointed specimens under uniaxial compression," *Arabian Journal of Geosciences*, vol. 13, no. 4, p. 164, 2020.

[4] M. Chen, S. Yang, R. Pathegama Gamage et al., "Fracture processes of rock-like specimens containing nonpersistent fissures under uniaxial compression," *Energies*, vol. 12, no. 1, p. 79, 2018.

[5] F. Xiong, X. Liu, X. Zhou et al., "Mechanical behaviours of sandstone containing intersecting fissures under uniaxial compression," *Journal of Rock Mechanics and Geotechnical Engineering*, vol. 14, no. 2, pp. 460–476, 2022.

[6] J. Lee, J. W. Hong, and J.-W. Jung, "The mechanism of fracture coalescence in pre-cracked rock-type material with three flaws," *Engineering Geology*, vol. 223, pp. 31–47, 2017.

[7] F. Feng, S. J. Chen, Y. J. Wang, W. P. Huang, and Z. Y. Han, "Cracking mechanism and strength criteria evaluation of granite affected by intermediate principal stresses subjected to unloading stress state," *International Journal of Rock Mechanics and Mining Sciences*, vol. 143, Article ID 104783, 2021.

[8] X. Cheng, "Damage and failure characteristics of rock similar materials with pre-existing cracks," *International Journal of Coal Science & Technology*, vol. 6, no. 4, pp. 505–517, 2019.

[9] S. J. Chen, F. Feng, Y. J. Wang et al., "Tunnel failure in hard rock with multiple weak planes due to excavation unloading of in-situ stress," *Journal of Central South University*, vol. 27, no. 10, pp. 2864–2882, 2020.

[10] S. Chen, C. Qiao, Y. Qing, and B. Deng, "Composite damage constitutive model of jointed rock mass considering crack propagation length and joint friction effect," *Arabian Journal of Geosciences*, vol. 11, no. 11, p. 283, 2018.

[11] A. Boone and P. Etchevers, "An intercomparison of three snow schemes of varying complexity coupled to the same land-surface model:local scale evaluation at an Alpine site," *Journal of Hydrometeorology*, vol. 2, no. 4, pp. 374–394, 2001.

[12] A. Boone, V. Masson, T. Meyers, and J. Noilhan, "The influence of the inclusion of soil freezing on simulations by a soil-vegetation-atmosphere transfer scheme," *Journal of Applied Meteorology*, vol. 39, no. 9, pp. 1544–1569, 2000.

[13] S. R. Wang, Y. L. Chen, J. Ni, M. D. Zhang, and H. Zhang, "Influence of freeze-thaw cycles on engineering properties of tonalite: examples from China," *Advances in Civil Engineering*, vol. 2019, Article ID 3418134, 12 pages, 2019.

[14] G. Chen, D. Jian, Y. Chen, Y. Wan, and Z. Lin, "Shear creep characteristics of red sandstone after freeze-thaw with different water contents," *Chinese Journal of Geotechnical Engineering*, vol. 43, no. 4, pp. 661–669, 2021.

[15] G. Chen, Y. Wan, X. Sun, and G. Zhang, "Research on creep behaviors and fractional order damage model of sandstone subjected to freeze-thaw cycles in different temperature ranges," *Chinese Journal of Rock Mechanics and Engineering*, vol. 40, no. 10, pp. 1962–1975, 2021.

[16] M. Fener and İ. İnce, "Effects of the freeze–thaw (F–T) cycle on the andesitic rocks (Sille-Konya/Turkey) used in construction building," *Journal of African Earth Sciences*, vol. 109, pp. 96–106, 2015.

[17] S. Huang, Q. Liu, A. Cheng, and Y. Liu, "A statistical damage constitutive model under freeze-thaw and loading for rock and its engineering application," *Cold Regions Science and Technology*, pp. 142–150, 2018.

[18] Q. Liu, S. Huang, Y. Kang, and X. Liu, "A prediction model for uniaxial compressive strength of deteriorated rocks due to freeze-thaw," *Cold Regions Science and Technology*, vol. 120, pp. 96–107, 2015.

[19] Y. Kang, Q. Liu, and S. Huang, "A fully coupled thermo-hydro-mechanical model for rock mass under freezing/thawing condition," *Cold Regions Science and Technology*, vol. 95, pp. 19–26, 2013.

[20] K. Zhao, S. Ran, P. Zeng, D. Yang, and T. Teng, "Effect of moisture content on characteristic stress and acoustic emission characteristics of red sandstone," *Rock and Soil Mechanics*, vol. 42, no. 4, pp. 899–908, 2021.

[21] *Ministry of Water Resources of the People's Republic of China, SL264-2001, Specifications for Rock Tests in Water Conservancy and Hydroelectric Power Engineering*, China Water & Power Press, Beijing, China, 2001.

[22] G. L. Song, L. X. Chen, K. S. Li et al., "Experiment and mechanism investigation on freezing-thawing of sandstone with different water contents," *Shock and Vibration*, vol. 2021, Article ID 2280348, 11 pages, 2021.

[23] J. Shen, S. Zhan, M. Karakus, and J. Zuo, "Effects of flaw width on cracking behavior of single-flawed rock specimens," *Bulletin of Engineering Geology and the Environment*, vol. 80, no. 2, pp. 1701–1711, 2021.

[24] S. Yang, Y. Dai, L. Han, Y. He, and Y. Gang, "Uniaxial compression experimental research on deformation and failure properties of brittle marble specimen with pre-existing fissures," *Chinese Journal of Rock Mechanics and Engineering*, vol. 28, no. 12, pp. 2391–2404, 2009.

[25] G. Wang, G. Yu, G. Li, and L. Gao, "Influence of initial crack dip angle on failure mode and peak strength of rock," *China Mining Magazine*, vol. 26, no. 10, pp. 173–176, 2017.

[26] C. Wang, C. Liu, and D. Liu, "Experimental study on volume effect of saturated fractured sandstone under uniaxial compression," *Chinese Journal of Underground Space and Engineering*, vol. 15, no. 5, pp. 1331–1340, 2019.

Hindawi
Advances in Materials Science and Engineering
Volume 2022, Article ID 8260107, 20 pages
https://doi.org/10.1155/2022/8260107

Research Article

Experimental and Numerical Investigation of Energy Evolution Characteristic of Granite considering the Loading Rate Effect

Feiyue Sun,[1] Junqi Fan,[2] Jiaqi Guo,[1] and Xiliang Liu[1]

[1]*School of Civil Engineering, Henan Polytechnic University, Jiaozuo 454003, Henan, China*
[2]*Research Institute for National Defense Engineering of Academy of Military Science PLA China, Luoyang 471023, Henan, China*

Correspondence should be addressed to Jiaqi Guo; gjq519@163.com

Received 21 July 2022; Accepted 18 August 2022; Published 20 September 2022

Academic Editor: Depeng Ma

In order to investigate the loading rate effect of energy evolution in granite, the indoor physical simulation test of single face fast unloading-three directions and five faces stress-vertical continuous loading under different loading rates was conducted using a new true triaxial rockbursttest system. The energy accumulation-dissipation-release characteristics in the process of rock deformation and failure were revealed. Based on the three-dimensional discrete element theory and the polycrystalline modeling technique (randomly generated Voronoi mineral grains), the entire process of rockburst inoculation-occurrence-development, as well as the energy evolution characteristics under true triaxial single face unloading conditions, were studied. The test results indicate that the energy transport and conversion of rock samples under different loading rates exhibit distinct stage characteristics. It can be divided into the initial energy accumulation stage, steady energy accumulation stage, rapid energy dissipation stage, and rapid energy release stage. With a rise in loading rate, the specimen in the process of energy accumulation is accompanied by energy dissipation, more external input energy, and elastic strain energy release amount into the kinetic energy of fragments, resulting in the rockburst phenomenon. As the loading rate increases, the elastic strain energy conversion rate (U_e/U) falls, while the dissipative energy conversion rate (U_d/U) increases. The higher the elastic strain energy conversion rate and the lower the dissipative energy conversion rate, the more serious the rockburst occurs. Numerical simulation results show that the entire process of rockburst inoculation-occurrence-development is successfully simulated using the crystal scale fine model (CSFM) considering the grain mineral composition. The ejection failure process can be divided into four stages, including grains ejection, rock spalling into plates, rock shearing into fragments, and rock fragments ejection. The relationships between the peak strength, elastic strain energy of rock samples, and loading rates are obtained, which is consistent with the laboratory test results. The high rate linear growth of kinetic energy evolution between the two inflection points can provide precursor information for rockburst prediction.

1. Introduction

With the competitive development of underground engineering construction, the excavation and boring speed of mines, large underground cavern groups, and tunnels (caves) have been accelerated, causing changes in the loading rate of surrounding rock mass in front of the working face. As a result, the mechanical properties of surrounding rock mass are changed, which in turn induces dynamic geological disasters such as rockburst, bringing high safety risks to the operators, and construction equipment in underground engineering. Rock dynamic response is essentially the outcome of energy drive exceeding the energy storage limit, based on the energy evolution mechanism that can reflect the dynamic process of rock failure [1–3]. According to studies, the loading rate is a significant factor in determining the occurrence of rockburst, and different loading rates have significant influences on the failure mode, strength characteristics, and energy evolution characteristics of the rock. Therefore, it is of theoretical importance and engineering application value to study the energy transport and conversion in the process of rock deformation and failure under different loading rates, as well as to reveal the essential characteristics of rock deformation

and failure, so as to enrich the dynamic response mechanism of rock.

Studies on the loading rate effect on the energy evolution of rockburst process features have received a great deal of interest from professionals in rock mechanics and engineering researchers around the world. In an experimental study, Chen et al. investigated the energy dissipation of fragments during rockburst [4]. Polito and Moldenhauer were involved in a novel method used to reveal the evolution and distribution law of elastic energy and dissipated energy density of rock samples [5]. Weyher et al. investigated the law of change in critical strain energy density [6]. Lu et al. investigated the effects of loading rate on rock deformation, strength, failure mode, and energy evolution [7]. Si et al. studied the influence of loading rate on the energy evolution of rockburst damage mechanism in circular tunnels [8]. The abovementioned research has significantly advanced the development of mechanical properties and energy evolution characteristics of rocks under different loading rates. However, the results achieved so far are primarily in uniaxial, biaxial, and conventional triaxial compression conditions to carry out research on energy transport and conversion in the process of rock deformation and failure, resulting in its difficulty in effectively simulating the real stress path and boundary condition transformation process of surrounding rock mass before and after excavation. Therefore, it is imperative to conduct research on the energy evolution characteristics of the loading rate effect on rockburst process under the true triaxial test conditions. In the aspect of numerical simulation, Zhang et al. studied the rock inner failure mechanisms under different loading rates based on the particle discrete element model [9]. Lee et al. developed a novel energy damage model based on continuum damage mechanics [10]. Ma et al. simulated laboratory experiments on coal-rock composite samples using the particle flow code [11]. Yu et al. studied the influence of loading rate on rock energy evolution and failure mode [12]. Most of the abovementioned results focus on the simulation of the rock static failure process, while there are few studies on the simulation of the dynamic failure process of rockburst reported in the literature, especially the numerical simulation of rock fragmentation ejection process based on polygonal crystal structure is still in a blank state, making it difficult to accurately reflect the physical reality of rock and to reasonably simulate the dynamic disaster of rockbursts at the engineering scale. Therefore, this paper adopts a computational grid based on a randomly distributed Voronoi diagram and discretizes the Voronoi polygon of rock mineral grain shape. In the entire process of simulating the ejection failure of rock fragments, the grid dependence of the model mechanical parameters on the general discrete element method is largely eliminated. It can accurately simulate the stress-strain curve and strength nonlinear characteristics of rocks, demonstrate the entire process of rockburst disaster, and reveal the inoculation mechanism of rockburst disaster.

This paper uses the new true triaxial rockburst test system, according to the new rockburst test method, new loading and unloading path to conduct physical simulation tests of single face fast unloading-three direction and five faces stress-vertical continuous loading under different loading rates. The influence of loading rate on the energy evolution characteristics during rock deformation and failure process is analyzed. Based on the energy principle, the transformation mechanism of energy storage, accumulation, dissipation, and release in each stage of rock deformation and failure under different loading rates is expounded. The study combines experimental results with the coupling of three-dimensional discrete element numerical analysis method and polycrystalline modeling theory (randomly generated Voronoi mineral grains) to construct a crystal scale fine model (CSFM) considering the composition of mineral grains. The entire process of rockburst inoculation-occurrence-development and the energy evolution characteristics under true triaxial single face unloading conditions are studied from the macro and micro levels. The study results to provide a fundamental scientific basis and significant theoretical support for the occurrence mechanism and prediction of rockbursts in underground engineering under high-stress states.

2. Test Equipment and Methods

2.1. Test Equipment. The test system mainly consists of true triaxial rockburst testing machine, loading system, control system, real-time data signal acquisition and monitoring system, high-speed camera system, and other subsystems (Figure 1). True triaxial rockburst testing machine is a new high-pressure servo rigid press, the maximum vertical loading pressure of 5000 kN, the maximum horizontal loading pressure of 3000 kN, through the full digital servo controller control can be realized in three vertical directions for independent loading and unloading. It has the special function of single face fast unloading under the three directions and six faces loading conditions. It can accurately simulate the process of rapid change of surrounding rock stress path at the moment of underground engineering excavation. With the aid of a high-speed camera, it is possible to observe the failure phenomenon of unloading faces in real-time.

2.2. Rock Samples Preparation. Grayish–white granite samples were collected in Wenshang County, Shandong Province, China (Figure 2). To ensure the comparability of tests and decrease the impact of material heterogeneity and dispersion on the test results, all specimens were extracted from the same intact rock. Before true-triaxial rockburst tests, the rectangular prismatic specimens, 100 mm (length) × 100 mm (width) × 200 mm (height), were prepared, and all sides and ends of specimens were finely ground and polished to minimize the local stress concentration and produce flat and smooth end surfaces. To ensure that rock samples are uniformly pressured in all directions, the processing accuracy is strictly in accordance with the standard of the International Society for Rock Mechanics [13], with a flatness error of ±0.05 mm for two opposite faces and a perpendicularity error of ±0.25° for two adjacent faces.

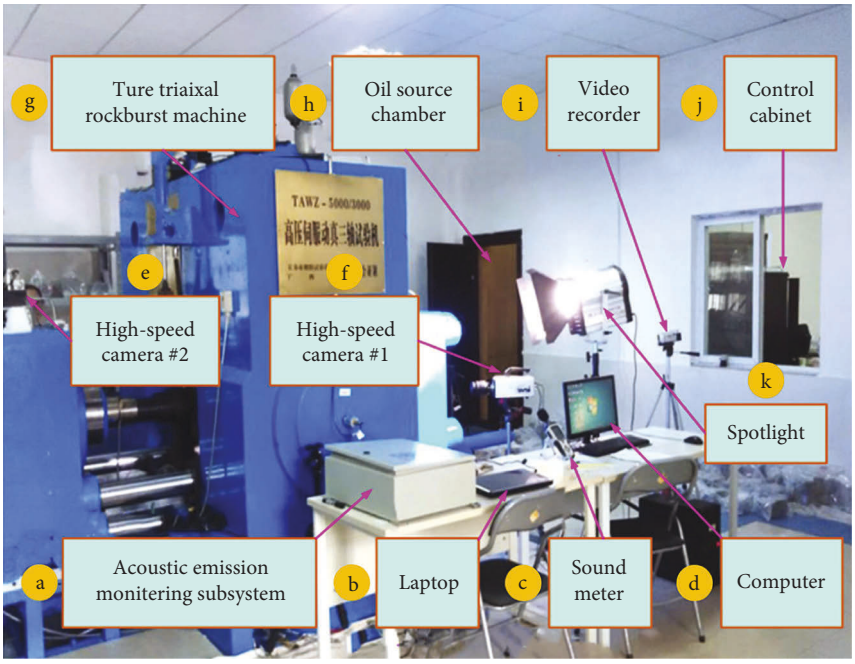

Figure 1: True triaxial rockburst testing system.

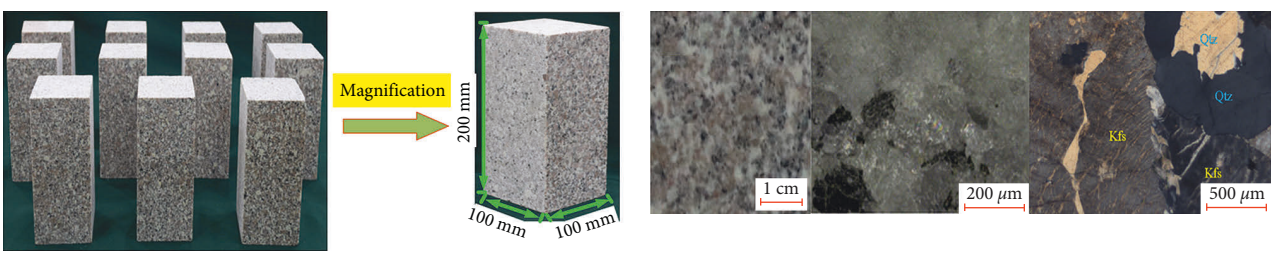

(a) (b)

Figure 2: Photo and microstructure of sample. (a) Photo of rock specimens; (b) naked-eye observations (left), 3D hyper-focal distance microscopic images (middle), and optical cross-polarized micrographs (right) of granite.

2.3. Test Methodology

2.3.1. Stress Path Design. Before excavation of the cavern, the rock mass is in a triaxial stress state. After the cavern excavation is unloaded, the unloading face of rock mass appears, and its radial stress decreases sharply (the corresponding principal stress is σ_3), the tangential stress increases gradually (the corresponding principal stress is σ_1), and the principal stress along the cavern axis remains the same as the initial stress field (the corresponding principal stress is σ_2), as depicted in Figure 3. For the rock unit in the area of concentrated compressive stress in the surrounding rock mass, the radial stress on the excavation boundary is zero, while the radial stress in the rock mass at a certain distance from the excavation surface rises sharply along the diameter direction, and the rock unit is in a special stress state of "one face zero load-three direction and five faces load."

According to the stress path and boundary condition transformation process of the surrounding rock mass after excavation of an underground cavern (Figure 3), the true triaxial rockburst test with single face fast unloading-three directions and five faces stress-vertical continuous loading can accurately reproduce the stress transformation process of radial stress plunge and tangential stress concentration after excavation and unloading of deep underground engineering. In addition, engineering practice demonstrates that rockburst typically occurs within 1~3 days after excavation [14, 15], indicating that the gradual concentration of tangential stress is one of the main factors leading to rockburst. Consequently, the process of continual concentration of tangential stress can be reproduced with vertical continuous loading. Figure 4 depicts the test method and loading-unloading path.

The specific testing procedures are described as follows: (I) The initial stress state of underground engineering rock mass before excavation is simulated according to the in-situ stress field inversion of measured geostress in a project, and the initial stress state in three directions is $\sigma_1/\sigma_2/\sigma_3 = 74.58/54.96/39.51$ MPa [17]. To achieve the loading and unloading in the tests, the values of σ_1, σ_2, and σ_3 under the initial ground stress condition in loading paths were set as 75, 55,

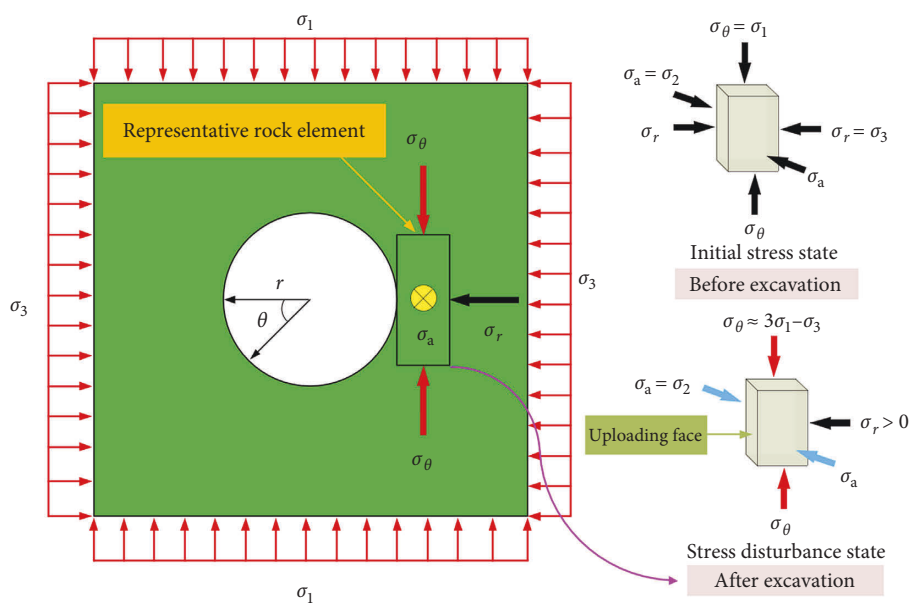

Figure 3: Mechanical environment of rock specimen in underground engineering before and after excavation: σ_1, σ_2, σ_3 are initial stresses, and $\sigma_1 > \sigma_2 > \sigma_3$; σ_θ, σ_a, and σ_r are stresses acting on representative rock specimen, and $\sigma_\theta > \sigma_a > \sigma_r$ (adapted from Su et al. [16]).

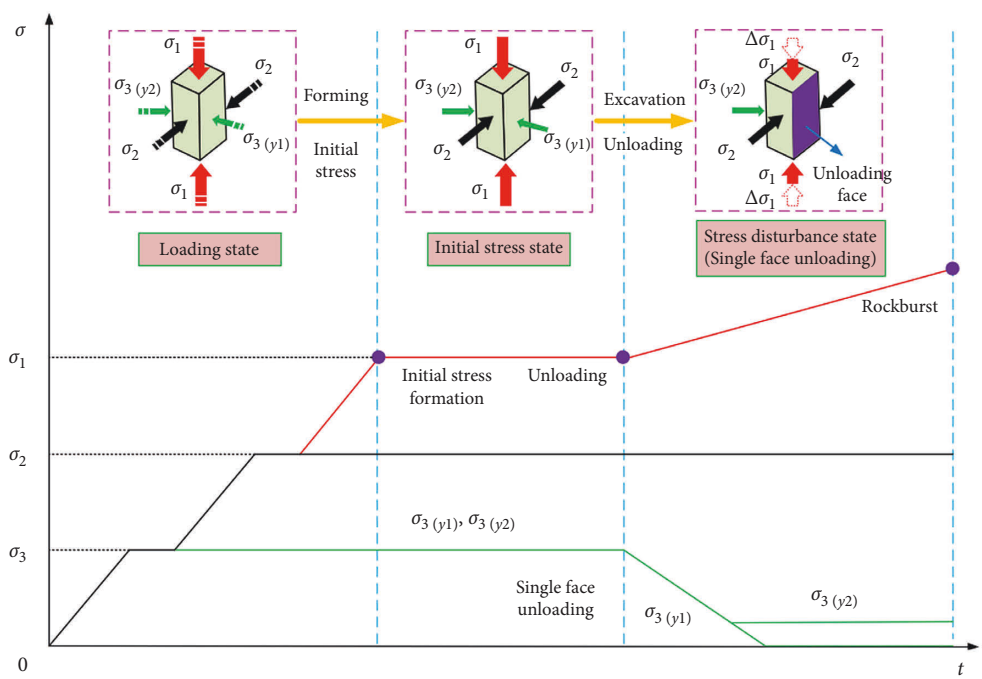

Figure 4: Sketch map of test method and loading-unloading path of rockburst.

and 40 MPa, respectively. Firstly, the principal stresses σ_1, σ_2, and σ_3 were loaded simultaneously to the predetermined values and then held for about 2~3 minutes. Secondly, the principal stresses σ_1 and σ_2 were loaded simultaneously to the predetermined values and then held for about 2~3 minutes. Finally, the principal stress σ_1 was loaded to the predetermined values. After the initial stress state is applied, the specimen is stabilized for approximately 6~8 minutes under the triaxial stress state of $\sigma_1 = 75$ MPa, $\sigma_2 = 55$ MPa, $\sigma_3 = 40$ MPa. (II) A single face fast unloading device (two springs) is used to unload the stress $\sigma_{3(y1)}$ to zero on one face in the Y-direction, while rapidly reducing the stress $\sigma_{3(y2)}$ to a predetermined value on the other face in the Y-direction. In order to simulate the radial stress reduction after excavation unloading in underground engineering, and to realize the conversion process the stress path and boundary conditions near the excavation boundary are under the effect of tangential stress. The stress $\sigma_{3(y2)}$ on the opposite face of the unloading face and the stress σ_2 in the X-direction are kept unchanged. Finally, the stress σ_2 in the vertical stress σ_1 is

continuously increased at different loading rates until the specimen is failure.

2.3.2. Testing Plan. In this experimental, four different loading rates of 0.05, 1.0, 3.0, and 5.0 MPa/s were designed, with strain rates of 1.7×10^{-6}, 3.4×10^{-5}, $1.0\times10^{-4,}$ and $1.7\times10^{-4}\,s^{-1}$ corresponding to the four different loading rates. The specific test procedures are detailed in Table 1. In our test, at least three specimens were prepared for each test with a given loading path to guarantee the repeatability of the experimental results. The typical failure process of each tested specimen was chosen to investigate the rockburst.

3. Stress-Strain Curve and Failure Mode of Granite Specimen

The stress-strain curves and failure modes of granite specimens with different loading rates are shown in Table 2.

Compared to the stress-strain curve of rock samples with static brittle failure rock sample no. *Z*-1, the typical stress-strain curve of rock sample with ejection failure has the following characteristics: (1) The failure process of rock samples under different loading rates roughly goes through four stages: the initial compaction stage (*OA*), the elastic deformation stage (*AB*), the prepeak unstable fracture stage (*BC*), and the postpeak failure stage (*CD*). (2) The prepeak curve has an obvious yield point, and the stress-strain curve between the yield point and the peak point changes more gently, corresponding to the splitting failure phenomena at the unloading face of rock samples and shear failure phenomena in the range of potential rockburst pits.

There is a correlation between the failure mode of granite specimens and the loading rate, and the failure mode characteristics of specimens vary depending on the different loading rates. *Z*-1 specimens display a relative rock plate splitting face on the unloading face, a large penetrating shear diagonal fracture on the inside of the rock body, and shear-tension fractures close to the unloading face, predominantly in the form of stable and slow slabbing failure. The failure modes of *Z*-2~*Z*-4 rock samples exhibit obvious multi-divisional failure characteristics, such as V-shaped or step-shaped rockburst pits, splitting cracks caused by tension appearing on the unloading face, and an uneven surface of rockburst pits.

4. Loading Rate Effect on Energy Evolution of Granite

4.1. Principle of Energy Analysis. The deformation and failure of rocks are mostly caused by energy-driven. From the viewpoint of energy, when a rock is deformed by an external force, assuming that the physical process has no heat exchange with the outside world, the total input energy generated by the external work is *U*. According to following energy conservation law [18]:

$$U = U_d + U_e, \tag{1}$$

Table 1: Testing plan.

Specimen no.	Loading rate (MPa/s)	σ_2 (MPa)	$\sigma_{3(y2)}$ (MPa)
Z-1	0.05	55	5
Z-2	1.0	55	5
Z-3	3.0	55	5
Z-4	5.0	55	5

where: U_d is the rock dissipation energy, which is used to generate internal damage and plastic deformation of rock, as depicted in the empty space encompassed by the curve in Figure 5; U_e is the rock releasable elastic strain energy, as depicted in the shaded area enclosed by the curve in Figure 5.

The total input energy *U*, elastic strain energy U_e, and dissipation energy U_d of a rock sample in the true triaxial stress state are calculated as follows [18]:

$$\begin{aligned} U &= \int_0^{\varepsilon_1}\sigma_1 d\varepsilon_1 + \int_0^{\varepsilon_2}\sigma_2 d\varepsilon_2 + \int_0^{\varepsilon_3}\sigma_3 d\varepsilon_3, \\ U_e &= \frac{\left[\sigma_1^2+\sigma_2^2+\sigma_3^2-2\nu\left(\sigma_1\sigma_2+\sigma_2\sigma_3+\sigma_1\sigma_3\right)\right]}{2E}, \\ U_d &= U - U_e, \end{aligned} \tag{2}$$

where: $\sigma_1, \sigma_2, \sigma_3$ is the maximum, intermediate, and minimum principal stress, respectively; $\varepsilon_1, \varepsilon_2, \varepsilon_3$ is the maximum, intermediate, and minimum principal strains, respectively; *E* is the initial elastic modulus; ν is the Poisson's ratio.

Based on the energy evolution mechanism in the process of rock deformation, the difference between dynamic and static rock failure is explained in detail [18]: due to the high-stress action of excavation unloading and disturbance load on the rock, a part of the rock is damaged intensifies in a very short time and its strength gradually decreases, while the elastic strain energy stored in the majority of rock rapidly reaches its limit value. When U_e reaches U_0 (the energy required for rock failure), i.e. $U_e = U_0$, U_e is completely released and the rock static fails. When $U_e > U_0$, the rock dynamic failure, the energy difference $\Delta U = U_e - U_0$ constitutes the kinetic energy to split the rock, inducing rockburst to occur.

4.2. Energy Evolutionary Process of Rockburst

4.2.1. Energy Evolution Characteristics of Specimens under Different Loading Rates. Using the energy calculation method in Section 4.1, the total input energy *U*, elastic strain energy U_e, dissipation energy U_d evolutionary process of granite rockburst test under different loading rates was obtained, as shown in Figure 6.

As can be seen from Figure 6, (a) The deformation and failure of rock is a dynamic imbalance process by energy-driven. The process of specimen deformation and failure under different loading rates is accompanied by energy input, accumulation, dissipation, and release. (b) Initial compression stage (stage I): The external energy input is utilized mostly for initial crack closure, frictional slip, etc. The total energy curve and the elastic strain energy curve

Table 2: Stress-strain curve and failure mode of granite specimens with different loading rates.

Loading rate (MPa/s)	Axial stress-strain curve	Peak stress (MPa)	Failure mode
0.05 (*Z*-1)	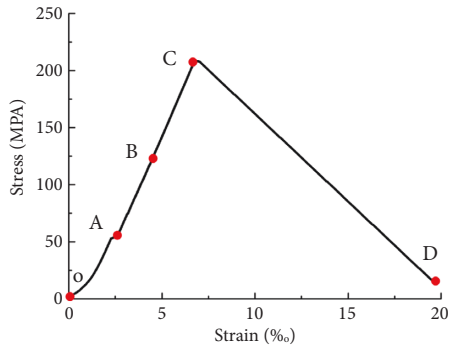	208.93	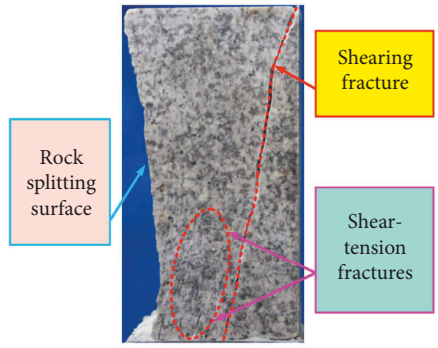
1.0 (*Z*-2)	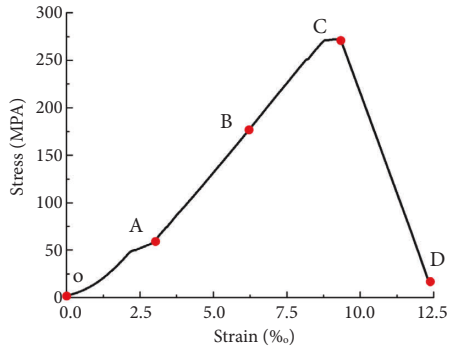	272.40	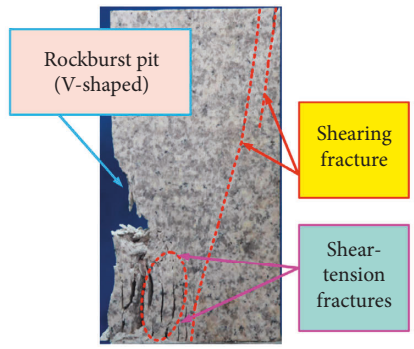
3.0 (*Z*-3)	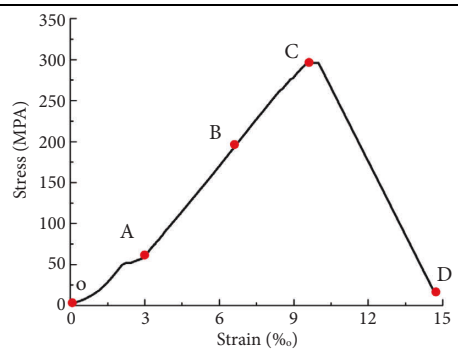	296.52	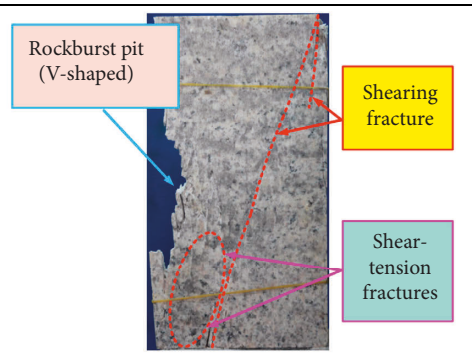
5.0 (*Z*-4)	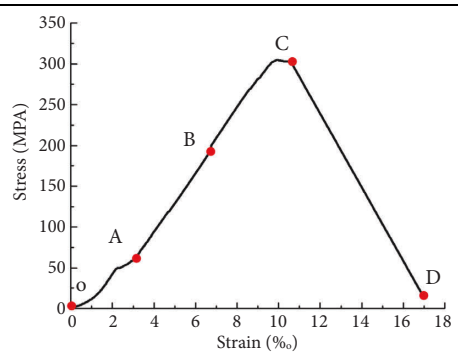	304.90	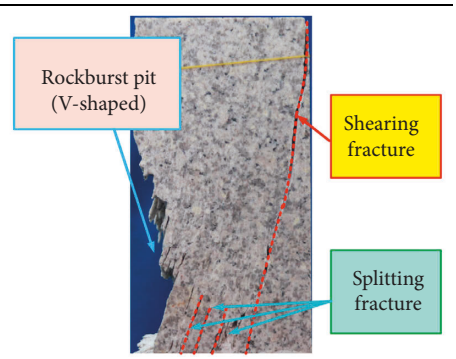

basically coincide, and the dissipation energy is close to zero, showing that the internal damage to the specimen at this stage is negligible. (c) Elastic deformation stage (stage II): With the continuous input of external energy, the micro-cracks inside the specimen begin to sprout, expand, and penetrate, and the dissipation energy begins to increase slowly. The total energy and elastic strain energy are positively correlated with the loading rate and are mainly stored in the specimen in the form of elastic strain energy. It indicates that the higher the loading rate is, the more obvious the brittle failure characteristics of specimen are, and the more complete the dynamic damage process is. (d) Prepeak unstable fracture stage (stage III): The accumulation capacity and rate of elastic strain energy are significantly greater than

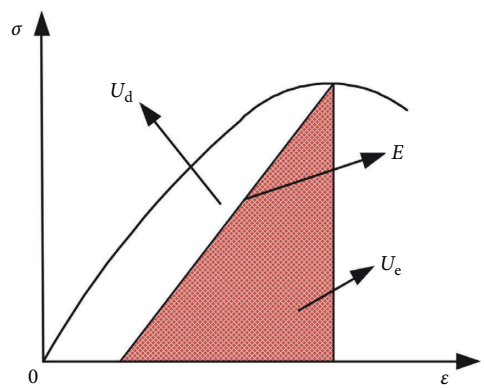

Figure 5: Stress-strain relation curve of rock [18].

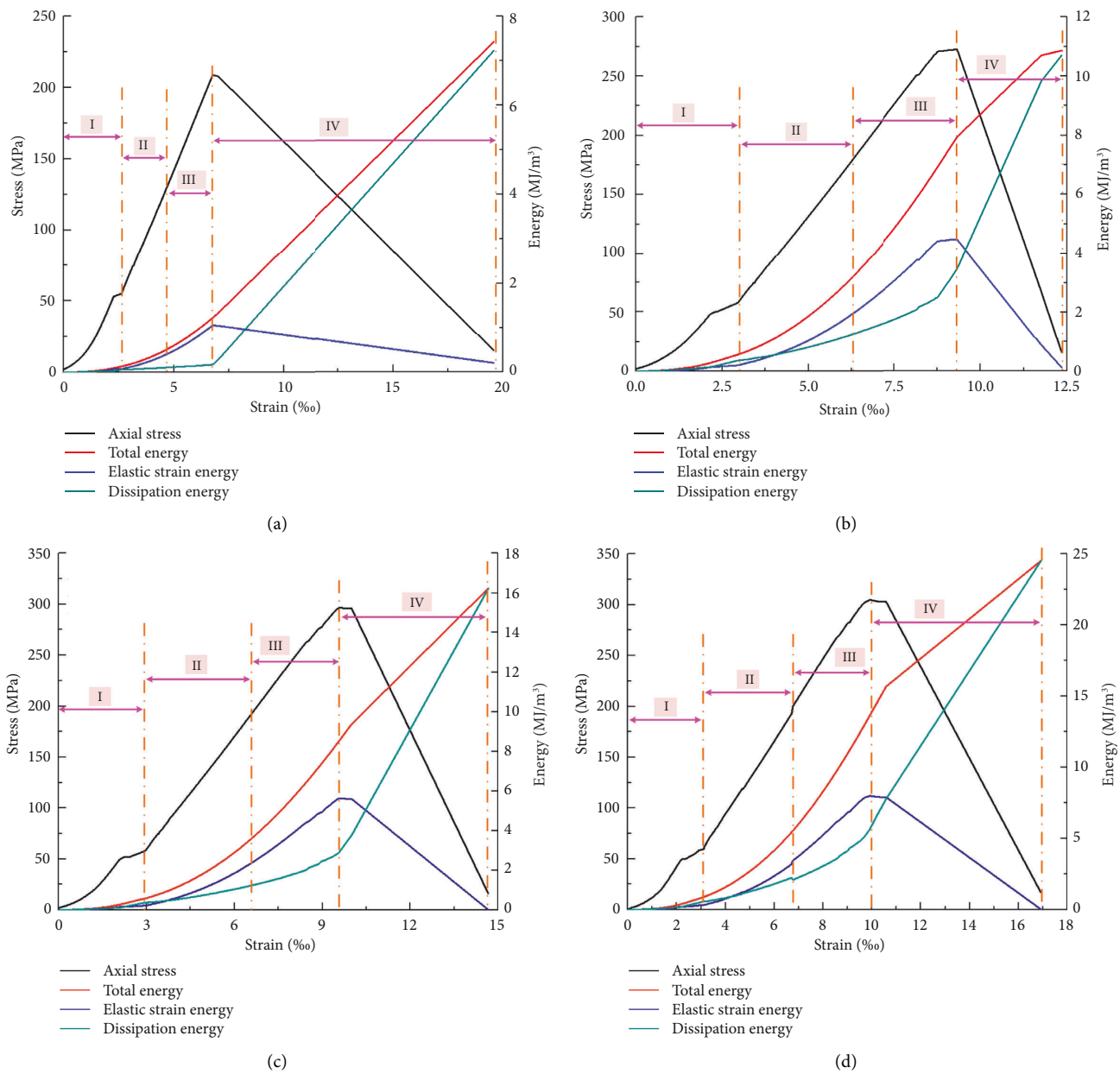

Figure 6: Energy evolution process of specimen with different loading rates during rockburst. (a) 0.05 MPa/s; (b) 1.0 MPa/s; (c) 3.0 MPa/s; and (d) 5.0 MPa/s.

the dissipation energy, and as the loading rate increases, the difference between the two values gradually increases. It indicates that the energy behavior of the specimen during prepeak stress process is primarily energy accumulation, and a part of the elastic strain energy is converted into fragment ejection kinetic energy in a small proportion, and the majority of elastic strain energy is converted into dissipation energy of rock cracking and sliding, and particle ejection begins to occur on the unloading face of specimen. (e) Postpeak failure stage (stage IV): When the peak stress is reached, the elastic strain energy curve decreases linearly while the dissipation energy curve increases linearly. This is mainly due to the instantaneous release of elastic strain energy accumulated in the specimen before the peak, and the dissipation energy increases sharply, leading to the formation of a macroscopic rupture surface through the crack and the destabilization of the specimen. It indicates that the energy behavior of specimen failure process is mainly reflected by energy release and energy dissipation. For specimen Z-1, the unloading face appears to be stable and slow slabbing failure. For other specimens, the fragments in the unloading face ejected at a relatively fast rate, and a rockburst dynamic disaster occurred. This further indicates that only a very small portion of the elastic strain energy stored before the peak of the specimen during the rockburst is converted into kinetic energy for fragment ejection, and the majority of the elastic strain energy is converted into fragment dissipation energy during the rockburst ejection failure.

From the aforementioned experimental tests, it is evident that the elastic strain energy increases gradually as the loading rate increases, the greater the accumulation of elastic strain energy, the greater the susceptibility of rockburst. It can be seen that the loading rate has a significant impact on the energy accumulation, so it is necessary to convert the loading rate under the laboratory scale to the speed of the working face under the engineering scale, take appropriate measures to reduce the elastic strain energy accumulated in the surrounding rock mass, and gradually release the energy in the surrounding rock mass to reduce the possibility of rockburst.

4.2.2. Energy Evolution Law at the Peak Stress of Specimen under Different Loading Rates. Figure 7 depicts the variation laws of total energy, elastic strain energy, and dissipation energy at the peak stress of the specimen under different loading rates. Table 3 displays the mathematical expressions of each energy characteristic value with the loading rate at the peak stress, where r denotes the loading rate.

As shown in Figure 7 and Table 3, (a) at the peak stress, the correlation coefficient values for each energy characteristic and the loading rate are all 0.999 (near to 1), showing a strong association. The change curve of elastic strain energy with an increase in loading rate exhibits a sharp increase followed by a slow rise. The overall change trend of total energy and dissipation energy curve is more similar, exhibiting a sharp increase followed by a short decline and then a sharp increase, with a cut-off value in the range of 1~3 MPa/s. (b) For the peak analysis of each energy characteristic, the elastic strain

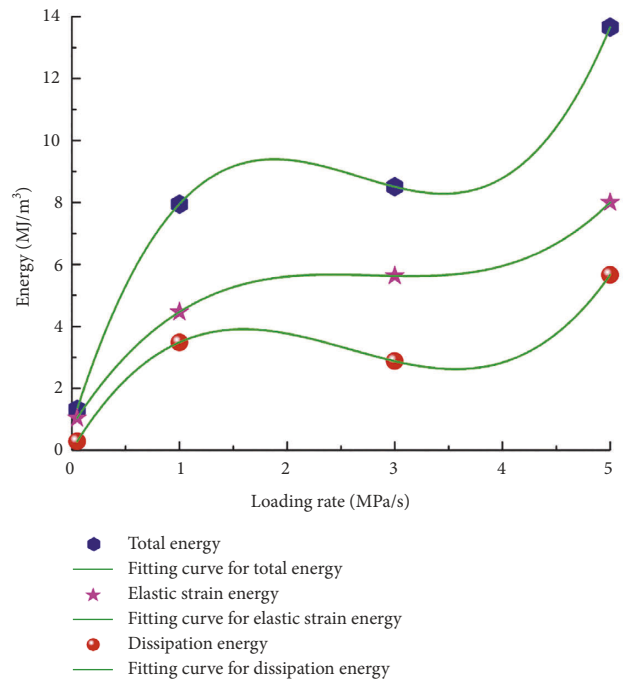

Figure 7: Energy variation characteristics at the peak value of specimen with different loading rates.

energy accumulation capacity, and the dissipation energy release capacity of the specimen are closely related to the loading rate effect. With a rise in loading rate, the specimen in the process of energy accumulation is accompanied by dissipation energy, more external input energy, and elastic strain energy released into the kinetic energy of breaking rock block, resulting in rockburst phenomenon. In addition, the greater the loading rate, the more pronounced the fracture traces remaining on the specimen failure surface, the more fully developed the through cracks, the more obvious the brittle failure characteristics, and the greater the failure strength. (c) Under different loading rates, the dissipation energy is significantly less than elastic strain energy. The lower the loading rate, the slower the expansion rate of specimen internal microfractures development. The longer the specimen damage accumulation time, resulting in the higher degree of internal deterioration of the specimen. When the loading rate progressively increases, it accelerates the expansion rate of microcracks and reduces their expansion time, so their development and expansion in a short period of time is insufficient. Therefore, raising the loading rate will minimize the degree of damage deterioration inside the rock, which is the fundamental reason for the regular variation of elastic strain energy and dissipative strain energy at the peak with the loading rate.

4.3. Energy Conversion Characteristics of Rockburst

4.3.1. Energy Conversion Characteristics of Specimens under Different Loading Rates. U_e/U is defined as the energy storage limit of rock, which is used to characterize the ability of the rock to release elastic strain energy during the

Table 3: Mathematical expression of energy eigenvalue and loading rate.

Name	Fitting curve	Correlation coefficient
Total energy	$U = 0.574r^3 - 4.594r^2 + 11.191r + 0.776$	0.999
Elastic strain energy	$U_e = 0.237r^3 - 1.986r^2 + 5.439r + 0.773$	0.999
Dissipation energy	$U_d = 0.337r^3 - 2.609r^2 + 5.752r + 0.003$	0.999

postpeak stage. The greater the rock's energy storage capacity, the less susceptible it is to energy-driven failure. U_d/U is defined to characterize the energy dissipation capability of rock. The higher the ratio, the easier the damage occurs inside the rock and the lower the energy storage capacity. Figure 8 depicts the energy conversion characteristics of the true triaxial rockburst test with different loading rates. Table 4 displays the energy values at the peak stress of specimens with different loading rates.

As shown in Figure 8 and Table 4, (a) The elastic strain energy conversion rate (U_e/U) decreases with increasing loading rate, whereas the dissipative energy conversion rate (U_d/U) increases with increasing loading rate. The average elastic strain energy conversion rate is 60.40%, whereas the average dissipative energy conversion rate is 39.60%, indicating that the elastic strain energy conversion rate is significantly greater than the dissipative energy conversion rate. Furthermore, combined with the failure mode of specimen can achieve the Z-2 specimen unloading faces V-shaped or step-shaped rockburst pits and its surface unevenness is much smaller than that of the Z-4 specimen. This demonstrates that in the rockburst test, the greater the elastic strain energy conversion rate and the lower the dissipation energy conversion rate, the more serious the rockburst. (b) As the loading rate increases, the development of microcrack expansion is insufficient, and the accumulation of elastic energy will be released in the form of particle ejection or fragmentation exfoliation, the greater the energy released when the rock is failure. This also demonstrates that the higher the loading rate is, the less the energy consumption of crack development and propagation of rock samples is, resulting in more elastic strain energy that can be converted into fragment ejection kinetic energy, leading to the occurrence of rockburst dynamic disaster. (c) Combined with the energy evolution characteristics of specimen under different loading rates, the initial compression stage elastic strain energy growth rate is greater than the growth rate of dissipation energy before the peak, and the majority of the external energy input is converted into elastic energy. In the postpeak failure stage, the elastic energy is released rapidly, the dissipation energy increases at a higher rate, and all the external energy input is converted into post-peak dissipation energy. This implies that the greater the loading rate, the amount of energy accumulated before the specimen failure is stored in the specimen in the form of elastic energy, the greater amount of energy released after the specimen destruction.

4.3.2. Conversion Rate of Energy Eigenvalues of Specimens with Different Loading Rates. The ratio of total energy increment ΔU, elastic strain energy increment ΔU_e, and dissipative energy increment ΔU_d to the corresponding time increment Δt of specimen between the loading-unloading onset point and the peak stress point is defined as the total energy conversion rate u, the elastic strain energy conversion rate u_e, and the dissipative energy conversion rate u_d [19, 20], respectively. The calculation expression is given as follows:

$$\begin{cases} u = \dfrac{\Delta U}{\Delta t}, \\ u_e = \dfrac{\Delta U_e}{\Delta t}, \\ u_d = \dfrac{\Delta U_d}{\Delta t}. \end{cases} \tag{3}$$

The energy conversion rates of specimen with different loading rates are shown in Figure 9. The mathematical expressions of u and loading rate are shown in Table 5; where, r is the loading rate.

As shown in Figure 9 and Table 5, (a) The correlation coefficient values for each energy eigenvalue conversion rate and loading rate are greater than 0.92, indicating a strong linear correlation between the two. The total energy conversion rate u, the elastic strain energy conversion rate u_e, and the dissipative energy conversion rate u_d are positively correlated with the loading rate. It indicates that as the loading rate increases, more energy is input to the specimen from the outside, the rock mainly undergoes shear failure, and the generation of shear cracks requires a high amount of energy consumption, resulting in a higher percentage of dissipative energy in the rock. (b) As the loading rate increases, the elastic strain energy accumulated inside the specimen increases, and as the external loading continues to grow, the resulting force is dispersed, resulting in a distinct type of energy transformation. This indicates that when the sum of external energy input to the specimen and the elastic strain energy release is greater than the dissipated energy required for rock fragmentation, the excess energy will be released as kinetic energy of fragments, specifically as loosening, spalling, throwing, or ejection of fragments. (c) Translating the loading rate at the test room scale into the working face boring rate during the underground cavity excavation should reduce the concentration of vertical stress in the tunnel surrounding rock mass, improve the bearing capacity of surrounding rock mass, control the deformation of surrounding rock mass, and enhance the stability of surrounding rock mass in order to lessen the seriousness of rockburst.

5. Numerical Simulation Analysis

5.1. Generation of Crystal Scale Fine Model

5.1.1. Geometry Model. Granite is a natural aggregate composed of mineral grains of varying sizes and shapes that have been accumulated by geological processes in

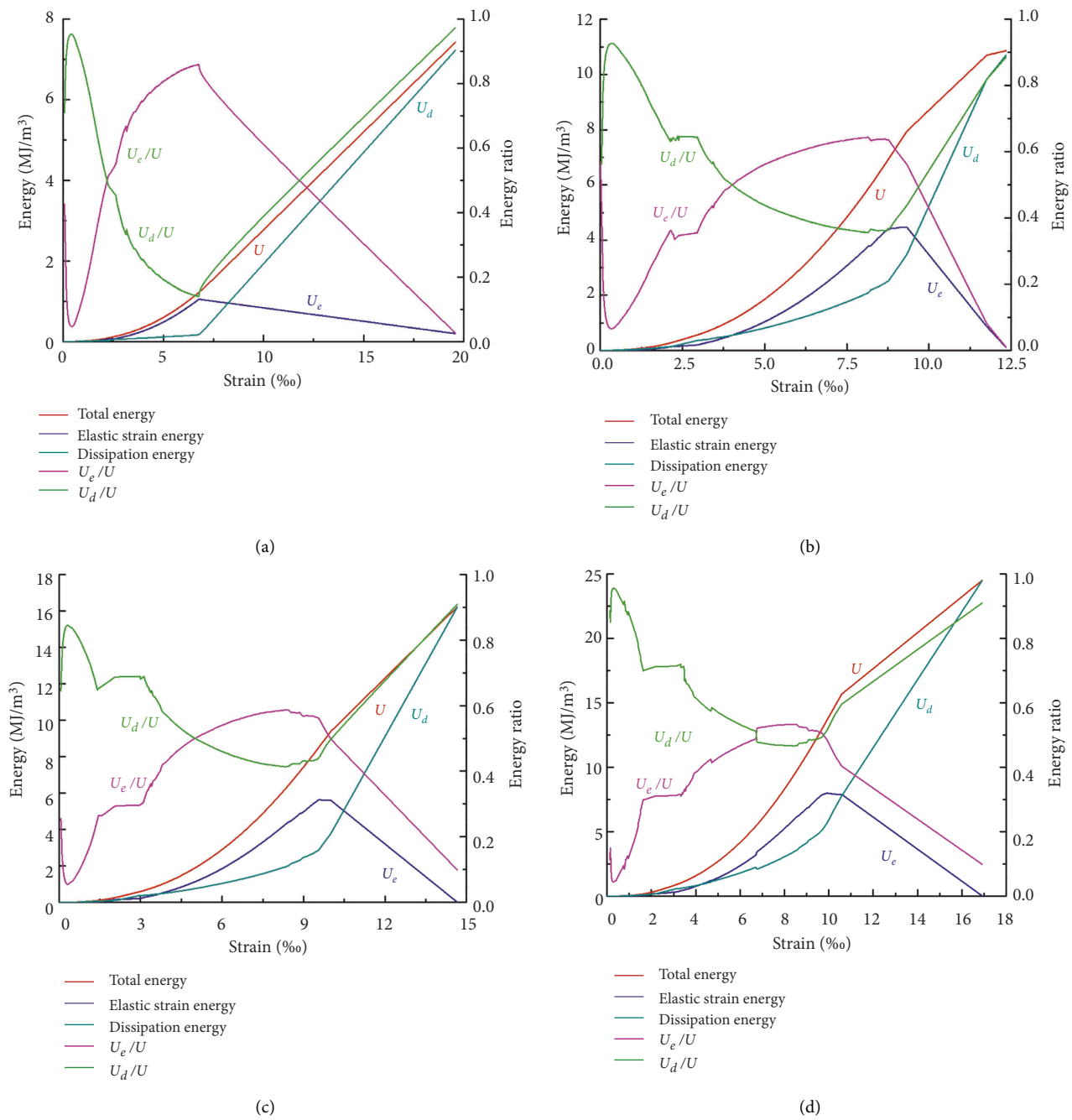

Figure 8: Energy transformation characteristics of specimen with different loading rates during rockburst. (a) 0.05 MPa/s; (b) 1.0 MPa/s; (c) 3.0 MPa/s; and (d) 5.0 MPa/s.

Table 4: Energy values at peak stress with different loading rates.

Loading rate (MPa/s)	U (MJ/m^3)	U_e (MJ/m^3)	U_d (MJ/m^3)	U_e/U	U_d/U
0.05	1.324	1.040	0.284	0.785	0.215
1.0	7.947	4.464	3.483	0.562	0.438
3.0	8.506	4.729	3.777	0.556	0.444
5.0	13.660	7.001	6.659	0.513	0.487

accordance with particular laws. The grains that makeup granite rocks resemble polygons; hence, the polygon mesh is more consistent with the internal fine structure characteristics of the rock. With the help of 3D Voronoi subdivision profile technology and regularization technology, a crystal scale fine model (CSFM) is built that accurately

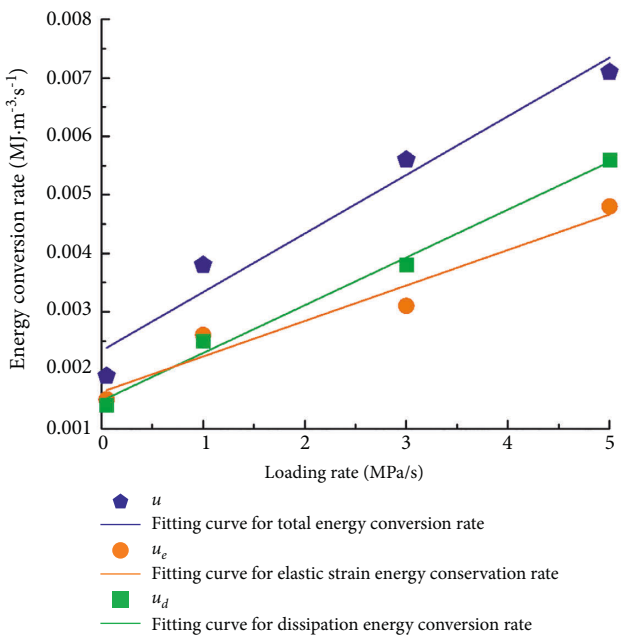

Figure 9: Energy conversion rate of specimen with different loading rates during rockburst.

Table 5: Mathematical expression of u and loading rate.

Energy conversion rate	Fitting curve	Correlation coefficient
u	$u = 0.0010r + 0.0020$	0.9620
u_e	$u_e = 0.0006r + 0.0016$	0.9472
u_d	$u_d = 0.0008r + 0.0015$	0.9924

represents the mineral grain composition. The CSFM is embedded into the secondary development block discrete element software platform by compiling the NEPER-DEM data interface calculation program using the FISH language embedded. The entire process of rockburst inoculation-occurrence-development and the energy evolution characteristics under true triaxial single face unloading conditions were studied. The simulation of interaction between mineral grains and failure process of microfracture eruption, expansion, and penetration will shed additional light on the rockburst formation mechanism.

Using a polarization microscope, the lithology and mineral composition of rock sample sections were determined. The granite specimen used in this study is mostly composed of potassium feldspar (48%), quartz (39%), plagioclase (8%), and black mica (5%). Due to the high content of quartz minerals and the brittle and hard texture, the granite sample has a material basis for brittle failure. The three-dimensional crystal scale fine model is shown in Figure 10.

5.1.2. Failure Criterion and Calibration Micro-Parameters. Crystal-scale cracks emerging from interparticle contact failure of CSFM can be further classified as tensile and shear cracks based on their fracture mechanisms. When the normal tensile stress of particles within a mineral crystal exceeds the tensile strength, tensile failure occurs in interparticle contact and produces intracrystalline tensile cracks. When the tangential shear stress of particles within a mineral crystal exceeds the shear strength, shear failure occurs in interparticle contact and produces intracrystalline shear cracks. This work uses the maximum tensile strain criterion and the SMP criterion to determine the methodologies for determining tensile and shear failure of the contact surface.

In this paper, Weibull distribution functions are introduced to describe the rock and joint mechanical parameters. A data interface program is prepared in FISH language to assign multiple sets of lithological parameters conforming to the Weibull distribution to the model. Firstly, an array of coefficients conforming to the Weibull distribution is generated. Secondly, suitable fine mechanical parameters are obtained by the "iterative test method" [21]. Finally, element k is randomly taken from the coefficient array as the Weibull distribution coefficient, and the coefficient k is multiplied by the average value of each component of the parameter to obtain multiple sets of rock mechanics parameters conforming to the Weibull distribution.

Tables 6 and 7 display the fine mechanical parameters of various mineral grains derived from the calibration results [22]. In Table 7, K_n is the contact normal stiffness, K_s is the contact shear stiffness, J_T is the contact tensile strength, J_C is the contact cohesion, and φ_r is the contact residual friction angle.

5.2. Comparison and Analysis of Stress-Strain Curve and Failure Mode of Rock Sample

5.2.1. Comparison and Analysis of Stress-Strain Curve of Rock Sample. Figure 11 compares the axial stress-strain curves of rock samples derived from physical experiments and numerical simulations.

From Figure 11, it is clear that (1) both the test curve and the simulation curve exhibit four stages: the initial compression stage, the elastic deformation stage, the prepeak unstable fracture stage, and the postpeak failure stage, and that the curve change trend is essentially identical. It demonstrates that the discrepancy between numerical calculation results and experimental results is not obvious and that the two curves are in good agreement. (2) As the loading rate increased, the peak strain and peak stress of rock sample exhibited an upward trend. This implies a positive correlation between the loading rate and the peak strain and peak stress of rock sample. Compared with the static brittle failure rock sample no. Z-1, the typical stress-strain curve of rock samples with ejection failure has an obvious yield platform, and the change is gentle and maintains a relatively stable state. (3) Analysis of the macroscopic failure process of rock sample: under the same stress path, the No. Z-1 granite specimen presents static brittle failure by slabbing, whereas the other granite specimens present dynamic failure by rockburst. On the typical stress-strain curves of granite specimens with different grain sizes, five characteristic points ($A \sim E$) were selected to depict the different stages experienced by rock samples during failure process. This

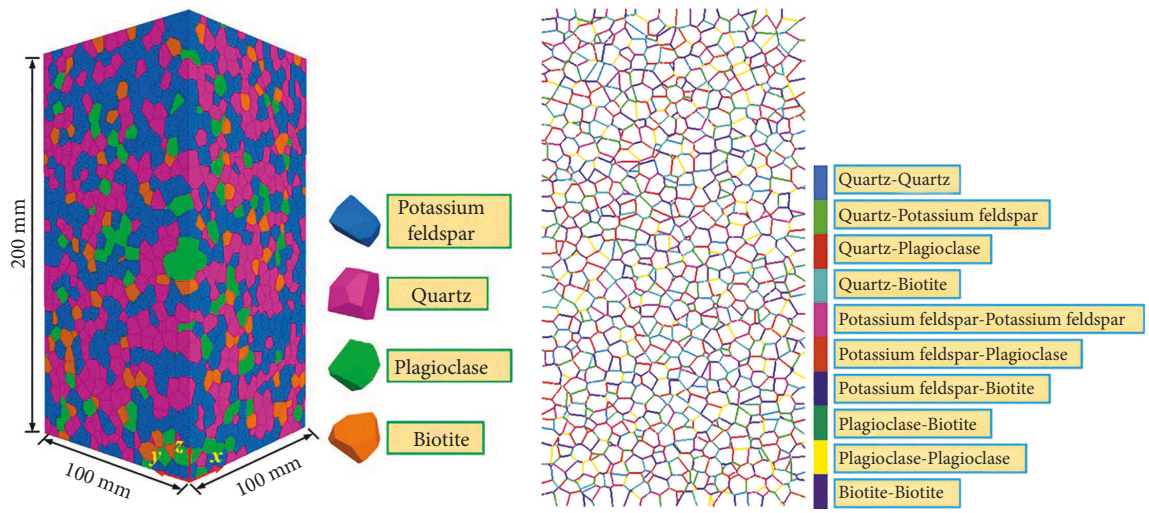

(a) (b)

Figure 10: Three-dimensional crystal scale fine model. (a) The 3D numerical rock specimen used with the grains assigned as potassium feldspar (blue), quartz (pink), plagioclase (green), biotite (peach) (as guided by the modal composition of the studied granite, the allocation of minerals is performed in a random manner). The outline of the polyhedral (the grains) can be seen. (b) 2D slice of a cube numerical specimen showing the different grain-to-grain contacts (color figure online).

Table 6: Microscopic parameters of mineral grains.

Mineral composition	Bulk modulus (GPa)	Shear modulus (GPa)	Poisson's ratio
Quartz	38.2	43.3	0.20
Potassium feldspar	55.6	29.5	0.25
Plagioclase	45.6	27.3	0.26
Biotite	59.7	42.3	0.27

Table 7: Microscopic parameters of grain contacts.

Contact	K_n (GPa/mm)	K_s (GPa/mm)	J_T (MPa)	J_C (MPa)	φ_r (°)
Quartz-quartz	836	418	47.69	201	8
Quartz-potassium feldspar	561	281	46.31	198	8
Quartz-plagioclase	502	251	32.59	187	9
Quartz-biotite	452	226	46.36	179	7
Potassium feldspar-potassium feldspar	365	183	52.26	169	8
Potassium feldspar-plagioclase	469	235	45.46	185	9
Potassium feldspar-biotite	359	180	32.15	179	9
Plagioclase-plagioclase	452	225	30.26	194	8
Plagioclase-biotite	587	294	29.68	161	7
Biotite-biotite	550	275	61.57	171	8

further verifies that the numerical simulation is in good agreement with the failure process variation of experimental test.

5.2.2. Comparison and Analysis of Failure Mode of Rock Sample. Figure 12 depicts a comparison between numerical simulation and experimental results for the ultimate failure modes of rock samples.

From Figure 12, it can be seen that (1) The characteristics of rock sample failure mode obtained from the numerical simulation under different loading rates are essentially the same as the results of experimental test. It indicates that the crystal scale fine model can better simulate the main macroscopic cracks that lead to the final failure of rock sample, particularly in the final failure mode of specimen, which demonstrates a high degree of agreement with the experimental test. (2) The numerical simulation reveals that the failure modes of rock samples primarily consist of tensile, shear, and tensile-shear composite failure. As the loading rate increases, the depth, and volume of rockburst pits increase, the splitting fractures become more fully developed, the penetration of shear diagonal fractures increases, and the shear failure activity within the seam intensifies, which is consistent with the results of experimental tests. (3) In addition, the failure modes of rock samples produced from numerical simulations are comparable to those of experimental tests, which further verifies the

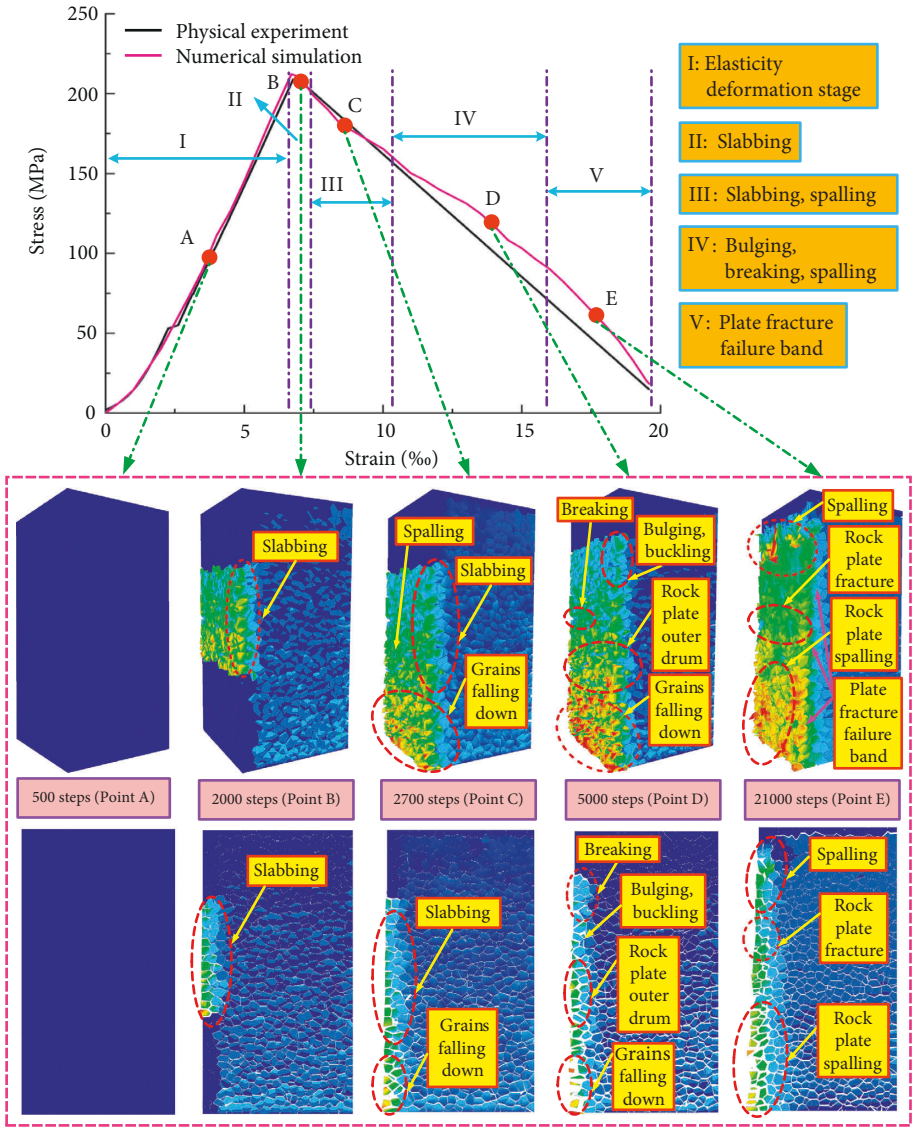

(a)

Figure 11: Continued.

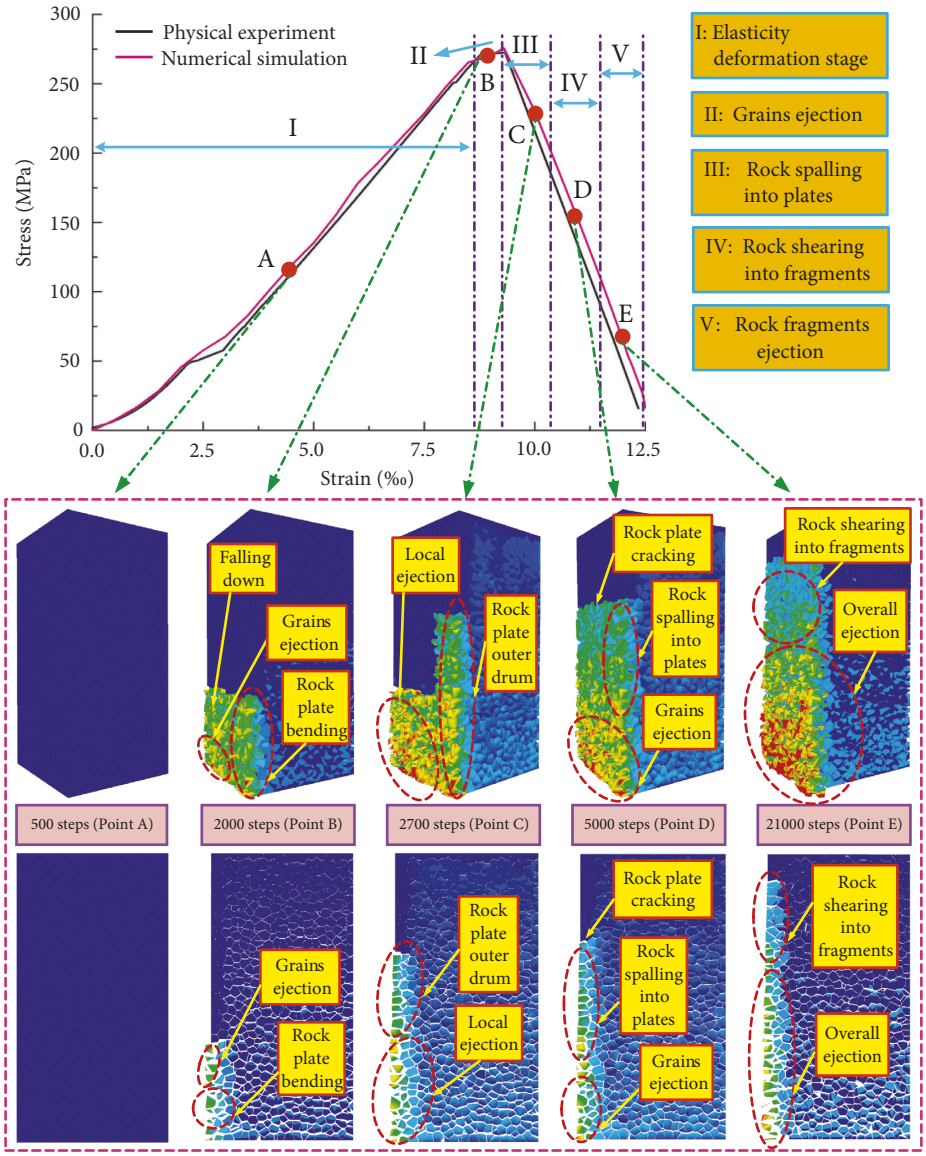

(b)

Figure 11: Continued.

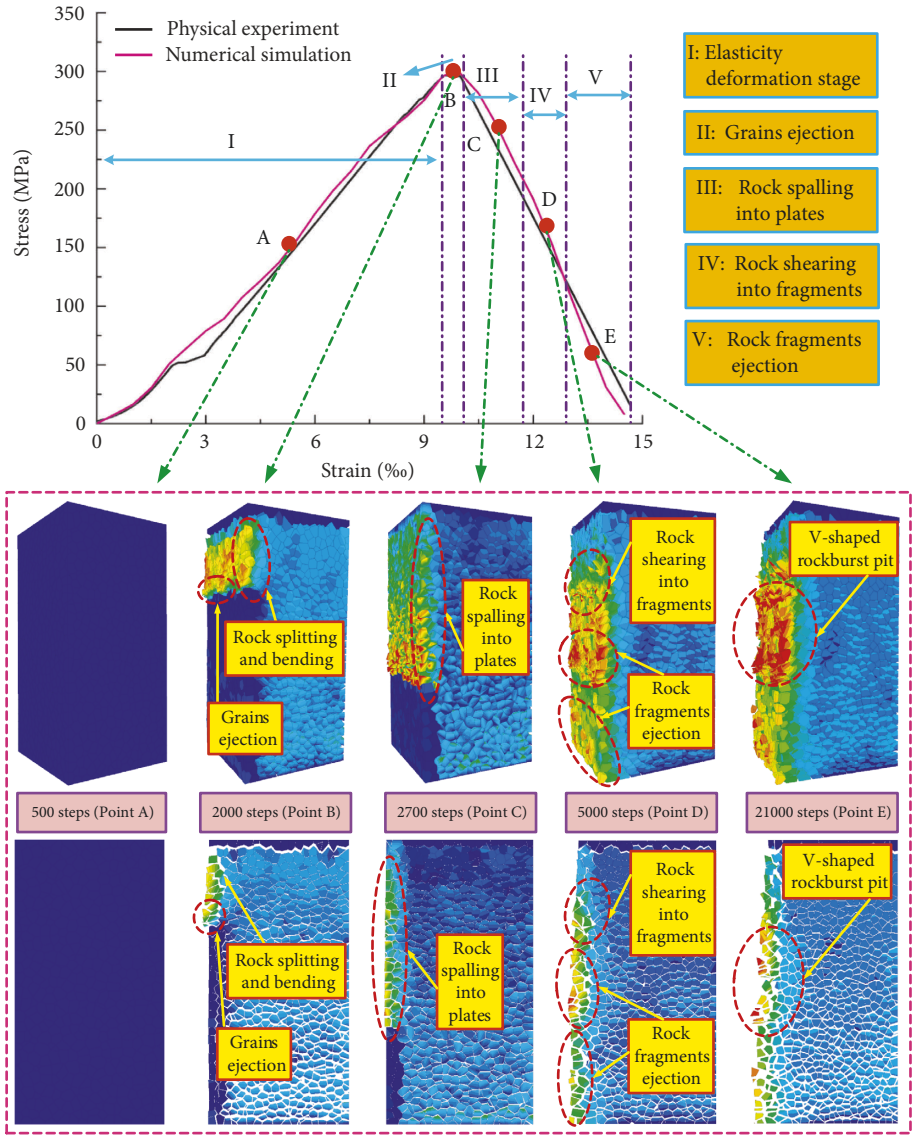

(c)

Figure 11: Continued.

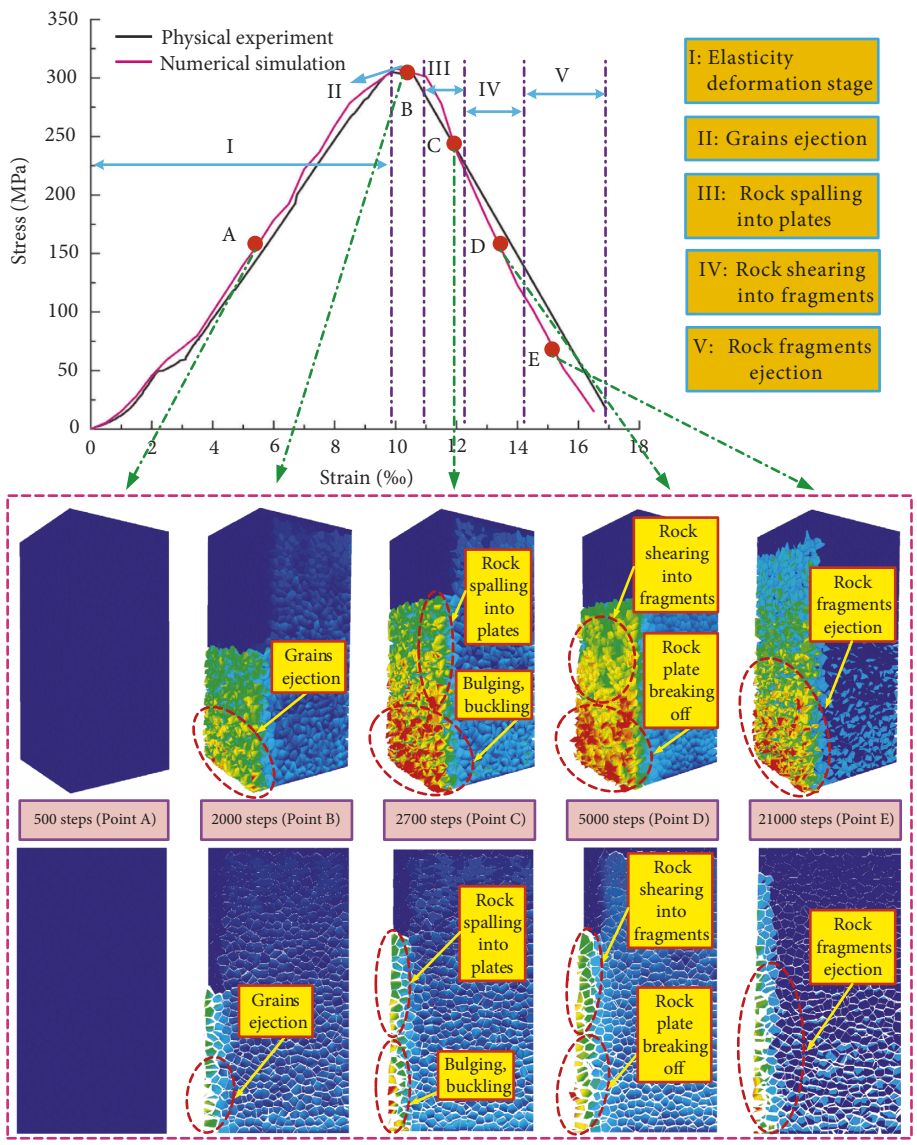

(d)

Figure 11: Numerical simulation and physical experiment stress-strain curve comparison and three-dimensional ejection photographs and corresponding central section of typical points (A–D). (a) 0.05 MPa/s; (b) 1.0 MPa/s; (c) 3.0 MPa/s; and (d) 5.0 MPa/s.

rationality of introduction of Weibull distribution function to describe the mechanical parameters of rock blocks and joints in this paper. The abovementioned also shows great agreement with the experimental results.

5.3. Loading Rate Effect on Evolution Process of Energy. The numerical calculation program is compiled by the FISH language embedded in the 3D discrete element software in order to monitor the elastic strain energy of each unit and the ejection kinetic energy of each block in real-time. Figure 13 shows the evolution process of the stored elastic strain energy and released kinetic energy of specimen with different loading rates.

According to Figure 13 and related data, we can find that: (1) the trends of elastic strain energy curves derived from experimental tests (Figure 6) and numerical simulations are essentially identical. The higher the loading rate, the more elastic strain energy is stored, and the limit of energy storage for specimens with loading rates of 1.0/3.0/5.0 MPa/s is 3.63 times, 4.59 times, and 5.56 times that for specimens with loading rates of 0.05 MPa/s, respectively. On the other hand, the growth rate of elastic energy of granite specimens in each group differs greatly, and the higher the loading rate, the faster the growth rate of elastic energy. (2) The ejection kinetic energy of specimens with different loading rates varied greatly. The ejection kinetic energy of specimens with loading rate of 5 MPa/s was significantly greater than that of other specimens. The final ejection kinetic energy of specimens with loading rate of 0.05/1.0/3.0 MPa/s decreased by 76.55%, 33.78%, and 6.76%, respectively, when compared to that of the specimens with loading rate of 5 MPa/s. This is

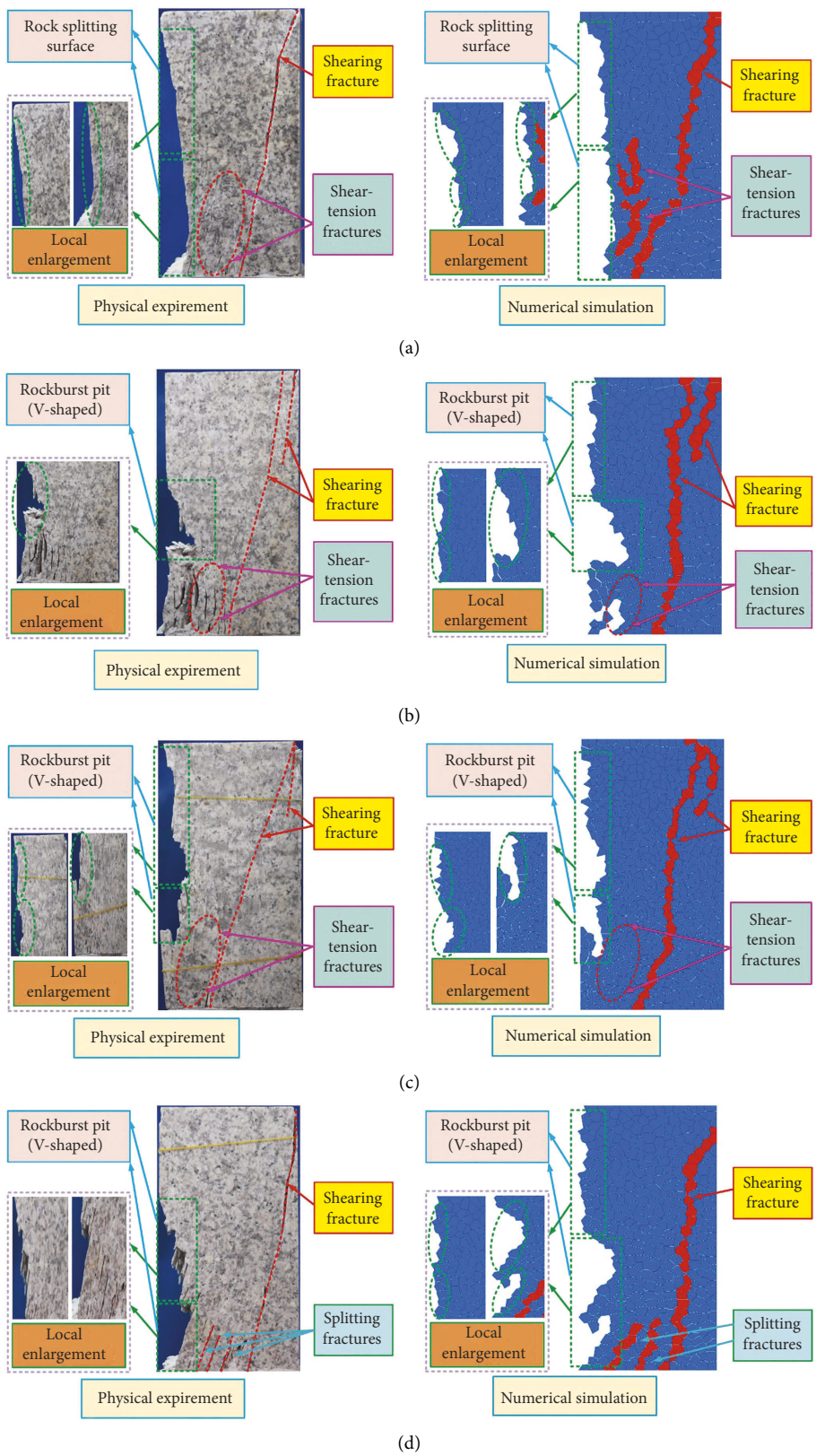

Figure 12: Comparison of rock specimen ultimate failure modes between experiment and simulation. (a) 0.05 MPa/s; (b) 1.0 MPa/s; (c) 3.0 MPa/s; and (d) 5.0 MPa/s.

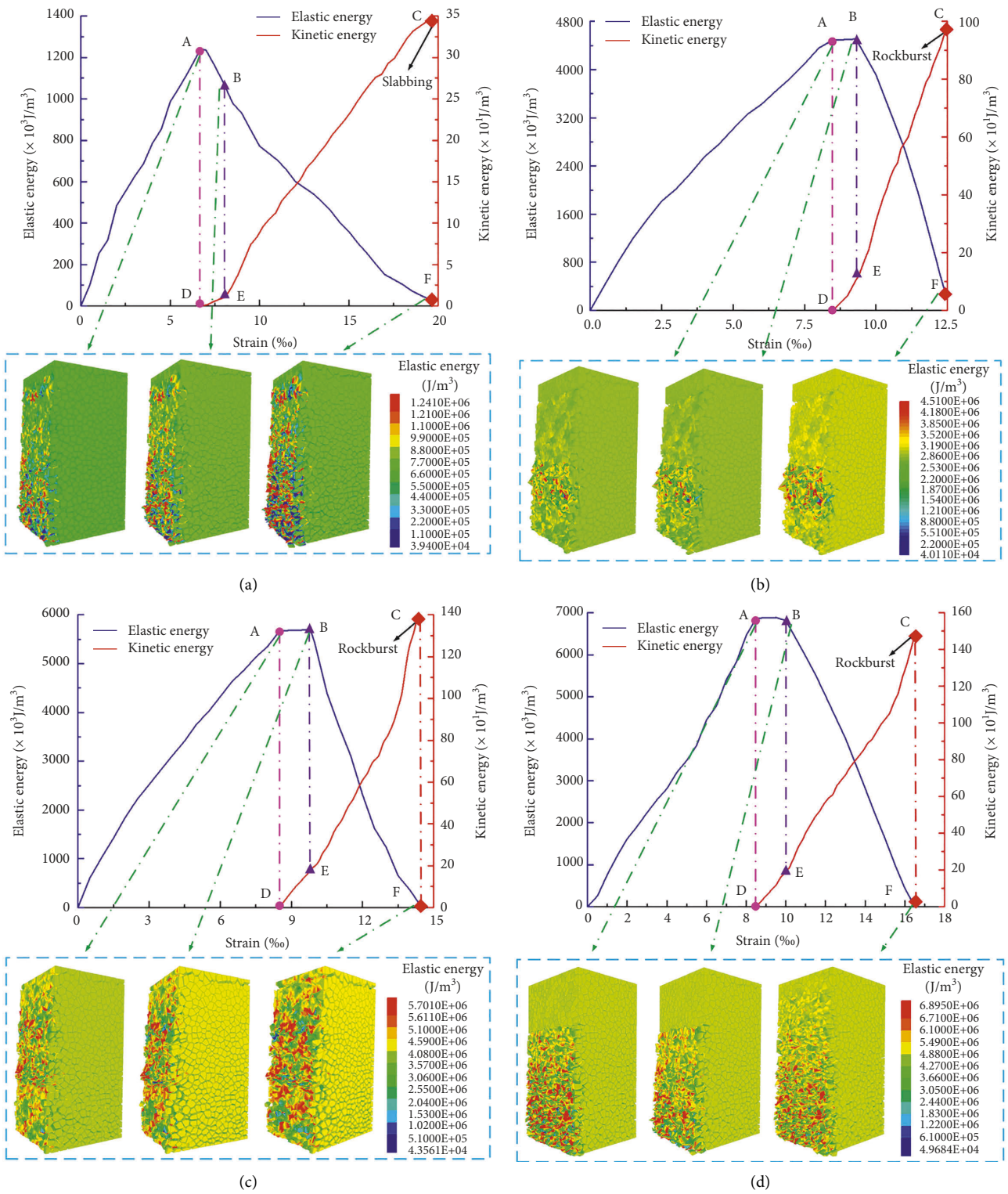

Figure 13: Evolution process of the stored elastic energy and released kinetic energy of specimen with different loading rates. (a) 0.05 Mpa/s; (b) 1.0 Mpa/s; (c) 3.0 Mpa/s; and (d) 5.0 MPa/s.

also the reason why 5 MPa/s loading rate specimens failure modes appeared relatively more ejected fragments of energy. (3) The elastic energy change curves of specimens subjected to loading rates of 1.0/3.0/5.0 MPa/s all contain two inflection points. These two inflection points correspond to the starting and ending points (points *A* and *B*) of the yield platform, respectively. The evolution of elastic energy grows approximately linearly at a low rate between the two inflection points (points *A* and *B*), while the evolution of kinetic energy grows approximately linearly at a high rate

between the D point and E point. The characteristics of the existing two inflection points and the high rate linear growth of kinetic energy evolution between point D and point E can provide precursor information for rockburst prediction. The kinetic energy is released abruptly in the postpeak stage, and at the moment of the elastic energy drops sharply, the kinetic energy suddenly increases from zero to a high value (points C and F). (4) The overall trends of elastic energy curves for specimens loaded at 1.0/3.0/5.0 MPa/s are similar, and the elastic energy decreases sharply after reaching its peak. The elastic energy curve of specimens loaded at 0.05 Mpa/s exhibited a sharp increase followed by a gradual drop.

6. Conclusions

(1) The energy evolution process of specimens under different loading rates can be summed up in four stages: the initial compression stage, the elastic deformation stage, the prepeak unstable fracture stage, and the postpeak failure stage. Among them, energy accumulation mainly occurs in the initial compression stage and elastic deformation stage, energy dissipation mainly occurs in the prepeak unstable fracture stage, and energy release mainly occurs in the postpeak failure stage. With the increase in loading rate, the specimen is in the process of energy accumulation accompanied by energy dissipation, more external input energy, and elastic strain energy released into the kinetic energy of breaking rock block, resulting in rockburst phenomenon.

(2) As loading rate increases, the elastic strain energy conversion rate (U_e/U) drops, whereas the dissipative energy conversion rate (U_d/U) increases. The higher the elastic strain energy conversion rate and the lower the dissipative energy conversion rate, resulting in a more powerful rockburst. The loading rate at the laboratory scale into the underground cavity excavation process of working face driving rate. It should reduce the excavation cycle footage, improve the bearing capacity of surrounding rock mass, control the deformation of surrounding rock mass, and increase the stability of surrounding rock mass in order to reduce the intensity of rockburst and delay its occurrence of rockburst.

(3) Using a three-dimensional discrete element numerical simulation platform, the entire process of inoculation-occurrence-development of rockburst was successfully simulated, supporting the conclusions of experimental physical testing. At a loading rate of 0.05 MPa/s, rock samples had static brittle failure by slabbing, at loading rates of 1.0/3.0/5.0 MPa/s, rock samples experienced varying degrees of rockburst failure. The rockburst ejection failure process can be summarized as four stages: grains ejection, rock spalling into plates, rock shearing into fragments, and rock fragments ejection. The failure mode of rockburst demonstrates multiplicity, that is, the unloading face appears as a rockburst pit due to tensile-shear failure, and splitting fractures due to tension, while the inside of the rock body appears as a penetrating shear fracture due to shear failure.

(4) The overall trend of elastic energy curves of specimens with loading rates of 1.0/3.0/5.0 MPa/s is relatively similar, with the elastic energy showing a sharp decrease after reaching the peak. The elastic energy curve of specimens with a loading rate of 0.05 MPa/s showed a sharp increase and then a slow decrease. The kinetic energy is released abruptly in the postpeak stage, and at the moment of the elastic energy drops sharply, the kinetic energy suddenly increases from zero to a high value. The high rate linear growth of kinetic energy evolution between the two inflection points can provide precursor information for rockburst prediction.

Data Availability

The data presented in this study are available on request from the corresponding author.

Conflicts of Interest

The authors declare that the research was conducted in the absence of any commercial or financial relationships that could be construed as potential conflicts of interest.

Acknowledgments

This research was funded by the National Natural Science Foundation of China (Grant nos. 52178388 and U1810203) and Natural Science Foundation of Henan Province (Grant no. 212300410146).

References

[1] M. Q. You and A. Z. Hua, "Energy analysis on failure process of rock specimens," *Chinese Journal of Rock Mechanics and Engineering*, vol. 21, no. 6, pp. 778–781, 2002.

[2] H. P. Xie, R. D. Peng, and Y. Ju, "Energy dissipation of rock deformation and fracture," *Chinese Journal of Rock Mechanics and Engineering*, vol. 23, no. 21, pp. 3565–3570, 2004.

[3] R. Yang, L. Jiakun, B. Zhou, and D. P. Ma, "Rock unloading failure precursor based on acoustic emission parametric fractal characteristics," *Lithosphere*, no. 11, Article ID 8221614, 2022.

[4] Z. Y. Chen, G. S. Su, J. W. Ju, and J. Q. Jiang, "Experimental study on energy dissipation of fragments during rockburst," *Bulletin of Engineering Geology and the Environment*, vol. 78, no. 7, pp. 5369–5386, 2019.

[5] C. P. Polito and H. H. M. Moldenhauer, "Energy dissipation and pore pressure generation in stress-and strain-controlled cyclic triaxial tests," *Geotechnical Testing Journal*, vol. 42, no. 4, pp. 20170437–20171089, 2019.

[6] R. D. Weyher, M. K. McCarter, and J. M. Wempen, "Energy partitioning following tensile failure in three-point loading tests of nugget sandstone specimens," *Mining, Metallurgy & Exploration*, vol. 37, no. 5, pp. 1499–1515, 2020.

[7] J. Lu, D. M. Zhang, G. Huang, X. Li, H. Gao, and G. Z. Yin, "Effects of loading rate on the compound dynamic disaster in

deep underground coal mine under true triaxial stress," *International Journal of Rock Mechanics and Mining Sciences*, vol. 134, Article ID 104453, 2020.

[8] X. F. Si, L. Q. Huang, F. Q. Gong, X. L. Liu, and X. B. Li, "Experimental investigation on influence of loading rate on rockburst in deep circular tunnel under true-triaxial stress condition," *Journal of Central South University*, vol. 27, no. 10, pp. 2914–2929, 2020.

[9] X. P. Zhang, Y. J. Jiang, G. Wang, J. C. Wang, X. Z. Wu, and Y. Z. Zhang, "Numerical experiments on rate-dependent behaviors of granite based on particle discrete element model," *Rock and Soil Mechanics*, vol. 37, no. 9, pp. 2679–3686, 2016.

[10] S. Lee, K. Ramos, and K. Matous, "Numerical study of damage in particulate composites during high-strain rate loading using novel damage model," *Mechanics of Materials*, vol. 160, Article ID 103944, 2021.

[11] Q. Ma, Y. L. Tan, X. S. Liu, Z. H. Zhao, D. Y. Fan, and L. Purev, "Experimental and numerical simulation of loading rate effects on failure and strain energy characteristics of coal-rock composite samples," *Journal of Central South University*, vol. 28, no. 10, pp. 3207–3222, 2021.

[12] L. Q. ., . Yu, Q. L. Yao, Q. Xu, W. N. Wang, Z. J. Niu, and W. D. Liu, "Experimental and numerical simulation study on crack propagation of fractured fine sandstone under the influence of loading rate," *Journal of China Coal Society*, vol. 46, no. 11, pp. 3488–3501, 2021.

[13] C. E. Fairhurst and J. A. Hudson, "Draft ISRM suggested method for the complete stress-strain curve for intact rock in uniaxial compression," *International Journal of Rock Mechanics and Mining Sciences*, vol. 36, no. 3, pp. 279–289, 1999.

[14] B. R. Chen, X. T. Feng, H. J. Ming et al., "Evolution law and mechanism of rockburtst in deep tunnel: time delayed rockburst," *Chinese Journal of Rock Mechanics and Engineering*, vol. 31, no. 3, pp. 561–569, 2012.

[15] X. C. Hu, G. S. Su, G. Y. Chen et al., "Experiment on rockburst process of borehole and its acoustic emission characteristics," *Rock Mechanics and Rock Engineering*, vol. 52, no. 3, pp. 783–802, 2019.

[16] G. S. Su, J. Q. Jiang, S. B. Zhai, and G. L. Zhang, "Influence of tunnel axis stress on strainburst: an experimental study," *Rock Mechanics and Rock Engineering*, vol. 50, no. 6, pp. 1551–1567, 2017.

[17] X. R. Ge and M. X. Hou, "A new 3D in-situ rock stresses measuring method: borehole wall stress relief method (BWSRM) and development of geostress measuring instrument based on BWSRM and its primary applications to engineering," *Chinese Journal of Rock Mechanics and Engineering*, vol. 30, no. 11, pp. 2161–2180, 2011.

[18] H. P. Xie, Y. Ju, and L. Y. Li, "Criteria for strength and structural failure of rocks baded on energy dissipation release principles," *Chinese Journal of Rock Mechanics and Engineering*, vol. 24, no. 17, pp. 3003–3010, 2005.

[19] D. Huang and Y. R. Li, "Conversion of strain energy in triaxial unloadingtests on marble," *International Journal of Rock Mechanics and Mining Sciences*, vol. 66, no. 1, pp. 160–168, 2014.

[20] G. Z. Yin, B. Ma, C. Liu, M. H. Li, J. Lu, and S. Y. Yin, "Effect of loading and unloading rates on mechanical properties and energy characteristics of sandstone under true triaxial stress," *Journal of China Coal Society*, vol. 44, no. 2, pp. 454–462, 2019.

[21] X. F. Li, H. B. Li, and J. Zhao, "3D polycrystalline discrete element method (3PDEM) for simulation of crack initiation and propa-gation in granular rock," *Computers and Geotechnics*, vol. 90, pp. 96–112, 2017.

[22] T. Xu, T. F. Fu, M. J. Heap, P. G. Meredith, T. M. Mitchell, and P. Baud, "Mesoscopic damage and fracturing of heterogeneous brittle rocks based on three-dimensional polycrystalline discrete element method," *Rock Mechanics and Rock Engineering*, vol. 53, no. 12, pp. 5389–5409, 2020.

Hindawi
Advances in Materials Science and Engineering
Volume 2022, Article ID 3196506, 12 pages
https://doi.org/10.1155/2022/3196506

Research Article

Study on Mechanical Properties and Acoustic Emission Characteristics of Sandstone under Freezing and Thawing

Ziyi Wang, Ping Liu, Chang Luo, Yichao Jia, and Zhen Chen

School of Mining, Guizhou University, Guiyang 550025, China

Correspondence should be addressed to Ping Liu; 373388719@qq.com

Received 12 July 2022; Revised 22 August 2022; Accepted 24 August 2022; Published 17 September 2022

Academic Editor: Depeng Ma

The cyclic freezing-thawing action in cold regions leads to the deterioration of rock damage, resulting in local damage and further threatening the safety of engineering. In order to study the degradation characteristics of green sandstone and yellow sandstone under freeze-thaw cycles from macroscopic and microscopic aspects, the sandstone of a mining area in Inner Mongolia was used as experimental material. The freeze-thaw cycles were divided into 20 times, 30 times, and 40 times. NMR images and mechanical test results of two different rock samples were analyzed by binarization, NMR, and mechanical test. The test results show that, except that the mass change is less than that of yellow sandstone, the physical index degradation degree of green sandstone is higher than that of yellow sandstone, and the frost resistance is less than that of yellow sandstone. The change of acoustic emission event rate of green sandstone is mainly in the elastic deformation stage and stable crack propagation stage, and the change of acoustic emission event rate of yellow sandstone is concentrated in the crack closure stage. In the loading process, the energy release trends of the two sandstones are similar; the 30 freeze-thaw cycles are the boundary of brittle-plastic transformation of green sandstone, and the increase of cumulative energy is the most obvious. The research results provide a theoretical basis for studying the rock failure mechanism and improving the stability of rock engineering in cold regions.

1. Introduction

In recent years, with the increase of construction efforts in Inner Mongolia, engineering activities have increased year by year, and there are many geological problems in cold regions. Among them, the most representative and key problem is rock freeze-thaw degradation, resulting in a series of disasters in cold regions. Different degrees of freeze-thaw disasters such as frost heaving cracking, freeze-thaw sliding, and slope instability bring great challenges to construction safety. Therefore, it is of great significance to study the damage and deterioration mechanism of freeze-thaw rock mass in Inner Mongolia to prevent further deterioration of engineering rock mass and understand the development law of freeze-thaw rock mass. The freeze-thaw cycle test of rock is one of the important methods to study the damage mechanism of freeze-thaw [1, 2]. Many scholars have made important contributions to the damage and deterioration of rock under the effect of freezing-thawing. In order to study the influence of freezing-thawing cycles on the dynamic tensile properties of sandstone, scholars used φ50 mm split Hopkinson pressure bar and three average loading rates to conduct dynamic splitting tensile tests on sandstone with different freezing-thawing cycles, and analyzed the failure characteristics and dynamic splitting tensile strength of sandstone [3, 4]. Jiang Haibo [5] in order to incorporate the freeze-thaw cycle test into the diversion tunnel project, under the conditions of the lowest freezing temperature of −40°C and the melting temperature of 20°C, two groups of different state andesite rock samples were tested, and the internal microstructure of rock samples under different freeze-thaw cycles was detected by magnetic resonance imaging. Zhou et al [6] combined macroscopic and microscopic methods with statistical methods to quantitatively analyze the damage degree of rock under freeze-thaw cycles and loads and established a fractal damage constitutive model considering the residual strength of rock. Liping et al. [7] studied the physical parameters and triaxial compression

mechanical properties of intact hard rock under different freeze-thaw cycles, with fine sandstone (UCS = 114.8 MPa) and coarse sandstone (UCS = 104.1 MPa) as representatives. In the work by Fang et al. [8], under freeze-thaw and loading conditions, the analytical expressions of model parameters and characteristic parameters in stress-strain curves under specific freeze-thaw cycles were established, and the attenuation model conforming to Newton 's law of material cooling was introduced. The relationship between elastic modulus, peak stress, and freeze-thaw cycles was developed. Si et al. [9] conducted a series of uniaxial compression tests on sandstone after freeze-thaw treatment. The purpose is to more quantitatively express the initial damage of rock after freeze-thaw treatment, study the influence of freeze-thaw damage on the crack propagation process of rock, and provide certain reference for the stability evaluation of rock engineering in cold regions. Qiao et al. [10] carried out uniaxial compression and acoustic emission synchronous test to study the deformation and failure characteristics of rock bridge of central locked specimen drilled in plateau in China. The effects of freeze-thaw cycles and rock bridge angles on fracturing and acoustic emission patterns were characterized. Based on orthogonal test method, Zhou et al. [11] designed a series of large-scale triaxial tests of soil-rock mixture under freeze-thaw environment. The influence of orthogonal test factors and confining pressure on the static characteristics of soil-rock mixture was analyzed by range and variance analysis. Lei et al. [12] studied the effect of freeze-thaw through a large number of shear tests. The effect of cyclic induced joint shear degradation on joint cohesion and friction Angle was considered. The variation law of shear strength parameters under freeze-thaw cycle was analyzed, and the evolution model of joint shear under freeze-thaw cycle was established. The cyclic property and joint durability of the model were further analyzed, and the feasibility of the model was also analyzed.

Based on the contribution of predecessors, this paper selects green sandstone and yellow sandstone in a mining area in Inner Mongolia as raw materials for this test specimen, and the geographical location of the mining area is shown in Figure 1. Through the core technology, the unified sample treatment and grinding are equivalent to the cylinder to form the A-F group. The samples are processed from the macro- and microaspects by the binary method, nuclear magnetic resonance (NMR), mechanical test, acoustic emission, and other methods, and the degradation mechanism of green sandstone and yellow sandstone under the action of freeze-thaw cycle is obtained, which has a certain reference value for preventing the further deterioration of rock mass in Inner Mongolia mining area and reducing the risk of engineering in cold regions.

2. Specimen Preparation and Experimental Scheme

The specimen of this test selects green sandstone and yellow sandstone from a mining area in Inner Mongolia as raw materials. Complete raw rock is selected on-site. Under the condition of avoiding its obvious cracks, a vertical core-taking machine is used to take out 50 mm diameter cores, and the raw materials are cut and processed by TY-450 stone sawing machine.The raw materials were uniformly processed into $\varphi 50\,\text{mm} \times 100\,\text{mm}$ cylindrical samples, and the end face was finally ground with a double-end grinding machine to ensure that the end face unevenness error was less than 0.05 mm. The green sandstone and yellow sandstone specimens were divided into three groups and numbered.

Figure 1: Geographical location of the mining area.

According to the actual working conditions of the mine in the cold area, the specimens of the two lithologies were put into the vacuum pressurized saturation device filled with water, frozen at −40°C for 6 hours, and then dissolved at 40°C for 6 hours. The period from the beginning of freezing to the end of dissolution was recorded as a cycle, with each cycle duration of 12 hours, as shown in Figure 2. The specimens were divided into 6 groups, with 3 specimens in each group. The freeze-thaw cycles mentioned above were carried out for 20, 30 and 40 times respectively, and the group numbers were marked as group A-F. Nuclear magnetic resonance system was used to measure each group of specimens after a freeze-thaw cycle, as shown in Figure 3.

3. Analysis of Test Results

3.1. Appearance Deterioration Characteristics of Specimens. After the six groups of specimens completed 20, 30, and 40 freezing-thawing cycles, their appearance deterioration degree was observed and analyzed, respectively. The freezing-thawing cycle results of yellow sandstone are shown in Figure 4, and the freezing-thawing cycle results of green sandstone are shown in Figure 5. Image binarization is a commonly used method in digital image processing. Through an appropriate threshold, the image contains only the target and background so that the changes in the appearance of time can be observed more intuitively. The local amplification results of the corresponding binarization samples are shown in Figure 6.

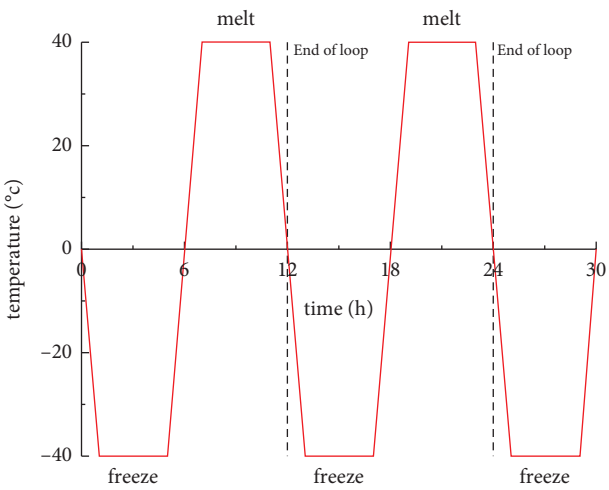

Figure 2: Schematic diagram of the freeze-thaw cycle.

Figure 3: NMR system.

Figure 4 shows that there is no obvious deterioration in the appearance of yellow sandstone during 40 freeze-thaw cycles. According to Figure 5, when freezing-thawing cycles were 20 times, the appearance of group A specimens did not change, which was basically the same as that after processing, indicating that freezing-thawing damage did not affect the outer surface of sandstone specimens. After 30 freezing-thawing cycles, the specimens in group B showed mild deterioration, and the surface of the specimens began to show microcracks and a small extent of skin peeling. Combined with Figure 6(a), it can be seen that the *B*-1 specimen produces horizontal cracks and body expansion, indicating that the pore water inside the specimen is frozen to generate ice crystals, and the pore space becomes larger when the ice crystal freezes and expands. However, the surface of the specimen is strongly bound, and the deterioration caused by the internal expansion changes does not seriously affect the surface, so only mild deterioration occurs. At the end of the freeze-thaw cycle, the specimens in group C showed a variety of deterioration forms and obvious grid-like staggered cracks. Combined with Figures 6(b)–6(d), it can be seen that both specimen *C*-1 and specimen *C*-3 have horizontal cracks, vertical cracks and reticular cross cracks, and there are a large number of microcracks in the specimen itself. The deterioration of freezing and thawing is intensified, and the particles with weak cementation on the microcracks are constantly falling off. The microcracks are continuously developed and expanded, and then developed to the surface of the specimen to form macro cracks. Small block shedding and oolitic structure appear in specimen *C*-2, which is considered to be due to the increase of freeze-thaw cycles, the continuous shedding of rock particles with weak cementation, and the formation of annular cracks. The deepening of circular cracks leads to the poor bonding ability between small block rock and the whole specimen, which leads to the shedding phenomenon. The shedding of rock particles near the crack has a sequence. The particles with poor cementation are preferentially shedding, and the particles with good cementation are subsequently shedding, so the oolitic phenomenon occurs near the crack of the specimen.

3.2. The Change of Specimen Quality and Porosity. The macroscopic physical properties of each specimen reflect the changes of the mesoscopic structure inside the specimen to a certain extent [1, 13, 14]. The quality of the specimen is one of the most important physical parameters. Under the action of freeze-thaw cycles, the change of specimen quality can be used as an important manifestation of specimen deterioration.

The average quality of the specimen is taken in each freeze-thaw cycle. In order to observe the overall law of the quality change of the specimen under different freeze-thaw cycles more intuitively, the test data of each specimen are statistically summarized, and the experimental data are fitted to obtain the relationship curve between the quality change rate and the number of freeze-thaw cycles. It can be seen from Figure 7 that the average mass of the two sandstones increased by about 1.6%. After 40 freeze-thaw cycles, the more the freeze-thaw cycles were, the more the water absorption of the specimen showed a continuous growth trend, and the mass change rate also increased. The tangent slope of the fitting curve of the mass change rate of the specimen increases with the increase of the number of freeze-thaw cycles, indicating that the water absorption of the specimen is less in the early stage and more in the later stage. The tangent slope of the fitting curve of the mass change rate of yellow sandstone decreases with the increase of the number of freeze-thaw cycles, indicating that the water absorption in the early stage of yellow sandstone is much larger than that in the later stage, and the average mass change rate of yellow sandstone is slightly larger than that of cyan sandstone.

Due to the different properties, shapes and particle sizes of rock particles, pores are formed in the space not filled by cement between particles. When the specimen is frozen, liquid water freezes into solid water, and the pore volume becomes larger due to frost heaving. When melting, solid water melts into liquid water. Because the original pore volume increases, the specimen will absorb more liquid water. In this way, the porosity increases continuously. However, due to the slight differences in the composition

(a) (b) (c)

Figure 4: Freeze-thaw cycle results of yellow sandstone specimens. (a) 20 cycles. (b) 30 cycles. (c) 40 cycles.

(a) (b) (c)

Figure 5: Freeze-thaw cycle results of green sandstone specimens. (a) 20 cycles. (b) 30 cycles. (c) 40 cycles.

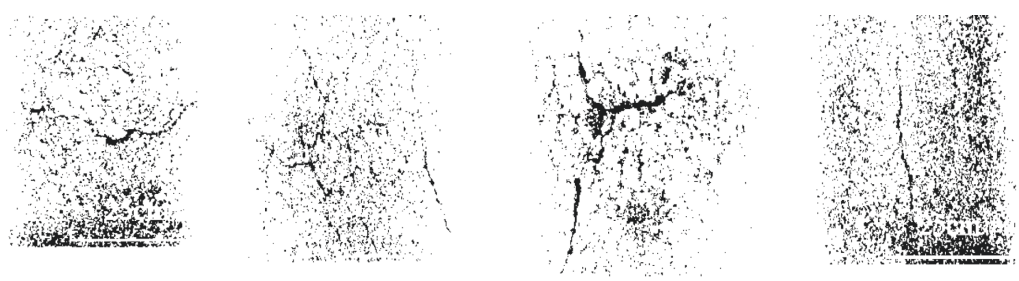

(a) (b) (c) (d)

Figure 6: Binary processing part of green sandstone specimen partial enlarged view. (a) *B*-1. (b) *C*-1. (c) *C*-2. (d) *C*-3.

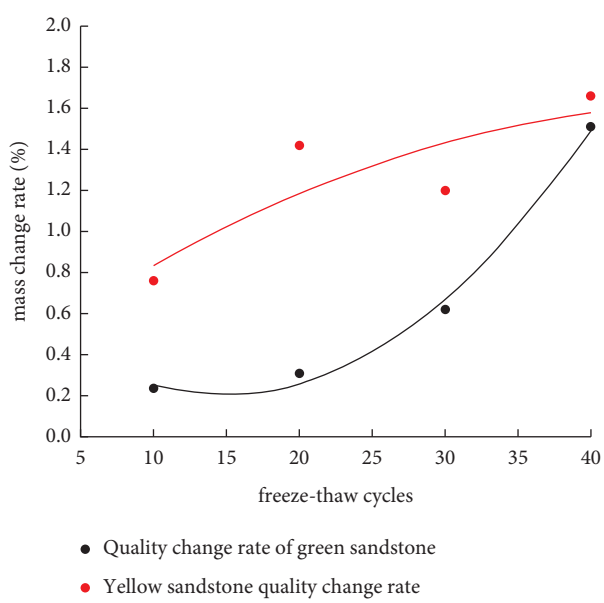

Figure 7: Fitting curve of mass change rate and number of freeze-thaw cycles.

and properties of different specimens, the influence of freeze-thaw cycles on the porosity changes is also different.

With the above method, the pore change rates of the two sandstone specimens are fitted, as shown in Figure 8. Combined with Figure 8, it can be seen that with the increase in the number of freeze-thaw cycles, the porosity of sandstone shows an overall upward trend, with an increasing trend. After the freeze-thaw cycle, the maximum variation of porosity of green sandstone is 2.06%, while that of yellow sandstone is only 0.55%. The porosity growth of the two sandstone samples shows a fluctuating upward trend, and is not completely positively correlated with the number of freeze-thaw cycles. With the increase of freeze-thaw cycles, the average porosity change rate will tend to be stable. From the change trend, the porosity will be stable at a relatively fixed value, which shows that the increase of rock porosity caused by freeze-thaw cycles is limited. The average porosity change rate of yellow sandstone is still slowly increasing, showing a linear growth trend, indicating that the freeze-thaw cycle can continue to increase the porosity of yellow sandstone.

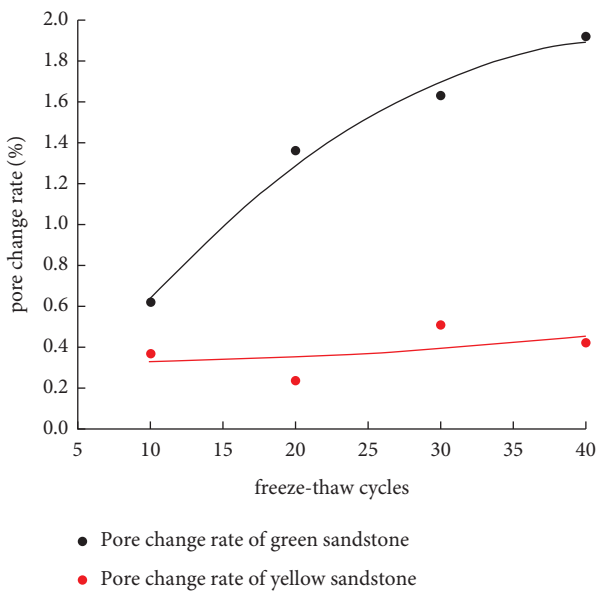

Figure 8: Fitting curve of porosity change rate and freeze-thaw cycles.

3.3. NMR T2 Spectrum Analysis. Nuclear magnetic resonance (NMR) technology reflects the pore structure by measuring the NMR relaxation signal of hydrogen atoms in pores. When the specimen is tested by nuclear magnetic resonance technology, the H proton in the rock pore fluid is subjected to an external magnetic field to make the atomic nucleus reach equilibrium and absorb electromagnetic energy. At this time, the H proton is excited by the radio frequency pulse to release the absorbed energy. This process produces a large number of energy signals, which is called relaxation. For fluids in pores, there are three independent relaxation types, namely volume relaxation, surface relaxation and diffusion relaxation. According to the above principle, the total transverse relaxation rate of NMR is expressed as follows:

$$\frac{1}{T_2} = \frac{1}{T_{2\ \text{free dom}}} + \rho_2\left(\frac{S}{V}\right)_{\text{pore}} + \frac{D\left(\gamma G T_E\right)^2}{12}. \quad (1)$$

Among them, $T_{2\text{freedom}}$ is free relaxation time of fluid (ms), S pore surface area (cm^2), ρ_2 is the relaxation intensity of the transverse plane (μm/ms), D is the diffusion coefficient, γ is the spin-magnetic ratio (rad/(s·T)), Gis the magnetic field gradient (Gs/cm), and T_E is echo time (ms). If the fluid in the pore is unique, the surface relaxation is much larger than the other two relaxations. The above formula can be simplified as follows:

$$\frac{1}{T_2} = \rho_2\left(\frac{S}{V}\right)_{\text{pore}}. \quad (2)$$

It can be seen from the above equation that the pore size is proportional to the distribution of T_2. At present, most domestic scholars classify pores by $T_2 = 10$ ms, pores corresponding to $T_2 < 10$ ms are micropores, large pores corresponding to $T_2 > 10$ ms, and the greater the signal strength, the more pores corresponding to T_2. The T_2 spectra of Group C and F sandstone specimens are shown in Figure 9.

It can be seen from Figure 9 that the T_2 distribution range of green sandstone rock samples is roughly between 10^{-1} ms and 10^4 ms, which is a state of coexistence of large and small pores. The T_2 distribution range of yellow sandstone rock samples is concentrated between 10 and 10^3 ms, indicating that the internal pores are mostly large pores. With the increase of freeze-thaw cycles, the T_2 distribution curves of green sandstone and yellow sandstone shifted to the right, but the right shift of green sandstone was more obvious than that of yellow sandstone, which indicated that the pores of green sandstone increased significantly under the influence of freeze-thaw cycles. The T_2 distribution curves of green sandstone samples are obvious bimodal structure, the first peak position is less than 10 ms, which is small pore, the second peak position is about 10^2 ms, which is a large pore. The T_2 distribution curve of yellow sandstone samples is a single peak structure, and the peak position is between 10^2 and 10^3 ms, which is large pores. According to the pore size of the spectrum peak position, the order is: yellow sandstone spectrum peak, green sandstone second spectrum peak, green sandstone first spectrum peak; the peak signal intensity of green sandstone sample is only close to 2000 n/a, while that of yellow sandstone sample is close to 5000 n/a. This shows that the proportion of pores of various sizes in the green sandstone sample is much lower than that in the yellow sandstone sample. With the increase of the number of freeze-thaw cycles, the signal strength of the first peak of the green sandstone decreased significantly, and the signal strength of the second peak increased significantly, which showed that the number of small pores decreased and the number of large pores increased with the increase of freeze-thaw cycles. The peak signal intensity of yellow sandstone increased, indicating that the pore size of yellow sandstone changed little, but the number increased significantly.

4. Deterioration Analysis of Sandstone Mechanical Properties

4.1. Experimental Design. After the surface moisture was wiped, two rubber bands were covered on the surface of the test rock sample to prevent sputtering after the rock sample was broken [15, 16]. When the rock sample is raised near the loading platform, the parameter setting of the testing machine is preloading 2 kN, and the loading rate is 0.1 mm/min. The uniaxial compression acoustic emission test is carried out by using SAS-2000 microcomputer controlled electro-hydraulic servo rock testing machine, as shown in Figure 10.

4.2. Analysis of Test Results. It can be seen from Figure 11 that with the increase of freeze-thaw cycles, the intersection of shear failure of the X-shaped conjugate inclined plane moves obviously to both ends after the failure of blue sandstone rock samples. During 20 freezing-thawing cycles, the failure mode of the sandstone sample was typical X-shaped conjugate inclined plane shear failure, but the intersection point moved up to 3/4 of the rock sample, and the upward movement was obvious. The failure mode of A-1 and A-3 specimens is still shear failure, but there is only one obvious main crack

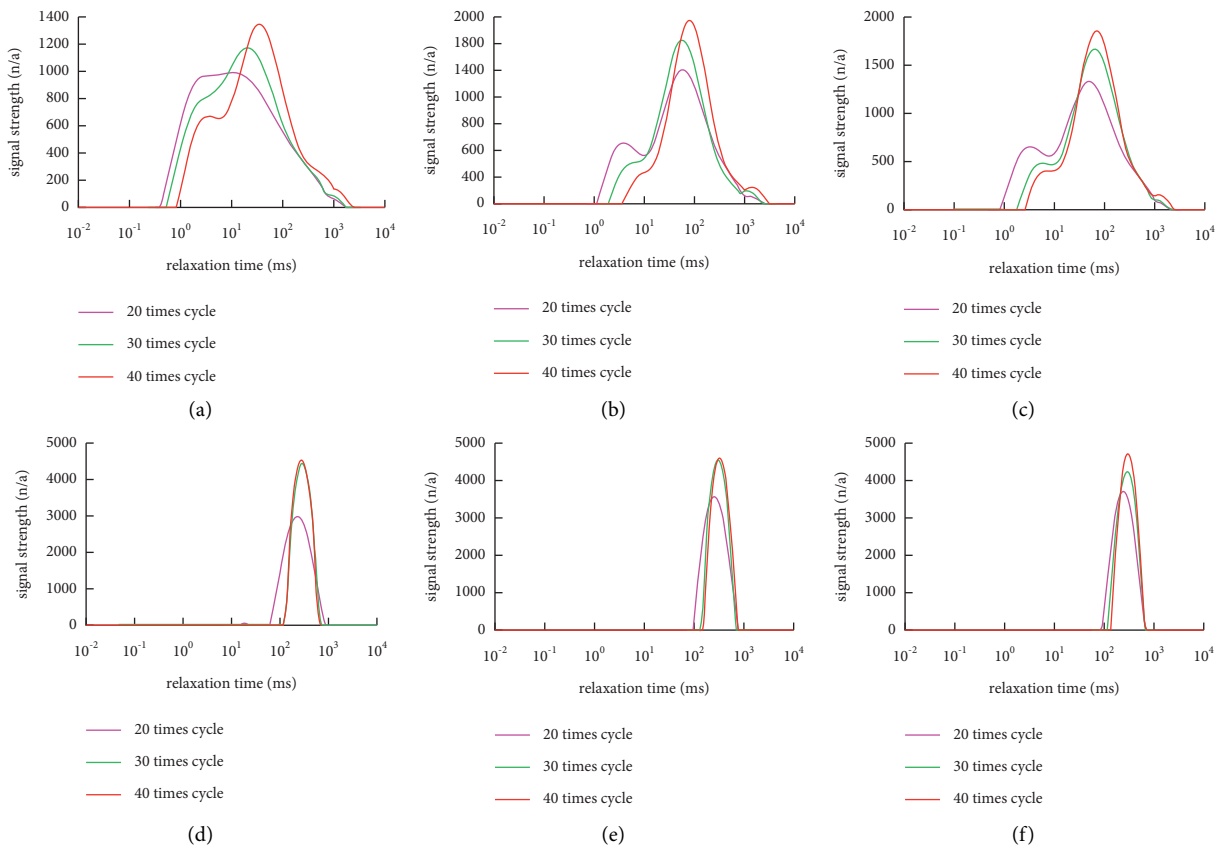

Figure 9: T_2 map of freeze-thaw cycles in group C and F. (a) C-1. (b) C-2. (c) C-3. (d) F-1. (e) F-2. (f) F-3.

Figure 10: Loading of the uniaxial compression specimen.

running through the rock specimen and obviously inclined, which belongs to typical single inclined shear failure, and a small number of short tensile cracks appear. It can be seen from Figure 11(b) that after 30 freeze-thaw cycles, the failure modes of specimens B-2 and B-3 are typical single-slope shear failure, but the number of tensile cracks increases, and their length also increases. The slope of the main crack of B-2 specimen increased slightly; the slope of the main crack of the B-1 rock sample is larger, and the tensile cracks appear more. The failure characteristics of the brittle rock are no longer obvious when the rock sample is destroyed. According to Figure 11(c), there was no obvious instability phenomenon in the whole loading process of the three rock samples after 40 freeze-thaw cycles, and there was basically no green sandstone particle powder after failure. At this time, the rock samples had shown plastic failure properties. The failure type is still single inclined plane shear failure, but the slope of the main fracture crack is very large, tends to be vertical, and accompanied by a large number of tensile cracks.

In summary, with the increase of freeze-thaw cycles, the change trend of the failure mode of green sandstone is as follows: X-shaped conjugate inclined plane shear failure ⟶ X-shaped conjugate inclined plane shear failure ⟶ monoclinic plane shear failure ⟶ monoclinic plane shear failure, which indicates that freeze-thaw will make the internal structure of rock change to a certain extent and then change the failure mode of rock.

The failure modes of yellow sandstone specimens under different freeze-thaw cycles are shown in Figure 12. It can be seen from Figure 12 that the failure mode of the yellow sandstone specimen is relatively simple, which is similar to that of green sandstone in 20, 30, and 40 freeze-thaw cycles. They are all single inclined plane shear failures and are accompanied by a small number of tension cracks. However, with the increase in freeze-thaw cycles, the slope of the inclined plane increases to a certain extent.

The axial stress-strain curve is an intuitive expression of the deformation law of rock specimen under external load. Figure 13 shows the stress-strain curves of green sandstone and yellow sandstone under different freeze-thaw cycles. According to Figures 13(a) and 13(d), the stress-strain curves of the two kinds of rock samples are similar and

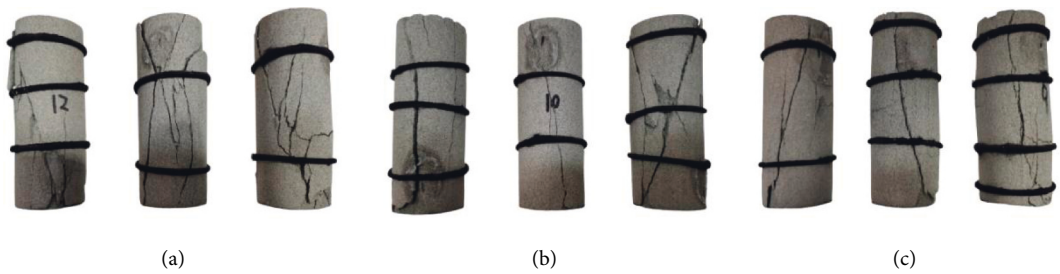

Figure 11: Uniaxial compression of green sandstone after freeze-thaw cycles. (a) Group A loading results. (b) Group B loading results. (c) Group C loading results.

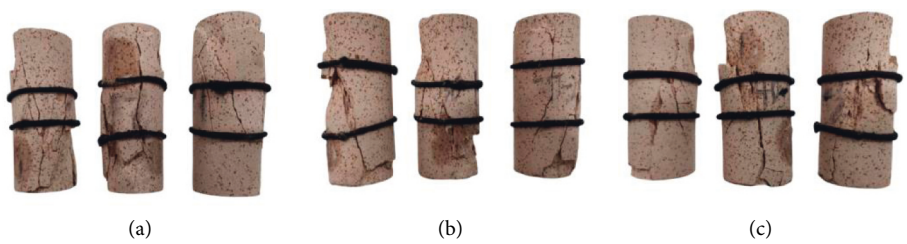

Figure 12: Uniaxial compression of yellow sandstone after freeze-thaw cycles. (a) Group D loading results. (b) Group E loading results. (c) Group F loading results.

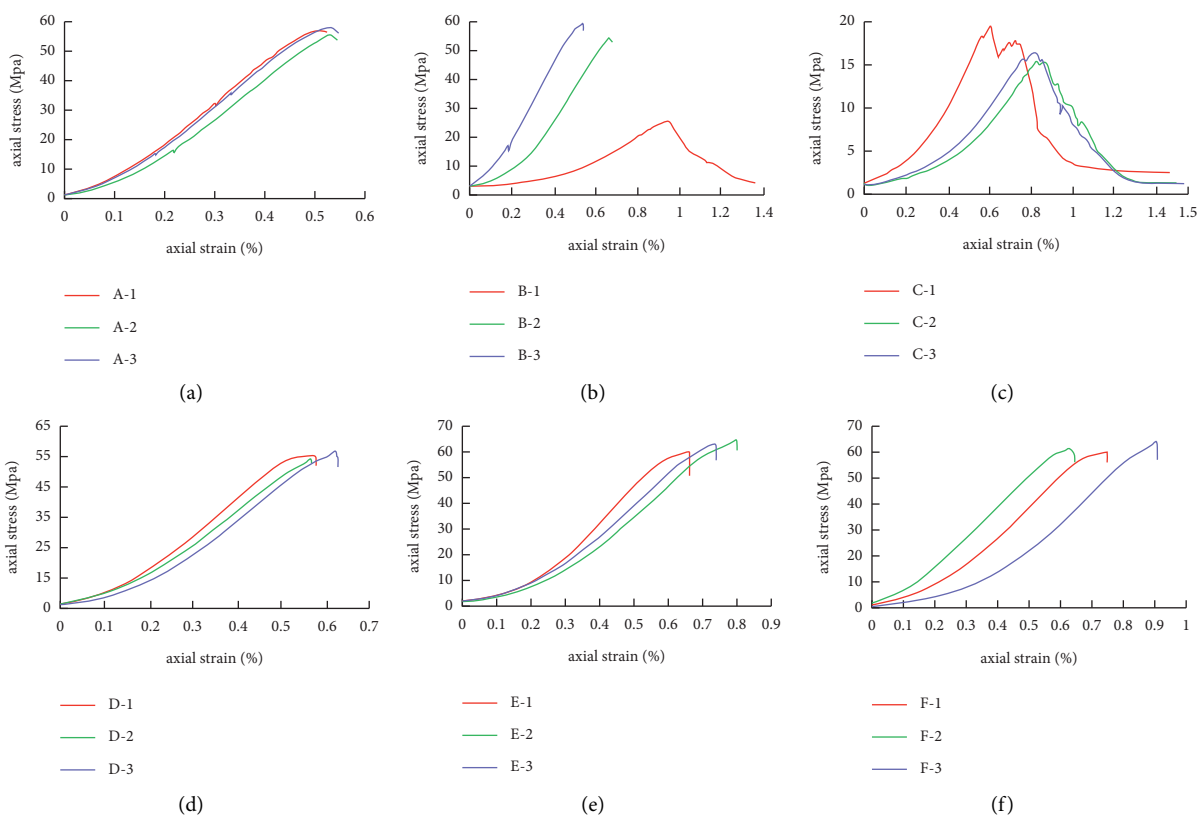

Figure 13: Axial stress-strain curve. (a) Group A specimens. (b) Group B specimens. (c) Group C specimens. (d) Group D specimens. (e) Group E specimens. (f) Group F specimens.

concentrated, and the discreteness is small, which shows that the mechanical properties of the rock samples are similar under the same number of freeze-thaw cycles. The peak strength of rock samples between different freeze-thaw cycles decreased to a certain extent, and the strain decreased slightly. It can be seen from Figure 13(b) that after 30 freeze-

thaw cycles, the stress-strain curve of green sandstone is inconsistent, and the curve trend of B-2 and B-3 specimens is similar, but the curve trend of B-2 is compared with B-3. The axial stress only decreases slightly, but the strain increases significantly; the curve trend of B-1 is similar to that of 40 freeze-thaw cycles. Compared with B-2 and B-3, the peak stress is significantly reduced and the axial strain is significantly increased. Figure 13(c) shows that the rock samples of 40 freeze-thaw cycles all show typical plastic failure characteristics, and the discreteness of the stress-strain curves of the three rock samples decreases slightly. Combined with the stress-strain curve of green sandstone, the rock sample begins to change from typical brittle failure characteristics to plastic failure characteristics during 30 freeze-thaw cycles, and the mechanical properties of the rock sample begin to change from brittle to plastic. Therefore, 30 freeze-thaw cycles can be used as the mechanical property boundary of green sandstone freeze-thaw degradation. According to Figures 13(d)–13(f), with the increase of freeze-thaw cycles, the peak stress of yellow sandstone rock samples gradually decreases, but the strain slightly increases, and the growth rate is between 0.1% and 0.2%. The specimen shows brittle failure characteristics as a whole, but with the increase in freeze-thaw cycles, it tends to transform into plastic failure. The curve discreteness of rock sample increases with the increase of freeze-thaw cycles.

It can be seen from Figure 14 that the overall trend of AE event rate of green sandstone rock samples after 20 freeze-thaw cycles is similar to the "U" type, that is, high event rate in the early stage, low event rate in the middle stage, and rapidly rising to high event rate in the late stage. After 30 freeze-thaw cycles, the whole loading process was a high event rate, and there was no obvious change trend. At this time, the stress-time curve was still the change trend of brittle rock, but the "U" type characteristics of AE event rate of rock samples after the first 20 freeze-thaw cycles had completely disappeared. After 40 freeze-thaw cycles, the AE event rate was opposite to the first 20 times. That is, the early low event rate, the middle high event rate, and the late event rate decreased gradually, showing a "convex "feature. With the increase in the number of freeze-thaw cycles, the AE events of stage II and III of Qingsha sandstone gradually increased, and the AE event rate increased, reaching the highest 120/s at 30 cycles (Figures 14(a) and 14(b)). The analysis is due to the continuous deterioration of freeze-thaw, the cementation between rock particles is weakening, the pores are more likely to rupture, and the microcracks are more likely to penetrate, resulting in more active acoustic emission activities. The internal deterioration of rock samples after 30 cycles was the most obvious; after 40 freeze-thaw cycles, the rock samples showed plastic failure characteristics. The AE event rate increases with the increase of stress, and the highest event rate is 118/s near stage IV.

It can be seen from Figure 15 that after 20 freeze-thaw cycles, the AE event rate of yellow sandstone shows the "√" type change trend of mid-early event rate, mid-low event rate, and late high event rate; after 30 freeze-thaw cycles, the loading process was high event rate, no obvious change trend, the overall gradually presented "U" type; after 40 freeze-thaw cycles, the overall trend of AE event rate is approximately "U" type. The AE event rates in the II and III stages of yellow sandstone increased slightly with the increase of freeze-thaw cycles; the AE event rate of stage IV and the AE event rate before and after peak stress are very stable, about 130/s. After 20 and 30 freeze-thaw cycles, the peak event rate appears in stage IV, and in 40 freeze-thaw cycles, the peak event rate appears in stage I. After 30 freeze-thaw cycles, the event rate of stage I was 2 times higher than that of 20 freeze-thaw cycles, which was close to the event rate near the peak stress. The event rate was high throughout the loading process, and there was no obvious change trend. After 40 freeze-thaw cycles, the event rate of stage I continued to rise and was higher than that near the peak stress, which was approximately "U" type. After 20, 30, and 40 freeze-thaw cycles, the maximum values are about 70, 120, and 140/s, respectively. This is because under the effect of freeze-thaw cycles, the porosity of yellow sandstone rock samples increases, the number of macropores increases, and the phenomenon of pore or crack pressure sealing increases, resulting in more active AE activities. This also shows that the degradation of rock samples by freeze-thaw cycles is mainly concentrated on the role of pores. The local stress that the cementation strength between particles of rock samples can withstand is smaller and smaller, and the pores inside the rock samples are larger and larger, and the number of pores is also increasing.

When the peak stress reaches, the two kinds of rock samples have an obvious AE low event rate missing phenomenon, which is a sign of the fracture precursor of rock samples, indicating that the acoustic emission activity is extremely active when the rock sample is damaged, and more macroscopic cracks appear at this time. However, with the increase of freezing and thawing times, the AE low event rate missing phenomenon of the two rock samples is not consistent. With the increase of cycles in the 20th and 30th freeze-thaw cycles, the area of low event rate missing is becoming smaller and smaller, and the high and low event rates coexist, and the failure mode is more complex. As shown in Figure 14(c), after 40 freeze-thaw cycles, the high event rate appears at the peak stress, and the obvious low event rate loss occurs at the same time. With the slow decline of stress, the event rate is also declining, the phenomenon of instantaneous instability of rock samples disappears, and the damage of pores and the development of microcracks are still emerging after the peak stress. However, the phenomenon of low event rate loss of yellow sandstone has no obvious change rule, and the area of low event rate loss has no obvious change. This is because the yellow sandstone rock samples in 40 freeze-thaw cycles, although there is a trend of ductile development, it did not reach the transition stage such as 30 freeze-thaw cycles of green sandstone. The brittle rock characteristics are obvious, and it is destroyed near the peak stress, forming a macroscopic crack that makes the rock samples unstable instantaneously.

In order to explore the effect of freeze-thaw on the acoustic emission energy release of rock samples, the stages of Figures 16 and 17 are divided, but most AE energy and cumulative energy-time curves only change significantly at

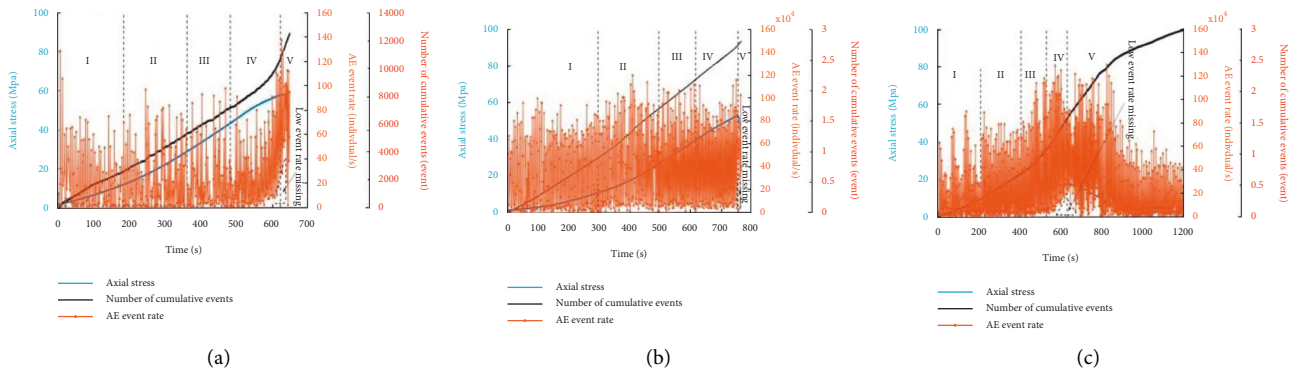

Figure 14: AE event rate, cumulative event number and stress-time curve of green sandstone. (a) 20 cycles. (b) 30 cycles. (c) 40 cycles.

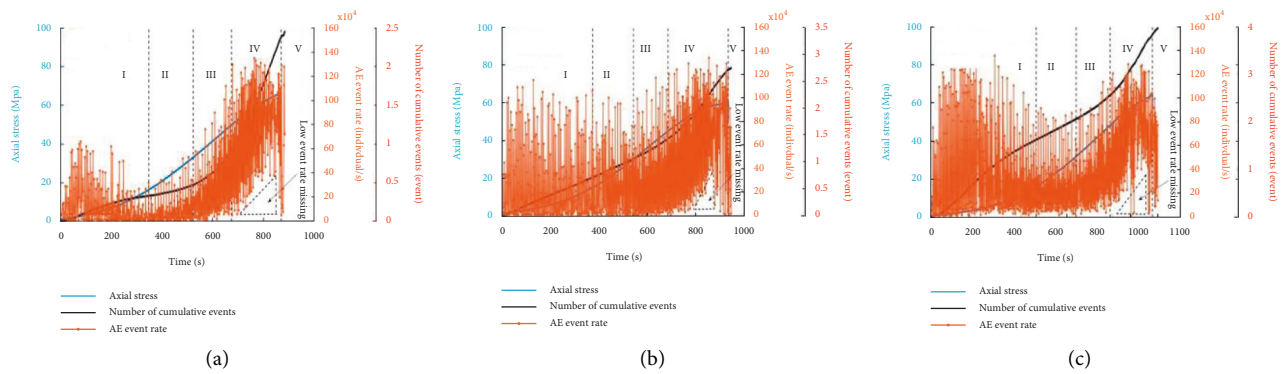

Figure 15: AE event rate, cumulative event number, and stress-time curve of yellow sandstone. (a) 20 cycles. (b) 30 cycles. (c) 40 cycles.

the peak stress. If the crack volume strain method such as Figure 15 is continued to be used, the stage division will not be applicable. Because the energy released by the rock near the peak stress is much larger than in other time periods, the order of magnitude is obvious, so according to the different order of magnitude of AE energy rate, the energy release stage is divided into two categories, in which the stage of higher acoustic emission energy release near the peak stress is defined as the "explosion period," and the stage of lower acoustic emission energy release is defined as the "stationary period." The "stationary period" and "explosion period" division results of each rock sample are shown in Figures 16 and 17. Figure 16(c) shows that in addition to the rock samples being divided into "stable period-explosion period-stable period" three stages, the rock samples are only divided into "stable period-explosion period" two stages. This is because the physical and mechanical properties of the rock sample deteriorate after repeated freeze-thaw cycles, and the deformation characteristics of the lithology gradually change from brittleness to plasticity. After reaching the peak stress, it does not immediately lose stability as the brittle rock does, and it can still continue to bear pressure. After the peak stress, the rock sample gradually destroyed and continued to emit acoustic energy under the action of external load, but the order of magnitude of the released energy was small, reaching the second "stationary period".

After 20 freeze-thaw cycles, there is almost no obvious energy release in the "stationary period" of Qingsha sandstone samples, and the average energy rate in the "stationary period" is about 1/90 of the peak energy rate, indicating that the energy release is concentrated in the outbreak period. After 30 cycles, there is a higher energy release in the "stationary period," and the average energy rate of the "stationary period" can reach about 1/10 of the peak energy rate, which shows that the intensity of acoustic emission activity of the rock sample after 30 cycles is larger and the energy release is more uniform. The deterioration of rock samples is the most obvious in the first 30 rocks with brittle characteristics; there are two "stationary periods" in the whole process of 40 cycles of rock samples, and the ratio of average energy rate and peak energy rate of "stationary period" decreases to 1/50, and the energy release is concentrated in the "explosive period." At this time, the acoustic emission energy rate of the "stationary period" is similar to that of 20 cycles of the "stationary period," and there is no obvious energy release, and the intensity of acoustic emission activity is much lower than that of 30 cycles. There was no obvious energy release during the 40 freeze-thaw cycles of yellow sandstone rock samples in the "stationary period," but the ratio of the average energy rate and the peak energy rate in the "stationary period" increased from 1/600 to 1/30, indicating that the energy release in the "stationary period" gradually increased. As shown in Figure 17(c), the "stationary period" produces a small outbreak. It can be predicted that if the number of cycles continues to increase, the "stationary period" will erupt in higher energy release, and

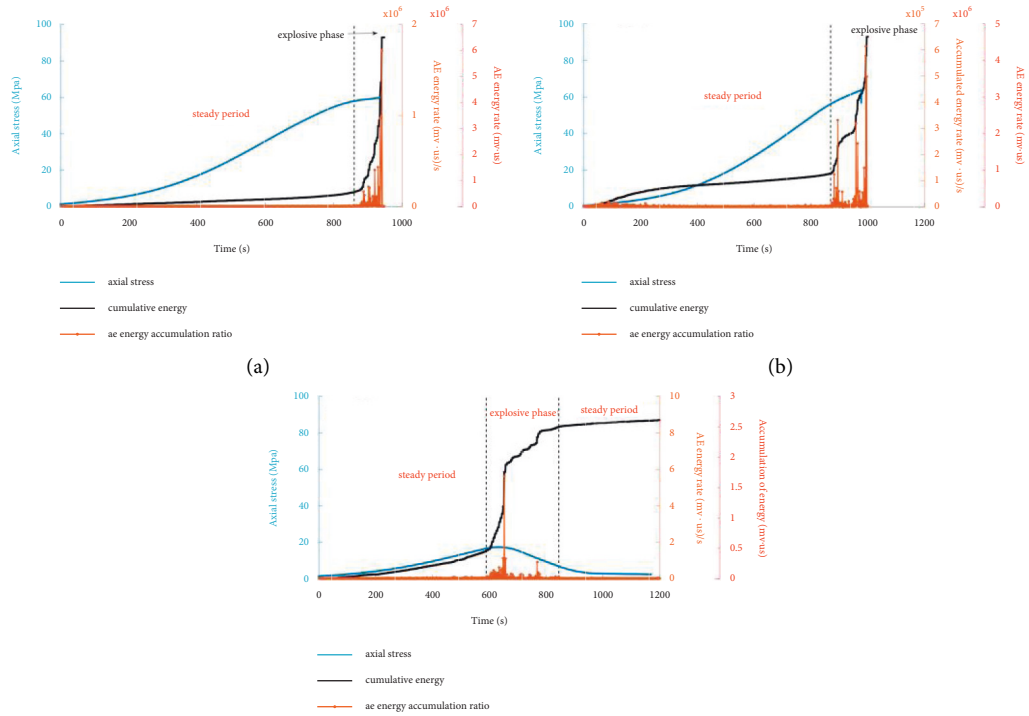

Figure 16: AE energy rate, cumulative energy and stress-time curve of green sandstone. (a) 20 cycles. (b) 30 cycles. (c) 40 cycles.

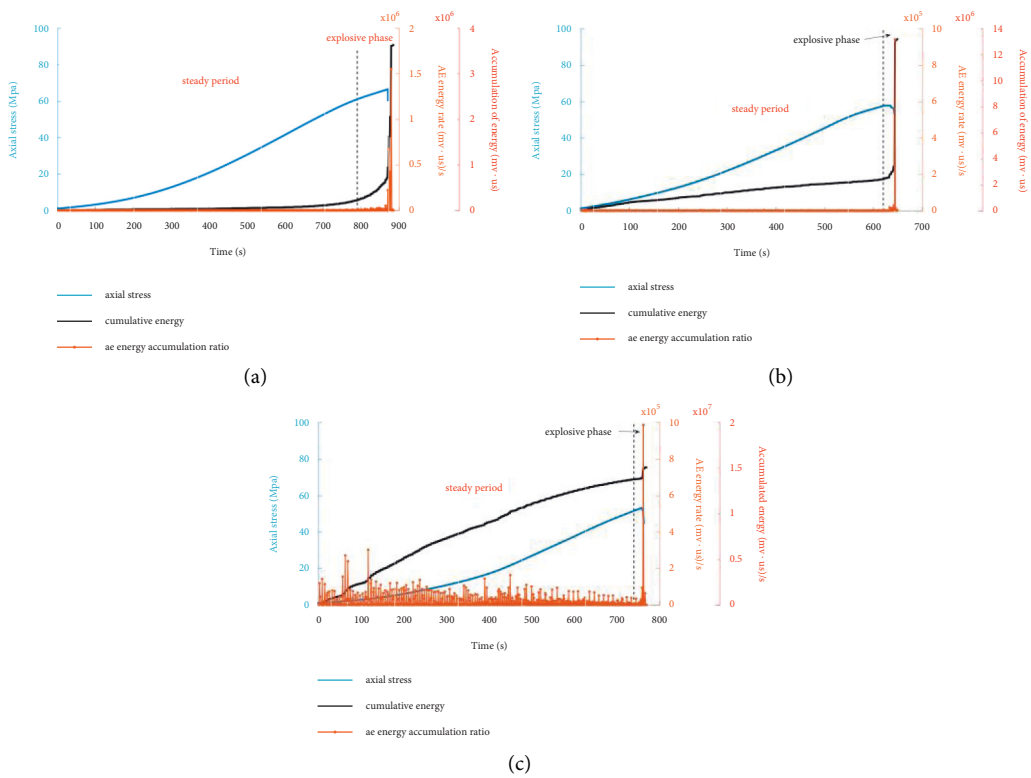

Figure 17: AE energy rate, cumulative energy and stress-time curve of yellow sandstone. (a) 20 cycles. (b) 30 cycles. (c) 40 cycles.

the change of cumulative energy and AE energy rate is close to the trend in Figures 16(b) and 16(c). With the increase in the number of freeze-thaw cycles, the number of pores in the rock sample increases, and the size of pores is also increasing. Under the action of external load, the pores continue to rupture, and the acoustic emission events increase, which is also accompanied by a large amount of energy release. Therefore, the energy release in the "stationary period" is gradually obvious, such as the whole process of the "stationary period" in Figure 16(b) and the small energy outbreak in the early stage of the "stationary period" in Figure 17(c). After 30 freeze-thaw cycles, the energy released by a single AE event in the green sandstone sample is more than that in the yellow sandstone sample. This reflects the freeze-thaw degradation of green sandstone is more serious than yellow sandstone. Under the action of the freeze-thaw cycle, the internal microcracks of cyan sandstone have a certain degree of initiation, which leads to the pore rupture of cyan sandstone accompanied by the initiation and penetration of microcracks under the action of external load, releasing a lot of energy; while the internal pores of yellow sandstone are broken, the initiation and penetration of microcracks are relatively small, thus releasing less energy. As shown in Figures 16 and 17, the AE energy "burst period" only exists near the peak stress. With the increase of the applied load, the pores inside the rock sample are continuously compacted, and the microcracks are also continuously pressed and sealed. During this period, huge energy is accumulated. When the peak stress is reached, a macroscopic fracture that makes the rock sample unstable instantaneously is formed. The accumulated energy is released instantaneously, and the AE energy rate increases instantaneously. At this time, the energy rate corresponds to the peak energy rate, and the accumulated energy is also rising linearly. After 40 freeze-thaw cycles, the peak energy rate decreased significantly, and the peak energy rate decreased significantly after the brittle-plastic transformation of rock samples. At this time, the release of energy increased and decreased with the increase and decrease of stress. This shows that the freeze-thaw cycle will reduce the energy released by acoustic emission activity because the freeze-thaw cycle weakens the internal structure of the rock, and the energy released by rock failure is also reduced.

5. Conclusions

(1) After several freeze-thaw cycles, the appearance of green sandstone samples showed obvious deterioration compared with yellow sandstone, and the degree of appearance deterioration also deepened. The average mass change rate of the yellow sandstone sample is slightly larger than that of the green sandstone sample; green sandstone absorbs water earlier, later more; the porosity of green sandstone is generally larger than that of yellow sandstone. The number of small pores in green sandstone decreases and the number of large pores increases, while the pore size of yellow sandstone changes little, but the number increases.

(2) The discreteness of stress-strain curves of two kinds of rock samples increases with the increase of freeze-thaw cycles. After 40 freeze-thaw cycles, the stress-strain curve of yellow sandstone still maintained the typical brittle characteristics, but it had the trend of plastic transformation. The curves of B-1 and 40 freezing-thawing cycles show obvious plastic characteristics, and 30 freezing-thawing cycles can be used as the dividing line of mechanical properties for the freezing-thawing degradation of green sandstone. The peak stress of yellow sandstone has no obvious change, and the peak stress of green sandstone decreases obviously.

(3) With the increase of cycles in the 20 th and 30 th freeze-thaw cycles, the area of low event rate missing is becoming smaller and smaller, and the high and low event rates coexist, and the failure mode is more complex. There is no obvious change in the low event rate loss phenomenon of yellow sandstone, and there is no obvious change in the area of low event rate loss. This is because the yellow sandstone rock samples in 40 freeze-thaw cycles, although there is a trend of ductile development, it did not reach the transition stage such as 30 freeze-thaw cycles of green sandstone. The energy released by a single AE event of the green sandstone rock sample is more than that of yellow sandstone. With the increase in freeze-thaw cycles, more and more energy is released during the stationary period.

Data Availability

The data used to support the findings of this study may be released upon request to the corresponding author.

Conflicts of Interest

The authors declare no conflicts of interest in this article.

Acknowledgments

This study was supported by Qiankehe Foundation ([2020] 1Z047).

References

[1] Y. L. Chen, J. Ni, L. H. Jiang, M. L. Liu, P. Wang, and R. Azzam, "Experimental study on mechanical properties of granite after freeze-thaw cycling," *Environmental Earth Sciences*, vol. 71, no. 8, pp. 3349–3354, 2014.

[2] Q. Liu, W. Chen, J. K Guo et al., "Fractional stress relaxation model of rock freeze-thaw damage," *Advances in Materials Science and Engineering*, pp. 2021–2028, 2021.

[3] J. Li, K. Zhou, W. Liu, and Hw Deng, "NMR research on deterioration characteristics of microscopic structure of sandstones in freeze-thaw cycles," *Transactions of Nonferrous Metals Society of China*, vol. 26, no. 11, pp. 2997–3003, 2016.

[4] T. T. Zhu, J. X. Chen, D. Huang, Y. Luo, Y. Li, and L. Xu, "A DEM-based approach for modeling the damage of rock under freeze-thaw cycles," *Rock Mechanics and Rock Engineering*, vol. 54, no. 6, pp. 2843–2858, 2021.

[5] H. Jiang, "The relationship between mechanical properties and gradual deterioration of microstructures of rock mass subject to freeze-thaw cycles," *Earth Sciences Research Journal*, vol. 22, no. 1, pp. 53–57, 2018.

[6] S. Zhou, N. Jiang, X. Luo, W. Fang, and X. He, "Uniaxial compression fractal damage constitutive model of rock subjected to freezing and thawing," *Periodica Polytechnica: Civil Engineering*, vol. 64, no. 2, pp. 500–510, 2020.

[7] W. Liping, Li Ning, Q. Jilin, T. Yanzhe, and X. Shuanhai, "A study on the physical index change and triaxial compression test of intact hard rock subjected to freeze-thaw cycles," *Cold Regions Science and Technology*, vol. 160, pp. 39–47, 2019.

[8] W. Fang, N. Jiang, and X. Luo, "Establishment of damage statistical constitutive model of loaded rock and method for determining its parameters under freeze-thaw condition," *Cold Regions Science and Technology*, vol. 160, pp. 31–38, 2019.

[9] K. Si, Z. Cui, R. Peng, L. Zhao, and Y. Zhao, "Crack propagation process and seismogenic mechanisms of rock due to the influence of freezing and thawing," *Applied Sciences*, no. 20, p. 9601, 2021.

[10] C. Qiao, Z. Song, Yu Wang, D. Tannant, and C. Li, "Fractures and acoustic emission features of non-persistent jointed rocks subjected to freeze-thaw-compression load: experimental insights," *Rock Mechanics and Rock Engineering*, vol. 55, no. 1, pp. 109–123, 2021.

[11] Z. Zhou, F. Li, H. Yang, W. Gao, and L. Miao, "Orthogonal experimental study of soil-rock mixtures under the freeze-thaw cycle environment," *International Journal of Pavement Engineering*, vol. 22, no. 11, pp. 1376–1388, 2019.

[12] D. Lei, H. Lin, and Y. Wang, "Damage characteristics of shear strength of joints under freeze–thaw cycles," *Archive of Applied Mechanics*, vol. 92, no. 5, pp. 1615–1631, 2022.

[13] J. Yu, X. Chen, H. Li, Jw Zhou, and Yy Cai, "Effect of freeze-thaw cycles on mechanical properties and permeability of red sandstone under triaxial compression," *Journal of Mountain Science*, vol. 12, no. 1, pp. 218–231, 2015.

[14] L. Zhou, Z. Ma, H. Xie, W. Yang, and H. Zheng, "Numerical simulation experimental study of the deformation and failure of granite with multiaxial tension," *Processes*, vol. 10, no. 5, p. 949, 2022.

[15] R. Yang, L. Jiakun, Bo Zhou, and D. Ma, "Rock unloading failure precursor based on acoustic emission parametric fractal characteristics," *Lithosphere*, vol. 2022, Article ID 8221614, 2022.

[16] H. Lin, D. Lei, C. Zhang, Y. Wang, and Y. Zhao, "Deterioration of non-persistent rock joints: a focus on impact of freeze-thaw cycles," *International Journal of Rock Mechanics and Mining Sciences*, vol. 135, no. 104515, Article ID 104515, 2020.

Hindawi
Advances in Materials Science and Engineering
Volume 2022, Article ID 6909248, 9 pages
https://doi.org/10.1155/2022/6909248

Research Article

Study on Complex Theory Solution and Numerical Simulation of Fracture Mechanics of Surrounding Rock Stress and Energy Field in Fault Type Rock Burst Stope

Haidong Zhang,[1,2,3] **Siyu Dou**,[2] **Guangchen Zhao**,[2] **Haiqing Yang**,[2] **and Chunyan Wu**[2]

[1]*School of Mines, China University of Mining and Technology, Xuzhou 221116, China*
[2]*Department of Civil and Construction Engineering, Shanxi Institute of Technology, Shanxi 045000, China*
[3]*University of Wollongong, NSW 2522, Australia*

Correspondence should be addressed to Haidong Zhang; haidongzhang221116@163.com

Received 12 July 2022; Accepted 23 July 2022; Published 13 September 2022

Academic Editor: Depeng Ma

Rock burst is one of the most sophisticated and threatening problems in the process of mining activities of underground coal mines, which can evolve into phenomena such as gas outburst, violent ground pressure behavior of surrounding rock of stope roadway, and high dynamic load energy event of roof overburden fracture through the interaction between various influencing factors. This paper deeply studies the causes, consequences, and disaster mechanism of "2–2 rock burst accident" in Xinjulong coal mine, gives the network diagram of the relationship between the main influencing factors of fault type rock burst and high-energy events, establishes a mechanical model on this basis, and explores the influence and evolution law of fault influencing factors on the elastic strain energy field of surrounding rock of stope roadway.

1. Background Introduction

On February 22, 2020, Xinjulong coal mine had a large rock burst accident in the upper roadway of 2305 s working face in the south wing of −810 m horizontal second mining area, resulting in four deaths and huge economic losses. Due to the jumping impact energy characteristics caused by its unique fault distribution at the mining area boundary, this case has become a research hot topic of experts and scholars at home and abroad in the field of rock burst for several years. At the same time, due to the complexity of its disaster causing mechanism and the overall systematicness of the stope, the factors that directly lead to the violent impact can only be delineated in the following three aspects: 1) fault stress concentration; 2) hard composite sandstone roof accumulating a large amount of elastic strain energy; 3) regional tectonic stress being affected by mining disturbance. This is a disadvantageous factor for the research on the means of impact prevention and control. Thanks to the detailed data support of Xinjulong coal mine of Shandong energy group, this paper only studies the formation, accumulation, and appearance process of impact energy for the interruption layer of this case and takes this as the basis to provide a theoretical basis for the impact prevention and control of mines under similar conditions.

2. Introduction

In the mining industry, transportation industry, underground space engineering construction, water conservancy, and hydropower engineering and other underground rock mechanics engineering fields, more and more large section roadways have been excavated and serve large-scale deep rock mechanics engineering in recent years [1]. With the average buried depth moving towards the geocenter at the speed of nearly 10 m/A, the surrounding rock state of deep roadway is subject to more complex mechanical boundary conditions, and a series of new dynamic load failure and

instability phenomena also appear [2]. In 1933, the phenomenon of strong dynamic pressure in rock burst mine, which occurred in Fushun Shengli coal mine for the first time in China and was officially statistically defined in 1959, also appeared unprecedented "jumping" disaster causing characteristics after the mining entered the deep stage, which undoubtedly launched a more arduous task for rock burst research experts and scholars, and even the emergence of this case challenged some previous research results on the starting and appearing mechanism of rock burst. Some theories that only apply to continuous coal seam impact have been questioned. Therefore, the in-depth study of Xinjulong 2–2 rock burst case is of great significance even after the stoppage of the mining area.

Rock burst is a violent and instantaneous throwing out of coal and rock mass in the process of deep coal seam mining. When the release energy is serious, it may cause the damage of roof and floor and even destroy the roadway, resulting in casualties and equipment damage [3].

At present, in the initiation and accumulation mechanism of rock burst, the theories that have a detailed classification and definition of the influencing factors of fault structure include dividing the rock burst phenomenon from the stope abutment pressure acting on the working face and near the stope roadway into "gravity type" rock burst. The rock burst events of the principle stope appearing in the advance position of the driving roadway and the upper and lower drift are divided into "structural" rock burst [4]. Then, the structural rock burst is divided into broken line type (rock burst in the area near the fault line, which is easy to burst when the roadway is under the influence of this stress due to the residual in situ stress in the fault zone) and section type (it occurs in the section within a certain range from the fault structure and is subject to the combination and superposition of mining stress and in situ stress). Tai et al. divided the rock burst induced by mining activities into coal compressive stress type, top and bottom plate tensile stress type, and fault strike slip shear type according to the force source [5]. The fault strike slip shear type rock burst takes the energy released by the sudden dislocation between bedding and fault discontinuity as the source of input energy of rock burst. In 2003, Pan further divided rock burst into coal compression rock burst, roof fracture rock burst, and fault dislocation rock burst and deeply expounded its mechanism: it is considered that the process of fault dislocation rock burst is due to the propagation, superposition, and amplification of mining stress in the form of energy through the rock material medium between faults when mining activities are close to the fault. Thus, the fault is suddenly staggered and damaged, with the magnitude often reaching 3~4 and the dominant frequency reaching 1~6 Hz [6]. Fault type rock burst is often not due to the impact damage of the energy of fault dislocation directly caused by natural tectonic stress on the stope roadway, but due to the disturbance stress caused by mining activities, it breaks the rock structure of the fault plane that has accumulated higher than the original rock stress level, resulting in the dislocation damage and energy release of the fault structure position, and then transfers the energy to the roadway surrounding rock, coal pillar, or stope coal wall. It leads to the sudden destruction of the bearing structure of the surrounding rock of the stope which is already bearing the peak stress, the release of energy to the free surface, and the violent rock burst accident.

In view of the prediction and early warning of the precursor of fault tectonic rock burst in coal mine, a microseismic monitoring station was established for the first time in the deep mine of Johannesburg, South Africa, at the early stage of Alhilton seismological society to monitor the microseismic activity of the mine [7]. More than 200 microseismic energy events caused by mining disturbance have been successfully monitored. Simple capture and analysis of microseismic event frequency and energy are difficult to combine its characterization characteristics with impact prediction. Therefore, B. Brady and others further studied microseismic energy events and roof collapse caused by mine mining and matched them from the characterization level [8]. Since entering the 21st century, Professor Dou et al.'s team [9] of China University of mining and technology has integrated monitoring equipment such as Aramis, ESG microseismic monitoring system, and electromagnetic radiometer into the rock burst microseismic monitoring system and used big data to build a multiparameter rock burst early warning cloud platform to achieve accurate and quantitative prediction of coal mine impact.

In addition, as per Pan et al. [10, 11], the roadway anti-impact support equipment is deeply explored according to the impact energy absorption mechanism.

Therefore, after the in-depth study of the mechanism of fault type rock burst and the establishment of quantitative discrimination formula, it is expected to realize the safe mining of resources with earthquake and without disaster under the guarantee of the above microseismic monitoring technology and anti-scour equipment.

In this paper, on the one aspect, the mechanical modeling of the fault round the roadway surrounding rock in the case is carried out, and the plate construction of elastic mechanics is adopted for analysis. In the assumption of boundary conditions and the selection of constitutive relationship, reference is made to the classical theories of fracture mechanics, material mechanics, and rock mechanics. In order to obtain the theoretical calculation formula of the stress field around the infinite crack plate, preestimate the stress concentration position and energy accumulation area of the surrounding rock of the stope in the case and similar boundary conditions and realize the formulation of quantitative measures for the scour prevention of the stope working face and roadway on this basis. Finally, the accuracy of the theoretical formula is verified by the simulation experimental results of FLAC3D numerical simulation software and field measured data records.

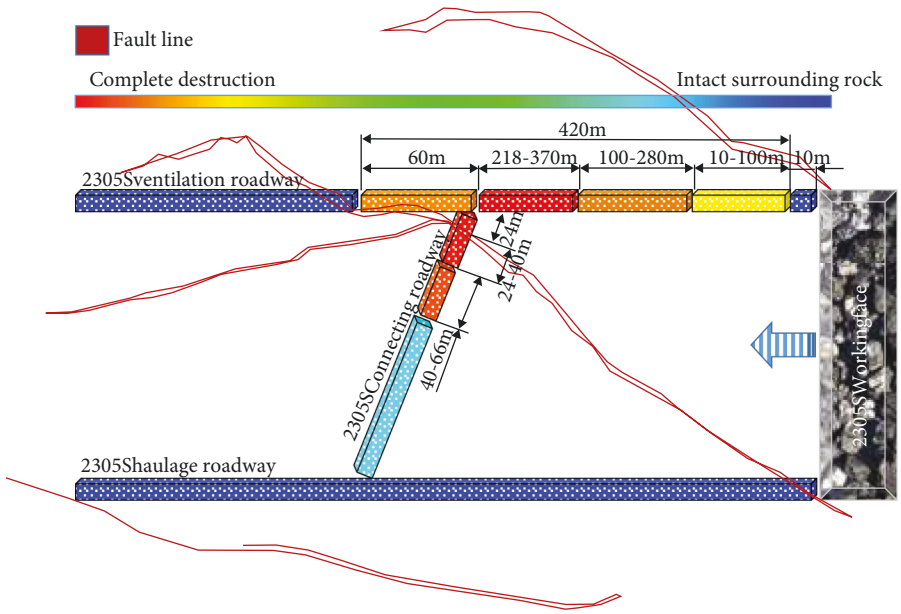

Figure 1: Schematic diagram of fault and impact damage degree of roadway in mining area (refer to Fan Shifu Prevention measures and methods of deep shaft rock burst in Xinjulong coal mine, Coal Mine Modernization, 2019 (4): 4).

3. Rock Burst Occurrence Process and Geological Details of Typical Fault Type Rock Burst

The accident occurred at 6 : 17 a.m. in the upper drift of −810 n level 2305 s fully mechanized top coal caving face. The average thickness of the main mining 3# coal seam is about 8.82 m, and its elastic energy index wet is calibrated as 1.2 by laboratory rock mechanics experiment. It belongs to the coal seam with medium risk of impact tendency. There are 6 faults in the working face with impact, of which FD8 and FD11 have a great impact on the mining operation. The FD8 fault penetrating the impact appearance roadway and connecting roadway is selected for in-depth study. The fault location and the damage degree of the working face roadway by impact are shown in Figure 1.

As shown in Figure 1, it is shown that FD8 fault passes through the intersection of 2305s upper drift and associated roadway, and the damage degree is the most serious. During the roadway excavation, no obvious features of the upper and lower drift and the surrounding plastic area of the combined roadway are found to be affected by the fault. However, after the accident site investigation, it is found that the roadway near the FD8 fault is the most severely damaged, the two sides move relatively close, the roof bolts, anchor cables, and roof beams break off, and only 1.0 m^2 of the minimum roadway section is left.

Therefore, modeling and analysis are mainly carried out for the relative spatial position of FD8 fault and 2305 s working face stope and service roadway and the geological conditions of rock mechanics.

The coal seam passes through the fault structure, and the horizons move and slip with each other. Affected by the regional tectonic stress of the plate, the coal seam reaches a stable state after long-term movement. Before the influence of artificial mining activities, it is difficult to form a strong source of elastic strain dynamic force by itself. Generally, it is only shown that the regional stress rise exceeds the original rock stress. When the mining disturbance is near the fault, the leading stress caused by mining and the regional elevated stress caused by tectonic stress are mutually superimposed, resulting in the breaking of the original stable state between faults, as shown in Figure 2. The movement law between rock layers shows that the fault rock layer near the mining free surface may sink, slide, rotate, or composite displacement. The support of the rock layer at the fault plane where the original rock is squeezed and engaged is changed from surface load to point load, resulting in the stress concentration of the rock layer at the fault plane. As a result, a large amount of elastic strain energy is accumulated in the rock layers on both sides, which is more dangerous. The trend surface of elastic strain energy release tends to the working face near the horizontal angle and the free end of the roadway.

In fracture mechanics, Volterra's [1] dislocation model [12, 13], and dislocation theory [14] and for the calculation of the normal stress field of the infinite crack surface, the mechanical model of the influence factors such as cohesion is introduced.

Among them, the Volterra dislocation model assumes that the relative position staggering amount between the two sides of the fault is equal everywhere, which is a constant, and the displacement discontinuity value can be easily obtained by taking the average value in the drill hole

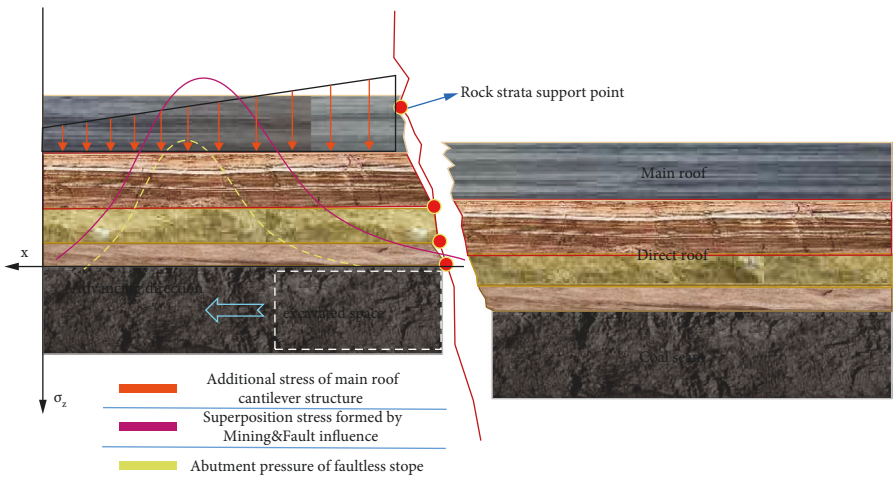

Figure 2: Suspension curve of fault stress and mining stress.

inspection map. However, the Volterra dislocation model has its major defect that when a specific value is obtained in the X direction, its shear stress τ_{xy} is greater than another certain value, and some singular values will appear in the calculation results of the stress field and displacement field on the crack surface,which will seriously affect the confidence of the calculation results.

The other two fault mechanics models are not suitable for calculating the displacement around the crack on the infinite plane because of their mechanical assumptions. Therefore, the linear elastic fracture mechanics model is introduced [15].

The final result of the calculation of the complex stress function in the complex variable function is

$$\begin{cases} \tau_{xy} = \mathrm{Im}\left[Z\phi_1''(z) + \psi_1'(z)\right], \\ \sigma_x = 2\mathrm{Re}\left[\phi_1'(z)\right] - \mathrm{Re}\left[Z\phi_1''(z) + \psi_1'(z)\right], \\ \sigma_y = 2\mathrm{Re}\left[\phi_1'(z)\right] + \mathrm{Re}\left[Z\phi_1''(z) + \psi_1'(z)\right], \end{cases} \tag{1}$$

$$\phi_1(z) = -\frac{1}{2\pi(1+\kappa)}\sum_{k=1}^{m}(x_k + iY_k)\ln(z - z_k) + \phi_{1*}(z),$$

$$\psi_1(z) = \frac{\kappa}{2\pi(1+\kappa)}\sum_{k=1}^{m}(x_k - iY_k)\ln(z - z_k) + \psi_{1*}(z).$$

Assume that the total stress componentaround the fault is σ_{XX}, σ_{YY}, τ_{XY}, disturbance stress field of fault is $\sigma^{C_{IJ}}$ $(i, j = 1, 2)$ [16], and stress function of direct conversion is as follows [16]:

$$Z_{\mathrm{II}}^{c} = \left(\frac{z}{\sqrt{z^2 - a^2}} - 1\right)\Delta\tau. \tag{2}$$

The disturbed stress component around the fault is

$$\begin{cases} \mathrm{Im}Z_{\mathrm{II}}^{c} = \dfrac{\left(\sigma_{xx}^{c} - \sigma_{yy}^{c}\right)}{2}, \\ \mathrm{Im}Z_{\mathrm{II}}^{c} + y\mathrm{Re}Z_{\mathrm{II}}^{'c} = \dfrac{\left(\sigma_{xx}^{c} - \sigma_{yy}^{c}\right)}{2}, \\ \mathrm{Re}Z_{\mathrm{II}}^{c} - y\mathrm{Im}Z_{\mathrm{II}}^{'c} = \tau_{xy,}^{c} \end{cases} \tag{3}$$

where $\mathrm{Im}Z_{\mathrm{II}}^{c}$ is the real part of the complex variable function of the disturbed stress component; $\mathrm{Re}Z_{\mathrm{II}}^{c}$ is the imaginary part of the complex variable function of the disturbed stress component; Z_{II}^{c} is called the Westergaard function of mode II crack, which can be taken as

$$Z_{\mathrm{II}}(z) = \frac{z\tau^{\infty}}{\sqrt{z^2 - a^2}} + D, \tag{4}$$

where $C = D = \tau^{\infty}$ take the boundary condition at infinity; A selects the center position for calculation; Z is the coordinate variable for calculating Westergaard function. Then, the displacement component around the fault is obtained as

$$\begin{cases} 2\mu\mu^{c} = \left(\dfrac{\kappa+1}{2}\right)\mathrm{Im}\tilde{Z}_{\mathrm{II}}^{c} + y\mathrm{Re}Z_{\mathrm{II}}^{c}, \\ 2\mu v^{c} = -\left(\dfrac{\kappa+1}{2}\right)\mathrm{Re}\tilde{Z}_{\mathrm{II}}^{c} - y\mathrm{Im}Z_{\mathrm{II}}^{c}. \end{cases} \tag{5}$$

The full field formula of mode II crack stress is

$$\begin{cases} \sigma_{xx} = 2\mathrm{Im}Z_{\mathrm{II}} + y\mathrm{Re}Z_{\mathrm{II}}', \\ \sigma_{yy} = -y\mathrm{Re}Z_{\mathrm{II}}', \\ \tau_{xy} = \mathrm{Re}Z_{\mathrm{II}} - y\mathrm{Im}Z_{\mathrm{II}}' - C. \end{cases} \tag{6}$$

By substituting formulas (5) into (6) of elastic strain energy [17, 18], the calculation formula of elastic strain energy field (scalar) around the crack can be obtained:

$$U^e = \frac{\left[\sigma_1^2 + \sigma_2^2 + \sigma_3^2 - 2\mu\left(\sigma_1\sigma_2 + \sigma_2\sigma_3 + \sigma_1\sigma_3\right)\right]}{2E},$$

$$\begin{aligned} U^e = \frac{1}{2E}\{&[(\Delta\sigma_x + \sigma_H) + \left(\Delta\sigma_y + \sigma_v\right)\cos\alpha)\sin\theta + \left(\left(\sigma_h + \Delta\tau_{xy}\right) + \left(\Delta\sigma_y + \sigma_v\right)\sin\alpha\right)\cos \\ &+\left(\left(\Delta\sigma_x + \sigma_H + \left(\Delta\sigma_y + \sigma_v\right)\cos\theta + \left(\sigma_h + \Delta\tau_{xy} + \left(\Delta\sigma_y + \sigma_v\right)\sin\theta\right)^2\right. \\ &+\Delta\tau_{xy}^2 - 2\mu\left(\left(\Delta\sigma_x + \sigma_H + \left(\Delta\sigma_y + \sigma_v\right)\cos\alpha\right)\sin\theta + \left(\sigma_h + \Delta\tau_{xy} + \left(\Delta\sigma_y + \sigma_v\right)\sin\alpha\right)\cos\theta\right) \\ &\cdot\left(\Delta\sigma_x + \sigma_H + \left(\Delta\sigma_y + \sigma_v\right)\cos\alpha\right)\cos\theta + \left(\sigma_h + \Delta\tau_{xy} + \left(\Delta\sigma_y + \sigma_v\right)\sin\alpha\right)\sin\theta) + \\ &\cdot\left(\Delta\sigma_x + \sigma_H + \left(\Delta\sigma_y + \sigma_v\right)\cos\alpha\right)\cos\theta + \left(\sigma_h + \Delta\tau_{xy} + \left(\Delta\sigma_y + \sigma_v\right)\sin\alpha\right)\sin\alpha)\Delta\tau_{xy}\right) \\ &+\Delta\tau_{xy}\left(\Delta\sigma_x + \sigma_H + \left(\Delta\sigma_y + \sigma_v\right)\cos\theta + \left(\sigma_h + \Delta\tau_{xy} + \left(\Delta\sigma_y + \sigma_v\right)\sin\theta\right)\right)]. \end{aligned} \tag{7}$$

The disturbed stress contour of linear elastic fault stress model is calculated, as shown in Figure 3.

It can be clearly seen that around the type II fracture, the maximum disturbed compressive stress around the fault initiation direction reaches 1.04 MPa, and the maximum disturbed tensile stress in the middle of the fault reaches 23.7 MPa. This shows that the stress state of the rock stratum near the fault structure is sophisticated, there is a sudden change in the stress direction, and the stress difference is obvious. This stress state of the surrounding rock of the fault makes it easier for the surrounding rock in the dominant stress direction to displace or transfer elastic strain energy to the surrounding rock in the weak stress direction under the influence of the external mining stress. As a result, the disturbance caused by mining causes further damage when the stress difference near the fault structure exceeds the strength limit of the surrounding rock under the stress state at that time. There is a 15.1 m thick hard rock near the FD8 fault with a length of about 240 m, accumulating a large amount of elastic strain energy. When it is subjected to a tensile stress of 23.7 MPa under its own confining pressure, it will be damaged, and the released energy will exceed 0.4393 kJ. It is far beyond the upper limit threshold of one-day total energy involved in micro earthquake shutdown warning of the coal mine by 0.27 kJ.

Therefore, through the analytical calculation of rock fracture mechanics theory, it is not difficult to find that the energy accumulated in the surrounding rock of the fault is enough to cause the occurrence of rock burst. In addition, through the analysis of the direction and contour map of the disturbed stress field around the fault fracture in Figure 3 obtained from the calculation results, it can be concluded that for the stope roadway and working face threatened by fault type rock burst, through large-diameter pressure relief drilling and hydraulic fracturing, the pressure relief and erosion prevention of high stress surrounding rock by means of deep space blasting and surface fracturing are not only required to create a certain range of plastic zone of fault surrounding rock, but also important to reasonably regulate the stress field of fault surrounding rock according to the stress direction and dominant weak stress relationship of fault surrounding rock obtained from theoretical calculation and field measurement, so as to reduce the stress around the fault and reduce the stress difference at the same time.

4. Numerical Simulation Experiment of Sudden Change Model of Surrounding Rock Stress Disturbed by Fault in Rock Burst Stope

According to the field survey and measured borehole histogram, the physical and mechanical properties of the top and bottom slate of 3# coal seam near FD8 fault in 2305S working face are obtained, and the column chart is shown in Figure 4. It can be seen that the direct roof of 1.5 m fine sandstone with moderate impact tendency and the basic roof of 15.45 m thick hard medium grained sandstone are unfavorable factors for the risk of rock burst in the stope and roadway of 2305 s working face. Firstly, the thick and hard basic roof of medium grained sandstone accumulates a large amount of elastic strain energy under the action of high in situ stress with −980 m buried depth, and because the direct roof is thin and close to the basic roof, it is difficult to fully protect the stope, so the dynamic pressure appears obviously in the process of fracture and instability of the basic roof. In addition, the 3# coal seam has a moderate impact tendency, and a large amount of elastic strain energy is bound to

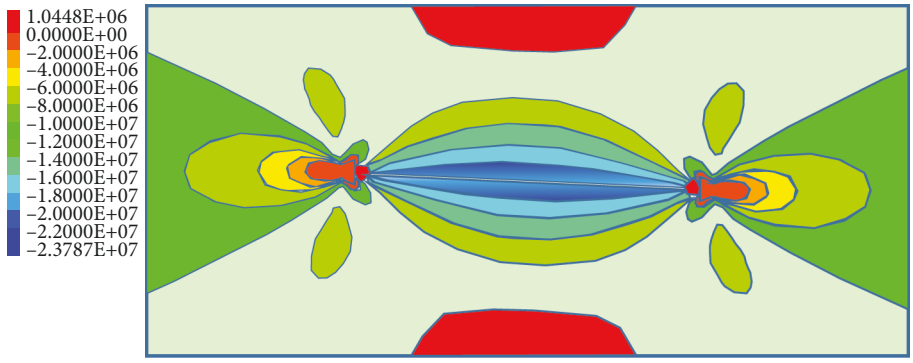

Figure 3: Isoline distribution of disturbed stress in linear elasticity II fault fracture mechanics model.

Rock stratum name	Lithology description	Thickness (m)	Bulk modulus (GPa)	Tensile strength (MPa)	Cohesion (MPa)
Mudstone	Dark gray,intercalated with thin layer of siltstone,with granular structure	3.5	1.72	3.36	1.8
Fine Sandstone	Gray,thin layer,with highly developed small fissures	9	2.22	2.81	0.73
Medium Grained Sandstone	Gray, mainlyc omposed of quartz and feldspar,with fine and medium particles and small vertical fissures	15.45	18.7	1.2	12.1
Fine Sandstone	Grayish black, rich in plant stem and leaf fossils and root fossils	1.5	8.05	11.9	15.3
3# coal seam	Black, mainly composed of bright coal anddark coal, with hard texture and stepped fracture	7.7	4.91	0.75	1.25
Siltstone	Grayish black,with oblique small cracks	2.38	10.83	1.84	3.75
Fine Sandstone	Gray, thin layer, occasionally mixed with thin layer of siltstone	8.45	21.01	1.29	3.2

Figure 4: Rock thickness and physical and mechanical property description histogram.

accumulate in the surrounding rock energy field of the stope. The following modeling and analysis are carried out for 2305 s working face in combination with geological conditions.

Flac3D 6.0 numerical simulation software is used to model the stope roadway, working face overburden strata, and baseplate of 2305 s working face. At the same time, FD8 fault is divided and constructed in the rock stratum. The spatial geometric position relationship is shown in Figure 5.

Based on the actual mining conditions of 2305 s working face, the experimental scheme and parameter selection mainly discuss the stage far away from the fault during working face and roadway excavation (stage I); approaching fault stage (stage II); the stress field distribution and the accumulation of elastic strain energy field in the overlying strata and floor of the stope during the four stages of passing through the fault (stage III) and leaving the fault (stage IV) to verify the accuracy of the energy field distribution in the calculation results of the elastic strain energy analytical formula around the fault derived above.

It can be seen in Figure 6 that the development shape of the stope collapse zone is similar in the mining influence stages I, II, and III. When passing through the fault, the height of the roof collapse zone is reduced from 15.4 m to 12.65 m due to the increase of the horizontal tectonic compressive stress and the decrease of the tensile stress in the surrounding rock stress area of the fault. During the period when the mining space crosses the fault (stages II and III), the stress of the surrounding rock of the roadway increases significantly and the stress of the overlying strata of the stope decreases to a certain extent, which is good news for the working condition of the support in the mining process of the working face. However, for the surrounding rock of the roadway, the existence of the fault further increases the stress of the surrounding rock of the roadway and increases the risk of rock burst accidents in the roadway.

In addition, by comparing the calculation results of the above rock fracture mechanics on the disturbed stress field around the fault in phase IV of Figure 5, it can be seen that the isoline distribution law of the stress state around the fault basically conforms to the conclusion of numerical simulation.

The displacement and stress data of the node element are postprocessed by Tecplot2021 software, and the stress tensor is calculated according to formula (6). The result is the elastic strain energy UE of each node. As shown in Figure 7, the concentration and accumulation position of elastic strain energy changes with the advance of the fault crossing stage.

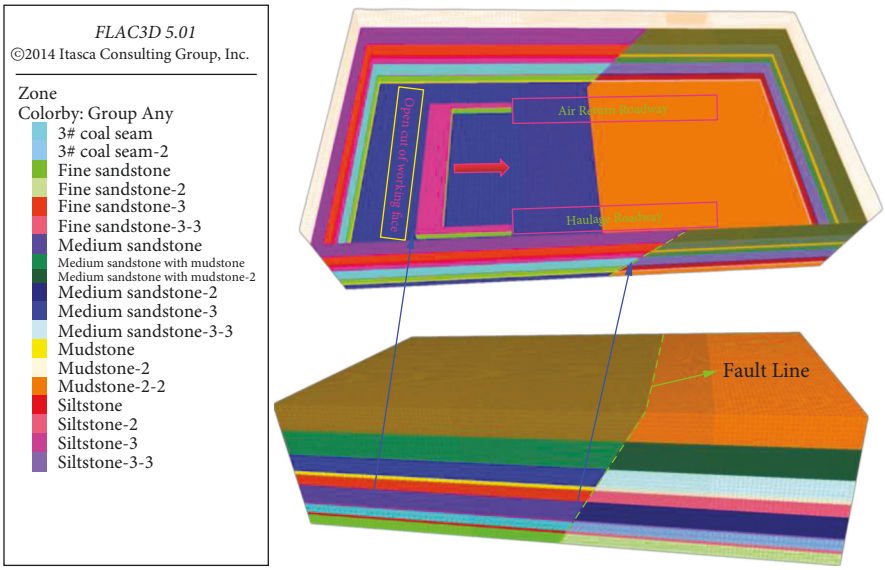

Figure 5: Relative position of FD8 fault and stope of numerical simulation experimental model.

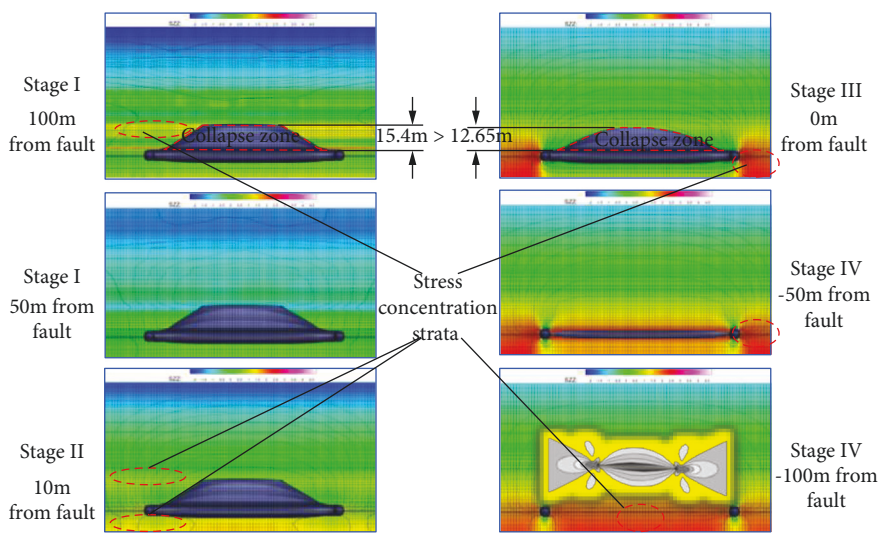

Figure 6: Evolution law of stress field in surrounding rock of stope at different stages of fault.

At stage I, the elastic strain energy is mainly accumulated in the coal seams, and the concentration degree is very weak. There is little difference between the elastic strain energy accumulated in the fine sandstone of the roof and siltstone of the floor, and the elastic strain energy of the node is less than 0.02 kJ as a whole. When the roadway near the fault reaches stage II, the bending moment of the roof increases, and the accumulated elastic strain energy in the fine sandstone layer increases significantly. Due to the influence of mining liberation, the accumulated elastic strain energy in the coal seam decreases. However, when the stope roadway and working face pass through the fault to reach stage III, a large amount of elastic strain energy accumulation occurs in the roof and floor strata at the same time. At this time, the elastic strain of the node element as a whole is close to 0.06 kJ, which is about three times higher due to the influence of the fault.

Therefore, it is not difficult to see that the presence of faults has a negative and dangerous impact on coal mining when theoretically explaining the mechanism of the initiation of rock burst caused by faults from the perspectives of stress source and elastic strain energy [19]. In order to reduce the threat of faults to a certain extent and the risk of rock burst in mines with faults around or inside the mining area [20], the antiscour process parameters shall be quantitatively formulated in combination with the analytical formula (7), and the relevant influence parameters of fault stress energy field are revealed by the numerical simulation test results.

5. Discussion and Conclusions

Based on the established mechanical model, combined with the calculation formula of stress field and energy field around type II structural fault derived from rock fracture

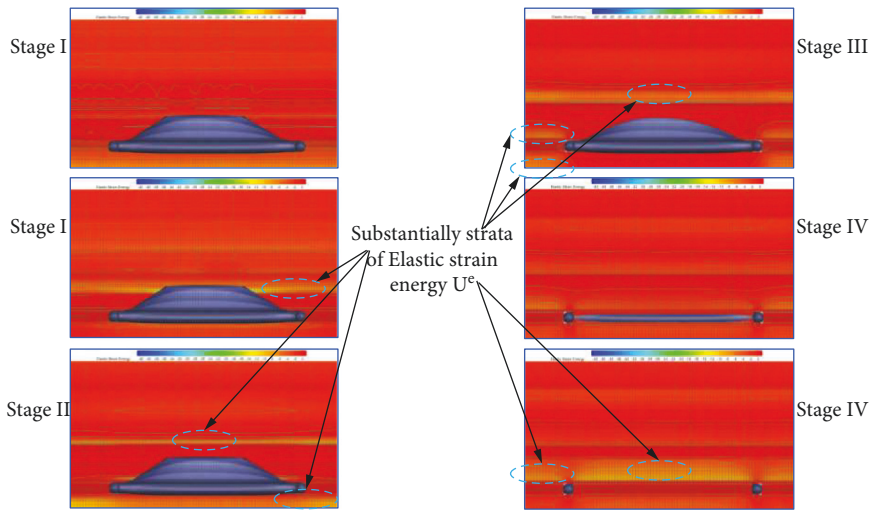

Figure 7: Evolution law of elastic strain energy field of stope surrounding rock at different stages of fault crossing.

mechanics and material mechanics, and the numerical simulation experiment of FD8 fault model, the influence of strata fault structure on the impact risk of stope surrounding rock from the perspective of force source and energy is obtained when the stope experiences different mining stages and spatial geometric position relationship of the fault.

In practice, the conclusion of this paper is as follows.

(1) Through the calculation formula of stress field and energy field around type II structural fault, the state of surrounding rock in different stages of mining is preliminarily calculated and estimated. It is a new effective auxiliary means to predict and estimate the impact tendency of mine threatened by fault type rock burst [21]. It can calculate the accumulation degree coefficient of elastic strain energy UE, the high-energy position of the roof and floor of the surrounding rock, and the high-stress and high-energy horizon that should be paid attention to in different mining stages.

(2) The parameters in the analytical formula explain that, in the prevention and control means and measures of type II structural fault type rock burst [22], while considering the pressure relief construction of high stress concentration in thick and hard basic roof strata, attention should also be paid to the phenomenon of high stress and high energy in the floor. The surrounding rock of the stope is an integral support and bearing system. When the floor stress is at a high level, the pressure relief of the basic roof strata may not be effective.

(3) During stage II and stage III, attention should be paid to reducing the advancing speed of the working face, using large-diameter pressure relief drilling and hydraulic fracturing to cut the hard basic roof strata to shorten the fracture layout and basic roof thickness. In addition, reducing the mining height to protect the floor and opening pressure relief grooves for the roadway floor are also theoretically feasible and effective on-site impact prevention measures [23]. What is more noteworthy is that, in the process of mining thick coal seams, the staggered roadway layout method [24] can be selected, and the roadway can be arranged along the coal seam roof [25]. Under the dual protection of the thin immediate roof protection and the roadway floor coal seam, the roadway surrounding rock can be slightly vibrated without obvious impact [26, 27].

Data Availability

The experimental and analytical calculation results data used to support the findings of this study are included within the article.

Conflicts of Interest

The authors declare that there are no conflicts of interest regarding the publication of this paper.

Acknowledgments

This research project was funded by the Science and Technology Project of Shanxi Institute of Engineering and Technology (2022HX-05), the National College Students' Innovation and Entrepreneurship Training Project (s202214527014), and Ecological Restoration of Mining Areas and Solid Waste Recycling Provincial and Municipal Joint Construction of Shanxi Provincial Key Laboratory Cultivation Base Project. This dissertation was funded by the Shanxi Province Overseas Students Management Committee.

References

[1] V. Volterra, *Theory of Functionals and of Integral and Integro-Differential Euations, Dover Publication*, Mineola, NY, USA, 1959.

[2] L. Cao, "China University of mining and technology XvZhou Jiangsu province China," *Occurrence Regularity and Prevention and Control Countermeasures of Mine Earthquake in Oblique Fault Area of 3305 Working Face*, in Chinese, 2021.

[3] W. Cai, L. M. Dou, G. F. Wang, and Y. W. Hu, "Mechanical mechanism of fault activation caused by coal mining activities and its mechanism of induced thrusting," *Journal of mining and safety engineering*, vol. 36, no. 06, pp. 1193–1202, 2019.

[4] N. P. Wang, "Discussion on the types of rockburst and its treatment," *Proceedings of Symposium on control of hard rock mass in mines*, vol. 11, no. 5, pp. 172–179, 1991.

[5] Y. L. Tai, L. G. Wang, and M. T. Zhang, "Classification of rockburst," *Coal Mining*, vol. 7, no. 01, pp. 27-28+64, 1998.

[6] Y. S. Pan, Z. H. Li, and M. T. Zhang, "Study on distribution, type, mechanism and prevention of rockburst in China," *Journal of rock mechanics and Engineering*, vol. 8, no. 11, pp. 1844–1851, 2003.

[7] D. Fowler and Z. S. Lian, "Seismic monitoring to prevent rock burst disaster," *Foreign mining technology express*, vol. 3, no. 10, pp. 13–15, 1986.

[8] B. T. Brady and F. W. Leighton, "Seismicity anomaly prior to a moderate rock burst: a case study," *International Journal of Rock Mechanics and Mining Sciences & Geomechanics Abstracts*, vol. 14, no. 3, pp. 127–132, 1977.

[9] L. M. Dou, Y. D. Jiang, A. Y. Cao et al., "Monitoring and early warning technology of "stress field vibration wave field" for dynamic and static load of rock burst in coal mine," *Journal of rock mechanics and engineering*, vol. 36, no. 04, pp. 803–811, 2017.

[10] Y. S. Pan, Q. X. Qi, A. W. Wang et al., "Three-level support theory and technology of coal mine rockburst roadway," *Journal of China Coal Society*, vol. 45, no. 05, pp. 1585–1594, 2020.

[11] Y. H. Xiao, Y. S. Pan, J. Q. Chen, K. L. Liu, A. W. Wang, and L. P. Dai, "Study on buckling energy absorption reliability of energy absorption components of roadway anti impact support," *Journal of mining and safety engineering*, vol. 39, no. 02, pp. 317–327, 2022.

[12] G. Gripenberg, S. O. Londen, and O. J. staffans, *Volterra Integral and Functional Equations*, Cambridge University Press, Cambridge, England, 2013.

[13] M. E Gurtin, *The Linear Theory of Elasticity*, USA, 1973.

[14] G. kimura, S. Maruyama, Y. Isozaki, and M. Terabayashi, "Well-preserved underplating structure of the jadeitized Franciscan complex, Pacheco Pass, California," *Geology*, vol. 24, no. 1, p. 75, 1996.

[15] S. Y. Li, T. M. He, and X. J. Yin, *Introduction to Rock Fracture Mechanics*, China University of science and Technology Press, China, 2010.

[16] H. M. Westergaard, "Bearing pressures and cracks: bearing pressures through a slightly waved surface or through a nearly flat part of a cylinder, and related problems of cracks," *Journal of Applied Mechanics*, vol. 6, no. 2, pp. a49–a53, 1939.

[17] E. H. Dai, Y. Wang, Y. Q. Lu, H. D. Qiu, S. H. Yan, and T. Yang, "Study on Application of TBM Construction Technology in Coal Mine Construction in Yunnan Guizhou Region," *Coal Science and Technology*, 2022.

[18] Z. Q. Wang, C. Wu, J. Q. Luo et al., "Mechanism and control of coal pillar instability in the section of fully mechanized mining face with thick roof in extra thick coal seam," *Journal of China Coal Society*, vol. 46, no. 12, pp. 3756–3770, 2021.

[19] J. G. Lv, C. Q. Nan, Y. Zhang, and Z. Tang, "Mechanism of rock burst induced by mining near thrust faults in Yima coalfield," *Journal of Mining and Safety Engineering*, vol. 35, no. 03, pp. 567–574, 2018.

[20] E. B. Yi, "Analysis of rock burst prevention and control in fault zone of deep working face," *Mining Research and Development*, vol. 38, no. 12, pp. 57–60, 2018.

[21] A. Y. Cao, Y. Q. Liu, S. Q. Jiang, Y. Hu, and Y. Peng, "Study on the mechanism and main controlling factors of rock burst in cutting mining," *Journal of Mining and Safety Engineering*, vol. 39, no. 01, pp. 36–44, 2022.

[22] J. Q. Luo, S. H. Yan, T. Yang et al., "Mechanism of hydraulic fracturing cutting hard basic roof to prevent rockburst," *Shock and Vibration*, vol. 2021, Article ID 4032653, 2021.

[23] Z. Xiao and K. Hongpu, "Pressure relief mechanism of directional hydraulic fracturing for gob-side entry retaining and its application," *Shock and Vibration*, vol. 2021, Article ID 6690654, 8 pages, 2021.

[24] J. Adachi, E. Siebrits, A. Peirce, and J. Desroches, "Computer simulation of hydraulic fractures," *International Journal of Rock Mechanics and Mining Sciences*, vol. 44, no. 5, pp. 739–757, 2007.

[25] L. Yuan, "Gas drainage theory of pressure relief mining and technical system of coal and gas CO mining," *Journal of China Coal Society*, vol. 34, no. 1, pp. 1–8, 2009.

[26] S. P. Timoshenko, *Theory of Elastic Stability*, p. 560, McGraw-Hill, New York City, 1936.

[27] Z. Q. Wang, J. L. Zhao, B. Y. Zhang, and P. C. Liu, "Stability characteristics of key strata in top coal caving mining with staggered roadway arrangement," *Journal of China Coal Society*, vol. 5, no. 09, pp. 961–965, 2008.

Hindawi
Advances in Materials Science and Engineering
Volume 2022, Article ID 9724275, 12 pages
https://doi.org/10.1155/2022/9724275

Research Article

Study on the Key Factors of Terminal Mining Line Layout in Repeated Mining of Close-Distance Thick Coal Seams

Fulian He,[1] Bingquan Liu,[1,2] Liang Li,[1] Xuhui Xu,[1] Kai Lv,[1] Wenli Zhai,[1] Jiayu Song,[1] and Deqiu Wang[1]

[1]*School of Energy and Mining Engineering, China University of Mining and Technology (Beijing), Beijing 100083, China*
[2]*Beijing Tiandi Huatai Mining Management Co., Ltd, China Coal Technology & Engineering Group, Beijing 100013, China*

Correspondence should be addressed to Liang Li; liangli96@foxmail.com

Received 10 July 2022; Revised 12 August 2022; Accepted 25 August 2022; Published 12 September 2022

Academic Editor: Qing Ma

In order to mater the reasonable layout basis of the terminal mining line position in the repeated mining of close-distance thick coal seams, taking Yan mine as the engineering background, we conducted theoretical analyses, numerical simulations, and field measurements to study the action mechanism of the stress arch. The results show that (1) with repeated mining, the shape of the left and right half arches of the stress arch changes in the order of time and space until it is stable; (2) the shape of the stress arch is highly related to the distribution of abutment pressure in the working face. If the shape is unchanged, the distribution of abutment pressure is unchanged; (3) in the final mining stage of repeated mining, when the shape of the right half arch is stable, the difference stagger distance of the terminal mining line has little effect on the distribution of abutment pressure of the working face where the front arch foot is located; (4) when the internal stagger distance between 3216 working face and terminal mining line of 4216 working face is greater than 22 m or the external stagger distance is greater than 30 m, 3216 working face is located in a relatively safe position. This study clarifies the key factors for the layout of terminal mining lines in close-distance thick coal seams, which can provide a scientific basis for similar projects.

1. Introduction

With the mining of the working face, a stress arch structure will be formed in the upper overburden. The front and rear arch feet are located in the nonmining body of the working face and the open cut, respectively, and the arch crown is located in the bending subsidence zone. The stress arch bears the load up to the surface rock layer and transmits it to the front and rear arch feet. The front arch foot is located in the elastic pressurization zone in front of the working face and determines its width. The layout of the terminal mining line should ensure that the main roadway is located outside the influence range of the front abutment pressure of the working face, but the repeated mining of close-distance coal seams will cause changes in the shape parameters of the stress arch, and meanwhile, when the final mining stage enters under the solid coal with the working face from the goaf, the longitudinal position of the front arch foot will be transferred to the lower coal seam. At this stage, the change law of the abutment pressure distribution of the working face is not clear, especially whether the different stagger distances of the terminal line will affect the distribution of the abutment pressure, which is related to the reasonable width of the stopping coal pillar. It is of great significance to study the mechanism of stress arch in close-distance thick coal seams.

Many scholars have widely researched on stress arch theory. Wang believed that the overburden of the working face would form a stress shell and studied the ground pressure law of the working face under the shell structure [1]. Wang established the mechanical model of the symmetrical pressure arch and studied its characteristics [2]. Wang analyzed the formation mechanism of the stress arch, established the corresponding mechanical model, and

clarified the evolution process of the stress arch [3]. Based on the pressure arch and key stratum theory, Yang established the structural model of the overburden pressure arch [4]. Based on monitoring data of ground pressure, Wang established a mechanical model of the surrounding rock to study the law of ground pressure [5]. Yue used numerical simulation to obtain the shape parameters of the stress arch in close-distance coal mining and thus obtained the distribution of additional stress in the floor roadway [6]. Some scholars have also studied this subject [7–10].

Many scholars have widely researched on ground pressure in the working face of close-distance coal seams [11–13]. Shang studied the destruction process of the lower coal seam chain pillar and gate road under the action of the coal pillar in close-distance coal seam mining [14]. Lv studied the stress environment of the stope at the end of the mining stage of the close-distance coal seams and proposed the surrounding rock control technology of the withdrawal channel [15]. Zhang studied the damage characteristics of interbedded strata in close-distance coal seams and studied the stability of gob-side entry under this condition [16]. Li studied the influence of roof stress and fracture distribution characteristics on the stability of surrounding rock in the stope under the condition of repeated mining of close-distance coal seams [17]. Liu studied the stress distribution law of the floor under the action of coal pillars in close-distance coal seams and determined the reasonable layout position of the roadway [18]. Some scholars have also studied this subject [19, 20].

To sum up, there are many studies on the location selection of mining roadways in close-distance coal seams, the law of stope ground pressure, and the stress arch structure of single coal seams. However, there is little research on the action mechanism of stress arch in close-distance, thick coal seams, and the reasonable staggering distance of the terminal mining line. The purpose of this study is to provide a scientific basis for the stopping project of close-distance thick coal seams.

2. Project Overview

4 # and 3# coal seams in Yan coal mine are close-distance, thick coal seams, with a thickness of 7.5 m and 5.5 m, respectively. The average spacing between the two coal seams is 25 m. The coal seam mining methods are downward mining and fully mechanized top coal caving longwall mining methods, as well as the roof span management method. Figure 1 shows the rock stratum histogram.

4216 working face is located above 3216 working face, as shown in Figure 2. 4216 working face has stopped mining, and the stopping coal pillar is about 110 m. 3216 working face is near the final mining, so it is necessary to determine a reasonable terminal mining line.

3. Theoretical Analysis of Stress Arch Shape

Comprehensively clarifying the evolutionary law of stress arch shape before and after repeated mining of close-distance, thick coal seams is the premise of studying the mechanism of stress arch.

	Thickness (m)	Depth (m)	lithology
	12.4	382.6	Coarse sandstone
	6.5	389.1	Fine sandstone
	3.4	392.5	Siltstone
	7.5	400.0	1# coal seam
	6.0	406.0	Fine sandstone
	8.0	414.0	Medium-fine sandstone
	4.5	418.5	Kaolinite rock
	5.3	423.8	Conglomerate
	1.2	425.0	Carbonaceous mudstone
	5.5	430.5	2# coal seam
	3.2	433.7	Carbonaceous mudstone
	3.6	437.3	Kaolinite rock
	5.5	442.8	Medium-fine sandstone

Figure 1: Rock stratum histogram.

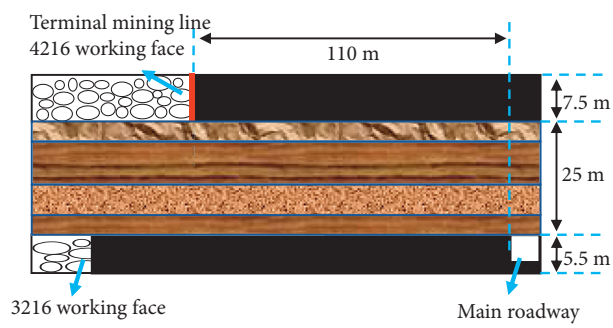

Figure 2: Strike profile of working face.

3.1. Upper Coal Seam Mining

(1) The working face starts mining from the open cut, and the roof of the goaf deflects and sinks under the action of the secondary stress field. Taking the nonmining body of the open cut and working face as the fulcrum, the roof concentrated stress area is formed, and its shape is similar to the shape of the arch, that is, the stress arch, as shown in Figure 3(a).

(2) With the continuous increase of the overhead distance of the roof, the first span fall of the immediate roof and the main roof occurred successively. The position of the rear arch foot of the stress arch remains unchanged, and the front arch foot moves forward continuously, always located in the elastic pressurization zone in front of the working face, and the arch crown moves up to the complete roof, as shown in Figure 3(b).

(3) With the mining of the working face, the roof is broken repeatedly, the breaking height is increasing, and the arch height and span are also increasing. When the working face reaches full subsidence, the arch height and span of the stress arch will no longer increase, and only the horizontal extension will occur at the arch crown, and the distribution of front

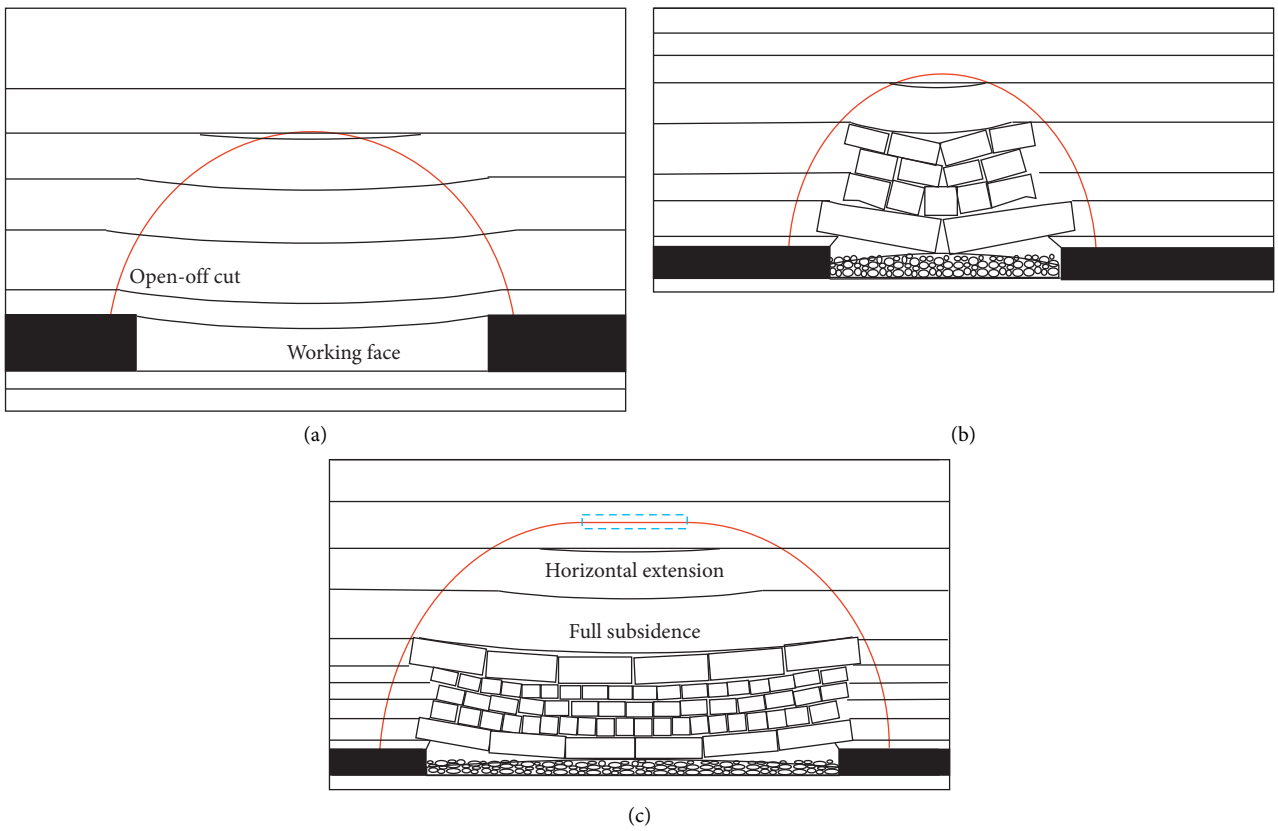

Figure 3: Stress arch shape of upper coal seam mining.

abutment pressure in the working face should no longer change, as shown in Figure 3(c).

3.2. Lower Coal Seam Mining

(1) With repeated mining, a small stress arch is formed in the interlayer, and the front and rear arch feet are located in the nonmining body of the working face and the open cut, respectively, and the stress arch shape of the upper coal seam remains unchanged, as shown in Figure 4(a).

(2) The goaf is connected to form a new stress arch. First, repeated mining affects the left half arch, and its arch height and span continue to increase until it is stable. The left and right half arches keep the stability of the stress arch under the action of horizontal restraint stress. Because the load borne by the right half arch remains unchanged, the distribution of abutment pressure in front of the working face in the upper coal seam remains unchanged, as shown in Figure 4(b).

(3) When repeated mining affects the right half arch, it has entered the final mining stage. The height and span of the right half arch continue to increase until they are the same as the left half arch, at which time a symmetrical arch structure is formed. The overlying load borne by the right half arch changes, causing the distribution of abutment pressure on the working face where the front arch foot is located to change. When the working face changes from internal stagger to external stagger at the terminal mining line, the longitudinal position of the front arch foot will change, as shown in Figures 4(c) and 4(d).

4. Numerical Simulation of Stress Arch and Abutment Pressure

4.1. Numerical Simulation Model Development. FLAC^{3D} numerical simulation software is used to study the change law of stress, arch shape, and abutment pressure of the working face in close-distance thick coal seams. According to the geological conditions, the model size was 600 m (X) × 10 m (Y) × 250 m (Z). The X-axis represents the strike direction of the working face. The displacements at the bottom, front, back, left, and right of the model were fixed, and a vertical stress of 4.75 MPa was applied to the upper boundary of the model to simulate the overburden pressure. Vertical and horizontal stresses were applied according to the measured in situ stress, and the side pressure coefficient was 1.2. The working face was excavated from the left side to the right side of the model.

The Mohr–Coulomb theory was adopted as the constitutive relation of the model. According to the literature [21–23], reasonable rock mechanics parameters can be obtained. Table 1 presents the rock mechanical parameters.

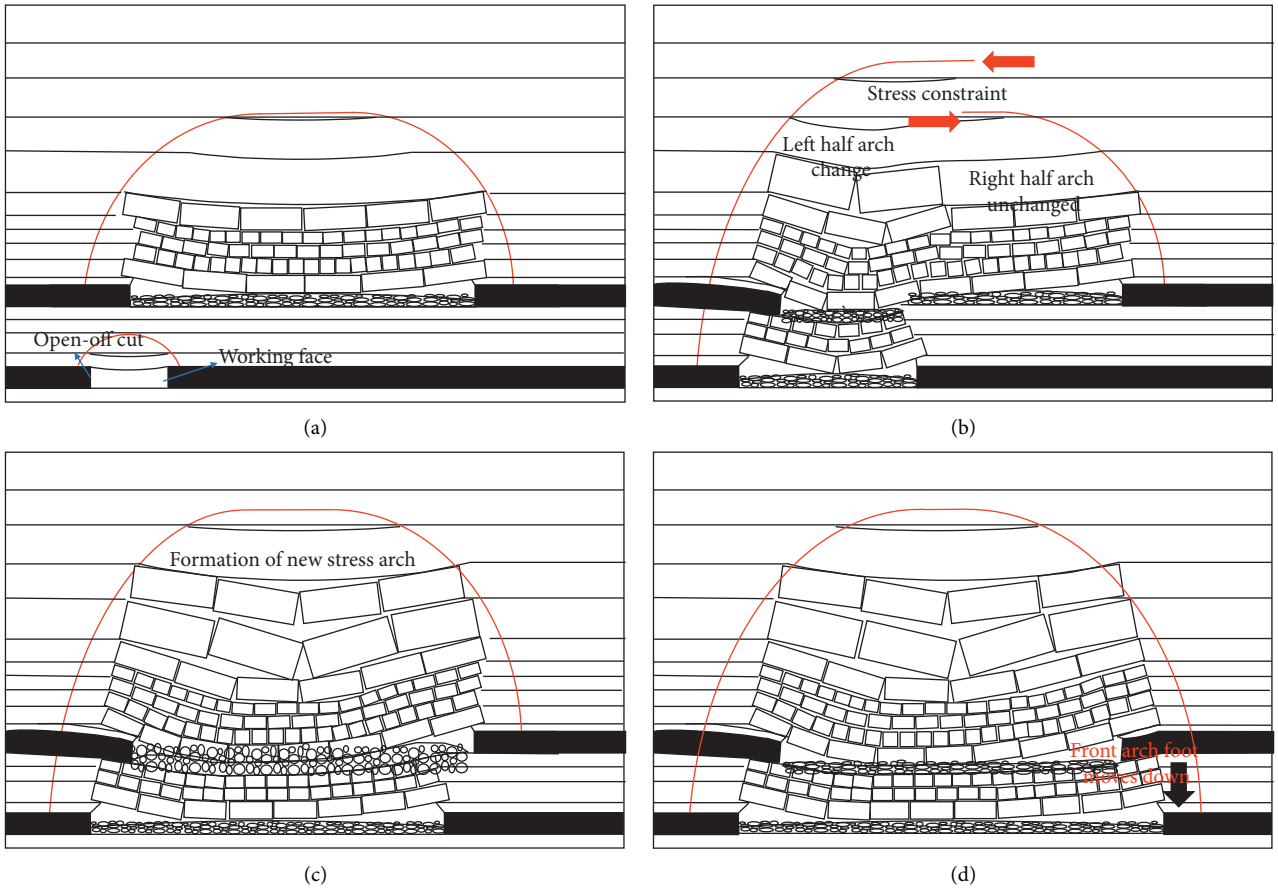

Figure 4: Stress arch shape of lower coal seam mining.

Table 1: Mechanical parameters of coal and rock mass in calculation model.

Layer	Natural density (kg/m^3)	Shear modulus (GPa)	Bulk modulus (GPa)	Cohesion (MPa)	Internal friction angle (°)	Tensile strength (MPa)
Overlying strata	2500	7.80	9.00	2.40	32	1.30
Coarse sandstone	2580	8.40	11.23	2.40	32	1.50
Fine sandstone	2612	8.24	11.79	2.83	33	1.60
Siltstone	2300	4.26	5.79	1.53	31	0.80
1# coal seam	1550	3.36	4.51	1.00	27	0.30
Fine sandstone	2612	8.24	11.79	2.73	31	1.50
Medium-fine sandstone	2580	7.90	9.30	2.20	32	1.30
Kaolinite rock	2450	6.89	8.76	2.10	30	1.20
Conglomerate	2520	7.54	9.23	2.30	31	1.40
Carbonaceous mudstone	2360	4.35	5.87	1.80	29	1.20
2# coal seam	1550	3.36	4.51	1.00	27	0.30
Carbonaceous mudstone	2360	4.35	5.87	1.80	29	1.20
Kaolinite rock	2450	6.89	8.76	2.30	30	1.40
Medium-fine sandstone	2580	7.90	9.30	2.40	32	1.30

It is particularly important for numerical simulation to accurately reflect the compaction of gangue in goaf. We used a double yield model to replace coal seam mining and simulate the caving of gangue in the goaf. The cap pressure in the double yield model was calculated using formulas (1)–(3) [24–26]:

Table 2: Cap pressures.

Strain	0.00	0.01	0.03	0.05	0.07	0.09	0.11	0.13	0.15	0.17
Stress (MPa)	0.00	0.53	1.78	3.37	5.44	8.26	12.34	18.76	30.30	57.23

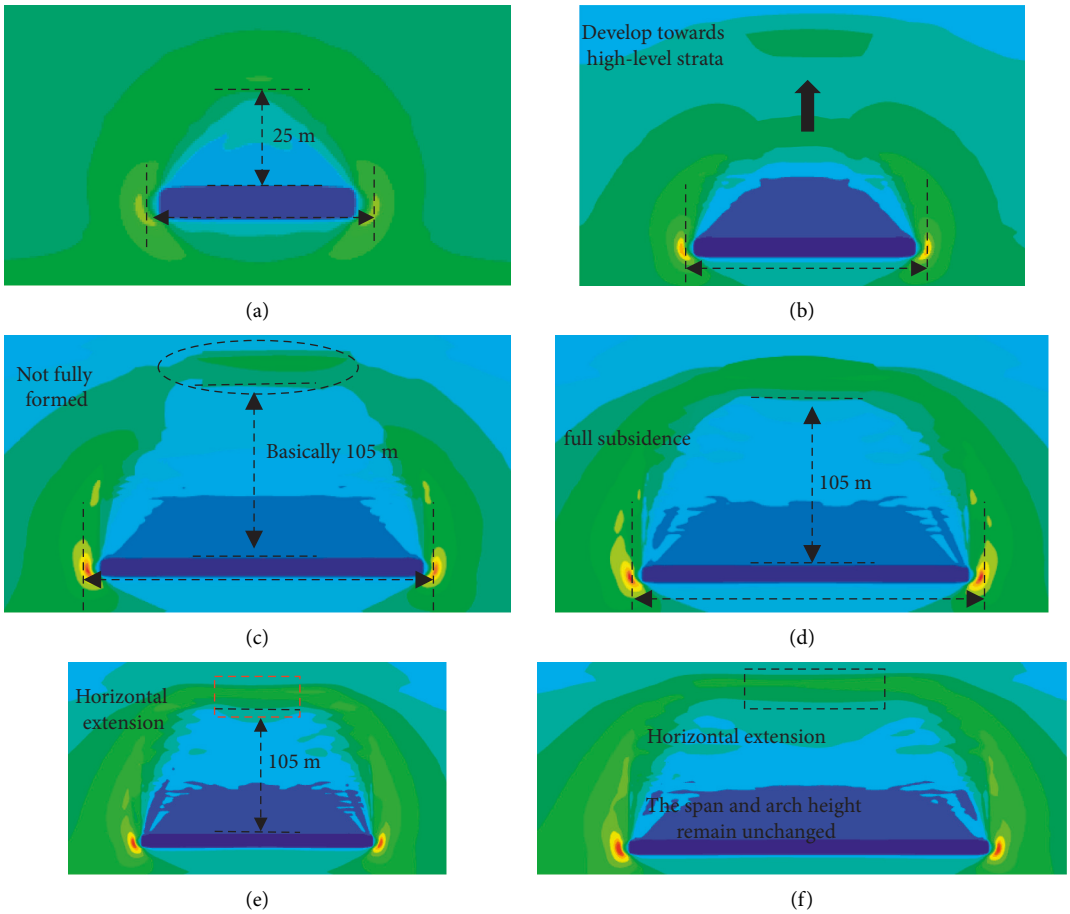

Figure 5: Evolution process of stress arch shape in upper coal seam mining. (a) 50 m, (b) 100 m, (c) 150 m, (d) 160 m, (e) 170 m, and (f) 210 m.

$$\sigma\text{cap} = \frac{E0\varepsilon}{1-(\varepsilon/\varepsilon\max)}, \quad (1)$$

$$\varepsilon\max = \frac{Kp-1}{Kp}, \quad (2)$$

$$E0 = \frac{10.39\sigma c^{1.042}}{Kp^{7.7}}, \quad (3)$$

where σcap is the pressure on the gangue in the goaf; ε is the volume strain of gangue in goaf under the action of σcap; ε max is the maximum volumetric strain that can be produced by gangue in goaf; $E0$ is the initial elastic modulus of gangue in goaf; Kp is the coefficient of dilatancy of caving rock mass, and 1.25; σc is the compressive strength of rock mass, 23.7 MPa. Then, formula (1) can get σcap, as shown in Table 2.

4.2. 4216 Working Face Mining. A 70 m boundary was set on the left side of the model for excavating the 4216 working face, and the excavation is carried out step by step to 210 m. The evolution of the stress arch shape is shown in Figure 5.

At the same time, stress monitoring points are arranged at an interval of 1 m in the front along the strike during the mining process of the working face, and the evolution of abutment pressure distribution with the mining of the working face is analyzed.

It can be seen from the analysis of Figures 5 and 6:

(1) When the 4216 working face is mined for 50 m–160 m, the shape of the stress arch changes constantly, and the peak value and influence range of abutment pressure also increase continuously. The peak value increased from 21 MPa to 30.5 MPa, and the influence range increased from 23 m to 75 m.

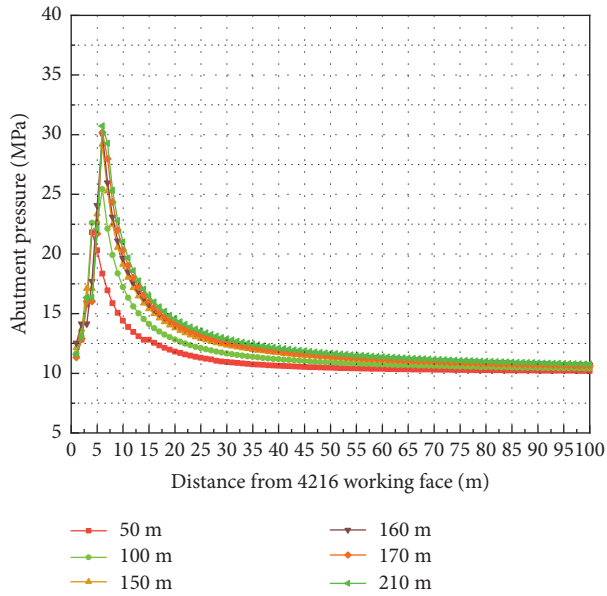

Figure 6: Abutment pressure of 4216 working face.

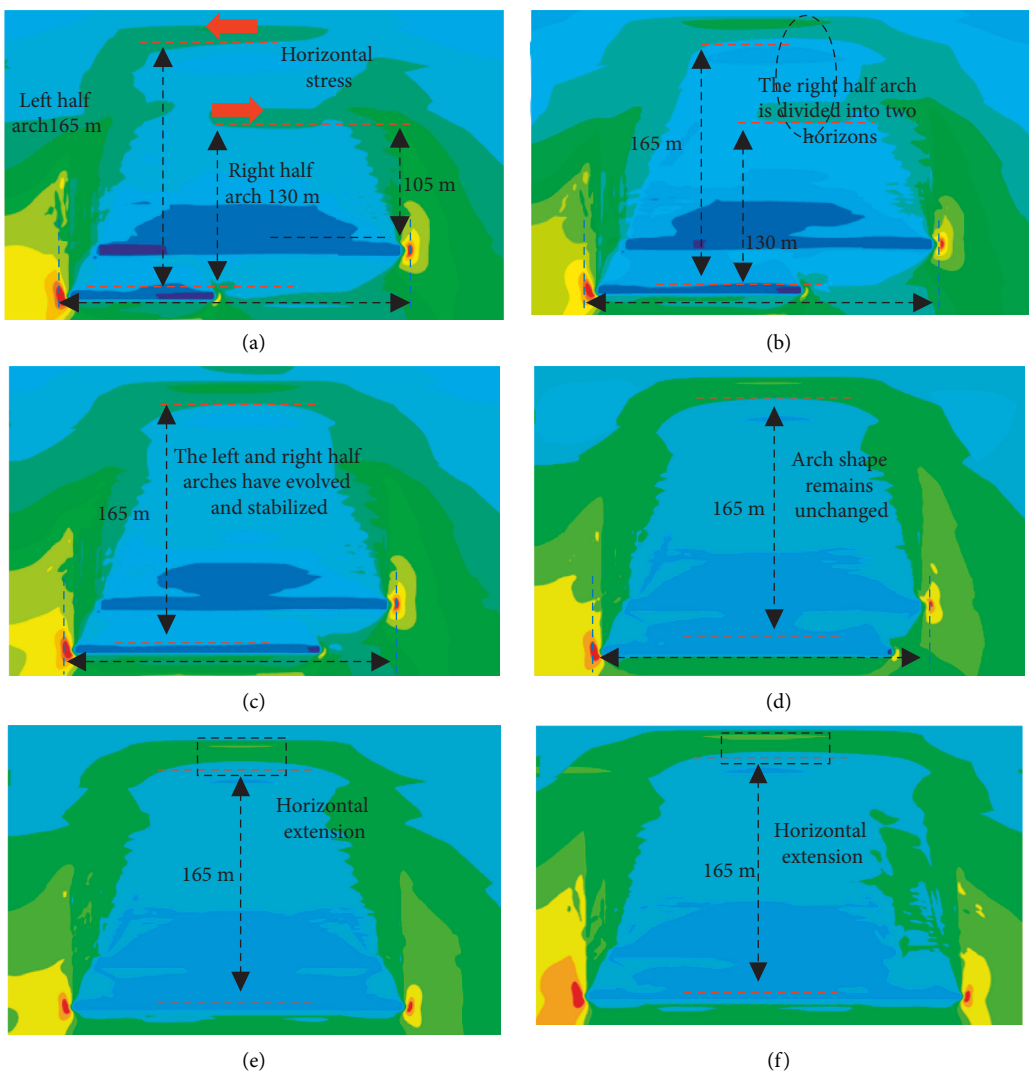

Figure 7: Evolution process of stress arch shape in repeated mining: (a)internal stagger 180 m, (b) internal stagger 90 m, (c) internal stagger 50 m, (d) internal stagger 20 m, (e) external stagger 20 m, and (f) external stagger 50 m.

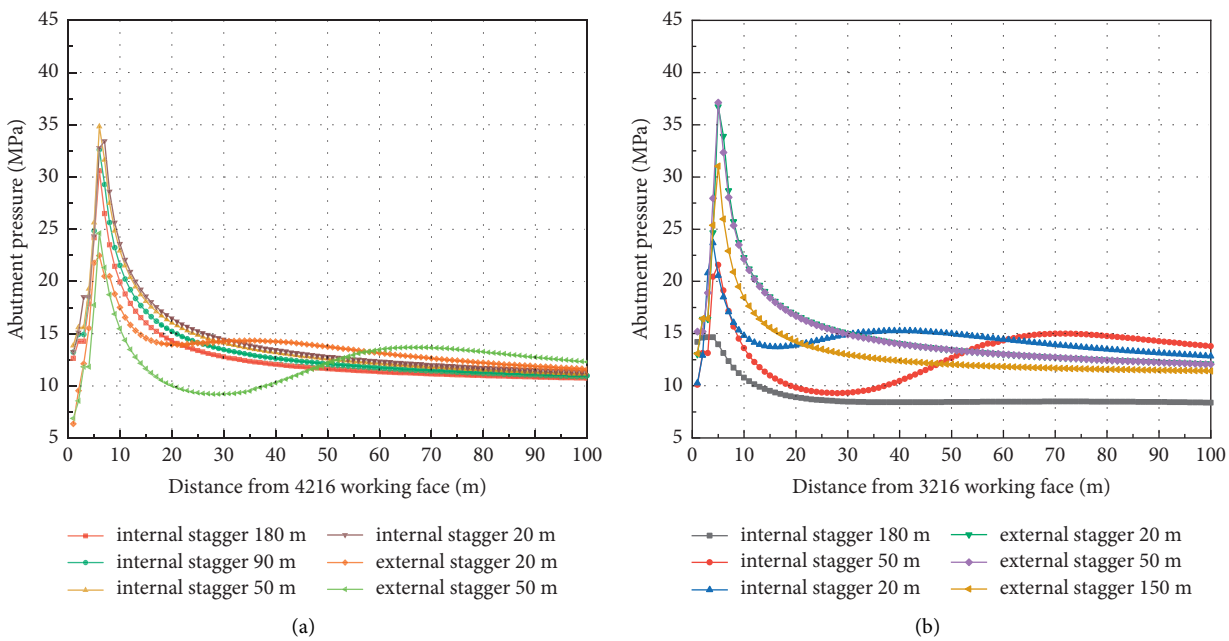

Figure 8: Abutment pressure of the two working faces. (a) Abutment pressure of 4216 working face, (b) Abutment pressure of 3216 working face.

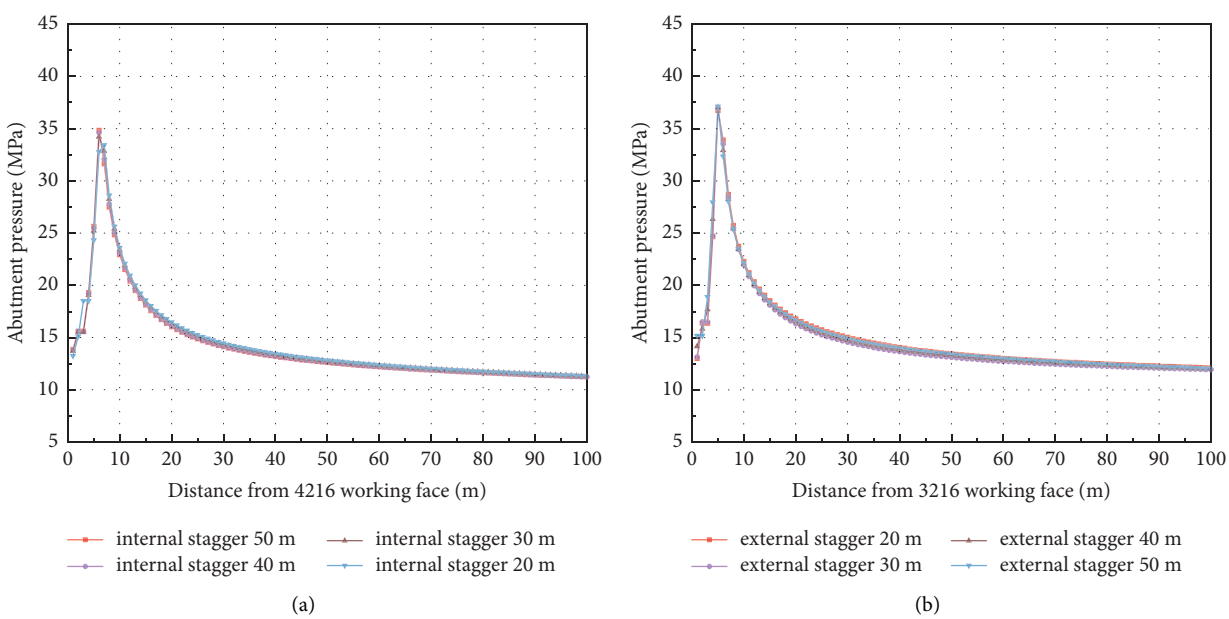

Figure 9: Abutment pressure of the two working faces. (a) Abutment pressure of 4216 working face, (b) Abutment pressure of 3216 working face.

(2) Mining to 160 m, reaching full subsidence, the shape of the stress arch remains unchanged, and the distribution of abutment pressure does not change.

(3) The numerical simulation results show that the shape of the stress arch is highly related to the distribution of abutment pressure, which is consistent with the theoretical analysis in Section 3.1.

4.3. 3216 Working Face Mining. Connected to 4216 working face mining 210 m, a 50 m boundary was set on the left side of the model for excavating 3216 working face, and the excavation is carried out step by step to 280 m. The relative position of 3216 working face and 4216 working face is described by the horizontal distance between them.

Table 3: Mechanical parameters of coal and rock mass in calculation model.

Layer	Natural density (kg/m^3)	Shear modulus (GPa)	Bulk modulus (GPa)	Cohesion (MPa)	Internal friction angle (°)	Tensile strength (MPa)
Coarse sandstone	2580	8.40	11.23	3.40	32	1.50
Fine sandstone	2612	8.24	11.79	5.83	33	2.60
Siltstone	2300	4.26	5.79	2.53	31	1.20
1# coal seam	1550	3.36	4.51	1.50	27	0.80
Fine sandstone	2612	8.24	11.79	3.73	31	2.50
Medium-fine sandstone	2580	7.90	9.30	5.20	32	1.40
Carbonaceous mudstone	2360	4.35	5.87	3.80	29	1.20
2# coal seam	1550	3.36	4.51	1.50	27	0.80
Carbonaceous mudstone	2360	4.35	5.87	2.80	29	1.80
Medium-fine sandstone	2580	7.90	9.30	2.40	32	1.30

Similarly, stress monitoring points are arranged at an interval of 1 m along the mining direction of the two working faces, and the evolution of abutment pressure distribution with repeated mining is analyzed.

It can be seen from the analysis of Figures 7 and 8 that

(1) In the case of an internal stagger, the front arch foot is located at 4216 working face, and in the case of an external stagger, the arch foot moves down to 3216 working face.

(2) As shown in Figure 7(a), when the internal stagger is 180 m, the shape of the left half arch changes, while the shape of the right half arch remains unchanged. This stage corresponds to Figure 4x(d). The front arch foot is located in the 4216 working face, and its abutment pressure distribution is basically unchanged. 3216 working face belongs to pressure relief mining;

(3) As shown in Figure 7(b), when the internal stagger is 90 m, the shape of the right half arch begins to change, and the peak value and influence range of the abutment pressure of the 4216 working face increase to 32.6 MPa and 85 m;

(4) As shown in Figures 7(c) and 7(d), when the internal stagger is 50 m, the peak value and influence range of abutment pressure of 4216 working face continue to increase to 35 MPa and 95 m. Continue mining to an internal stagger of 20 m, the shape of the right half arch remains stable, and its abutment pressure distribution remains unchanged. This stage corresponds to Figure 4(c);

(5) When the external stagger is 20–50 m, the shape of the stress arch is stable, the front arch foot is transferred to the 3216 working face, and the peak value and influence range of the abutment pressure of the 4216 working face are greatly reduced. The peak value and influence range of the abutment pressure of 3216 working face were increased to 36.5 MPa and 95 m and remained unchanged. This stage corresponds to Figure 4(d).

(6) When the external stagger is 150 m, the peak value and influence range of abutment pressure of 3216 working face are significantly reduced, which is similar to the mining of 4216 working face.

(7) The numerical simulation results show that the shape of the stress arch is highly related to the distribution of abutment pressure, which is consistent with the theoretical analysis in Section 3.2.

When the internal stagger is 50 m to the external stagger, 50 m, the abutment pressure distribution of the working face where the front arch foot is located is extracted, as shown in Figure 9. Analysis shows that:

(1) When the working face changes from an internal stagger of 50 m to an external stagger of 50 m, the shape of the stress arch remains unchanged, only the front arch foot moves down, and the load borne by the stress arch does not change, so the abutment pressure distribution of the working face where the front arch foot is located does not change;

(2) Under the action of the stress arch structure, the layout of the terminal mining line only needs to consider the influence range of the front abutment pressure of the working face where the front arch foot is located, and the stagger distance of the terminal mining line only needs to ensure the safety of the working face.

5. Numerical Simulation of Reasonable Stagger Distance of Terminal Mining Line

5.1. Numerical Simulation Model Development. In this section, UDEC numerical simulation software is used to study the reasonable stagger distance of the terminal mining line. According to geological conditions, the model size was 200 m (X) × 105 m (Y). The displacement at the bottom, left, and right of the model were fixed, and a vertical stress of 9.01 MPa was applied to the upper boundary of the model to simulate the overburden pressure. Vertical and horizontal stresses were applied according to the measured in situ

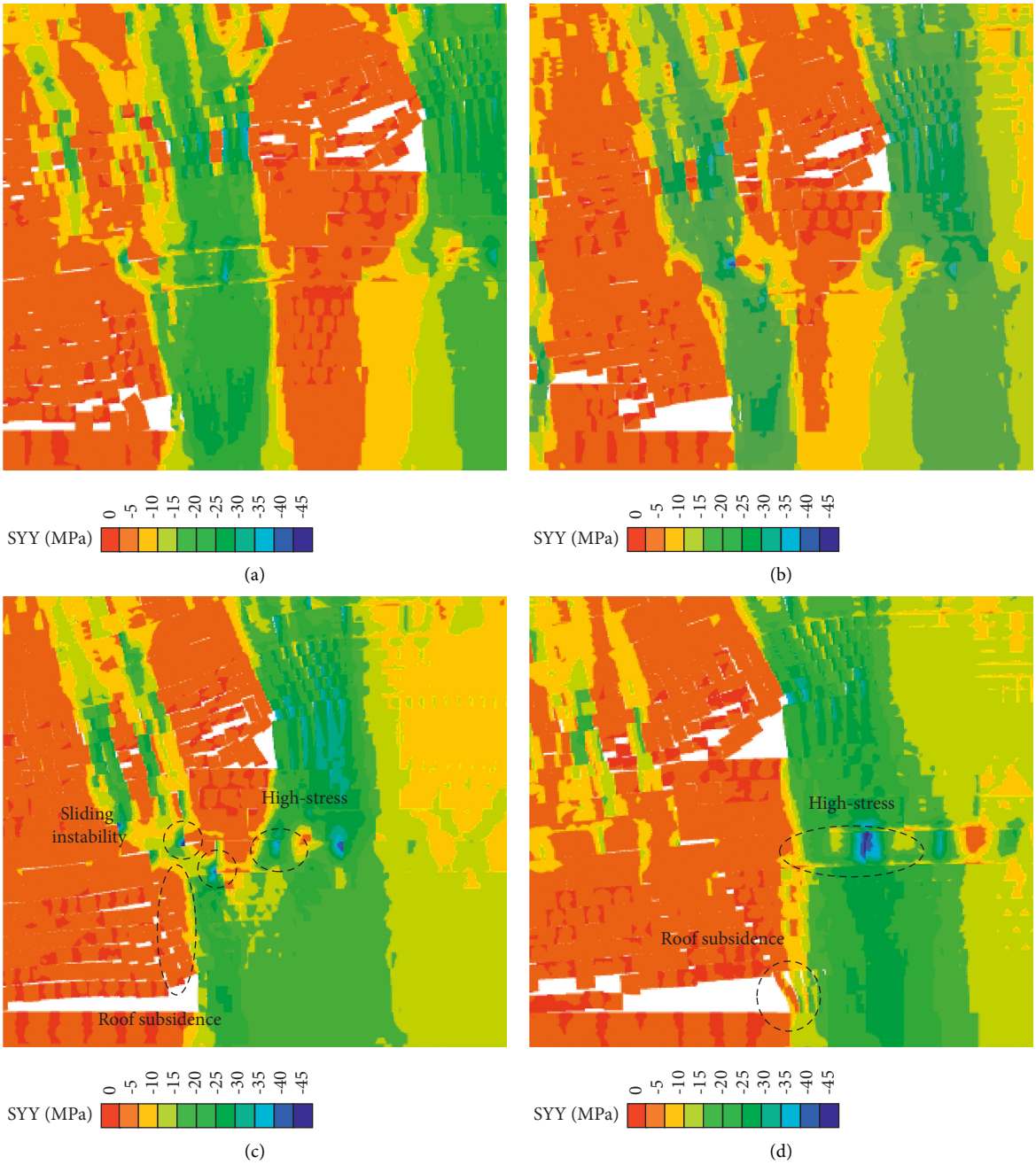

Figure 10: Continued.

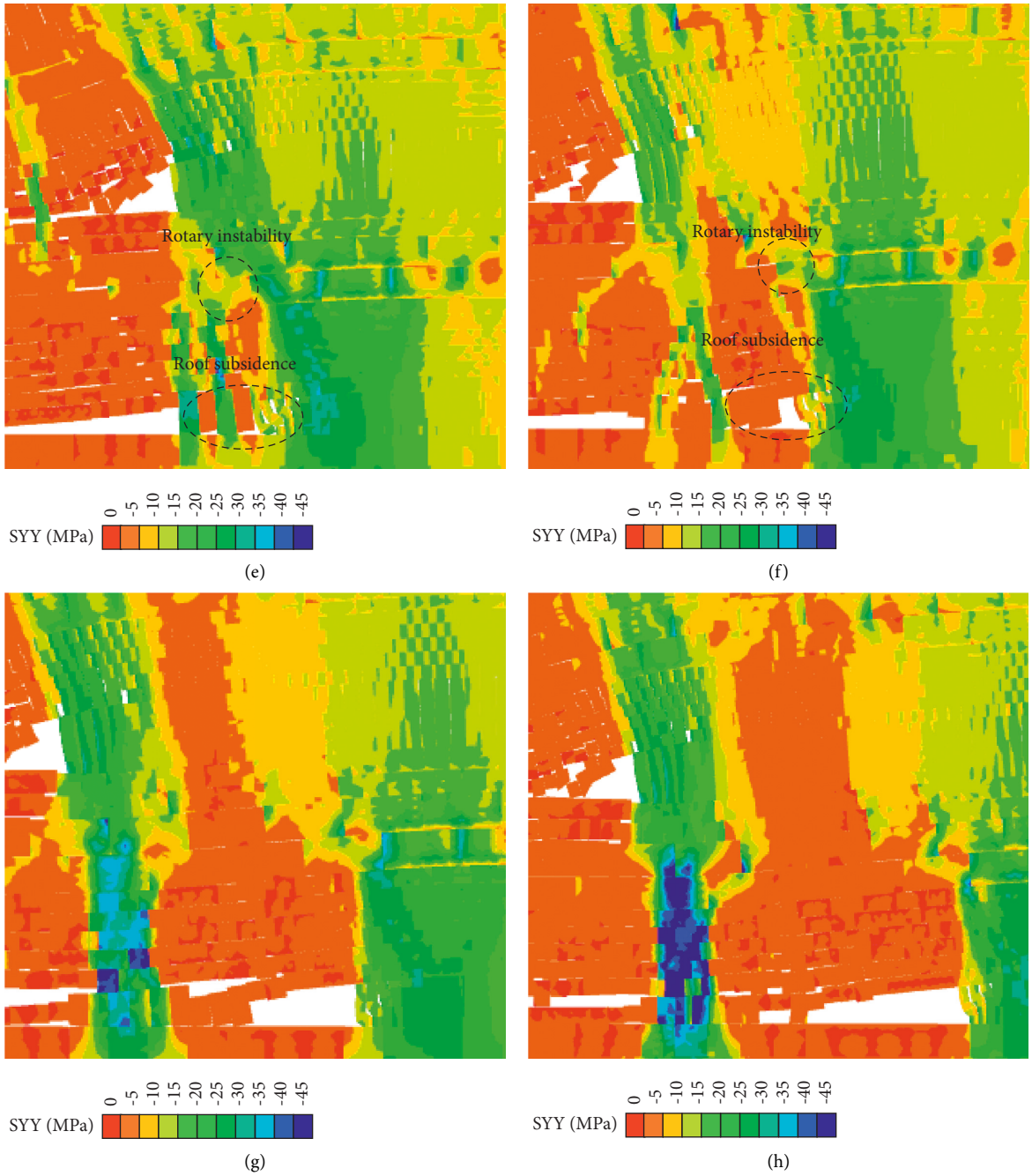

Figure 10: Ground pressure of working face in different stagger distance: (a) internal stagger 30 m, (b) internal stagger 20 m, (c) internal stagger 10 m, (d) overlap, (e) external stagger 10 m, (f) external stagger 20 m, (g) external stagger 30 m, and (h) external stagger 40 m.

stress, and the side pressure coefficient was 1.2. The Mohr–Coulomb theory was adopted as the constitutive relation of the model. Table 3 presents the rock mechanical parameters.

5.2. Model Excavation. First, we excavate the 4216 working face of 120 m. Then, we excavate 3216 working face to 90 m, 100 m, 110 m, 120 m, 130 m, 140 m, 150 m, and 160 m. The working face was excavated from the left side to the right side of the model. The relative position of 3216 working face and 4216 working face is described by the horizontal distance between them.

It can be seen from the analysis of Figure 10 that

(1) When the internal stagger is greater than 20 m, the main roof of the interlayer is well spliced, and the high stress range of the main roof is not large, as shown in Figures 10(a) and 10(b);

(2) When the internal stagger is 10 m to the external stagger, 10–20 m, the stress range of the main roof of the interlayer is large, and sliding and rotary

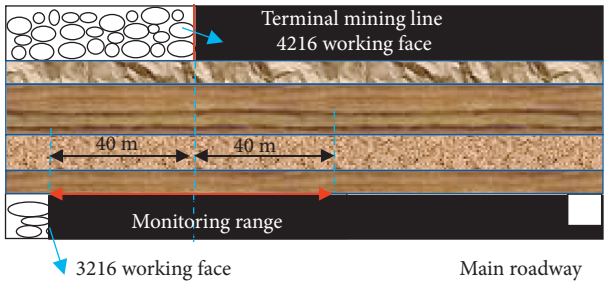

Figure 11: Monitoring scheme.

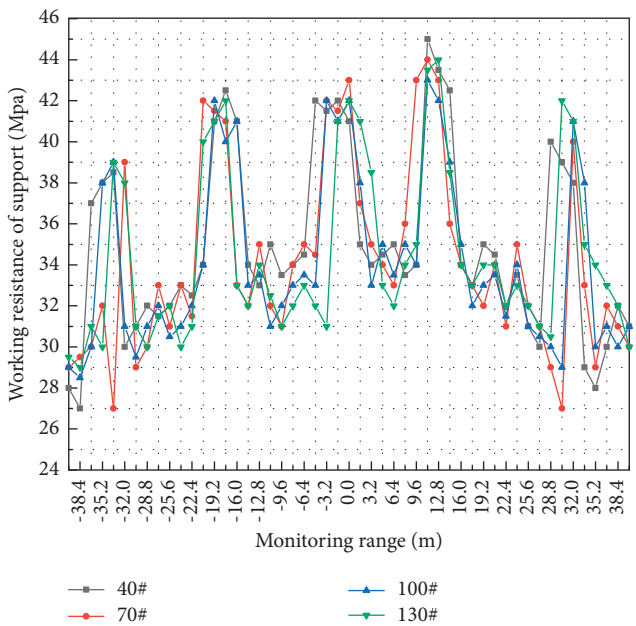

Figure 12: Working resistance curve of supports.

instability of the main roof are shown in Figures 10(c)–10(f);

(3) When the external stagger is greater than 30 m, the main roof splicing is good, the roof subsidence is small, and the surrounding rock of 3216 working face is relatively complete, as shown in Figures 10(g) and 10(h).

To sum up, the 3216 working face should be staggered at least 20 m internally or 30 m externally at the terminal mining line of the 4216 working face.

6. Field Measurement

In order to determine the reasonable internal and external stagger distance of the terminal mining line, install the support working resistance monitoring station at the 40#, 70#, 100#, and 130# supports of 3216 working face to monitor the roof pressure in the final mining stage in real time, as shown in Figure 11.

It can be seen from the analysis of Figure 12 that

(1) A total of five times of periodic weighting is monitored at a distance of 80 m. When the internal stagger is about 33 m, the main roof is weighted, and the periodic weighting strength is not large;

(2) When the internal stagger is 22 m to the external stagger, 26 m, the pressure of the supports increases significantly;

(3) When the external stagger is more than 26 m, the pressure of the supports begins to decrease.

Comprehensive numerical simulation and field measurement results: 3216 working face should be staggered at least 22 m internally or 30 m externally at the terminal mining line of 4216 working faces.

7. Conclusions

(1) During the mining of 4216 working face, the peak value and influence range of abutment pressure continue to increase until the shape of the stress arch is stable. With repeated mining, the shape of the left and right half arches of the stress arch changes in order of time and space until it is stable. When the shape of the right half arch changes, the distribution of abutment pressure on the working face where the arch foot is located also changes until the shape is stable.

(2) Under the action of the stress arch structure, the layout of the terminal mining line in close-distance thick coal seams only needs to consider the influence range of the front abutment pressure of the working face where the front arch foot is located, and the stagger distance of the terminal mining line only needs to ensure the safety of the working face in the lower coal seam.

(3) When the internal stagger distance between 3216 working face and the terminal mining line of 4216 working face is greater than 22 m or the external stagger distance is greater than 30 m, the left stopping coal pillar has little impact on 3216 working face, and 3216 working face is located in a relatively safe position, which can be regarded as the minimum safe stagger distance.

Data Availability

The data used to support the findings of this research are included within the paper.

Conflicts of Interest

The authors declare that they have no conflicts of interest.

Acknowledgments

This work was supported by the National Natural Science Foundation of China (No. 51974317), the Fundamental Research Funds for the Central Universities (2022YJSNY09), and the China Scholarship Council (Nos. 202106430048 and 202106430055).

References

[1] G. X. Xie, "Numerical investigation on the influence of surrounding rock stress hell on fractured field," *Journal of China Coal Society*, vol. 40, no. 9, pp. 2009–2014, 2015.

[2] S. R. Wang, X. G. Wu, Y. H. Zhao, P. Hagan, and C. Cao, "Evolution characteristics of composite pressure-arch in thin bedrock of overlying strata during shallow coal mining," *International Journal of Applied Mechanics*, vol. 11, no. 03, Article ID 1950030, 2019.

[3] F. Wang and T. Chen, "Formation mechanism of stress arch during longwall mining based on key strata theory," *Energy Exploration & Exploitation*, vol. 40, Article ID 01445987211042701, 2021.

[4] D. M. Yang and W. B. Guo, "Structural characteristics and evolution mechanism of overlying strata pressure arch in shallow and flat seams," *Journal of Mining & Safety Engineering (In Chinese)*, vol. 36, no. 2, pp. 323–330, 2019.

[5] S. R. Wang, X. G. Wu, Y. Zhao, and P. Hagan, "Mechanical performances of pressure arch in thick bedrock during shallow coal mining," *Geofluids*, vol. 2018, Article ID 2419659, 13 pages, 2018.

[6] X. Z. Yue and M. Xu, "Calculation of subsidiary mining stress in floor roadway under the remaining boundary pillar of close coal seam mining," *Journal of Mining & Safety Engineering (In Chinese)*, vol. 38, no. 02, pp. 246–252+259, 2021.

[7] Y. H. Zhao and J. Yu, "Characterization of pressure arching effect of arch shell surrounding rock considering deviation of principal stress axis," *Chinese Journal of Geotechnical Engineering*, vol. 43, no. 10, pp. 1842–1850+1958, 2021.

[8] Y. H. Zhao, S. R. Wang, P. Hagan, L. Ren, and Z. Zou, "Pressure-arching characteristics in roof blocks during shallow coal mining," *Advances in Civil Engineering*, vol. 2018, Article ID 6817059, 12 pages, 2018.

[9] B. W. Xia, X. Zhang, B. Yu, and J. Jia, "Weakening effects of hydraulic fracture in hard roof under the influence of stress arch," *International Journal of Mining Science and Technology*, vol. 28, no. 6, pp. 951–958, 2018.

[10] C. Y. Jin, A. L. Shao, D. Liu, T. Han, F. Fan, and S. Li, "Failure mechanism of highly stressed rock mass during unloading based on the stress arch theory," *International Journal of Geomechanics*, vol. 18, no. 11, Article ID 04018146, 2018.

[11] H. B. Zhao and H. Cheng, "Study of the mechanism and evolution law of unsymmetrical failure of the mining roadway in close distance coal seam," *Journal of China University of Mining & Technology*, vol. 50, no. 6, pp. 1029–1040, 2021.

[12] G. Y. Peng G and M. Z. Gao, "Investigation on mining mechanics behavior of deep close distance seam group," *Journal of China Coal Society*, vol. 44, no. 7, pp. 1971–1980, 2019.

[13] F. L. He, K. Lv, X. Li, B. Qin, and L. Li, "Failure mechanism and control of lower retracement channel in close-distance double-thick coal seams," *Shock and Vibration*, vol. 2021, Article ID 6651099, 19 pages, 2021.

[14] H. F. Shang, J. G. Ning, S. Hu, S. Yang, and P. Qiu, "Field and numerical investigations of gateroad system failure under an irregular residual coal pillar in close-distance coal seams," *Energy Science & Engineering*, vol. 7, no. 6, pp. 2720–2740, 2019.

[15] K. Lv and F. L. He, "Field and simulation study of the rational retracement channel position and control strategy in close-distance coal seams," *Energy Science & Engineering*, vol. 10, 2022.

[16] Z. Z. Zhang, M. Deng, J. Bai, S. Yan, and X. Yu, "Stability control of gob-side entry retained under the gob with close distance coal seams," *International Journal of Mining Science and Technology*, vol. 31, no. 2, pp. 321–332, 2021.

[17] Q. Li, G. Y. Wu, and D. Kong, "Study on stability of stope surrounding rock under repeated mining in close-distance coal seams," *Geofluids*, vol. 2022, Article ID 9630942, 17 pages, 2022.

[18] X. J. Liu and X. M. Li, "Analysis on the floor stress distribution and roadway position in the close distance coal seams," *Arabian Journal of Geosciences*, vol. 9, no. 83, pp. 1–8, 2016.

[19] S. B. Li, L. Wang, C. Zhu, and Q. Ren, "Research on mechanism and control technology of rib spalling in soft coal seam of deep coal mine," *Advances in Materials Science and Engineering*, vol. 2021, Article ID 2833210, 9 pages, 2021.

[20] R. Gao, T. J. Kuang, X. B. Meng, and B. Huo, "Effects of ground fracturing with horizontal fracture plane on rock breakage characteristics and mine pressure control," *Rock Mechanics and Rock Engineering*, vol. 54, no. 6, pp. 3229–3243, 2021.

[21] Y. X. Zhao and T. Wang, "Application of Hoek-Brown criterion in numerical simulation of ground pressure features in multi-seam longwall mining," *Journal of China Coal Society*, vol. 38, no. 6, pp. 970–976, 2013.

[22] H. W. Wang, B. A. Poulsen, B. Shen, S. Xue, and Y. Jiang, "The influence of roadway backfill on the coal pillar strength by numerical investigation," *International Journal of Rock Mechanics and Mining Sciences*, vol. 48, no. 3, pp. 443–450, 2011.

[23] N. Mohammad, D. J. Reddish, and L. Stace, "The relation between in situ and laboratory rock properties used in numerical modelling," *International Journal of Rock Mechanics and Mining Sciences*, vol. 34, no. 2, pp. 289–297, 1997.

[24] S. L. Wang, S. P. Hao, Y. Chen, J. B. Bai, X. Y. Wang, and Y. Xu, "Numerical investigation of coal pillar failure under simultaneous static and dynamic loading," *International Journal of Rock Mechanics and Mining Sciences*, vol. 84, pp. 59–68, 2016.

[25] M. Shabanimashcool and C. C. Li, "A numerical study of stress changes in barrier pillars and a border area in a longwall coal mine," *International Journal of Coal Geology*, vol. 106, pp. 39–47, 2013.

[26] Z. Z. Zhang, J. B. Bai, Y. Chen, and S. Yan, "An innovative approach for gob-side entry retaining in highly gassy fully-mechanized longwall top-coal caving," *International Journal of Rock Mechanics and Mining Sciences*, vol. 80, pp. 1–11, 2015.

Hindawi
Advances in Materials Science and Engineering
Volume 2022, Article ID 8176721, 10 pages
https://doi.org/10.1155/2022/8176721

Research Article

Effect of Loading Rates on Mechanical Characteristics and Rock Burst Tendency of Coal-Rock Combined Samples

Jiang Hu and Jingang Li

Bulianta Coal Mine of National Energy Shendong Coal Group, Shenmu, Shannxi 719300, China

Correspondence should be addressed to Jiang Hu; qingma@sdust.edu.cn

Received 11 May 2022; Accepted 13 August 2022; Published 9 September 2022

Academic Editor: Depeng Ma

According to the universal law of thermodynamics, the failure of any substance is closely related to its energy change. Understanding the strain energy and rock burst tendency of rock or coal under different loading rates is critical in many geological projects, such as mining, tunneling, and other underground engineering project. The mechanical and energy evolution characteristics of the coal-rock combined sample under different loading rates of uniaxial compression were numerically investigated. And, the rock burst tendency was also calculated by the Rock Burst Energy Index K_E. The results show that with the increase of the loading rate, the total input energy, elastic strain energy, and dissipation energy all show an increasing trend. But the growth trend is different. And, under the five loading rates, the Rock Burst Energy Index K_E of the coal-rock combined sample were all between $1.5 \leq K_E < 5$. That is, they all have weak rock burst tendency. And the rock burst energy index increases first and then decreases with the increase of loading rates. This study provides references for propulsion speed of working face in the field mining practice.

1. Introduction

The coal-rock combined sample is often seen in the process of coal mining, such as the combined structure formed by coal pillars and roof and floor rocks [1–3]. Affected by the propulsion speed of working face, construction of adjacent working face, blasting, and other engineering disturbances, the coal-rock combined structure will be affected by different load rates [4–6]. Currently, the loading rate in rock mechanics is a variable parameter. Different loading rates should be considered for different engineering problems. Different loading rates have a great influence on the mechanical and energy characteristics of rock materials [7–10].

Scholars have done a lot of research on the strength and failure characteristics of coal-rock combined samples. The research focuses on theoretical research, numerical simulation tests, indoor rock mechanics tests and so on [11–13]. These studies have a good reference value for the strength and deformation characteristics of coal-rock combined samples. For a long time, the rock strength and failure criterion based on the classical elastic-plastic theory has been the basis for judging engineering failure. However, as a description of a specific mechanical state, stress-strain is only one aspect of the thermodynamic state of the rock. The mechanical parameters such as the stress-strain curve and rock strength obtained from laboratory tests are very discrete. Even the specimens from the same rock mass of the same rock will be quite different, and the engineering calculation will produce errors due to the inaccurate selection of parameters. Energy conversion is the essential feature of the material physical process, so it is necessary to study the energy characteristics of the coal-rock combined sample [14–17]. According to the structural characteristics of coal and rock, and the mechanical characteristics of the coal-rock combined sample, Chen et al. [18] gives the calculation formula of energy distribution before failure of equal diameter coal and rock combination and nonequal diameter coal and rock combination, and uses the energy distribution calculation formula to calculate the energy distribution before failure of the combination. Li et al. [19] used a split Hopkinson compression bar (SHPB) to carry out impact compression tests on coal and rock monomer and combined

samples, and analyzed the energy dissipation and fragmentation characteristics of the specimens. Yang et al. [20] analyzed the evolution laws of mechanical parameters such as input energy density, elastic energy density, dissipated energy density, elastic modulus, and uniaxial compressive strength of the coal-rock combined sample and obtained the energy storage characteristics of different samples. Zhao et al. [21] used the DYD-10 electronic universal testing machine and PCI-8 acoustic emission signal acquisition system to carry out the mechanical and energy characteristics experiments of the whole process of deformation and failure of coal-like rock materials with different coal thickness under a uniaxial load. Ma et al. [15, 17] studied the energy characteristics of the coal-rock combined sample with different coal-rock height ratios through numerical simulation. In conclusion, it can be seen that the research on the mechanical and energy characteristics of the coal-rock combined sample has made a wealth of research results. However, there is a lack of research on the energy characteristics and rock burst tendency of the coal-rock combined sample under uniaxial compression with different loading rates.

Therefore, taking the combined structure formed by roof rock, coal, and floor rock in mining engineering as the research background, according to the size standard recommended by the International Society of Rock Mechanics (ISRM), the energy evolution characteristics of the coal-rock combined samples under different loading rates are studied by numerical simulation, and the rock burst tendency of coal-rock combined samples under different loading rates is calculated by the Rock Burst Energy Index K_E.

2. Numerical Model and Energy Calculation Method for the Combined Sample

2.1. Numerical Model. The meso parameters of coal and rock in reference [2, 3, 22, 23] are selected for coal-rock combined sample simulation, as shown in Table 1. The ratio of normal stiffness to tangential stiffness of coal and rock particles, and the ratio of normal stiffness to tangential stiffness of parallel bond are set to 2.5. The multipliers of the parallel bond radius are all set to 1, and the particle contact modulus is equal to the parallel bond modulus. The normal strength of the parallel bond is equal to the tangential strength of the parallel bond (rock : coal = 3 : 1). The physical and numerical model is shown in Figure 1.

2.2. Energy Calculation Method for the Coal-Rock Combined Sample. The energy evolution characteristics in the uniaxial compression process of the coal-rock combined sample is complicated, accompanied by the transfer and transformation of energy between coal and rock. The dissipative energy (U^d) is used to form internal damage and plastic deformation of the coal-rock combined sample. U^d is shown by the blue shadow area in Figure 2.

The releasable strain energy (U^e) is the elastic strain energy released after the coal-rock combined sample unit is unloaded. This part of energy is directly related to the unloading elastic modulus and the unloading Poisson's ratio. The red shadow area (U^e) under the stress-strain curve shown in Figure 2 represents the releasable strain energy stored in the coal-rock combined sample. From a thermodynamic point of view, energy dissipation is unidirectional and irreversible, while energy release is bidirectional, as long as certain conditions are met [5, 24].

Considering the deformation of a rock under the action of external force, it is obtained from the first law of thermodynamics [5, 24].

$$U = U^d + U^q, \tag{1}$$

$$U = \int \sigma_1 d\varepsilon_1 = \sum_{i=1}^{n} \frac{1}{2}\left(\sigma_{1i} + \sigma_{1i-1}\right)\left(\varepsilon_{1i} + \varepsilon_{1i-1}\right), \tag{2}$$

$$U^e = \frac{1}{2\bar{E}}\left[\sigma_1^2 + \sigma_2^2 + \sigma_3^2 - 2\bar{\nu}\left(\sigma_1\sigma_2 + \sigma_2\sigma_3 + \sigma_1\sigma_3\right)\right], \tag{3}$$

where $\bar{E}$ and $\bar{\nu}$ are the average values of unloading elastic modulus and Poisson's ratio, respectively.

Equation (3) is the calculation formula of elastic strain energy that can be released under triaxial compression. When the rock is under uniaxial compression ($\sigma_2 = \sigma_3 = 0$), equation (3) becomes

$$U^e = \frac{\sigma_1^2}{2\bar{E}}. \tag{4}$$

In this paper, the energy accumulation and dissipation characteristics of the coal-rock combined sample under different loading rates are calculated according to the abovementioned formulas.

3. Results and Analysis

3.1. Strength and Deformation Characteristics. The stress-strain curves of coal-rock combined samples under different loading rates are shown in Figure 3. It can be seen from Figure 3 that under different loading rates, the change trends of the stress-strain curves of the coal-rock combined samples are basically the same. Generally, they all experience three stages: initial compaction, linear elasticity, and macroscopic failure. At low loading rates, the postpeak stress-strain curve shows a "step-like" drop, while at high loading rates, the curve drops more smoothly with a smaller slope. As the loading rate increases, the opening of the stress-strain curve also increases.

The variation trends of elastic modulus, peak strength, and peak strain of coal-rock combined samples under different loading rates are shown in Figure 4. It can be seen from Figure 4(a) that with the increase of the loading rate, the elastic modulus of the coal-rock combined sample shows a nonlinear decreasing trend. Its change trend can be represented by $y = 9.503 + 0.988/(1 + (x + 0.055)^{3.535})$, $R^2 = 99.74\%$. The deceleration rate shows a trend of increasing first and then decreasing. It can be seen from Figures 4(b) and 4(c) that the peak strength and peak strain of the coal-rock combined sample increase nonlinearly with the loading rate. The increasing trend of peak strain can be

Table 1: Micromechanical parameters of coal and rock [2, 3, 22, 23].

Mechanical parameters	ρ/kg·m^{-3}	Rmin/mm	Rmax/Rmin	E_c/GPa	K_n/K_s	$\bar{E}$/GPa	$\bar{K}_n/\bar{K}_s$	$\bar{\sigma}_c$/MPa	$\bar{\tau}_c$/MPa	μ
Roof rock	2600	0.2	1.5	12	2.5	12	2.5	45	45	0.5
Coal	1800	0.2	1.5	4	2.5	4	2.5	15	15	0.5
Floor rock	2600	0.2	1.5	12	2.5	12	2.5	45	45	0.5

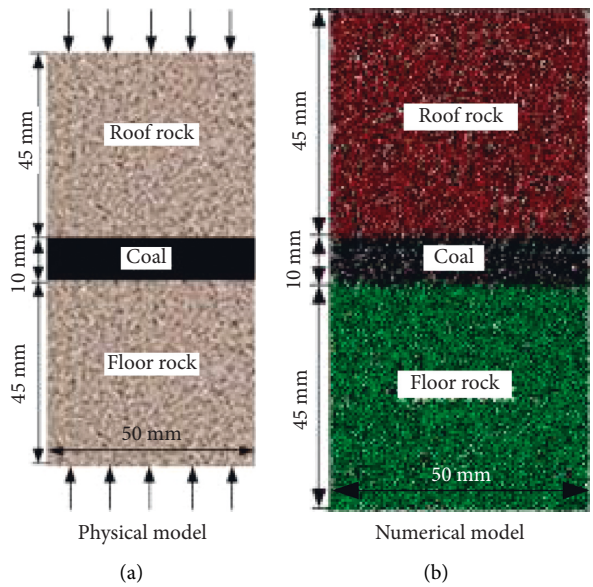

Figure 1: Physical and numerical model of the coal-rock combined sample. (a) Physical model. (b) Numerical model.

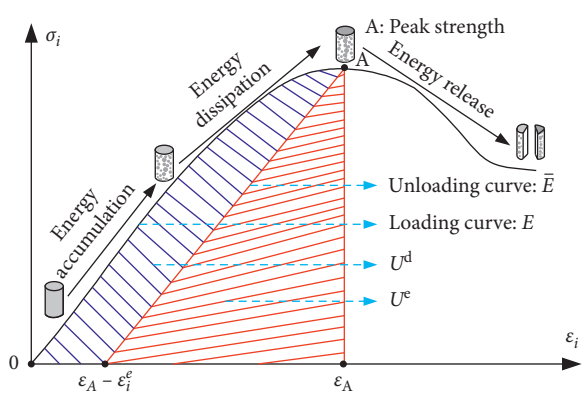

Figure 2: Relationship between dissipated energy and releasable strain energy in rock [5, 24].

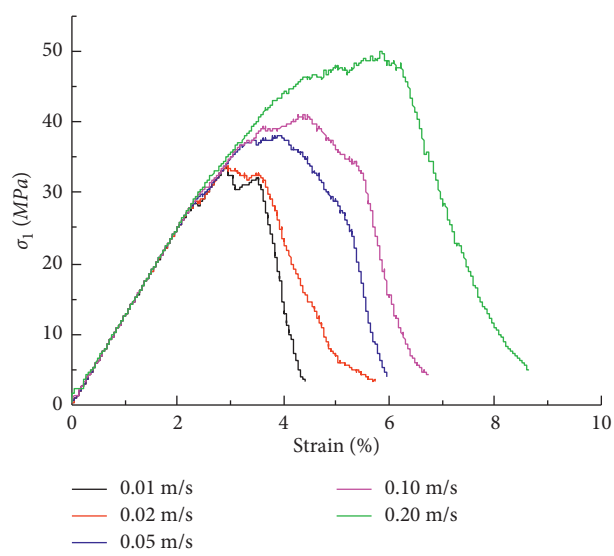

Figure 3: The stress-strain curves of coal-rock combined samples under different loading rates.

represented by $y = 0.085 + 3.152/(1 + \exp((x + 0.996)/dx))$, $R^2 = 92.74\%$, and the increasing trend of peak strength can be represented by $y = 8.633 - 5.382/(1+(x/18057.417)^{0.947})$, $R^2 = 96.53\%$.

3.2. AE Characteristics. In the PFC2D parallel bonding model, each crack forms an AE signal [13]. When the loading rates are different, the AE characteristics and generation mechanism of coal-rock combined samples under loading are also different. By recording the number of cracks and data postprocessing during uniaxial compression of coal-rock combined samples under different loading rates, the AE counts during the failure process can be simulated. The AE characteristics of the coal-rock combined samples under different loading rates are shown in Figure 5.

The stress-strain, AE counts, and failure modes of coal-rock combined samples with different loading rates

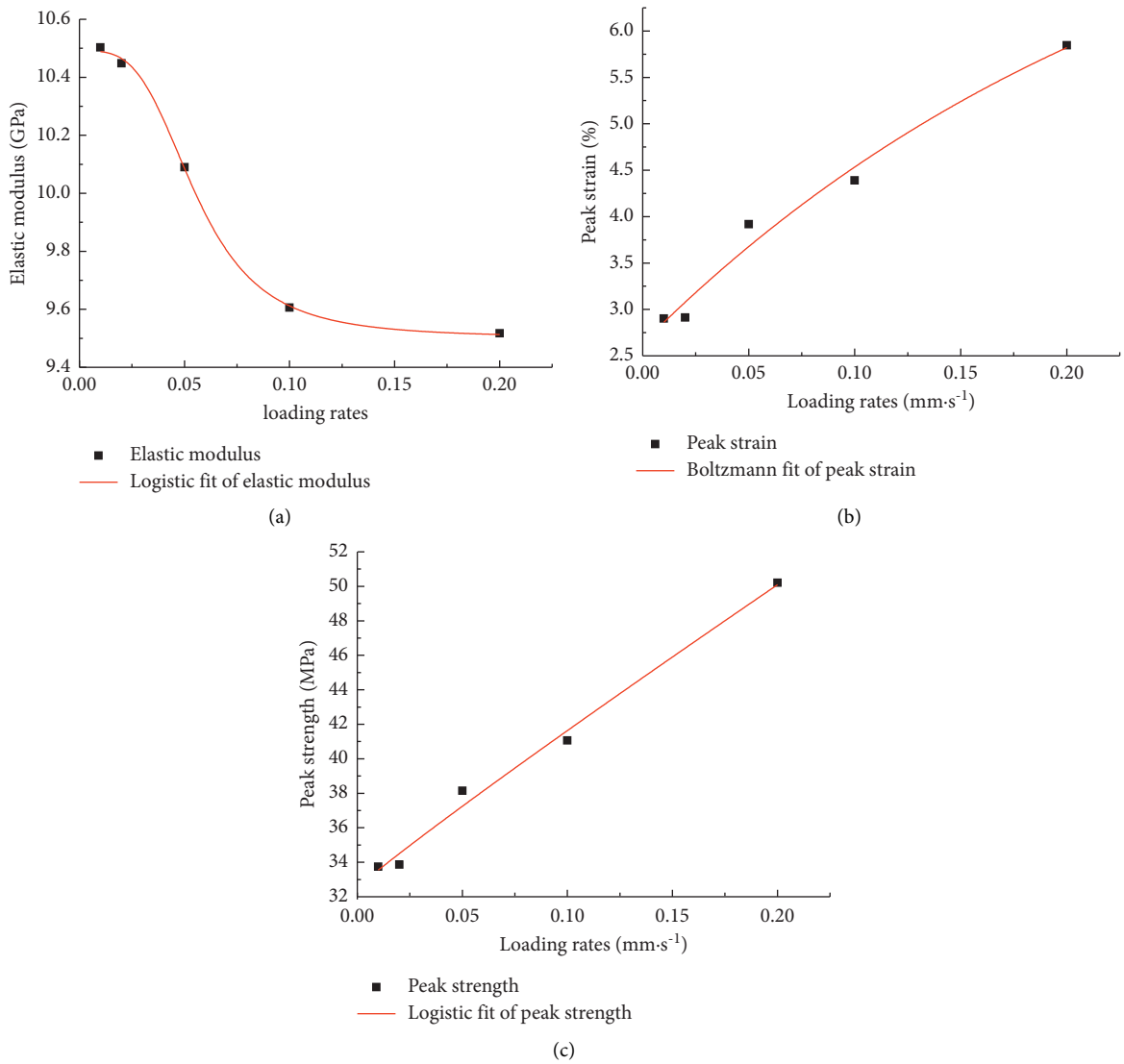

Figure 4: The variation trends of elastic modulus, peak strength, and peak strain of coal-rock combined samples under different loading rates. (a) Elastic modulus. (b) Peak strain. (c) Peak strength.

are shown in Figure 5. It can be seen from Figure 5 that under uniaxial compression conditions, the AE counts variation characteristics of coal-rock combined samples are basically the same. In the initial stage of uniaxial compression, when the stress of coal-rock combined samples is relatively small, AE counts are also small. With the increase of loading stress, internal cracks in the coal-rock combined samples propagate, secondary cracks form and propagate, and the number of AE counts increases gradually. Near the peak of the stress-strain curve, AE counts reach the maximum. Then, as the loading continued, AE counts gradually decreased. Until the loading was completed, internal cracks in the coal-rock combined samples penetrated, macro-cracks formed, and AE counts decreased significantly towards zero. When the loading rates are 0.05 mm/s and 0.10 mm/s, the maximum value of the AE counts is not synchronized with the peak strength, and the maximum value of AE counts coincides with the peak strength of other loading rates. In addition, the maximum AE count value increases with the increase of loading rates.

It can also be seen from Figure 5 that with the increase of loading rates, the failure of the coal-rock combined sample occurs not only in the coal part, but also in the rock part on both sides. And, with the increase of the loading rate, the failure of the rock parts on both sides of the coal-rock combined sample is becoming more and more serious.

3.3. Energy Evolution Characteristics. The stress-strain curves and the energy evolution of coal-rock combined samples at different loading rates are illustrated in Figure 6. It can be seen that the energy evolution curves at different loading rates exhibit similar trends: most of U, U_d, and U_e curves increase slowly first, fast afterwards, and changed very sharply at the peak stress points. Before failure, the total input energy, accumulated elastic properties, and dissipated

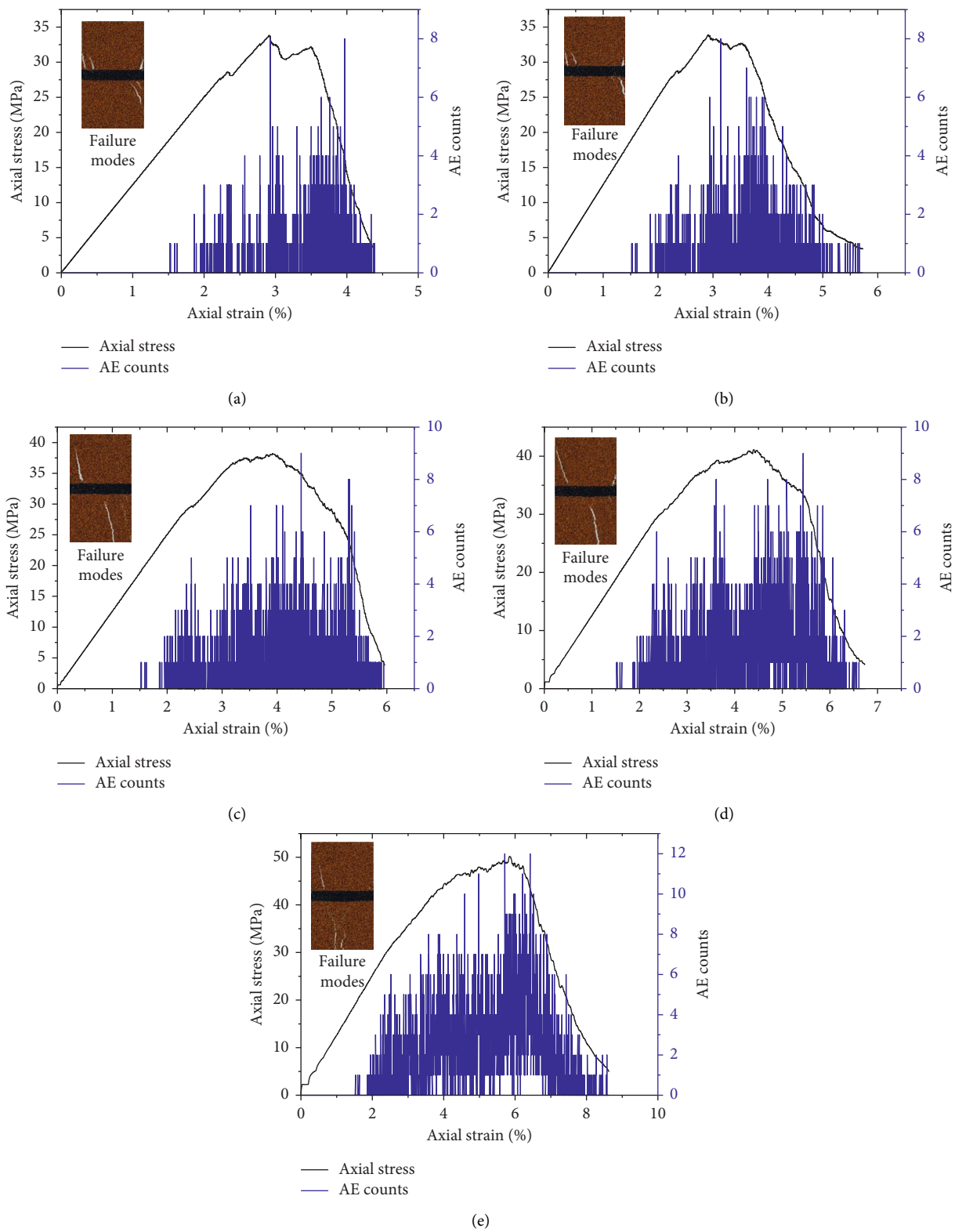

Figure 5: Stress-strain-AE count curves of the coal-rock combined sample under different loading rates. (a) 0.01 mm/s. (b) 0.02 mm/s. (c) 0.05 mm/s. (d) 0.10 mm/s. (e) 0.20 mm/s.

energy increase with the increase of stress. The total input energy increases the fastest, followed by elastic energy, and the dissipated energy is the slowest. The elastic energy increases nonlinearly with the axial stress. The growth rate is small at the initial stage of loading, then increases slowly, and slows down near failure. The dissipative energy increases slowly at first and increases significantly in the stage of impending failure.

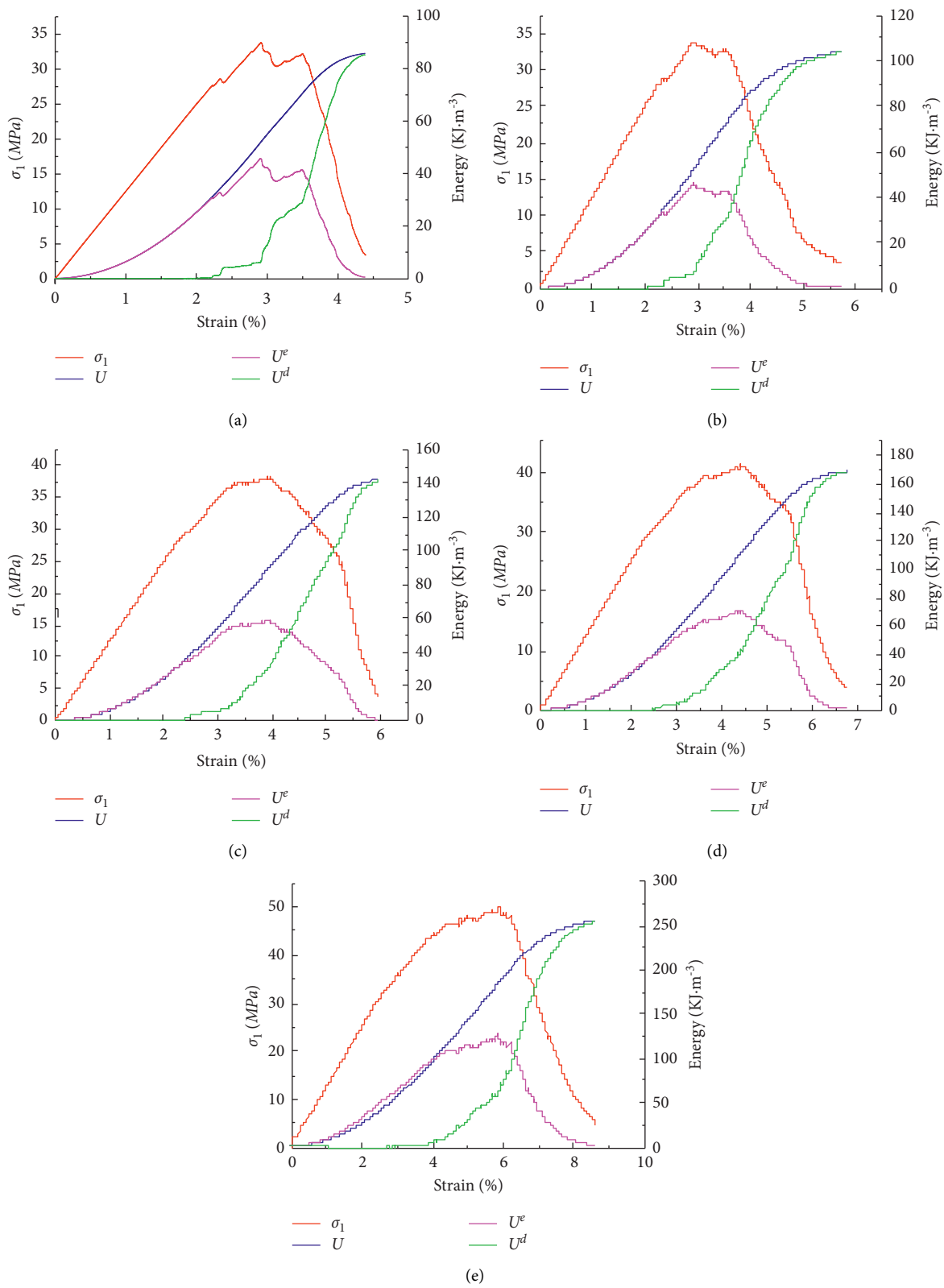

Figure 6: Stress-energy-strain curves under different loading rates. (a) 0.01 mm/s. (b) 0.02 mm/s. (c) 0.05 mm/s. (d) 0.10 mm/s. (e) 0.20 mm/s.

To compare the energy evolution of the coal-rock combined sample with different loading rates directly, the energy evolution curves are plotted in a single figure, as shown in Figure 7. As it can be seen, the accumulated input energy of the coal-rock combined sample increases approximately linearly with the strain and it also increases

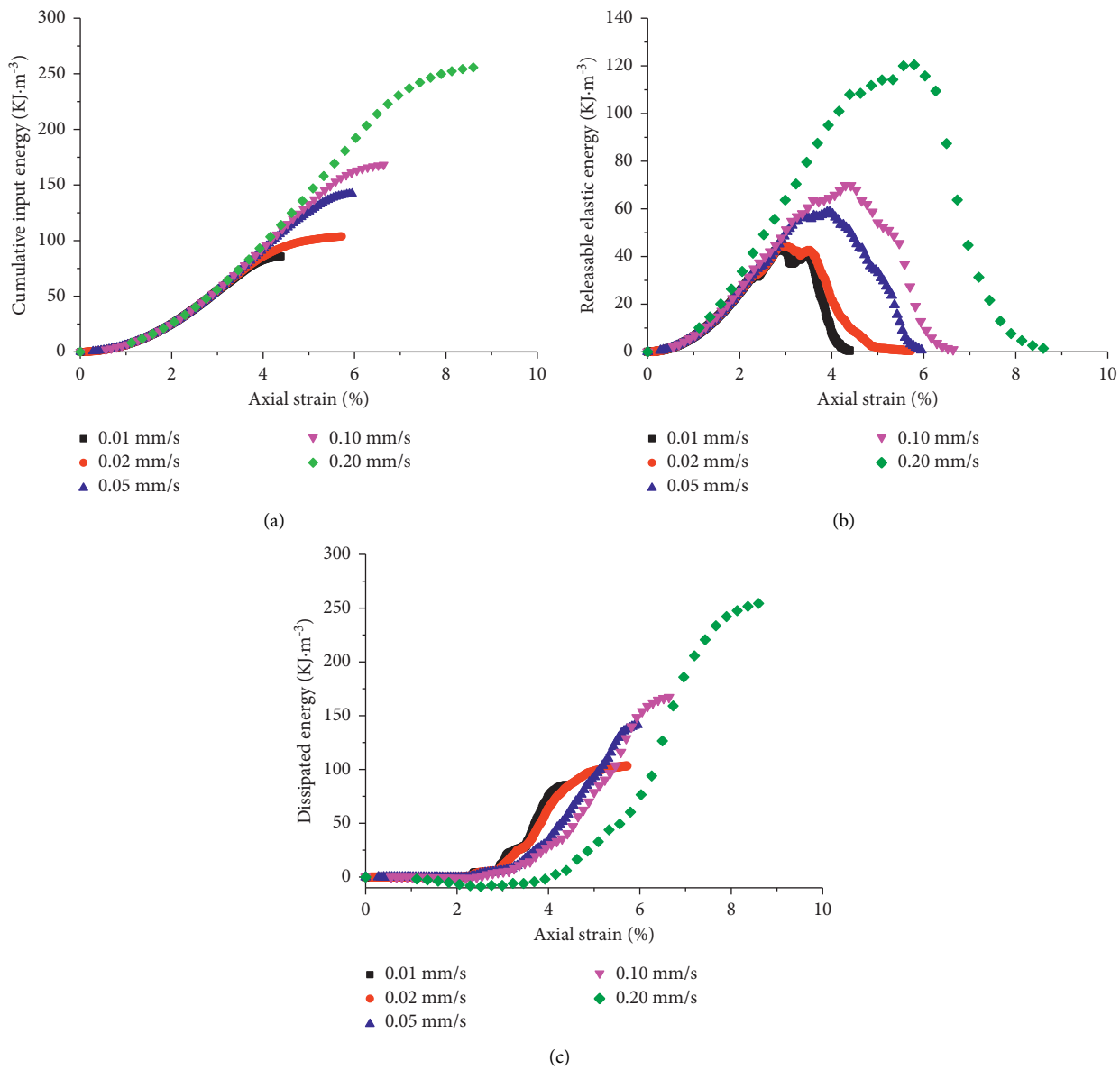

Figure 7: Correlation between energy and strain of the coal-rock combined sample with different loading rates. (a) Cumulative input energy. (b) Releasable energy. (c) Dissipated energy.

with loading rates (Figure 7(a)), reaching a maximum of 257.4 kJ/m^3 at 0.20 mm/s. Elastic energy reaches the maximum at the peak strength of stress-strain. In addition, the dissipated energy of the coal-rock combined sample increases more rapidly with loading rates (Figure 7(c)), and the peak value is also higher, reaching a maximum of 254.3 kJ/m^3 at 0.20 mm/s.

3.4. Energy Characteristics in the Peak Strength Point. Based on the variation of the coal-rock combined sample energy with the strain at different loading rates, the energy at the peak strength is further discussed. The total absorbed energy U, recoverable elastic strain energy U_e, and dissipated energy U_d at the peak point of stress-strain curve are designated as U_A,U_A^e, and U_A^d (Table 2), respectively. The relationships between U_A, U_A^e, U_A^d, U_A^e/U_A, and U_A^d/U_A and the loading rates are illustrated in Figure 8 in an energy vs. loading rate plot.

It can be seen from Table 2 and Figure 8 that the accumulation and dissipation of energy at the peak strength are closely related to loading rates. U_A,U_A^e, and U_A^d have the same variation trend with the loading rates of RCR and show an increasing trend with the increase of the loading rate. As the loading rate increases from 0.01 to 0.20 mm/s, U_A increases from 51.93 to 183.93 kJ/m^3, U_A^d increases from 6.20 to 57.30 kJ/m^3, and U_A^e increases from 45.73 to 126.62 kJ/m^3, respectively.

With the increase of loading rates, U_A^e/U_A decreases first and then increases. U_A^e/U_A decreases from 88.1% to 64.0% first, then increases from 64.0% to 68.8%. The U_A^d/U_A increases first and then decreases with the increase of loading

Table 2: Total input energy U_A, recoverable elastic strain energy U_A^e, and dissipated energy U_A^dat the peak strength.

Coal-rock height ratio	U_A(kJ/m^3)	U_A^e (kJ/m^3)	U_A^d (kJ/m^3)	U_A^e/U_A	U_A^d/U_A
0.01	51.93	45726.4212	6200.1228	0.881	0.119
0.02	52.32	45526.7667	6753.621	0.871	0.129
0.05	89.35	59110.9172	30229.7903	0.662	0.338
0.10	110.26	70515.3816	39662.7844	0.640	0.360
0.20	183.93	126620.68	57304.492	0.688	0.312

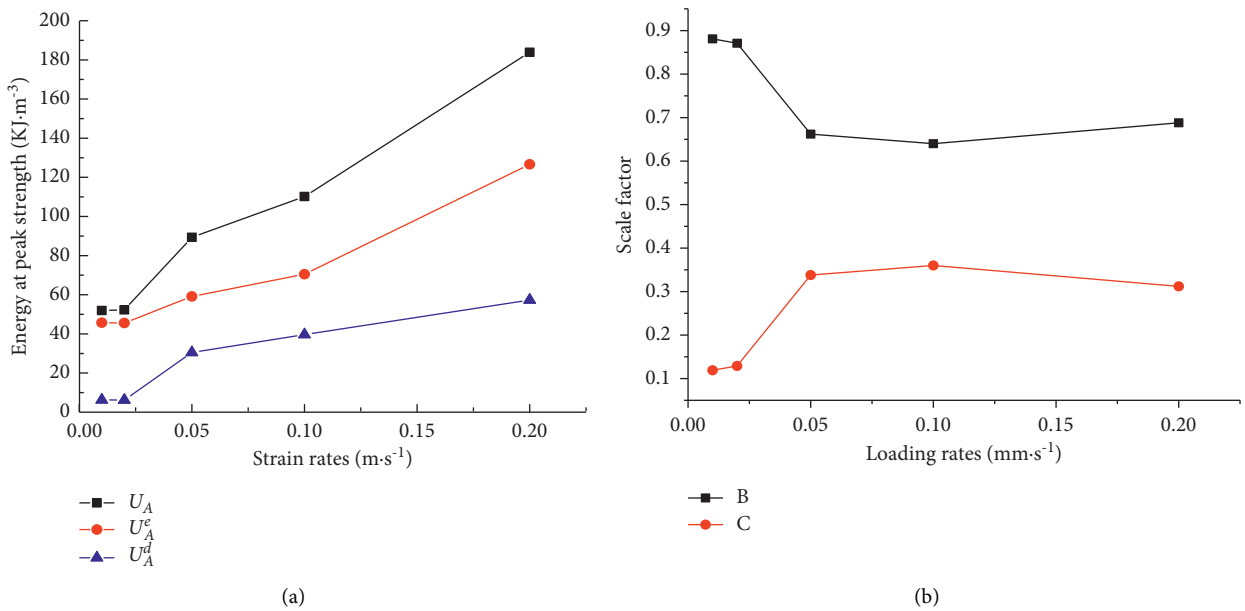

Figure 8: Total input energy $(U)_A$, recoverable elastic strain energy U_A^e,dissipated energy U_A^d, $U_A^e/(U)_A$, and $U_A^d/(U)_A$ at the peak strength.

rates. U_A^d/U_A increases from 11.9% to 36.0% first, then increases from 36.0% to 31.2%.

3.5. Rock Burst Energy Index. According to China's coal industry standard MT/T174-2000 classification and determination method of the Coal Seam Impact Tendency Index, the identification indexes of coal seam impact tendency include the Rock Burst Energy Index K_E, Elastic Energy Index W_{ET}, and dynamic failure time D_T [25, 26]. The Rock Burst Energy Index K_E is an important classification index to judge whether coal seam has rock burst tendency. The calculation formula of the Rock Burst Energy Index K_E is as follows:

$$K_E = \frac{A_S}{A_X}, \tag{5}$$

where A_S is the deformation energy accumulated before the peak value and A_x is the deformation energy lost after the peak value. When $K_E < 1.5$, there is no rock burst tendency; when $1.5 \le K_E < 5$, there is a weak rock burst tendency; when $K_E \ge 5$, there is a strong rock burst tendency. KE actually refers to the ratio of the area of the rising section (A_S) to the area of the falling section (A_x) of the whole stress-strain curve (as shown in Figure 9). σ_c is the peak stress.

The Rock Burst Energy Index of the coal-rock combined sample with different loading rates is shown in Figure 10(a).

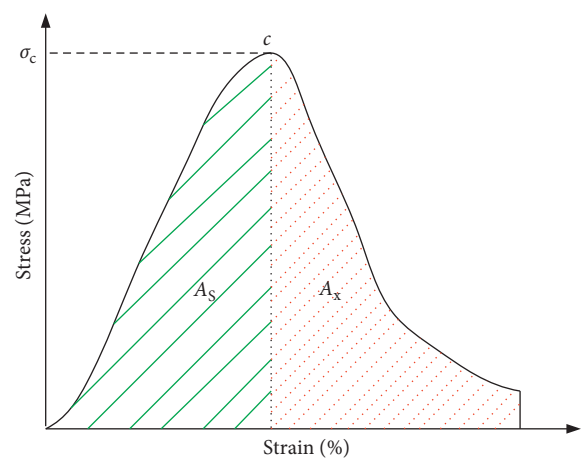

Figure 9: Calculation chart of ?? [25, 26].

It can be seen from the figure that under the five loading rates, the Rock Burst Energy Index K_E of the coal-rock combined sample is between $1.5 \le K_E < 5$. That is, they all have weak rock burst tendency. With the increase of the loading rate, the Rock Burst Energy Index increases first and then decreases. That is, there is a critical loading rate, which is consistent with the study of Li et al. [27]. It is also consistent with the field observations of Dou et al. [28, 29]. Dou et al. [28, 29] pointed out that there is no nonlinear

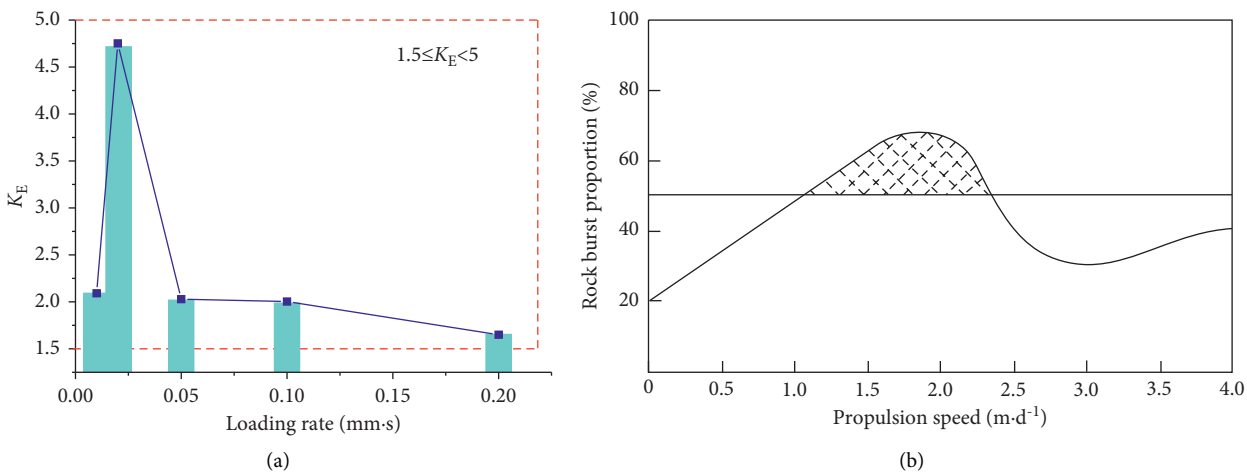

Figure 10: The Rock Burst Energy Index with different loading rates and rock burst proportion with propulsion speed.

relationship between the propulsion speed and the times of rock burst after counting the data of several mines. When the propulsion speed of the working face is less than 1 m/d or the propulsion speed of the working face is about 3 m/d, the number of rock burst is the least. When the propulsion speed is 1.3~2.5 m/d, the rock burst times are the most frequent, which is the most unfavorable to safe mining, as is shown in Figure 10(b).

The Rock Burst Energy Index with different loading rates and rock burst proportion with propulsion speed by Dou et al. [28, 29].

4. Conclusions

(1) With the increase of loading rates, the elastic modulus of the coal-rock combined samples shows a nonlinear decreasing trend. And, the deceleration rate shows a trend of increasing first and then decreasing. The peak strength and peak strain of the coal-rock combined sample increase nonlinearly with the loading rates.

(2) The accumulated input energy of the coal-rock combined sample increases approximately linearly with the strain and it also increases with loading rates, reaching a maximum of 257.4 kJ/m^3 at 0.20 mm/s. The elastic energy reaches the maximum at the peak strength of stress-strain. In addition, the dissipated energy of the coal-rock combined sample increases more rapidly with loading rates, and the peak value is also higher, reaching a maximum of 254.3 kJ/m^3 at 0.20 mm/s.

(3) The accumulation and dissipation of energy at peak strength are closely related to the loading rates. U_A, U_A^d, and U_A^e have the same variation trend with the loading rates of the coal-rock combined sample and show an increasing trend with the increase of the loading rate. With the increase of loading rates, U_A^e/U_A decreases first and then increases. The U_A^d/U_A increases first and then decreases with the increase of loading rates.

(4) With the increase of loading rates, the Rock Burst Energy Index increases first and then decreases, which is consistent with the indoor study and field observations of the former study. Therefore, in the field mining practice, when the propulsion speed is too slow or too fast, it is beneficial to safe mining. At this time, the occurrence times of rock burst are relatively small.

Data Availability

The data presented in this study are available upon request from the first author or the corresponding author.

Conflicts of Interest

The authors declare that they have no conflicts of interest.

Acknowledgments

The authors thank the support of the Natural Science Foundation of Shaanxi Province (2020JZ-52).

References

[1] J. Zuo, Z. Wang, H. Zhou, J Pei, and J Liu, "Failure behavior of a rock-coal-rock combined body with a weak coal interlayer," *International Journal of Mining Science and Technology*, vol. 23, no. 6, pp. 907–912, 2013.

[2] W. Y. Guo, Y. L. Tan, F. H. Yu et al., "Mechanical behavior of rock-coal-rock specimens with different coal thicknesses," *Geomechanics and Engineering*, vol. 15, no. 4, pp. 1017–1027, 2018.

[3] S. J. Chen, D. W. Yin, N. Jiang, F. Wang, and W. J. Guo, "Simulation study on effects of loading rate on uniaxial compression failure of composite rock-coal layer," *Geomechanics and Engineering*, vol. 14, no. 4, pp. 333–342, 2019.

[4] F. Gong, Y. E. Hao, and Y. Luo, "Rate effect on the burst tendency of coal-rock combined body under low loading rate range," *Journal of China Coal Society*, vol. 42, no. 11, pp. 2852–2560, 2017.

[5] B. X. Huang and J. W. Liu, "The effect of loading rate on the behavior of samples composed of coal and rock," *International Journal of Rock Mechanics and Mining Sciences*, vol. 61, pp. 23–30, 2013.

[6] D. W. Yin, S. Chen, W. Xing, D Huang, and X. Liu, "Experimental study on mechanical behavior of roof-coal pillar structure body under different loading rates," *Journal of China Coal Society*, vol. 284, no. 05, pp. 67–75, 2018.

[7] Y. L. Chen and Y. Zhang, "Influence of loading rate on the Kaiser effect for different lithological rocks," *Journal of China Coal Society*, vol. 43, no. 04, pp. 959–966, 2018.

[8] Z. L. Zhou, Y. Chang, and X. Cai, "Experimental study of infrared radiation effects of rock with different loading rates," *Journal of Central South University*, vol. 50, no. 5, pp. 1127–1134, 2019.

[9] X. Wang, E. Wang, X. Liu, and X. Zhou, "Failure mechanism of fractured rock and associated acoustic behaviors under different loading rates," *Engineering Fracture Mechanics*, vol. 247, no. 16, Article ID 107674, 2021.

[10] X. Wang, J. C. Li, X. B. Zhao, and Y. Liang, "Propagation characteristics and prediction of blast-induced vibration on closely spaced rock tunnels," *Tunnelling and Underground Space Technology*, vol. 123, Article ID 104416, 2022.

[11] S. N. Dong, A. Li, Y. D. Ji, Y. X. Yang, and Q. Mu, "Mechanical and failure characteristics of rock-coal-rock combined body under different strain rates: a numerical study from micro perspective," *Geotechnical and Geological Engineering*, vol. 39, pp. 1–7, 2020.

[12] J. Liu, E. Y. Wang, D. Z. Song, S Wang, and Y Niu, "Effect of rock strength on failure mode and mechanical behavior of composite samples," *Arabian Journal of Geosciences*, vol. 8, no. 7, pp. 4527–4539, 2014.

[13] J. P. Zuo, Y. Chen, and F. Cui, "Investigation on mechanical properties and rockburst tendency of different coal-rock combined bodies," *Journal of China University of Mining & Technology*, vol. 7, no. 1, pp. 81–87, 2018.

[14] L. Qiu, Y. Zhu, D. Song et al., "Study on the nonlinear characteristics of EMR and AE during coal splitting tests," *Minerals*, vol. 12, no. 2, p. 108, 2022.

[15] Q. Ma, Y. L. Tan, X. S. Liu, Z. H. Zhao, and D. Y. Fan, "Mechanical and energy characteristics of coal-rock composite sample with different height ratios: a numerical study based on particle flow code," *Environmental Earth Sciences*, vol. 80, no. 8, p. 309, 2021.

[16] H. P. Xie, R. D. Peng, Y. Ju, and H. W. Zhou, "On energy analysis of rock failure," *Chinese Journal of Rock Mechanics and Engineering*, vol. 15, pp. 5–10, 2005.

[17] Q. Ma, Y. L. Tan, X. S. Liu, Q. H. Gu, and X. B. Li, "Effect of coal thicknesses on energy evolution characteristics of roof rock-coal-floor rock sandwich composite structure and its damage constitutive model," *Composites Part B: Engineering*, vol. 198, Article ID 108086, 2020.

[18] G. Chen, T. Li, G. Zhang, P. Teng, and B. Gong, "Energy distribution law of dynamic failure of coal-rock combined body," *Geofluids*, vol. 2021, no. 7, Article ID 6695935, 14 pages, 2021.

[19] C. J. Li, Y. Xu, and Z. Y. Ye, "Energy dissipation and crushing characteristics of coal-rock-like combined body under impact loading," *Chinese Journal of Geotechnical Engineering*, vol. 350, no. 05, pp. 190–197, 2020.

[20] L. Yang, F. Q. Gao, X. Q. Wang, and J. Z. Li, "Energy evolution law and failure mechanism of coal-rock combined specimen," *Journal of China Coal Society*, vol. 44, no. 12, pp. 3894–3902, 2020.

[21] P. Y. Zhao, Y. C He, S. G. Li, H. F. Lin, Y. Y. Jia, and E. H. Yang, "Coal thickness effect on mechanics and energy characteristics of coal-rock combination model," *Journal of Mining & Safety Engineering*, vol. 37, no. 5, p. 10, 2020.

[22] Y. L. Tan, W. Y. Guo, Q. H. Gu et al., "Research on the rock burst tendency and AE characteristics of inhomogeneous coal-rock combination bodies," *Shock and Vibration*, vol. 2016, Article ID 9271434, 11 pages, 2016.

[23] D. W. Yin and X. X. Meng, "Numerical simulation on uniaxial compression failure of a roof rock-coal-floor rock composite sample with coal persistent joint," *Geotechnical & Geological Engineering*, vol. 37, no. 1, pp. 13–23, 2019.

[24] Z. Zhang, H. Xie, R. Zhang et al., "Deformation damage and energy evolution characteristics of coal at different depths," *Rock Mechanics and Rock Engineering*, vol. 52, no. 5, pp. 1491–1503, 2018.

[25] Q. X. Qi, Y. W. Peng, H. Y. Li, J. Q. Li, Y. G. Wang, and C, R Li, "Study on burst liability of coal and rock," *Chinese Journal of Rock Mechanics and Engineering*, vol. S1, pp. 2736–2742, 2011.

[26] Y. S. Pan, L. Geng, and Z. H. Li, "Research on evaluation indices for impact tendency and danger of coal seam," *Journal of China Coal Society*, vol. 12, pp. 1975–1978, 2010.

[27] H. T. Li, L. Song, H. W. Zhou, Y. D. Jiang, and H. W. Wang, "Evaluation method and application of coal burst performance under the effect of loading rate," *Journal of China Coal Society*, vol. 40, no. 12, pp. 21–29, 2005.

[28] L. M. Dou and X. Q. He, *Theory and Technology of Rock Burst Prevention and Control*, China University of mining and Technology Press, Xuzhou, Jiangsu, 2001.

[29] L. M. Qiu, Z. T. Liu, E. Y. Wang, X. Q. He, J. J. Feng, and B. L. Li, "Early-warning of rock burst in coal mine by low-frequency electromagnetic radiation," *Engineering Geology*, vol. 279, Article ID 105755, 2020.

Hindawi
Advances in Materials Science and Engineering
Volume 2022, Article ID 1212584, 13 pages
https://doi.org/10.1155/2022/1212584

Research Article

Energy Dissipation and Damage Evolution Characteristics of Shale under Triaxial Cyclic Loading and Unloading

Ziyun Li,[1] **Song Xie**,[1] **Qianghui Song**,[2] **Peiyong Wang**,[2] **Dongyan Liu**,[3,4] **Baoyun Zhao**,[1] **and Wei Huang**[1]

[1]*School of Civil Engineering and Architecture, Chongqing University of Science & Technology, Chongqing 400000, China*
[2]*Chongqing Key Laboratory of Geomechanics & Geoenvironment Protection, Army Logistics University of PLA, Chongqing 401311, China*
[3]*Chongqing University, Chongqing 400000, China*
[4]*Chongqing College of Architecture and Technology, Chongqing 400000, China*

Correspondence should be addressed to Ziyun Li; liziyun130@126.com

Received 24 June 2022; Revised 11 August 2022; Accepted 16 August 2022; Published 30 August 2022

Academic Editor: Depeng Ma

Rock engineering is highly susceptible to cyclic loads resulting from shale gas exploitation; it is very important to study the failure mechanism of underground rock mass under cyclic load. To investigate the energy dissipation and damage evolution characteristics of shale under triaxial cyclic loading and unloading conditions, a series of triaxial incrementally cyclic loading and unloading tests under different confining pressures (10 MPa, 15 MPa, 20 MPa, and 30 MPa) were carried out. The variation of plastic strain of shale under four confining pressures was analyzed, and the evolution characteristics of dissipated energy and energy dissipation ratio were discussed. The results show that: the peak strength and peak strain of shale increase with the increase in confining pressures. Meanwhile, the plastic strain of rock under cyclic loading increases rapidly first, then develops steadily, and finally increases sharply with the increase in axial strain. The energy dissipation ratio-strain curve presents a spoon-shaped evolution feature, and can be divided into three stages: a linear decline stage, a steady development stage, and a rapid increase stage, respectively. However, the trend of elastic modulus of shale was opposite to that of the energy dissipation ratio. Accordingly, the energy dissipation ratio can be regarded as the damage factor to describe the degradation of shale. Based on the evolution of dissipated energy, a theoretical equation of shale stress-strain evolution was established. By substituting the test data into the formula, it is found that the calculated results are basically consistent with the test data, and the peak strains and peak stress calculated by the equation are in good agreement with the test data. The findings could provide important theoretical support for the energy dissipation and damage evolution analysis in the failure process of shale under cyclic stress conditions.

1. Introduction

In the process of shale gas exploitation, the underground stress condition is very complex, and the shale is constantly damaged in the deformation process, which is accompanied by the absorption, accumulation, and release of energy, and the release of energy inside the shale is the main cause of engineering accidents. Therefore, from the perspective of mechanical behavior, the deformation and failure of rock under different loading states is a process from crack initiation, plastic deformation, to global failure. According to the law of thermodynamics, energy transformation is the essential characteristic of physical change, and material destruction is the state instability phenomenon driven by energy [1]. Therefore, rock failure is also a kind of instability phenomenon driven by energy; energy plays a fundamental role in rock deformation and failure process; the ability of rocks to absorb, accumulate, dissipate, and release energy is also a way to evaluate the rock-bearing capacity.

The deep rock mass is in a state of high in-situ stress, and the stress state of the rock mass is redistributed under the influence of excavation. Taking shale gas extraction as an

example, the instability of shale gas wellbore surrounding rock, such as wellbore collapse, sticking, and borehole expansion, has become a prominent and significant problem in the exploration and development of shale gas resources. In the process of shale gas extraction, the wellbore surrounding rock experiences multiple cycles of loading and unloading, and its mechanical properties and deformation mechanism are very complex. Since the fundamental cause of rock damage and yielding is energy-driven [2], studying the damage evolution and deformation characteristics of shale under cyclic loading and unloading from the perspective of dissipated energy can more essentially reveal its strength failure and destabilization mechanism, and can provide a new perspective for stability analysis of wellbore surrounding rock.

Gong et al. [3] investigate the energy evolution characteristics of rock materials under uniaxial compression. For rock materials, input energy density, elastic energy density, and dissipated energy density nonlinearly increase with increasing unloading stress levels. The input energy is mainly converted into elastic energy and dissipated energy during the experiment. Elastic energy density and dissipated energy density linearly increase with an increase in input energy density. Meanwhile, the ratio of the elastic energy to dissipation energy of rack materials can reflect the damage of the rock. The ratio of dissipated energy to elastic energy increases gradually with the increase in cycle times and reaches the maximum at peak stress.

Xie et al. [1, 2, 4] pointed out that the deformation and failure of rock is a process of exchanging energy with the external environment, and revealed the intrinsic connection between rock deformation and failure, energy dissipation, and energy release. Singh [5] proposed the burst energy release index to characterize the degree of rock damage. It was found that the stronger the energy storage capacity of the rock, the greater the energy release index when reaching the peak strength, and the greater the damage degree. Mikhalyuk and Zakharov [6] considered the elastic limit of the rock and carried out relevant experiments to study the energy dissipation of the rock during the elastic deformation stage. Munoz et al. [7] analyzed the energy characteristics of the rock pre-peak stage based on conventional uniaxial and triaxial rock compression tests. Meng et al. [8, 9] carried out triaxial cyclic loading and unloading tests on sandstone, marble, and limestone, and revealed the relationship between the energy evolution of rock samples and the confining pressure, cycle times, and stress. Ai et al. [10] analyzed the axial stress-axial strain curves and proposed a brittleness evaluation standard based on the energy principle to reveal the correlation between rock brittleness and energy evolution. Li et al. [11] conducted triaxial compression tests on different types of granite specimens under different loading and unloading stress paths, and found that the total strain energy, elastic strain energy, and circumferential strain energy all increased with the increase in the initial confining pressures, while the dissipated energy decreases. During unloading, hard rock is more prone to rock burst than soft rock under conventional triaxial loading conditions. Zhang et al. [12] did triaxial cyclic loading and unloading tests on sandstone under six different confining pressures. The total absorbed energy density, elastic energy density, and dissipated energy density of rock specimens under different confining pressures were obtained. The influence mechanism of confining pressure on energy evolution was analyzed. Zhou et al. [13] studied the post-peak energy evolution characteristics of Beishan granite under cyclic loading and unloading based on the acoustic emission test. The above researches revealed the basic characteristics of energy evolution of rocks under load to failure: a large amount of elastic energy is accumulated in the rock before the peak strength, while the stored elastic energy in the rock after the peak strength is rapidly released and transformed into the energy consumed by rock breakage.

The process of rock loading is a gradual process of damage, and the dissipated energy is mainly used for the generation of new fractures. The results are closer to the nature of rock damage by exploring the damage evolution during rock loading from the perspective of energy dissipation. He et al. [14] introduced the dissipated energy coefficient to study the energy evolution characteristics of rocks and proposed a method to determine the rock burst proneness and crack propagation in rocks. Liu et al. [15] established a damage constitutive model of rocks from the perspective of dissipated energy to describe the behavior of rocks under cyclic loading. Wang et al. [16] used the constitutive model and multi-criteria model established for rock failure from the perspective of energy. Zhao et al. [17] found that the variation of dissipated energy can be used to define the damage variable of the rock, and the damage variable also increases with the increase in loading rate. Li et al. [18] established a damage model of fractured rocks related to dissipated energy. Chen and Guo [19] analyzed the fracture closure effect and the relationship between fracture parameters and height-diameter ratio (H/D) through the uniaxial compression test of sandstone. A nonlinear model of energy dissipation based on the crack closure effect was established. Pei et al. [20] carried out cyclic loading and unloading tests on granites under six different confining pressures, and proposed four energy parameters, namely energy storage rock, energy storage limit, energy storage ratio, and energy dissipation ratio, to describe the energy storage and energy dissipation characteristics of rocks. Duan and Yang [21] conducted cyclic loading and unloading tests on sandstone, and found that dissipated energy can represent fatigue deformation of rock samples, and the curves of dissipated energy-cycle numbers present a U-shaped curve. Wang et al. [22] carried out triaxial compression tests on marble with different bedding angles, and found that compared with conventional triaxial tests, more energy was consumed for complete failure of rock samples under stress disturbance. Wang et al. [23] performed fatigue tests under different maximum cycling stresses on salt rock specimens to study the microstructural variations and damage evolvement of salt rock under cyclic loading; the fatigue damage evolvement equation of salt rock under cyclic loading was established based on the change in porosity. Hou et al. [24] combined microscopic tests and a thermal damage simulation to evaluate the changes in the internal structure of the

coal caused by the LN2 cooling. Xue et al. [25] conducted triaxial compression tests of coal under different gas pressure conditions, and the mechanical properties, acoustic emission (AE) energy characteristics, and nonlinear characteristics of the energy evolution of coal were obtained.

When the external force applied to the rock is in the elastic range (below the lower threshold), there will be no plastic deformation or crack initiation. When the force reaches the upper threshold of strength, failure will occur. When the force is between the upper and lower thresholds, each loading will cause damage to the rock. With the accumulation of damage caused by cyclic loading, when a certain damage threshold is reached, instability failure will occur. The physical manifestations of damage include plastic deformation, crack propagation, and crack friction, which can be expressed as the weakening of the elastic modulus in mechanical properties and energy dissipation in energy level. Therefore, how to quantitatively describe the damage characteristics of rocks subjected to cyclic loading and evaluate its stability (such as shale gas reservoir rock) has always been the focus of research.

In this paper, the variation trend of plastic strain under cyclic loading was firstly discussed. Considering damage mechanics, a plastic strain damage model including confining pressure parameters, damage accumulation factor, and average damage factor was established. Based on the conservation law of energy, the evolution law of total energy, elastic energy, and dissipated energy under cyclic loading was analyzed, and the relationship between the energy dissipation ratio and plastic strain was discussed. The criterion of rock failure is established. This research provides theoretical guidance for the quantitative analysis of the mechanical response and parameters (strength, elastic modulus, etc.), degradation of rocks during the excavation and unloading process of underground engineering (such as drilling, underground chamber, carbon sequestration, tunnel excavation), and the failure mechanism of rock under cyclic load is studied from the perspective of energy. These results can provide a theoretical basis for support design, stability analysis, and risk prediction in the process of underground engineering development.

2. Experimental Design

2.1. Sample Preparation. The shale samples were taken from Jiangjin District, Chongqing, and were collected in strict accordance with the relevant test procedures of the International Society for Rock Mechanics [26] to prepare $\varphi 50\,\text{mm} \times 100\,\text{mm}$ cylindrical samples. Before the test, in order to ensure the flatness of the upper and lower faces of the rock samples, the samples were drilled perpendicular to the bedding plane of shale. Parts of the specimens are shown in Figure 1.

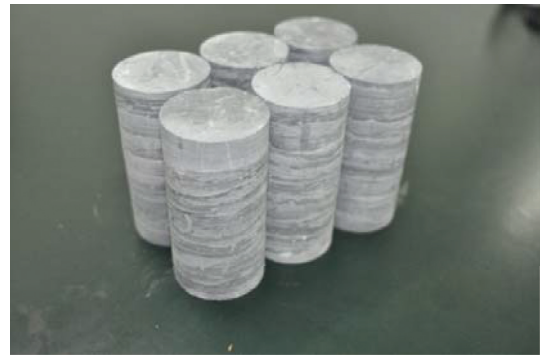

Figure 1: Parts of the samples.

2.2. Experimental Equipment. To explore the energy evolution characteristics of loaded rock samples under different confining pressures, the experimental stress path of constant confining pressure and unloading axial pressure was designed by applying a constant axial displacement increment at each loading cycle, and triaxial cyclic loading and unloading tests under four confining pressures were carried out. It is worth noting that this study mainly focusses on the energy evolution characteristics of shale before failure; the tests were ended after the sample reaches its peak strength.

The tests were conducted on TFD–2000 (as shown in Figure 2). The equipment comprises axial loading, confining pressure loading, hydraulic pressure loading, numerical control, and a measuring system. The maximum axial load is 2000 kN and the measurement resolution is 10 N. The maximum confining pressure is 100 MPa and the measurement resolution is 0.001 MPa. The maximum hydraulic pressure is 70 MPa, the maximum axial deformation is 10 mm, the measurement accuracy is ±0.5%, and the temperature range is from atmospheric temperature to 200°C. This equipment can perform controlled tests and data analysis by computerized and robotized operations, which ensures the accuracy, timeliness, and safety of the test results.

2.3. Experimental Procedure. The procedure of triaxial cyclic loading and unloading tests can be described as follows. Firstly, an initial axial load of 1.0 kN was applied to fix the rock sample; then the confining pressure was applied to the design value (10, 15, 20, 30 MPa) by stress control at a speed of 0.5 kN/s. The confining pressure was kept constant during the whole test process. The displacement control rate of 0.05 mm/min was used to apply the axial stress up to each unloading point (10, 20, 30, 40, 50 MPa), and then the axial stress was unloaded to 1 MPa and reloaded to the previous unloading stress at the unloading and reloading rate of 0.5 kN/s. Upon reaching the unloading stress value of the last cycle, the displacement method was used to continue the next loading cycle at a rate of 0.05 mm/min. The schematic diagram of the loading path is shown in Figure 3, and the blue and green lines are displacement loading and stress loading paths, respectively. The recording frequency of stress and strain during the tests was 0.1 s/time and the test scheme is shown in Table 1.

2.4. Energy Calculation Method. According to the first law of thermodynamics, thermal energy can be transferred, its form can be transformed, and total energy in various forms

(a) (b) (c)

Figure 2: TFD-2000 microcomputer servo-controlled triaxial rheological testing machine. (a) The test system. (b) Confining pressure device and loading device. (c) Installation of rock specimens.

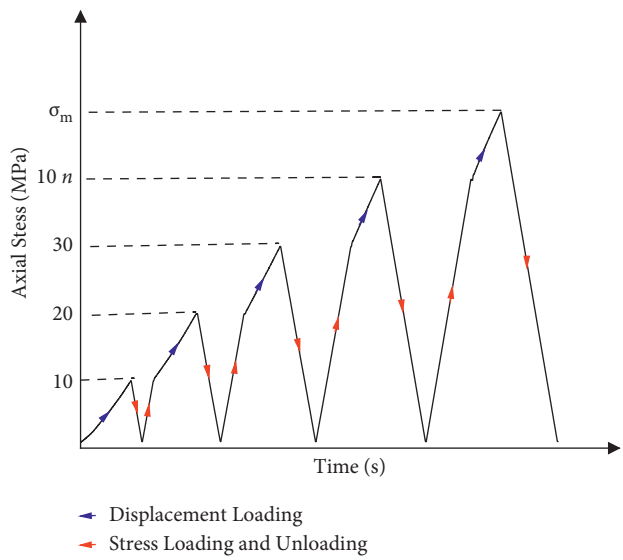

Figure 3: The path of loading.

Table 1: Test scheme.

specimen number	Confining pressure/MPa	Initial unload value/MPa	Increment/MPa	Unload endpoint/MPa
S1	5	10	10	0
S2	10	10	10	0
S3	20	10	10	0
S4	30	10	10	0

is constant in the process of transfer and conversion. In the process of cyclic loading and unloading, the work input by the testing machine is transformed into mechanical energy and heat energy [27, 28]. Therefore, the work input by the testing machine is the main source of mechanical energy of the rock sample. For the reason that rock is a typical elastic-plastic material, the input mechanical energy is mainly divided into two types: one is stored in the form of elastic energy, and the other is the dissipated energy used for crack expansion, friction, and plastic deformation. In the triaxial cyclic loading and unloading experiments, axial stress σ_1 exerts positive work on rock samples. Under the condition of triaxial constant confining pressure, for a unit volume of rock sample sheet, the stress state is biaxial compression, and there are both axial strain ε_1 and radial strain ε_2 and ε_3. To simplify the calculation, we assumed that ε_2 was equal to ε_3;

thus, when we evaluated u_3, the value of u_3 was twice of the unilateral radial diffusion energy. Confining pressure σ_3 exerted negative work by restraining lateral deformation on rock samples. In this study, it was assumed that the whole test process was a closed system and there was no heat exchange with external environment, according to the law of conservation of energy,

$$u = u_1 + u_3 = \int_0^{\varepsilon_1} \sigma_1 d\varepsilon_1 + 2\int_0^{\varepsilon_3} \sigma_3 d\varepsilon_3, \quad (1)$$

u is the total energy input from the electrohydraulic servo testing machine, u_1 is the axial strain energy, and u_3 is the energy consumed for radial deformation; u^{e} is the elastic energy accumulated in the rock, and u^{d} is the energy dissipated due to pore compaction, plastic deformation, and crack propagation. σ_1 is the axial stress and σ_3 is the confining pressure, ε_1 is the axial strain, and ε_3 is the radial strain; considering that the distribution of the annular deformation along the rock sample is not uniform during the compression process, especially after the rock sample was damaged, this effect was more obvious. Therefore, when calculating according to (1), it was assumed that ε_3 is 1/2 of the central annular deformation value of the measured rock sample.

As shown in Figure 4, the area of the loading stress-strain curve projected onto the X coordinate axes is the total energy input to the rock sample, i.e., the work done by the testing machine on the rock sample. The area of the unloading stress-strain curve projected onto the X coordinate axes is the elastic energy accumulated in the rock sample, and the difference between the total energy and the elastic energy is the dissipated energy.

$$u_{\mathrm{i}}^{d} = u_{\mathrm{i}} - u_{\mathrm{i}}^{\mathrm{e}} = \int_0^{\varepsilon_{\mathrm{i}}} \sigma_{\mathrm{i}} d\varepsilon - \int_{\varepsilon_{\mathrm{i}}^{d}}^{\varepsilon_{\mathrm{i}}} \sigma_{\mathrm{i}} d\varepsilon, \quad (2)$$

where u_{i} is the total energy of a single loading and unloading, including the energy input by the machine and the energy consumed by radial strain expansion, $u^{\mathrm{e}}i$ is the elastic energy accumulated in the rock sample, $u^{d}i$ is the dissipated energy, ε_{i} is the strain corresponding to the unloading point, $\varepsilon^{d}i$ is the corresponding strain when unloading is completed, and σ_{i} is the stress.

As a discontinuous, elastic-plastic material with initial defects, the rock dissipated energy irreversibly closes the micropores and natural cracks, reduces plastic deformation, and propagates cracks during the loading process; thus, the dissipated energy exists in the whole process of rock deformation from compaction to failure. Obviously, the damage of the rock is positively correlated with the amount of dissipated energy; therefore, the energy dissipation ratio (the ratio of dissipated energy to input energy) is proposed to characterize the damage inside the rock and is calculated as:

$$\eta = \frac{1 - u^{\mathrm{e}}}{u^{\mathrm{i}}} = \frac{u^{\mathrm{d}}}{u}. \quad (3)$$

As a parameter to describe the damage characteristics of the rock such as plastic deformation and crack propagation, the ratio of dissipated energy to total input energy reflects the degree of rock damage under different stress states to a certain extent.

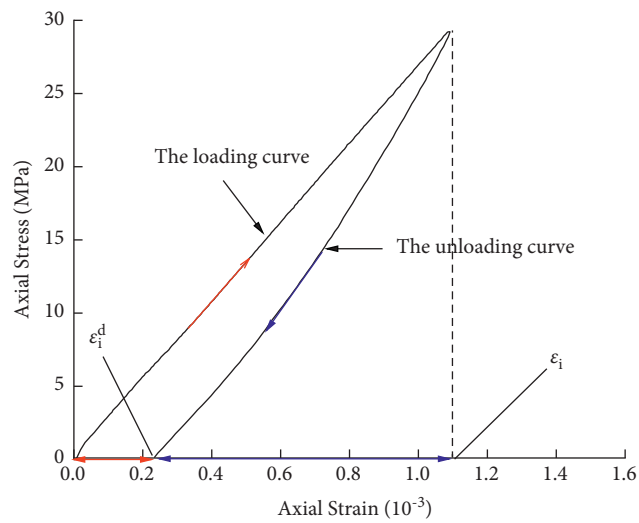

Figure 4: The relationship between elastic energy and dissipated energy of rocks during loading and unloading.

3. Experimental Results

3.1. Mechanical behavior. The triaxial cyclic loading and unloading tests were carried out on shale, and the confining pressure was kept constant in the loading process to restore the in-situ stress state of the rock. The axial load was imposed on the sample, and the rock's deformation occurred in each cycle (including the axial strain and radial strain). When the bearing capacity of the rock sample was reached, the rock sample was destroyed. Through this test, the influence of reciprocating load on the rock mass was simulated. The axial stress-axial strain curves of typical shale samples obtained from the experiments were presented in Figure 5. It can be found that the peak strength and peak strain increase with the increase in confining pressures. The greater the confining pressure, the greater the peak strength of rock samples. Meanwhile, the rock changed from brittleness to ductility under higher confining pressures, and the peak strain of rock samples increases with the increase in confining pressure. It can be seen from Figure 5 that in the process of a single cyclic loading and unloading, the unloading curve does not completely coincide with the loading curve and is lower than the loading curve due to damage and elastic hysteresis. As a geological material, micropores and natural cracks contained in the rock make the unloading curves unable to completely coincide with the loading curves. As an experimental phenomenon, hysteresis loop is not only a manifestation of stress path, but also a manifestation of energy dissipation. With the increase in loading times, the area of the hysteresis loop gradually increases, which means that the dissipated energy is larger. Before failure, the area of the hysteresis loop is proportional to the number of cycles. After reaching the peak strength, shear failure occurs in the rock sample with internal cracks converging to a main fracture surface, and the dissipated energy reaches the largest.

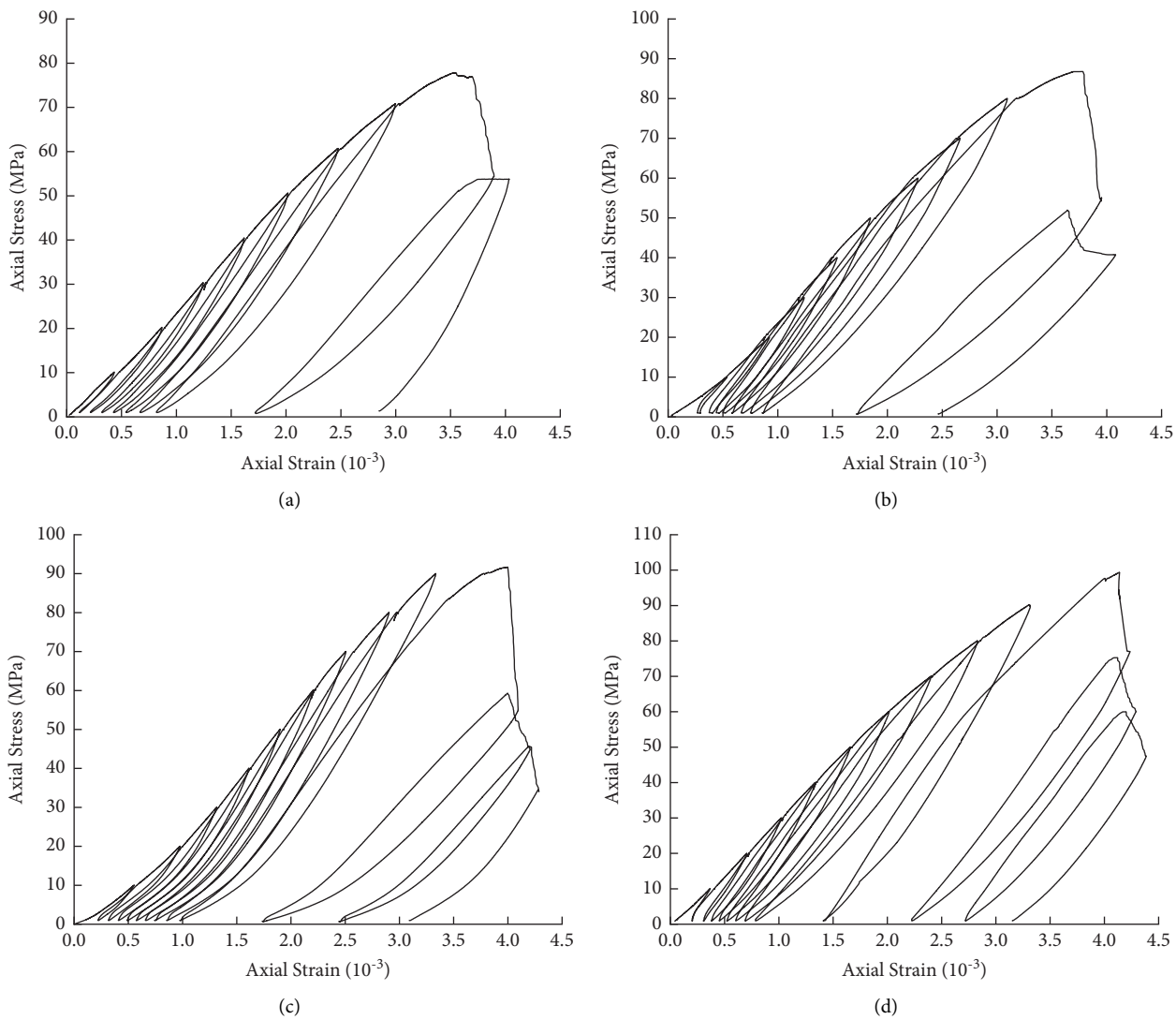

Figure 5: The axial stress-axial strain curves of typical shale samples.

3.2. Energy Evolution Characteristics. According to the triaxial cyclic loading and unloading test curves and the energy calculation method in section 2.4, the evolution law of total energy, elastic energy, and dissipated energy of shale under cyclic loading and unloading under different confining pressures can be obtained. As can be seen from Figure 6, energy evolution of rock samples under different confining pressures is similar, and the energy of rock samples under different confining pressures shows nonlinear growth with an increase in strain. In the elastic stage, the growth rate of elastic energy is slow, and in the plastic stage, the elastic energy increases rapidly. When the peak strength is reached, elastic energy is released rapidly, resulting in macroscopic fractures of the sample. The dissipated energy also presents a nonlinear growth trend with the increase in strain, with slow growth in the elastic stage and sharp growth in the plastic stage. The maximum values of input energy, dissipated energy, and energy dissipation ratio all appear at the peak strength point. In the pre-peak strength stage, the difference between the input energy and the dissipated energy increases gradually with the increase in the number of cycles, indicating that most of the energy input by the testing machine is accumulated in the form of elastic energy. When reaching the peak strength point, a large amount of energy is consumed due to the expansion of a large number of fractures and the bearing capacity of rock samples decreases gradually until failure.

The damage of rock samples under specific stress or strain conditions can be reflected by the change in the energy dissipation ratio. As shown in Figure 6, the energy dissipation ratio-axial strain curves of rock samples under different confining pressures presents a "scoop" shape. The energy dissipation ratio of rock samples decreases linearly first (the stages of compaction), then develops steadily (the stages of elasticity), and then increases rapidly (the stages of plastic), respectively. In the elastic stage, rock samples are in a stable state, elastic energy and dissipation energy both increase slowly, most cracks in rock samples gradually close, and the energy dissipation ratio decreases relatively slowly. The junction of the elasticity stage and the plastic stage is the

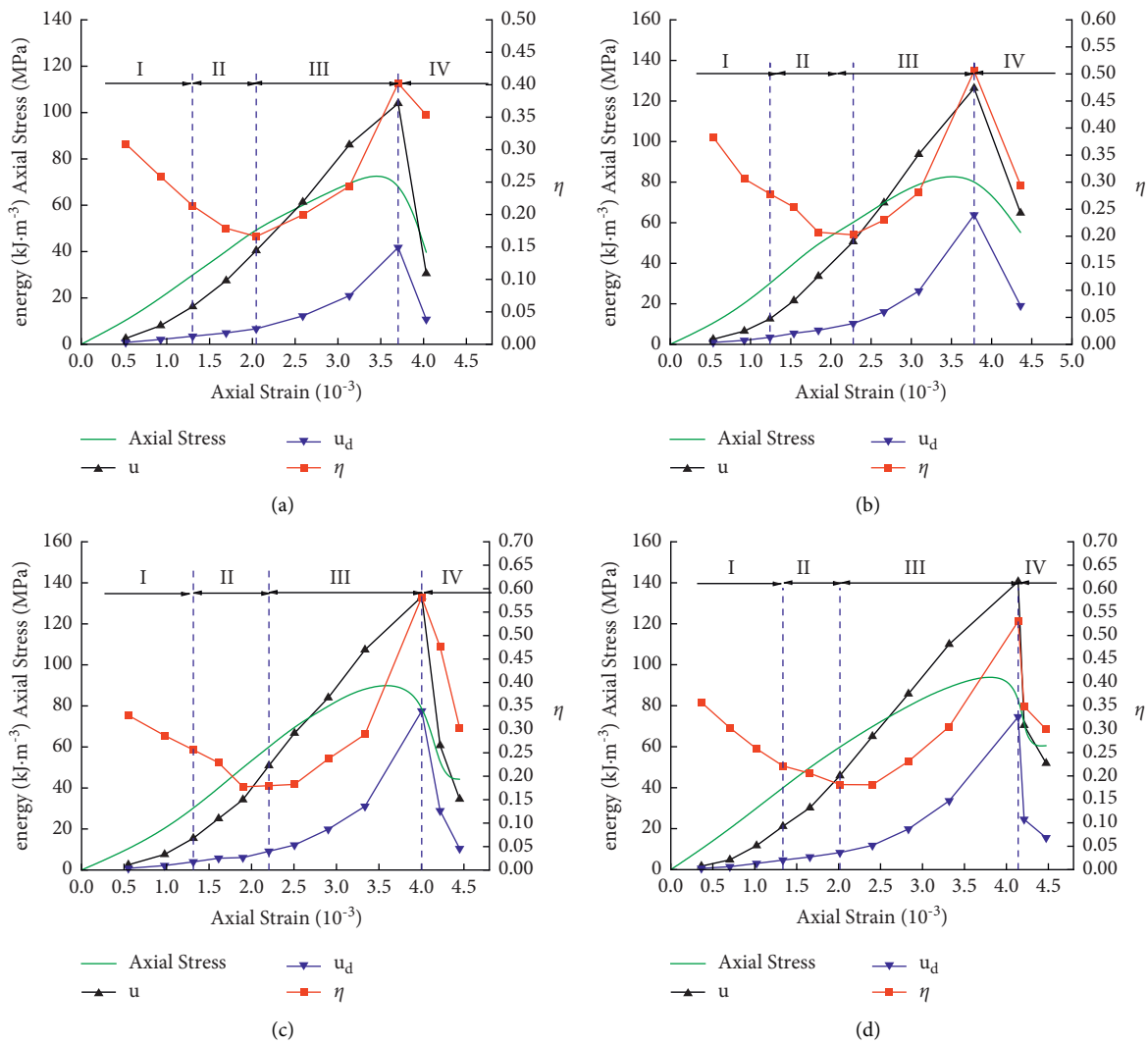

Figure 6: Axial stress-strain and energy evolution curves under cyclic loading and unloading. (a) $\sigma_3 = 10$ MPa. (b) $\sigma_3 = 15$ MPa. (c) $\sigma_3 = 20$ MPa. (d) $\sigma_3 = 30$ MPa.

turning point between the elastic deformation stage and the plastic deformation stage, and the energy dissipation ratio reaches minimum at this turning point. After entering the plastic deformation stage, the growth rate of the dissipated energy increases rapidly, and the energy dissipation ratio increases gradually. In this stage, new cracks and plastic deformation begin to occur inside the rock samples. Before approaching the peak strength, the dissipated energy of rock samples increases due to a large number of new cracks, but the rock sample has not yet failed. At this point, the elastic energy stored in the rock sample reaches the energy storage limit of the rock samples, and the main fracture is about to penetrate. When the peak stress is reached, shear failure occurs in the rock sample with internal cracks converging to a main fracture surface, and the slip of the main fracture dissipates a large amount of energy derived from the accumulated elastic energy as well as the input energy. The rock samples' failure behavior made the dissipated energy increase sharply, and the energy dissipation ratio reaches its maximum.

3.3. Damage Characteristics of the Specimens Under Cyclic Loading. Damage mechanics is an important way to study rock properties. Density [29], wave velocity [30], elastic modulus [31], and plastic strain [32] are usually used to quantitatively describe the deterioration of rock mechanical properties. The generation of plastic strain is the most intuitive physical manifestation of rock damage, and the accumulation of plastic strain is the cause of rock failure. The triaxial cyclic loading and unloading tests were carried out using the TFD-2000 test system, and the cracks of the rocks were propagated to different degrees and then caused damage. In order to better describe the variation of plastic strain under cyclic loading, the following equation is used to reveal the relationship between plastic strain and axial strain:

$$\varepsilon_c = \varepsilon_m - \beta \log\left(\frac{k}{\varepsilon} - \lambda\right), \tag{4}$$

ε_c is the plastic strain under single cyclic loading, ε is the axial strain corresponding to ε_c, and ε_m is the average value of the

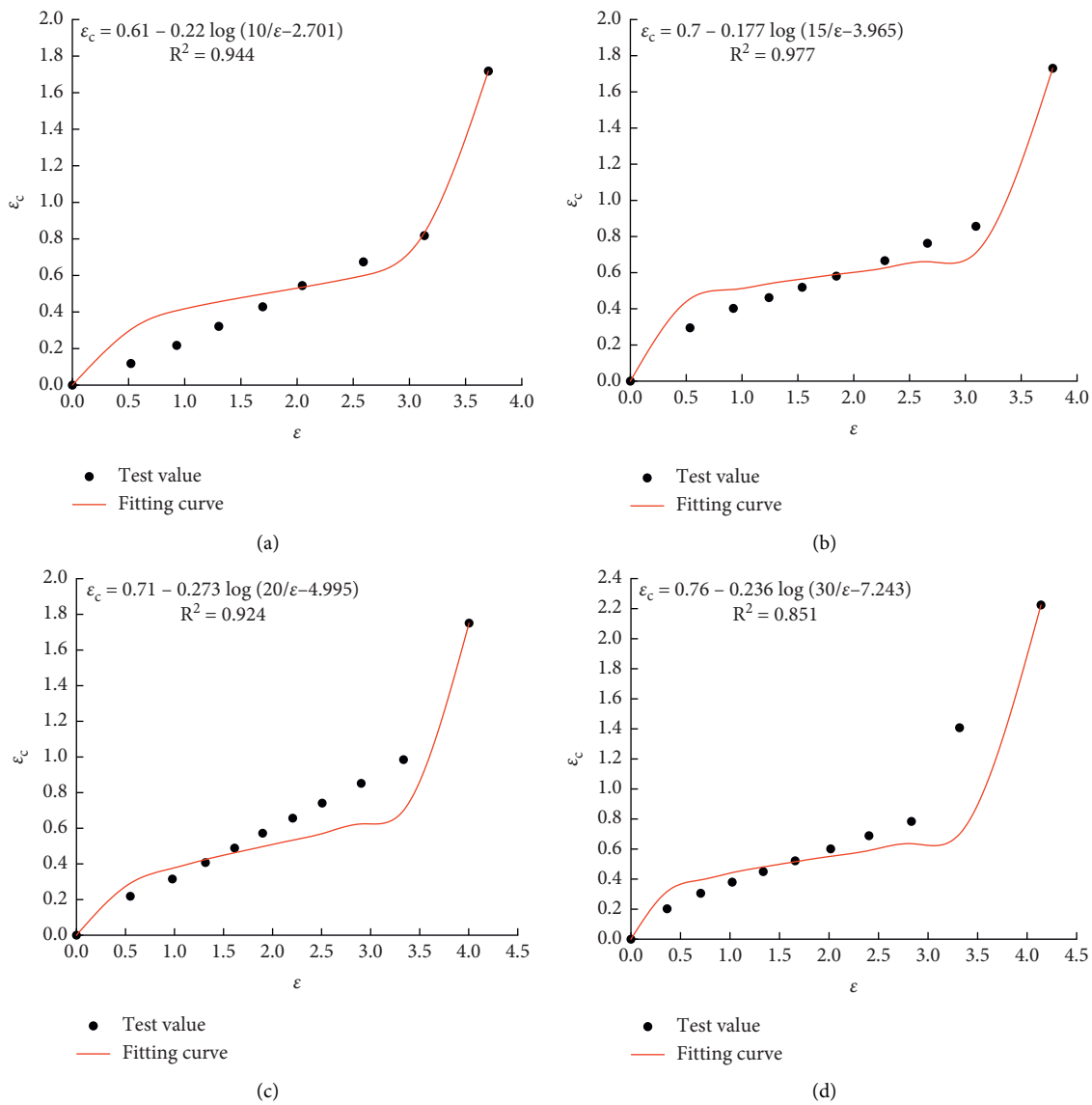

Figure 7: Trend of plastic strain under different confining pressures.

plastic strain of multiple cyclic loading and unloading, representing the cumulative damage of the whole loading process. β is the slope of the stable development stage of the plastic strain curve of rock, k is the confining pressure value, λ is the damage accumulation rate factor in the crack development stage, and its value range is $0-k/\varepsilon$. According to the test results, the variation of plastic strain in single cycle of rock under different confining pressures was obtained, as shown in Figure 7. In the first cycle, the plastic strain increases rapidly under the action of compaction, while the plastic strain value caused by the intermediate cycle increases linearly. In critical failure, the cyclic load accelerates the crack propagation and transfixion, resulting in a sharp increase in plastic strain. With the increase in confining pressure, the number of cycles increases, indicating that the existence of confining pressure enhances the bearing capacity and the deformation capacity of rock samples. Under cyclic loading and unloading conditions, the plastic strain increases with an increase in strain.

As can be seen from Figure 4, input energy is mainly divided into elastic energy and dissipated energy, while dissipated energy is mainly used for the plastic of rock. Plastic deformation occurs in rocks under cyclic loading, and the ultimate macroscopic failure of rocks is caused by accumulative plastic strain exceeding its bearing capacity. Dissipated energy is the energy that causes microcrack propagation, plastic deformation, and stiffness deterioration of rocks. Therefore, the relationship between the energy dissipation ratio and plastic strain is analyzed. The function relation between the energy dissipation ratio and plastic deformation is established:

$$\eta = a\varepsilon_c + \frac{b}{c\varepsilon_c} + d, \tag{5}$$

where a, b, c, and d are fitting parameters.

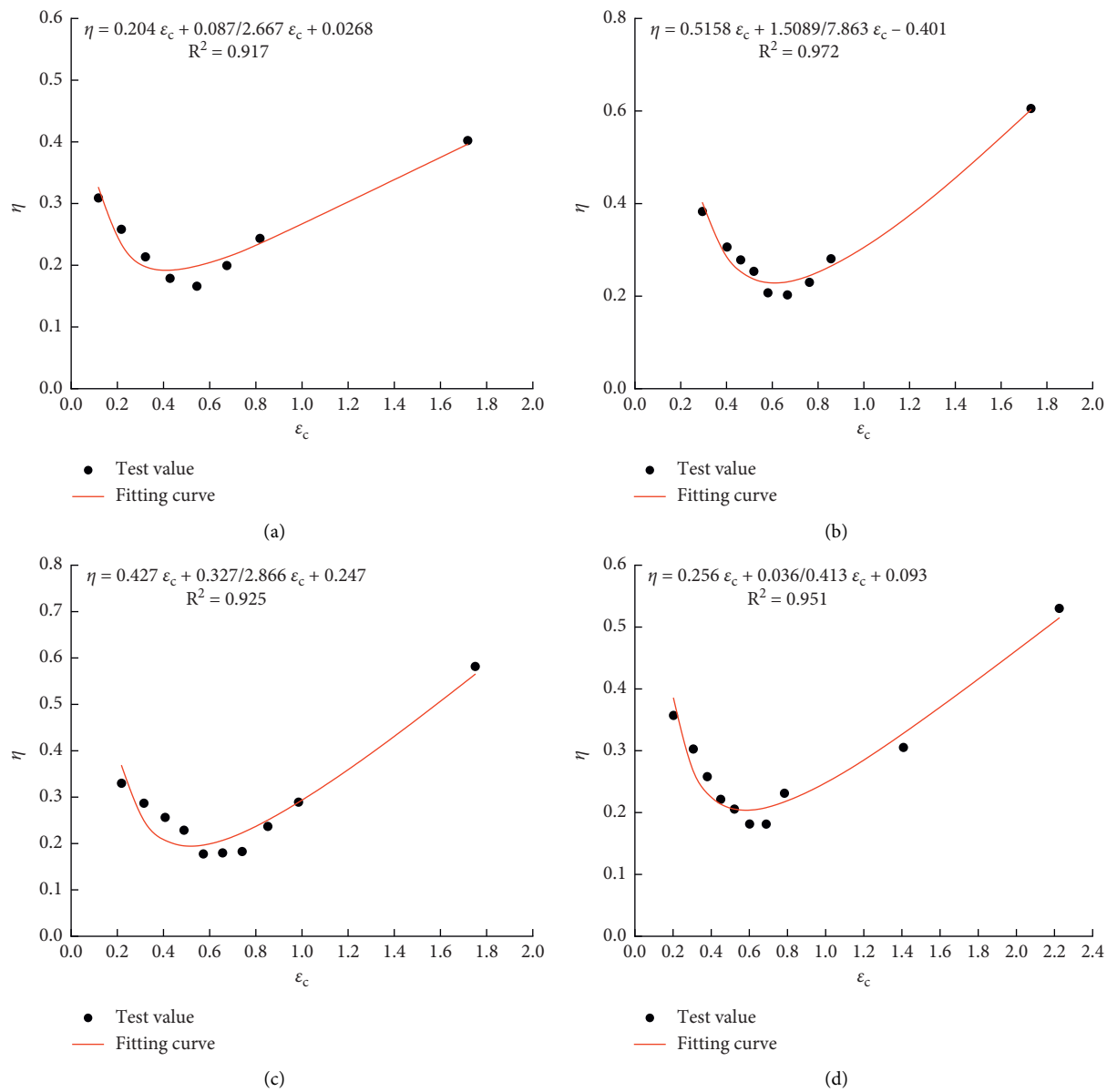

Figure 8: Fitting curves of the energy dissipation ratio-plastic strain under cyclic loading and unloading.

The energy dissipation ratio-plastic strain curves under different confining pressures were drawn by (5). The fitting curves were compared with the experimental curves (as shown in Figure 8), and the fitting curves were found to be similar to the experimental curves showing a "spoon" shape.

3.4. Correlation Between the Energy Dissipation Ratio and Elastic Modulus Evolution. Elastic modulus is a basic mechanical parameter of rock, and the weakening of elastic modulus during loading and unloading reflects the internal structural damage of rocks. Dissipated energy is the intrinsic reflection of rock damage, the elastic modulus of single cycle loading and unloading is calculated by the tangent modulus of the loading stage. To explore the correlation between mechanical characteristic degeneration and the evolution of dissipated energy of shale, the elastic modulus-strain curves (Figure 9) were drawn to compare with the energy dissipation ratio-strain curves, and the equation of correlation was established.

It can be seen from Figure 9 that the elastic modulus of rock samples increases at first, then gently develops, and finally decreases; the change of the elastic modulus reflects the stress state of the rock, namely compaction process, elastic stage, plastic stage, and post-peak stage. Meanwhile, the change of the elastic modulus is also driven by energy; the change in the energy dissipation ratio reflects the damage in the rock, which leads to a change in the elastic modulus.

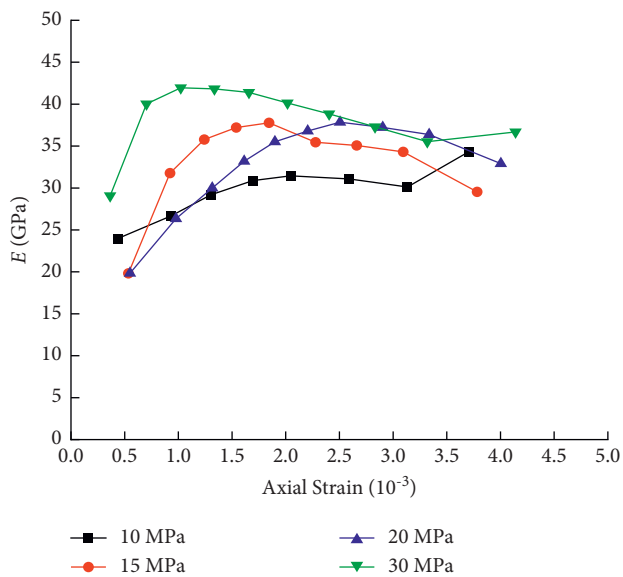

Figure 9: Elastic modulus—-strain curve during cyclic loading and unloading.

(With the progress of the loading, in stages I and II, the elastic modulus increases greatly, and in stage III, the elastic modulus decreases slightly).

The maximum elastic modulus of 10, 15, 20, and 30 MPa is 31.4, 37.8, 37.9, and 41.9 GPa, respectively. Compared with Figure 6, the variation trend of the elastic modulus and the energy dissipation ratio is the opposite; the ratio of the dissipated energy to input energy reflects the weakening characteristics of the elastic modulus to a certain extent. From the energy point of view, the dissipated energy can be used as a factor of the damage and crack propagation of rocks. From the perspective of mechanical characteristics, the decrease of the elastic modulus can also reflect the damage degree of the rocks. Therefore, the energy dissipation ratio is used to characterize the degradation of the elastic modulus, and the relationship between the elastic modulus and the energy dissipation ratio can be expressed as:

$$E = \varphi E_0 (1 - \eta). \tag{6}$$

E_0 is the maximum loading modulus in the cyclic loading and unloading process, E is the elastic modulus corresponding to the energy dissipated ratio, and the value of φ depends on the confining pressure.

3.5. Strength Failure Criterion Based on Energy Dissipation and Strain Damage. In the underground space, the ultimate instability failure of rocks usually occurs when the internal damage of rocks accumulates to a certain threshold under cyclic loading. In Section 3.3, we discussed the relationship between plastic strain and total strain. Under cyclic loading, as the total strain increases, the plastic strain also gradually increases. When the plastic strain reaches a certain value, the internal damage of rock sample reaches the limit that it can bear, leading to the failure of rock sample.

As shown in Figure 4, the total strain of single loading and unloading consists of recoverable strain and plastic strain:

$$\varepsilon_i = \varepsilon_i^e + \varepsilon_i^d, \tag{7}$$

εi, εe i, and εd i are the total strain, elastic strain, and plastic strain of a single cycle loading and unloading, respectively.

According to (3), the relationship between the total strain, elastic deformation, and energy dissipation ratio of single loading and unloading is as follows:

$$\varepsilon_e^i = (1 - \eta_i)\varepsilon, \tag{8}$$

η_i is the energy dissipation ratio of a single cycle of loading and unloading.

The stress of the rock sample under load is divided into the effective elastic part and damage part. The effective elastic part satisfies Hooke's law and can be expressed as:

$$\sigma = E\varepsilon^e. \tag{9}$$

The energy dissipation ratio of rock samples can be obtained using the above (8) and (10), and the corresponding stress under the strain can be obtained by the following equation:

$$\sigma = \varphi E_0 (1 - \eta)^2 \varepsilon, \tag{10}$$

where ε is the strain, and σ is the stress corresponding to ε.

According to (5) and (10), the stress solution equation can be obtained,

$$\sigma = \varphi E_0 \left[1 - \left(a\varepsilon_c + \frac{b}{c\varepsilon_c} + d \right) \right]^2 \varepsilon, \tag{11}$$

$$\sigma = \varphi E_0 \left[1 - \left(a\left(\varepsilon_m - \beta \log\left(\frac{k}{\varepsilon} - \lambda \right) \right) \right) \right.$$

$$\left. + \frac{b}{c(\varepsilon_m - \beta \log(k/\varepsilon - \lambda))} + d) \right]^2 \varepsilon. \tag{12}$$

(12) can be used to fit the envelopes of cyclic loading and unloading stress-strain curves under different confining pressures, as shown in Figure 10. When φ is 1.2, 1.15, 1.1, and 1.05, respectively, the envelopes of the stress-strain curves in the pre-peak stage under 10,15, 20, and 30 MPa confining pressures can be obtained. The equation includes confining pressure-related parameters β and k, plastic strain-related parameters β , and damage accumulation factor λ at the critical damage stage. Compared with the experimental curves, the theoretical axial stress-strain curves containing various parameters can well predict the stress-strain variation under cyclic loading and unloading. From Figure 10, it can be seen that the envelope curves calculated by (12) are in good agreement with the experimental curves. Under different confining pressures, the calculated peak strength points of the theoretical curves are basically consistent with the experimental curves. The stress and strain values of the actual strength failure, the stress and strain values of the theoretical

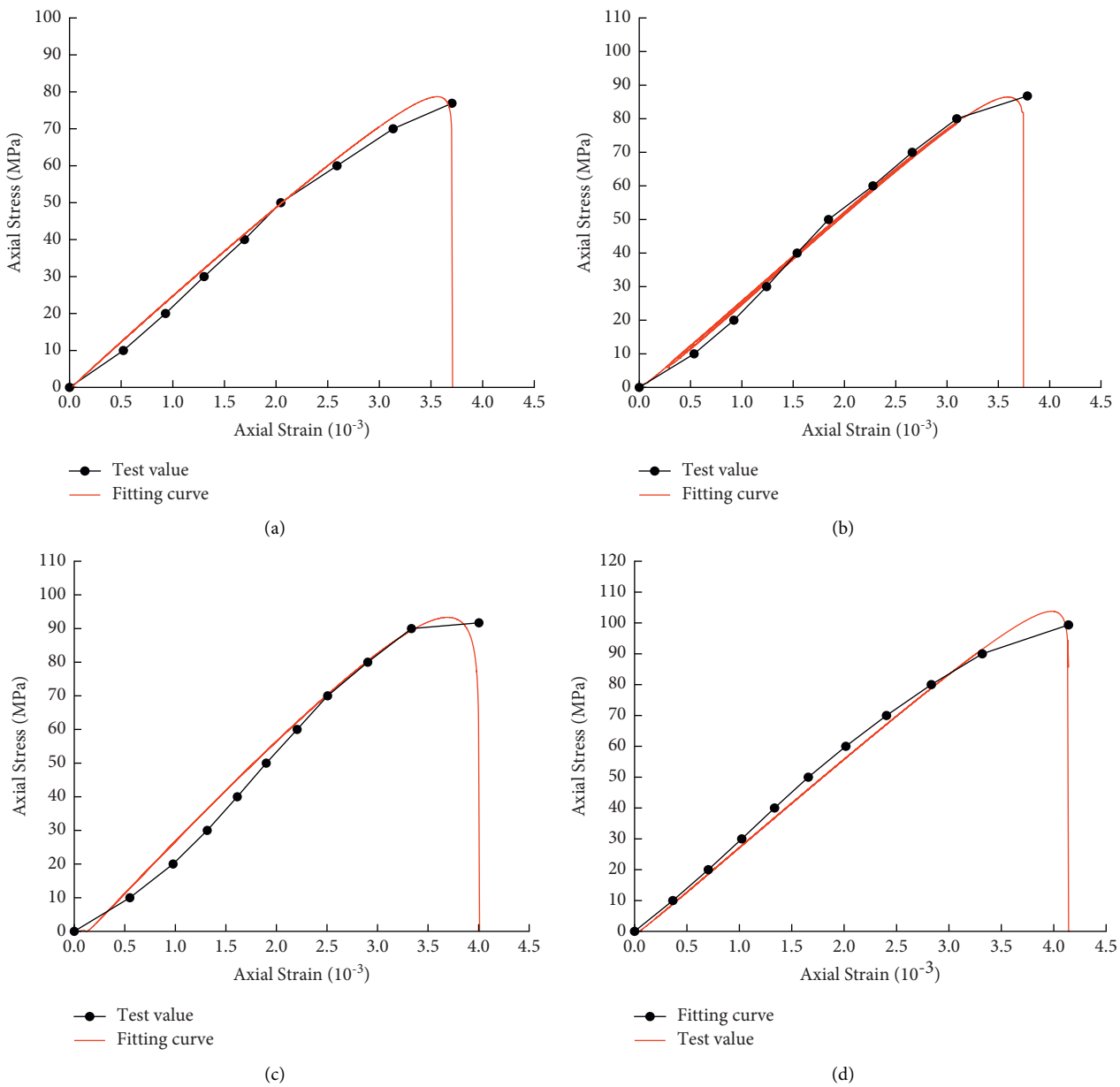

Figure 10: Axial stress-strain curves and theoretical curves under different confining pressures (10 MPa, 15 MPa, 20 MPa, and 30 MPa).

strength failure, and relative errors are shown in Figure 10. The relative errors of stress and strain are less than 10%, which indicates the equation can predict the strength failure point.

4. Discussion

A large number of studies show that it is feasible to study the dynamic strength variation of rock under external load from the perspective of energy. Many researchers have put forward different viewpoints to define rock damage in terms of energy, and have achieved quite important research results [33–36], which greatly promote the application of the energy principle in geotechnical engineering.

In this study, the relationship between peak strain and plastic strain under cyclic loading was studied, and an equation containing many mechanical parameters was established. The relationship between energy dissipation and plastic deformation was investigated based on the energy principle. In this test, only triaxial cyclic loading and unloading of shale was carried out, and other rocks, such as brittle granite and soft marble, were not tested. Future research needs to be further deepened.

This paper studies the mechanical properties and energy dissipation characteristics of shale under general triaxial quasistatics loading conditions. The second stress and the third principal stress were the same in the test, which cannot reflect the influence of intermediate principal stresses on rock deformation and energy dissipation in the actual situation. In the future, relevant cyclic loading and unloading research will be carried out under true triaxial stress.

5. Conclusions

(1) In the triaxial cyclic loading and unloading experiments of shale, the greater the confining pressure, the greater the peak strength and peak strain values the rock samples can achieve. Due to the existence of confining pressure, the strength and deformation ability of rock samples are enhanced. With the increase in the number of cycles, the energy absorbed and dissipated by the rock sample increases, and the energy dissipated reaches the maximum at the peak strength. After failure, the rock sample still has a certain degree of bearing capacity.

(2) The equation of plastic strain and total strain including confining pressure and damage accumulation factor was established. It is found that plastic strain increases with the increase in total strain and confining pressure. It shows a trend of rapid increase at first, steady development, and sharp increase at last.

(3) The accumulation of damage is the cause of the ultimate failure of shale. The energy dissipated in the test process is mainly used for irreversible plastic deformation and crack propagation. The curve fitting method is used to fit the correlation between the energy dissipation ratio and plastic strain, and it is found that the energy dissipation ratios of shale under different confining pressures all show a "spoon" shape with an increase in strain.

(4) In general, the greater the confining pressure, the greater the elastic modulus. The elastic modulus increases first, then develops steadily, and finally decreases with an increase in strain. The ratio of the dissipated energy to input energy reflects the damage of the rock; therefore, the energy dissipation ratio is available to characterize the degradation of the elastic modulus.

(5) A theoretical stress-strain calculation equation was established based on the evolution characteristic of the dissipated energy, and the results obtained by the equation were used to draw the envelope curves of the stress-strain curves. It is found that the calculated results are basically consistent with the test data, as well as the peak strains and peak stress.

Data Availability

The data used to support the findings of this study are included within the article.

Conflicts of Interest

The authors declare no conflicts of interest.

Authors' Contributions

Ziyun Li wrote the manuscript and administered the project; the original draft was prepared by Song Xie and the author was also responsible for project administration; Dongyan Liu and Qianghui Song were in charge of acquiring resources; Peiyong Wang and Baoyun Zhao acquired the funding for this project; Wei Huang curated the data. All authors have read and agreed to the published version of the manuscript.

Acknowledgments

This research was funded and supported by the National Natural Science Foundation of China, under Grant no. 51908097, the Natural Science Foundation of Chongqing, (Grant nos. cstc2020jcyj-msxm1078, cstc2020jcyj-msxmX0558, cstc2019jcyj-msxmX0258, and cstc2020jcyj-msxmX0567),the Science and Technology Innovation Project of Chongqing Social Work and People's Livelihood Guarantee (no. cstc2017shmsA00002), the Special Funding for Chongqing Postdoctoral Research Projects (Grant no. Xm2017006), and the Science and Technology Research Program of Chongqing Municipal Education Commission (no. KJZD-K202101505).

References

[1] H. P. Xie, L. Y. Li, Y. Ju, R. Peng, and Y. Yang, "Energy analysis for damage and catastrophic failure of rocks," *Science China Technological Sciences*, vol. 54, no. S1, pp. 199–209, 2011.

[2] H. P. Xie, L. Y. Li, R. D. Peng, and Y. Ju, "Energy analysis and criteria for structural failure of rocks," *Journal of Rock Mechanics and Geotechnical Engineering*, vol. 1, no. 1, pp. 11–20, 2009.

[3] F. Q. Gong, J. Y. Yan, S. Luo, and X. B. Li, "Investigation on the linear energy storage and dissipation laws of rock materials under uniaxial compression," *Rock Mechanics and Rock Engineering*, vol. 52, no. 11, pp. 4237–4255, 2019.

[4] J. J. Hu, C. Gao, H. Xie, J. Wang, M. Li, and C. Li, "Anisotropic characteristics of the energy index during the shale failure process under triaxial compression," *Journal of Natural Gas Science and Engineering*, vol. 95, Article ID 104219, 2021.

[5] S. P. Singh, "Burst energy release index," *Rock Mechanics and Rock Engineering*, vol. 21, no. 2, pp. 149–155, 1988.

[6] A. V. Mikhalyuk and V. V. Zakharov, "Dissipation of dynamic-loading energy in quasi-elastic deformation processes in rocks," *Journal of Applied Mechanics and Technical Physics*, vol. 38, no. 2, pp. 312–318, 1997.

[7] H. Munoz, A. Taheri, and E. K. Chanda, "Rock drilling performance evaluation by an energy dissipation based rock brittleness index," *Rock Mechanics and Rock Engineering*, vol. 49, no. 8, pp. 3343–3355, 2016.

[8] L. Y. Yu, Z. H. Zhu, Q. B. Meng, H. J. Su, and M. He, "Dynamic characteristics of marble damaged by cyclic loading," *Explosion and Shock Waves*, vol. 39, pp. 63–73, 2019.

[9] Q. B. Meng, M. W. Zhang, Z. Z. Zhang, L. J. Han, and H. Pu, "Research on non-linear characteristics of rock energy evolution under uniaxial cyclic loading and unloading conditions," *Environmental Earth Sciences*, vol. 78, p. 650, 2019.

[10] C. Ai, J. Zhang, Y. W. Li, J. Zeng, X. l. Yang, and J. Wang, "Estimation criteria for rock brittleness based on energy analysis during the rupturing process," *Rock Mechanics and Rock Engineering*, vol. 49, no. 12, pp. 4681–4698, 2016.

[11] D. Y. Li, Z. Sun, T. Xie, X. B. Li, and P. G. Ranjith, "Energy evolution characteristics of hard rock during triaxial failure

with different loading and unloading paths," *Engineering Geology*, vol. 228, pp. 270–281, 2017.

[12] M. W. Zhang, Q. B. Meng, SH. D. Liu, and M. Zappalorto, "Energy evolution characteristics and distribution laws of rock materials under triaxial cyclic loading and unloading compression," *Advances in Materials Science and Engineering*, vol. 2017, pp. 1–16, Article ID 5471571, 2017.

[13] H. W. Zhou, Z. H. Wang, C. S. Wang, and J. F. Liu, "On acoustic emission and post-peak energy evolution in beishan granite under cyclic loading," *Rock Mechanics and Rock Engineering*, vol. 52, no. 1, pp. 283–288.

[14] M. M. He, F. Pang, H. T. Wang, J. W. Zhu, Y. S. Chen, and F. Rizzo, "Energy dissipation-based method for strength determination of rock under uniaxial compression," *Shock and Vibration*, vol. 2020, pp. 1–13, Article ID 8865958, 2020.

[15] X. S. Liu, J. G. Ning, Y. L. Tan, and Q. H. Gu, "Damage constitutive model based on energy dissipation for intact rock subjected to cyclic loading," *International Journal of Rock Mechanics and Mining Sciences*, vol. 85, pp. 27–32, 2016.

[16] C. Wang, B. He, X. L. Hou, J. Y. Li, and L. Liu, "Stress–energy mechanism for rock failure evolution based on damage mechanics in hard rock," *Rock Mechanics and Rock Engineering*, vol. 53, pp. 1–17, 2019.

[17] K. Zhao, X. Yu, Y. Zhou, Q. Wang, J. Q. Wang, and J. Hao, "Energy evolution of brittle granite under different loading rates," *International Journal of Rock Mechanics and Mining Sciences*, vol. 132, Article ID 104392, 2020.

[18] T. T. Li, X. J. Pei, D. P. Wang, R. Q. Huang, and H. Tang, "Nonlinear behavior and damage model for fractured rock under cyclic loading based on energy dissipation principle," *Engineering Fracture Mechanics*, vol. 206, pp. 330–341, 2018.

[19] Y. Chen and B. H. Guo, "Crack closure effect and energy dissipation model for rocks under uniaxial compression," *Geotechnical & Geological Engineering*, vol. 38, no. 1, pp. 621–629, 2020.

[20] F. Pei, H. G. Ji, and T. H. Zhang, "Energy evolution and mechanical features of granite subjected to triaxial loading-unloading cycles," *Advances in Civil Engineering*, vol. 209, pp. 63–73 2019.

[21] H. Q. Duan and Y. J. Yang, "Deformation and dissipated energy of sandstone under uniaxial cyclic loading," *Geotechnical & Geological Engineering*, vol. 36, no. 1, pp. 611–619, 2018.

[22] Y. Wang, W. K. Feng, and C. H. Li, "On anisotropic fracture and energy evolution of marble subjected to triaxial fatigue cyclic-confining pressure unloading conditions," *International Journal of Fatigue*, vol. 134, p. 105524, 2020.

[23] J. B. Wang, Q. Zhang, Z. P. Song, X. R. Liu, X. P. Wang, and Y. W. Zhang, "Microstructural variations and damage evolvement of salt rock under cyclic loading," *International Journal of Rock Mechanics and Mining Sciences*, vol. 152, Article ID 105078, 2022.

[24] P. Hou, Y. Xue, F. Gao et al., "Effect of liquid nitrogen cooling on mechanical characteristics and fracture morphology of layer coal under Brazilian splitting test," *International Journal of Rock Mechanics and Mining Sciences*, vol. 151, Article ID 105026, 2021.

[25] Y. Xue, J. Liu, P. G. Ranjith, Z. Zhang, F. Gao, and S. Wang, "Experimental investigation on the nonlinear characteristics of energy evolution and failure characteristics of coal under different gas pressures," *Bulletin of Engineering Geology and the Environment*, vol. 81, no. 1, p. 38, 2022.

[26] R. Ulusay, "The ISRM suggested methods for rock characterization, testing and monitoring," *Springer International Publishing*, vol. 15, pp. 47-48 2014, 2007-2014.

[27] T. T. Li, X. J. Pei, J. Guo, M. H. Meng, and R. Q. Huang, "An energy-based fatigue damage model for sandstone subjected to cyclic loading," *Rock Mechanics and Rock Engineering*, vol. 53, pp. 5069–5079, 2020.

[28] E. D. Steffler, J. S. Epstein, and E. G. Conley, "Energy partitioning for a crack under remote shear and compression," *International Journal of Fracture*, vol. 120, no. 4, pp. 563–580, 2003.

[29] G. Brown and D. J. Reddish, "Experimental relations between rock fracture toughness and density," *International Journal of Rock Mechanics and Mining Sciences*, vol. 34, no. 1, pp. 153–155, 1997.

[30] M. Oda, T. Yamabe, and K. Kamemura, "A crack tensor and its relation to wave velocity anisotropy in jointed rock masses," *International Journal of Rock Mechanics and Mining Sciences & Geomechanics Abstracts*, vol. 23, no. 6, pp. 387–397, 1986.

[31] J. Q. Xiao, D. X. Ding, F. L. Jiang, and G. Xu, "Fatigue damage variable and evolution of rock subjected to cyclic loading," *International Journal of Rock Mechanics and Mining Sciences*, vol. 47, no. 3, pp. 461–468, 2022.

[32] Z. l. Wang, Y. C. Li, and J. G. Wang, "A damage softening statistical constitutive model considering rock residual strength," *Computers & Geosciences*, vol. 33, pp. 1–9, 2007.

[33] W. Chen, H. Konietzky, X. Tan, and T. Frühwirt, "Pre-failure damage analysis for brittle rocks under triaxial compression," *Computers and Geotechnics*, vol. 74, pp. 45–55, 2015.

[34] D. Huang and Y. R. Li, "Conversion of strain energy in triaxial unloading tests on marble," *International Journal of Rock Mechanics and Mining Sciences*, vol. 66, pp. 160–168, 2013.

[35] G. Y. Zhao, B. Dai, L. J. Dong, and C. J. Yang, "Energy conversion of rocks in process of unloading confining pressure under different unloading paths," *Transactions of Nonferrous Metals Society of China*, vol. 25, no. 5, pp. 1626–1632, 2015.

[36] N. Li, Y. Zou, S. C. Zhang et al., "Rock brittleness evaluation based on energy dissipation under triaxial compression," *Journal of Petroleum Science and Engineering*, vol. 183, p. 106349, 2019.

Hindawi
Advances in Materials Science and Engineering
Volume 2022, Article ID 8281362, 13 pages
https://doi.org/10.1155/2022/8281362

Research Article

Mechanical Behaviors and Damage Evolution Characteristics of Predamaged Rock under Triaxial Compression Experiment

Jinshuai Guo,[1] **Wenzheng Shang**,[2] **Jianbo Yuan**,[2] **and Zhigang Liu**[2,3,4]

[1]*School of Civil Engineering, Xuzhou University of Technology, Xuzhou, Jiangsu 221018, China*
[2]*Institute of Mining Engineering, Shandong University of Science and Technology, Tai'an 271019, China*
[3]*Shandong Energy Group, Jinan 250013, China*
[4]*A Key Laboratory of Deep Coal Resource Mining, School of Mines, Ministry of Education of China, China University of Mining and Technology, Xuzhou 221116, China*

Correspondence should be addressed to Zhigang Liu; 15865721818@163.com

Received 2 July 2022; Accepted 25 July 2022; Published 23 August 2022

Academic Editor: Depeng Ma

The underground rock was disturbed repeatedly during the excavation, resulting in its damage degree gradually accumulated. Therefore, the rock in practical engineering can be regarded as predamaged (PD) rock, and its mechanical behaviors are different from conventional intact rock. This paper proposed the calibrate method to evaluate the predamaged degree of rock based on acoustic emission (AE) ring counts, and the PD rock samples were prepared by uniaxial cyclic loading and unloading test. Then, the triaxial compression experiment of predamaged rock was carried out to study the influence of different predamaged degrees on mechanical behaviors and damage evolution characteristics. The results show that the peak stress and axial strain of PD rock decrease gradually with the increase of predamaged degree. The yield stage of PD rock was significantly shorter than that of intact rock, and it entered the dilation deformation earlier. Furthermore, the constitutive equation of the PD rock based on energy was constructed and the damage evolution characteristics of PD rock were analyzed. It was observed that the bigger the predamaged degree was, the earlier the rock entered the damage, and the failure mode was more complex and crushed. The research results can provide the theoretical basis for the stability control of engineering disturbed rock.

1. Introduction

The surrounding rock experienced multistress paths during the engineering disturbance, such as roadway excavation, blasting, and coal seam mining, resulting in the generation and accumulation of damage in the rock [1, 2]. Therefore, the rock in practical engineering generally belongs to the predamaged rock [3, 4]. The study of the mechanic's behavior, damage, and failure characteristics of the PD rock are of great significance for the field of engineering.

However, the existing research on mechanical behaviors of rock mainly focused on intact rock, while the research studies on the PD rock were still in exploration [5–7]. Some scholars prefabricated regular cracks in rock samples to simulate the predamaged rock, and studied the influence of cracks number, length, and angle on mechanical behaviors and failure modes [8, 9]. The results indicated that the strength parameters (uniaxial compressive strength, residual strength, and elastic modulus) and deformation parameters (peak axial, radial, and volume strain) decrease with the increase in the number of preexisting cracks [9–13]. Wu et al. proposed that the yield platform was presented in the cracked rock sample with the length of preexisting cracks more than 23 mm [10]. Cao et al. analyzed the rock with different cracks angle and found that the rock sample takes a turn from wing crack propagation failure to crack coalescence failure with the increase of the angle [8]. Cheng proposed that the failure mode changed from shear failure to tensile failure as the length of preexisting crack increased [9]. Huang and Li proposed that the compaction stage of prefabricated crack rocks was obviously prolonged, and the brittleness of samples with cracks was more significant than that of intact samples [14]. With the increase of the crack angle, the peak strength of the sample first decreases and

then increases. The fracture dip angle of 45° was the dividing point of the variation of mechanical and deformation parameters [15, 16]. The variation of mechanical and deformation parameters of the sample with the crack length does not turn at the middle crack length, and the increase of the crack length will directly degrade the strength and mechanical and deformation behaviors of the rock [17].

Based on the comprehensive analysis of the above literature, the existing research mostly uses prefabricated regular cracks to study the influence law of predamaged rock mechanical behaviors. Although this method can study its basic influence characteristics and mechanism to a certain extent, the predamaged cracks in the existing research are mostly macrocracks with regular distribution, which is somewhat different from the random distribution and closure characteristics of microcracks in natural rocks.

Some scholars prepared rock samples with different predamaged degrees through a preloading test. Qiu et al. used the ratio of the stress level loaded on a rock to the peak strength under the corresponding conditions of rock to characterize the predamaged degree [18]. Hou et al. defined the predamaged degree based on the axial strain and elastic modulus and prepared samples with different initial damage degrees through a uniaxial preloading test [19]. Huang et al. defined the predamaged degree of coal samples based on strain energy and prepared coal samples with different initial damage degrees by cyclic loading and unloading test [20]. In conclusion, there is no uniform definition of PD rock, and the relevant research studies were still in exploration.

In view of the above problems, this paper used an AE ring count to calibrate the predamaged degree of rock and prepared rock samples with different predamaged degrees through grading cyclic loading and unloading test. Then, the triaxial mechanical experiment of PD rock was carried out to study the influence of different predamaged degrees on rock mechanical behaviors, damage evolution, and failure characteristics.

2. Preparation of PD Rock Samples

The damage to rock is essentially the development and expansion process of internal cracks and which is accompanied by energy change. Therefore, the damage degree of rock can be calibrated by the accumulated energy [21]. The energy of rock is gradually accumulated during cyclic loading and unloading, and the damage degree is also changing. Then, rock samples with different predamaged degrees were prepared by grading cyclic loading and unloading test.

2.1. Definition of Predamage. AE technology has been used to study the material damage and fracture process for a long time. It is found that the release of strain energy during the generation, propagation, and penetration of internal microcracks will produce an AE ring count [22]. Therefore, the study on the change rule of AE ring count during the loading process of rock is helpful to reveal the damage evolution.

The microelement strength obeys a certain statistical distribution considered the statistical principle [23]. Therefore, the damaged area of the rock cross section can be described as follows [24]:

$$S_d = S\int_0^{\varepsilon}\varphi(x)\mathrm{d}x, \tag{1}$$

where S is the cross-sectional area of the material without damage; $\varphi(x)$ was the statistical distribution of microelement strength.

Then, the damage D can be obtained [22],

$$D = \frac{S_{\mathrm{d}}}{S} = \int_0^{\varepsilon}\varphi(x)\mathrm{d}x. \tag{2}$$

Assuming that the number of AE ring counts per unit area of the damage element is n, then the number of AE ring counts of damage area ΔS to be generated can be expressed as follows:

$$\Delta N = n\Delta S = N_{\mathrm{d}}\frac{\Delta S}{S}, \tag{3}$$

where N_d is the accumulated AE ring counts when the damaged area is Sd.

When the sample strain increment is $\Delta\varepsilon$, the damaged area corresponding to the sample ΔS can be calculated as follows:

$$\Delta S = S_d\varphi(x)\Delta\varepsilon. \tag{4}$$

When the strain produced by the sample increased to ε, the ratio of accumulated AE ring counts to which at complete damage can be obtained as follows:

$$\frac{N_d}{N} = \int_0^{\varepsilon}\varphi(x)\mathrm{d}x. \tag{5}$$

Combining the above (2) and (5), the relationship between damage and AE ring counts can be obtained as follows:

$$D = \frac{N_d}{N}. \tag{6}$$

The circular loading and unloading methods were adopted in this paper. Assuming that the rock was failure after n cycles of loading and unloading, then the predamage can be expressed as follows:

$$D_0(k) = \frac{\sum_{i=1}^{k} N_i}{\sum_{i=1}^{n} N_i}. \tag{7}$$

where $D_0(k)$ is the predamaged degree of k cycles of loading and unloading test; $\sum_{i=1}^{k} N_i$ is the accumulated AE ring counts of k cycles of loading and unloading test; $\sum_{i=1}^{n} N_i$ is the accumulated AE ring counts of n cycles of loading and unloading test.

2.2. Test System. The MTS compression machine and PCI-2 AE monitoring system were adopted to prepare the PD rock, as shown in Figure 1. MTS machine circularly loads and unloads rock samples through the set stress path, and

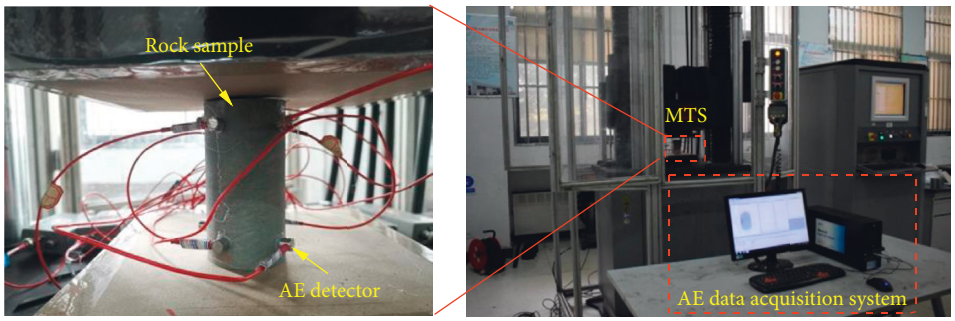

Figure 1: Cyclic loading and unloading test.

collects stress-strain data in real-time. PCI-2 AE monitoring system collects the AE data during the compression test.

2.3. AE Characteristics of PD Rock Samples. Firstly, a rock sample (S-5) was selected to be cyclic loading and unloading until it was a failure. The accumulated AE ring counts during the whole loading and unloading process were monitored. The stress-strain and AE data are shown in Figure 2.

The S-5 rock sample was a failure after 19 cycles of loading and unloading. Comparing the accumulated AE ring counts and energy variation curve, it was observed that the loading peak of each cycle would correspond to the sudden rise of ring and energy. In the 7th cycle loading, the increase of the AE ring counts curve was significantly greater than in the previous cycles and the energy curve also showed a sharp rise. Therefore, the S-5 rock sample in the 7th cycle began to damage the rock. When the 17th cyclic loading was carried out, the AE ring counts and energy change degree were significantly larger than those of the previous cycles. Meanwhile, the microcracks in the rock began to connect. The S-5 rock sample formed a penetrating fracture and failure in the 19th cycle.

Based on the experimental results of the S-5 rock sample, four kinds of PD rock samples with different predamaged degrees were prepared by cyclic loading and unloading 7, 10, 13, and 16 times, respectively (S-1, S-2, S-3, and S-4). The stress-strain and AE data during the test are shown in Figure 3.

Comparing the stress and AE data in Figure 3, it can be seen that the accumulated AE ring counts and energy curve also show a sudden rise when the 4th, 6th, 7th, and 11th loading and unloading cycles were carried out, indicating that the rock sample begins to damage. Therefore, the cracks in the rock began to develop, and the damage continued to increase as the loading and unloading cycle increased.

According to the calculation method of the predamaged degree of rock in (7), the acculturated AE ring counts after loading and unloading cycles of S-1, S-2, S-3, and S-4 were counted, respectively. The predamaged degree of different rock samples can be obtained by comparing the accumulated AE ring counts of the S-5 rock sample, as shown in Table 1.

3. Triaxial Compression Experiment of PD Rock

3.1. Triaxial Experimental System. The experimental equipment adopts GDS triaxial system (Figure 4). The stress loading system is divided into an axial compression control system and confining pressure control system. The axial compression is applied by the axial hydraulic servo machine, and the confining pressure is applied by injecting hydraulic oil into the cell through the plunger pump.

3.2. Triaxial Experimental Scheme. First, the axial pressure and confining pressure were loaded to the original rock stress level, then the confining pressure was kept constant and the axial pressure was continuously loaded until the rock was a failure. OA section: equally loading axial pressure and confining pressure to 5.0 MPa ($\sigma 1 = \sigma 3$); section AB: keep confining pressure constant ($\sigma 3 = 5.0$ MPa) and continue to load axial pressure until the rock was a failure (Figure 5).

4. Mechanical Behaviors of PD Rock

4.1. Peak Stress. The axial strain, radial strain, and volumetric strain curves of S-0, S-1, S-2, S-3, and S-4 rock samples are shown in Figure 6.

The peak stress of each rock sample was fitted with the predamaged degree, as shown in Figure 7.

$$\sigma_f = 91.2D_0^3 - 111.7D_0^2 + 13.5D_0 + 42.2. \quad (8)$$

The peak stresses of S-1, S-2, S-3, and S-4 PD rock samples were 42.0 MPa, 40.0 MPa, 36.0 MPa, and 28.0 MPa, respectively, which were smaller than those of S-0 intact rock samples (42.2 MPa). Figure 7 indicates that peak stresses of PD rock gradually decrease with the increase of predamaged degree.

4.2. Deformation Characteristics. The stress-strain curves of S-1, S-2, S-3, and S-4 were similar to S-0, which can be divided into fracture compaction stage, elastic deformation

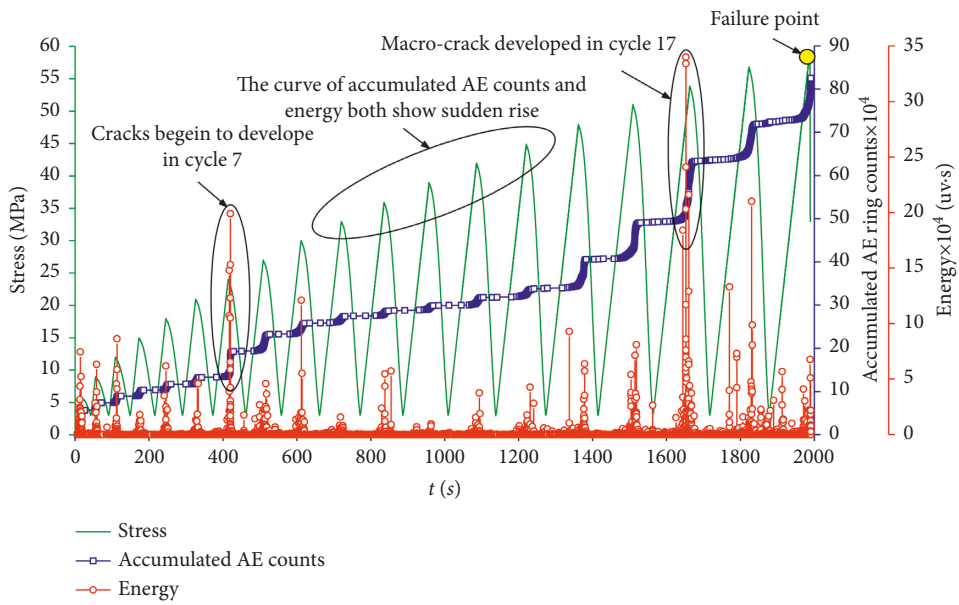

Figure 2: AE data of S-5 rock sample.

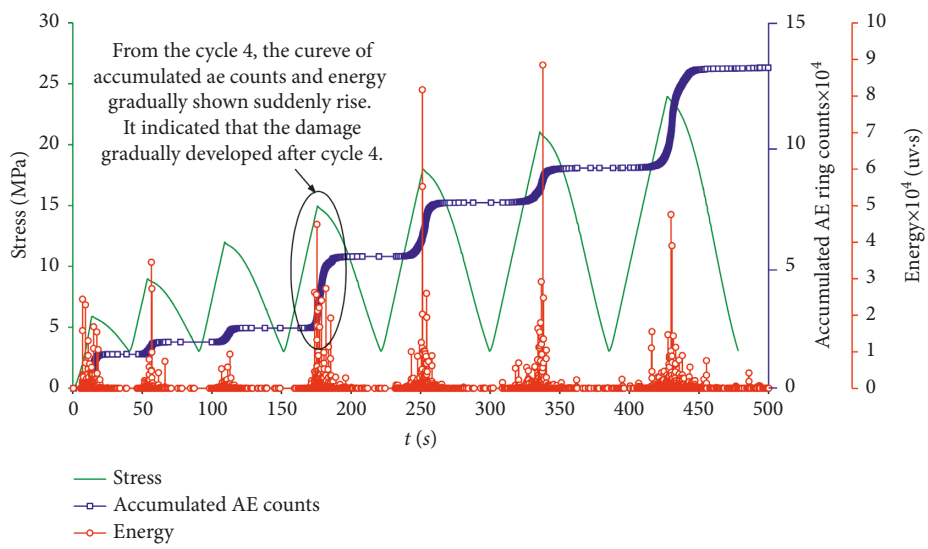

(a)

Figure 3: Continued.

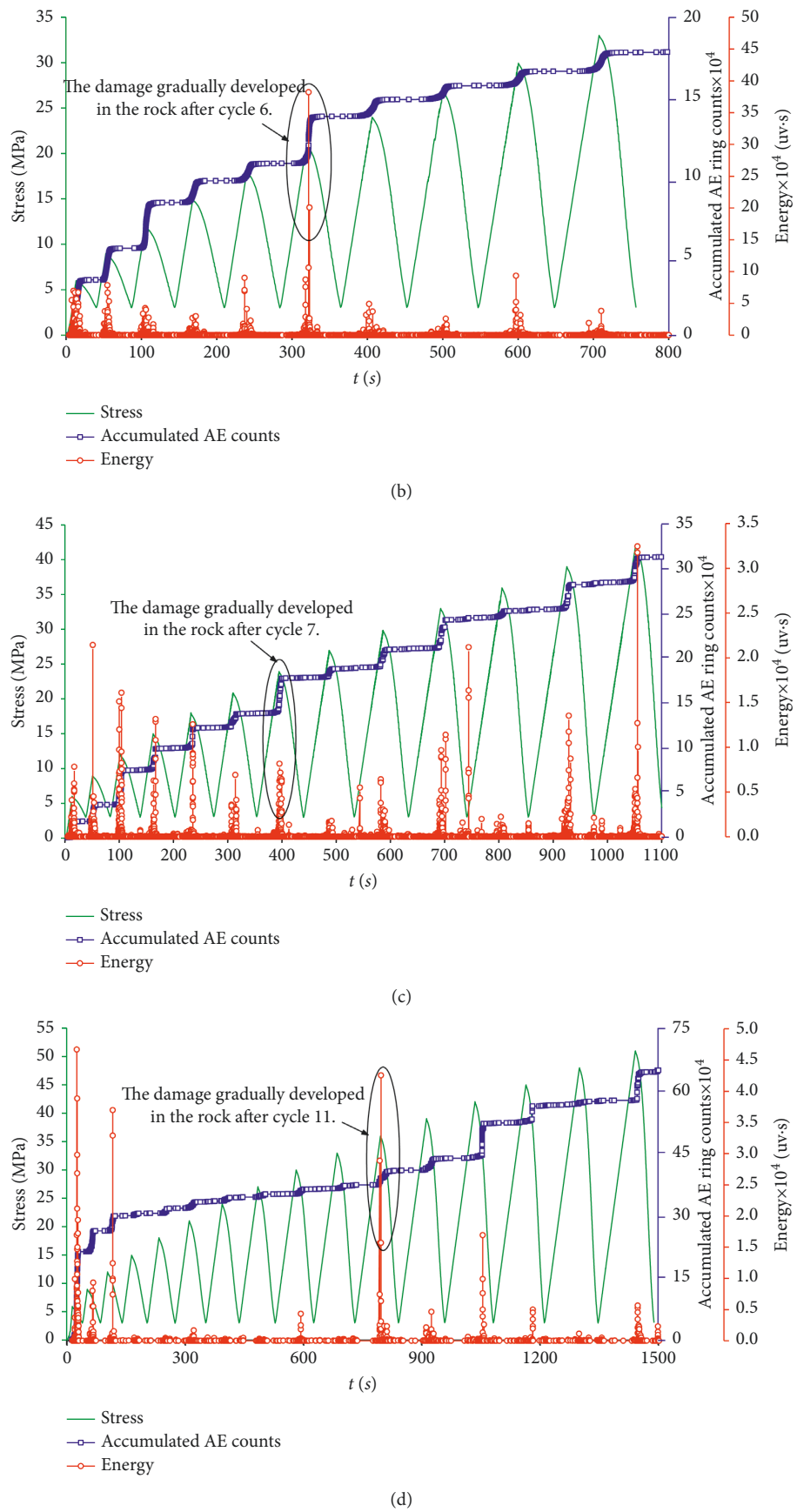

Figure 3: AE data of PD rock sample. (a) S-1 rock sample. (b) S-2 rock sample. (c) S-3 rock sample. (d) S-4 rock sample.

Table 1: Predamaged degree of a rock sample.

Sample	Number of cycles	Accumulated AE ring counts	Predamaged degree/$D0$
S-0	0.0	0.0	0.0
S-1	7.0	14.0	0.1
S-2	10.0	19.8	0.2
S-3	13.0	32.2	0.4
S-4	16.0	61.1	0.7
S-5	19.0	82.6	1.0

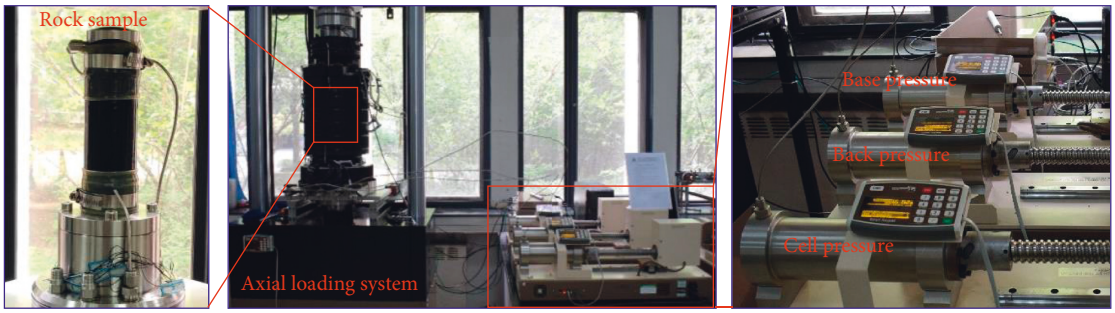

Figure 4: Triaxial experimental system of GDS.

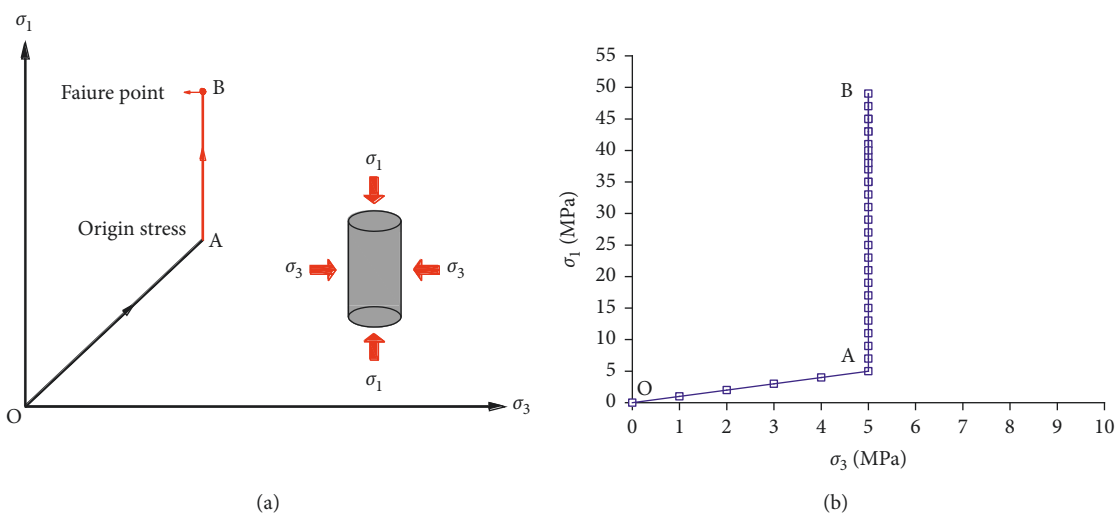

Figure 5: Triaxial experimental stress path. (a) Designed stress path. (b) Experimental stress path.

stage, yield deformation stage, and postpeak stage, as shown in Figure 8.

The peak axial strain of PD rock samples (1.0%, 1.0%, 1.1%, and 1.2%) was significantly smaller than that of intact rock samples (1.3%), and the peak axial strain of rock samples decreases gradually with the increase of predamaged degree. Meanwhile, the ratio of YDS to the total strain of PD rock samples (51.3%, 52.9%, 58.1%, and 59.7%) was significantly bigger than that of intact rock samples (48.7%).

4.3. Dilation Characteristics. The volumetric strain curves of S-1, S-2, S-3, and S-4 PD rock samples and S-0 intact rock samples were compared and analyzed to study the influence of predamaged degree on rock deformation, as shown in Figure 9.

The dilatancy onset point (DOP) of S-1, S-2, S-3, and S-4 was 0.6%, 0.5%, 0.4%, and 0.4% of axial strain, respectively, which were less than 0.7% of intact rock. It indicated that the PD rock more easily entered the dilation deformation, and the volume deformation is smaller at the DOP.

5. Damage Evolution and Failure Characteristics of PD Rock

5.1. Damage Constitutive Equation. The damage variable was generally defined as the ratio of the number of failed units to the total number of units as $D = N_d/N$ [25]. The distribution of rock materials, in reality, was not homogeneous. The Weibull equation was usually used to simulate this non-uniform distribution in existing studies [26, 27]. The

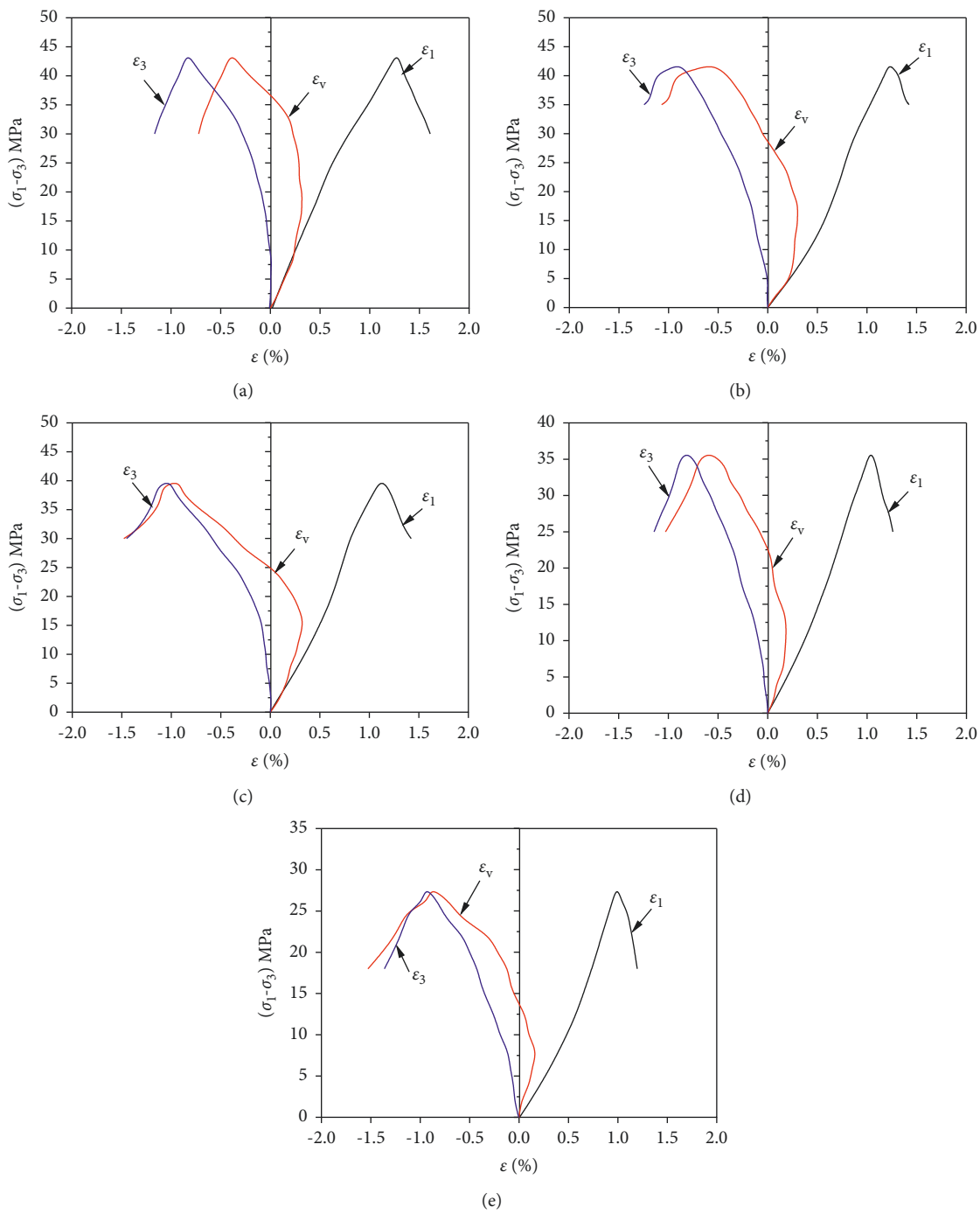

Figure 6: Stress-strain curve of the PD rock. (a) S-0 rock sample. (b) S-1 rock sample. (c) S-2 rock sample. (d) S-3 rock sample. (e) S-4 rock sample.

distribution function and probability density function were expressed as follows:

$$\begin{cases} F(u) = 1 - e^{\left(-\left(u/u_0\right)^m\right)}, \\ f(u) = F'(u) = \dfrac{m}{u_0}\left(\dfrac{u}{u_0}\right)^{m-1} e^{\left(-\left(u/u_0\right)^m\right)}. \end{cases} \tag{9}$$

where u was the mechanical parameter (such as strength, strain, and elastic modulus) of the element, and the scaling parameter u_0 was related to the average value of the element parameter. m was the scale parameter, the larger the value means the more uniform the material.

The internal damage of rock was accompanied by the dissipation process of energy. Therefore, when the energy U was selected as the mechanical parameter u, (9) can be written as follows:

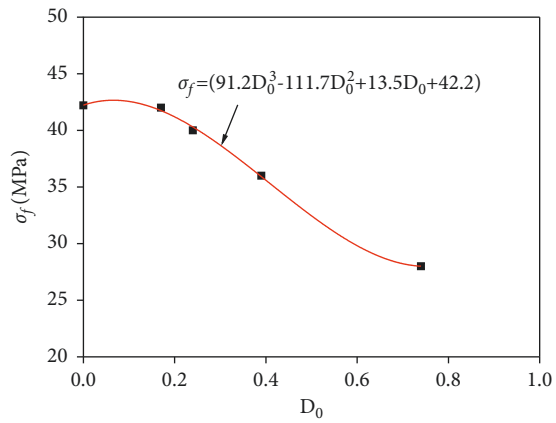

Figure 7: Fitting relationship of peak stress with a predamaged degree.

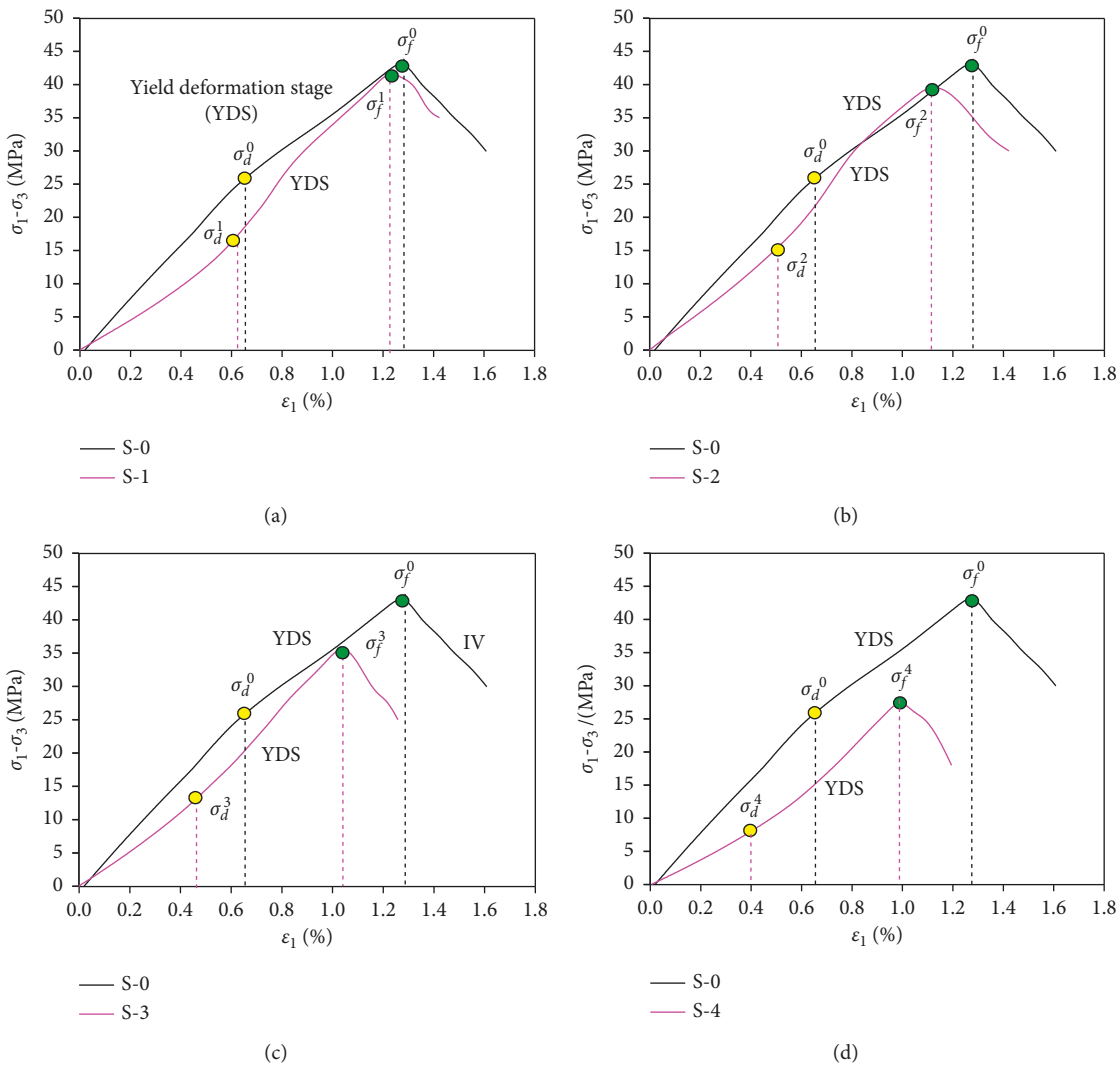

Figure 8: Stress-strain curve comparison of PD rock and intact rock. (a) S-1 rock sample. (b) S-2 rock sample. (c) S-3 rock sample. (d) S-4 rock sample.

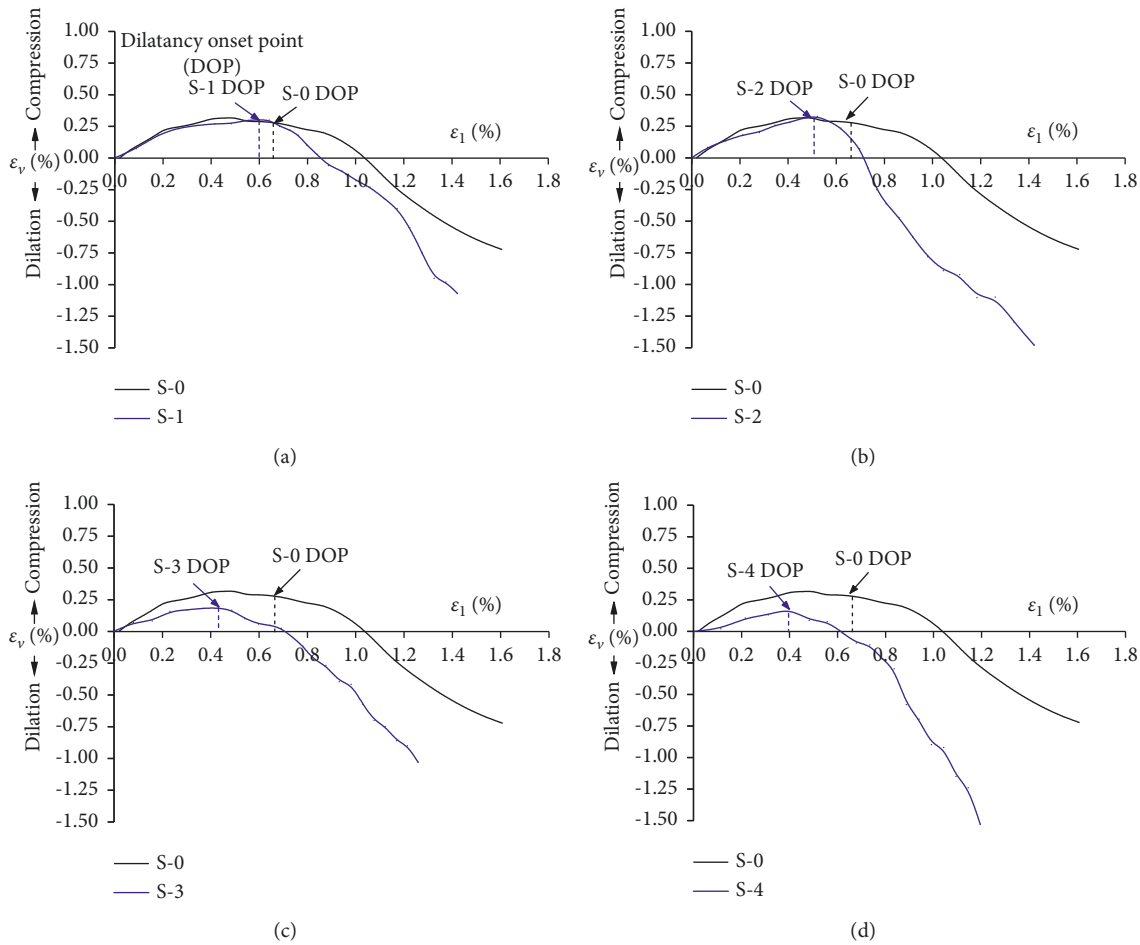

Figure 9: Volumetric strain variation curve of PD rock. (a) S-1 rock sample. (b) S-2 rock sample. (c) S-3 rock sample. (d) S-4 rock sample.

$$f(\varepsilon) = \frac{m}{U_0}\left(\frac{U}{U_0}\right)^{m-1} e^{\left(-\left(u/u_0\right)^m\right)}. \tag{10}$$

When the rock was in a stress state F, there were as follows:

$$N_d = \int_0^F N f(U)\mathrm{d}F = N\left\{1 - e^{-\left(u/u_0\right)^m}\right\}. \tag{11}$$

Then, the damage variable D can be expressed as follows:

$$D = \frac{N_\mathrm{d}}{N} = 1 - e^{-\left(u/u_0\right)^m}. \tag{12}$$

According to relevant research studies, the energy absorbed by rock can be divided into two parts as follows: (1) the energy obtained by volume deformation; (2) the distortion specific energy leading to deformation. The energy of volumetric deformation will not cause damage, so the energy absorbed by rock damage U can be expressed as $U = (\sigma 1 - \sigma 3)2/6G = E(1+\nu)\ (\varepsilon 1)2/3$.

According to the Lemaitre strain equivalence hypothesis, there were $\sigma 1 = (1-D)\ E\varepsilon 1$, which can be expressed as $\sigma 1 = (1-D)E\varepsilon 1 + \nu(\sigma 2 + \sigma 3)$ in the triaxial state, in which $E = (1 - D_0)$, E_0, E_0 was the elastic modulus of intact rock. Then, the constitutive equation of the rock can be expressed as follows:

$$\sigma_1 = e^{-\left(E(1+\nu)\varepsilon_1^2/3U_0\right)^m} E\varepsilon_1 + \nu\left(\sigma_2 + \sigma_3\right). \tag{13}$$

5.2. Damage Evolution of PD Rock. According to the experimental data, the parameters U_0 and m can be determined by fitting with (13), and then the damage variable changes of each rock sample can be obtained by substituting the (12), as shown in Figure 10.

Figure 10 shows that the damage degree of rock samples before the yield point was 0, because the initial cracks inside the rock have been completely closed, but no new cracks have been generated. The damage variable increases gradually after the yield point, which can be divided into initial development stage and accelerated development stage. In the initial stage of development, new cracks began to generate inside the rock, and the damage degree gradually developed. As the stress continues to increase, more macrocracks in the rock begin to generate, and the damage degree accelerates until the peak was completely failure.

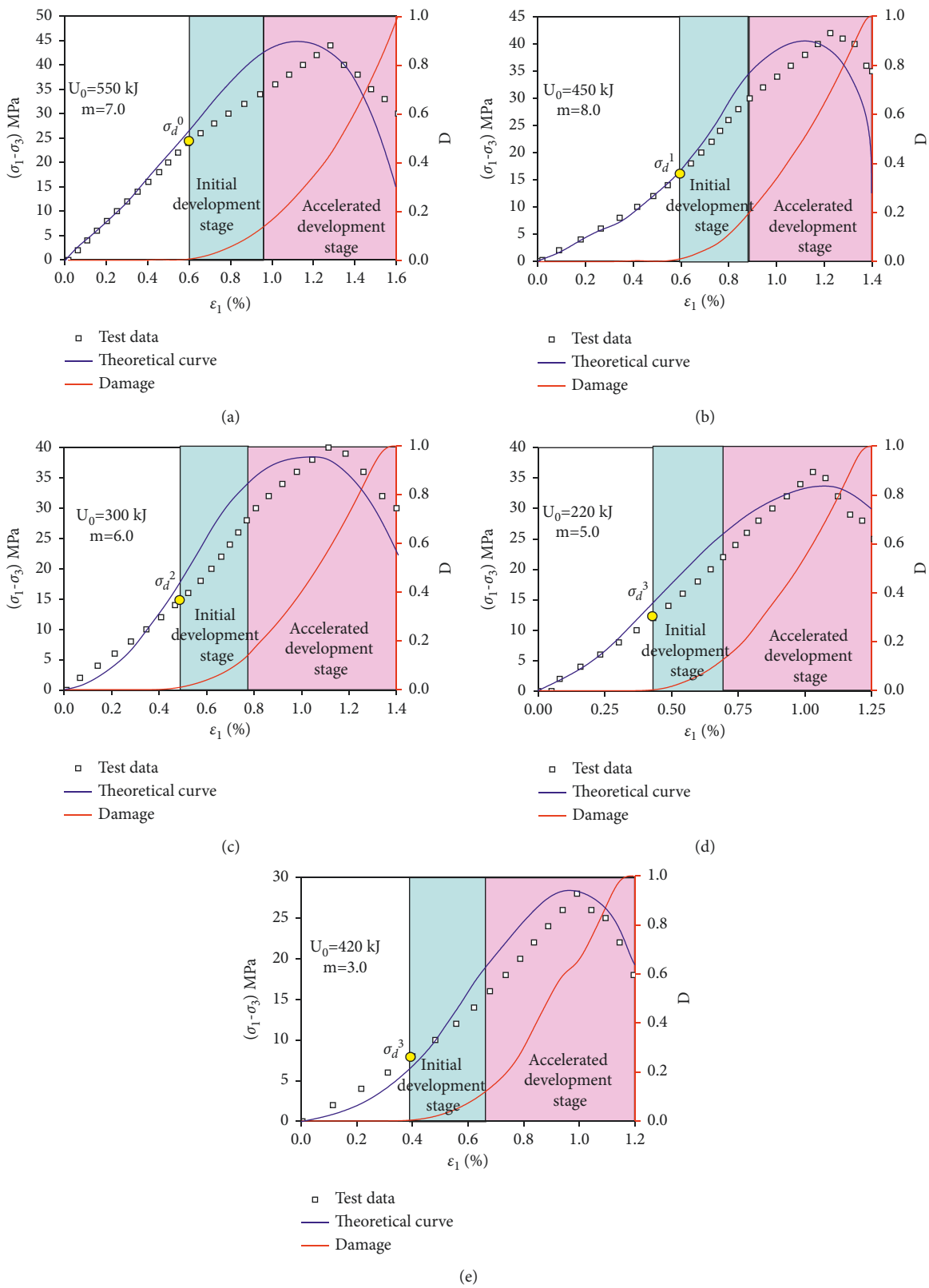

Figure 10: Damage variable of PD rock. (a) S-0 rock sample. (b) S-1 rock sample. (c) S-2 rock sample. (d) S-3 rock sample. (e) S-4 rock sample.

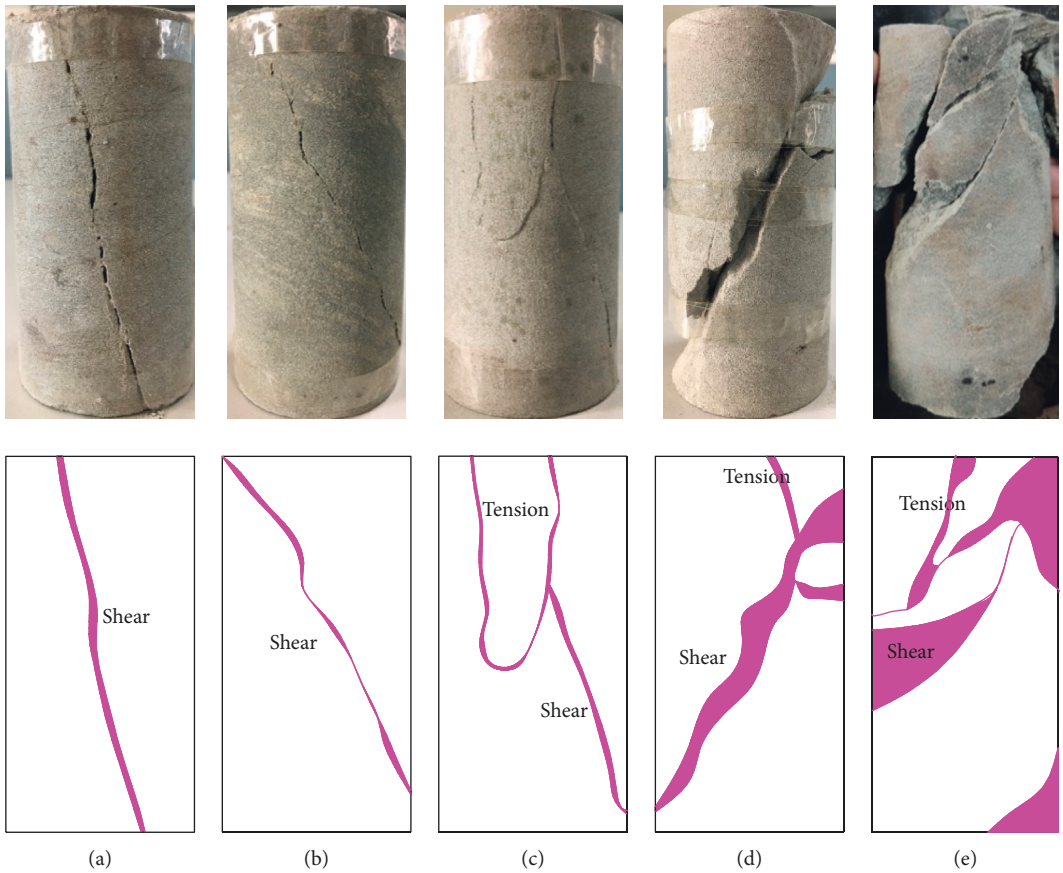

Figure 11: Failure characteristics of PD rock. (a) S-0 rock sample. (b) S-1 rock sample. (c) S-2 rock sample. (d) S-3 rock sample. (e) S-4 rock sample.

The critical point of S-0, S-1, S-2, S-3, and S-4 PD rock samples which entered the initial development stage was 0.7%, 0.6%, 0.5%, 0.4%, and 0.4% of axial strain, respectively, and the critical point which entered the accelerated development stage was 1.0%, 0.9%, 0.8%, 0.7%, and 0.7% of axial strain, respectively. It indicated that the rock was more prone to damage as the increase of the predamaged degree.

5.3. Failure Characteristics. The crack distribution of S-0, S-1, S-2, S-3, and S-4 rock samples after failure is shown in Figure 11.

The crack propagation form was a present shear failure when the predamaged degree was small (S-0 and S-1 sample). But with the increase of predamaged degrees, the crack propagation form becomes more complicated. For instance, the cracks propagation form of the S-2, S-3, and S-4 rock samples were composed of tension and shear. Moreover, the failure form of rock was more crushed with the increase of predamaged degrees.

6. Conclusions

(1) For the cumulative damage characteristics of rock caused by multimining disturbances, a method for preparing rock samples with different predamaged degrees by cyclic loading and unloading test was proposed. The variation laws of AE data during the loading and unloading process were analyzed, and definition for calibrating the predamaged degree of rock based on AE ring counts was put forward.

(2) The triaxial compression experiment of PD rock samples was carried out. The experiment results show that the peak stress and axial strain of PD rock was less than that of intact rock, and which gradually decreased with the increase of predamaged degree. The ratio of yield stage to the total strain of PD rock was obviously larger than that of intact rock. The PD rock more easily entered the dilation deformation with the predamaged degree increased.

(3) The constitutive equation of PD rock based on energy was constructed, and the damage evolution characteristics were analyzed. The damage evolution process can be divided into the initial development stage and the accelerated development stage. The PD rock was more prone to damage as the increase of the predamaged degree. Moreover, the crack propagation and failure form of rock was more complex and crushed with the increase of predamaged degree.

Data Availability

Data in the manuscript were obtained by experiments, and the data were effectively collected and correctly presented. Data used to support the findings of this study were included in the article.

Conflicts of Interest

The authors declare no conflicts of interest.

Authors' Contributions

The work presented herein was carried out in collaboration between all the authors. Jinshuai Guo proposed the innovative points and wrote the paper. Wenzheng Shang and Jianbo Yuan conducted the triaxial compression test. Zhigang Liu analysed the test data.

References

[1] A. R. Fotovvat and A. Sadrekarimi, "Instability of a gold mine tailings subjected to different stress paths," *Journal of Geotechnical and Geoenvironmental Engineering*, vol. 148, no. 5, pp. 1–13, Article ID 04022020, 2022.

[2] C. H. Fu, H. P. Xie, M. Z. Gao et al., "Mechanical behaviour and seepage characteristics of coal under the loading path of roadway excavation and coal mining," *Geomatics, Natural Hazards and Risk*, vol. 12, no. 1, pp. 1862–1884, 2021.

[3] M. L. Doan and V. D'Hour, "Effect of initial damage on rock pulverization along faults," *Journal of Structural Geology*, vol. 45, no. 12, pp. 113–124, 2012.

[4] Y. G. Cao, M. Y. Liu, Y. Zhang, J. Hu, and S. C. Yang, "Effect of strain rates on the stress-strain behavior of FRP-confined pre-damaged concrete," *Materials*, vol. 13, no. 5, p. 1078, 2020.

[5] J. H. Hu, P. P. Zeng, D. J. Yang et al., "Experimental investigation on uniaxial compression mechanical behavior and damage evolution of pre-damaged granite after cyclic loading," *Energies*, vol. 14, no. 19, p. 6179, 2021.

[6] C. K. Ma, R. Garcia, S. Yung, A. Z. Awang, W. Omar, and K. Pilakoutas, "Strengthening of pre-damaged concrete cylinders using post-tensioned steel straps," *Proceedings of the ICE - Structures and Buildings*, vol. 14, no. 19, pp. 1–9, 2019.

[7] J. Peng and W. C. Zhu, "Dynamic-static coupling analysis on rockburst mechanism in jointed rock mass," *Journal of Central South University*, vol. 19, pp. 3285–3290, 2012.

[8] P. Cao, T. Y. Liu, C. Z. Pu, and H. Lin, "Crack propagation and coalescence of brittle rock-like specimens with pre-existing cracks in compression," *Engineering Geology*, vol. 187, pp. 113–121, 2015.

[9] X. Y. Cheng, "Damage and failure characteristics of rock similar materials with pre-existing cracks," *International Journal of Coal Science&Technology*, vol. 6, no. 4, pp. 505–517, 2019.

[10] J. Y. Wu, M. M. Feng, B. Y. Yu, and G. Han, "The length of pre-existing fissures effects on the mechanical properties of cracked red sandstone and strength design in engineering," *Ultrasonics*, vol. 82, no. 1, pp. 188–199, 2018.

[11] J. Y. Wu, Z. Q. Chen, M. M. Feng, Y. M. Wang, and G. S. Han, "The length of pre-existing fissure effects on the dilatancy behavior, acoustic emission, and strength characteristics of cracked sandstone under different confining pressures," *Environmental Earth Sciences*, vol. 77, no. 12, p. 430, 2018.

[12] S. Q. Yang, Y. H. Dai, L. J. Han, and Z. Q. Jin, "Experimental study on mechanical behavior of brittle marble samples containing different flaws under uniaxial compression," *Engineering Fracture Mechanics*, vol. 76, no. 12, pp. 1833–1845, 2009.

[13] I. Gratchev, D. H. Kim, and C. K. Yeung, "Strength of rock-like specimens with pre-existing cracks of different length and width," *Rock Mechanics and Rock Engineering*, vol. 49, no. 11, pp. 4491–4496, 2016.

[14] M. Huang and T. L. Li, "Study on mechanical and deformation properties of prefabricated single fissure rock under uniaxial compression," *Journal of Changji University: Natural Science Edition*, vol. 17, no. 1, pp. 1–6, 2020.

[15] I. A. Tijani, Y. F. Wu, and C. W. Lim, "Effects of pre-damaged on stress-strain relationship of partially confined concrete," *ACI Structural Journal*, vol. 17, no. 1, pp. 115–120, 2021.

[16] D. J. Yang, J. H. Hu, G. P. Wen, and P. P. Zeng, "Analysis of fracture deformation field and energy evolution of granite after high confining pressure cyclic load pre-damaged," *Royal Society Open Science*, vol. 21, no. 6, pp. 1–12, 2021.

[17] C. Wei, B. Zhang, W. Zhu, S. Wang, J. Li, and C. Yang, "Fracture propagation of rock like material with a fluid-infiltrated pre-existing flaw under uniaxial compression," *Rock Mechanics and Rock Engineering*, vol. 54, no. 2, pp. 875–891, 2021.

[18] S. L. Qiu, X. T. Feng, C. Q. Zhang, and J. B. Yang, "Experimental research on mechanical properties of deep marble under different initial damage levels and unloading paths," *Chinese Journal of Rock Mechanics and Engineering*, vol. 31, no. 8, pp. 1686–1697, 2012.

[19] R. B. Hou, Y. K. Shi, L. G. Xu, J. W. Fu, and K. Zhang, "Evaluating Long-Term Strength and Time to Failure of Sandstone with Different Initial Damage," *Hindawi Limited*, vol. 2020, pp. 1–15, Article ID 7149148, 2020.

[20] P. Huang, J. X. Zhang, N. J. Damascene, Z. J. Wang, and M. Li, "Effect of loading rate on mechanical behavior of coal samples with initial damage accumulation," *Mechanics of Time-dependent Materials*, vol. 26, no. 2, pp. 309–322, 2021.

[21] W. Liu, L. Ma, H. Sun, and N. Muhammad Khan, "An experimental study on infrared radiation and acoustic emission characteristics during crack evolution process of loading rock," *Infrared Physics & Technology*, vol. 118, no. 1, Article ID 103864, 2021.

[22] J. S. Guo, L. Q. Ma, and D. S. Zhang, "Management and utilization of high-pressure floor-confined water in deep coal mines," *Acta Geotechnica*, vol. 17, no. 5, pp. 1753–1763, 2021.

[23] K. Zhao, D. Q. Yan, C. H. Zhong, X. Y. Zhi, and X. Q. Xiong, "Comprehensive analysis method and experimental vertification for in-situ stress measurement by acoustic emission tests," *Chinese Journal of Geotechnical Engineering*, vol. 34, no. 8, pp. 1403–1411, 2012.

[24] Q. S. Wang, J. X. Chen, J. Q. Guo, Y. B. Luo, H. Y. Wang, and Q. Liu, "Acoustic emission characteristics and energy mechanism in karst limestone failure under uniaxial and triaxial compression," *Bulletin of Engineering Geology and the Environment*, vol. 78, no. 3, pp. 1427–1442, 2019.

[25] X. W. Liu, Q. S. Liu, B. Liu, and Q. Liu, "Acoustic emission characteristics of pre-cracked specimens under biaxial

compression," *Journal of Geophysics and Engineering*, vol. 16, no. 6, pp. 1164–1177, 2019.

[26] Q. Q. Zheng, Y. H. Cheng, Q. Zong, Y. Xu, F. H. Li, and P. Y. Chen, "Failure mechanism of different types of shotcrete based on modified Weibull distribution model," *Construction and Building Materials*, vol. 224, no. 10, pp. 306–316, 2019.

[27] B. C. Yang, L. Xue, and M. M. Wang, "Evolution of the shape parameter in the Weibull distribution for brittle rocks under uniaxial compression," *Arabian Journal of Geosciences*, vol. 11, no. 12, p. 321, 2018.

Hindawi
Advances in Materials Science and Engineering
Volume 2022, Article ID 9681481, 14 pages
https://doi.org/10.1155/2022/9681481

Research Article

Study on Creep Mechanical Properties of Non-Water Reacting Polyurethane Grouting Material

Heng Liu,[1] **Mingyang Ren**,[1] **Mingsheng Shi**,[2] **Dengping Hu**,[3] **and Jianuo Tan**[1]

[1]*School of Civil and Transportation Engineering, Henan University of Urban Construction, Pingdingshan, Henan 467036, China*
[2]*School of Hydraulic Science and Engineering, Zhengzhou University, Zhengzhou 450002, China*
[3]*School of Civil Engineering, Guangzhou University, Guangzhou 510006, Guangdong, China*

Correspondence should be addressed to Mingyang Ren; 20201017@hncj.edu.cn

Received 19 May 2022; Revised 5 July 2022; Accepted 15 July 2022; Published 31 July 2022

Academic Editor: Qing Ma

Non-water reacting polyurethane is a new type of grouting material for support reinforcement and emergency rescue, whose creep mechanical behavior is directly related to the stability and safety of the reinforcement project. To investigate the creep properties of non-water reacting polyurethane grouting material, a series of multistage loading creep tests were performed under uniaxial compression conditions. Then, the creep curves, creep strain rate, and creep failure modes of non-water reacting polyurethane grouting material were obtained. In addition, the effects of temperature and density on the creep properties of non-water reacting polyurethane grouting material were also analyzed. Finally, based on the finite difference program, the numerical simulation of the uniaxial compression creep test of non-water reacting polyurethane grouting material was conducted by employing the Burgers–Mohr creep model. The simulated creep curve was in good agreement with the test curve, which verified the feasibility of the model to describe the creep characteristics of non-water reacting polyurethane grouting material. The research results can provide a reference for studying the creep behavior of polyurethane grouting material and also contribute to the development and application of polyurethane material grouting technology.

1. Introduction

With the development of underground engineering, water inrush disasters occur frequently. The grouting technology is considered to be an effective means to prevent and control these engineering accidents [1–10]. Non-water reacting two-component polyurethane is a new type of grouting material, which is different from the traditional grouting material represented by cement mortar. It has the advantages of rapid hardening, large expansion, and a small permeability coefficient [11–15]. In recent years, it has gradually become a hot topic of international research. At present, it has been widely used in seepage prevention, infrastructure reinforcement, and as support materials in infrastructure engineering projects [16–24].

As non-water reacting polyurethane is a new type of material gradually emerging in recent years, the research on it is limited by test equipment and experimental data. Scholars have made slow progress in the study of its physical and mechanical properties, and the theoretical research is far behind the engineering practice [25–28]. Liu [29] conducted a uniaxial compression test and splitting test for low-density polyurethane materials ($\rho < 0.3\,\mathrm{g/cm^3}$), and obtained the relationship between the density of polyurethane materials and the uniaxial compressive strength and splitting tensile strength. Pan [30] tested the expansion performance of non-water reacting polyurethane grouting material and obtained the law that the expansion force increases exponentially with the increase of density in fixed volume space. Shi et al. [31] studied the permeability, bending, and temperature characteristics of non-water reacting polyurethane grouting material and pointed out that the permeability of polyurethane materials decreases with the increase of density. Liu [32] tested the tensile properties of non-water reacting polyurethane grouting material by direct tensile test. The results showed that the tensile strength increased

exponentially with the increase in density. Aiming at non-water reacting polyurethane grouting material used for repairing highways, settlement lifting for ballastless track of high-speed rail, and impermeable reinforcement of dams or dikes in a seismic region, Li et al. [33] investigated dynamic viscoelastic properties of polyurethane grouting material and proposed a viscoelastic constitutive model based on the generalized Maxwell model. Sham [34] studied the relationship between the viscoelasticity of polyurethane and frequency or temperature by using the Dynamic Mechanical Thermal Analysis method. Bagley and Torvik [35] studied creep and relaxation behaviors of polyurethane materials and proposed a fractional viscoelastic model.

However, despite the recent improvements in the research on the mechanical properties of non-water reacting polyurethane grouting material by many scholars, the current research mainly focuses on the conventional mechanical behavior of polyurethane materials, and there are only a few research reports on the creep mechanical behavior. In practical engineering, the creep phenomenon of materials widely exists in all kinds of engineering. A large number of field measurements and engineering practices show that the grouting materials in highway and railway tunnels, large slopes, mine roadways, and tunnel surrounding rocks exhibit creep characteristics [12–14]. Therefore, it is of great significance to study the creep characteristics of non-water reacting polyurethane materials. The research results can provide a scientific basis for the analysis of long-term deformation characteristics of subgrade and provide theoretical guidance for jacking settlement pipeline and tunnel support.

Due to the similarity of the mechanical properties of non-water reacting polyurethane grouting material with geotechnical materials and asphalt mixtures, this study employed the rheological mechanical properties of geotechnical materials and asphalt mixtures to study the creep mechanical properties of non-water reacting polyurethane grouting material. First, a series of multistage loading creep tests were carried out to obtain the creep curves of non-water reacting polyurethane grouting material. Then, the effects of density and temperature on the creep rate and creep failure mode of polyurethane grouting material were analyzed. Finally, the viscoelastic mechanical parameters of polyurethane grouting material were obtained by the fitting method, and the creep test curve of polyurethane material was simulated by a finite difference program. The reliability of the Burgers–Mohr creep model to describe the creep behavior of non-water reacting polyurethane grouting material was verified.

2. Creep Tests

2.1. Testing Equipment. In our study, the uniaxial compression creep tests were conducted using the CMT5105 series microcomputer-controlled electronic universal testing system, as shown in Figure 1. The test system has high accuracy and sensitivity for the measurement and control of load, deformation, and displacement. It can also carry out the automatic control test of constant velocity loading, constant velocity deformation, and constant velocity displacement, and has the functions of low-frequency load cycle, deformation cycle, and displacement cycle. It can be competent for the tensile, compression, bending, shear, peeling, tearing, and other tests of various solid material samples. The maximum test force of the test equipment is 100 kN and the resolution of the test force is 1/300000 FS (full scale). The deformation measurement range is 0.2 ~ 100% FS and the relative error of deformation indication is ±0.5%. In order to study the temperature effect on creep characteristics of non-water reacting polyurethane, a high-low temperature test chamber was equipped with a temperature control range of −40°C to 150°C.

Figure 1: CMT5105 series microcomputer-controlled electronic universal testing system.

2.2. Sample Preparation. The non-water reacting polyurethane material is a two-component foam (polyols and isocyanate) that exhibits liquid properties before curing, with fluidity and expansion. The specimen used for the creep test was a cylinder with a diameter of 50 mm and a height of 50 or 100 mm. Therefore, the sample-making mold was specially developed, as shown in Figure 2.

Since the non-water reacting polyurethane grouting material can generate a large expansion force after mixing, the mold was made of steel to ensure sufficient rigidity. The grouting hole was set in the steel plate above the mold. In order to facilitate demolding, it is necessary to apply grease to the inner wall of the mold before grouting. It should be noted that the specimens with different densities were prepared by controlling the injection volume of polyols and isocyanate.

Due to the limitation of the testing equipment, some cylindrical samples with a height of 100 mm were cut into two cylindrical samples with a height of 50 mm by the numerical control punching machine. In order to ensure the smoothness of the end face of the specimen, the specimen with an uneven end face was polished with sandpaper. The surface deviation of the two ends was within a range of 0.05 mm. Figure 3 shows some of the prepared specimens.

The mass, height, and diameter of the specimen were measured by a digital display balance and vernier caliper with an accuracy of 0.1 g, and then the density of the polyurethane specimen was calculated. The uniaxial compressive strength

Figure 2: Polyurethane sample preparation mold.

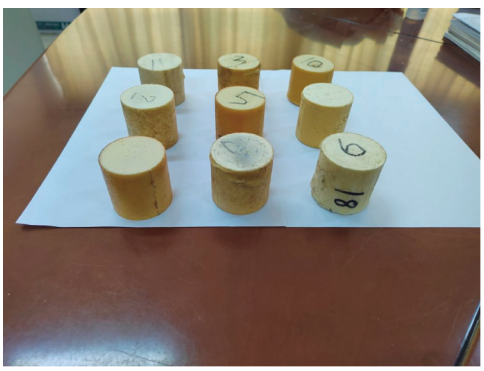

Figure 3: Photos of the prepared specimens.

of each specimen was calculated according to the empirical formula, as listed in Table 1. The empirical formula for uniaxial compressive strength is as follows [32]:

$$y = 67.289x^2 - 4.3758x + 1.1339, \quad (1)$$

where x denotes the density of the polyurethane specimen and y denotes the uniaxial compressive strength of the polyurethane specimen.

2.3. Creep Test Scheme. Previous studies have shown that density and temperature are important factors affecting the mechanical properties of polyurethane materials. Therefore, the effects of density and temperature were considered in this study. For creep tests to study the density effect, the multistep loading test method was used to reduce the influence of sample inhomogeneity. The axial stress was divided into several different levels. At present, no one has studied the creep mechanical properties of non-water reacting polyurethane grouting materials by laboratory tests. We also have no relevant literature for reference. Through a large number of tests, it is found that non-aqueous reactive polyurethane grouting materials have similar viscosity characteristics to asphalt mixture. Therefore, we searched the literature and relevant test procedures and referred to some test methods for the study of the rheological properties of asphalt mixture [25, 36–38]. The loading time for each step was tentatively determined to be approximately 1800 s (30 minutes). When the loading time of each step reached the predetermined value, the next step of the axial stress level was applied. The axial stress was increased step by step until the sample failed. In order to be consistent with the engineering environment as much as possible, the local average temperature (25°C) was taken as the reference temperature for creep tests. When considering the effect of temperature on the creep properties of the polyurethane grouting material, 25°C was taken as the initial temperature; the temperature increased or decreased by 10°C for each stage until the sample failed. It should be noted that the axial stress remained constant since loading throughout the creep experiment to study the temperature effect. After the temperature of each stage lasted for 1800 s, the temperature of the next stage was applied.

All of the creep test data were recorded during the test and the creep test scheme is outlined in Table 2. Before carrying out each creep test, a load of 50 N shall be pre-applied to the specimen at a loading speed of 1 mm/min, and the load shall be kept constant for 30 s.

3. Test Results Analysis

3.1. Creep Strain. Figure 4 illustrates the relationship curves of axial strain with time for the polyurethane grouting material. From Figure 4(a), it can be observed that the axial strain curves of polyurethane samples with different densities show typical creep characteristics, including attenuation creep, steady-state creep, and accelerated creep. When the axial stress was small, the polyurethane grouting material showed attenuation creep and steady-state creep behavior. With the gradual increase of axial stress, the creep of polyurethane grouting material gradually transited to the accelerated creep stage. In addition, polyurethane samples with higher density experienced a longer creep process. Taking the creep curves with densities of 0.141 and 0.357 g/cm^3 as an example, the former creep loading time lasted for about 5800 s, while the latter lasted for nearly 11000 s, which was more than twice that of the former. Moreover, polyurethane samples with higher density experienced a higher creep failure strength. For lower density specimens (less than 0.233 g/cm^3), the averaged creep failure strength is about 0.76 UCS. However, for the specimens with higher density (more than 0.233 g/cm^3), their creep failure strength is basically above 0.9 UCS. This is because the polyurethane samples with higher densities showed larger strength, and thus the loading time was longer to reach higher creep failure strength. Therefore, in engineering practice, its service life can be improved by increasing the density of the polyurethane grouting material. Furthermore, it is also found that when the axial stress was less than 50% of the compressive strength, the polyurethane grouting material showed attenuated creep behavior. When it was 95% of the compressive strength, the polyurethane grouting material showed accelerated creep behavior. While it was 50% ~ 95% of the compressive strength, the polyurethane grouting material showed steady-state creep behavior.

Table 1: Physical and mechanical parameters of each specimen.

Specimen number	Mass (g)	Diameter (mm)	Height (mm)	Volume (cm^3)	Density (g/cm^3)	Uniaxial compressive strength (MPa)
*S*1	29.4	50.0	49.9	97.93	0.300	5.86
*S*2	28.9	50.0	50.0	98.13	0.295	5.68
*S*3	55.6	50.0	49.9	97.93	0.567	20.26
*S*4	57.4	49.9	50.0	97.73	0.585	21.60
*S*5	39.9	50.0	49.9	97.93	0.407	9.08
*S*6	40.0	50.0	50.0	98.13	0.408	9.11
*S*7	22.9	50.0	50.0	98.13	0.233	3.78
*S*8	22.7	50.0	50.0	98.13	0.231	3.72
*S*9	44.1	49.9	49.9	97.53	0.449	12.76
*S*10	45.5	50.0	50.0	98.13	0.461	13.40
*S*11	9.0	49.9	49.9	97.53	0.092	1.30
*S*12	8.0	50.0	49.8	97.73	0.082	1.22
*S*13	19.2	50.0	49.8	97.73	0.196	2.85
*S*14	20.8	50.0	50.0	98.13	0.212	3.23
*S*15	35.0	50.0	50.0	98.13	0.357	8.13
*S*16	34.8	50.0	49.9	97.93	0.355	8.05
*S*17	13.8	50.0	50.0	98.123	0.141	1.85
*S*18	13.8	50.0	49.9	97.93	0.141	1.85
*S*19	61.8	50.0	50.0	98.13	0.630	25.7
*S*20	68.2	50.0	50.0	98.13	0.695	30.60
*S*21	17.4	50.0	50.0	98.13	0.177	2.47
*S*22	19.0	50.0	49.9	97.93	0.194	2.81

Table 2: Creep test scheme.

Factor	Specimen number	Density (g/cm^3)	UCS (MPa)	Factor level
Temperature	*S*18	0.141	0.92	25°C, 35°C, 45°C
	*S*8	0.231	2.24	25°C, 35°C
	*S*16	0.355	4.00	25°C, 15°C, 5°C, −5°C, −15°C, −25°C, −35 °C
Density	*S*17	0.141	1.85	0.4 UCS, 0.5 UCS, 0.6 UCS, 0.7 UCS
	*S*21	0.177	2.47	0.5 UCS, 0.6 UCS, 0.7 UCS, 0.8 UCS
	*S*22	0.194	2.81	0.45 UCS, 0.55 UCS, 0.65 UCS
	*S*14	0.212	3.23	0.5 UCS, 0.6 UCS, 0.7 UCS, 0.8 UCS, 0.9 UCS
	*S*7	0.233	3.78	0.55 UCS, 0.65 UCS, 0.75 UCS
	*S*2	0.295	5.68	0.2 UCS, 0.3 UCS, 0.4 UCS, 0.5 UCS, 0.6 UCS, 0.7 UCS, 0.8 UCS, 0.9 UCS, 1.0 UCS, 1.1 UCS
	*S*15	0.357	8.13	0.4 UCS, 0.5 UCS, 0.6 UCS, 0.7 UCS, 0.8 UCS, 0.9 UCS
	*S*5	0.407	10.48	0.3 UCS, 0.35 UCS, 0.4 UCS, 0.5 UCS, 0.6 UCS, 0.7 UCS, 0.8 UCS, 0.9 UCS, 1.0 UCS
	*S*6	0.408	10.53	0.6 UCS, 0.67 UCS, 0.74 UCS, 0.81 UCS, 0.88 UCS
	*S*10	0.461	13.40	0.5 UCS, 0.57 UCS, 0.64 UCS, 0.71 UCS, 0.78 UCS, 0.85 UCS, 0.92 UCS
	*S*3	0.567	20.26	0.4 UCS, 0.47 UCS, 0.54 UCS, 0.61 UCS, 0.68 UCS, 0.75 UCS, 0.82 UCS, 0.89 UCS, 0.96 UCS, 1.03 UCS, 1.1 UCS
	*S*4	0.585	21.60	0.5 UCS, 0.6 UCS, 0.7 UCS, 0.8 UCS, 0.9 UCS, 0.95 UCS, 1.0 UCS, 1.05 UCS, 1.1 UCS, 1.15 UCS
	*S*19	0.630	25.07	0.4 UCS, 0.48 UCS, 0.56 UCS, 0.64 UCS, 0.69 UCS, 0.74 UCS, 0.79 UCS, 0.84 UCS, 0.88 UCS, 0.92 UCS, 0.96 UCS, 1.0 UCS, 1.04 UCS
	*S*20	0.695	30.60	0.5 UCS, 0.58 UCS, 0.66 UCS, 0.74 UCS, 0.82 UCS, 0.9 UCS, 0.98 UCS, 1.06 UCS

Note. UCS represents uniaxial compressive strength.

Polyurethane samples with densities of 0.408 and 0.567 g/cm^3 were taken as examples. Table 3 lists the axial total strain ε_t, axial instantaneous strain ε_i, axial creep strain ε_c, and at instantaneous elastic modulus E_i different loading levels during the creep test.

From Table 3, the contribution of creep to axial total deformation increased with the increasing axial stress. In particular, the creep strain was less than 30% of the amount of axial total strain for the first loading level, when the axial creep strain exceeded 90% of the amount of axial total strain for the last loading level. In addition, it is also noticed that the elastic modulus of the polyurethane sample first increased and then decreased during the whole creep process. This is because the polyurethane grouting material had many internal voids, and with the increase of the axial stress, the elastic modulus of the polyurethane sample reached the maximum. Then, as the

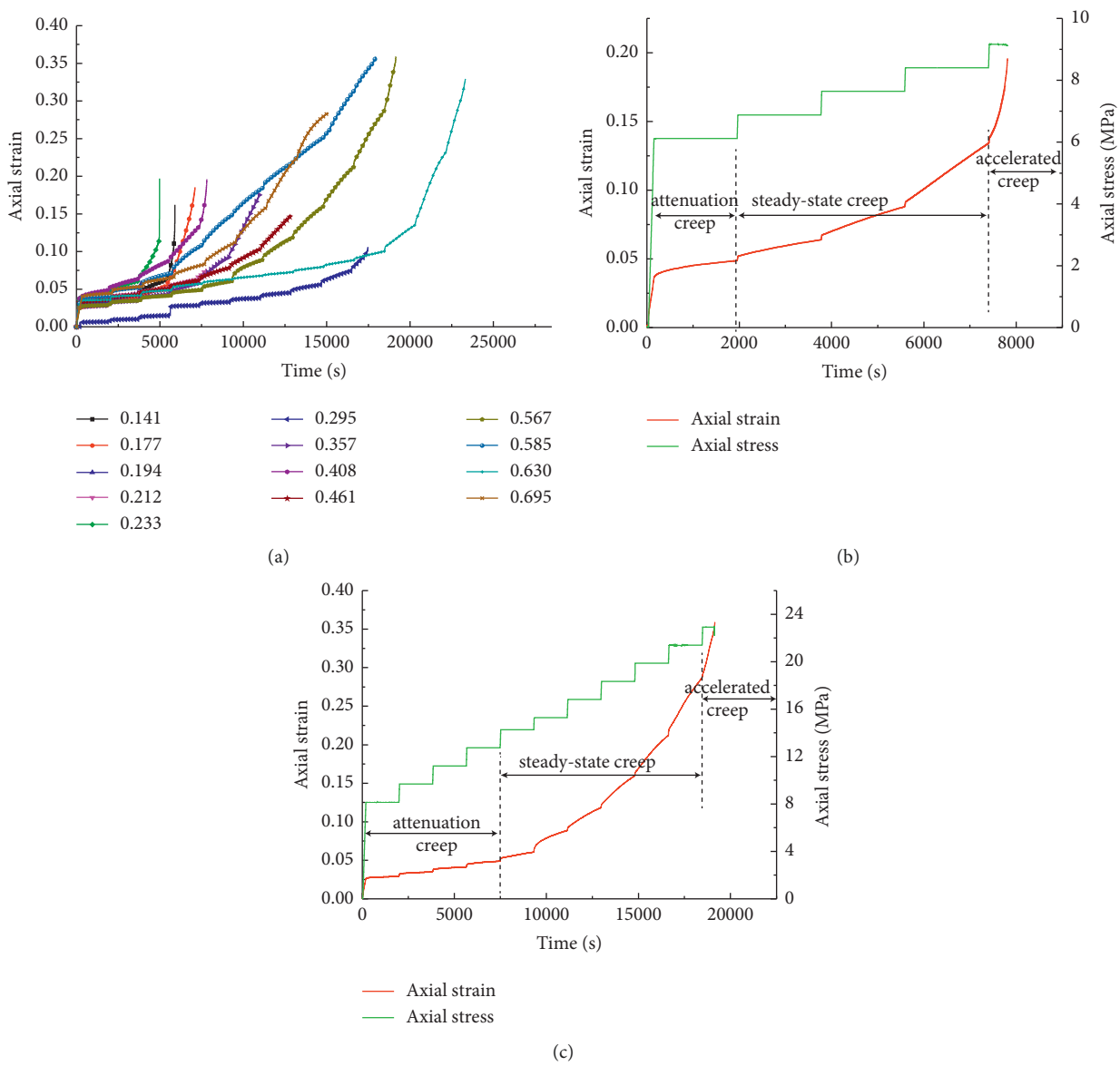

Figure 4: Curves of axial strain with time for the polyurethane grouting material. (a) Different density conditions. (b) Density = 0.408 g/cm^3. (c) Density = 0.567 g/cm^3.

Table 3: Axial strain and elastic modulus in each loading stage during the creep test.

Density (g/cm^3)	Loading level	ε_t	ε_i	ε_c	$\varepsilon_c/\varepsilon_t$	E_i (MPa)
	Preloading	0.17	0.17	—	0	—
	58.1%	4.70	3.48	1.22	25.96%	192
	65.3%	1.52	0.30	1.22	80.26%	235
0.408	72.6%	2.41	0.31	2.10	87.14%	233
	79.8%	4.62	0.33	4.29	92.86%	225
	87.1%	6.18	0.36	5.82	94.17%	217
	Sum	19.60	4.95	14.65	74.74%	220

Table 3: Continued.

Density (g/cm^3)	Loading level	ε_t	ε_i	ε_c	$\varepsilon_c/\varepsilon_t$	E_i (MPa)
0.567	Preloading	0.18	0.18	—	0	—
	40.2%	2.72	2.48	0.24	8.82%	399
	47.8%	0.58	0.35	0.23	39.66%	450
	55.3%	0.64	0.35	0.29	45.31%	445
	62.9%	0.78	0.35	0.43	55.13%	435
	70.4%	1.17	0.35	0.82	70.08%	432
	75.4%	2.80	0.40	2.40	85.71%	260
	83.0%	2.97	0.39	2.58	86.87%	390
	90.6%	4.12	0.41	3.71	90.05%	374
	98.1%	5.61	0.41	5.20	92.69%	365
	105.6%	7.13	0.43	6.70	93.97%	357
	Sum	35.87	6.54	29.33	81.77%	405

axial stress continued to increase, a certain degree of damage occurred inside the polyurethane sample, resulting in the deterioration of its stiffness. On the whole, the density had a great influence on the elastic modulus of polyurethane grouting material. The average elastic modulus of a polyurethane sample with a density of 0.567 g/cm^3 was nearly twice larger than that of a polyurethane sample with a density of 0.408 g/cm^3.

3.2. Creep Strain Rate. In order to study the law of creep strain rate, Figure 5 shows the variation curve of axial strain with time during each loading level for polyurethane samples with different densities. It is clearly seen that the polyurethane grouting material exhibits an obvious creep stress threshold, that is, the creep phenomenon occurs only after the axial stress reaches a certain value. Moreover, the lower the density, the lower the creep stress threshold of polyurethane samples. For specimens with lower density (less than 0.295 g/cm^3), when the axial stress is lower than 0.4 UCS, no creep phenomenon will occur. However, for specimens with higher density (more than 0.295 g/cm^3), the creep stress threshold is about 0.5 ~ 0.6 UCS. In addition, it can also be seen that all specimens entered the accelerated creep stage before reaching the expected loading time (1800 s) during the final loading level. At the same time, the specimen did not fail when the axial load was applied. The final failure of the specimens occurred within 1800 s of the final loading level, i.e., creep failure. Moreover, the creep strain rate in the steady-state stage showed an increasing trend with the increase of density. However, when the density of the sample was too large, due to the compression of the voids in the sample, the deformation ability decreased, resulting in a decrease in the creep rate in the steady-state creep stage. Furthermore, with the increase of the axial stress, the creep strain rate in the steady-state creep stage also showed an increasing trend. The creep strain rate in the steady-state creep stage was usually 4% to 21% of the creep rate in the accelerated creep stage.

3.3. Creep Failure Characteristics. Figures 6~10 illustrate the failure forms of non-water reacting polyurethane samples.

It can be found that the creep failure modes of polyurethane specimens with different densities were significantly different. When the sample density was low, the sample was mainly a compressed deformation failure (see Figures 6 and 7). In addition, due to the difference in density and hardness, there were differences in the manifestations of compression failure of the specimens. The deformation of the two groups of samples with densities of 0.141 and 0.194 g/cm^3 was only the wrinkle on the sample surface, without fracture failure on the sample surface (see Figure 7). For the sample with a density of 0.233 g/cm^3, in addition to the same wrinkle, some wrinkles on the surface of the sample were broken (see Figure 7). When the density of the specimen was larger, there was a macro fracture surface. Vertical cracks appeared on the side surface of the sample with a density of 0.407 g/cm^3. It indicates that the specimen occurred splitting tensile failure. For the samples with a density of 0.567 and 0.585 g/cm^3, in addition to the vertical crack, there was a shear fracture surface with an inclination of 45°. When the density was large, the polyurethane sample showed tensile-shear composite failure.

3.4. Temperature Effect. Figure 11 shows the variation curves of axial strain with time for polyurethane samples with different densities under heating and cooling conditions. Clearly, the temperature had a significant effect on the creep behavior of polyurethane grouting material. When the temperature rose, the creep rate of the polyurethane sample was larger, and there was steady-state creep and accelerated creep stages. While the temperature decreased, the creep rate also decreased, and the polyurethane specimens only exhibited attenuated creep behavior. Therefore, it can be concluded that high temperature can enhance the creep of polyurethane grouting material, while low temperature can inhibit its creep behavior. The reason for this phenomenon is probably that the increase in temperature will increase the activity of the molecules in the polyurethane grouting material, causing the creep rate to increase significantly and thus inducing the accelerated creep behavior. In the low-temperature environment, the molecular activity inside the polyurethane grouting material was low, and thus the creep rate was greatly reduced, and only attenuated creep behavior occurs. In addition, by comparing Figures 11(a) and 11(b), it is found that the polyurethane specimen with a density of 0.231 g/cm^3 had accelerated creep at 35°C, while the

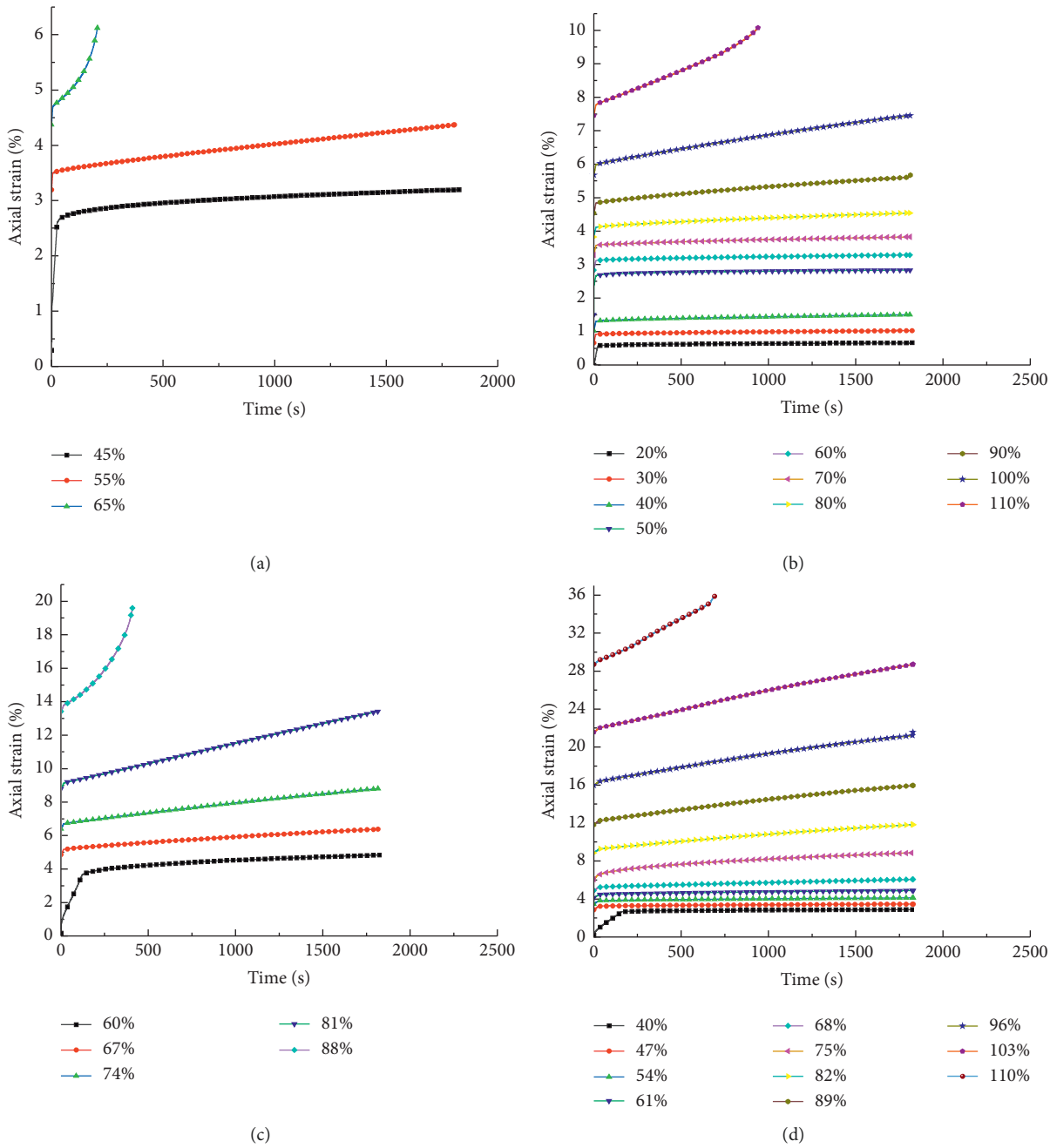

Figure 5: Continued.

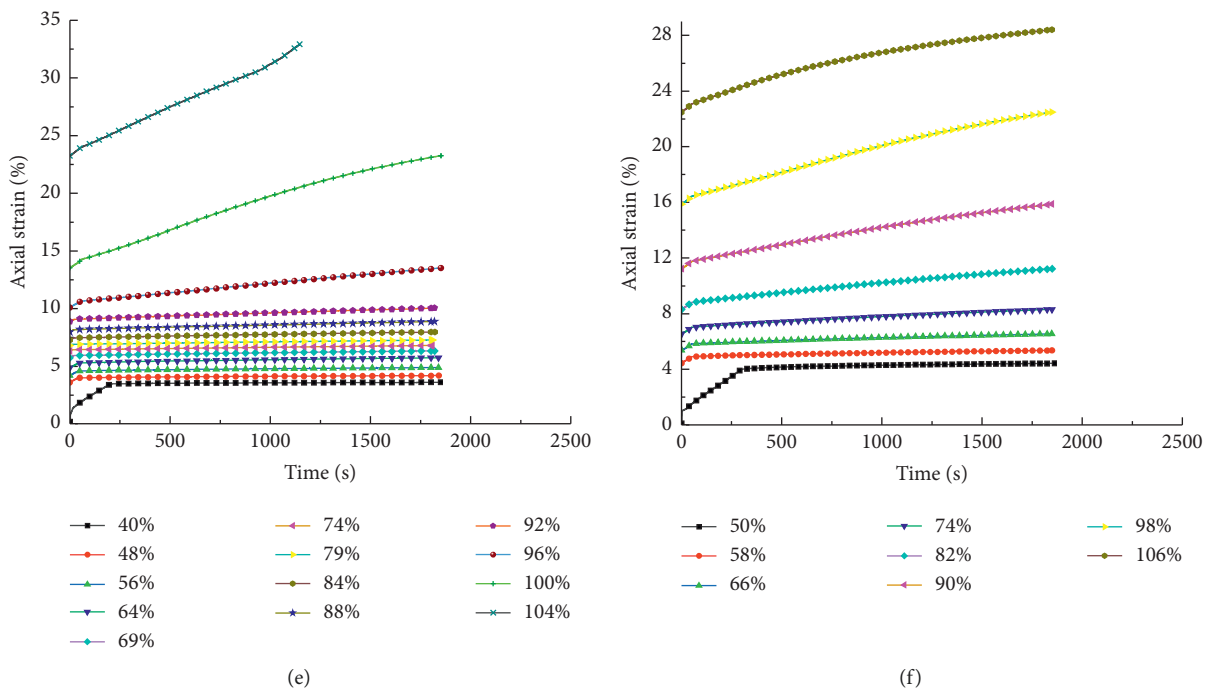

Figure 5: Variation curve of axial strain with time during each loading level for polyurethane samples with different densities. (a) Density = 0.194 g/cm^3. (b) Density = 0.295 g/cm^3. (c) Density = 0.408 g/cm^3. (d) Density = 0.567 g/cm^3. (e) Density = 0.630 g/cm^3. (f) Density = 0.695 g/cm^3.

specimen with a density of 0.141 g/cm^3 was only in the steady-state creep stage at 35°C, and the accelerated creep behavior occurred at 45°C. This further verified the above findings. The specimen with a smaller density contained less polyurethane grouting material, and the active energy of internal molecules was lower at the same temperature. Therefore, the temperature to reach the accelerated creep stage should be higher.

4. Numerical Simulation

4.1. Burgers–Mohr Creep Model. From the above analysis, the polyurethane grouting material had the three-stage characteristics of a typical creep curve, i.e., attenuation creep, steady-state creep, and accelerated creep. The Burgers creep model can well describe the viscoelastic characteristics of attenuation creep and steady-state creep. In order to better describe the accelerated creep characteristics, the FLAC3D finite difference program provided a Burgers-Mohr creep model which connects a Mohr–Coulomb plastic cell in series with the Burgers model [39], as shown in Figure 12. The Burgers part of the model was used to describe the first two stages of the creep curve. When the deviatoric stress exceeded yield strength and entered the accelerated creep stage, the Mohr–Coulomb plastic cell started to work. Next, the feasibility of using this model was explored to describe the creep mechanical behavior of polyurethane grouting material under uniaxial compression conditions. For the convenience of illustration, the polyurethane specimen with a density of 0.408 g/cm^3 was taken as an example.

4.2. Model Parameter Solution. From Figure 12, it is found that the Burgers–Mohr creep model includes five mechanical parameters, i.e., Kelvin module E_1, Kelvin visibility coefficient η_1, Maxwell module E_2, Maxwell visibility coefficient η_2, and yield strength σ_s. Since this study was limited to uniaxial compression, the yield strength here was taken as uniaxial compressive strength (9.11 MPa). In addition, in order to describe the lateral deformation, the mechanical parameter Poisson's ratio was also needed. According to the uniaxial compression test results, the Poisson's ratio was 0.25.

Under the one-dimensional condition, the creep equation of the Burgers creep model can be written as

$$\varepsilon = \frac{\sigma_0}{E_2} + \frac{\sigma_0}{\eta_2} t + \frac{\sigma_0}{E_1}\left(1 - e^{-(E_1/\eta_1)t}\right), \tag{2}$$

where σ_0 denotes the current stress level and t denotes the loading time.

Referring to the previous study [40], (2) was adopted to fit the axial strain curve under each level of stress level, and the fitted model parameters are listed in Table 4. The creep parameters of each stress level varied greatly, indicating that the creep parameters of polyurethane grouting material were non-stationary in the whole creep test process.

Figure 13 shows the comparison between the fitted curves and the test value. It is found that the fitted curves were in good agreement with the test data at each stress level, and the correlation coefficient was close to 1. It indicates that the Burgers creep model can well describe the viscoelastic characteristics of polyurethane grouting material under uniaxial compression creep.

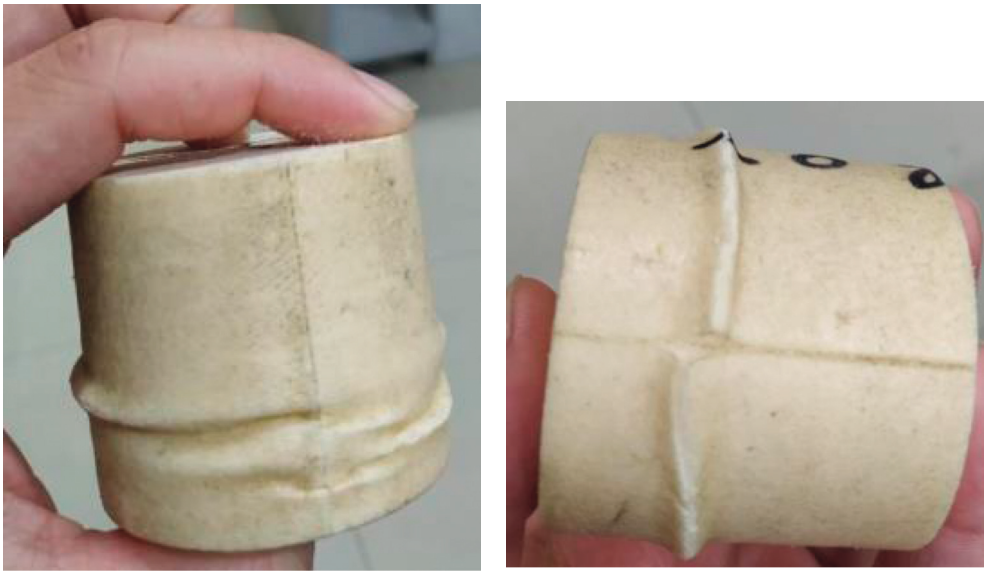

(a) (b)

Figure 6: Failure forms of samples with a density of 0.141 and 0.194 g/cm^3. (a) Density = 0.141 g/cm^3. (b) Density = 0.194 g/cm^3.

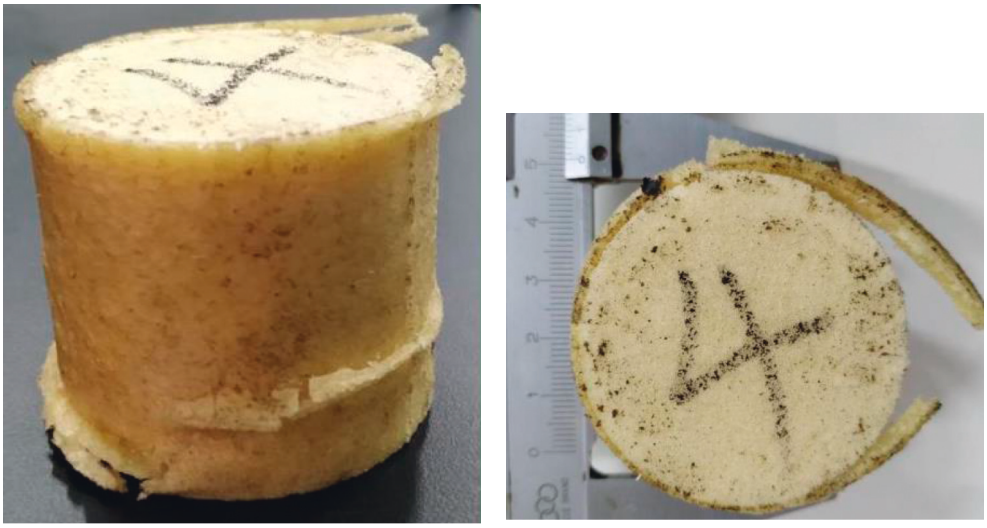

(a) (b)

Figure 7: Failure forms of the sample with a density of 0.233 g/cm^3. (a) Sample compression. (b) Top view of specimen failure.

4.3. Model Verification. According to the parameters in Table 4, the Burgers–Mohr creep model built-in FLAC3D was employed to simulate the uniaxial compression creep of the specimen with a density of 0.408 g/cm^3. The loading level classification and creep time in the numerical simulation were completely consistent with the actual test. Figure 14 shows the comparison between the test curve and the simulated curve. It is observed that the simulated curve was in good agreement with the experimental curve, and the accelerated creep stage was successfully obtained. It has strongly proved that the Burgers–Mohr creep model can better describe the viscoelastic plastic creep characteristics of polyurethane grouting material under uniaxial compression conditions.

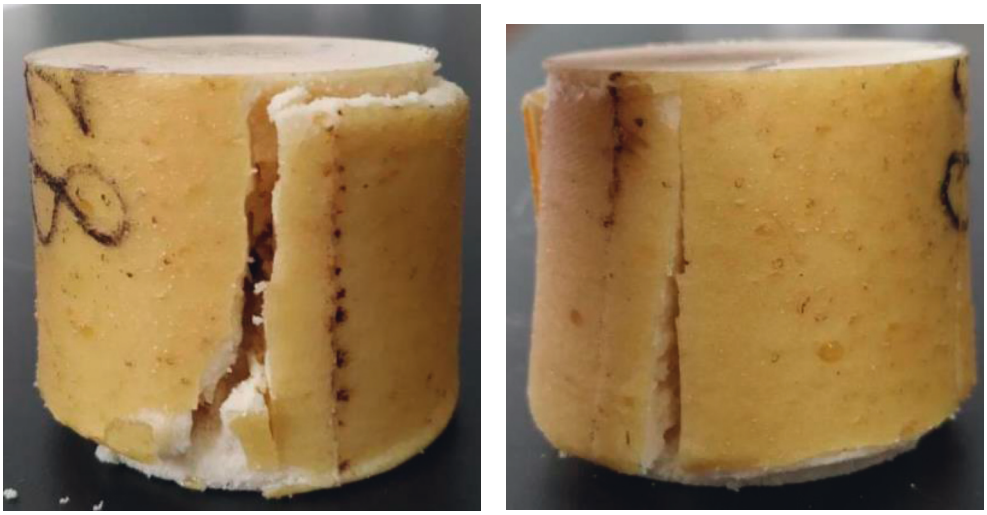

(a) (b)

Figure 8: Failure forms of the sample with a density of 0.407 g/cm^3. (a) Fracture surface of the sample. (b) Vertical crack on the specimen side.

(a) (b)

Figure 9: Failure forms of the sample with a density of 0.567 g/cm^3. (a) Cracks with an inclination of 45° on the specimen side. (b) Vertical crack on the specimen side.

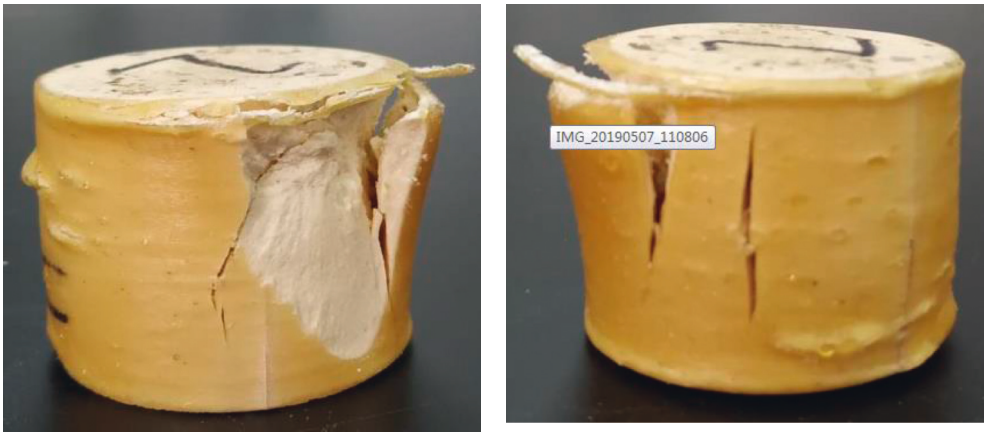

(a) (b)

Figure 10: Failure forms of the sample with a density of 0.585 g/cm^3. (a) Fracture surface of the sample. (b) Vertical crack on the specimen side.

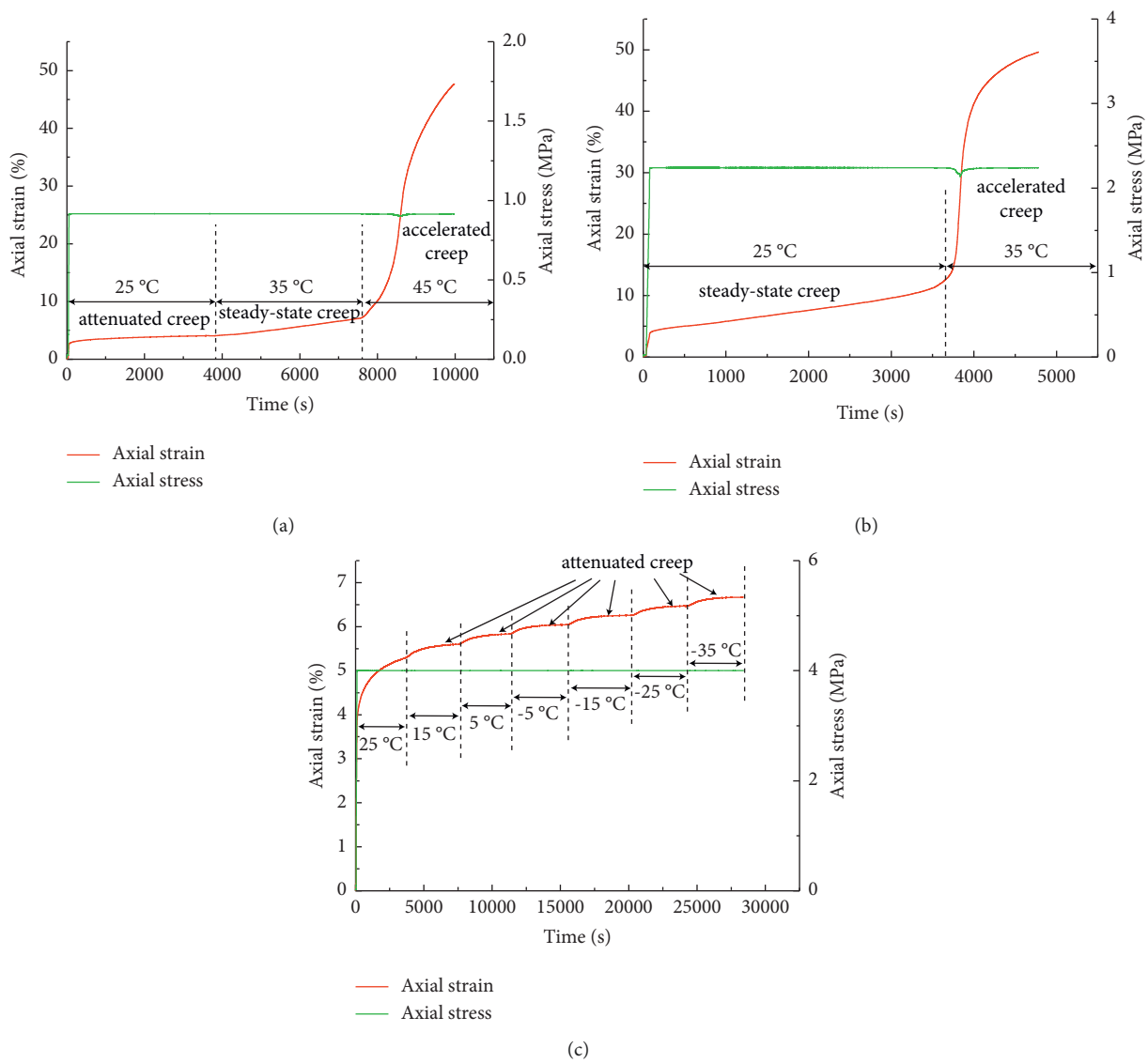

Figure 11: Variation curves of axial strain with time for the polyurethane sample with different densities under heating and cooling conditions. (a) Density = 0.141 g/cm^3. (b) Density = 0.231 g/cm^3. (c) Density = 0.355 g/cm^3.

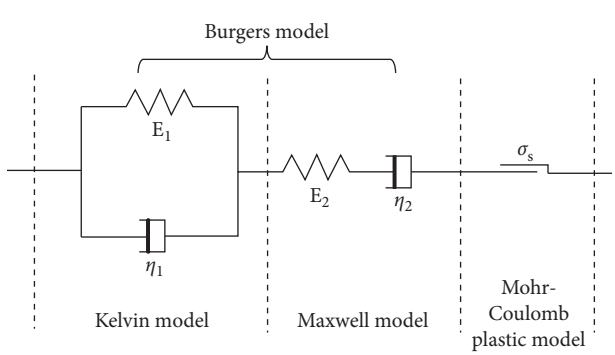

Figure 12: Schematic of the Burgers–Mohr creep model.

Table 4: Fitted parameters of the polyurethane specimen with a density of 0.408 g/cm^3.

Stress level (MPa)	E_1 (MPa)	η_1 (GPa·s)	E_2 (MPa)	η_2 (GPa·s)	Correlation coefficient
6.1	1370	1850	163	1700	0.98
6.9	1220	1430	132	1590	0.99
7.7	880	700	115	830	0.99
8.4	345	610	92	780	0.99

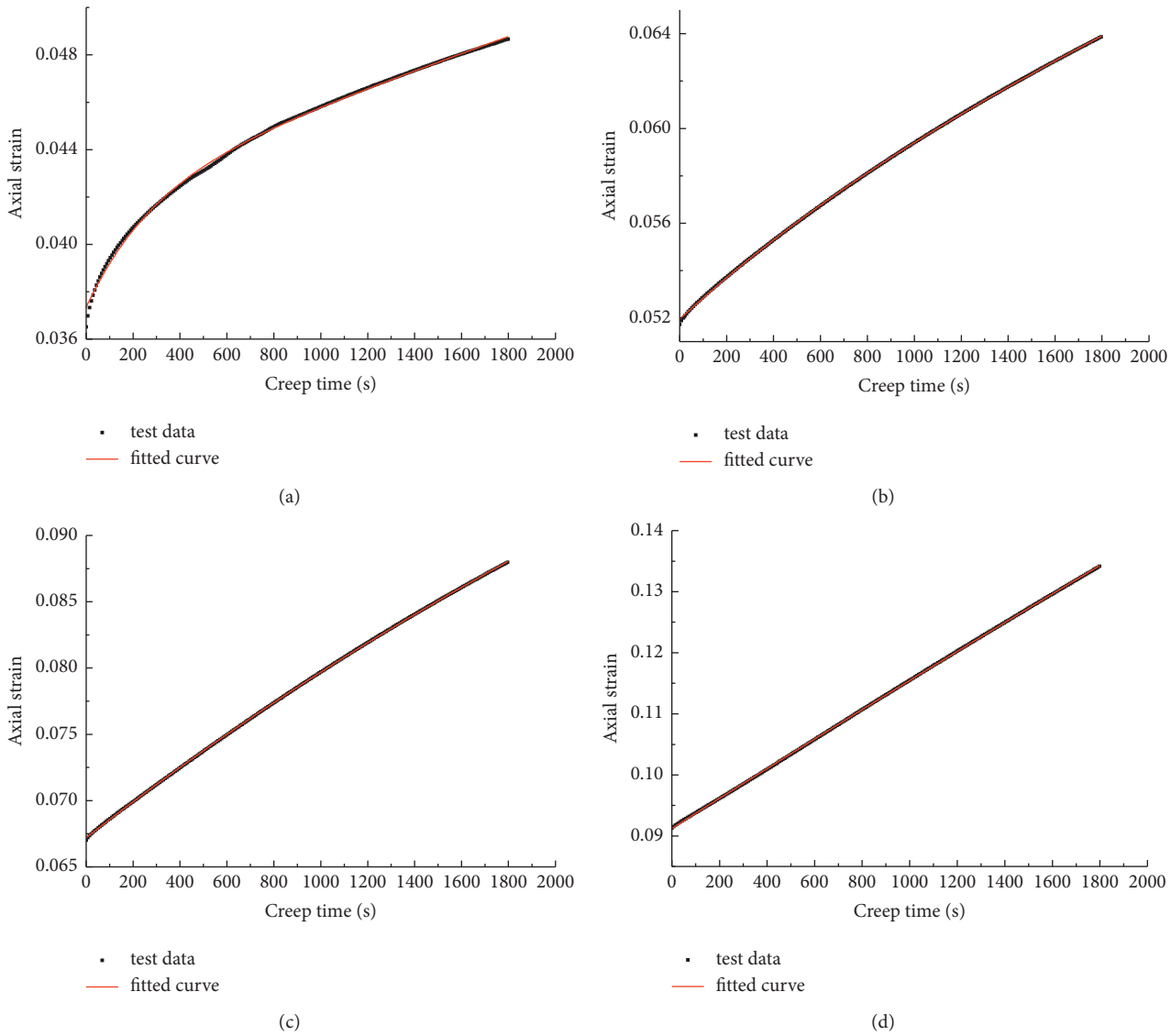

Figure 13: Comparison between test data and fitted curves. (a) $\sigma_0 = 6.1$ MPa. (b) $\sigma_0 = 6.9$ MPa. (c) $\sigma_0 = 7.7$ MPa. (d) $\sigma_0 = 8.4$ MPa.

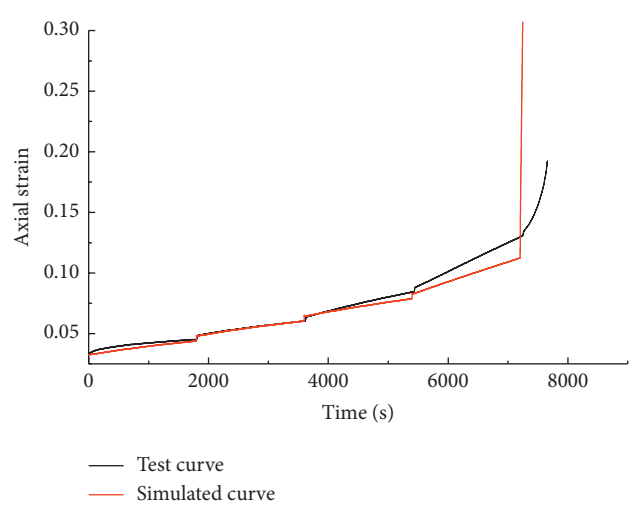

Figure 14: Comparison between the test curve and simulated curve.

5. Conclusions

In this study, a series of uniaxial compression creep tests were performed to study the creep properties of polyurethane grouting material. The main conclusions are as follows:

(1) Polyurethane grouting material showed typical creep characteristics under uniaxial compression. Density is the dominant factor affecting the creep behavior of polyurethane grouting material. Higher density can significantly increase the creep failure strength, stiffness, and creep failure time of polyurethane grouting material.

(2) The contribution of creep to polyurethane grouting material deformation increased with the increasing axial stress level. The steady-state creep strain rate increased with the increase of the axial stress level.

(3) The creep failure mode of polyurethane grouting material under uniaxial compression was significantly affected by the density. When the density was small (less than 0.2 g/cm^3), the polyurethane sample showed the compression deformation failure mode with wrinkles on the surface. When the density was medium (0.2 ~ 0.5 g/cm^3), the polyurethane sample shows splitting failure. When the density was high (more than 0.5 g/cm^3), the polyurethane sample showed tensile-shear composite failure.

(4) The creep characteristics of polyurethane grouting material were significantly dependent on temperature. High temperature (more than 35°C) can enhance the creep of polyurethane grouting material, while low temperature (less than 35°C) can inhibit its creep behavior.

(5) Burgers–Mohr creep model can better describe the attenuated creep, steady-state creep, and accelerate the creep of polyurethane grouting material under uniaxial compression conditions. It will provide a reference for the research on the creep behavior of polyurethane grouting material, and contribute to the development and application of polyurethane grouting material grouting technology.

Data Availability

The data presented in this study are available on request to the corresponding author. The data are not publicly available due to the data also form part of an ongoing study.

Conflicts of Interest

The authors declare that they have no conflicts of interest.

Acknowledgments

This research was funded by the Scientific Research Project of Education Department of Henan Province of China (Grant no. 22A56008); Science and Technology Research Project of Department of Science and Technology of Henan Province of China (Grant no. 212102310965); and Young Backbone Teacher Training Project of Henan Urban Construction University (Grant no. YCJQNGGJS202202).

References

[1] S. Li, X. Zhang, Q. Zhang et al., "Research on mechanism of grout diffusion of dynamic grouting and plugging method in water inrush of underground engineering," *Chinese Journal of Rock Mechanics and Engineering*, vol. 30, pp. 2377–2396, 2011.

[2] L. Li, S. Li, and J. Cui, "Experimental research on chemical grout for treating water inrush in rock mass," *Rock and Soil Mechanics*, vol. 30, pp. 3642–3648, 2009.

[3] D. Zhang, F. Sun, and P. Li, "Mechanism of composite grouting in subsea tunnel and its application," *Chinese Journal of Rock Mechanics and Engineering*, vol. 32, pp. 445–452, 2012.

[4] X. Xie, B. Su, and Y. Gao, "Numerical study on water inrush above a confined aquifer in coal mining using hydro-fracturing," *Chinese Journal of Rock Mechanics and Engineering*, vol. 24, pp. 987–993, 2005.

[5] X. Hua and G. Xie, "Research on grouting material for bolt and grouting reinforcement of soft rock tunnel and its application," *Rock and Soil Mechanics*, vol. 25, pp. 1642–1646, 2004.

[6] M. J. Yang, Z. Q. Yue, P. K. Lee, and L. G. SuTham, "Prediction of grout penetration in fractured rocks by numerical simulation," *Canadian Geotechnical Journal*, vol. 39, no. 6, pp. 1384–1394, 2002.

[7] Z. Li, Z. Sun, and X. Wang, "Grouting technology for water blockage of weathered slot F1 in Xiamen Xiang'an subsea service tunnel," *Chinese Journal of Rock Mechanics and Engineering*, vol. 26, pp. 3841–3848, 2007.

[8] D. Ma, H. Duan, and J. Zhang, "Solid grain migration on hydraulic properties of fault rocks in underground mining tunnel: radial seepage experiments and verification of permeability prediction," *Tunnelling and Underground Space Technology*, vol. 126, Article ID 104525, 2022.

[9] D. Ma, H. Duan, J. Zhang, X. Liu, and Z. Li, "Numerical Simulation of Water–Silt Inrush Hazard of Fault Rock: A Three-phase Flow Model," *Rock Mechanics And Rock Engineering*, vol. 55, 2022.

[10] Y. Tan, Q. Ma, and X. Liu, "Failure prediction from crack evolution and acoustic emission characteristics of roof rock-coal-floor rock sandwich composite structure under uniaxial compression," *Bulletin of Engineering Geology and the Environment*, vol. 81, pp. 1–13, 2022.

[11] F. M. Wang, M. S. Shi, H. J. Li, and Y. H. Zhong, "Experimental study on the anti-permeability properties of polymer grouting materials," *Advanced Materials Research*, vol. 284-286, pp. 1952–1955, 2011.

[12] C. Guo and F. Wang, "Research on polymer injection technology for quick tunnel repairment," in *Proceedings of the Geo-Hunan International Conference*, pp. 3–6, Hunan, China, August 2009.

[13] F. Wang, J. Wang, M. Shi, C. Guo, Y. Zhong, and B. Zhang, "Directional fracture grouting method with polymer for seepage control of dikes and dams," *U.S. Patent*, vol. 8, 2012.

[14] M. Shi, *Research on Polymer Grouting Material Property and Directional Fracturing Grouting Mechanism for Dikes and Dams*, Ph.D. Thesis, Dalian University of Technology, Dalian, China, 2012.

[15] C. Guo and F. Wang, "Mechanism study on the constructing of ultra-thin anti-seepage wall by polymer injection," *Journal of Materials in Civil Engineering*, vol. 24, pp. 1183–1192, 2012.

[16] J. Li, B. Wang, and J. Zhang, "Dynamic centrifuge test on seismic acceleration response of earth dike and dam with polymer anti-seepage wall," *Earthq. Eng. Eng. Dyn.*vol. 36, pp. 1–6, 2016.

[17] X. Ma, F. Wang, C. Guo, and B. Sun, "Seismic isolation effect of non-water reacted two-component polymeric material coating on tunnels," *Applied Sciences*, vol. 10, no. 7, p. 2606, 2020.

[18] M. Hao, F. Wang, X. Li, B. Zhang, and Y. Zhong, "Numerical and experimental studies of diffusion law of grouting with expansible polymer," *Journal of Materials in Civil Engineering*, vol. 30, no. 2, Article ID 04017290, 2018.

[19] O. Buzzi, S. Fityus, Y. Sasaki, and S. Sloan, "Structure and properties of expanding polyurethane foam in the context of foundation remediation in expansive soil," *Mechanics of Materials*, vol. 40, no. 12, pp. 1012–1021, 2008.

[20] L. Cong, F. Yang, G. Guo, and L. RenShiTan, "The use of polyurethane for asphalt pavement engineering applications: a state-of-the-art review," *Construction and Building Materials*, vol. 225, pp. 1012–1025, 2019.

[21] H. Fang, B. Li, F. Wang, Y. Wang, and C. Cui, "The mechanical behaviour of drainage pipeline under traffic load before and after polymer grouting trenchless repairing," *Tunnelling and Underground Space Technology*, vol. 74, pp. 185–194, 2018.

[22] A. Naudts, "Irreversible Changes in the Grouting Industry Caused by Polyurethane Grouting: An Overview of 30 Years of Polyurethane Grouting," *Geotechnical Special Publication*, vol. 2, pp. 1266–1280, 2003.

[23] L. P. Priddy and J. K. Newman, "Full-scale field testing for verification of mechanical properties of polyurethane foams for use as backfill in PCC repairs," *Journal of Materials in Civil Engineering*, vol. 22, no. 3, pp. 245–252, 2010.

[24] S. Saleh, N. Z. M. Yunus, K. Ahmad, and N. Ali, "Improving the strength of weak soil using polyurethane grouts: a review," *Construction and Building Materials*, vol. 202, pp. 738–752, 2019.

[25] K. Liu, W. Liang, F. Ren, and H. RenWangDing, "The study on compressive mechanical properties of rigid polyurethane grout materials with different densities," *Construction and Building Materials*, vol. 206, pp. 270–278, 2019.

[26] Y. Wei, F. Wang, X. Gao, and Y. Zhong, "Microstructure and fatigue performance of polyurethane grout materials under compression," *Journal of Materials in Civil Engineering*, vol. 29, no. 9, pp. 04017101.1–04017101, 2017.

[27] X. Bian, C. Cheng, F. Wang, L. Jiang, and Y. Chen, "Experimental study on dynamic performance and long-term durability of high-speed railway subgrade rehabilitated by polymer injection technology," *Chinese Journal of Geotechnical Engineering*, vol. 36, pp. 562–568, 2014.

[28] Z. Lin, C. Guo, D. Cao, and F. NiWang, "An experimental study on the cutting failure of polymer grouting," *Construction and Building Materials*, vol. 258, Article ID 119582, 2020.

[29] Z. Liu, "Experimental Study on Engineering Characteristics of Polymer Grouting Materials," Master. Thesis, Zhengzhou University, Zhengzhou, China, 2007.

[30] Y. Pan, "Experimental Study on Expansion Force of Polymer Grouting Material," Master. Thesis, Zhengzhou University, Zhengzhou, China, 2008.

[31] M. Shi, D. Yu, and F. Wang, "Bending properties of a polymer grout," *Journal of Materials Science and Engineering*, vol. 28, pp. 514–517, 2010.

[32] H. Liu, "Experimental Study on Polyurethane Polymer anchorage Grouting Material," Master. Thesis, Zhengzhou University, Zhengzhou, China, 2011.

[33] J. Li, J. Zhang, and S. Chen, "Study on dynamic viscoelastic properties and constitutive model of non-water reacted polyurethane grouting materials," *Measurement*, vol. 176, Article ID 109115, 2021.

[34] R. Shamsi, G. Mir Mohamad Sadeghi, and G. H. Asghari, "Dynamic mechanical analysis of polyurethanes and carbon nanotube based composites obtained from PET waste," *Polymer Composites*, vol. 39, no. S2, pp. E754–E764, 2018.

[35] R. L. Bagley and P. J. Torvik, "On the fractional calculus model of viscoelastic behavior," *Journal of Rheology*, vol. 30, no. 1, pp. 133–155, 1986.

[36] Q. Zhang, X. Gu, Z. Yu, J. Liang, and Q. Dong, "Viscoelastic damage characteristics of asphalt mixtures using fractional rheology," *Materials*, vol. 14, no. 19, p. 5892, 2021.

[37] Y. Cheng, H. Li, L. Li, and Y. ZhangWangBai, "Viscoelastic properties of asphalt mixtures with different modifiers at different temperatures based on static creep tests," *Applied Sciences*, vol. 9, no. 20, p. 4246, 2019.

[38] H. Li, J. Zhang, and X. Huang, "Uniaxial static creep test of the high temperature stability of asphalt mixture," *Journal of Henan University of Science and Technology: Natural Science*, vol. 27, pp. 48–52, 2006.

[39] H. Yuan, P. Cao, W. Xu, and Y. Chen, "Visco-elasto-plastic constitutive relationship of rock and modified Burgers creep model," *Chinese Journal of Geotechnical Engineering*, vol. 28, pp. 796–799, 2006.

[40] L. Xiong, L. Yang, Y. Zhang, M. Shen, and Z. Shi, "Experimental study on creep behaviors of green schist specimen from Jinping hydropower station under biaxial compression," *Chinese Journal of Rock Mechanics and Engineering*, vol. 27, pp. 3928–3934, 2008.

Hindawi
Advances in Materials Science and Engineering
Volume 2022, Article ID 4027231, 14 pages
https://doi.org/10.1155/2022/4027231

Research Article

Analysis of the Regularity and Mechanism of Fault Activation Caused by Deep Continuous Mining of Shizishan Copper Mine, China

Yanhui Guo,[1] **Luo Luo**,[1] **Hanhua Xu**,[2] **and Chun Zhu**[3]

[1]*Faculty of Public Safety and Emergency Management, Kunming University of Science and Technology, Kunming 650093, China*
[2]*Kunming Prospecting Design Institute of China Nonferrous Metals Industry Co, Ltd., Kunming 650051, China*
[3]*School of Earth Sciences and Engineering, Hohai University, Nanjing 210098, China*

Correspondence should be addressed to Yanhui Guo; guoyanhui0818@kust.edu.cn

Received 12 May 2022; Revised 16 June 2022; Accepted 21 June 2022; Published 14 July 2022

Academic Editor: Depeng Ma

In order to study the law and mechanism of fault activation induced by deep continuous mining, this paper takes the fault activation caused by underground mining of Shizishan Copper Mine as the research object. On the basis of field investigation and theoretical analysis of fault activation, the law and mechanism of fault group activation induced by deep continuous mining in the Shizishan mining area are analyzed in detail based on the three-dimensional discrete element method software 3DEC. The results show that the fault effect of rock movement in the footwall of the main orebody in the mine area is obvious. The en echelon steep dipping fault group in the footwall of the goaf will move each fault block in the direction of the goaf and slip along the fault plane when the balance between mining and gravity is disrupted. The fault activation has a domino effect in time and space, and the mechanism of this effect is revealed. The research results have great significance for the deep mining area development, mining alignment arrangement, and disaster prevention and control caused by fault activation.

1. Introduction

In underground mining, with the deepening of mining depth and the expansion of goaf, there are many mine disasters [1, 2]. The fault is a geological structure [3] in which rock mass breaks under the action of tectonic stress and has evident displacement along the fracture surface. Its existence destroys the continuity and integrity of rock strata and changes the stress and displacement field of surrounding rock mass [4, 5]. The fault activation phenomenon caused by various influencing factors will cause many mine disasters such as rock burst, mine water inrush, surface subsidence, and others, resulting in many casualties, equipment damage, and loss of mineral resources. These disasters will also seriously threaten the life and property safety of workers in the mining area, which also have a negative social impact, and seriously restrict the development of the national economy and mining enterprises [6, 7]. The fault activation caused by mining has always been an important factor affecting underground mining safety [8].

In recent years, many scholars have researched the regularity and mechanism of fault activation induced by deep continuous mining. In terms of theoretical analysis, Zhang et al. [9] proposed a multi-slip-spring model of fault activation and considered fault activation as a local to global linkage instability. Yin et al. [10] considered fault activation as a displacement extreme point-type instability with a sudden jump in force. Pan [11] proposed a criterion for discriminating the disturbance response that the leading cause of fault activation is an increase in fault shear stress or a decrease in normal stress. Zhao et al. [12] and Wang et al. [13] analyzed the changing law of Coulomb stress at the fault face and concluded that the failure of the coal body at the working face was the main reason for fault activation. Li [14]

and Pan et al. [15] proposed a viscous slip-viscoelastic brittle body mutation theory and a folded mutation model to classify the fault activation mechanism into dynamic and steady-state cases. They described the stability mechanism of the system in the precursor stage and post-activation stage of fault activation. For experiments, Cai et al. [16] and Han et al. [17] combined numerical simulation and similar simulation experiments to propose the mechanical mechanisms of two types of fault activation, namely, mining stress dominated and mining vibration load dominated. Zuo et al. [18], Wang et al. [13], and Wu [19] reproduced the physical process of fault activation based on similar simulation experiments, and the mechanism of fault activation caused by coal mining was analyzed and revealed the mode of induced fault activation under different mining sequences in the hanging wall and footwall working face. In terms of numerical simulation, Islam et al. [20] used the boundary element method to simulate coal mining to analyze the law of fault activation induced by mining. The results showed that the deformation and stress field of the fault and the surrounding rock in its vicinity under the effect of mining disturbance produced significant changes. The stress concentration at the fault end is high. Jiang et al. [21] used a 3D numerical calculation method to simulate and analyze the characteristics of coal seam roof movement and the law of fault activation. They compared the analysis with engineering examples for verification. Sainoki and Mitri [22] studied the influence of stress waves, fault plane roughness, and other factors on fault activation based on FLAC3D secondary development simulation.

In summary, the current research on mining-induced fault activation mainly focuses on coal mines, and there are few studies on fault activation caused by deep continuous mining in non-coal mines. Moreover, there are few reports on the domino law effect and induced mechanism of fault activation caused by continuous mining in deep mining. In this paper, based on field rock movement investigation and theoretical analysis of fault activation sliding criterion and the discrete element numerical simulation software 3DEC, the law and mechanism of fault activation induced by deep continuous mining in Shizishan Copper Mine are analyzed. The research results have great significance for the deep mining area development, mining alignment arrangement, and disaster prevention and control caused by fault activation.

2. Overview of Engineering Geology in Mining Area

Shizishan Copper Mine is located in Xiaojie township, Yimen County, Yunnan Province, China, which is located at the junction of Yimen, Shuangbai, and Lufeng counties. It is 51 km away from Yimen County, with convenient transportation. The geographical location and surrounding geological map of the Shizishan Copper Mine are shown in Figure 1. The mining area is located on the west side of the fault of the Yimen depression basin. Under the influence of the east-west extrusion force, a north-south structural system is formed, and the bending faults are very developing. The main backbone structure in the mining area is mainly composed of the fault of Tanglang-Yimen and Yuanmou-Lvzhijiang, which is more than 100 km long and extends northward to Sichuan. It is one of the major faults in the north-south structural system of Sichuan and Yunnan. The strata of the Kunyang group exposed in the mining area can be divided into seven groups: Lvzhijiang formation, Etouchang formation, Luoxue formation, Yinmin formation, Meidang formation, Dalongkou formation, and Heishantou formation from top to bottom, respectively. It is a set of shallow marine clastic rock formations and carbonate formations, with a total thickness of more than 10,000 m. After the Jinning movement, the area was relatively calm, and there was activity after the Yanshan movement. The activity in this period was mainly manifested in superimposing on the NNW fault in Jinning period, staggering the Mesozoic red bed, which is characterized by counterclockwise horizontal torsion, destructing the orebody and was a post-mineralization fault [23].

The dip angle of the orebody is 70~80°, which is a steep orebody with a thickness of 20 m~160 m. The designed mining and selection scale is 1700 t/d, and the actual production scale is 1750 t/d–2200 t/d. The mine began production in October 1977. The highest surface elevation of the mine is 2143 m, and the design elevation of the project's first phase is 1807 m~1587 m (sublevel 4 to 8). The design of the mine capacity is 1750 t/d, and stoping has been completed. The design elevation of the project's second phase is 1587 m~337 m (sublevel 8 to 13). The designed ore capacity is 1000 t/d. The design elevation of the third phase project is 1337 m~1237 m (sublevel 14 to 15). The designed ore capacity is 1000 t/d. The basic stoping of the third phase project is completed. The design elevation of the project's fourth phase is 1237 m~787 m (sublevel 16 to 24).

The authors have measured the distribution of in situ stress field in the mining area. According to the three-dimensional in situ stress measurement results, in the regional tectonic gravitational field, the maximum principal stress direction is NNW-SSE, and the trend of the maximum principal stress is consistent with the direction of the maximum principal stress. It shows that the dominant direction of the maximum principal stress in the mining area is consistent with the direction of the maximum principal stress and perpendicular to the orebody's strike. The maximum and minimum principal stress difference is significant, and the average ratio is 2.54. This indicates that the dominant direction of the principal stress in the mining area is evident. The three principal stresses in the field investigation show an increasing linear trend with the increase of mining depth. The increasing rate of vertical principal stress and minimum principal stress is less than that of maximum principal stress. It can also be seen that the dominant stress in the mining area is the maximum principal stress. The linear regression equation of in situ stress value (MPa) in three directions with depth H (m) is, respectively, shown in formulas (1)–(3) [23].

$$\sigma_{h,\max} = -0.0163 + 0.0511H, \tag{1}$$

$$\sigma_{h,\min} = -0.3883 + 0.021H, \tag{2}$$

Figure 1: Geographical location and surrounding geological map of Shizishan Copper Mine.

$$\sigma_v = -0.6018 + 0.0307H, \quad (3)$$

where $\sigma_{h,\max}$ is the maximum principal stress, $\sigma_{h,\min}$ is the minimum principal stress, σ_v is the vertical principal stress, and H is the mining depth.

According to the results of in situ stress measurement in mining area, the indoor rock mechanics test results, and the quantitative standard of high in situ stress [24–26], the mining area should belong to the category of high in situ stress area.

The deposit structure of the mining area is the same as the regional geological structure. The dominant fault group that has a significant impact on the deep mining of the mine is the NE trending longitudinal fault group. They are fault F2 (strike 222°, dip direction 132°, dip angle 69°), fault F3 (strike 221°, dip direction 131°, dip angle 71°), fault F4 (strike 219°, dip direction 129°, dip angle 78°), fault FC2 (strike 272°, dip direction 182°, dip angle 35°), and fault FC3 (strike 311°, dip direction 221°, dip angle 33°) located in the footwall of the main orebody. Among them, faults F2 and F3 extend from sublevel 10 to 15, extending more than 200 m, and there are many engineering revelations in sublevels 11 and 12. Fault F4 extends from sublevel 6 to 18, which are weak intercalation of carbonaceous slate. Faults FC2 and FC3 are a pair of parallel ore-controlling faults located below sublevel 18, dislocating the deep orebody to the right. The distribution of each fault is shown in Figure 2.

3. The Field Situation of Fault Activation Slip in Mining Area

The authors have carried out several investigations on the rock mass movement status of the footwall from sublevel 7 to 15 of the main orebody in the Shizishan mining area. These investigations focus on identifying the dominant faults in the footwall that have an important impact on the stability of the project, and selecting appropriate monitoring points for the layout of the rock movement monitoring network. The investigation in April 2010 showed that the footwall of fault F2 had a significant influence on rock mass movement. The maximum slip of fault F2 was 0.50 m in the area exposed by the project, and severe deformation and failure of roadway and chamber were controlled by fault. The entire hanging wall of the fault sinks, which leads to the abandonment of many works. In contrast, faults F3 and F4 are not activated, and faults FC2 and FC3 in the lower part of sublevel 18 have not been exposed. The field investigation in April 2015 showed that during the past few years, affected by deep mining, the slip amount of fault F2 continued to increase and reached about 1.6 m, while fault F3 was activated due to the influence of deep mining, and the fault dislocation was obvious. The slip amount reached about 0.30 m. Tectonic development, such as faults in the footwall of the main orebody of the mine, and the objective presence of soft surfaces create conditions for roadway deformation, span fall, collapse, and rock movement. Figure 3 shows photos of a partial slip of fault F2.

4. Slip Criterion Analysis of Mining-Induced Fault Activation

Under the redistribution of stress field of surrounding rock caused by mining, fault dislocation between hanging wall and footwall is called "fault activation." Under the action of ground pressure, the fault activation is a process in which the mining disk of the fault undergoes shear deformation along the fault plane and then generates new fractures at one or both ends of the fault so that the fault can expand. The cracks located in the mining disk will also change accordingly.

4.1. Coulomb–Mohr Criterion. For non-water-conducting faults, activation plays two important roles. Firstly, through activation, the cement on the fault plane is "cut off," which makes the "bonding" state between the hanging wall and footwall of the fault transform into a "breaking" state, which makes it easier to introduce groundwater. Secondly, the fault tip and fault-derived joints expand through activation, which significantly enhances the permeability of the fault zone and its adjacent rock mass. When the fault zone has groundwater or imports groundwater, the softening effect of groundwater can reduce the shear strength of the fault zone and fault material modulus of deformation. The potential energy of the excavated rock mass will be transformed into plasticity work to a high extent. In contrast, the magnitude of

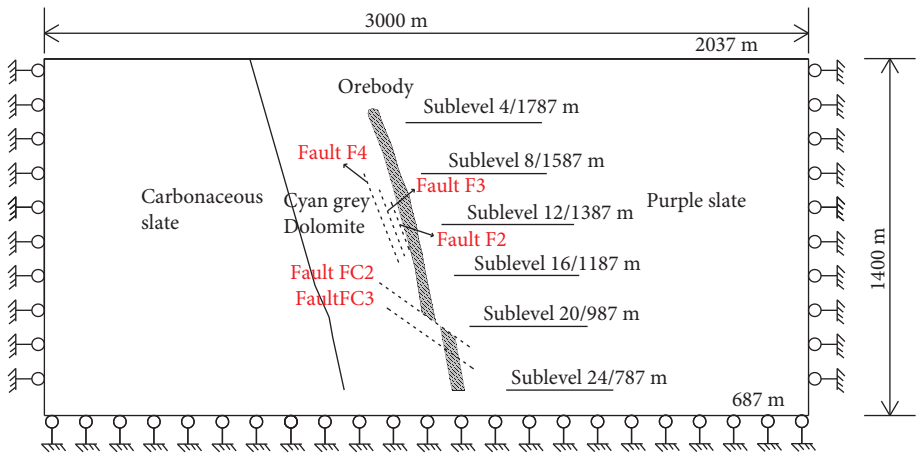

Figure 2: Distribution diagram of fault and orebody.

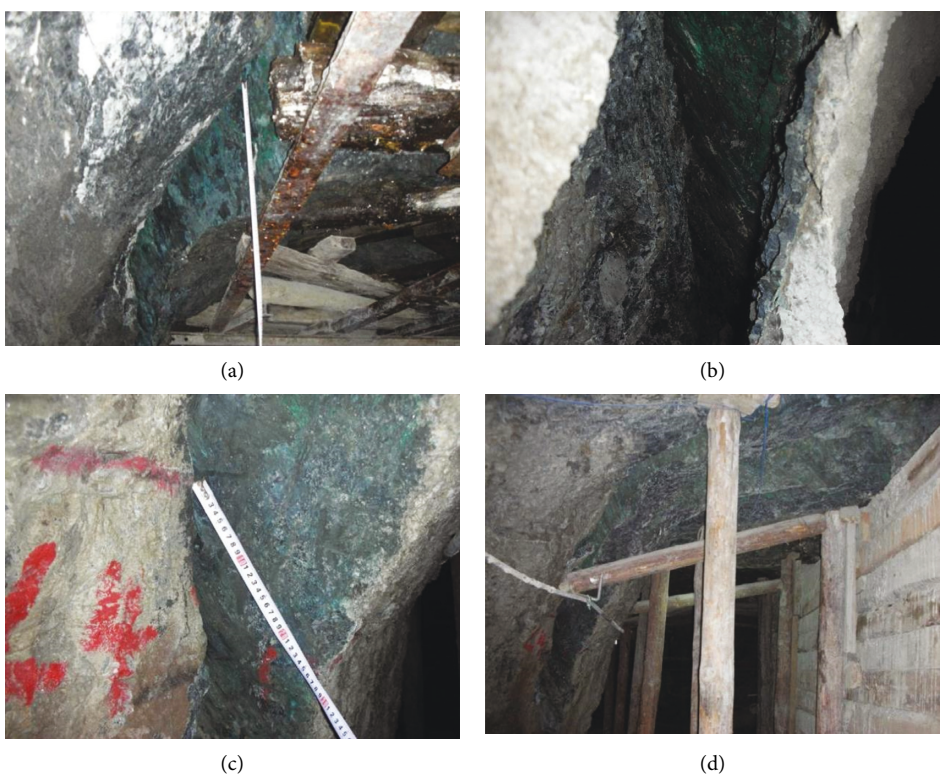

Figure 3: Photograph of partial slip on fault F2: (a) the displacement of the main roadway along the fault in sublevel 12, (b) dislocations along the faults of the ore slip bypass in sublevel 12, (c) the slip of the fault near the pass in sublevel 12, and (d) fault dislocation of material chamber in sublevel 12.

rock movement is bound to be greater, the process is more rapid, and the activation of faults is more pronounced.

Assuming that the hanging wall and footwall of the fault are elastic rock bodies, the fault plane is the contact surface of the hanging wall and footwall, and the initial activation of the fault is marked by the shear motion of the hanging wall and footwall. Modeling the fault activation force state [3, 27] is shown in Figure 4.

Assume that the fault plane dip is α, the fault is subjected to the maximum compressive stress, and the minimum compressive stress is σ_1 and σ_3. The bond coefficient of the fault plane is c, and the internal friction angle is φ. The shear and normal stresses acting on the fault plane are given in the following formula:

$$\begin{cases} \tau = \sigma_1 \sin\alpha + \sigma_3 \cos\alpha, \\ \sigma_n = \sigma_1 \cos\alpha - \sigma_3 \sin\alpha, \end{cases} \tag{4}$$

$$\tau_n = c + (\sigma_n - P_0)\tan\varphi, \tag{5}$$

where P_0 is the pore water pressure and τ_n is the shear strength of the fault plane, and when the pore water pressure

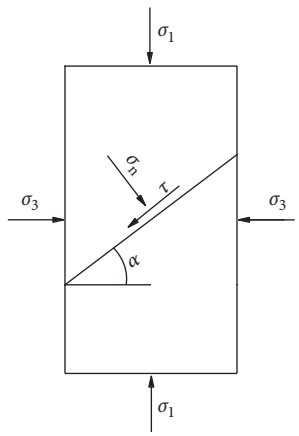

Figure 4: Mechanical models of fault activation.

is not considered, the residual shear stress $\Delta\tau$ is shown in the following formula:

$$\Delta\tau = \tau - \tau_n = \sigma_1 (\sin\alpha - \cos\alpha \tan\varphi) - \sigma_3 (\cos\alpha - \sin\alpha \tan\varphi) - c. \quad (6)$$

The criterion for fault activation is shown in the following formula:

$$\Delta\tau \geq 0. \quad (7)$$

4.2. The Sliding Criterion of Byerlee. The main problem in determining the stability of faults in rock masses is the correct selection of the sliding criterion (frictional strength). At present, it is difficult to determine the slip characteristics and criteria of the fault by accurately determining the shear strength parameters of the fault. Byerlee supplemented the Coulomb–Mohr criterion by using the spring-slider experiment in the laboratory and obtained the practical value of the sliding friction coefficient. According to Byerlee's sliding criterion formula [3], $\tau = \mu(\sigma_n - P_0)$, where P_0 is the pore water pressure. When the fault is dry and closed, the sliding criterion formula is $\tau = \mu\sigma_n$. According to many rock friction experiments, Byerlee proposed that the conditions for the frictional sliding of rocks along the sliding plane should satisfy formulas (8) and (9).

$$\tau = 0.85\sigma_n, \quad 3\text{MPa} < \sigma_n < 200\text{MPa}, \quad (8)$$

$$\tau = 50 + 0.6\sigma_n, \quad 200\text{MPa} \leq \sigma_n < 1700\text{MPa}, \quad (9)$$

where τ is the shear stress and σ_n is the normal stress.

5. Regularity and Mechanism Analysis of Fault Activation Induced by Continuous Mining in Deep Mining Area

5.1. Establishment of Numerical Calculation Model. Based on the schematic diagram of the distribution of faults and orebodies in Section 40 of the mining area, the 3D discrete unit method software 3DEC was used to build the calculation model. The top boundary of the numerical calculation model is taken to the surface, and the bottom boundary of the model is taken to 1400 m below the surface. In order to eliminate the influence of too close boundary, the left and right boundary are extended outward for a certain distance. The length of the model along the X direction is 3000 m, and 100 m is taken along the direction of the orebody strike, simplifying the surface at the top of the model into a horizontal plane. Figure 5 shows the schematic diagram of the final calculation model. The model dimensions are 3000 m, 1400 m, and 100 m in x, y, and z directions, respectively. In order to ensure the calculation accuracy and ensure that the unit has no distortion, the entire model is divided into 634,500 units and 126,850 nodes.

5.2. Parameter Selection and Calculation Scheme. The Mohr–Coulomb elastoplastic constitutive model is adopted for calculation. Except for setting free boundary conditions on the ground of the calculation model, the bottom of the model restricts the vertical displacement, and other boundaries restrict the horizontal displacement. The in situ stress is applied inside the model according to the actual measurement in the mining area. Based on the rock physical and mechanical parameters obtained from the laboratory test and the RMR value of the rock mass quality evaluation, the Hoek–Brown strength criterion is used to reduce and correct the rock mass mechanical parameters to estimate the rock mass mechanical parameters. The macroscopic rock mass physical and mechanical parameters of the Shizishan Copper Mine finally determined are shown in Table 1. The shear stiffness is 0.6 GPa, the normal stiffness is 0.285 GPa, the tensile strength is 0.43 MPa, the cohesion is 0.25 MPa, and the internal friction angle is 25° which are the parameters used in the fault calculation. Fault mechanics parameters were determined from the inversion of slip on fault F2 after mining the orebody in deep sublevel 14, sublevel 15, and above.

The calculation scheme is one-time mining in a single sublevel, each mining height above sublevel 18 is 50 m, and from sublevel 19 to 24, each mining height is 30 m. It has been continuously mined from the level of 1787 m in sublevel 4 to the level of 787 m in sublevel 24. In order to analyze the stress field and slip variation of each fault during calculation, monitoring points are set up on each fault, namely, points A, B, C, D, and E, as shown in Figure 6.

5.3. Analysis of Calculation Results

5.3.1. Activation Law and Mechanism Analysis of Fault F2

(1) Effect of Continuous Mining at Depth on the Stress Field of the Fault Plane. Figure 6 shows the positive and shear stress curves on fault F2 plane with the mining depth. When the mining depth is above fault F2 in sublevel 10, the positive stress on fault F2 plane is 3.49 MPa. When mining to sublevel 13, fault F2 plane is affected by mining. Additional tensile stress is generated on the fault plane, the positive stress on the fault plane decreases sharply to 0.15 MPa, and the positive

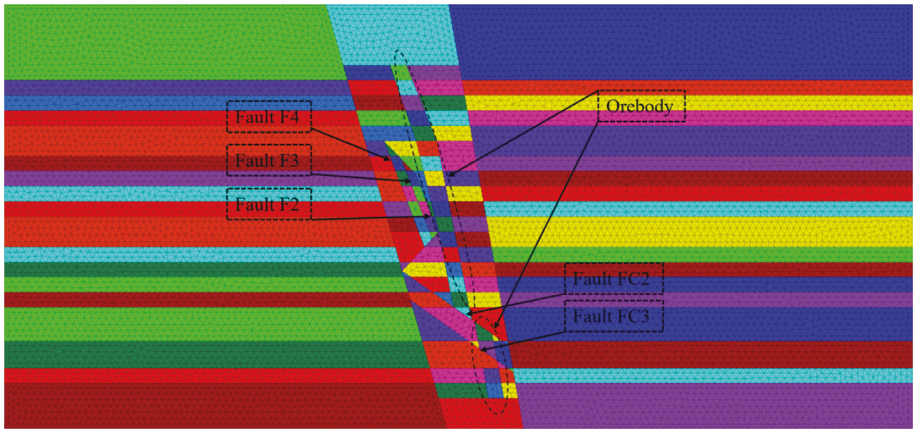

Figure 5: 3D discrete cell method 3DEC model cross-sectional logical block distribution profile.

Table 1: Macroscopic rock mechanics parameters of Shizishan Copper Mine.

Lithology	Density ρ (g/cm^3)	Modulus of elasticity E (GPa)	Poisson's ratio	Tensile strength σ_t (MPa)	Cohesive force C (MPa)	Angle of internal friction Φ (°)
Bluish grey dolomite	2.85	20.0149	0.269	2.1966	2.6110	41.99
Faded dolomite	2.84	13.0620	0.280	2.1796	2.5504	34.05
Orebody	2.84	17.8847	0.214	2.2577	2.9637	47.42
Purple slate	2.63	4.5676	0.284	1.0431	1.5710	31.68
Carbonaceous slate	2.70	2.2416	0.350	0.9298	1.3848	35.42

stress decreases more. The positive stress on the fault plane decreased sharply to 0.15 MPa, with a large reduction in positive stress. Then, the positive stress on the fault plane showed a slightly decreasing trend with the increase of mining depth, and the change of positive stress was relatively stable. When mining to sublevel 10, the shear stress on the fault plane is 1.0 MPa. When mining to sublevels 11 and 12, the shear stress on the fault plane decreases to 0.45 MPa. When mining to sublevel 13, the shear stress on the fault plane increases sharply to the peak, the shear stress is 0.80 MPa, and then the shear stress decreases gradually. When mining reaches sublevel 16, the shear stress decreases to 0.05 MPa, and the shear stress on the fault plane changes steadily from 0 MPa to 0.25 MPa during mining from sublevel 16 to 24.

According to the discussion of the fault activation slip criterion in Section 4 of this paper, the slip properties of fault F2 were analyzed using the Coulomb–Mohr criterion and Byerlee slip criterion, respectively. $\Delta\tau(\tau - 0.85\sigma_n)$ is the difference between shear stress and shear strength at tracking point A on the plane of fault F2. The variation curve of $\Delta\tau$ with the mining depth is shown in Figure 7. It can be seen from the calculation result that when mining from sublevel 10 to 12, the shear stress on the fault plane is less than the shear strength, indicating that the fault is in the static equilibrium state. After mining to sublevel 13, $\Delta\tau$ was positive and peaked at sublevel 13, with a maximum value of 0.20 MPa, indicating that the shear stress on the fault plane was greater than the shear strength fault slipped unstably. Then, $\Delta\tau$ gradually decreases. After mining to sublevel 14, $\Delta\tau$ is mainly negative because the cohesive force c disappeared

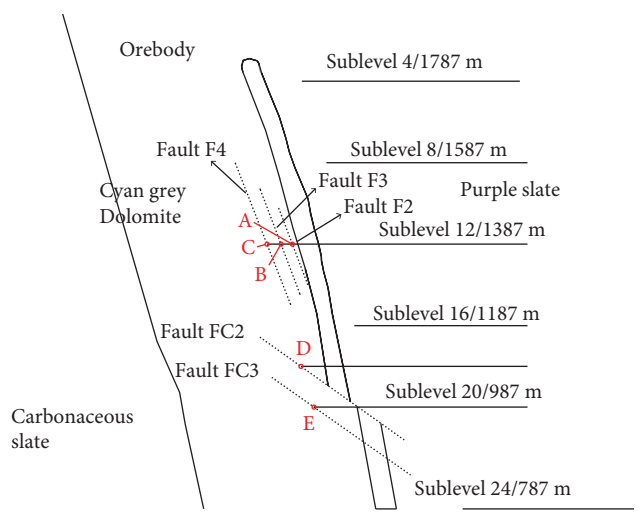

Figure 6: Schematic diagram of fault monitoring point layout.

after the fault's activation slip. The cohesive force is still taken into account in the calculation. Therefore, the Mohr–Coulomb criterion is only applicable to static equilibrium but not when the fault is activated and slipped.

Based on the Byerlee sliding criterion, the criterion for the occurrence of sliding on the fault plane is $\tau \geq 0.85\sigma_n$. By calculation, the variation curve of $\tau - 0.85\sigma_n$ on fault F2 plane with the mining depth is shown in Figure 8, and the value of $\tau - 0.85\sigma_n$ increases linearly with the increase of mining depth from sublevel 10 to sublevel 13. The ratio of shear stress to normal stress also increases rapidly at this

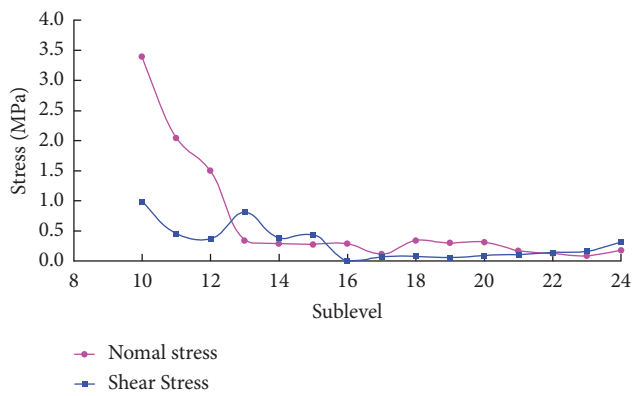

Figure 7: Relationship of the stress state of fault F2 with the mining depth.

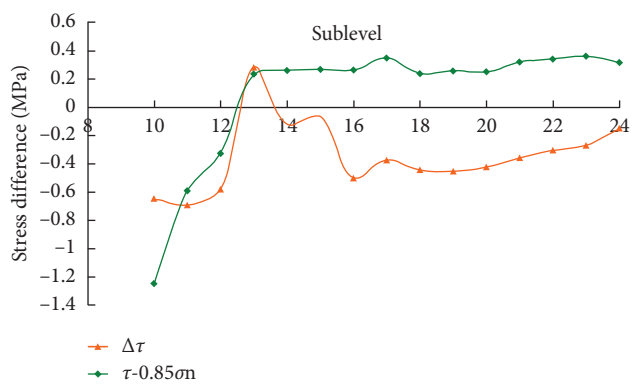

Figure 8: The slip property of fault F2 varies with mining depth.

time, the value of $\tau - 0.85\sigma_n$ is positive at sublevel 13, and the peak value is 0.24 MPa, indicating that the fault had been activated and started to slip at this point. After that, the value of $\tau - 0.85\sigma_n$ showed a stable trend with the increase of mining depth, and the values were all greater than 0.

(2) Influence of deep Continuous Mining on Fault Slip. Figure 9 shows the spatial and temporal variation curve of fault F2 slip with the mining depth. The results show that when mining above sublevel 12, fault F2 did not slip, and the fault was not activated. In contrast, after mining to sublevel 13, fault F2 was activated by mining, and the slip amount was 0.129 m. When sublevels 14 and 15 were mined, the slip amount of the fault increased to 0.630 m. According to the field monitoring, after mining to sublevel 15, the slip amount of fault F2 increases greatly, and the slip amount of fault F2 is 0.56 m. The calculated results agree well with the measured ones. The calculated results show that the slip of fault F2 increased to 2.44 m after the mining of sublevel 18. As the deep mining continued, the slip of fault F2 gradually increased, and when sublevel 22 to sublevel 24 (−1150 m to −1300 m) were mined, the slip of fault F2 finally increased to 4.491 m. According to the calculated results of the fault slip, after mining sublevel 13, the fault slipped, which is consistent with the prediction result of the Byerlee slip criterion, indicating that it is feasible to use Byerlee's law to determine mining-induced fault activation slip.

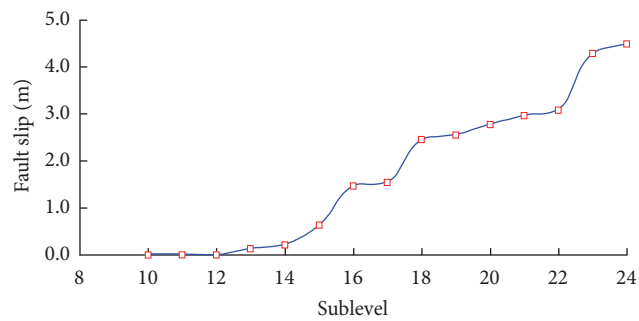

Figure 9: Relationship of slip amount of fault F2 with mining depth.

(3) Analysis of Activation Mechanism of Fault F2 Induced by Deep Continuous Mining. According to the above analysis, the activation mechanism of fault F2 under the effects of mining is as follows. As the deep mining of the main orebody continues until sublevel 10, the stress around the excavation area is redistributed under the influence of mining, and the mining influence scope spreads to fault F2, resulting in the decrease of normal stress on fault F2 plane and the apparent additional tensile stress $\Delta\sigma_n$. At this time, the shear strength $\tau = (\sigma_n - \Delta\sigma_n)\tan\varphi + c$ of the fault plane decreased. After mining to sublevel 13, the difference between the fault plane's shear stress and shear strength was greater than 0, and the Byerlee fault slip criterion is satisfied. The fault was activated by mining and began to slip steadily towards the goaf which is consistent with the actual situation on site. The analysis of this paper shows that the activation of steep dip fault is mainly caused by the decrease of normal stress of fault plane caused by mining. It is caused by additional tensile stress generated by excavation unloading.

5.3.2. Activation Law and Mechanism Analysis of Fault F3

(1) Influence of Deep Continuous Mining on Stress Field of the Fault Plane. Figure 10 shows the normal and shear stress curve of fault F3 plane with the mining depth. When mining from sublevel 10 to 13, the normal stress of fault F3 plane is 2.889 MPa, showing a steady trend. When mining from sublevel 14 to 16, the normal stress on the fault plane decreases greatly, and a large additional tensile stress is generated on the fault plane. After mining from sublevel 17 to 24, the normal stress on the fault plane shows a steady trend, ranging from 0 MPa to 0.1 MPa. When mining from sublevel 10 to 12, the shear stress on fault F3 plane is about 0.95 MPa, showing a steady trend. After mining from sublevel 13 to 15, the shear stress on the fault plane was reduced to 0.21 MPa. The shear stress on the fault plane was reduced, but the reduction was much less than the reduction in the positive stress on the fault plane. After mining to sublevel 16, the shear stress on the fault plane increased slightly to 0.43 MPa, indicating that additional shear stress was produced along the fault plane. After that, the shear stress on the fault plane varied steadily between 0.1 MPa and 0.2 MPa during mining from sublevel 17 to 24.

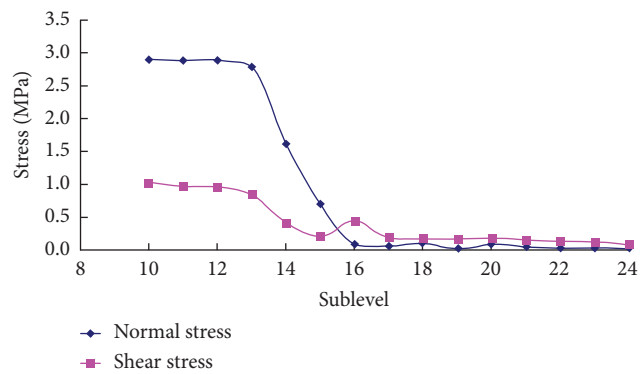

Figure 10: Relationship of stress state of fault F3 with mining depth.

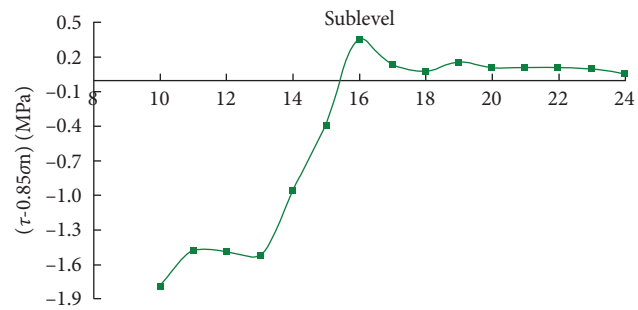

Figure 11: Sliding property of fault F3 changes with mining depth.

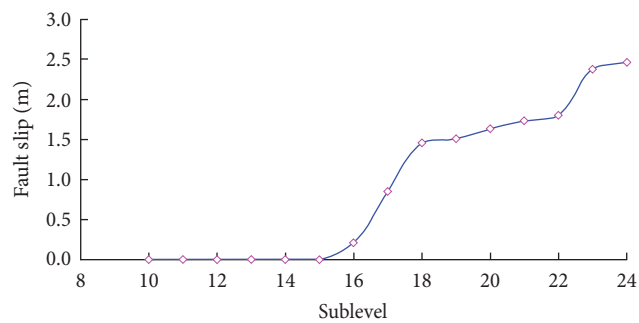

Figure 12: Relationship of slip amount of fault F3 with mining depth.

Figure 11 shows the curve of $\tau - 0.85\sigma_n$ on fault F3 with mining depth. When mining from sublevel 10 to 13, the value of $\tau - 0.85\sigma_n$ slightly increased with the increase of mining depth. When mining from sublevel 14 to 16, the shear stress to normal stress ratio increases rapidly. The value of $\tau - 0.85\sigma_n$ is greater than 0 after mining to sublevel 16, and the peak value is 0.35 MPa, indicating that the fault has been activated and has started slipping. Later, with the increase of mining depth, when the value of $\tau - 0.85\sigma_n$ is slightly reduced, it shows a stable trend with little change, but all positive, indicating that fault F3 has been sliding after mining to sublevel 16.

(2) Influence of Deep Continuous Mining on Fault Slip. Figure 12 shows the spatial and temporal relationship curve of fault F2 slip with mining depth. The results show that when the orebody above sublevel 15 was mined, fault F3 did not slip, i.e., the fault was not activated. In contrast, after the end of mining sublevel 16, fault F3 was activated by mining, and the slip amount was 0.21 m. When sublevel 17 and sublevel 18 were mined, the slip amount of the fault increased sharply to 1.46 m; however, during the mining period from sublevel 18 to sublevel 22, the increase rate of slip on the fault plane decreases. The slip on the fault plane was 1.798 m at the end of mining sublevel 22, and the rate of increase in a slip on the fault plane increased again after mining from sublevel 23 to sublevel 24. Furthermore, the slip on the fault plane was 2.46 m after mining sublevel 24, showing a staged increase in the slip on the fault plane.

(3) Analysis of Activation Mechanism of Fault F3 Induced by Deep Continuous Mining. Through the above analysis, the mechanism of activation of fault F3 by mining is as follows. As the main orebody continues to be mined from sublevel 13 to 15, the stresses around the excavation area are redistributed by mining, and the mining influence spreads to fault F3, causing a corresponding decrease in the positive and shear stresses on fault F3, the decreasing range of normal stress is much smaller than that of shear stress and additional tensile stress, and the additional tensile stress on the fault $\Delta\sigma_n$ increases; the shear strength $\tau = (\sigma_n - \Delta\sigma_n)\tan\varphi + c$ of the fault plane decreases, but the shear stress on the fault plane is still less than the shear strength. When sublevel 16 is mined, according to the Byerlee fault sliding criterion, the value of $\tau - 0.85\sigma_n$ is greater than 0. The difference between the shear stress and shear strength on the fault plane is $\Delta\tau > 0$, indicating that the fault is activated by the mining influence and starts to slip steadily in the direction of the goaf, which is consistent with the actual situation on site.

5.3.3. Activation Law and Mechanism Analysis of Fault F4

(1) Influence of Deep Continuous Mining on Stress Field of Fault Plane. Figure 13 shows the normal and shear stress curve on fault F4 plane with the mining depth. When mining from sublevel 10 to 16, the normal stress on fault F4 plane is 2.635 MPa, showing a steady trend. After mining from sublevel 20 to 24, the normal stress on the fault plane began to change steadily, with the normal stress range varying in a steady trend around 0.1 MPa. When mining from sublevel 10 to 16, the shear stress on fault F4 plane shows a stable trend, varying from 1.148 MPa to 1.005 MPa, and after mining from sublevel 17 to 18, the shear stress on the fault plane decreased to 0.226 MPa. The shear stress on the fault plane decreases, but the decrease is much smaller than that of the normal stress on the fault plane. The shear stress on the fault plane increased slightly to 0.338 MPa after mining to sublevel 19, indicating that additional shear stress was generated along the fault plane. After that, the shear stress on the fault plane varied steadily around 0.15 MPa from sublevel 20 to 24.

Figure 14 shows the variation curve of $\tau - 0.85\sigma_n$ on fault F4 with mining depth. When mining from sublevel 10 to 18, the value of $\tau - 0.85\sigma_n$ is −1.2 MPa; as mining depth

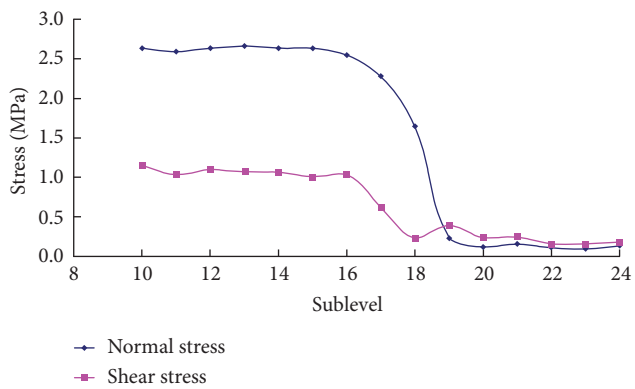

Figure 13: Relationship of stress state of fault F4 with mining depth.

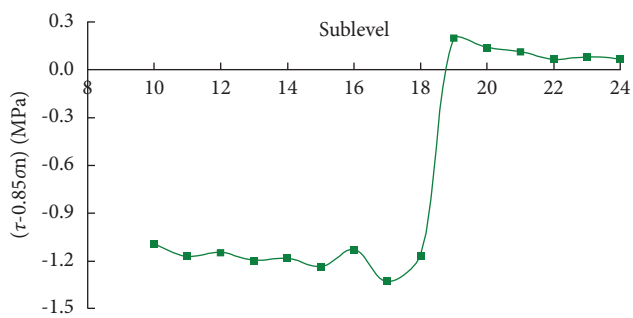

Figure 14: The sliding property of fault F4 varies with the mining depth.

increases, the curve shows a smooth change. When mining from sublevel 18 to 19, shear stress to normal stress increases steeply. The value of $\tau - 0.85\sigma_n$ is greater than 0 after mining to sublevel 19, and the peak value is 0.196 MPa. It means that the fault has been activated and started to slide. After that, when mining depth increases, the value of $\tau - 0.85\sigma_n$ decreases slightly and then stabilizes, but all of them are positive, indicating that after mining sublevel 19, fault F4 is activated by mining and is sliding.

(2) Influence of Deep Continuous Mining on Fault Slip. Figure 15 shows the relationship of the slip amount of fault F4 with mining depth. The results show that fault F4 does not slip after mining the orebody above sublevel 18, which means that the fault was not activated. After sublevel 19 was mined, fault F3 affected by mining was activated, and the slip amount was 0.18 m. When the orebody in sublevel 21 was mined, the slip amount of fault F4 rapidly increased to 0.767 m. Finally, after mining the orebody from sublevel 22 to 24, the slip amount on the fault plane increased to 1.008 m, and the slip amount on the fault plane showed an increasing trend in stages.

(3) Analysis of Activation Mechanism of Fault F4 Induced by Deep Continuous Mining. In summary, the mechanism of activation of fault F4 by mining is as follows. As the deep part of the main orebody continues to be mined until sublevel 18, the stress around the excavation area is redistributed by

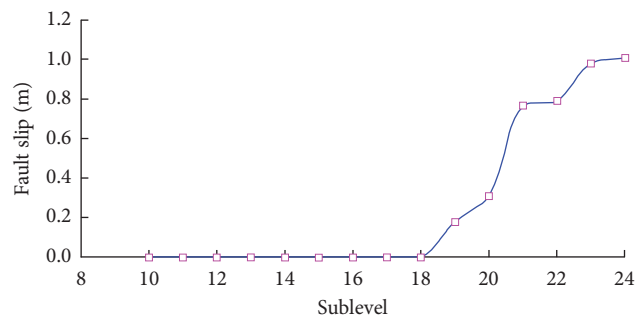

Figure 15: Relationship of slip amount of fault F4 with mining depth.

mining, and the impact of mining spreads to fault F4, causing the normal stress and shear stress on fault F4 plane to decrease accordingly, the reduction of normal stress is much larger than that of shear stress, and the normal stress on the fault plane $\Delta\sigma_n$ increases and obvious additional tensile stress is produced. The shear strength of the fault plane $\tau = (\sigma_n - \Delta\sigma_n)\tan\varphi + c$ decreases, but the shear stress on the fault plane is still less than the shear strength. When sublevel 19 was mined, according to the Byerlee fault sliding criterion, the value of $\tau - 0.85\sigma_n$ was greater than 0. It shows that the fault is activated by mining and began to slide towards the goaf.

5.3.4. Activation Law and Mechanism Analysis of Fault FC2

(1) Influence of Deep Continuous Mining on the Stress Field of Fault Plane. Figure 16 shows the curve of the positive and shear stress on fault FC2 plane with the mining depth. When mining from sublevel 10 to 20, the positive stress on fault FC2 plane is 16.23 MPa, showing a steady trend. When mining from sublevel 21 to 22, the positive stress on the fault plane decreases significantly. After mining to sublevel 22, the positive stress on the fault plane is 2.01 MPa. The fault plane has a large additional tensile stress generated. After mining from sublevel 23 to 24, the positive stress on the fault plane showed a stable trend, with a range of positive stresses around 1.70 MPa. The shear stress on fault FC2 plane was from 6.11 MPa to 5.43 MPa when mining from sublevel 10 to 21, showing a steady trend. The shear stress on the fault plane increased slightly to 2.670 MPa after mining to sublevel 22, indicating that additional shear stresses along the fault plane were generated at this time. The shear stress on the fault plane changes steadily at about 2.30 MPa during the mining of the sublevel 23 to sublevel 24.

Figure 17 shows the curve of the value of $\tau - 0.85\sigma_n$ on fault FC2 plane changing with the mining depth. When mining from sublevel 10 to 21, with the increase of the mining depth, the value of $\tau - 0.85\sigma_n$ is -7.50 MPa, showing a continuous change. When sublevels 21 and 22 were mined, the shear stress to normal stress ratio increased rapidly. The value of $\tau - 0.85\sigma_n$ is greater than 0 after mining to sublevel 22, and the peak value is 0.97 MPa. It shows that the fault has been activated and began to slide. As mining depth increases, the value of $\tau - 0.85\sigma_n$ decreased slightly, showing a stable

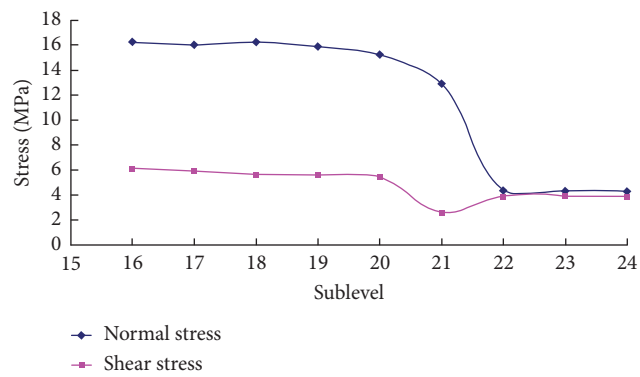

Figure 16: Relationship of stress state of fault FC2 with mining depth.

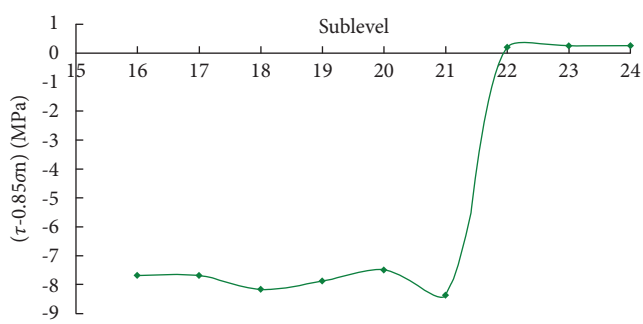

Figure 17: The sliding property of fault FC2 varies with mining depth.

trend with little change. However, all were positive, indicating that after mining to sublevel 22, fault FC2 was activated, and sliding after the mining was affected.

(2) Influence of Deep Continuous Mining on Fault Slip. Figure 18 shows the spatial and temporal relationship between the slip amount of fault FC2 and the mining depth. The results show that when the orebody above sublevel 21 was mined, fault FC2 did not slip, i.e., the fault was not activated, while at the end of the mining of sublevel 22, fault FC2 was activated by mining and the slip amount was 0.15 m. When the orebody from sublevel 22 to sublevel 24 was mined, the slip amount on the fault plane finally increased to 0.68 m.

(3) Activation Mechanism Analysis of Fault FC2 Induced by Deep Continuous Mining. In summary, the mechanism of activation of fault FC2 by mining is as follows. As the main orebody continues to be mined until sublevel 21, the stresses around the excavation area are redistributed by mining, and the mining influence spreads to fault FC2, resulting in the corresponding decrease of normal stress and shear stress on fault FC2 plane. The amplitude of normal stress is much smaller than the amplitude of shear stress. Moreover, the reduction in the normal stress on the fault plane $\Delta\sigma_n$ increased, resulting in an obvious additional tensile stress. At this time, the shear strength of the fault plane $\tau = (\sigma_n - \Delta\sigma_n)\tan\varphi + c$ declines, but the shear stress on the fault plane is still less than the shear strength. When sublevel 22 was

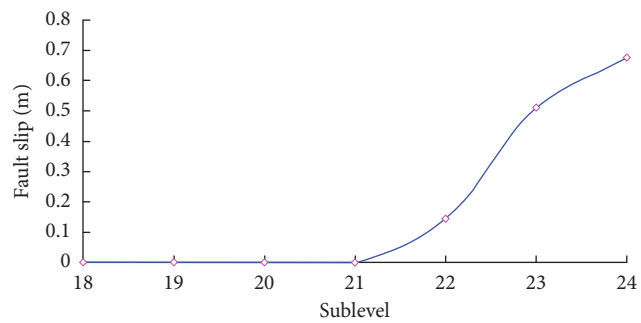

Figure 18: Relationship of the slip amount of fault FC2 with mining depth.

mined, according to the Byerlee fault sliding guidelines, the value of $\tau - 0.85\sigma_n$ greater than 0 indicates that the fault is activated by mining and begins to slide towards goaf. The change of fault slip amount with mining depth also proves this conclusion.

5.3.5. Activation Law and Mechanism Analysis of Fault FC3

(1) Influence of Deep Continuous Mining on Stress Field of Fault Plane. Figure 19 shows the normal and shear stress curve on fault FC3 plane with the mining depth. When sublevel 10 to sublevel 21 were mined, the normal stress on fault FC3 plane was 17.03 MPa, showing a steady trend. When sublevel 22 to sublevel 23 were mined, the normal stress on the fault plane was greatly reduced. After sublevel 23 was mined, the normal stress on the fault plane was 2.05 MPa, and a large additional tensile stress was generated on the fault plane. After mining from sublevel 23 to 24, the normal stress on the fault plane began to show a stable trend again, with the range of normal stress varying in a stable trend around 1.40 MPa. The shear stress on fault FC3 plane ranged from 5.28 MPa to 5.77 MPa when mining from sublevel 10 to 21, showing a steady trend. After sublevels 21 and 22 were mined, the shear stress on the fault plane decreased to 2.15 MPa, and the shear stress on the fault plane decreased, but the decrease was much smaller than the normal stress on the fault plane. After mining to sublevel 23, the shear stress on the fault plane increased slightly to 2.650 MPa. This means that additional shear stresses were generated along the fault plane, and the shear stress on the fault plane was 0.91 MPa after the orebody was mined in sublevel 24.

According to the Byerlee sliding criterion, the criterion for the occurrence of sliding on the fault plane is $\tau \geq 0.85\sigma_n$. Figure 20 shows the variation curve of $\tau - 0.85\sigma_n$ on fault FC3 plane with mining depth. When mining from sublevel 10 to 21, the value of $\tau - 0.85\sigma_n$ is −8.90 MPa, which is a smooth change. When mining from sublevel 22 to 23, the shear stress to normal stress ratio increases rapidly during this time. The value is greater than 0 after mining sublevel 23, and the peak value is 0.95 MPa, which means that the fault has been activated and began to slide. After that, as the mining depth increases, the value of $\tau - 0.85\sigma_n$ slightly decreases. It is a stable trend, not much change, but all

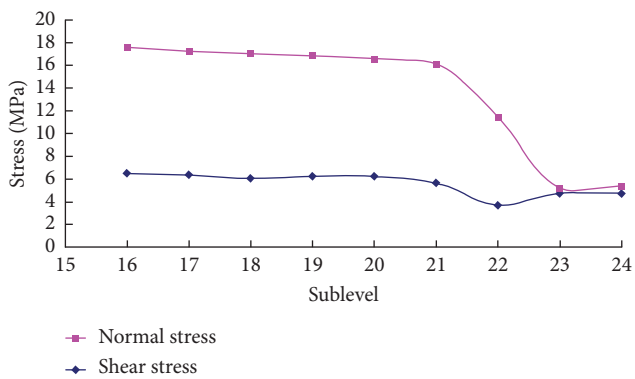

Figure 19: Relationship of stress state of fault FC3 with mining depth.

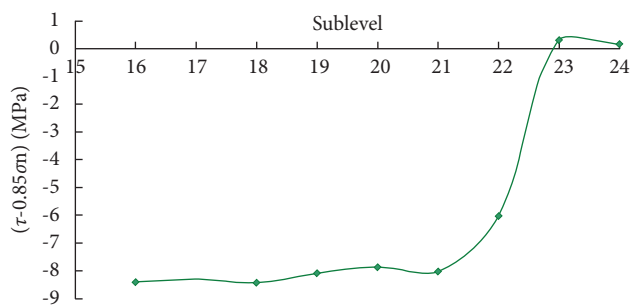

Figure 20: The sliding property of fault FC3 varies with mining depth.

positive, indicating that after mining to sublevel 23, fault FC3 was activated and slipped after being affected by the mining.

(2) Influence of Deep Continuous Mining on Fault Slip. Figure 21 shows the spatial and temporal relationship of the slip amount of fault FC3 with mining depth. The results show that when the orebody above sublevel 22 was mined, fault FC3 did not slip, i.e., the fault was not activated. In contrast, at the end of the mining of sublevel 23, fault FC3 may have been activated by mining, and the slip amount was 0.143 m, and when the orebody of sublevel 24 was mined, the slip amount of fault FC3 increased to 0.223 m.

(3) Analysis of Activation Mechanism of Fault FC3 Induced by Deep Continuous Mining. As a result of mining, the mechanism of activation of fault FC3 is as follows. As the deep part of the main orebody continues to be mined until sublevel 22, the stresses around the mining area are redistributed by mining, and the mining influence spreads to fault FC3, causing the normal stress and shear stress on fault FC3 to decrease accordingly; compared to the reduction in shear stress, the reduction in normal stress is much greater, and the reduction in the normal stress on the fault plane $\Delta\sigma_n$ increased, resulting in an obvious additional tensile stress. At this time, the shear strength of the fault plane $\tau = (\sigma_n - \Delta\sigma_n)\tan\varphi + c$ has declined, but the shear stress on the fault plane is still less than the shear strength. When mining to sublevel 23, according to the Byerlee fault sliding criterion,

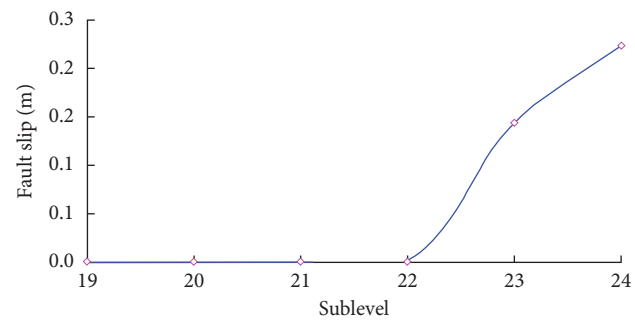

Figure 21: Relationship of the slip amount of fault FC3 with mining depth.

the value of $\tau - 0.85\sigma_n$ is greater than 0, indicating that the fault is activated by the mining effect and starts to slip towards the goaf. The change of the slip amount of the fault with mining depth also proves this conclusion.

5.3.6. Domino Effect and Mechanism Analysis of Fault Activation under the Influence of Deep Continuous Mining. Figure 22 shows the spatial and temporal relationship of the slip of the faults in the footwall of the main orebody with mining depth. The analysis shows that the activation law of the footwall fault of the main orebody is that the movement law of the footwall rock mass of the main orebody in the mining area is mainly controlled by the dominant fault. There is a barrier effect of the fault on the distribution of stress and displacement fields in the footwall rock of the main orebody. With the end of stoping of the orebody in sublevel 13 (burial depth 700 m), the influence of mining spreads to fault F2, and fault F2 was activated by mining, and the rock body on the hanging wall of the fault near the mining area began sliding along the fault towards the mining area; when stoping of the orebody in sublevels 14 and 15 was completed, the slip of fault F2 gradually increased to 0.63 m. With the development, preliminary mining and stoping of the orebody in the sublevel 16. Mining also caused fault F3 to be activated, and the rock on the hanging wall of fault F3 began to slip along the fault in the direction of the goaf, and the slip of faults F2 and F3 was 1.476 m and 0.210 m, respectively, after the end of stoping in sublevel 16. When the deep mining continued to sublevel 19 (buried depth 1000 m), fault F4 was also activated under the influence of mining, and the rock mass from the hanging wall of the fault to the side of the goaf produces slip towards the goaf. After the end of stoping of sublevel 19, the slip of faults F2, F3, and F4 was 2.553 m, 1.506 m, and 0.18 m, respectively. After the end of stoping of the orebody in sublevel 22, fault FC2 was also activated by mining and started to slip. The slip of faults F2, F3, F4, and FC2 was 3.078 m, 1.798 m, 0.791 m, and 0.144 m, respectively. When the orebody in deep sublevel 23 (burial depth 1350 m) finished stoping, fault FC3 was also activated by mining and started to slip, and the slip of fault FC3 was 0.143 m. The slip amount on faults F2, F3, F4, FC2, and FC3 was 4.491 m, 2.460 m, 1.008 m, 0.675 m, and 0.223 m, respectively, after stoping of the orebody in deep sublevel 24. Based on the spatial and temporal correlation

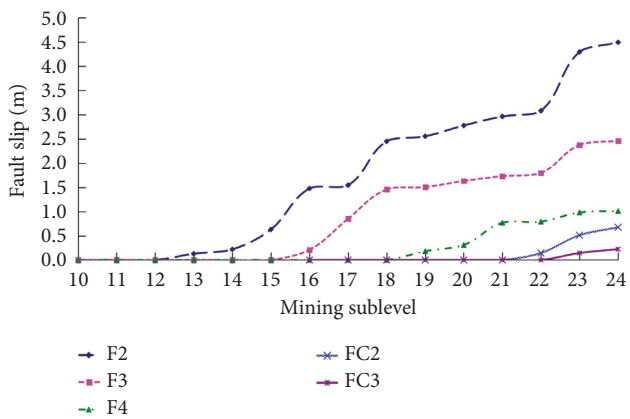

Figure 22: The time-space relationship curve of the slip amount of each fault with mining depth.

between the activation and slip of the fault group under the main orebody, the activation of the faults induced by the continuous mining conditions at depth has a "domino effect." In an interconnected system, small initial energy may produce a series of successive activation of faults and slip of the hanging wall towards the extraction area during deep and continuous mining, i.e., the "domino effect." Therefore, similar to the Shizishan Copper Mine, the steeply dipping geese column fault group in the footwall of the mining area induces fault activation under mining, which results in the hanging wall of the fault moving towards the mining area and slipping along the fault plane.

By calculating normal stress and shear stress on each fault with mining depth, according to Byerlee's law, the criterion of fault plane sliding is $\tau \geq 0.85\sigma_n$. Figure 23 shows the temporal and spatial relationship curve of additional tensile stress on each fault plane with mining depth. Figures 24 and 25 show the temporal and spatial relationship curve of fault values of $\tau - 0.85\sigma_n$ on the footwall of the main orebody with mining depth. Through analysis, the domino effect mechanism of fault activation in the footwall of the main orebody is as follows. As mining enters sublevel 10, as a result of mining, the additional tensile stress is first generated on fault F2 plane. With the downward mining, the additional tensile stress on fault F2 plane increases gradually, and the shear strength $\tau = (\sigma_n - \Delta\sigma_n)\tan\varphi + c$ of the fault plane decreases gradually. After mining the orebody to sublevel 13, additional tensile stress reaches a maximum value of 3.05 MPa. Currently, the shear stress on the fault plane exceeds the shear strength and satisfies Byerlee's law. The value of $\tau - 0.85\sigma_n$ is greater than 0. Under the influence of mining, the fault F2 starts to active and began to slip. The rock body on the hanging wall of the fault near the mining area starts to slide along the fault plane in the direction of the goaf, and then the additional tensile stress on the fault plane tends to stabilize. When the orebody is mined from the sublevel 14 to the sublevel 16, Fault F3 plane starts to generate additional tensile stress and reaches a maximum value of 2.799 MPa after mining the orebody to sublevel 16, and fault F3 also satisfies Byerlee's law. Fault F3 was activated under the influence of mining, and the rock body on the hanging wall of fault F3 began to slip along the fault

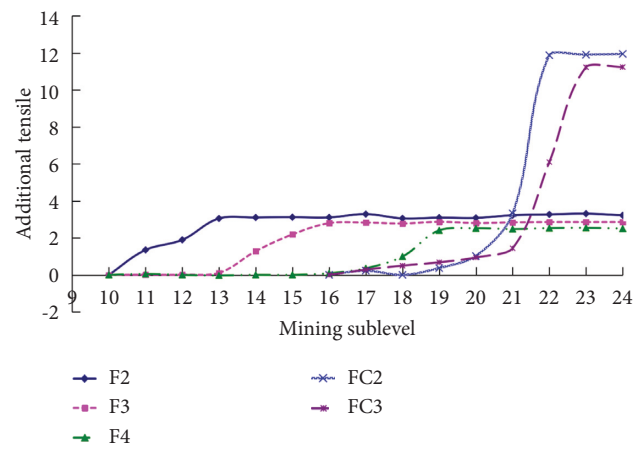

Figure 23: Temporal and spatial relationship curve of additional tensile stress on each fault plane with mining depth.

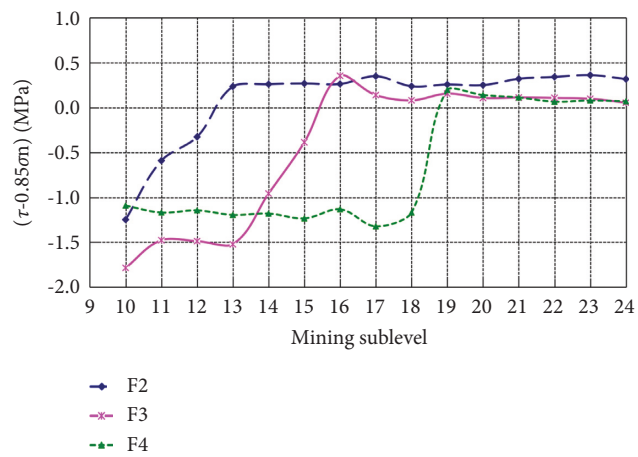

Figure 24: Temporal and spatial relationship curves of fault F2, F3, and F4 values changing with mining depth.

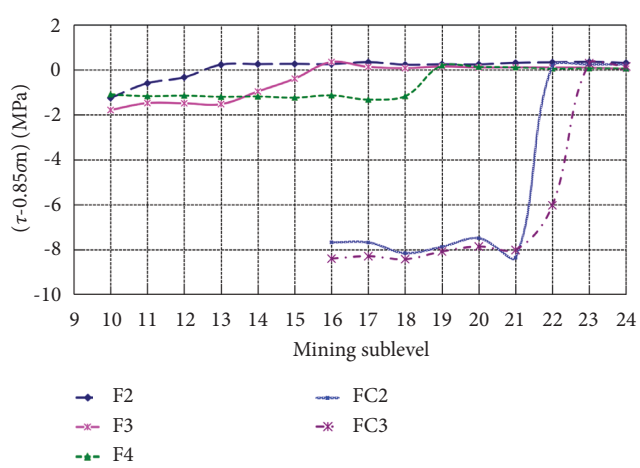

Figure 25: Temporal and spatial relationship curve of fault FC2 and FC3 values changing with mining depth.

plane in the direction of the goaf. When the deep mining continued to sublevel 19 (buried depth 1000 m), the additional tensile stress on fault F4 plane also reached a peak of

2.409 MPa, and fault F4 shows greater shear stress than its strength, and mining affected the fault's activation as well. The additional tensile stress on the fault plane also increases to the peak value of 11.23 MPa. It is also activated and begins to slip under the influence of mining.

From the analysis of the additional tensile stress and the spatial and temporal relationship of the fault activation slip with mining depth on each fault plane in the footwall of the main orebody, the positive and shear stresses on the fault plane decrease simultaneously after mining of the orebody, i.e., additional tensile stress and additional shear stress are generated. At this time, the additional tensile stress acts to reduce the shear strength of the fault plane and promotes fault activation. In contrast, the shear stress on the fault plane is reduced by the additional shear stress, preventing the activation of the fault. Through analysis, shear stress to positive stress ratios increase after mining on each fault plane, indicating that the nature of fault activation in the mine area is caused by the additional tensile stress generated on the fault plane due to excavation and unloading. In contrast, the increase of additional tensile stress on fault F2 leads to the reduction of the positive stress acting on the footwall by the rock body on fault F2. The footwall of fault F2 is the hanging wall of fault F3, which, according to the principle of force transfer, is the essence of the domino effect of fault activation under the influence of mining on the steep dip fault group.

6. Conclusion

(1) Within the area affected by underground excavation, the existence of fault plane and fault zones will change the normal distribution pattern of the displacement field and secondary stress field of the surrounding rock and become a barrier affecting the deformation and stress propagation of the surrounding rock, resulting in different characteristics of rock movement and deformation on both sides of the fault plane or fault fracture zone. With the change of potential energy of the rock in the excavation influence area, the work done by the self-weight volume force is mainly consumed in the slip action of the fault plane and the plastic deformation and slip deformation of the fault fracture zone, which makes it difficult to completely cross the fault fracture zone to the deeper part of the surrounding rock. The extrusion displacement and rebound deformation pointing to the mining space are mostly restricted within the fault fracture zone. This is the essence of displacement and stress barrier effect of faults and is also the main reason for the large deformation and high-stress concentration in the surrounding rock between the fault and the mining area.

(2) The normal stress and shear stress on each fault plane decrease simultaneously after mining the orebody, and additional tension stress and shear stress are generated. At this time, the additional tensile stress reduces the shear strength of the fault plane and promotes the fault's activation. The effect of the additional shear stress on the fault plane is to prevent the activation of the fault, but the decrease of normal stress on the fault plane is much greater than that of shear stress, and the shear stress on the fault plane is greater than the shear strength, resulting in fault activation. It also shows that the essence of fault activation in the mining area is caused by additional tensile stress on the fault plane caused by excavation unloading.

(3) The fault effect of rock movement in the footwall of the main orebody of the mine is obvious. The en echelon steep dipping fault group in the footwall of the mining area will move each fault block in the direction of the mining area and slip along the fault plane when the balance between mining and gravity is broken. The activation of the fault has a domino effect in time and space. After mining, the increase of additional tensile stress of fault F2 leads to the decrease of the normal stress exerted by the hanging wall rock mass of fault F2 on the footwall. The footwall of fault F2 is the hanging wall of fault F3. According to the principle of force transfer, the normal stress exerted by the hanging wall rock mass of fault F3 on the footwall rock mass will decrease, resulting in a decrease in the shear strength of fault F3. Similarly, the normal stress exerted by the hanging wall of fault F4 on the footwall decreases, and the shear strength of fault F4 also decreases, which is the essence of the domino effect of fault activation of en echelon steep dipping fault group under the influence of mining.

Data Availability

The data used to support the findings of this study are included within the article.

Conflicts of Interest

The authors declare that they have no conflicts of interest.

Acknowledgments

This study was supported and funded by the Scientific Research Fund Project of Yunnan Provincial Department of Education, China (no. 2022J0065), Key Projects of Analysis and Testing Fund of Kunming University of Science and Technology, China (no. 2021T20200145), China Postdoctoral Science Foundation Project (no. 2017M620433), and General Projects of Yunnan Basic Research Program (no. 2018FB075).

References

[1] H. P. Xie, F. Gao, and Y. Ju, "Research and development ofrock mechanics in deep ground engineering," *Chinese Journal of Rock Mechanics and Engineering*, vol. 34, no. 11, pp. 2161–2178, 2015.

[2] M. C. Xie, H. P. Xie, S. P. Peng, and Y. D. Jiang, "Study on rock mechanics in deep mining engineering," *Chinese Journal of Rock Mechanics and Engineering*, vol. 16, no. 11, pp. 2803–2813, 2005.

[3] D. Chen, H. Chen, W. Zhang, J. Lou, and B. Shan, "An analytical solution of equivalent elastic modulus considering confining stress and its variables sensitivity analysis for fractured rock masses," *Journal of Rock Mechanics and Geotechnical Engineering*, vol. 14, 2021.

[4] G. W. Lei, C. H. Yang, G. Wang, S. Chen, X. Wei, and L. Huo, "The development law and mechanical causes of fault influenced zone," *Chinese Journal of Rock Mechanics and Engineering*, vol. 35, no. 02, pp. 231–241, 2016.

[5] H. Luo, Z. H. Li, A. W. Wang, and Y. H Xiao, "Study on the evolution law of stress field when approaching fault in deep mining," *Journal of China Coal Society*, vol. 39, no. 02, pp. 322–327, 2014.

[6] Q. Wang, M. C. He, S. C. Li et al., "Comparative study of model tests on automatically formed roadway and gob-side entry driving in deep coal mines," *International Journal of Mining Science and Technology*, vol. 31, no. 04, pp. 591–601, 2021.

[7] C. Zhu, M. Karakus, M. He et al., "Volumetric deformation and damage evolution of Tibet interbedded skarn under multistage constant-amplitude-cyclic loading," *International Journal of Rock Mechanics and Mining Sciences*, vol. 152, 2022.

[8] Q. H. Yu, H. X. Zhang, Y. J. Zhang, W. N. Deng, and G. Y. Zhang, "Analysis of fault activation mechanism and influencing factors causedby mining," *Journal of China Coal Society*, vol. 44, no. S1, pp. 18–30, 2018.

[9] D. D. Zhang, Y. Y. Duan, W. Du, and Chai, "Experimental study on physical similar model of fault activation law based on distributed optical fiber monitoring," *Shock and Vibration*, vol. 2021, pp. 1–11, Article ID 4846977, 2021.

[10] Y. Q. Yin, P. E. Li, and Y. Di, "Instability and jumping phenomenon of rock structure," *Chinese Journal of Rock Mechanics and Engineering*, vol. 34, no. 05, pp. 945–952, 2015.

[11] Y. S. Pan, *Study on Rockburst Initiation and Failure Propagation*, Tsing University, Beijing, China, 1999.

[12] D. Y. Zhao, H. Wang, Z. G. Lu, and B. Cao, "Characteristics of tremor time-space evolution and Coulomb stress distribution along the fault during workface excavation," *Journal of China Coal Society*, vol. 43, no. 2, pp. 340–347, 2018.

[13] T. Wang, Y. D. Jiang, and Y. X. Zhao, "Experimental research on fault reactivation and relating coal bumps," *Journal of Mining & Safety Engineering*, vol. 31, no. 2, pp. 180–186, 2014.

[14] Z. H. Li, *Research on Rockburstmechanism Induced by Fault Slipduring Coal Mining Operation*, China University of Mining and Technology, Xuzhou, Jiangsu, China, 2009.

[15] Y. Pan, J. Y. Xie, and S. F. Gu, "Catastrophe theory analysis of mining faultrockburst under nonuniform surrounding pressure," *Chinese Journal of Rock Mechanics and Engineering*, vol. 03, pp. 310–314, 2001.

[16] W. Cai, L. M. Dou, G. F. Wang, and Y. W. Hu, "Mechanism of fault reactivation and its induced coal burst caused by coal-mining activities," *Journal of Mining & Safety Engineering*, vol. 36, no. 06, pp. 1193–1202, 2019.

[17] K. M. Han, Q. H. Yu, H. X. Zhang, and F. M. Li, "Mechanism of fault activation when mining on hanging-wall and footwall," *Journal of China Coal Society*, vol. 45, no. 04, pp. 1327–1335, 2019.

[18] J. P. Zuo, Z. H. Chen, H. W. Wang, X. P. Liu, and Z. P. Wu, "Experimental investigation on fault activation pattern under deep mining," *Journal of China Coal Society*, vol. 34, no. 03, pp. 305–309, 2009.

[19] Q. S. Wu, *Study on Mining Effect and Dynamic Response Characteristics in normal Fault-Affected Area*, Doctor, Shandong University of Science and Technology, Qingdao, Shandong, China, 2019.

[20] M. R Islam and R. Shinjo, "Mining-induced fault reactivation associated with the main conveyor belt roadway and safety of the Barapukuria Coal Mine in Bangladesh: c," *International Journal of Coal Geology*, vol. 79, no. 4, pp. 115–130, 2009.

[21] J. Q. Jiang, Q. L. Wu, and H. Qu, "Characteristic of mining stress evolution and activation of the reverse faultbelow the hard-thick strata," *Journal of China Coal Society*, vol. 40, no. 02, pp. 267–277, 2015.

[22] A. Sainoki and H. S. Mitri, "Effect of slip-weakening distance on selected seismic source parameters of min-ing-induced fault-slip," *International Journal of Rock Mechanics and Mining Sciences*, vol. 34, pp. 2161–2178, 2015.

[23] Y. H. Guo and K. P. Hou, "In-situ stress measurement and prediction analysis of rockburst in deep mining of Shizishan copper mine," *Electronic Journal of Geotechnical Engineering*, vol. 19, pp. 2513–2524, K, 2014.

[24] G. Herget, *Stresses in Rock,* pp. 50–58, A. A. Balkema, Ottawa, Ontario, Canada, 1rd edition, 1988.

[25] Z. Y. Tao, "On characteristics of rock mass in high in-situ stress area," *Underground Engineering*, vol. 3, pp. 5–9, 1983.

[26] Z. Guo, "Deformation characteristics of rock mass in high stress area," *The third National Engineering Geology Conference*, vol. I, pp. 300–305, 1988.

[27] M. F. Cai, *Rock Mechanics and Engineering,* pp. 31–68, Science Press, Beijing, China, 2rd edition, 2002.

Hindawi
Advances in Materials Science and Engineering
Volume 2022, Article ID 7893477, 8 pages
https://doi.org/10.1155/2022/7893477

Research Article

Study on Relationship between Joint Surface's Shear Strength and Morphology Parameter Deterioration of Typical Bank Slope in Wudongde

Jing Yu Zhang,[1,2] Huafeng Deng,[1] Xushu Sun,[1,2] Yunjie Feng,[1] Wendong Wang,[1] Lei Xiao,[3] and Wenhua Li[4]

[1]*Key Laboratory of Geological Hazards on Three Gorges Reservoir Area, Ministry of Education, China Three Gorges University, Yichang 443002, China*
[2]*College of Hydraulic & Environmental Engineering, China Three Gorges University, Yichang 443002, China*
[3]*Power China GuiYang Engineering Co. Ltd, Guiyang, Guizhou 550081, China*
[4]*China Three Gorges Construction Engineering Co. Ltd., Chengdu, Sichuan 610041, China*

Correspondence should be addressed to Huafeng Deng; dhf8010@ctgu.edu.cn

Received 28 May 2022; Accepted 24 June 2022; Published 11 July 2022

Academic Editor: Depeng Ma

The change of typical bank slope's water occurrence environment and the special climatic condition of dry hot valley in Wudongde reservoir area will make the shear characteristics of jointed rock mass on bank slope deteriorate continuously. Based on this, the shear test of joint surface under heat-wet cycles is carried out. The results show the following. (1) The shear strength and joint roughness deteriorate significantly with the increasing test cycles, and the deterioration ranges are 70.90%–84.48% and 29.33%–61.56% in the first 5 cycles. (2) The shear strength's deterioration caused by repeated shear is mainly in the initial state, and the shear strength's deterioration caused by heat-wet cycles increases firstly and decreases later with the test cycles. (3) By introducing the equivalent damage coefficient of morphology, the shear strength calculation formula is improved, and it can be seen that the estimated value coincides with the modified test value. The research results can provide a reference for long-term variation and calculation method of joint surface's shear strength under different water-rock interactions.

1. Introduction

Reservoir water level fluctuation will change the water occurrence environment of bank slope, and different ways of water-rock interaction such as long-term immersion and dry-wet cycles will weaken the physical and mechanical parameters of rock to different degrees on bank slope. Actually, the stability of rock slope is mainly controlled by the joint surface inside rock mass. As the joint surface frequently reacts with water, its shear strength will deteriorate over time [1, 2] that will eventually lead to partial instability of the slope and even cause a wider range of collapse. Therefore, affected by the rise and fall of reservoir water level with the influence of changing water levers, the shear characteristics' long-term variation of joint surfaces in hydro-fluctuation belt is crucial to the study of slope stability.

There are many studies on shear characteristics about joint surface or fracture under different water-rock interactions. For example, some scholars [3–7] studied the variation law of joint surface's shear characteristics under different immersion times and found that the shear characteristics deteriorated significantly. Some scholars [8–14] also found the regular pattern of influence on dry-wet cycle on joint surface's shear characteristics and deduced the deterioration formula of shear strength combined with the change of morphology parameters. The rock itself is a bad heat conductor, so in the process of water-rock interaction, it is necessary to consider the influence of temperature. Especially in the hot and dry valley areas of the Jinsha River

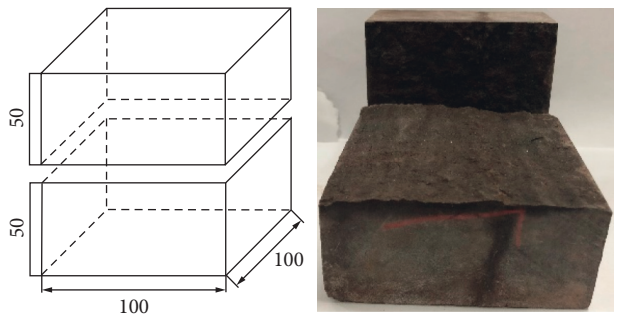

Figure 1: Single-joint specimen.

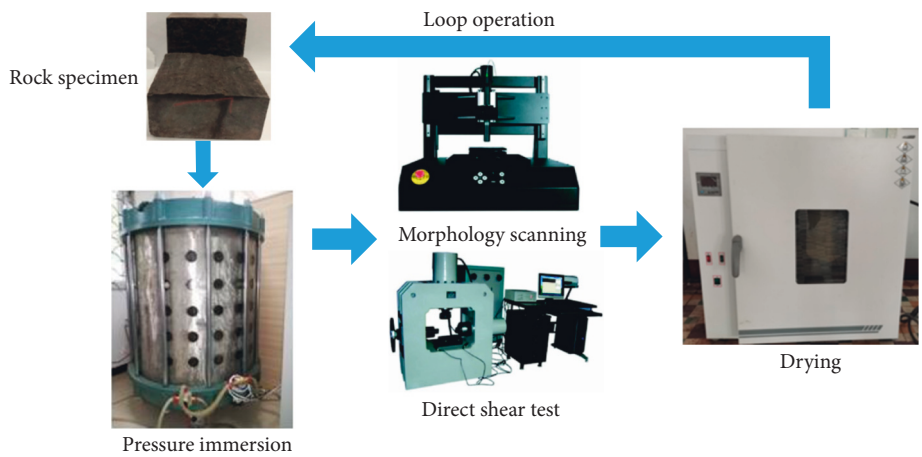

Figure 2: Test flowchart.

where there are abundant light and heat resources, the shear characteristics of the jointed rock mass on the surface of the bank slope under the heat-wet cycles need attention. In particular, large reservoirs such as Baihetan and Wudongde make part of the jointed rock mass on the bank slope in this water environment.

At present, there are many studies on the deterioration of rock physical and mechanical parameters under heat-wet cycles [15–17], but there are few results about joint surface or fracture. Therefore, this paper carried out the test on influence of heat-wet cycles about the shear strength and morphology parameters of joint surface and obtained the variation law of shear characteristics and morphology parameters and then deduced the shear strength deterioration formula. The results can provide ideas for the analysis on the stability of bank slopes under long-term operation conditions of large reservoir in hot and dry valley.

1.1. Experimental Procedure. In this paper, in order to reduce the discrete effect caused by the difference of joint surface morphology, the single-joint repeated shear method was adopted [18]. The sandstone rock from the typical bank slope in upstream of Wudongde reservoir area was made into a cube block with a length of 100 mm. Then, the block was split along its axis to form a single-joint specimen, as shown in Figure 1. From the prepared single-joint specimens, the specimens with similar morphology parameters of joint surface were chosen as the test specimen.

As the height of Wudongde reservoir hydro-fluctuation belt is 30 m (945 m–975 m) and the jointed rock mass at the bottom of hydro-fluctuation belt still bears a certain water pressure, its deterioration effect is more obvious [19]. For experimental convenience, 0.3 MPa water pressure was set. Referring to the actual situation, the heating temperature is set to 70°C and the heating time is 8 h. According to the water quality test report of Wudongde reservoir, the pH of the immersion solution was set to 8.35. A total of 12 test cycles were set. After the end of initial saturated state, 1st, 3rd, 5th, 8th, and 12th immersion, the joint surface morphology scanning and shear test of the joint specimen were carried out. The normal stress of the direct shear test was set to 0.5 MPa, 1.0 MPa, 1.5 MPa, and 2.0 MPa. The test process is shown in Figure 2. The main test instruments include YRK-2 rock immersion-air drying test instrument (Figure 3),

Figure 3: YRK-2 rock immersion-air drying test instrument.

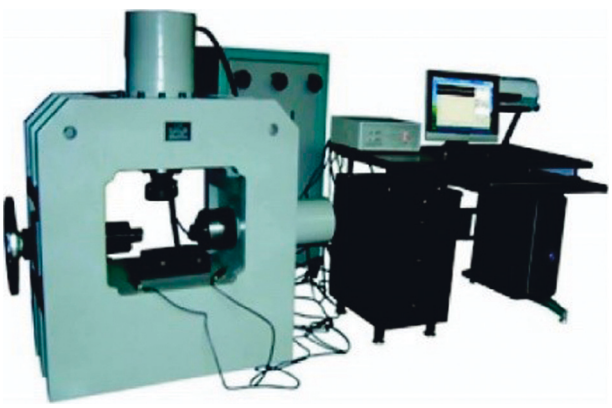

Figure 4: YZW1000 microcomputer-controlled electric direct shear instrument.

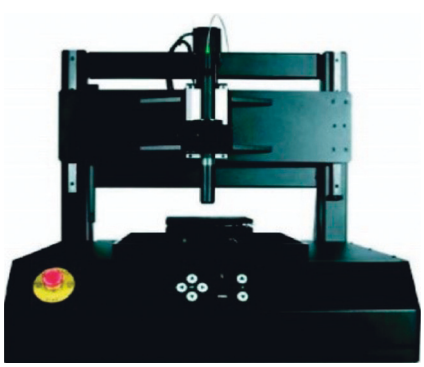

Figure 5: ST500 ultrafast large area profilometer.

YZW1000 microcomputer-controlled electric direct shear instrument (Figure 4), and ST500 ultrafast large area profilometer (Figure 5).

2. Analysis of Joint Surfaces' Shear Strength Deterioration Law

2.1. Joint Surface's Shear Strength Curve. Under different normal stresses, the variation curves of shear strength of joint surface with test cycles and shear times are shown in Figure 6.

As shown in Figure 6, the difference of 6 times shear strength in the initial state is significant. With the increase of test cycle, different strengths of repeated shear in each cycle gradually decrease. Taking the average value of the repeated shear strengths at each cycle, it can be seen that with the increase of the test cycle, the joint surface's shear strength under different normal stresses decreases evidently in the first five cycles, and then slowly later. In general, under the combined action of repeated shear and heat-wet cycles, the joint surface's shear strength deteriorates significantly.

2.2. Analysis of Joint Surfaces' Shear Strength Deterioration Value. According to the method proposed in reference [18], the effects of repeated shear and heat-wet cycles on shear strength are distinguished, as shown in Figure 7. The deterioration value of joint surface's shear strength caused by repeated shear is the most obvious one in the initial state, then decreases sharply, and tends to be stable with the increase of test cycles. The deterioration value of shear strength caused by heat-wet cycles is larger at the 1st and 3rd test cycle and then decreases sharply and gradually after the 5th cycle.

By eliminating the influence of repeated shear, the deterioration law curve of joint surface's shear strength only under heat-wet cycles is obtained, as shown in Figure 8.

From Figure 8, it can be seen that under heat-wet cycles only, with the increase of the test cycle, the joint surface's shear strength shows a decreasing trend of "being fast at first and slow later" and gradually tends to be stable after the 5th cycle. At the same test cycle, the normal stress has a great influence on the deterioration of joint surface's shear strength. The greater the normal stress is, the greater the deterioration will be because in the shear process, the greater the normal stress is, the greater the damage of the joint surface will be and the more serious the structural damage in mineral particles of the joint surface will be. Finally, the deterioration effect of the heat-wet cycle on the joint surface is also magnified.

3. Analysis of Joint Surface Roughness and Shear Strength

The research shows that the roughness of joint surface has a strong association with the root mean square of slope of joint surface [20]. After each test, the morphology of joint surface was scanned. The morphology scanning result of typical joint surface is shown in Figure 9. The root mean square of slope is extracted. The roughness coefficient JRC of joint surface is calculated by the following formula:

$$JRC = 32.69 + 32.98 \cdot \lg\left(S_{dq}\right), \tag{1}$$

where S_{dq} is the joint surface's root mean square of slope.

The normalized roughness coefficient curves of joint surfaces in different test cycles are shown in Figure 10.

From Figure 10, it can be seen that under different normal stresses, the deterioration law of JRC is consistent, and the overall deterioration trend is "fast at first and slow

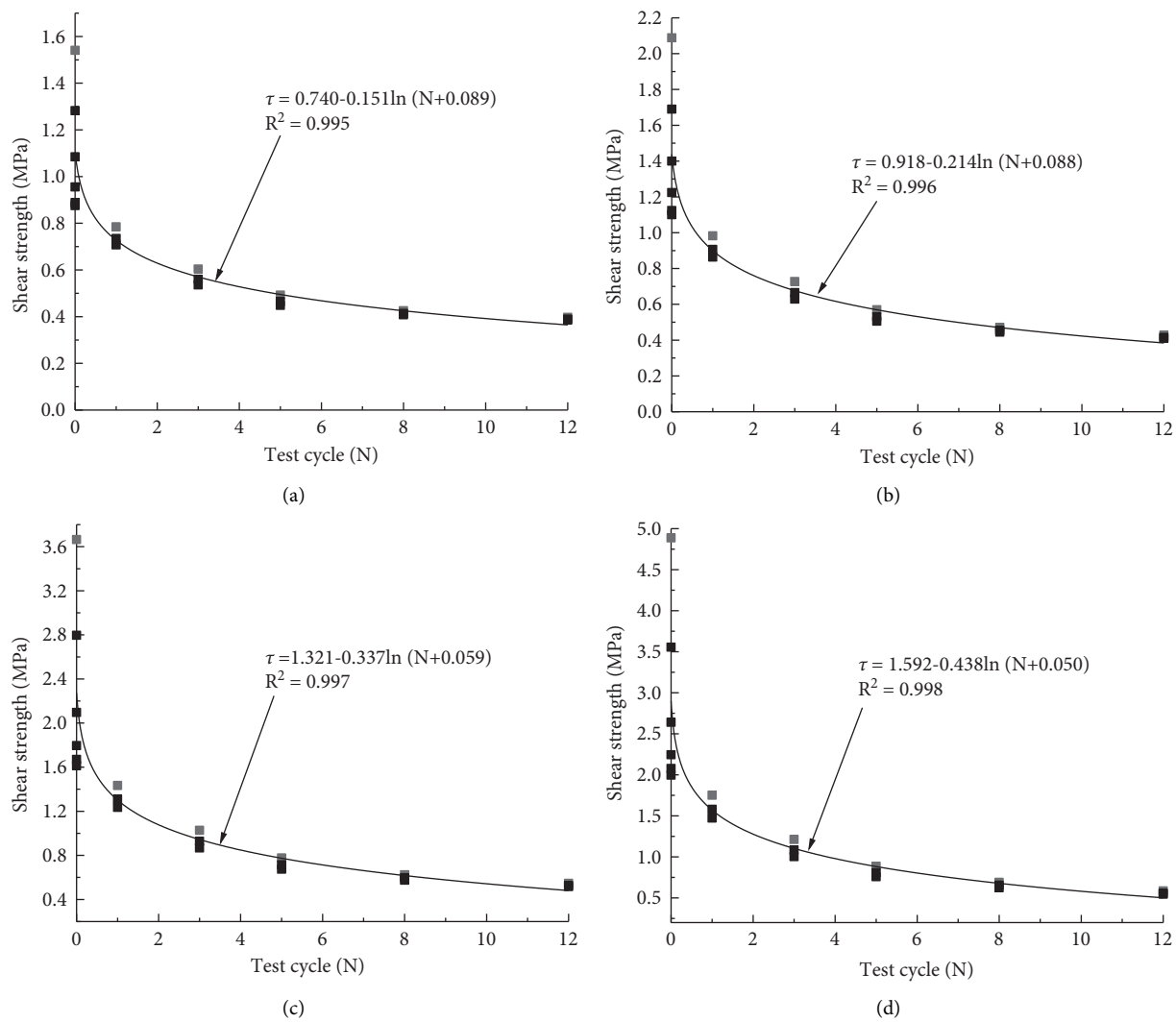

Figure 6: Variation of joint surface's shear strength under different normal stresses. (a) 0.5 MPa. (b) 1.0 MPa. (c) 1.5 MPa. (d) 2.0 MPa.

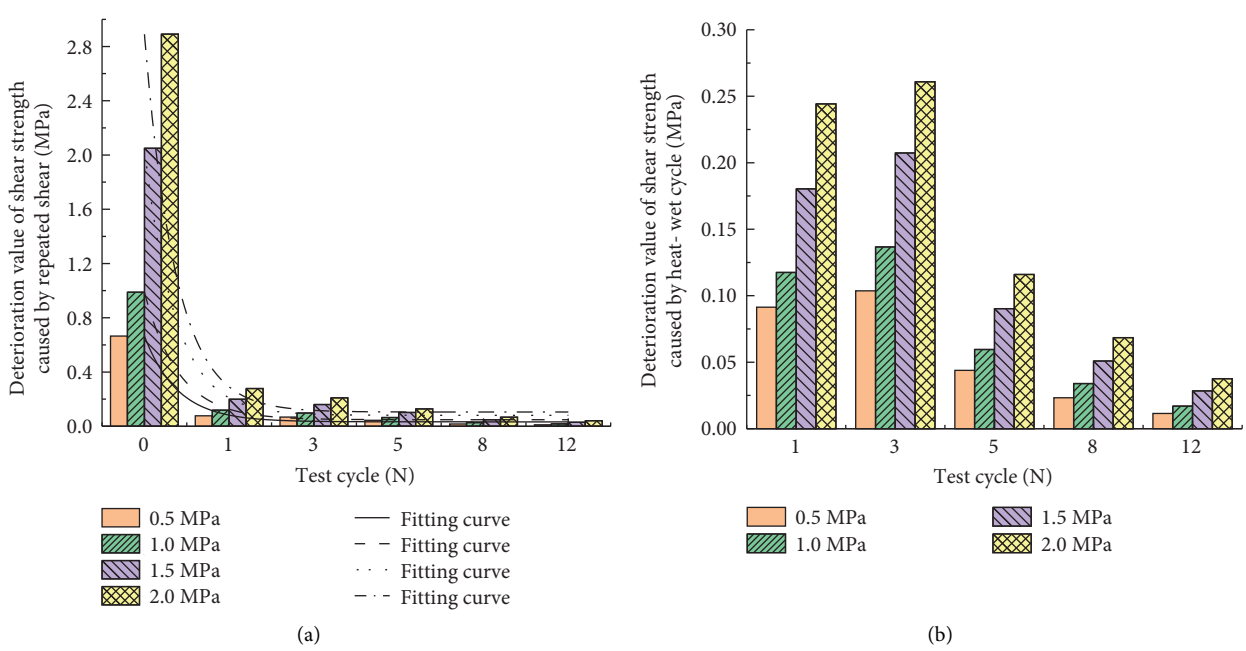

Figure 7: Deterioration value of shear strength caused by repeated shear and heat-wet cycles. (a) Deterioration value of shear strength caused by repeated shear. (b) Deterioration value of shear strength caused by heat-wet cycles.

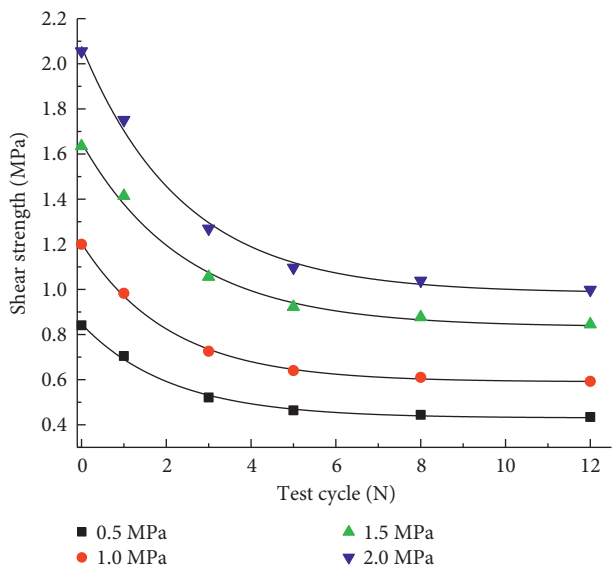

Figure 8: Deterioration law curve of shear strength of joint surface under heat-wet cycles.

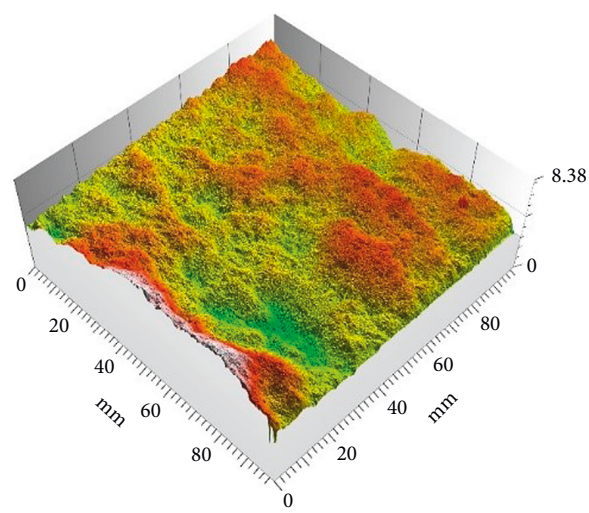

Figure 9: Scanning image of typical joint surface morphology.

Table 1: Damage coefficient of JRC by heat-wet cycle.

Test cycle/N	Normal stress/MPa			
	0.5	1.0	1.5	2.0
1	0.517	0.563	0.491	0.530
3	0.784	0.781	0.769	0.788
5	0.612	0.612	0.606	0.611
8	0.458	0.446	0.447	0.432
12	0.419	0.468	0.481	0.477

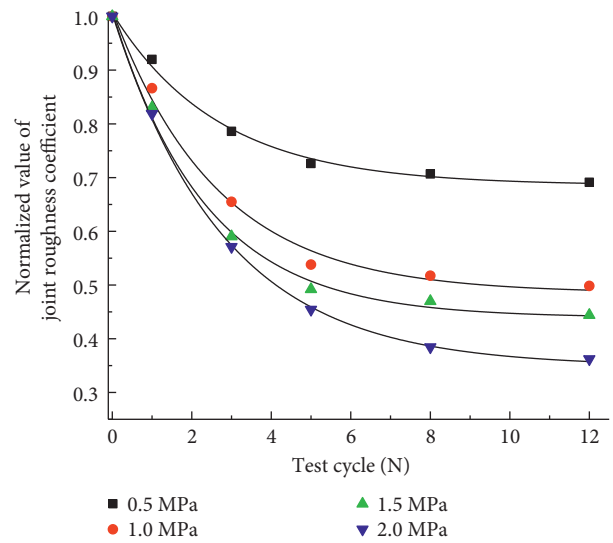

Figure 10: Normalized JRC change curves under heat-wet cycles and repeated shear.

Table 2: JRC under heat-wet cycles.

Test cycle/N	Normal stress/MPa			
	0.5	1.0	1.5	2.0
0	15.569	12.739	12.545	12.546
1	14.894	11.892	11.534	11.483
3	13.632	10.323	9.836	9.760
5	13.166	9.607	9.257	9.064
8	12.991	9.460	9.114	8.620
12	12.869	9.340	8.956	8.486

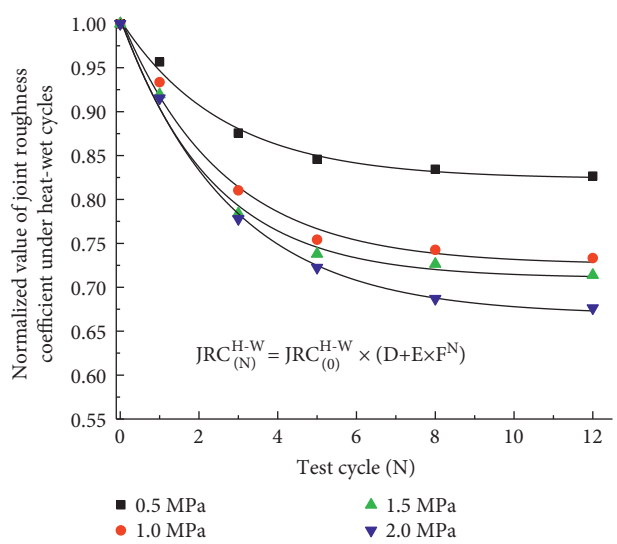

Figure 11: Deterioration curve of JRC under heat-wet cycles.

later." After the fifth cycle, the change of JRC gradually tends to be stable, which is consistent with the deterioration law of the shear strength.

However, the change of morphology parameters in test is the result of both repeated shear and heat-wet cycles. As the sandstone structure used in the test is relatively dense, the influence of heat-wet cycle on joint surface's morphology parameters cannot be reflected directly, which can only be reflected from the modified influence on joint surface's shear strength under heat-wet cycle. Therefore, in this paper, the ratio of shear strength's deterioration value caused by heat-

Table 3: Fitting formula and parameter statistics of JRC with heat-wet cycles.

Normal stress/MPa	Fitting formula	D	E	F	R^2
0.5	$JRC_{(N)}^{H-W} = JRC_{(0)}^{H-W}(D + E \times F^N)$	0.823	0.181	0.681	0.993
1.0		0.726	0.282	0.679	0.992
1.5		0.711	0.296	0.653	0.993
2.0		0.669	0.337	0.699	0.998

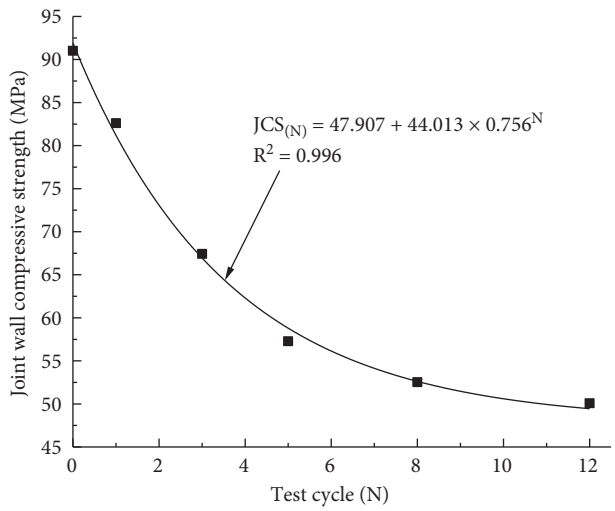

Figure 12: Strength deterioration curve of rock wall on joint surface under heat-wet cycles.

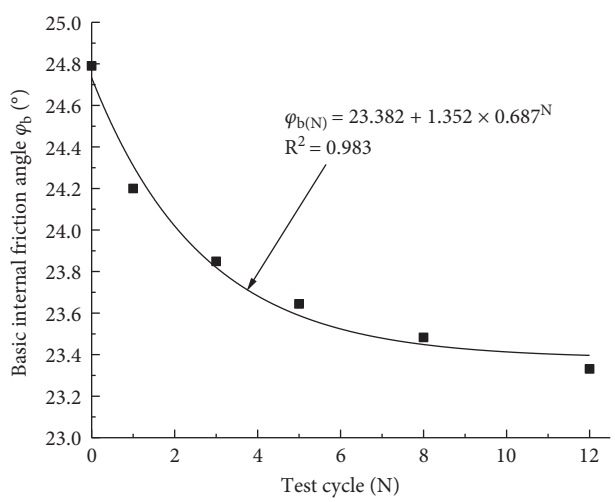

Figure 13: Deterioration curve of basic internal friction angles under heat-wet cycles.

wet cycle to the current total deterioration is considered as the damage coefficient of the joint surface roughness coefficient *JRC* under the heat-wet cycle only, as shown in the following formula:

$$\delta_{(N)} = \frac{\Delta\tau_{(N)}^{H-W}}{\Delta\tau_{(N)}}, \quad (2)$$

where $\delta_{(N)}$ is the damage coefficient of joint surface roughness under the heat-wet cycle, $\Delta\tau_{(N)}$ is the total shear strength's deterioration value in the N_{th} test cycle, and $\Delta\tau_{(N)}^{H-W}$ is the shear strength's deterioration value caused by heat-wet cycles in the N_{th} test cycle.

According to formula (2), $\delta_{(N)}$ is counted and the results are shown in Table 1.

The calculation formula of joint surface roughness coefficient in different test cycles is shown in the following formula:

$$JRC_{(N+1)}^{H-W} = JRC_{(N+1)} + \sum_{N=0}^{N} \left[\left(1 - \delta_{(N+1)}\right)\Delta JRC_{(N+1)}\right], \quad (3)$$

where $JRC_{(N+1)}^{H-W}$ is the roughness coefficient caused by heat-wet cycles in $(N+1)_{\text{th}}$ test cycle, $\Delta JRC_{(N+1)}$ is the deterioration value of joint surface roughness coefficient in $(N+1)_{\text{th}}$ test cycle, and $\delta_{(N+1)}$ is the damage coefficient of joint surface roughness coefficient in $(N+1)_{\text{th}}$ test cycle.

Based on the variation curve of joint surface roughness coefficient and $\delta_{(N)}$ in Table 1, according to formula (3), the modified joint surface roughness coefficient under heat-wet cycle (Table 2) can be obtained. The normalized curve of joint surface roughness coefficient $JRC_{(N)}^{H-W}$ only varying with heat-wet cycle is drawn, as shown in Figure 11.

From Figure 11, it can be seen that the JRC presents a deterioration trend of "fast at first and slow later" under heat-wet cycles only. The greater the normal stress is, the greater the deterioration range will be. The fitting results of joint surface roughness coefficient with heat-wet cycles under different normal stresses are shown in Table 3.

4. The Shear Strength Deterioration Formula of Joint Surface under Heat-Wet Cycles

According to the JRC-JCS model proposed by Barton and Choubey [21, 22], the shear strength of rock joint surface can be calculated by the following formula:

$$\tau = \sigma_n \tan\left[JRC \cdot \lg\left(\frac{JCS}{\sigma_n}\right) + \varphi_b\right], \quad (4)$$

where τ is the shear strength of joint surface, σ_n is the normal stress, JRC is the roughness coefficient of joint surface, JCS is the rock wall strength of joint surface, and φ_b is the basic internal friction angle.

The uniaxial compressive strength of specimens with different heat-wet cycles is taken as the rock wall strength of joint surface. The variation curve is shown in Figure 12.

At the same time, the basic internal friction angles of joint surface with different heat-wet cycles were tested and counted. The variation curve is shown in Figure 13.

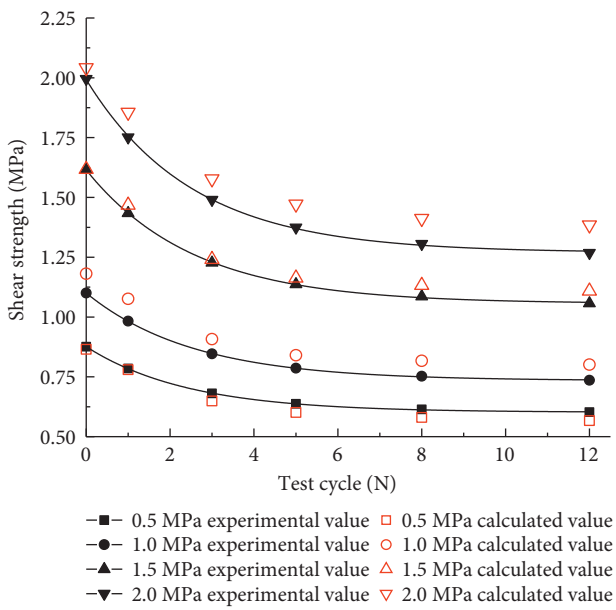

Figure 14: Comparison between test and calculated valves of joint surface's shear strength under heat-wet cycles.

According to the test results and analysis above, bring the modified roughness coefficient $JRC_{(N)}^{H-W}$ of joint surface, the rock wall strength $JCS_{(N)}$, and the basic internal friction angle $\varphi_{b(N)}$ at each heat-wet test cycle into formula (4). The deterioration formula of joint surface shear strength under heat-wet cycles can be obtained as follows:

$$\tau_{(N)} = \sigma_n \tan\left[JRC_{(N)}^{H-W} \cdot \lg\left(\frac{JCS_{(N)}}{\sigma_n}\right) + \varphi_{b(N)}\right], \quad (5)$$

where $JRC_{(N)}^{H-W}$, $JCS_{(N)}$, and $\varphi_{b(N)}$ are the relationship functions among roughness coefficient of joint surface, rock wall strength of joint surface, and basic internal friction angle of joint surface and heat-wet cycle N under different normal stress.

The shear strength of joint surface at each heat-wet cycle under different normal stresses can be calculated by formula (5). The calculated values are compared with the modified test values, as shown in Figure 14.

From Figure 14, the shear strength of joint surface calculated by formula (5) coincides with the modified test values. The error range is −5.94%~−0.61%, 6.82%~9.50%, 0.16%~4.88%, and 2.32%~9.19% under different normal stress. The error is within the allowable range of estimation. It indicates that the above *JRC* equivalent deterioration method is reasonable and can estimate the shear strength of joint surface under heat-wet cycles well.

5. Conclusions

In this paper, the shear test of joint surface under heat-wet cycles is carried out and the following conclusions are obtained:

(1) The shear strength and roughness coefficient of joint surface show a deterioration trend of "fast at first and slow later" with the increase of test cycles, and the deterioration rate is larger in the first 5 test cycles.

(2) The deterioration of shear strength caused by repeated shear is the most obvious one in the initial state, then decreases sharply, and tends to be stable with the increase of test cycles. The deterioration value of shear strength caused by heat-wet cycle is obvious in the first 3 test cycles, then decreases significantly, and tends to be stable.

(3) Considering the ratio coefficient of shear strength deterioration value caused by heat-wet cycles to the total deterioration value at current cycle as the equivalent damage coefficient of joint surface morphology parameters under heat-wet cycles, an improved method for calculating the shear strength of joint surface under heat-wet cycles is proposed. The estimated results coincide with the modified test values.

Data Availability

All data included in this study are available upon request by contact with the corresponding author.

Conflicts of Interest

The authors declare that they have no conflicts of interest.

Acknowledgments

This research was supported by the National Natural Science Foundation of China (52009067 and U2034203).

References

[1] X. Liu, W. Yuan, Y. Fu, Z. Wang, L. Miao, and W. Xie, "Tests on shear strength deterioration of sandstone under the action of chemical solution and drying-wetting cycles and analysis of chemical thermodynamics," *Chinese Journal of Rock Mechanics and Engineering*, vol. 35, no. 12, pp. 2534–2541, 2016.

[2] L. Xin-rong, W. Yuan, Y. Fu, Z. J. Wang, L. W. Zhu, and Y. K. Xie, "Deterioration rules of shear strength in sandstones under wetting and drying cycles in acid and alkali environment," *Chinese Journal of Geotechnical Engineering*, vol. 39, no. 12, pp. 2320–2326, 2017.

[3] Z. Dou, Z. Zhao, T. Gao, J. Li, and Q. Yang, "Evolution law of water-rock interaction on the shear behavior of granite fractures," *Tsinghua Univ (Sci & Technol)*, vol. 61, no. 8, pp. 792–798, 2021.

[4] Q. Yao, W. Wang, S. Yang, J. Fang, and B. Zhou, "Direct shear and acoustic emission characteristics of sandy mudstone under the effect of moisture content," *Journal of China Coal Society*, vol. 46, no. 09, pp. 2910–2922, 2021.

[5] L. Peng, J. Liu, Li Guo-he, J. B. Zhu, and S. G. Liu, "Experimental study for shear strength characteristics of sandstone under water-rock interaction effects," *Rock and Soil Mechanics*, vol. 32, no. 2, pp. 380–386, 2011.

[6] D. Zhang, L. Li, and X. Hu, "Effect of long-term immersion in static water on the physical, chemical, and mechanical properties of sliding zone soil in the Three Gorges Reservoir

area," *Bulletin of Geological Science and Technology*, vol. 40, no. 05, pp. 281–289, 2021.

[7] X. Yao, H.-F. Deng, L. Jian-lin, Y.-Y. Zhi, and Y. Xiong, "The deterioration effect of fractured rock mass strengthened by grouting method under long-term immersion," *Rock and Soil Mechanics*, vol. 40, no. S1, pp. 143–151+180, 2019.

[8] L. Xin-rong, Y. Fu, Y.-X. Wang, L. W. Huang, and X. Y. Qin, "Deterioration rules of shear strength of sand rock under water-rock interaction of reservoir," *Chinese Journal of Geotechnical Engineering*, vol. 9, pp. 1298–1302, 2008.

[9] W. B. An, L. Wang, and H. Chen, "Mechanical properties of weathered feldspar sandstone after experiencing dry-wet cycles," *Advances in Materials Science and Engineering*, vol. 2020, Article ID 6268945, 15 pages, 2020.

[10] L. Xin-rong, Y. Fu, Y.-X. Wang, L. W. Huang, and X. Y. Qin, "Stability of reservoir bank slope under water-rock interaction," *Rock and Soil Mechanics*, vol. 30, no. 3, pp. 613–616+627, 2009.

[11] X. Liu, Z. Tang, L. Li, Q. Zhang, and F. Su, "Experimental study on shear properties of red sandstone joints after cyclic wetting-drying treatment," *Chinese Journal of Rock Mechanics and Engineering*, vol. 39, no. S2, pp. 3316–3325, 2020.

[12] J. Fang, H. Deng, Y. Qi, Y. Xiao, H. Zhang, and J. Li, "Analysis of changes in the micromorphology of sandstone joint surface under dry-wet cycling," *Advances in Materials Science and Engineering*, vol. 2019, no. 7, Article ID 8758203, 11 pages, 2019.

[13] L. Zeng, J. Luo, P. Hou, and H. Bian, "Crack development and strength characteristics of pre-disintegrated carbonaceous mudstone under dry-wet cycles," *China Journal of Highway and Transport*, vol. 33, no. 9, pp. 1–11, 2020.

[14] B. Chen, Z. Le-yi, Y.-L. Zhao, Z.-C. Wang, D.-J. Chao, and G.-N. Jia, "Relationship between microstructure and shear strength of weak interlayer of red sandstone under dry and wet cycles," *Rock and Soil Mechanics*, vol. 39, no. 5, pp. 1633–1642, 2018.

[15] B. Zhang, L. Wang, and S. Zhang, "Study on constitutive model for unloading damage of sandstone under effect of heat-wet cycle," *Water Resources and Hydropower Engineering*, vol. 49, no. 12, pp. 162–168, 2018.

[16] L. Wang, J. Jin, and B. Zhang, "Experimental study on loading and unloading mechanical properties of sandstone under heat and wet cycles," *Chinese Journal of Rock Mechanics and Engineering*, vol. 37, no. 3, pp. 699–708, 2018.

[17] L. Wang, J. Jin, and E. Zhao, "Study on degradation effect of typical sandstone in three gorges reservoir area under the action of heat and moisture," *Journal of Yangtze River Scientific Research Institute | J Yangtze River Sci Res Inst*, vol. 34, no. 06, pp. 76–80, 2017.

[18] H. Deng, L. Duan, Y. Zhi, D. Pan, J. Li, and L. Wan, "Evolution of shear mechanical properties of jointed surface under dry-wet cycle," *Chinese Journal of Rock Mechanics and Engineering*, vol. 37, no. S2, pp. 3958–3967, 2018.

[19] Y. Qi, *Deterioration Effect and Mechanism of Shear Mechanical Properties of Jointed Rock Mass under Water - Rock Interaction*, China Three Gorges University, Yichang, China, 2021.

[20] C. Xia, "Study on surface morphology of rock structure surface," *Journal of Engineering Geology*, vol. 3, pp. 71–78, 1996.

[21] N. Barton, "Review of a new shear-strength criterion for rock joints," *Engineering Geology*, vol. 7, no. 4, pp. 287–332, 1973.

[22] N. Barton and V. Choubey, "The shear strength of rock joints in theory and practice," *Rock Mechanics and Rock Engineering*, vol. 10, no. 1-2, pp. 1–54, 1977.